Antonella Macagnano
Emiliano Zampetti
Erich Kny   *Editors*

Electrospinning for High Performance Sensors

Springer

NanoScience and Technology

Series editors

Phaedon Avouris, Yorktown Heights, USA
Bharat Bhushan, Columbus, USA
Dieter Bimberg, Berlin, Germany
Klaus von Klitzing, Stuttgart, Germany
Roland Wiesendanger, Hamburg, Germany

The series NanoScience and Technology is focused on the fascinating nano-world, mesoscopic physics, analysis with atomic resolution, nano and quantum-effect devices, nanomechanics and atomic-scale processes. All the basic aspects and technology-oriented developments in this emerging discipline are covered by comprehensive and timely books. The series constitutes a survey of the relevant special topics, which are presented by leading experts in the field. These books will appeal to researchers, engineers, and advanced students.

Antonella Macagnano • Emiliano Zampetti
Erich Kny

Editors

Electrospinning for High Performance Sensors

Editors

Antonella Macagnano
Institute of Atmospheric Pollution
    Research (IIA)
CNR, Monterotondo-Rome, Italy

Emiliano Zampetti
Institute of Atmospheric Pollution
    Research (IIA)
CNR, Monterotondo-Rome, Italy

Erich Kny
Centre of Electrochemical
    Surface Technology (CEST)
Wiener Neustadt, Austria

To my beloved dad
Antonella Macagnano

To my parents, to my wife Claudia and my son
Damiano, to be always close to me
Emiliano Zampetti

The COST Action created not only a lot of
good relationships between colleagues, but
even friendships; only then it was possible to
create this great book together
Erich Kny

Preface

The first International Workshop on Electrospinning for High Performance Sensing (EHPS) was held in Rome on April 29–30, 2014, within a European Concerted Research Action, designed as COST MP1206 and entitled "Electrospun nano-fibres for bio inspired composite materials and innovative industrial applications". The workshop, organized and hosted by the Institute of Atmospheric Pollution Research of the National Research Council (CNR-IIA), was intended to be the first one of a series of forthcoming meetings devoted to share and spread novel ideas for innovative and more attractive sensors. Some recent and encouraging results concerning novel micro-nanofibrous sensors reported in literature confirmed a multitude of supplies. Indeed the electrospinning technology, allowing an easy integration of long fibres (organics, inorganics and composites) with microcircuits in different configurations and on several substrates, seems to be a very promising strategy to fabricate advanced sensing systems. Thus, world-renowned scientists, several companies and young researchers from all over the world (19 countries) joined the workshop. The general industrial potentials of electrospinning as well as the limitations of such a technology were discussed by both scientists and enterprises. In other presentations, mathematical models were proposed to control the electrospinning process in designing and manufacturing high performing materials for several applications, such as health and environmental monitoring, security, food quality, etc. Electroactive and optical properties of the fibres were also described, focusing on single fibres, 3D fabrics of polymers, polymer blends, nanocomposites and metal-oxides, as well as on different types of structures (hollow-fibres, core-shell) and on different functionalization. Several strategies in technical customisation of the procedure were proposed and described by scientists to obtain differently performing fibrous structures. Other issues of the workshop focused on the state of the art of nanosensors, and the description of materials, methods and advanced technologies to design and construct a plethora of functionalized nanofibres with different features suitable for sensing. All contribution concurred to a unique "symposium of knowledge". Briefly, all talks were focused on very innovative, technological and smart issues, but in a friendly way,

as well as in a comfortable environment, establishing a perfect synergy of intents, a full immersion in debating and sharing scientific findings and thoughts. The main subjects presented in that event and concerning both chemical and physical sensors and biosensors based on electrospinning, and their related sensor market prospects, have been collected in the present book hoping to give the reader the same exciting atmosphere of those days.

Rome, Italy   Antonella Macagnano
Wiener Neustadt, Austria   Erich Kny
Rome, Italy   Emiliano Zampetti

Contents

Introduction to Electrospinning for High Performance Sensors

A strategy to improve the sensing features of chemical sensors is to increase the specific surface of the interacting material: the higher the specific surface area of a sensing material the higher its sensor ability to interact, such as biological sensing structures do. Indeed, in nature, surfaces and receptors are in essence a macroscopical extension of the molecular structure of a material, where the properties of surfaces and receptors are directly related to their structure down to the molecular level. Similar structures can be reconstructed 'in vitro' for sensor and detecting systems of exceptional sensitivity and remarkable specificity. As a consequence, many techniques have been used to augment the surface of sensing layers with fine structures, especially to form controlled nanostructures, as it happens in natural systems, taking advantage of the large specific area of nanostructured materials. Accordingly nanostructured sensors, when compared to the conventional ones, showed desired properties like faster adsorption and minimized bulk effects (i.e. long diffusion–desorption time, analyte entrapment, etc.). From recent literature, electrospinning has been confirmed to be one of the best candidates among the various nanotechnologies for designing and developing smart and ultra-sensitive sensing systems, both for the uniqueness of the resulting nanostructures and for production rate and cost. Parameters like the extremely rapid formation of the nanofibres structure, which occurs on a millisecond scale, the large coverage in continuous mode, the easy tuning of size and shape, and the nanofibres assembling in situ have raised great scientific interest, confirmed from the number of publications over the last 10 years and reported in the following figure. Since the dimension of fibres is roughly comparable to that of the interacting molecules, people may exploit the tiny size with some size effects, such as quantization, and the single-molecule sensitivity. About the morphology of the fibres, it depends on the solution properties (system parameters), process conditions (operational parameters) and environmental conditions. The resulting aligned or non-woven nanofibres, arranged in 2D- or 3D-fibrous structures with tuneable porosity and high specific surface area, can be placed directly onto suitable transducers, often without further expensive refinement. Developments of electrospun nanomaterials have allowed chances

to fabricate more efficient interfaces with electronic components also due to their compatibility with semiconductor processes. Since electrospinning is a technique capable of continuously creating polymeric fibres, i.e. with no interruption during the process, it sounds appropriate for the production of huge quantities of nanofibres (micron size yarns consisting of nanofibres can be produced at high rates, up to 70 m/min), then also potentially appealing to the sensor market. Electrospinning apparatus, using multiple nozzles, as well as needleless electrospinning processes using a range of spinnerets, is able to increase further the production rate and to control jet formation, jet acceleration and the collection of nanostructures.
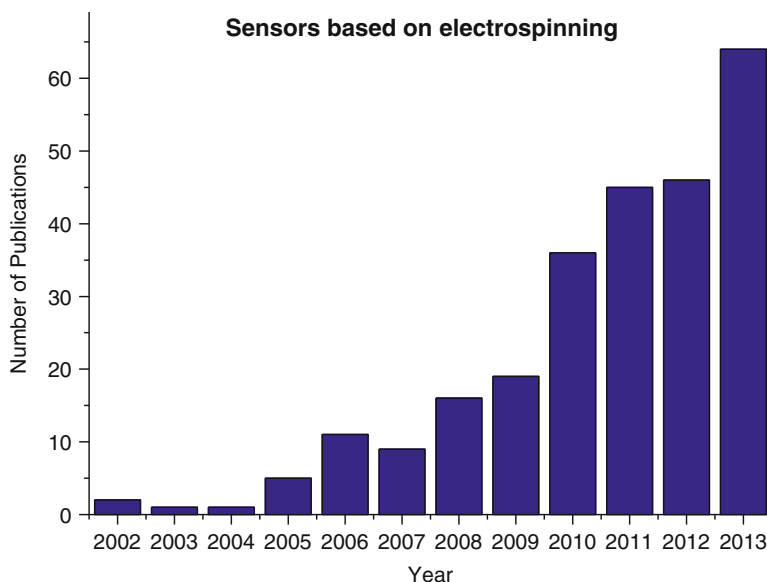
Number of publications related to electrospinning technology for sensors (Source: Web of Science accessed on 27 Apr 2014)

The further opportunity to customise and functionalise these micro-nanofibres on a large-scale enables the electrospinning technique to match a wide range of requirements for specific sensing applications, giving a benefit over other methods commonly used for the production of micro-nanostructures. Another advantage of this top-down nano-manufacturing process is the relatively low cost of the equipment and its functioning compared to that of most bottom-up methods. Despite the increased interest in sensors from scientists and the industrial potentials of the technology, the percentage of the number of patents about electrospinning for sensor was still about 0.3 % (2011, source EspaceNET) of all the patents related to electrospinning. An apparent lack of interest of manufacturers, of both chemical sensors and electrospun fibrous products, in this application is noticed. Some of the challenges are supposed to be related to the difficulty in exploring the application without significant funding, the perceived danger of working with nanofibres,

which is worsened by the lack of clearly defined terms, the lack of control over material supply as a result of the relatively small volume requirements for electrospinning compared with other industries and the lack of involvement of manufacturers in nanofibre development projects until the final stages of laboratory-scale optimisation. However, nowadays the technology sounds mature. It is progressing going beyond the laboratory and towards industrial setting, with the rise of start-ups and the interest of large multinationals. Increasing dissemination and involving even further industries urgently need to proceed into the next step, that is the actual manufacturing of high performing electrospinning based sensors for answering to real requirements.

In this book, thanks to the significant cooperation of scientists and manufacturers involved in a European Concerted Research Action, designed as COST MP1206 and entitled "Electrospun Nano-fibres for bio inspired composite materials and innovative industrial applications", and after the successful participation in the first "Electrospinning for High Performance Sensors" workshop held in 2014 in Rome, we collected some recent progress and predominant developments of several electrospinning sensing approaches, including gravimetric, resistive, photoelectric, optical, electrochemical sensors and biosensors. Thus the present book is the first collection of chapters focusing on the potentials of electrospinning in several specific sensing applications, through the usage of several transduction mechanisms based on organic, inorganic and composite materials. Their crucial role in quickly revealing molecules in traces, which are often the urgent needs in health, security, environment and food monitoring, will be described in detail. Finally, the situation of the electrospinning industry is discussed, including recent advances in commercial-scale electrospinning. The opening shortly describes the aim of the COST Action MP1206 that currently is the greatest platform of European scientists, young researchers and industrials for fabricating, investigating and sharing the potentials of such a technology. This Action is joined too by scientists, institutions and companies from COST Near Neighbour Countries and International Partner Countries thereby increasing the chances of succeeding. The book starts with a detailed description about the manufacturing of facile and ultrasensitive sensors based on synergic layers of electrospun polymer fibres added with electrospun-nanonets and investigated through gravimetric and optical transducers. Then, an accurate description of the polymer dynamics during the ejection process follows, trying to analyze, through the image analysis and mathematical models, the distribution and orientation of the charged molecules in the various segments of the fibres, ranging between the Taylor cone and the grounded substrate. Therefore the unique features of chemical sensors based on nanocomposite fibres are described, where the performance of conventional to electrospun sensors have been compared to detect gases in traces. The conductivity of the fibres has been explored too, both in individual and crossed nanofibres, supposing that the improved gas sensing performance were determined by diode effect. The photoconductivity of ceramic fibres to develop gas sensors operating at room temperature represents a further chance to get low cost sensors with low power consumption. Optical properties of nanofibrous sensors with a collection of specific applications in security, health and

food are the main topic of the following three chapters. They have been introduced by an overview of the properties of fluorescent electrospun nanofibres reporting illustrative examples of their application as optical sensors for the detection of heavy metal ions, explosive compounds and bio-systems. Some of the latest advances in bio-mimicking and biological sensors have been summarized, dealing with the preparation, bio-immobilization and the role of nanostructures for electrochemical and gravimetric biosensing systems for protein biomarkers and DNA detection. Two tremendously innovative and intriguing applications of electrospinning have also been reported, dealing with smart nanofibrous textiles and a brain mimicking system, respectively, before concluding with an overview on electrospinning from a manufacturer's perspective. Here the current state of the electrospinning industry is debated, including recent advances in commercial-scale electrospinning and other competing technologies. The challenges that are faced by commercial electrospinning companies are highlighted, helping to explain the limited commercialisation and uptake of electrospinning by industry. To finish, some examples of nanofibre products that are currently available or being commercialised are given, with an outlook on what the future may hold for electrospun nanofibre technologies in the years to come, comprising smart sensing systems.

<div align="right">
Antonella Macagnano
Erich Kny
Emiliano Zampetti
</div>

Electrospinning and the COST Action MP1206

Electrospinning, an electro-hydrodynamic process, has lately become an exciting and versatile platform technology for the production of nanofibrous materials. The electrospinning process takes place between a spinning head with a capillary opening or a rotating drum and a collector counter electrode where a high voltage is applied (typical 10–30 kV). The spinning head (nozzle or nozzle-less) is connected with and (usually) pressure fed by a reservoir of a polymer solution. The high voltage applied draws at very high speed a nano- to micron-sized fibre jet out of the Taylor cone, which forms at the opening of the nozzle. The solvent is rapidly evaporating in this process and the endless nanofibres are collected and deposited at the collector. The electrospun nanofibres are deposited either in an irregular and chaotic fashion to form a nonwoven web or as organized (e.g. parallelized) fibre patches.

The uniqueness of electrospun nanofibres is due to their high surface-to-volume ratio, high fibre interconnectivity and nano scale interstitial space, compared to conventional fibrous structures. As a result, they are of high interest in a diverse range of applications where highly porous structures or structures with a high surface area are desirable making them potentially very useful for a range of innovative biomedical and technical applications. Biomedical applications include biomimetic scaffolds for tissue engineering, sustained/controlled drug release systems, regenerative medicine, wound dressings, implants, artificial skin and biosensors. Other emerging applications of electrospun nanofibres are in the field of textiles and of filtration for air and liquids and personal respiratory systems for protection from biological and chemical agents. Electrospun nanofibres have been established to be very good candidates for the development of advanced sensors for environmental and biomedical applications (e.g. ultra-sensitive gas sensors, electronic noses, halochromic sensors, flexible reversible low-cost pH-sensors, biosensors, biomolecules microchip array). Indeed such a technique would be compatible and well matching with common microelectronics processes and is promising to be a non-expensive technique. Electrospun nanofibres play an important role in the food area, which includes separation operations, enzyme

immobilization, encapsulation of food bioactive compounds and microorganisms, and the fabrication of sensor devices, and in food packaging applications to make them active and intelligent. Other emerging uses are for energy applications (batteries, fuel cells, photovoltaic), catalyst applications and for various electronics and optoelectronics uses.

This topic is therefore very important and timely and presents numerous opportunities to contribute towards solving the pressing global challenges in health, water, food, environment and energy issues.

The electrospinning technique, as a base tool for novel product development, has gained outstanding relevance in many different research and technical fields. In the same breath, the technique itself remains the same for all application areas. The research done within a particular application area may be very relevant for the other electrospun nanofibres-related areas.

Thus a COST networking Action was considered to be very appropriate to create great benefit out of these many potential synergies. That makes this COST-networking Action MP1206 an ideal forum to bring all researchers from the different application areas together to exchange and merge the different approaches of the electrospinning procedures. Other national or international funding programs with a more focussed area cannot create these high synergistic effects among that many different approaches and application fields. It is also crucial to strengthen all the scattered research know-how on electrospinning nanofibres all over Europe as to make Europe more competitive on this high value domain.

Electrospinning is at the borderline between pure basic research and industrial implementations in many fields. When looking at the urgent need of European industry (particularly the polymer processing, biomaterials, and the textile and advanced technical systems such as energy, sensors, food packaging and filtering systems) for higher competitiveness, it is of outstanding importance to lead researchers towards the hot spots of research in terms of process and materials improvement and innovative applications. In that way, research institutions as well as European industry are profiting from a highly interconnected COST networking Action and an improved knowledge base within the field of electrospinning.

By forming an interdisciplinary knowledge platform the COST Action MP1206 on Electrospinning will strengthen the European R&TD on electrospun nanofibrous materials and nanofibrous composites and will generate fast progress in the state of the art. The COST Action will cover scientific breakthroughs and innovations in the electrospinning process itself, nanofibrous materials and nanofibrous composite advancements and the post-treatment processing of electrospun materials. Applications in the biomedical and technical fields as well as health, societal and environmental issues are considered.

The COST networking Action MP1206 on Electrospinning is also very advantageous and beneficial for young researchers, to obtain a basic overview and improved ideas in the field of electrospinning and the resulting materials applications.

By meeting the objectives of the COST Action MP1206 an important step towards the creation of an innovative, knowledge-based and competitive European industry will be accomplished. Moreover, the characteristic high added-value of electrospinning nanofibres-based materials means that the related industry would require highly qualified personnel to run the corresponding facilities, with the creation of new professional skills for working within interdisciplinary teams. The COST action will aim for maximal productive outcome by providing:

- New integrated experimental/theoretical methodologies for designing and producing electrospinning nanofibres
- Databases of application relevant electrospinning nanofibres properties
- An improved and enlarged knowledge base by scientific articles on electrospinning nanofibres
- Tutorial material for training young and more experienced researchers entering the field

The COST Action MP1206 will devote special attention to electrospun nanofibres of major technological interest and will disseminate its outcome to academia, industry and to the general public. In conclusion the COST networking activity MP1206 within the 36 COST countries will be the ideal instrument to gain strength and speed in these latest and important scientific and industrial developments in the area of electrospinning nanofibres. The COST Action MP1206 will run till May 2017, and since COST is an open and flexible network new participants interested in electrospinning will always be welcome, please consult www.electrospinning-cost.eu.

September 2014   Erich Kny

Chapter 1
Facile and Ultrasensitive Sensors Based on Electrospinning-Netting Nanofibers/Nets

Yan Li, Jianyong Yu, and Bin Ding

Abstract Due to rapid growth of industrialization, urbanization and modern agricultural development, there has resulted a heavy backlog of gaseous and liquid pollution in all over the world and threated the health of human beings. Driven by the actual demand, the sensors possess good portability, easy usability, excellent selectivity and sensitivity for water and air pollution monitoring are highly desirable. Among versatile sensing platforms, quartz crystal microbalance sensors and colorimetric sensor gained increasing attention for their easy accessibility, favorable expansibility and good associativity. Based on above two platforms, nanofibrous materials have been choose as an idea substrate to either capture the marker or amplify the signal associated with detection. In this chapter, we reviewed recent progress in the development of electrospun nanofibrous materials having applications in two predominant sensing approaches (quartz crystal microbalance and colorimetric sensors), illustrate them with current examples showing how they have been applied, optimized and discuss their intrinsic fundamentals and optimal designs. Moreover, we will also highlight gaps requiring further research.

1.1 Introduction

Due to rapid growth of industrialization, urbanization and modern agricultural development [1–4], there has resulted a heavy backlog of gaseous and liquid pollution in all over the world, which include inorganic gases (NH_3, CO_2, SiO_2,

Y. Li
Key Laboratory of Textile Science & Technology, Ministry of Education, College of Textiles, Donghua University, Shanghai 201620, China

J. Yu
Nanomaterials Research Center, Modern Textile Institute, Donghua University, Shanghai 200051, China

B. Ding (✉)
Key Laboratory of Textile Science & Technology, Ministry of Education, College of Textiles, Donghua University, Shanghai 201620, China

Nanomaterials Research Center, Modern Textile Institute, Donghua University, Shanghai 200051, China
e-mail: binding@dhu.edu.cn

N(CH₃)₃, etc.) [5–7], volatile and semi-volatile organic hydrocarbons, aldehydes, and heavy metals (Hg(II), Pb(II), Cu(II), Cr(IV), etc.) [8–10]. As is known to all, the air we breathe and the water we drink are essential ingredients for our wellbeing and a healthy life [11, 12]. Unfortunately, we are all routinely exposed to a broad range of pollutants that are present within the environment. Over the last three decades there has been increasing global concern over the public health impacts attributed to environmental pollution, in particular, the global burden of disease [13–16]. As the World Health Organization (WHO) stated, one sixth of the world's population, approximately 1.1 billion people do not have access to safe water and 2.4 billion lack basic sanitation [17]. Especially some trace heavy metals in polluted water are seriously harmful to human health [9]. On the other hand, in a recent study, WHO reports that in 2012 around seven million people died – one in eight of total global deaths – as a result of air pollution exposure. This finding more than doubles previous estimates and confirms that air pollution is now the world's largest single environmental health risk [18, 19]. Consequently, rapid detection of contaminants in the environment by emerging technologies is of paramount significance [5, 12, 20]. A tool providing interactive qualitative and quantitative information about pollution is essential for policy makers to protect massive populations.

Driven by the actual demand, various equipment have been built up for the quantification of water and air pollution in the past decade, such as inductively coupled plasma mass spectrometry [21, 22], atomic absorption spectrometry [23, 24], anodic stripping voltammetry [25, 26], and high performance liquid chromatography [27]. Although these strategies provide accurate, ultrasensitive detection, most of them require tedious sample pretreatment before analysis, and generally are not amenable to be handled by unskilled personnel. Therefore, it is highly desirable to develop a portable, easy use, selective and sensitive method for water and air pollution monitoring. Compared with those sophisticated equipment, quartz crystal microbalance sensors and colorimetric sensors gained increasing attention for their easy-to-use, relatively low cost and no requirement for skillful technicians [28, 29]. Until now, considerable efforts have been devoted to the assay of hazard gases and polluted water based on above two platforms. However, the sensitivity of those previously reported QCM and colorimetric sensors are still not sufficient magnitude to allow for practical applications [30–33].

In parallel, as one kind of the most important nanomaterials, electrospun nanofibrous materials have gained an increasing of interest in the environmental applications because of their unique chemical and physical properties, for instance, small size, large specific surface area (SSA), three dimensional (3D) porous structure, amenable to surface modification, etc. [34–36]. Under this circumstance, nanofibrous materials are used to either capture the marker or amplify the signal associated with detection [35]. Both of these capabilities are important for trace level pollution detection which are also hardly realized by utilizing conventional materials. Benefiting these unique properties, nanofibrous materials based sensors have be applied to assay, degrade and scavenge pollutants in water and air in the past decades [37–39].

In this chapter, we will review recent progress in the development of electrospun nanofibrous materials having applications in two predominant sensing schemes (QCM and colorimetric sensors), illustrate them with current examples showing

how they have been applied and optimized. Moreover, we will also discuss their intrinsic fundamentals and optimal designs. Ultimately, we will also highlight gaps requiring further research.

1.2 Electrospinning and Electro-Spinning/Netting (ESN)
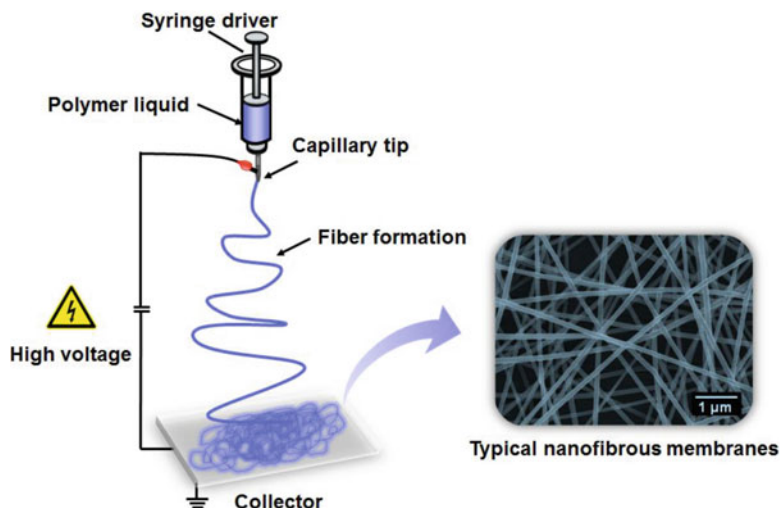
1.2.1 Electrospinning

Amongst number of processing techniques have been used to prepare polymer nanofibers, electrospinning is currently the most effective technique that allows the fabrication of continuous fibers with diameters down to a few nanometers, which shares characteristics of both electrospraying and conventional solution dry spinning [40].

1.2.1.1 The Process of Electrospinning

Electrospinning, also known as electrostatic spinning, is a powerful, rather simple and highly versatile technique which allows fabricating micro-and nanoscale fibers from process solutions or melts using and electrically forced fluid jet [41]. A schematic diagram to interpret electrospinning of polymer nanofibers in shown in Fig. 1.1. During the electrospinning, a high voltage electric field, is applied to the polymer liquid (a solution or melt), the repulsion among the charges on the surface of the drop at capillary tip competes with the surface tension, which tends to stabilize the drop [42, 43]. Once a critical condition is reached at which surface charge repulsion dominates, the hemispherical surface of the liquid at the tip elongates to form a conical shape known as the Taylor cone [44, 45]. Further increasing the intensity of the electric field, a jet is drawn from the spinneret under a constant flow rate. Before reaching the collector, the solution jet evaporates or solidifies, and is collected as an interconnected mats of small fibers on the oppositely charged grounded collector [46]. The diameters of polymer fibers are around nanometers, from few tens nanometers to micrometers, a typical example of polyacrylonitrile (PAN) nanofibers is displayed in Fig. 1.1.

1.2.1.2 Rich and Varied Electrospun Nanofibers

As a nanofabrication technique, electrospinning has been identified as a remarkably robust and versatile method for fabricating fibers with diameters down to the nanometer length scale by applying a high voltage on a polymer solution or melt. A variety of materials such as polymers [47–50], ceramics [51–53], carbon [54–56] and even metals [57] have been electrospun into uniform fibers with well-controlled

Fig. 1.1 Schematic diagram of fundamental setup for electrospinning

sizes, compositions, and morphologies. In most occasion, electrospun nanofibers are usually smooth solid fibers and they are collected as nonwoven membranes with randomly arranged structures, which have great limited their applications in various areas, for instance, electronic devices, biomedical areas, etc. [58] Thus it is important to have a basic understanding of the different group of materials and versatile nanofibrous structures before selecting the most appropriate electrospun fibers for sensing application. In order to fully explore the application of nanofibers, more and more scientists try to fabricate nanofibers with rich and varied structures. Different nanofiber structures and morphologies can be obtained *via* control of the processing conditions, these structure regulations could be mainly divided into two categories: single fiber structure and aggregate structure.

The single fiber structure is of significant importance as far as the packing of the fibers is concerned in nonwovens-that is, the total porosity. Furthermore, the structure is of significance with respect to the internal specific surface as controlled by geometric effects, but also with respect to the shape of the pores controlled by intersecting fibers as well as with respect to the flow of fluids or gases around the fibers that is, the permeation properties [40, 59]. So far, by regulating different parameters include the solution properties such as viscosity, elasticity, conductivity, and surface tension; governing variables such as hydrostatic pressure in capillary tube, electric potential at the capillary tip, and the distance between the tip and the collector; and the ambient parameters such as solution temperature, humidity, and air velocity in the electrospinning chamber, the nanofibers with porous [60], ribbon-like [61], helical [62], necklace-like [63], pine-needle-like [64], firecracker shape [65], multi-channel tubular [66], nanowire-in-microtube [67, 68] are successfully fabricated, as shown in the Fig. 1.2.
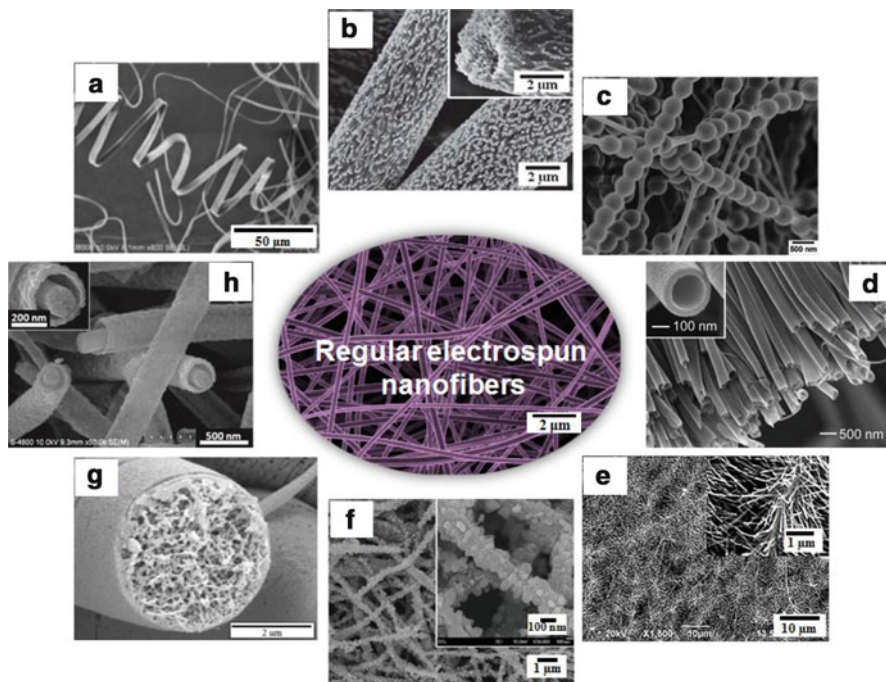
Fig. 1.2 Various micro-and single nanofibrous structures fabricated by electrospinning. (**a**) ribbon-like, reprinted with permission from [61]. ©2014 American Chemical Society; (**b**) porous, reprinted with permission from [69]. ©2012 Royal Society of Chemical; (**c**) necklace-like, reprinted with permission from [55]. ©2012 American Chemical Society; (**d**) hollow, reprinted with permission from [70] ©2004 American Chemical Society; (**e**) pine-needle-like, reprinted with permission from [64]. ©2012 Elsevier Ltd.; (**f**) firecracker-shaped, reprinted with permission from [68]. ©2014 Royal Society of Chemical; (**g**) inner porous, reprinted with permission from [71]. ©2010 American Chemical Society; (**h**) wire-in-tube structures, reprinted with permission from [68]. ©2010 American Chemical Society

Besides controllable fabricating versatile of single fiber structure, many groups have demonstrated that electrospun nanofibers could be collected as uniaxial aligned arrays since the collection of fibers aligned along a preferential direction is a very relevant aspect to be considered for various applications [72, 73]. For instance, Ding et al. use the high speed rotating roller as collecting electrodes, the strong stretching of the roller makes the fiber to be aligned among the rotating orientation, the highly alignment Poly(m-phenylene isophthalamide) (PMIA) nanofibers have been successfully fabricated, as shown in the Fig. 1.3a. Here is another typical example, Li et al. reported that nanofibers could be uniaxially aligned by introducing insulating gas into conductive collectors [74]. The more complex aggregate structure of nanofibers such as hierarchically organized nanofiber composites could also realize. To electrospun nanofiber membranes, lack of structural integrity is a persist problem and restrict its commercial viability.
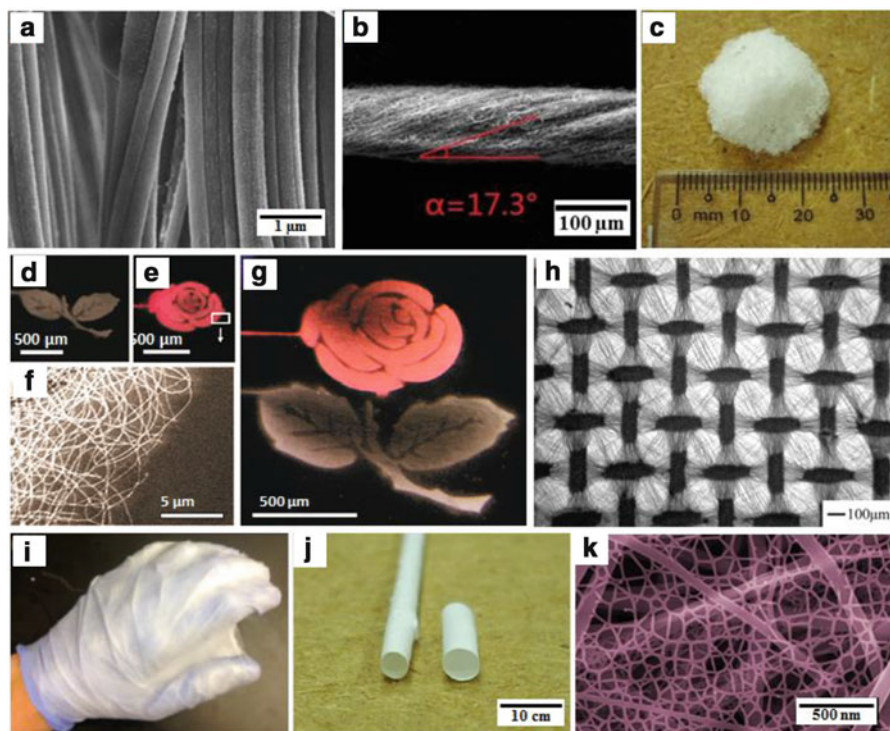
Fig. 1.3 Different aggregate structure of electrospun nanofiber: (**a**) alignment nanofiber, (**b**) yarns, reprinted with permission from [81], ©2013 Springer Science + Business Media; (**c**) 3D assemblies, (**d–h**) patterning nanofibers, (d–g) reprinted with permission from [75]. ©2010 American Chemical Society; (**h**) reprinted with permission from [76]. © 2007 WILEY-VCH Verlag GmbH & Co.; (**i**) glove sharp nanofibers, reprinted with permission from [76]. ©2014 American Chemical Society; (**j**) tubular nanofibers structure, reprinted with permission from [82]. © 2011 IOP Publishing Ltd.; (**k**) 2D nanonets, reprinted with permission from [83]. © 2011 Royal Society of Chemistry

Hierarchically organized nanofiber composites have great potential to solve this problem because they allow for interfacing nanofibers with other structural surfaces, and therefore the advantages of both components can be utilized synergistically. For example, as shown in Fig. 1.3d–g, Cho et al demonstrated selectively deposited architectures, well aligned fibrous architectures, and multilayered architectures [75]. Zhang et al fabricated the uniform mesh-like PLLA patterning nanofibers by using electroconductive collector with woven structure, which is displayed in Fig. 1.3h [76]. Furthermore, there are numerous hierarchically organized nanofiber composites, such as yarns, multiple interconnecting tubes, glove shaped, 3D assemblies, etc. [77–80] It has been shown that the outstanding properties and multifunctionality of such nanofibers and nanofibrous aggregates are highly attractive to numerous applications, including biological engineering,

composite, filters, textiles, etc. Additionally, this technique has become particularly powerful when combining other remarkable features with unique chemical, physical, and mechanical functions provided by adding other components with ease and control. Last but not least, electrospinning opens a door to creating various micro- or nanostructures for sensing application.

Notwithstanding the ability to fabricate micro- and nanoscale fibers of electrospinning which provide great potential in different fields, it is still difficult to electrospun polymer into uniform nanofibers with diameter as several nanometers up to now [84]. On the other hand, enormous researches in the past 10 year have indicated that the large average diameter (100–500 nm) of common electrospun fibers blocked their further applications in ultrafiltration, ultrasensitive sensors, catalyst, etc. In a meantime, when the fiber diameter falls below 20 nm [85], the extra SSA and porosity become more significant. Therefore, developing a robust strategy for manufacturing large-scale and extremely small nanofibers (<50 nm) has been a hotspot in the field of nanotechnology. As shown in Fig. 1.3k, a 2D soap bubble-like structured nanonets are fabricated for the first time by Ding et al in which the primary electrospun fibers acted as a support for the nanonets comprising interlinked ultrathin nanowires with diameter of 5–40 nm. This new types of aggregate structure was termed as "electrospun nanofibers/nets (NFN) membranes" was obtained by employing the novel one-step "electro-spinning/netting (ESN)" process which will be detailed introduced in the following part [86]. This inimitable structure exhibits several amazing characteristics, such as an extremely large SSA, high porosity and superior mechanical performance.

1.2.2 ESN Technique

In the past few years, significant progresses have been made in term of our fundamental understanding of the ESN process, the controllable fabrication of NFN membranes based on different polymer systems also have been explored. ESN NFN membranes has undoubtedly risen as a shining star in the horizon on the path of the scientists' searching for new materials for future environment, energy and healthcare applications [87]. Benefitting several fundamental properties of itself, such as extremely small diameter, high porosity, Steiner tree network geometry, controllable coverage rate, and controllable density, there is no doubt that NFN membrane are also an attractive candidate as sensing substrate loaded with receptors for ultrasensitive sensors. The following sections will fully illustrate the strategies for the controllable fabrication of NFN membranes.

1.2.2.1 History of ESN

The origins of the NSN process can be traced to the year of 2006 through a research article published in the journal of "*Nanotechnology*" by Ding and coworkers. An

incompletely spited polyacrylic acid (PAA) spider-web-like or soap-bubble-like structure were observed, then such unexpected unique structure was officially named as "nanonets" on account of its fascinating features [87]. In the meantime, the principles of structure control and a possible formation mechanism was also preliminary studied. It is at this time, the concept of "ESN" was introduced. As a variant of electrospinning process, ESN process involves the use of a high voltage to induce the formation of a liquid jet. In addition to the formation of liquid jet, the ESN process also comprise an electro-netting process, which defined as the phase separation-induced splitting of a small charged droplet in a high electric field. Since then, the research on exploration of spinnable polymers, influencing parameter, morphology control, application optimize has grown exponentially.

1.2.2.2   Formation Mechanism of NFN Membrane

About 8 years after the fantastic ESN was demonstrated by Ding, a wealth of researchers continued to expand the suitable application areas of NFN membranes and fell over themselves to learn as much as they could understanding the formation mechanism of NFN membrane on the other side. The questions keep arising during the research process, such as where is this structure come from? What happens to the charged polymer jets and droplet during their running in such small distance between the capillary tip and grounded collector? All these questions have triggered more rigorous experimental and theoretical work to reveal the secrets behind ESN process [72]. We are very delighted to hear and see that more and more researchers devoted themselves in this domain, but it is also worth to point out that the formation mechanism of NFN structures is complex and consensus on the formation mechanism has not been reached.

Up till the present moment, there are four predominant mechanism to explain the formation of NFN membrane which include the "ions initiated splitting up of the electrospun fibers" that proposed by Kim et al [88]. According their recent work, the nanonets are formed by the joints between many fibers and the possible joints occur at the apex of Taylor cone. In addition of "ions initiated splitting up of the electrospun fibers", Kim and his coworkers have proposed the "hydrogen bond formation" between nano-nets and PA6 nanofiber scaffold based on the investigation of PA6 and methoxy poly (ethylene glycol) (MPEG) oligomer/PA-6 NFN membranes [89, 90]. Another plausible mechanism of nanonets is "intertwine among branching jets", which is put forward by Tsou et al. base on their theoretic, the formation of nano-nets is associated with the complicated interaction between the subsidiary jets [91]. The last one is a mechanization proposed by Ding et al. That is "phase separation of charged droplets" theoretic which also has been well known and we will emphatically introduces next [92].

Since Ding et al observed the defect PAA films and partly split PAA nano-nets during 2006, they proposed the mechanism of "phase separation of charged droplets" for the first time depended on those observation described above. According to
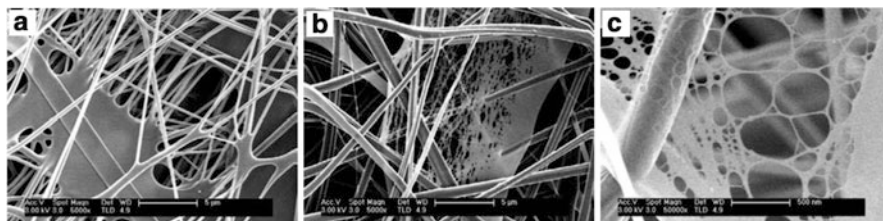
Fig. 1.4 SEM images of PAA fibers formed in PAA solution combined with (**a**) H_2O and (**b**) ethanol at a concentration of 6 wt%, voltage of 30 kV, spinning distance of 15 cm and relative humidity of 20 %. (**c**) High magnification SEM image taken from the sample shown in (**b**) (Reprinted with permission from [92]. © 2006 IOP Publishing Ltd)

the mechanism, the formation of nano-nets is on account of the phase separation of charged droplets generated during electrospinning. They suggested that during the ESN process, in addition to the formation of polymer solution jet, it also splitted some small charged droplets in a high electric field [93]. The discharged polymer solution jet undergoes an instability and elongation process, which allows the jet to become very long and thin and eventually form the polymer nanofibers. For small charged droplet, it deforms significantly to a thin liquid film, which undergoes rapid phase separation with the solvent rich domains to transform into pores. Actually, the presumption of small charged droplets formation is not an idiosyncratic views. The break-up of a jet and the formation of small charged droplets is a very old and interesting problem and the relevant research can be trace back to last century. For instance, in 2000, Hartman et al. presented a physical numerical model to describe the harmonic perturbations on the jet surface based on a cylindrical coordinate system, thereby to model the jet break-up process with analytical relations [94] (Fig. 1.4).

A schematic diagram illustrating the possible formation procedure of nano-nets is shown in Fig. 1.5. After the microsized charged droplets generated accompanying with the electrospun jet, There are various forces act on the charged droplet when it flights with a high speed in the electric field, including electrostatic force, drag force, gravity, Coulombic repulsion force, surface tension and viscoelastic force [95–97]. Above forces all play an important roles during the process of nano-nets formation. The electrostatic force is response to carry the charged droplet from capillary tip to collector. The drag force between the surrounding air and the charged droplet is the main cause that deforms the droplets into films. As to the Coulombic repulsion force, the main function is keep expanding the droplet. In addition, the contraction of charged droplet is attributed to the surface tension and viscoelastic forces. Since the electric field could be increased by increasing the applied voltage within a constant distance, the electrostatic and Coulombic repulsion forces of charged droplet were reinforced with increasing of electric field consequently. Then, the moving of charged droplet is further accelerated due to the increased electrostatic force, which led to an increased drag force. This
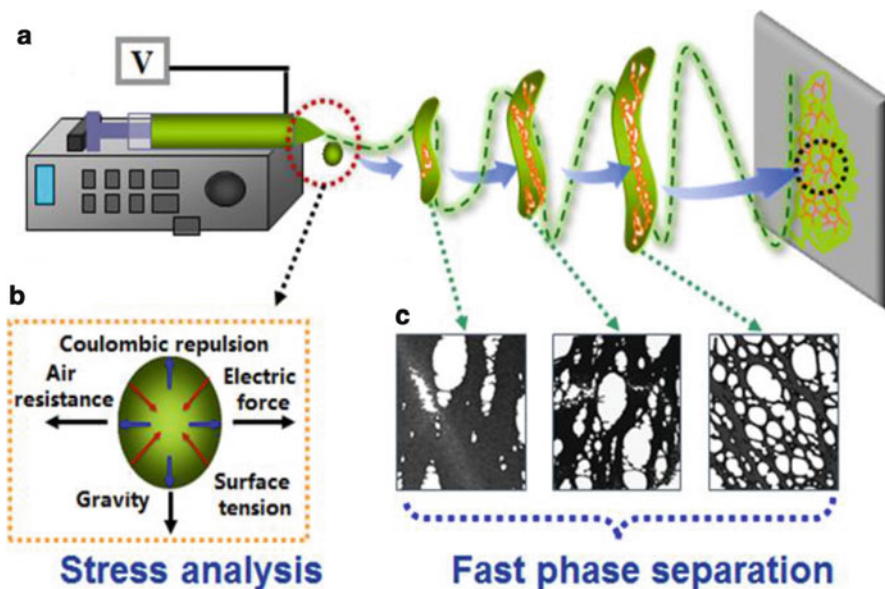
Fig. 1.5 (**a**) Schematic diagram of setup of electro-spinning/netting apparatus, reprinted with permission from [98]. © 2011 Royal Society of Chemistry. (**b–c**) Show drawings of the forces acting on the charged droplet and the possible process of nano-nets formation during ESN process (Reprinted with permission from [92]. © 2006 IOP Publishing Ltd)

phenomenon of charged droplet distortion and expansion in the electric field was also reported by Grimm and Beauchamp during their research on electrospraying [95]. The further expansion could happen when the electric field increased further to form thin films from droplets with the effect of increased Coulombic repulsion and drag forces. Moreover, the increased radial charge repulsion force also has a tendency to expand the charged films. As a result, the deformation of charged droplet was strongly affected by the electric field.

1.2.2.3 NFN Membrane Based on Different Polymer Systems

As introduced above, much effort has been applied to NFN membranes to comprehend the fundamental phenomena of fabrication process as well as the physical and chemical properties from the material science viewpoint. Consequently, ESN has been applied to numerous kind of polymer systems, including polymers soluble and spinnable from water, biocompatible and biodegradable polymers, polymer blends and polymers into which nanoparticles, salts, surfactants and other functional materials have been incorporated. Here is a comprehensive summary of polymers that have been successfully ESN into NFN structures to-date (Table 1.1).

Table 1.1 Different polymers to have been ESN into NFN membranes

Polymer system	Molecular weight	Solvent	Applications	Ref.
PA-6	18,000	Formic acid	Filter; sensors	[83, 99, 100]
PA-66	15,000	Formic acid	Filter	[101]
PAA	250,000	H_2O/Formic acid/ Ethanol	Sensors	[92, 97, 102]
PVA	90,000	H_2O	Filter; sensors	[88]
PU	180,000	DMF, DMF/THF	Filter; protective clothing; tissue engineering	[96]
CS	210 KDa	Acetic acid/H_2O	Tissue engineering; wound healing	[103]
Gelatin	–	Formic acid/ acetic acid	Tissue engineering; wound healing	[104]
PAA/PA-6	–	Formic acid	Sensors	[105]
CS/PA-6	–	Formic acid	Tissue engineering	[106, 107]
PANI/PA-6	–	Formic acid	Sensors	[108]
PANI/PVB/ PA-6	–	Formic acid	Sensors	[109]
NC/PA-6	–	Formic acid	Sensors	[110]

PA-6 polyamide-6, *PA-66* polyamide-66, *PVA* polyvinyl alcohol, *PU* polyurethane, *CS* chitosan, *PANI* polyaniline, *PVB* polyvinylbutyral, *NC* nitrocellulose, *DMF N,N*-dimethylformamide, *THF* Tetrahydrofuran

As shown in the Fig. 1.6, the typical morphologies of NFN membranes based on different polymer systems, such as PAA, PA-6, PMIA, gelatin, CS, and PU, which have been synthesized in Ding's laboratory. By regulating the different polymer systems and optimizing the nano-nets morphology (e.g. fiber and nanowire diameter, pore-width and coverage rate of nano-nets), they have found out that similar to electrospinning, the ESN process is also influenced by many parameters, classified broadly into solution parameters, process parameters, and ambient parameters. Solution parameters include concentration, conductivity, viscosity, surface tension, and solvent all influence the phase separation process during the ESN [86, 96, 98, 99]. As to process parameters, which include applied voltage and tip to collector distance. Each of these parameters significantly affects the NFN morphology. Except these influence factors, ambient parameters enclose the temperature and humidity of the surroundings, which also play a significant role in determining the morphology of NFN membranes. Although we already have a general knowledge of formation mechanism and influence factors of NFN membranes as well as successfully fabricated a broad range of polymers into NFN membranes, it is worth pointing out that the relationship lie behind appearances between spinnable polymers and NFN membranes is still waiting us to reveal.
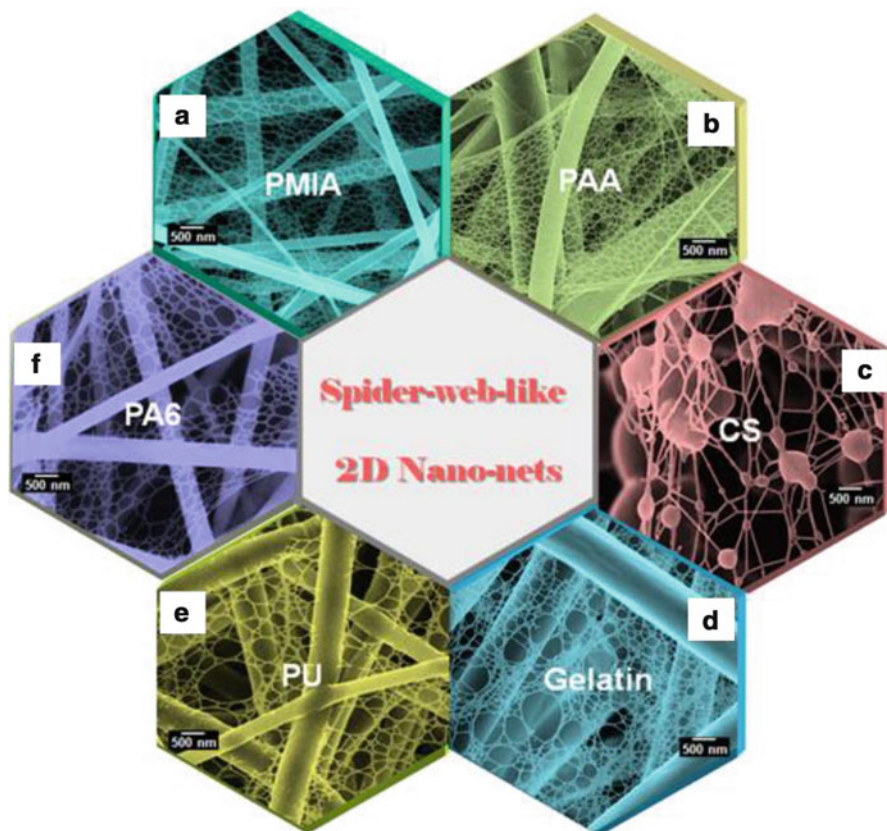
Fig. 1.6 Several typical electrospun nano-fibers/nets membranes based on different polymer systems. (**a**) PMIA; (**b**) PAA; (**c**) CS; (**d**) gelatin, reprinted with permission from [104]. © 2011 Elsevier Ltd.; (**e**) PU, reprinted with permission from [96]. © 2011 WILEY-VCH Verlag GmbH & Co.; (**f**) PA6

1.3 Sensors Based on Electrospun Nanofibers and ESN NFN Membranes

In recent years, considerable efforts have been made to develop varied sensors for the assay of environmental contaminants. Benefiting from the large surface-area-to-volume ratio, tailored pore structures, large stacking density and ease to surface modification of electrospun nanofibrous membranes, the nanofiber and NFN membranes-based sensors achieve high sensitivity, fast response, and good reversibility. In this section, we will review recent progress in the development of electrospun and ESN materials based QCM and colorimetric sensors, illustrate them with current examples showing how they have been applied, and discuss their intrinsic fundamentals and optimal designs.

1.3.1 QCM Sensors

In 1959, Sauerbrey demonstrated the dependence of quartz oscillation frequency on the change in surface mass [111]. He coined the term QCM in late 1950s, and it was his work that led to the use of quartz plate resonators as sensitive microbalances for thin films. When voltage is applied to a quartz crystal causing it to oscillate at a specific frequency, the change in mass on the quartz surface is directly related to the change in frequency of the oscillating crystal, the mass-frequency shift relation for quartz crystal resonators as follows [112, 113]:

$$\Delta f = -2f_0^2 \Delta m / A(\mu \rho)^{1/2} \tag{1.1}$$

Where Δf the measured frequency shift, f_0 fundamental frequency of a bare QCM chip, Δm the mass change per unit area, A the electrode area, ρ the density of quartz, and μ the shear modulus of quartz crystal.

For QCM, the most unique feature is the change in frequency can determine the mass of analyte adsorbed in ng/cm^2. Consequently, enormous materials such as metals, ceramics, polymers, self-assembled monolayers, lipids, and waxes, have been used as sensitive coatings on QCM to improve the sensor sensitivity and selectivity for chemical analytes [114, 115]. One major challenge lies in that the flat electrode surface limits the immobilization degree of the absorbing sites per unit area accompanies with the rapid development of QCM sensors [116]. Driven by the actual need, increasing attention has been paid to the development of nanostructured coatings on QCM to improve the sensor sensitivity, for instance, nanofibers [117]. Taking advantage of large specific surface area of the nanostructured sensing materials, the performance of the QCM sensors is greatly enhanced. In this part, we review recent progress in the development of electrospun and ESN nanomaterials having applications in QCM sensing approaches.

Formaldehyde is one of the volatile organic compounds (VOCs) that are widely used in household materials, which is associated with many health risk factors and has been identified as a major cause of sick building syndrome [118–120]. Consequently, the WHO has set a 30 min exposure limit of 0.08 ppm, while the US National Institute for Occupational Safety and Health has established a maximum long-term exposure limit of 0.016 ppm [121]. Considering the harmfulness of formaldehyde, the fast, selective and sensitive detection seems extremely important. Polyethyleneimine (PEI), a cationic polyelectrolyte, has been investigated not only as an immobilization material for biosensors, but also as a sensing materials for various gases and vapors. PEI has an affinity with formaldehyde, resulting from the interaction between formaldehyde molecules and amine groups of PEI [122]. Therefore, we are going to introduce a series of QCM formaldehyde sensor utilizing the PEI as the sensing material.

1.3.1.1 PEI Functionalized Polystyrene (PEI@PS) Nanofibrous Membranes Based Formaldehyde Sensors

SSA as a vital factors of QCM surface which determines the immobilization degree of the absorbing sites per unit area, thereby plays a decisive role in sensitivity. Since developing materials with a porous structure is an accepted way to enhance the available surface area, Zhang et al. [117] fabricated a formaldehyde sensors by depositing the three-dimensional (3D) fibrous PS membranes with different porous structure on the QCM surface (Fig. 1.7a). Then modified PEI solutions onto fibrous PS membranes, through which fibrous PEI@PS membranes were obtained. The resultant composite membranes were investigated as sensitive coatings on QCM for formaldehyde detection at room temperature. As shown in Fig. 1.7b, BET surface area test and N_2 adsorption/desorption isotherm demonstrated that PS fibers electrospun from higher concentration of PS solution (13 wt%) tended to possess larger pore volume and SSA (42.25 m^2/g), offering an excellent sensing template for the modification of PEI. In this case, when exposed to 140 ppm of formaldehyde, QCM-based PEI@PS (13 wt%) sensors has achieved the largest response value, approximately four times as much as PEI@PS (7 wt%) sensors. As it displayed in Fig. 1.7c, the developed formaldehyde-selective sensors exhibited fast response and achieved a detection limit of 3 ppm at room temperature.

In order to further improve the sensitivity of PEI@PS based sensors, Zhang et al subsequently investigated the influence of PEI depositing quantity, as shown in Fig. 1.7d, when exposed to 140 ppm of formaldehyde, the maximum frequency shifts of the PEI@PS based QCM sensors with various PEI coating loads (1,000, 2,000, and 6,000 Hz) were 5, 33, and 75 Hz, respectively. It was observed that the response of the sensor coated with 6,000 Hz PEI was almost 15 times as much as that of the sensor coated with 1,000 Hz PEI. As expected, the detecting sensitivity increased with the amount of PEI deposited on the QCM electrode due to more absorbing sites. Unfortunately, the optimal quantity of PEI to achieve the best performance of formaldehyde is not obtained here, because the QCM system would overload when the coating load of PEI is above 6,000 Hz. Additionally, from the Fig. 1.7e we can know that the developed sensors perform excellent selectivity toward formaldehyde when exposed to other interfering VOCs.

1.3.1.2 PEI Functionalized Titanium Dioxide (PEI@TiO2) Nanofibrous Membranes Based Formaldehyde Sensors

On the consideration of semiconductor metal oxides fibrous materials' advances in facilitating rapid mass transfer of the analyte molecules to and from the interaction region and requiring charge carriers to traverse any barriers introduced by molecular recognition events along the entire fibers [123, 124]. Wang et al. [120] developed another nanostructured complex of PEI functionalized TiO_2 nanofiber (PEI@TiO_2) as sensing coating on QCM for formaldehyde detection. As shown
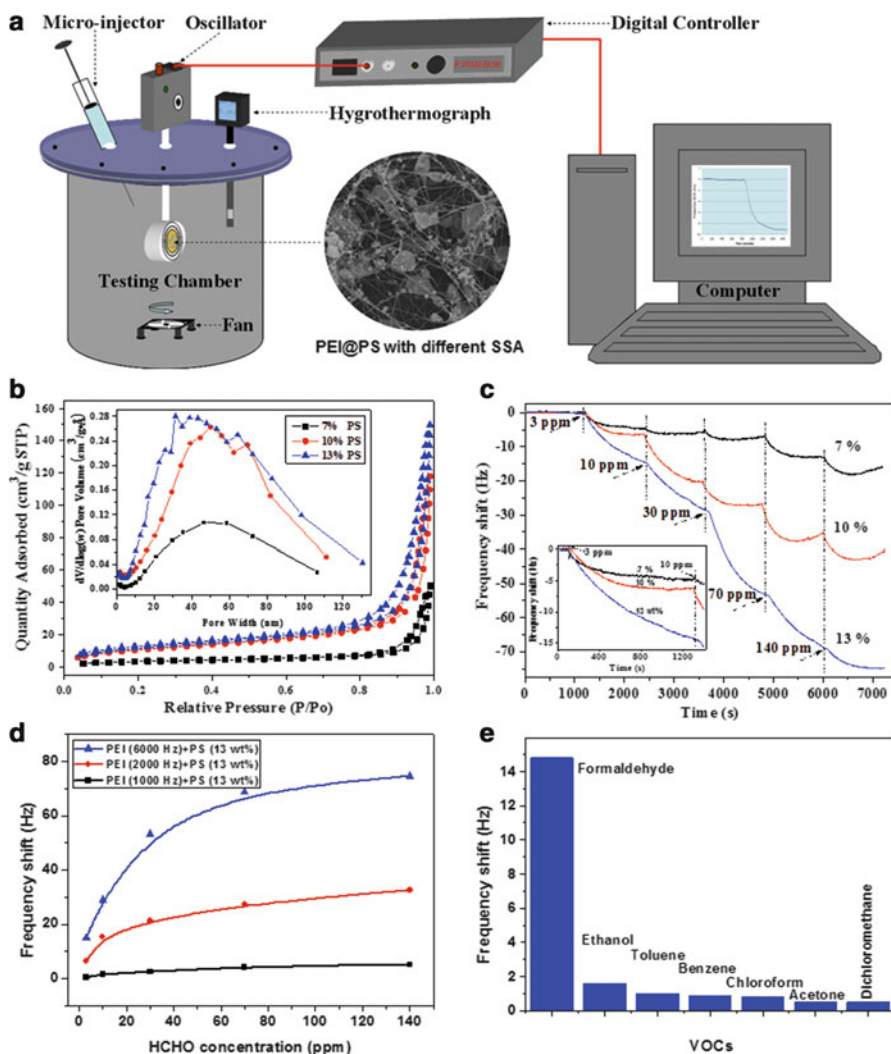
Fig. 1.7 Schematic diagram of a gas testing system based on PEI@PS with different SSA for formaldehyde monitoring (**a**). Nitrogen adsorption and desorption isotherm of fibrous PS membranes with different concentration, the inset image shows the pore size distribution (**b**). Response of QCM-based PEI-PS sensors formed from various concentrations of PS solutions (**c**). The influence of PEI loading amount (**d**), and the frequency shift of QCM-based PEI@PS sensors versus 30 ppm of various VOCs (**e**) (Reprinted with permission from [117]. © 2011 Elsevier Ltd)

in Fig. 1.8, the 3D porous TiO_2 fibrous membranes with porous structure were successfully fabricated by calcining the TiO_2/PS fibers at 450 °C. The porous structure of TiO_2 fibers was also confirmed by the nitrogen adsorption–desorption isotherm, the nitrogen adsorption–desorption isotherm of the TiO_2 fibers exhibits a type IV adsorption branch with a combination of H1 and H3 hysteresis loops
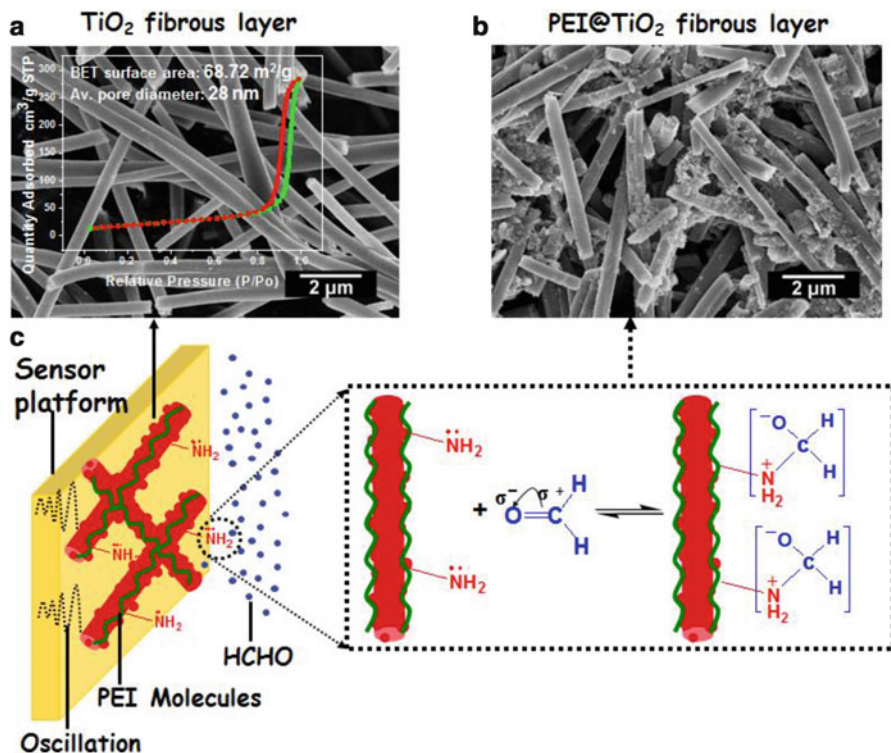
Fig. 1.8 The typical FE-SEM images of TiO$_2$ (**a**) and PEI@TiO$_2$ nanofibrous membranes (**b**), the inset image of (**a**) shows the nitrogen adsorption and desorption isotherm of TiO$_2$ membranes. And the (**c**) schematic represents the detecting platform of formaldehyde vapor based on PEI@TiO$_2$ fibers (Reprinted with permission from [120]. © 2012 Elsevier Ltd)

characteristic of a predominantly mesoporous system [125, 126]. The calculated BET surface area and average pore diameter are 68.72 m^2/g and 28 nm, respectively. All these versatile structures make the TiO$_2$ to be a candidate for applications of formaldehyde sensing.

The formaldehyde-sensing properties of PEI@TiO$_2$ porous fibers on QCM were investigated by measuring the frequency changes when the fibers were exposed to formaldehyde vapors. During the exposure process, the porous fibers on the QCM act as sensing layers for target formaldehyde molecules and the interaction of formaldehyde molecules with the sensing layer causes the frequency to decrease. The sensor responses (ΔF) for each concentration were obtained from the frequency differences between the corresponding QCM frequencies at the beginning and the end of the exposure process. Figure 1.9a shows time courses of response of PEI@TiO$_2$ sensors with different PEI coating loads upon exposure to increasing formaldehyde concentrations (1–100 ppm) in a cell. The QCM sensor coated with only TiO$_2$ fibers exhibited only 0.2 Hz frequency shift under exposure to 1 ppm formaldehyde vapor. The ΔF of the TiO$_2$ fibers coated QCM sensors exposed to
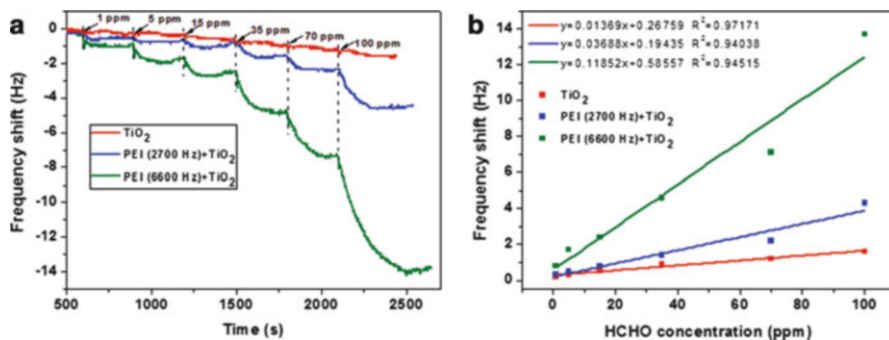
Fig. 1.9 Response of PEI@TiO$_2$ based QCM sensors with different PEI coating loads (i.e. 0, 2,700, 6,600 Hz) upon exposure to increasing formaldehyde concentrations (1–100 ppm) at ambient temperature of 25 °C (**a**). The frequency shift versus formaldehyde concentration. The coating load of TiO$_2$ was 1,300 Hz (**b**) (Reprinted with permission from [120]. © 2012 Elsevier Ltd)

5, 15, 35, 70 and 100 ppm of formaldehyde were 0.3, 0.5, 0.9, 1.2 and 1.6 Hz, respectively. It can be seen that the present PEI@TiO$_2$ based QCM sensor has not only the lowest detection limit (1 ppm) but also the fastest time response (<120 s). Figure 1.9b shows the ΔF values of sensors with different PEI coating loads (0, 2,700, and 6,600 Hz) in sensing formaldehyde with various concentrations of 1–100 ppm. The QCM isotherm to formaldehyde shows a Henry-type sorption at the concentration range [127]. This sorption behavior also proved the PEI@TiO$_2$ sensor possess a good linear relationship between frequency shift and concentration of formaldehyde which may give the sensors an extra advantage over their opponents.

1.3.1.3 PEI Functionalized PA-6 NFN Membranes Based Formaldehyde Sensors

Although the PEI@PS and PEI@TiO$_2$ membranes based QCM sensors have presented good performance to formaldehyde sensing, the detect limitation of above two sensors still cannot satisfy the WHO's standard. Facing with this obstacle, researchers turned their attention to explore new kind of substrates. Benefiting to several attractive features of NFN membranes such as extremely large specific surface area, high porosity, large stacking density and strongly tight adhesive force to the devices, it can lead to further enhancement in the facilitation of the analytes diffusion and oscillation transmission into the membranes, so as to detect formaldehyde at lower concentration level [83]. Recently, an effective formaldehyde detection system was developed by ESN depositing PA-6 NFN membranes on QCM and then modifying sensing PEI onto the NFN membranes (PEI@PA-6). As shown in Fig. 1.10d–f, the modification process did not disturb the NFN structure. When exposed to 100 ppm of formaldehyde, PEI@PA-6 NFN
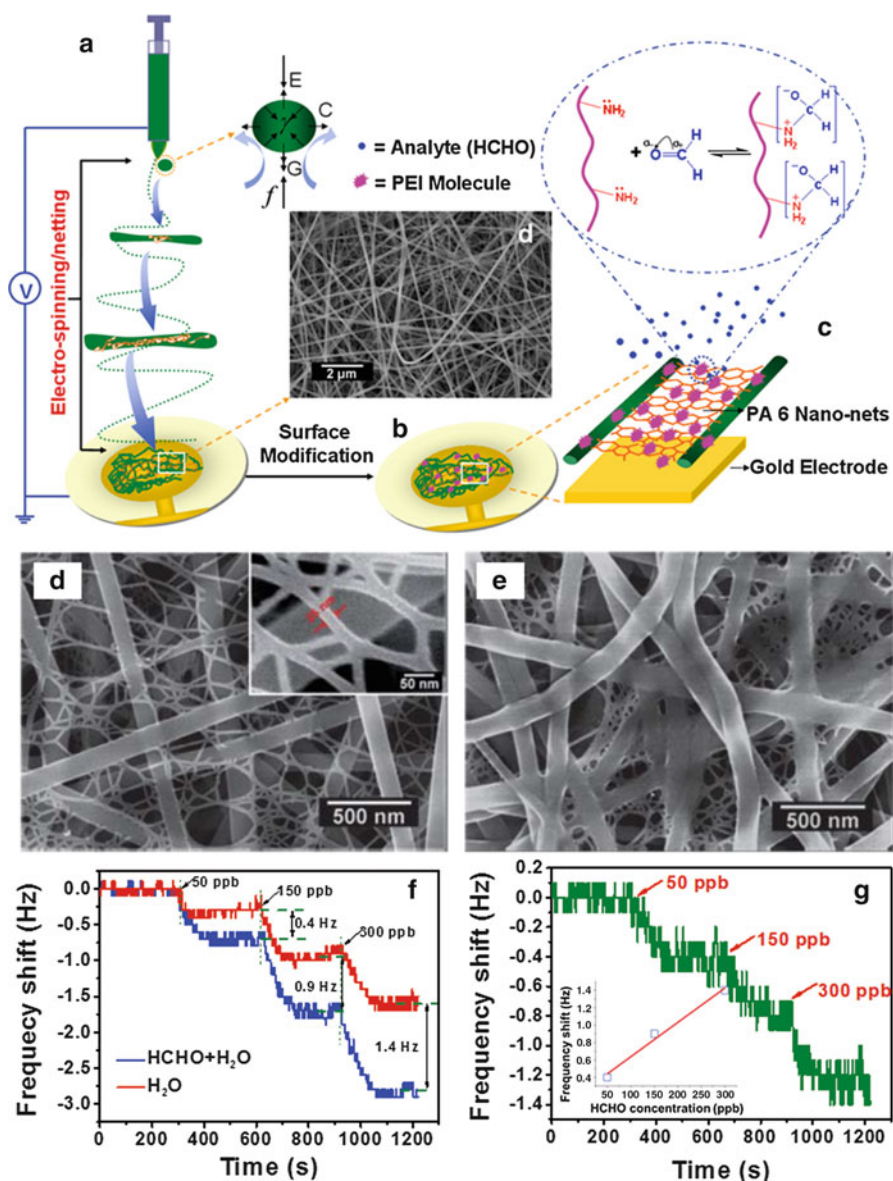
Fig. 1.10 Schematic diagram illustrating the fabrication of sensing layers on QCM. (**a**) ESN deposition of fibrous membranes onto the electrode of QCM. (**b**) Surface modification of NFN with diluted PEI solutions. (**c**) Illustration of PEI@PA-6 NFN on gold electrode and the reaction mechanism between formaldehyde and PEI. Typical FE-SEM image of PA-6 NFN membranes (**d**) and its corresponding samples modified with PEI (**e**). Responses of QCM-based PEI@PA-6 NFN (30 kV) sensors upon injection of water and the dilute formaldehyde solution, respectively (**f**). Response of the QCM sensor to formaldehyde (50, 150, and 300 ppb) (**g**), which derivate from (**f**) and removes effects of water. The inset in (**f**) shows the frequency shift versus the formaldehyde concentration (Reprinted with permission from [83]. © 2011 Royal Society of Chemistry)

(30 kV) based QCM sensor has achieved the largest response value, approximately three times as much as PEI flat film coated sensor. Subsequently, in order to detect formaldehyde with very low concentration, a moisture-compensating-based detecting method have been developed, i.e., firstly injected the dilute formaldehyde aqueous solution (1 wt%) into the chamber and then eliminated the influence of moisture. Figure 1.10f shows the responses of PEI@PA-6 NFN based QCM sensors upon injection of water and the dilute formaldehyde solution. The response of moisture-compensating QCM sensor exposing to formaldehyde was shown in Fig. 1.10g, indicating that the PEI@PA-6 NFN based QCM sensors exhibits a reduced detection limit for formaldehyde down to 50 ppb and a rapid response time (<100 s). In comparison with aforementioned works using QCM platform for formaldehyde sensing, the present PEI@PA-6 NFN based QCM sensors had not only the lowest detection limit but also the fastest time response, implying a high selectivity to formaldehyde and can be considered as an excellent candidate for gas sensing applications.

In addition to formaldehyde sensors, various kinds of QCM sensors based on electrospun nanofibers and NFN membranes have been developed such as sensors for humidity [99], trimethylamine [97], HCl [87] assaying and so on. There is no doubt that electrospun nanofibers have already become a desired substrate for QCM construction. Although the nanofibers based QCM sensors have gained an increased attention and achieved great progress. There is still a long distance from present condition to practical applications. Here are some possible reasons, first of all, the QCM system is still a little bit complex for people carrying around, so try to simplify the system and achieve the feature of direct reading are very important. Secondly, some performance of QCM system need further improve, including response time, stability, and reproducibility. Apart from QCM system, there are other structure features, such as viscoelastic, stiffness will influent the sensitivity waiting us to explore.

1.3.2 Colorimetric Sensors

Colorimetric sensors on patterned paper, fibrous material or plastic were developed as the least expensive, user-friendly alternative to conventional analytical instrumentations for 'point-of-care' medical diagnosis, environmental monitoring, and food quality control [128–131]. These low-cost platforms have been integrated with both colorimetric, and electrochemical detection systems. Such sensors are miniaturized and disposable and can be used for on-site analysis. In this section, we will focus on the application of electrospun nanofibers and NFN membranes on formaldehyde and heavy metal ions colorimetric sensing.

1.3.2.1 Colorimetric Strips for Formaldehyde Assaying

It goes without saying that the formaldehyde is one of most serious indoor air pollutant, can cause serious health damage. Wang et al. [132] demonstrated a label-free colorimetric sensor strip for real-time formaldehyde detection based on fluoral-p decorated PAN nanofibrous membranes. When the sensor strip was exposed to formaldehyde, the color of strips was dramatically changed from white to yellow attributed to the formation of symmetrically substituted 1, 4-dihydropyridines through the derived Hantzch reaction (Fig. 1.11a).

Because of selectivity is crucial for analytical chemistry grade, they systematically investigated the selectivity of the PAN/fuoral-p colorimetric strips by testing various VOCs (1 ppm) involving acetaldehyde, acetone, ethanol, dichloromethane, benzene, toluene, xylene, chloroform, ammonia, and DMF, which were possible interference vapors to assay. It is clearly observed from Fig. 1.11b that only formaldehyde induced a remarkable reflectance decrease at 417 nm and a distinct color change from white to yellow, implying that the interferential vapors have a negligible influence due to the specific reaction between formaldehyde and fuoral-p. It is worthwhile to note that acetaldehyde also cannot cause the color change, although acetaldehyde can also undergo the first stage with fuoral-p. This may be
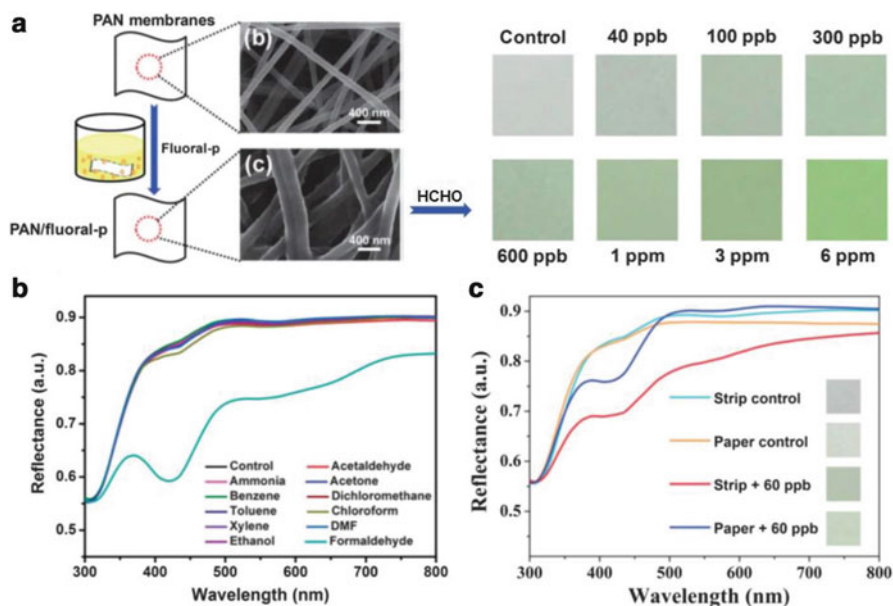
Fig. 1.11 The procedure for the fabrication of PAN/fluoral-p colorimetric sensor strips and the corresponding color changes after exposure to different concentration of HCHO (**a**). The UV-vis reflectance spectra of colorimetric strips after exposure to various VOCs (1 ppm) for 30 min (**b**). The UV-vis reflectance spectra and photographs of the PAN/fluoral-p nanofibrous strips and filter paper-based strips after exposure to 60 ppb formaldehyde (**c**) (Reprinted with permission from [132]. © 2013 Royal Society of Chemistry)

due to the fact that acetaldehyde molecules contain three active hydrogen atoms, the water molecule will be eliminated from methyl in the second stage which would lead to the formation of different end products (Mannich base), and so it would not induce the color change [133].

In corroboration of the superiority of electrospun nanofibers as the substrate, Wang et al. further compared their strips with the filter paper based strips. After espousing the PAN/fuoral-p nanofibrous strips and filter paper-based strips to 60 ppb formaldehyde under the optimized conditions. Figure 1.11c revealed that the reflectance intensity decrease at 417 nm of nanofibrous strips, substantially larger than filter paper strips which might be attributed to the large specific surface area and high porosity of fibrous membranes. Additionally, the corresponding color change of the nanofibrous membranes-based strips was much more obvious than the filter paper-based ones. Moving forward, this work also promotes a strategy for the design and development of versatile label-free colorimetric sensors toward various analytes in the future.

1.3.2.2 Colorimetric Strips for Mercury (II) Ions

Mercury, one of the most toxic metals, has drawn much attention due to its toxicity and impact on the public health. Mercury ions (Hg^{2+}) is released into the environment as a result of both natural processes and human activities, which can accumulate in the human body and readily penetrate through biological membranes, thus inactivating important cell functions and causing a wide variety of diseases such as brain damage, serious cognitive, motion disorders and Minamata disease [30, 134, 135]. Because of its high toxicity, Hg^{2+} ions has been included on the list of priority pollutants by U.S. EPA with a mandatory discharge limit of 50 nM for wastewater and a maximum concentration level of 10 nM for drinking water [136, 137]. Among the numerous analytical methods that are available for the detection of Hg^{2+} ions, colorimetric strategies offer distinct advantages in terms of sensitivity, selectivity, response time, and local observation.

Si et al. [109] report a novel, ultrasensitive, selective and flexible sensor strip based on PANI/PA-6/PVB NFN membranes for naked-eye colorimetric detection of Hg^{2+} ions in water. The sensing mechanism involves the transformations between different oxidation and doping forms of PANI. Figure 1.12a, b presents the changes of FE-SEM and optical images that accompany the treatment of PANI/PA-6/PVB NFN membranes with hydrazine aqueous solution. During the process, a series of redox and doping reactions took place. In the first stage, the benzenoid segments in leucoemeraldine base (fully reduced, PANI-LB) are oxidized by Hg^{2+} to form quinoid segment, yielding the emeraldine base (half oxidized, PANI-EB), thus inducing the first "turn-on" singles assigned to the charge transfer from the benzenoid to quinoid rings. Following, there are two competitive doping reaction of PANI-EB, protonation doping and Hg^{2+} complexation doping, and thus the color changed from green to blue vividly [138, 139]. Upon exposure to Hg^{2+} aqueous solution, the sensors exhibit two significant reflectance intensity decreasing bands
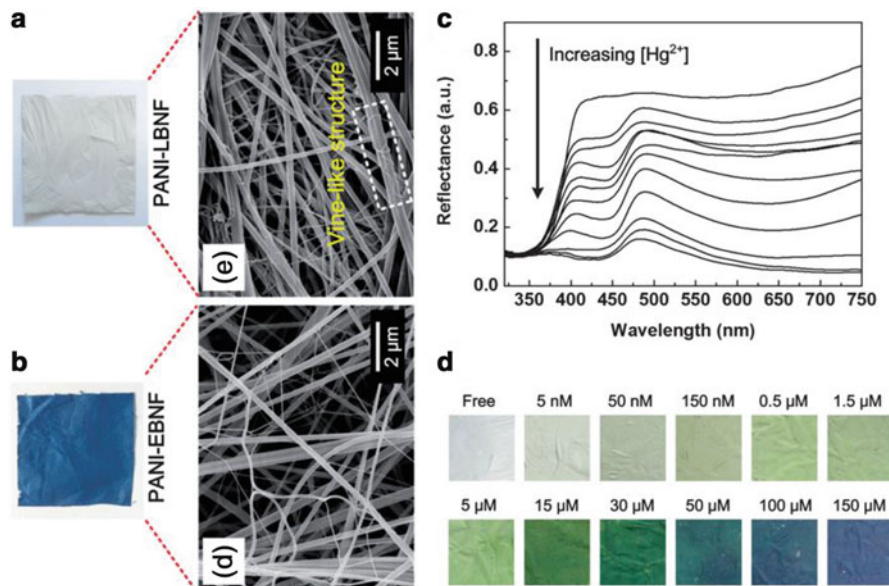
Fig. 1.12 FE-SEM and optical images of the PANI/PA-6/PVB NFN membranes (**a**) before (over) and (**b**) after (down) treated with hydrazine aqueous solution (40 wt%) for 2 h. (**c**) Reflectance spectra and (**d**) optical colorimetric response of the sensor strips after incubation for 20 min in Hg^{2+} aqueous solutions with concentrations of (0, 5 nM, 50 nM, 150 nM, 0.5 μM, 1.5 μM, 5 μM, 15 μM, 30 μM, 50 μM, 100 μM, and 150 μM) (Reprinted with permission from [109]. © 2014 Royal Society of Chemistry)

at 440 and 645 nm which induce the color changes from white to blue dramatically (Fig. 1.12c, d). This new sensor shows colorimetric response specifically to Hg^{2+} ions (white-to-blue color change) over other possible interfering metal cations and allows for detection of Hg^{2+} in aqueous solution with a low detection limit of 5 nM observing by naked eye.

The kinetic sensing response was also studied by continuously monitoring the reflectance spectra of sensor strips as a function of time after the addition of Hg^{2+}. It was found that the reflectance intensity of 440 nm decreased gradually over the entire time range, meanwhile the intensity of 645 nm showed a relatively stable region (>7 min) after the first slight decrease (Fig. 1.13a), thus leading to a continuous enhancement of the yellow/green color (Fig. 1.14c). This result suggests that the oxidation of benzenoid segments would be slowly saturated due to the weak oxidizability of the solution with low Hg^{2+} concentration (e.g., 5 μM), while the doping of quinoid rings (either protonation or Hg^{2+} complexation) was a constant, ongoing process. More interestingly, the dynamic responses upon exposure to high Hg^{2+} concentration (e.g., 150 μM) exhibited a dramatic difference from that of 5 μM. As shown in Fig. 1.13b, the reflectance intensity of 440 nm further decreased owing to the strong complexation doping with a large amount of Hg^{2+}. A rapid decrease of the intensity at 645 nm was also observed and it reached almost 0 after
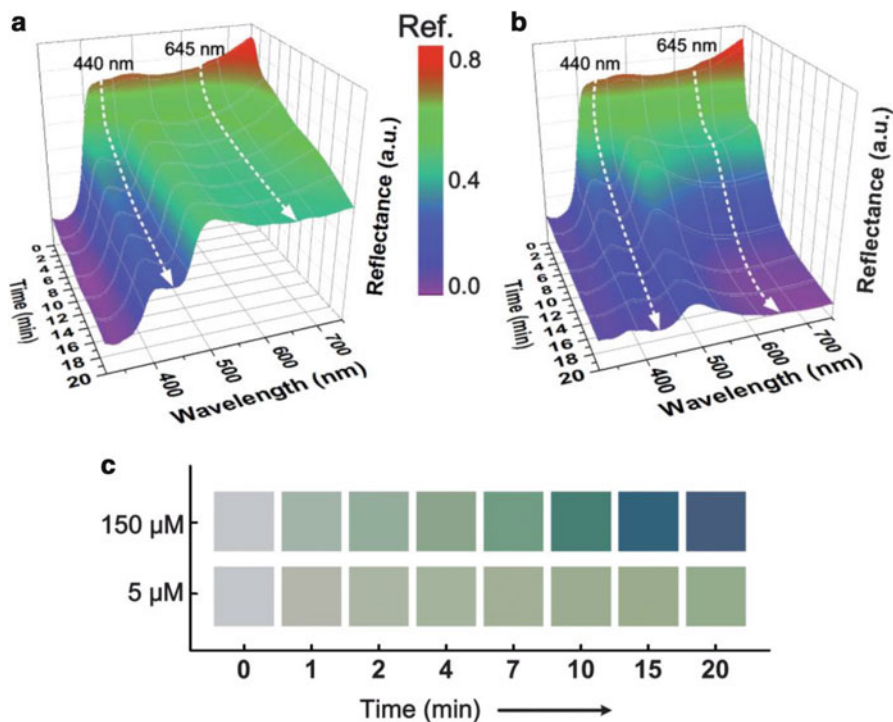
Fig. 1.13 The kinetic reflectance response of the PANI-LBNF sensor strips as a function of time for different Hg^{2+} concentrations: (**a**) 5 µM and (**b**) 150 µM. (**c**) The corresponding time dependent visualization of CIELAB color changes *versus* Hg^{2+} concentration (Reprinted with permission from [109]. © 2014 Royal Society of Chemistry)

15 min, indicating a complete oxidation of benzenoid segments into fully oxidized PANI-PB, and finally resulted in the vivid blue color [140].

1.3.2.3   Colorimetric Strips for Lead (II) Ions

Lead ion (Pb^{2+}) is another ubiquitous metallic pollutant in the environment and had been used recklessly until very recently. Nowadays, lead pollution has become a persisting problem and caused a long-lasting danger to human health. Even very low level of lead exposure can correspondingly result in high blood pressure, neurological, cardiovascular and hypertension developmental disorders, which lead to particularly serious problems in children including slowed motor responses, IQ decreasing and developmental disorders hypertension [141–143]. The Centers for Disease Control and Prevention has defined that the whole blood lead concentration >0.48 µM (100 µg/L) in children as indicative of significant exposure and recommends chelation therapy [144]. Due to the toxicity of Pb^{2+}, it is highly
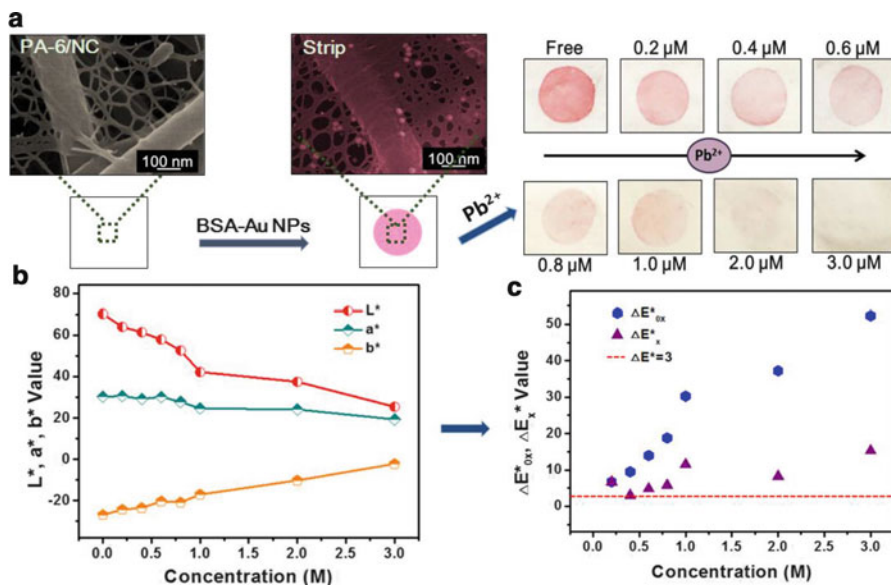
Fig. 1.14 (**a**) Schematic illustration of the colorimetric detection of Pb^{2+} based on the PA-6/NC NFN membranes and corresponding optical images of strips after incubated with different concentration of Pb^{2+} solution for 30 min at 60 °C. (**b**) The $L*a*b*$ values converted from the UV-vis absorbance spectra of colorimetric strips variation *versus* the concentration of Pb^{2+}. (**c**) ΔE_x* (color-difference of adjacent detecting samples) and $\Delta E_{0x}*$ (the color-difference between detecting samples and free sample) calculated from $L*a*b*$ values *versus* a series of Pb^{2+} concentrations (Reprinted with permission from [110]. © 2013 Elsevier Ltd)

desirable to develop a portable, easy use, house-hold use on-site, selective and sensitive method for Pb^{2+} assaying.

Li et al. [110] developed a simple colorimetric strip for assaying Pb^{2+}, constructed by immobilizing bovine serum albumin (BSA) decorated Au NPs (BAu probe) on PA-6/NC NFN membrane, which fabricated *via* multi-jet electrospinning. As shown in Fig. 1.14a, the successfully spotting BAu probe on PA-6/NC NFN membranes was confirmed by FE-SEM image. After the leaching liquor (pH = 10, 0.27 M Na$_2$S$_2$O$_3$ and 0.25 M 2-mercaptoethanol) was spiked with various concentrations of Pb^{2+} and incubated for 30 min, the color of strips gradually fade away from deep pink to white which is attribute to the fact that Pb^{2+} ions accelerate the leaching rate of Au NPs induced by S$_2$O$_3{}^{2-}$ and 2-mercaptoethanol [145].

In order to further quantitatively investigate the color-difference between two detecting samples as displayed in Fig. 1.14a, a converting method was used to convert a UV-vis absorbance spectrum into $L*a*b*$ values for given illuminant. In this work, the CIE normalized D65 is used, which closely matches that of the sky daylight. ΔE_x* (the color-difference of two adjacent detecting samples) and $\Delta E_{0x}*$ (the color-difference between detecting samples to free sample), is calculated in $L*$,

$a*$ and $b*$. ΔE is defined as the Euclidean distance between these two sets of color coordinates, were evaluated as [146, 147],

$$\Delta E*_x = \sqrt{(L*_x - L*_{x-1})^2 + (a*_x - a*_{x-1})^2 + (b*_x - b*_{x-1})^2} \qquad (1.2)$$

$$\Delta E_0*_x = \sqrt{(L*_x - L*_0)^2 + (a*_x - a*_0)^2 + (b*_x - b*_0)^2} \qquad (1.3)$$

As shown in Fig. 1.14c, the values of $\Delta E_{0x}*$ and ΔE_x* *versus* Pb^{2+} concentration revealed in Fig. 1.14a, all the results obtained were higher than 3 CIE LAB units, which could readily be identified by naked eyes.

The further, In addition, they compared two kinds of substrates here to evaluate the performance of the NFN membranes. As shown in Fig. 1.15c, the UV-vis absorbance spectra and photographs of NC based colorimetric film after incubated in optimized leaching liquor (0.27 M $Na_2S_2O_3$, 0.25 M 2-ME) spiked with 1 μM Pb^{2+}. The colorimetric responses of film obtained were substantially lower than strip and it was conspicuous that the $\Delta E_{0film}*$ could hardly be appreciated by human eyes. Because the strips have approximately one to two orders of magnitude larger surface area than that of films, which supplied more active sites. Apart from that, the morphology of film showed in Fig. 1.15a, b also gave a reasonably good explanation of less BAu probes binding amount. After analyzing the FE-SEM image, it was shown that the through-hole width distribute in range of 0.25–3 μm (major in micropore range) within the film. Unlike NFN membranes, the nanofibers overlap each other in a completely random manner during electrospinning procedure, giving a rise to the silt-shape pore structure which is ideal for membranes binding BAu probe.

1.4 Summary and Perspectives

In summary, this chapter presents a comprehensive review of the progress in QCM and colorimetric sensors based on electrospinning-netting nanofibers/nets. In virtue of the large surface-area-to-volume ratio, high length-to-diameter ratio, tailored pore structure, large stacking density, nanofiber-based sensors achieved high sensitivity, fast response and recovery, excellent stability. In further study, the following aspects should be taken into consideration: for QCM sensors, the sensing materials need further explore. Since the interfacial parameters, like roughness, surface free energy and surface charge will confound the responses of sensors, further regulate is also very important. In addition, there are other structure features, such as viscoelastic, stiffness will influent the sensitivity waiting us to explore. For colorimetric sensors, it still have a lot of problems need we to explore. How to decrease the response time? How to achieve the long-term storage, and how to improve the loading uniformity and fastness are still waiting for us to figure out. Furthermore, the structure of nanofibers also need further regulate. For instance,
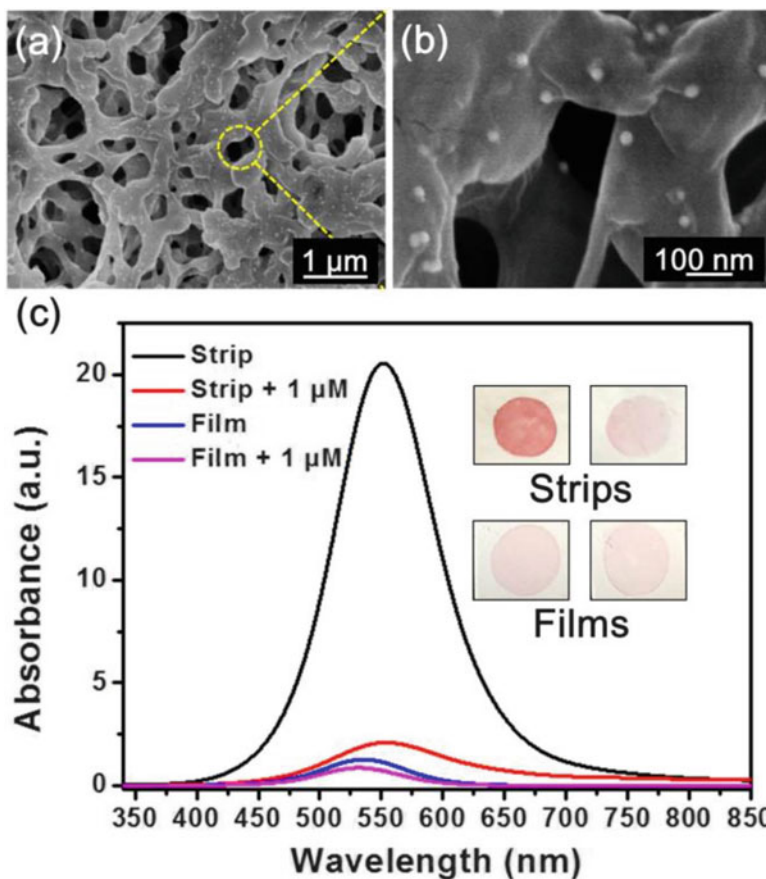
Fig. 1.15 UV-vis spectra and colorimetric responses of the colorimetric strips and commercial NC films having been incubated in two leaching liquors added with 0 and 1 μM Pb^{2+}, respectively (Reprinted with permission from [110]. © 2013 Elsevier Ltd)

high porosity and large SSA. Moving forward, it is reasonable to believe the electrospun nanofiber-based sensors may throw a light on the development of sensors in future.

References

1. C.D. Holmes, Air pollution and forest water use. Nature **507**(7491), E1–E2 (2014). doi:10. 1038/nature13113

2. C.C. Macpherson, Climate change matters. J. Med. Ethics **40**(4), 288–290 (2014). doi:10. 1136/medethics-2012-101084

3. S. Rodrıguez, X. Querol, A. Alastuey, M.-M. Viana, M. Alarcón, E. Mantilla, C.R. Ruiz, Comparative PM10–PM2.5 source contribution study at rural, urban and industrial sites during PM episodes in Eastern Spain. Sci. Total Environ. **328**(1–3), 95–113 (2004). doi: http://dx.doi.org/10.1016/S0048-9697(03)00411-X

4. M. Kampa, E. Castanas, Human health effects of air pollution. Environ. Pollut. **151**(2), 362–367 (2008). doi:http://dx.doi.org/10.1016/j.envpol.2007.06.012

5. P.D. Noyes, M.K. McElwee, H.D. Miller, B.W. Clark, L.A. Van Tiem, K.C. Walcott, K.N. Erwin, E.D. Levin, The toxicology of climate change: environmental contaminants in a warming world. Environ. Int. **35**(6), 971–986 (2009). doi:http://dx.doi.org/10.1016/j.envint. 2009.02.006

6. W. Gan, M. Koehoorn, H. Davies, P. Demers, L. Tamburic, M. Brauer, Long-term exposure to traffic-related air pollution and the risk of coronary heart disease hospitalization and mortality. Epidemiology **22**(1), S30 (2011). doi:10.1097/1001.ede.0000391750. 0000338925.0000391750f

7. P. Brown, *Toxic Exposures: Contested Illnesses and the Environmental Health Movement* (Columbia University Press, New York, 2013)

8. F. Fu, Q. Wang, Removal of heavy metal ions from wastewaters: a review. J. Environ. Manage. **92**(3), 407–418 (2011). doi:http://dx.doi.org/10.1016/j.jenvman.2010.11.011

9. B. Wei, L. Yang, A review of heavy metal contaminations in urban soils, urban road dusts and agricultural soils from China. Microchem. J. **94**(2), 99–107 (2010). doi:http://dx.doi.org/10. 1016/j.microc.2009.09.014

10. C. Luo, C. Liu, Y. Wang, X. Liu, F. Li, G. Zhang, X. Li, Heavy metal contamination in soils and vegetables near an e-waste processing site, south China. J. Hazard. Mater. **186**(1), 481–490 (2011). doi:http://dx.doi.org/10.1016/j.jhazmat.2010.11.024

11. B.R. Gurjar, A. Jain, A. Sharma, A. Agarwal, P. Gupta, A.S. Nagpure, J. Lelieveld, Human health risks in megacities due to air pollution. Atmos. Environ. **44**(36), 4606–4613 (2010). doi:http://dx.doi.org/10.1016/j.atmosenv.2010.08.011

12. H. Kan, R. Chen, S. Tong, Ambient air pollution, climate change, and population health in China. Environ. Int. **42**(0), 10–19 (2012). doi:http://dx.doi.org/10.1016/j.envint.2011.03.003

13. M.H. Yu, H. Tsunoda, M. Tsunoda, *Environmental Toxicology: Biological and Health Effects of Pollutants*, 3rd edn. (Taylor & Francis, Boca Raton, 2011)

14. L.B. Lave, E.P. Seskin, *Air Pollution and Human Health* (Taylor & Francis, Boca Raton, 2013)

15. N.Z. Muller, R. Mendelsohn, W. Nordhaus, Environmental accounting for pollution in the United States economy. Am. Econ. Rev. **101**(5), 1649–1675 (2011). doi:10.1257/aer.101.5. 1649

16. T. Kjellstrom, A. Butler, R. Lucas, R. Bonita, Public health impact of global heating due to climate change: potential effects on chronic non-communicable diseases. Int. J. Public Health **55**(2), 97–103 (2010). doi:10.1007/s00038-009-0090-2

17. World Health Organization, UNICEF, Water Supply and Sanitation Collaborative Council, WHO/UNICEF Joint Water Supply and Sanitation Monitoring Programme, *Global Water Supply and Sanitation Assessment 2000 Report* (World Health Organization, Geneva, 2000)

18. Y.F. Lee, C.C. Huang, Colorimetric assay of lead ions in biological samples using a nanogold-based membrane. ACS Appl. Mater. Interfaces **3**(7), 2747–2754 (2011). doi:10. 1021/am200535s

19. T. Jasarevic, G. Thomas, N. Osseiran, 7 million premature deaths annually linked to air pollution (2014), http://www.who.int/mediacentre/news/releases/2014/air-pollution/en/

20. L.D. Zhang, X.S. Fang, Controlled growth and characterization methods of semiconductor nanomaterials. J. Nanosci. Nanotechnol. **8**(1), 149–201 (2008). doi:10.1166/jnn.2008.N02

21. R. Purkhart, A. Hillmann, R. Graupner, G. Becher, Detection of characteristic clusters in IMS-Spectrograms of exhaled air polluted with environmental contaminants. Int. J. Ion Mobil. Spectrom. **15**(2), 63–68 (2012). doi:10.1007/s12127-012-0090-4

22. A. Masiá, J. Campo, C. Blasco, Y. Picó, Ultra-high performance liquid chromatography–quadrupole time-of-flight mass spectrometry to identify contaminants in water: an insight on environmental forensics. J. Chromatogr. A **1345**(0), 86–97 (2014). doi:http://dx.doi.org/10.1016/j.chroma.2014.04.017

23. C. Arpa Şahin, M. Efeçınar, N. Şatıroğlu, Combination of cloud point extraction and flame atomic absorption spectrometry for preconcentration and determination of nickel and manganese ions in water and food samples. J. Hazard. Mater. **176**(1–3), 672–677 (2010). doi:http://dx.doi.org/10.1016/j.jhazmat.2009.11.084

24. J.C. Van Loon, *Analytical Atomic Absorption Spectroscopy: Selected Methods* (Academic, New York, 1980)

25. K.C. Armstrong, C.E. Tatum, R.N. Dansby-Sparks, J.Q. Chambers, Z.-L. Xue, Individual and simultaneous determination of lead, cadmium, and zinc by anodic stripping voltammetry at a bismuth bulk electrode. Talanta **82**(2), 675–680 (2010). doi:http://dx.doi.org/10.1016/j.talanta.2010.05.031

26. Z. Bi, P. Salaün, C.M.G. van den Berg, Study of bare and mercury-coated vibrated carbon, gold and silver microwire electrodes for the determination of lead and cadmium in seawater by anodic stripping voltammetry. Electroanalysis **25**(2), 357–366 (2013). doi:10.1002/elan.201200446

27. A. Cavazzini, L. Pasti, A. Massi, N. Marchetti, F. Dondi, Recent applications in chiral high performance liquid chromatography: a review. Anal. Chim. Acta **706**(2), 205–222 (2011). doi:http://dx.doi.org/10.1016/j.aca.2011.08.038

28. T. Wagner, S. Haffer, C. Weinberger, D. Klaus, M. Tiemann, Mesoporous materials as gas sensors. Chem. Soc. Rev. **42**(9), 4036–4053 (2013). doi:10.1039/C2CS35379B

29. A. Afzal, N. Iqbal, A. Mujahid, R. Schirhagl, Advanced vapor recognition materials for selective and fast responsive surface acoustic wave sensors: a review. Anal. Chim. Acta **787**(0), 36–49 (2013). doi:http://dx.doi.org/10.1016/j.aca.2013.05.005

30. A.N. Uglov, A. Bessmertnykh-Lemeune, R. Guilard, A.D. Averin, I.P. Beletskaya, Optical methods for the detection of heavy metal ions. Russ. Chem. Rev. **83**(3), 196 (2014)

31. A. Allouch, S. Le Calvé, C.A. Serra, Portable, miniature, fast and high sensitive real-time analyzers: BTEX detection. Sens. Actuators B **182**(0), 446–452 (2013). doi:http://dx.doi.org/10.1016/j.snb.2013.03.010

32. A. Wilson, Diverse applications of electronic-nose technologies in agriculture and forestry. Sensors **13**(2), 2295–2348 (2013)

33. F. Long, A. Zhu, H. Shi, Recent advances in optical biosensors for environmental monitoring and early warning. Sensors **13**(10), 13928–13948 (2013)

34. S. Su, W. Wu, J. Gao, J. Lu, C. Fan, Nanomaterials-based sensors for applications in environmental monitoring. J. Mater. Chem. **22**(35), 18101–18110 (2012). doi:10.1039/C2JM33284A

35. L. Zhang, M. Fang, Nanomaterials in pollution trace detection and environmental improvement. Nano Today **5**(2), 128–142 (2010). doi:http://dx.doi.org/10.1016/j.nantod.2010.03.002

36. A. Vaseashta, M. Vaclavikova, S. Vaseashta, G. Gallios, P. Roy, O. Pummakarnchana, Nanostructures in environmental pollution detection, monitoring, and remediation. Sci. Technol. Adv. Mater. **8**(1–2), 47 (2007)

37. B.S. Kim, I.S. Kim, Recent nanofiber technologies. Polym. Rev. **51**(3), 235–238 (2011). doi:10.1080/15583724.2011.599507

38. J. Miao, M. Miyauchi, T.J. Simmons, J.S. Dordick, R.J. Linhardt, Electrospinning of nanomaterials and applications in electronic components and devices. J. Nanosci. Nanotechnol. **10**(9), 5507–5519 (2010). doi:10.1166/jnn.2010.3073

39. B. Ding, M. Wang, J. Yu, G. Sun, Gas sensors based on electrospun nanofibers. Sensors **9**(3), 1609–1624 (2009). doi:10.3390/s90301609

40. D. Li, Y. Xia, Electrospinning of nanofibers: reinventing the wheel? Adv. Mater. **16**(14), 1151–1170 (2004). doi:10.1002/adma.200400719

41. H.R. Darrell, C. Iksoo, Nanometre diameter fibres of polymer, produced by electrospinning. Nanotechnology **7**(3), 216 (1996)

42. P. Zahedi, I. Rezaeian, S.-O. Ranaei-Siadat, S.-H. Jafari, P. Supaphol, A review on wound dressings with an emphasis on electrospun nanofibrous polymeric bandages. Polym. Adv. Technol. **21**(2), 77–95 (2010). doi:10.1002/pat.1625

43. M. Inagaki, Y. Yang, F. Kang, Carbon nanofibers prepared via electrospinning. Adv. Mater. **24**(19), 2547–2566 (2012). doi:10.1002/adma.201104940

44. P. Ramesh Kumar, N. Khan, S. Vivekanandhan, N. Satyanarayana, A.K. Mohanty, M. Misra, Nanofibers: effective generation by electrospinning and their applications. J. Nanosci. Nanotechnol. **12**(1), 1–25 (2012). doi:10.1166/jnn.2012.5111

45. W.D. Luedtke, U. Landman, Y.H. Chiu, D.J. Levandier, R.A. Dressler, S. Sok, M.S. Gordon, Nanojets, electrospray, and ion field evaporation: molecular dynamics simulations and laboratory experiments. J. Phys. Chem. A **112**(40), 9628–9649 (2008). doi:10.1021/jp804585y

46. N. Bhardwaj, S.C. Kundu, Electrospinning: a fascinating fiber fabrication technique. Biotechnol. Adv. **28**(3), 325–347 (2010). doi:http://dx.doi.org/10.1016/j.biotechadv.2010.01.004

47. B. Ding, H.Y. Kim, S.C. Lee, D.R. Lee, K.J. Choi, Preparation and characterization of nanoscaled poly(vinyl alcohol) fibers via electrospinning. Fibers and Polymers **3**(2), 73–79 (2002). doi:10.1007/BF02875403

48. B. Kim, H. Park, S.H. Lee, W.M. Sigmund, Poly(acrylic acid) nanofibers by electrospinning. Mater. Lett. **59**(7), 829–832 (2005). doi:http://dx.doi.org/10.1016/j.matlet.2004.11.032

49. X. Li, L. Lin, Y. Zhu, W. Liu, T. Yu, M. Ge, Preparation of ultrafine fast-dissolving cholecalciferol-loaded poly(vinyl pyrrolidone) fiber mats via electrospinning. Polym. Compos. **34**(2), 282–287 (2013). doi:10.1002/pc.22402

50. C. Chen, L. Wang, Y. Huang, Electrospinning of thermo-regulating ultrafine fibers based on polyethylene glycol/cellulose acetate composite. Polymer **48**(18), 5202–5207 (2007). doi:http://dx.doi.org/10.1016/j.polymer.2007.06.069

51. D. Li, Y. Xia, Fabrication of titania nanofibers by electrospinning. Nano Lett. **3**(4), 555–560 (2003). doi:10.1021/nl034039o

52. A. Nikfarjam, S. Fardindoost, A. Iraji zad, Fabrication of Pd Doped WO3 nanofiber as hydrogen sensor. Polymers **5**(1), 45–55 (2013)

53. M. Fan, W. Hui, Z. Li, Z. Shen, H. Li, A. Jiang, Y. Chen, R. Liu, Fabrication and piezoresponse of electrospun ultra-fine $Pb(Zr_{0.3}, Ti_{0.7})O_3$ nanofibers. Microelectron. Eng. **98**(0), 371–373 (2012). doi:http://dx.doi.org/10.1016/j.mee.2012.07.026

54. L. Deng, R.J. Young, I.A. Kinloch, Y. Zhu, S.J. Eichhorn, Carbon nanofibres produced from electrospun cellulose nanofibres. Carbon **58**(0), 66–75 (2013). doi:http://dx.doi.org/10.1016/j.carbon.2013.02.032

55. H. Yan, N.K. Mahanta, B. Wang, S. Wang, A.R. Abramson, M. Cakmak, Structural evolution in graphitization of nanofibers and mats from electrospun polyimide–mesophase pitch blends. Carbon **71**(0), 303–318 (2014). doi:http://dx.doi.org/10.1016/j.carbon.2014.01.057

56. Y. Si, T. Ren, Y. Li, B. Ding, J. Yu, Fabrication of magnetic polybenzoxazine-based carbon nanofibers with Fe3O4 inclusions with a hierarchical porous structure for water treatment. Carbon **50**(14), 5176–5185 (2012). doi:http://dx.doi.org/10.1016/j.carbon.2012.06.059

57. A. Khalil, R. Hashaikeh, M. Jouiad, Synthesis and morphology analysis of electrospun copper nanowires. J. Mater. Sci. **49**(8), 3052–3065 (2014). doi:10.1007/s10853-013-8005-2

58. V. Thavasi, G. Singh, S. Ramakrishna, Electrospun nanofibers in energy and environmental applications. Energy Environ. Sci. **1**(2), 205–221 (2008). doi:10.1039/B809074M

59. D. Bin, Y. Jianyong, *Electrospinning and Nanofibers* (China Textile & Apparel Press, Beijing, 2011)
60. C. Tran, V. Kalra, Co-continuous nanoscale assembly of Nafion-polyacrylonitrile blends within nanofibers: a facile route to fabrication of porous nanofibers. Soft Matter **9**(3), 846–852 (2013). doi:10.1039/C2SM25976A
61. Y. Yao, W. Yin, J. Cao, M. Yang, J. Li, S. Zhao, Y. Li, X. He, J. Leng, Manipulation and formation mechanism of silica one-dimensional periodic structures by roller electrospinning. Langmuir **30**(9), 2335–2345 (2014). doi:10.1021/la4037277
62. Q. Du, D.R. Harding, H. Yang, Helical peanut-shaped poly(vinyl pyrrolidone) ribbons generated by electrospinning. Polymer **54**(25), 6752–6759 (2013). doi:http://dx.doi.org/10.1016/j.polymer.2013.10.029
63. S. Li, J. Leng, Y. Fan, C. Fu, H. Shen, Y. Xue, D. Xu, Electrospinning synthesis and structural characterization of manganese oxyborate (Mn2OBO3) necklace-like nanofibers. Phys. Status Solidi A **208**(1), 114–117 (2011). doi:10.1002/pssa.201026499
64. J. Li, K.I. Lee, X. Lu, S. Bao, T. Hua, J.H. Xin, B. Fei, In-situ growth of pine-needle-like tungsten oxide nanowire arrays on carbon nanofibers. Mater. Lett. **99**(0), 131–133 (2013). doi:http://dx.doi.org/10.1016/j.matlet.2013.02.077
65. Z. Chang, "Firecracker-shaped" ZnO/polyimide hybrid nanofibers viaelectrospinning and hydrothermal process. Chem. Commun. **47**(15), 4427–4429 (2011). doi:10.1039/C0CC05634K
66. H.-Y. Chen, T.-L. Zhang, J. Fan, D.-B. Kuang, C.-Y. Su, Electrospun hierarchical TiO2 nanorods with high porosity for efficient dye-sensitized solar cells. ACS Appl. Mater. Interfaces **5**(18), 9205–9211 (2013). doi:10.1021/am402853q
67. H. Chen, N. Wang, J. Di, Y. Zhao, Y. Song, L. Jiang, Nanowire-in-microtube structured core/shell fibers via multifluidic coaxial electrospinning. Langmuir **26**(13), 11291–11296 (2010). doi:10.1021/la100611f
68. F. Mou, J.-G. Guan, W. Shi, Z. Sun, S. Wang, Oriented contraction: a facile nonequilibrium heat-treatment approach for fabrication of maghemite fiber-in-tube and tube-in-tube nanostructures. Langmuir **26**(19), 15580–15585 (2010). doi:10.1021/la102830p
69. J. Lin, B. Ding, J. Yang, J. Yu, G. Sun, Subtle regulation of the micro- and nanostructures of electrospun polystyrene fibers and their application in oil absorption. Nanoscale **4**(1), 176–182 (2012). doi:10.1039/c1nr10895f
70. D. Li, Y. Xia, Direct fabrication of composite and ceramic hollow nanofibers by electrospinning. Nano Lett. **4**(5), 933–938 (2004). doi:10.1021/nl049590f
71. J. Lin, B. Ding, J. Yu, Y. Hsieh, Direct fabrication of highly nanoporous polystyrene fibers via electrospinning. ACS Appl. Mater. Interfaces **2**(2), 521–528 (2010). doi:10.1021/am900736h
72. B. Ding, M. Wang, X. Wang, J. Yu, G. Sun, Electrospun nanomaterials for ultrasensitive sensors. Mater. Today **13**(11), 16–27 (2010). doi:http://dx.doi.org/10.1016/S1369-7021(10)70200-5
73. J. Wu, N. Wang, Y. Zhao, L. Jiang, Electrospinning of multilevel structured functional micro-/nanofibers and their applications. J. Mater. Chem. A **1**(25), 7290–7305 (2013). doi:10.1039/C3TA10451F
74. D. Li, Y. Wang, Y. Xia, Electrospinning of polymeric and ceramic nanofibers as uniaxially aligned arrays. Nano Lett. **3**(8), 1167–1171 (2003). doi:10.1021/nl0344256
75. S.J. Cho, B. Kim, T. An, G. Lim, Replicable multilayered nanofibrous patterns on a flexible film. Langmuir **26**(18), 14395–14399 (2010). doi:10.1021/la102467u
76. D. Zhang, J. Chang, Patterning of electrospun fibers using electroconductive templates. Adv. Mater. **19**(21), 3664–3667 (2007). doi:10.1002/adma.200700896
77. M. Abbasipour, R. Khajavi, Nanofiber bundles and yarns production by electrospinning: a review. Adv. Polym. Technol. **32**(3), n/a–n/a (2013). doi:10.1002/adv.21363
78. G. Sun, D. Wei, X. Liu, Y. Chen, M. Li, D. He, J. Zhong, Novel biodegradable electrospun nanofibrous P(DLLA-CL) balloons for the treatment of vertebral compression fractures.

Nanomed. Nanotechnol. Biol. Med.. **9**(6), 829–838 (2013). doi:http://dx.doi.org/10.1016/j.nano.2012.12.003

79. A.M. Behrens, B.J. Casey, M.J. Sikorski, K.L. Wu, W. Tutak, A.D. Sandler, P. Kofinas, In situ deposition of PLGA nanofibers via solution blow spinning. ACS Macro Lett. **3**(3), 249–254 (2014). doi:10.1021/mz500049x

80. D. Ahirwal, A. Hebraud, R. Kadar, M. Wilhelm, G. Schlatter, From self-assembly of electrospun nanofibers to 3D cm thick hierarchical foams. Soft Matter **9**(11), 3164–3172 (2013). doi:10.1039/C2SM27543K

81. J. He, Y. Zhou, K. Qi, L. Wang, P. Li, S. Cui, Continuous twisted nanofiber yarns fabricated by double conjugate electrospinning. Fibers Polym. **14**(11), 1857–1863 (2013). doi:10.1007/s12221-013-1857-x

82. T. Wee-Eong, I. Ryuji, R. Seeram, Technological advances in electrospinning of nanofibers. Sci. Technol. Adv. Mater. **12**(1), 013002 (2011)

83. B. Ding, X. Wang, J. Yu, M. Wang, Polyamide 6 composite nano-fiber/net functionalized by polyethyleneimine on quartz crystal microbalance for highly sensitive formaldehyde sensors. J. Mater. Chem. **21**(34), 12784–12792 (2011). doi:10.1039/c1jm11847a

84. K. Lin, K.-N. Chua, G.T. Christopherson, S. Lim, H.-Q. Mao, Reducing electrospun nanofiber diameter and variability using cationic amphiphiles. Polymer **48**(21), 6384–6394 (2007). doi:http://dx.doi.org/10.1016/j.polymer.2007.08.056

85. H. Chaobo, C. Shuiliang, L. Chuilin, H.R. Darrell, Q. Haiyan, Y. Ying, H. Haoqing, Electrospun polymer nanofibres with small diameters. Nanotechnology **17**(6), 1558 (2006). doi:10.1088/0957-4484/17/6/004

86. X. Wang, B. Ding, G. Sun, M. Wang, J. Yu, Electro-spinning/netting: a strategy for the fabrication of three-dimensional polymer nano-fiber/nets. Prog. Mater. Sci. **58**(8), 1173–1243 (2013). doi:http://dx.doi.org/10.1016/j.pmatsci.2013.05.001

87. X. Wang, J. Wang, Y. Si, B. Ding, J. Yu, G. Sun, W. Luo, G. Zheng, Nanofiber-net-binary structured membranes for highly sensitive detection of trace HCl gas. Nanoscale **4**(23), 7585–7592 (2012). doi:10.1039/c2nr32730a

88. N.A.M. Barakat, M.A. Kanjwal, F.A. Sheikh, H.Y. Kim, Spider-net within the N6, PVA and PU electrospun nanofiber mats using salt addition: novel strategy in the electrospinning process. Polymer **50**(18), 4389–4396 (2009). doi:http://dx.doi.org/10.1016/j.polymer.2009.07.005

89. H.R. Pant, M.P. Bajgai, K.T. Nam, K.H. Chu, S.-J. Park, H.Y. Kim, Formation of electrospun nylon-6/methoxy poly(ethylene glycol) oligomer spider-wave nanofibers. Mater. Lett. **64**(19), 2087–2090 (2010). doi:http://dx.doi.org/10.1016/j.matlet.2010.06.047

90. H.R. Pant, M.P. Bajgai, C. Yi, R. Nirmala, K.T. Nam, W.-i. Baek, H.Y. Kim, Effect of successive electrospinning and the strength of hydrogen bond on the morphology of electrospun nylon-6 nanofibers. Colloids Surf. A Physicochem. Eng. Asp. **370**(1–3), 87–94 (2010). doi:http://dx.doi.org/10.1016/j.colsurfa.2010.08.051

91. S.Y. Tsou, H.S. Lin, C. Wang, Studies on the electrospun Nylon 6 nanofibers from polyelectrolyte solutions: 1. Effects of solution concentration and temperature. Polymer **52**(14), 3127–3136 (2011). doi:http://dx.doi.org/10.1016/j.polymer.2011.05.010

92. B. Ding, C. Li, Y. Miyauchi, O. Kuwaki, S. Shiratori, Formation of novel 2D polymer nanowebs via electrospinning. Nanotechnology **17**(15), 3685–3691 (2006). doi:10.1088/0957-4484/17/15/011

93. C. Mit-uppatham, M. Nithitanakul, P. Supaphol, Ultrafine electrospun polyamide-6 fibers: effect of solution conditions on morphology and average fiber diameter. Macromol. Chem. Phys. **205**(17), 2327–2338 (2004). doi:10.1002/macp.200400225

94. R.P.A. Hartman, D.J. Brunner, D.M.A. Camelot, J.C.M. Marijnissen, B. Scarlett, Jet break-up in electrohydrodynamic atomization in the cone-jet mode. J. Aerosol Sci. **31**(1), 65–95 (2000). doi:http://dx.doi.org/10.1016/S0021-8502(99)00034-8

95. R.L. Grimm, J.L. Beauchamp, Dynamics of field-induced droplet ionization: time-resolved studies of distortion, jetting, and progeny formation from charged and neutral methanol

droplets exposed to strong electric fields. J. Phys. Chem. B **109**(16), 8244–8250 (2005). doi:10.1021/jp0450540

96. J. Hu, X. Wang, B. Ding, J. Lin, J. Yu, G. Sun, One-step electro-spinning/netting technique for controllably preparing polyurethane nano-fiber/net. Macromol. Rapid Commun. **32**(21), 1729–1734 (2011). doi:10.1002/marc.201100343

97. X. Wang, B. Ding, J. Yu, Y. Si, S. Yang, G. Sun, Electro-netting: fabrication of two-dimensional nano-nets for highly sensitive trimethylamine sensing. Nanoscale **3**(3), 911–915 (2011). doi:10.1039/c0nr00783h

98. S. Yang, X. Wang, B. Ding, J. Yu, J. Qian, G. Sun, Controllable fabrication of soap-bubble-like structured polyacrylic acid nano-nets via electro-netting. Nanoscale **3**(2), 564–568 (2011). doi:10.1039/c0nr00730g

99. X. Wang, B. Ding, J. Yu, M. Wang, Highly sensitive humidity sensors based on electro-spinning/netting a polyamide 6 nano-fiber/net modified by polyethyleneimine. J. Mater. Chem. **21**(40), 16231–16238 (2011). doi:10.1039/c1jm13037d

100. X. Wang, Y. Si, J. Wang, B. Ding, J. Yu, S.S. Al-Deyab, A facile and highly sensitive colorimetric sensor for the detection of formaldehyde based on electro-spinning/netting nano-fiber/nets. Sens Actuators B Chem. **163**(1), 186–193 (2012). doi:10.1016/j.snb.2012.01.033

101. N. Wang, X. Wang, B. Ding, J. Yu, G. Sun, Tunable fabrication of three-dimensional polyamide-66 nano-fiber/nets for high efficiency fine particulate filtration. J. Mater. Chem. **22**(4), 1445–1452 (2012). doi:10.1039/c1jm14299b

102. X. Wang, B. Ding, J. Yu, M. Wang, F. Pan, A highly sensitive humidity sensor based on a nanofibrous membrane coated quartz crystal microbalance. Nanotechnology **21**(5), 055502 (2010). doi:10.1088/0957-4484/21/5/055502

103. N. Wang, X. Wang, Y. Jia, X. Li, J. Yu, B. Ding, Electrospun nanofibrous chitosan membranes modified with polyethyleneimine for formaldehyde detection. Carbohydr. Polym. **108**(0), 192–199 (2014). doi:http://dx.doi.org/10.1016/j.carbpol.2014.02.088

104. X. Wang, B. Ding, J. Yu, J. Yang, Large-scale fabrication of two-dimensional spider-web-like gelatin nano-nets via electro-netting. Colloids Surf. B Biointerfaces **86**(2), 345–352 (2011). doi:http://dx.doi.org/10.1016/j.colsurfb.2011.04.018

105. D.C. Parajuli, M.P. Bajgai, J.A. Ko, H.K. Kang, M.S. Khil, H.Y. Kim, Synchronized polymerization and fabrication of poly(acrylic acid) and nylon hybrid mats in electrospinning. ACS Appl. Mater. Interfaces **1**(4), 750–757 (2009). doi:10.1021/am800191m

106. R. Nirmala, R. Navamathavan, M.H. El-Newehy, H.Y. Kim, Preparation and electrical characterization of polyamide-6/chitosan composite nanofibers via electrospinning. Mater. Lett. **65**(3), 493–496 (2011). doi:http://dx.doi.org/10.1016/j.matlet.2010.10.066

107. R. Nirmala, R. Navamathavan, H.-S. Kang, M.H. El-Newehy, H.Y. Kim, Preparation of polyamide-6/chitosan composite nanofibers by a single solvent system via electrospinning for biomedical applications. Colloids Surf. B Biointerfaces **83**(1), 173–178 (2011). doi:http://dx.doi.org/10.1016/j.colsurfb.2010.11.026

108. B. Ding, Y. Si, X. Wang, J. Yu, L. Feng, G. Sun, Label-free ultrasensitive colorimetric detection of copper(II) ions utilizing polyaniline/polyamide-6 nano-fiber/net sensor strips. J. Mater. Chem. **21**(35), 13345–13353 (2011). doi:10.1039/c1jm11851j

109. Y. Si, X. Wang, Y. Li, K. Chen, J. Wang, J. Yu, H. Wang, B. Ding, Optimized colorimetric sensor strip for mercury(ii) assay using hierarchical nanostructured conjugated polymers. J. Mater. Chem. A **2**(3), 645–652 (2014). doi:10.1039/c3ta13867d

110. Y. Li, Y. Si, X. Wang, B. Ding, G. Sun, G. Zheng, W. Luo, J. Yu, Colorimetric sensor strips for lead (II) assay utilizing nanogold probes immobilized polyamide-6/nitrocellulose nano-fibers/nets. Biosens. Bioelectron. **48**(0), 244–250 (2013). doi:http://dx.doi.org/10.1016/j.bios.2013.03.085

111. C.K. O'Sullivan, G.G. Guilbault, Commercial quartz crystal microbalances – theory and applications. Biosens. Bioelectron. **14**(8–9), 663–670 (1999). doi:http://dx.doi.org/10.1016/S0956-5663(99)00040-8

112. B. Ding, J.H. Kim, Y. Miyazaki, S.M. Shiratori, Electrospun nanofibrous membranes coated quartz crystal microbalance as gas sensor for NH3 detection. Sens Actuators B Chem. **101**(3), 373–380 (2004). doi:10.1016/j.snb.2004.04.008

113. B. Ding, M. Yamazaki, S. Shiratori, Electrospun fibrous polyacrylic acid membrane-based gas sensors. Sens Actuators B Chem. **106**(1), 477–483 (2005). doi:10.1016/j.snb.2004.09.010

114. S. Casilli, C. Malitesta, S. Conoci, S. Petralia, S. Sortino, L. Valli, Piezoelectric sensor functionalised by a self-assembled bipyridinium derivative: characterisation and preliminary applications in the detection of heavy metal ions. Biosens. Bioelectron. **20**(6), 1190–1195 (2004). doi:http://dx.doi.org/10.1016/j.bios.2004.04.028

115. A.J. Ricco, R.M. Crooks, G.C. Osbourn, Surface acoustic wave chemical sensor arrays: new chemically sensitive interfaces combined with novel cluster analysis to detect volatile organic compounds and mixtures. Acc. Chem. Res. **31**(5), 289–296 (1998). doi:10.1021/ar9600749

116. A. Palaniappan, X. Li, F.E.H. Tay, J. Li, X. Su, Cyclodextrin functionalized mesoporous silica films on quartz crystal microbalance for enhanced gas sensing. Sens. Actuators B **119**(1), 220–226 (2006). doi:http://dx.doi.org/10.1016/j.snb.2005.12.015

117. C. Zhang, X. Wang, J. Lin, B. Ding, J. Yu, N. Pan, Nanoporous polystyrene fibers functionalized by polyethyleneimine for enhanced formaldehyde sensing. Sens. Actuators B **152**(2), 316–323 (2011). doi:http://dx.doi.org/10.1016/j.snb.2010.12.028

118. Y.I. Korpan, M.V. Gonchar, A.A. Sibirny, C. Martelet, A.V. El'skaya, T.D. Gibson, A.P. Soldatkin, Development of highly selective and stable potentiometric sensors for formaldehyde determination. Biosens. Bioelectron. **15**(1–2), 77–83 (2000). doi:http://dx.doi.org/10.1016/S0956-5663(00)00054-3

119. R. Kataky, M.R. Bryce, L. Goldenberg, S. Hayes, A. Nowak, A biosensor for monitoring formaldehyde using a new lipophilic tetrathiafulvalene-tetracyanoquinodimethane salt and a polyurethane membrane. Talanta **56**(3), 451–458 (2002). doi:http://dx.doi.org/10.1016/S0039-9140(01)00567-7

120. X. Wang, F. Cui, J. Lin, B. Ding, J. Yu, S.S. Al-Deyab, Functionalized nanoporous TiO2 fibers on quartz crystal microbalance platform for formaldehyde sensor. Sens. Actuators B **171–172**, 658–665 (2012). doi:10.1016/j.snb.2012.05.050

121. P.-R. Chung, C.-T. Tzeng, M.-T. Ke, C.-Y. Lee, Formaldehyde gas sensors: a review. Sensors **13**(4), 4468–4484 (2013). doi:10.3390/s130404468

122. S. Srisuda, B. Virote, Adsorption of formaldehyde vapor by amine-functionalized mesoporous silica materials. J. Environ. Sci. **20**(3), 379–384 (2008). doi:http://dx.doi.org/10.1016/S1001-0742(08)60059-5

123. V.V. Sysoev, J. Goschnick, T. Schneider, E. Strelcov, A. Kolmakov, A gradient microarray electronic nose based on percolating SnO2 nanowire sensing elements. Nano Lett. **7**(10), 3182–3188 (2007)

124. J. Huang, Q. Wan, Gas sensors based on semiconducting metal oxide one-dimensional nanostructures. Sensors **9**(12), 9903–9924 (2009). doi:10.3390/s91209903

125. S. Bag, I.U. Arachchige, M.G. Kanatzidis, Aerogels from metal chalcogenides and their emerging unique properties. J. Mater. Chem. **18**(31), 3628–3632 (2008). doi:10.1039/B804011G

126. R. Liang, H. Cao, D. Qian, MoO3 nanowires as electrochemical pseudocapacitor materials. Chem. Commun. **47**(37), 10305–10307 (2011). doi:10.1039/C1CC14030B

127. M. Kimura, R. Sakai, S. Sato, T. Fukawa, T. Ikehara, R. Maeda, T. Mihara, Sensing of vaporous organic compounds by TiO₂ porous films covered with polythiophene layers. Adv. Funct. Mater. **22**(3), 469–476 (2012). doi:10.1002/adfm.201101953

128. A.W. Martinez, S.T. Phillips, M.J. Butte, G.M. Whitesides, Patterned paper as a platform for inexpensive, low-volume, portable bioassays. Angew. Chem. Int. Ed. **46**(8), 1318–1320 (2007). doi:10.1002/anie.200603817

129. A.W. Martinez, S.T. Phillips, G.M. Whitesides, E. Carrilho, Diagnostics for the developing world: microfluidic paper-based analytical devices. Anal. Chem. **82**(1), 3–10 (2009). doi:10.1021/ac9013989

130. W. Zhao, M.M. Ali, S.D. Aguirre, M.A. Brook, Y. Li, Paper-based bioassays using gold nanoparticle colorimetric probes. Anal. Chem. **80**(22), 8431–8437 (2008). doi:10.1021/ac801008q

131. R. Pelton, Bioactive paper provides a low-cost platform for diagnostics. TrAC Trends Anal. Chem. **28**(8), 925–942 (2009). doi:http://dx.doi.org/10.1016/j.trac.2009.05.005

132. X. Wang, Y. Si, X. Mao, Y. Li, J. Yu, H. Wang, B. Ding, Colorimetric sensor strips for formaldehyde assay utilizing fluoral-p decorated polyacrylonitrile nanofibrous membranes. Analyst **138**(17), 5129–5136 (2013). doi:10.1039/c3an00812f

133. S. Mukherjee, J.W. Yang, S. Hoffmann, B. List, Asymmetric enamine catalysis. Chem. Rev. **107**(12), 5471–5569 (2007). doi:10.1021/cr0684016

134. B.C. Ye, B.C. Yin, Highly sensitive detection of mercury(II) ions by fluorescence polarization enhanced by gold nanoparticles. Angew. Chem. Int. Ed. **47**(44), 8386–8389 (2008). doi:10.1002/anie.200803069

135. M. Zhang, L. Ge, S. Ge, M. Yan, J. Yu, J. Huang, S. Liu, Three-dimensional paper-based electrochemiluminescence device for simultaneous detection of Pb^{2+} and Hg^{2+} based on potential-control technique. Biosens. Bioelectron. **41**(0), 544–550 (2013). doi:http://dx.doi.org/10.1016/j.bios.2012.09.022

136. C.X. Tang, Y. Zhao, X.W. He, X.B. Yin, A "turn-on" electrochemiluminescent biosensor for detecting Hg2+ at femtomole level based on the intercalation of $Ru(phen)_3^{2+}$ into ds-DNA. Chem. Commun. **46**(47), 9022–9024 (2010). doi:10.1039/C0CC03495A

137. J. Liu, Y. Lu, Rational design of "turn-on" allosteric DNAzyme catalytic beacons for aqueous mercury ions with ultrahigh sensitivity and selectivity. Angew. Chem. Int. Ed. **46**(40), 7587–7590 (2007). doi:10.1002/anie.200702006

138. H.S. Kolla, S.P. Surwade, X. Zhang, A.G. MacDiarmid, S.K. Manohar, Absolute molecular weight of polyaniline. J. Am. Chem. Soc. **127**(48), 16770–16771 (2005). doi:10.1021/ja055327k

139. C. Alemán, C.A. Ferreira, J. Torras, A. Meneguzzi, M. Canales, M.A.S. Rodrigues, J. Casanovas, On the molecular properties of polyaniline: a comprehensive theoretical study. Polymer **49**(23), 5169–5176 (2008). doi:http://dx.doi.org/10.1016/j.polymer.2008.09.023

140. A. Varela-Álvarez, J.A. Sordo, G.E. Scuseria, Doping of polyaniline by acid – base chemistry: density functional calculations with periodic boundary conditions. J. Am. Chem. Soc. **127** (32), 11318–11327 (2005). doi:10.1021/ja051012t

141. D.P. Pompeani, M.B. Abbott, B.A. Steinman, D.J. Bain, Lake sediments record prehistoric lead pollution related to early copper production in North America. Environ. Sci. Technol. **47** (11), 5545–5552 (2013). doi:10.1021/es304499c

142. H. Cheng, Y. Hu, Lead (Pb) isotopic fingerprinting and its applications in lead pollution studies in China: a review. Environ. Pollut. **158**(5), 1134–1146 (2010). doi:http://dx.doi.org/10.1016/j.envpol.2009.12.028

143. G. Li, L. Zhang, Z. Li, W. Zhang, PAR immobilized colorimetric fiber for heavy metal ion detection and adsorption. J. Hazard. Mater. **177**(1–3), 983–989 (2010). doi:http://dx.doi.org/10.1016/j.jhazmat.2010.01.015

144. L. Fewtrell, World Health Organization, R. Kaufmann, A. Prüss-Üstün, World Health Organization Protection of the Human Environment, *Lead: Assessing the Environmental Burden of Disease at National and Local Levels* (World Health Organization, Protection of the Human Environment, 2003), http://www.who.int/quantifying_ehimpacts/publications/en/leadebd2.pdf

145. M.G. Aylmore, Treatment of a refractory gold-copper sulfide concentrate by copper ammoniacal thiosulfate leaching. Miner. Eng. **14**(6), 615–637 (2001). doi:http://dx.doi.org/10.1016/S0892-6875(01)00057-7

146. G.H. Liu, J.Y. Yang, Content-based image retrieval using color difference histogram. Pattern Recogn. **46**(1), 188–198 (2013). doi:http://dx.doi.org/10.1016/j.patcog.2012.06.001

147. M.M. Hawkeye, M.J. Brett, Optimized colorimetric photonic-crystal humidity sensor fabricated using glancing angle deposition. Adv. Funct. Mater. **21**(19), 3652–3658 (2011). doi:10.1002/adfm.201100893

Chapter 2
Controlling the Nanostructure of Electrospun Polymeric Fibers

Israel Greenfeld and Eyal Zussman

Abstract The high strain rate extensional flow of a semi-dilute polymer solution can cause substantial stretching and disentanglement of the polymer network. In this study, we conducted a theoretical and experimental investigation of the effects of electrospinning, a flow governed by high strain rate and rapid evaporation, on the polymer matrix of the resulting nanofibers. Modeling of the dynamic evolution of the entangled polymer network in an electrospinning jet predicted substantial longitudinal stretching and radial contraction of the network, a transformation from an equilibrium state to an almost fully-stretched state. This prediction was verified by X-ray phase-contrast imaging of electrospinning jets, which revealed a noticeable increase in polymer concentration at the jet center, within a short distance from the jet start. Additionally, polymer entanglement loss in consequence of stretching was evidenced in jet fragmentation and appearance of short nanofibers, affecting the entanglements density and molecular orientation of as-spun fibers. The stretching model was expanded to semi-flexible conjugated polymer chains, and scanning near field optical microscopy of electrospun nanofibers of such optically active polymers revealed that the network's dense elongated conformation effectively remains after jet solidification. By tuning the electrospinning conditions, the unique size-dependent properties of nanofibers can be controlled and improved, potentially leading to novel applications in engineering and life sciences.

I. Greenfeld (✉)
Department of Mechanical Engineering, Technion – Israel Institute of Technology, Haifa 32000, Israel

Department of Materials and Interfaces, Weizmann Institute of Science, Rehovot 76100, Israel
e-mail: green_is@netvision.net.il

E. Zussman
Department of Mechanical Engineering, Technion – Israel Institute of Technology, Haifa 32000, Israel

2.1 Introduction

Electrospinning has attracted considerable attention in the past decade as an accessible and scalable process for creating nanostructures. An electrospinning jet is created when a polymer solution is drawn from a capillary and stretched by the force of a strong electric field (Fig. 2.1), producing very thin fibers – nanofibers – of diameters ranging typically from 50 to 1,000 nm [1–4].

Electrospun polymeric nanofibers exhibit unique properties. For example, below a certain crossover diameter, dependent on the polymer molar mass, the nanofiber elastic moduli begin to rise sharply [5–11]. Similarly, in optically active polymers, the effective conjugation length of chromophores increases as a result of electrospinning, and their optical absorption and emission become polarized along the fiber axis [12, 13]. Better understanding of the mechanisms behind these phenomena can help improving the mechanical, electrical and optical properties of nanofibers, and can lead to novel applications in engineering and life sciences.

Electrospinning is an extensional flow characterized by high strain rates of order 10^3 s^{-1} [14–20]. Such stretching can potentially increase the structural order within as-spun nanofibers and enhance their mechanical properties such as elastic modulus
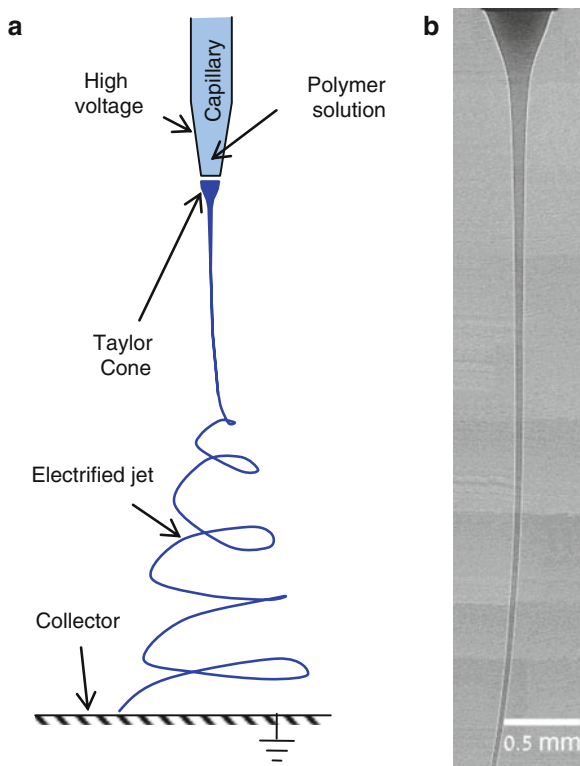
Fig. 2.1 (**a**) Schematics of the electrospinning setup and process. (**b**) Example of the rectilinear section of a jet (~5 mm length), imaged by fast phase-contrast X-ray. Conditions: molar mass 600 kDa PEO, concentration 5 wt% in water, electric field 0.6 kV/cm, flow rate 3.2 mL/h, electric field gap 6.5 cm
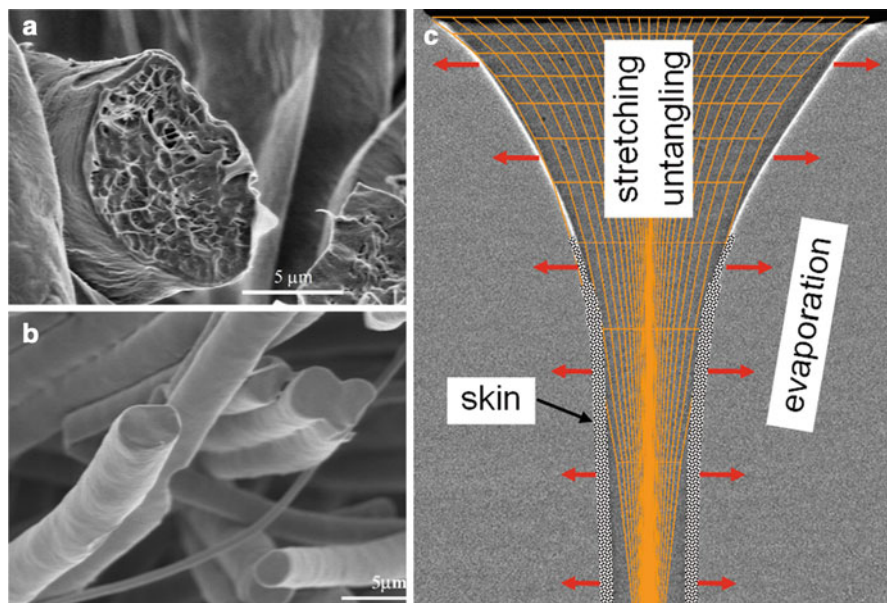
Fig. 2.2 Stretching and evaporation during electrospinning. (**a**)(**b**) SEM images of electrospun nanofibers of 10 wt% PCL with molar mass 80 kDa, dissolved in DCM/DMF (75:25 wt%), under an electric field of 0.63 kV/cm. (**a**) High flow rate of 20 ml/h resulting in heterogeneous fibers. (**b**) Low flow rate of 3 ml/h resulting in homogeneous fibers. (**c**) Illustration of stretching, untangling and evaporation effects [21]

and strength [5, 8–11, 21, 22]. At the same time, rapid solvent evaporation during electrospinning can lead to increased polymer concentrations at the jet boundary [23–26], sometimes forming a solid skin and a heterogeneous and porous structure [21, 25, 27]. The simultaneous effects of stretching and evaporation are illustrated in Fig. 2.2. Hence, study of electrospinning polymer solution jets, and specifically of the evolution of the polymer entangled network during electrospinning, is of interest in clarifying the microstructure of as-spun nanofibers.

The presentation in this text is broadly based on [12, 13, 21, 28–30]. In this study, modeling and random walk simulations of the dynamic evolution of the entangled polymer network in an electrospinning jet predicted substantial longitudinal stretching and radial contraction of the network, a transformation from an equilibrium state to an almost fully-stretched state [21]. This prediction was verified by fast X-ray phase-contrast imaging of electrospinning jets, which revealed a noticeable increase in polymer concentration at the jet center, as well as a concentration crossover within a short distance from the jet start [28].

Furthermore, modeling showed that polymer entanglement loss, due to network stretching under very high strain rates, reduces the fiber diameter and enhances the homogeneity and alignment of the nanostructure. This effect was evidenced by jet fragmentation and appearance of short nanofibers during extreme electrospinning conditions [29].

To examine whether the compact stretched network conformation remains after jet solidification, we electrospun MEH-PPV nanofibers. This conjugated semi-flexible optically active polymer has high absorption in the visible waveband, and is shown by the simulation to have a fast response to stretching owing to its long rigid segments. Scanning near field optical microscopy (SNOM) of such nanofibers at nano-resolution revealed a dense core with an increased elastic modulus [12], as well as an axial molecular alignment that affects the polarization of optical absorption and emission, which can be tuned [13].

The following sections expand on these findings and explain their meaning in the context of the question whether we can control and tune the nanostructure of electrospun fibers for the benefit of improving their properties.

2.2 Polymer Dynamics During Electrospinning

The flow of an electrospinning jet is viscoelastic and consists of axial and radial velocity components (Fig. 2.3). Analysis of electrically driven fluid jets has shown that the axial jet velocity v_z reaches an asymptotic regime sufficiently far from the needle orifice, which can be described by a power law of the distance z:
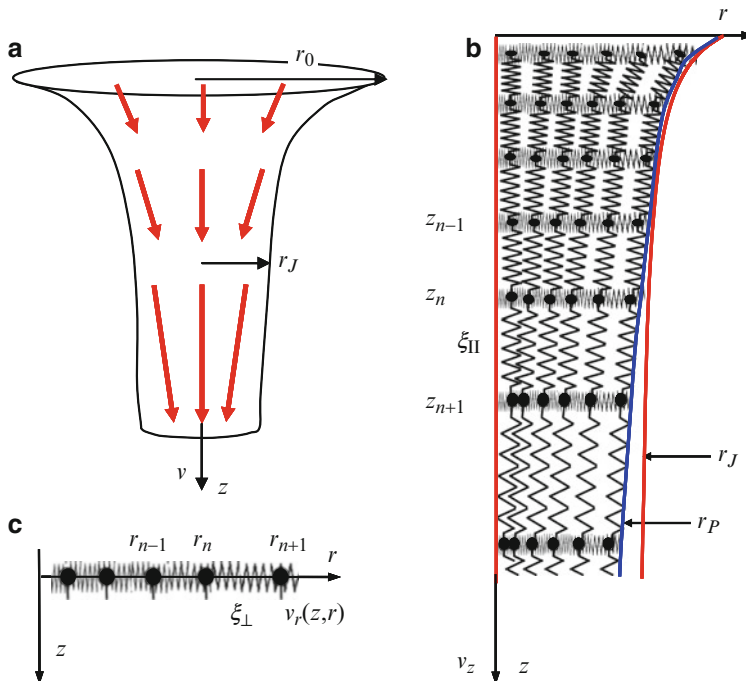
Fig. 2.3 (**a**) Illustration of the flow of an electrospinning jet. (**b**) Definition of an effective 1D beads-and-springs system in the axial direction and (**c**) the radial direction [21]

$$\frac{v_z}{v_0} \approx k^2 \left(\frac{z}{r_0}\right)^{2\beta}, \tag{2.1}$$

where β varies between 1/4 and 1 [31–35], r_0 is the jet initial radius, and v_0 is the initial velocity. Assuming volume conservation, the jet local radius $r_J/r_0 \cong (v_z/v_0)^{-1/2}$ and the radial velocity v_r can be derived.

We can obtain a rough approximation of the dimensionless parameter k by using a simple scaling approach: the velocity gradient scales as $\nabla v \sim v_0 k^2/r_0^2$; the upper bound for the electric charge surface density, assuming static conditions, scales as $s \sim \sigma E$, where σ is the solution's electric conductance and E is the electric field intensity; the electric shear stress is therefore $\tau_t \approx sE \sim \sigma E^2$, producing a velocity gradient $\nabla v \approx \tau_t/\eta \sim \sigma E^2 \eta^{-1}$, where η is the solution viscosity; hence, $k \sim \nabla v^{1/2} v_0^{-1/2} r_0$, or $k \sim r_0^1 \sigma^{1/2} \eta^{-1/2} v_0^{-1/2} E^1$. A more accurate calculation yields $k \cong r_0^{2/3} v_0^{-2/3} \sigma^{1/4} \eta^{-5/12} E^{5/6} \sim 1$ [35].

Polymer chains dissolved in a sufficiently concentrated semi-dilute solution create an entangled network (Fig. 2.3b), a prerequisite for the polymer solution successful spinability. A chain section between two subsequent entanglements is a strand, or a subchain, consisting of N_s rigid segments (Kuhn monomers), each of size $b \sim 1_{nm}$.

Given the solution concentration ϕ (in terms of the polymer volume fraction), the network mesh size (i.e., average subchain length) is given by $\xi_0 \approx b\phi^{-1} \approx b N_s^{1/2}$ for ideal chains, allowing the modeling of the network as a 3D beads and springs lattice, where each bead represents the mass m and size ξ_{eff} of a subchain, and the springs represent the linear entropic elasticity T/ξ_0^2 (T is the temperature in units of the Boltzmann constant k_B) of the subchains connected to each bead. Using the known rheology of electrified jets, the hydrodynamic force acting on a subchain can be defined, and the dynamics of the network can be described by difference-differential equations [21]:

$$m\frac{d^2 z_n}{dt^2} = \xi_{eff}\eta\left[v_z(z_n) - \frac{dz_n}{dt}\right] + \frac{T}{\xi_0^2}\{[z_{n+1} - z_n - \xi_0] - [z_n - z_{n-1} - \xi_0]\}$$
$$\xi_{eff}\eta v_r(r_n) + \frac{T}{\xi_0^2}\{[r_{n+1} - r_n - \xi_\perp] - [r_n - r_{n-1} - \xi_\perp]\} = 0. \tag{2.2}$$

The solution of this equation in the axial direction z, depicted in Fig. 2.4, predicts an affine stretching of the network

$$\frac{\xi_{||}(z)}{\xi_0} \approx \frac{v_z/v_0}{1 - \frac{1}{\alpha}d(v_z/v_0)/d(z/r_0)} \approx \frac{v_z(z)}{v_0}, \tag{2.3}$$

where the dimensionless parameter $\alpha \gg 1$ [21].
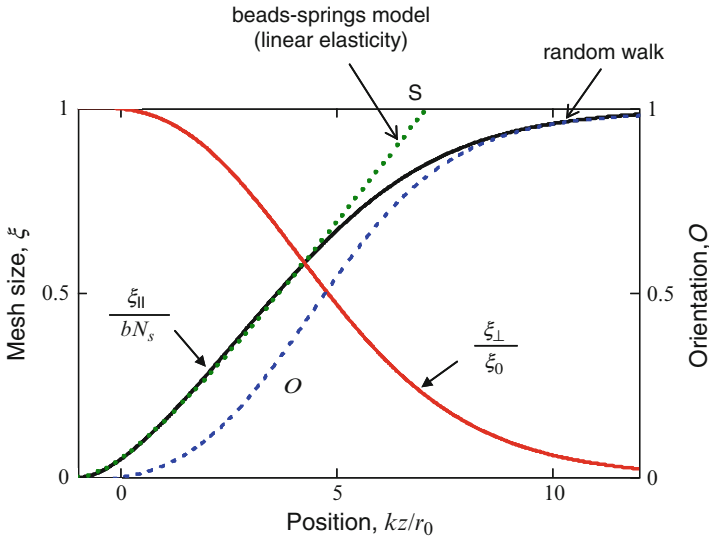
Fig. 2.4 Universal plot of the polymer network conformation. Relative axial stretching, $\xi_{\parallel}/bN_s$, radial contraction, $\xi_{\perp}/\xi_0$, and molecular orientation O, vs. the normalized axial position, kz/r_0. bN_s is the length of a fully extended subchain. The results were obtained by random walk simulation and theoretical modeling. The point S indicates the criterion for 'full' network extension [21]

Fig. 2.5 Forces acting on a subchain: external forces act at chain ends, and a hydrodynamic force acts on each monomer
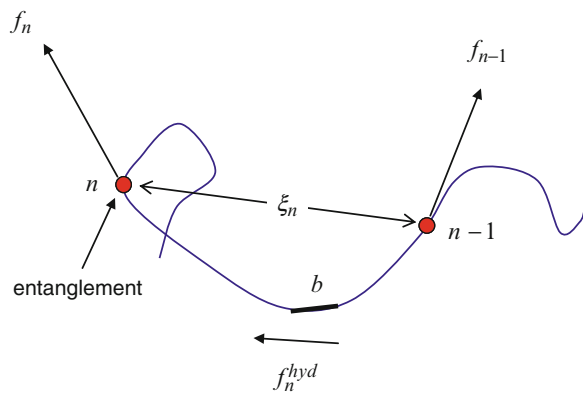
The dynamic conformation of subchains can be described by a random walk simulation, where each step represents a single monomer. The probability to step in a specific direction is determined by an effective potential, which arises from the external forces acting at the subchain ends, which propagate along the subchain, and the local hydrodynamic force acting directly on monomers (Fig. 2.5).

For a given force vector F acting on a monomer [normalized as $f = Fb/(k_BT)$], the probabilities for a random walk step are

$$P_x^{\pm} = \frac{\exp(\pm f_x)}{2\sum_x \cosh(f_x)}, \quad x = z, \rho, \varphi, \tag{2.4}$$

in each of the 6 Cartesian directions [21]. The monomer forces in the radial and axial directions are given by

$$f_\rho \cong f_0 \approx 3b/\xi_0 \approx 3\phi$$
$$f_z \cong f_0 + \sum_{i=1}^{n} f_i^{hyd} \cong f_0 + \tau_0(v_z - v_0)/b, \tag{2.5}$$

where f_0 is caused by an effective stretching force acting on subchains in a network at rest, and $\tau_0 \approx \eta_s b^3/(k_B T)$ is the monomer relaxation time given the solvent viscosity η_s. The hydrodynamic force in the radial direction is small compared to the force in the axial direction, since $f_\rho/f_z \cong v_\rho/v_z \approx \rho/z << 1$, and was therefore neglected.

Since the dominant force acts at the subchain ends, the stepping probabilities remain uniform along the subchain, and the axial stretching and radial contraction can be written using (2.4) and (2.5) [21]:

$$\xi_{\parallel}/\xi_{\max} \cong \sinh(f_z)/Q$$
$$\xi_{\perp}/\xi_{\max} \cong \sinh(f_\rho)/Q \tag{2.6}$$
$$Q = \cosh(f_z) + 2\cosh(f_\rho).$$

Shortly after the jet start, but before the network approaches full stretching ($f < 1$), the relative longitudinal elongation of a subchain can be approximated by

$$\frac{\xi_{\parallel}}{\xi_0} \approx \frac{\xi_0 v_0 \tau_0}{3b^2}\left(\frac{v_z}{v_0}\right) \approx \frac{v_z}{v_0}, \tag{2.7}$$

as obtained by the dynamic model (2.3). The condition for affine stretching is satisfied when the prefactor $\xi_0 v_0 \tau_0/(3b^2) = 1$, in which case the vertical force simplifies to $f_z \cong 3\phi v_z/v_0$.

The simulation allows expansion of the analysis to large chain elongations with non-linear elasticity, and shows that subchains approach full extension not far (<1 mm) from the jet start (Fig. 2.4). The criterion established for such full extension [marked by point S in Fig. 2.4, using (2.3) or (2.7)] is when the jet velocity rises above its initial value by a factor equal to the inverse of the polymer volume fraction:

$$\frac{v_{zS}}{v_0} \approx \frac{\xi_{\parallel S}}{\xi_0} \approx \frac{bN_s}{bN_s^{1/2}} \approx N_s^{1/2} \approx \phi^{-1}, \tag{2.8}$$

which occurs at a jet radius reduction ratio of $r_0/r_S \approx N_s^{1/4} \approx \phi^{-1/2} \sim 2 \div 10$. Note that the relative velocity and radius at the stretching crossover point depend

only on the solution concentration, and are completely independent of the electrospinning materials and conditions (e.g., molar mass and electric field).

The transformation of subchains from a coil-like equilibrium state into a stretched state occurs as a continuous crossover, and no phase transition is observed, in contrast to the well-known coil stretch transition in unentangled chains described by de Gennes [36, 37]. The dominant local force on a subchain is the elastic force arising from the action of the linked subchains, whereas the local hydrodynamic forces, whose accumulation along the network gives rise to the global elastic stretching, are negligible. Theoretically, since a vertical sequence of subchains in a network is analogous to a very long chain, a network stretch transition is possible if the jet strain rate is very low; however, under such conditions, the flow will be dominated by viscosity and network relaxation rather than elasticity.

The strong increase in the longitudinal mesh size, $\xi_{\parallel}$, results in a decrease in the radial mesh size, $\xi_{\perp}$, due to redistribution of the random walk stepping probabilities (Fig. 2.4). The result is a lateral contraction of the network toward the jet center (Fig. 2.6), which is proportional to the decrease in the subchains radial mesh size.

An approximation for the decrease of the polymer network radius with respect to the jet radius is given by

$$r_P(z) \cong \frac{\xi_{\perp}(z)}{\xi_0} r_J(z) \qquad (2.9)$$
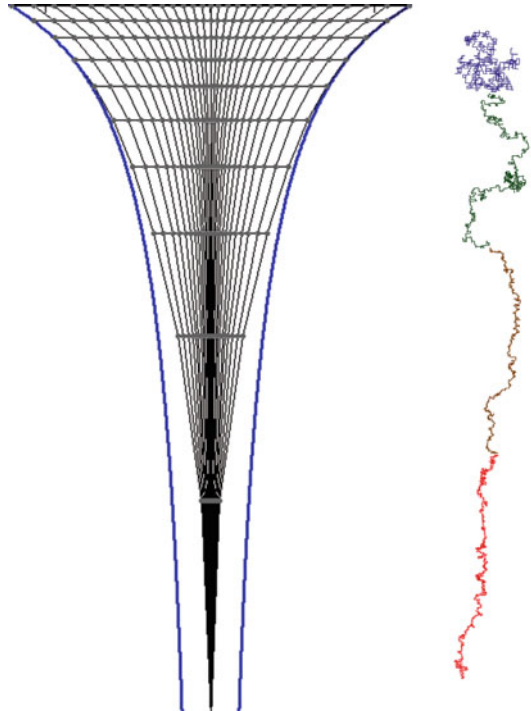
Fig. 2.6 Typical simulated conformation of a polymer network during electrospinning (*left*, diluted x800), and a vertical sequence of linked subchains (*right*, not to scale)

Fig. 2.7 Universal plot of the simulated polymer network radius, r_P/r_0, vs. the normalized axial position, kz/r_0, compared to the jet radius r_J/r_0 [21]
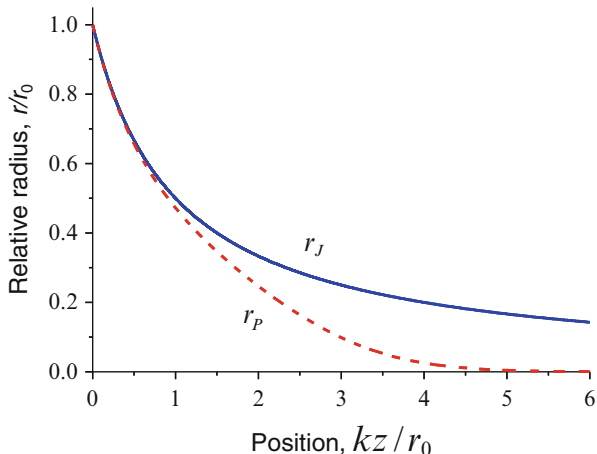
(depicted in Fig. 2.7), showing the dominant effect of axial stretching on the radial contraction [21]. This result allows predicting a significant increase of the polymer concentration at the jet center. The concentration (in terms of the polymer volume fraction) can be calculated by $\phi_p = b^3 N_s/(\xi_\parallel \xi_\perp^2)$ or by

$$\phi_p = \phi\left(\frac{r_J}{r_P}\right)^2 = \phi\left(\frac{\xi_0}{\xi_\perp}\right)^2 \cong \frac{\phi}{9}\left[\cosh\left(3\phi\frac{v_z}{v_0}\right) + 2\right]^2, \qquad (2.10)$$

using (2.6) and (2.9) and the relationship $\phi \approx b/\xi_0$, where ϕ is the solution initial concentration. The right term assumes affine stretching by means of the vertical force $f_z \cong 3\phi v_z/v_0$. When full stretching occurs, the polymer at the jet core is fully compacted ($\phi_p \cong 1$), and the corresponding jet radius can be approximated by $r_S/r_0 \cong [3/\ln(6/\sqrt{\phi})]^{1/2}\phi^{1/2} \approx \phi^{1/2}$, the same result as in (2.8). These predictions were validated by X-ray absorption measurements of electrospinning jets, which indicated a significant increase in polymer concentration close to the jet center (see Fig. 2.12).

The validity of the network modeling is restricted to the initial stage of the jet (first few millimeters), where elastic elongation is still possible, and therefore the model does not describe the final state of the polymer matrix in electrospun nanofibers. Additional processes, such as rapid solvent evaporation and polymer entanglement loss, which can result in chain relaxation, are not accounted for in the model, and are further addressed in later sections. Nevertheless, the results strongly indicate non-equilibrium, ordered nanostructures that could remain in the nanofibers after solidification, structures which may set a new internal scale, and affect the nanofiber elasticity through confinement.

2.3   X-ray Imaging of Electrospinning Jets

The theoretically predicted longitudinal stretching and lateral contraction of the
polymer network, as well as the additional effects of rapid evaporation, were
investigated experimentally by fast X-ray, phase-contrast, high-resolution imaging
of the first 10 mm of electrospinning jets, using solutions of PEO [poly(ethylene
oxide)] and PMMA [poly(methyl methacrylate)]. The experimental setup is shown
in Fig. 2.8.

The power law jet rheology (2.1), assumed in the theoretical model, was
validated by detailed measurements of the jet profile under a wide range of
electrospinning conditions and polymer solutions, demonstrating that the jet diam-
eter narrows faster under higher electric fields, lower flow rates, and lower polymer
concentrations (Fig. 2.9). The measurements validate the theoretical expression of
the parameter k defined in (2.1).

Comparison of velocity measurements obtained by particle tracing velocimetry
to estimates based on volume conservation assumption, showed an abrupt deviation
1–2 mm from the jet start, a possible indication for full extension of the network
that retards the jet velocity, as well as an indication for a substantial mass loss due to
evaporation (Fig. 2.10).

The flow regime inside the jet was found to be laminar, with observed stream-
lines and an almost uniform vertical velocity across the jet (Fig. 2.11).

The polymer concentration mapping along and across the jet makes use of the
different X-ray mass absorption coefficients of the polymer and solvent, ε_p and
ε_s, respectively. The absorption coefficient of the polymer solution is given by
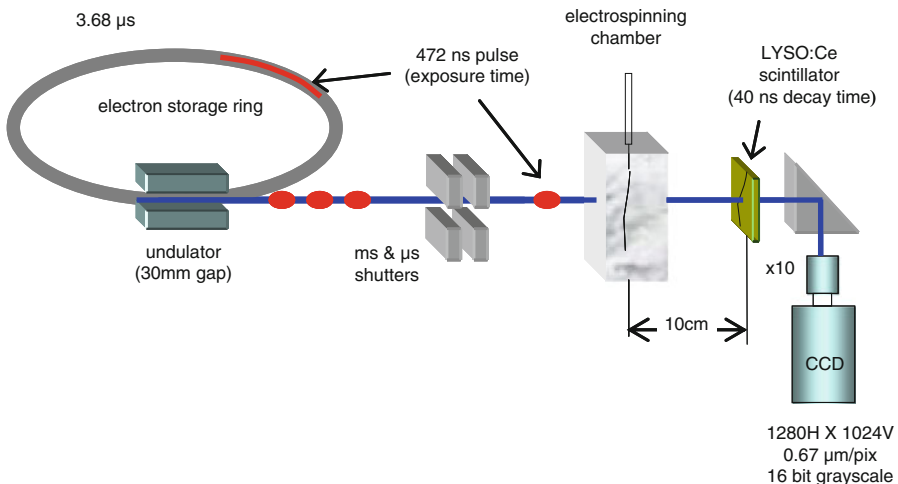
Fig. 2.8 Experimental setup of X-ray imaging of electrospinning jets. A millisecond shutter was
set up in series with a very fast galvano-based shutter that opened the path for less than 100 μs each
second. The beam penetrated the jet, and was converted to a digital image by a scintillator. The
CCD camera was timed to capture the first released pulse [28]
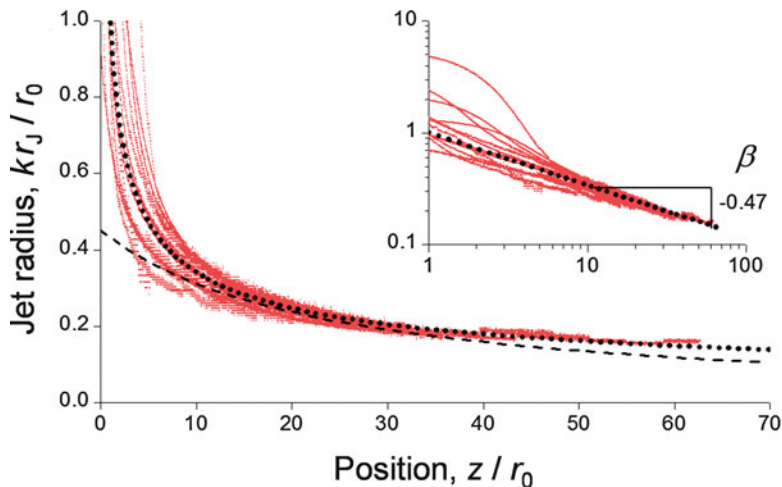
Fig. 2.9 Normalized jet radius kr_J/r_0 at position z/r_0 along the jet, for the combined data of 13 electrospinning tests, where each test set was multiplied by the constant k pertaining to that test. The power fit exponent β is shown in the *inset*. The measured dimensionless parameter k compares well with the theoretical prediction [28]
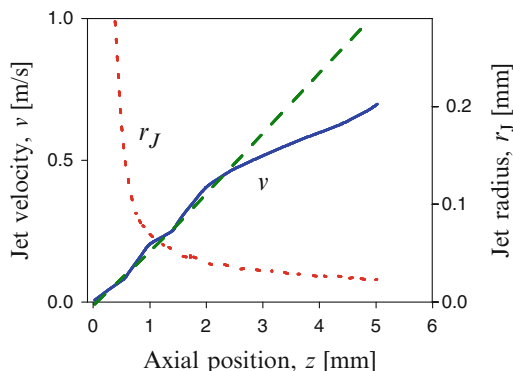
Fig. 2.10 Example of vertical velocity measurement using silica microbeads (*solid line*), compared to velocity estimation from the measured jet radius r_J assuming mass conservation (*dashed line*). Electrospinning of PEO 5 %, under an electric field of 4 kV/cm, at flow rate of 6.4 mL/h [28]

$\alpha(r,z) = \varepsilon_p c_p(r,z) + \varepsilon_s c_s(r,z)$ [38], where c_p and c_s denote the mass concentrations of the polymer and solvent, respectively, and the coordinates (r,z) are the radial and axial position in the jet, respectively. Thus, the change in the local polymer concentration, $\Delta c_p(r,z)$, is linearly dependent on the change in the local absorption coefficient $\Delta\alpha(r,z)$:

$$\Delta c_p(r,z) = \frac{\Delta\alpha(r,z)\rho_p}{\varepsilon_p\rho_p - \varepsilon_s\rho_s}, \tag{2.11}$$

where and ρ_p and ρ_s are the densities of the polymer and solvent, respectively [28]. $\Delta\alpha(r,z)$ is calculated by comparing the measured X-ray transmission (*exp*) to

Fig. 2.11 Typical flow field during electrospinning of PEO 5 % solution in water, mixed with 0.9 vol % silica microbeads, under an electric field of 4 kV/cm and flow rate of 6.4 mL/h. Obtained by two-pulsed X-ray imaging (73.6 µs time interval) of a 1 mm-long jet section [28]
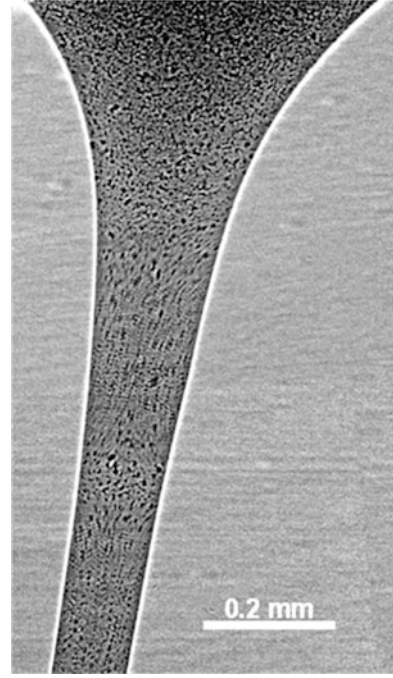
a simulated transmission for a 'still' jet (*sim*), at a given beam travel distance through the jet $d(r, z)$ [28]:

$$\Delta\alpha(r,z) \cong -\frac{1}{d(r,z)}\ln\left[\frac{T_{\exp}(r,z)}{T_{sim}(r,z)}\right]\left[\frac{\alpha_0}{\alpha_{sim}(r,z)}\right]. \tag{2.12}$$

The correction factor α_0/α_{sim} filters out the effects of scattering in a homogenous jet, and is used as an approximation for the non-homogenous electrospinning jet.

Concentrations were found to rapidly increase below a critical jet radius of ~25 µm (equivalent to radius reduction ratio of 0.2) (Fig. 2.12), a possible evidence for full network extension and of rapid evaporation that occurs much earlier than theoretical predictions found in the literature. When depicted versus the jet radius, the concentration curves collapse into groups of common initial solution concentration. The concentration crossover occurs at a lower radius for the lower solution concentration, as predicted in (2.8). The concentration theoretical prediction (2.10), depicted in the inset of Fig. 2.12, conforms well to the experimental results, hence favoring the stretching premise over evaporation. These results confirm that the stretching crossover position depends predominantly on the solution initial concentration, and is invariant with respect to the electrospinning materials and conditions. Note that the concentration increase is slightly slower in the experiment compared to the theoretical curve, possibly accounting for the stretching and compacting retardation caused by the untangling of chains.
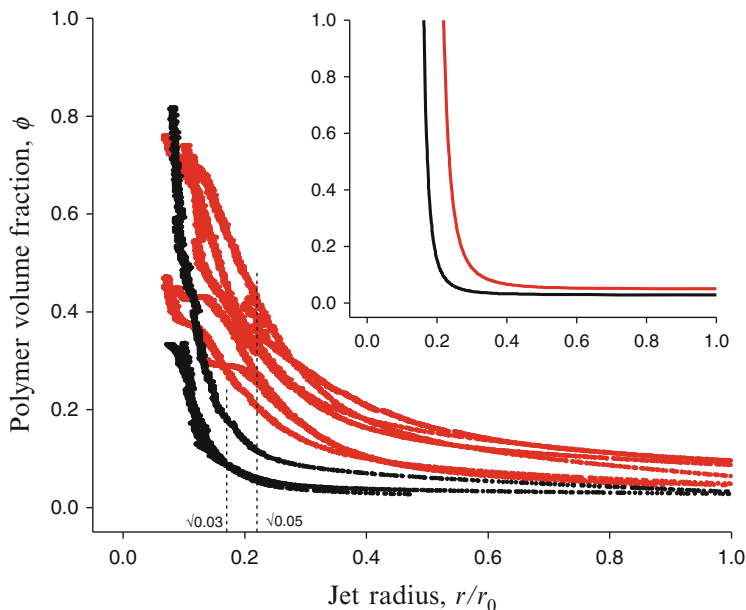
Fig. 2.12 Polymer volume fraction, ϕ_p, vs relative jet radius, r_J/r_0, derived from the X-ray absorption measurements at jet center, for 13 tests of PEO 3 % (*black lines*) and 5 % (*red lines*). The predicted crossover radius from (2.8) is indicated for both solution concentrations at position $\sqrt{\phi}$. The *inset* depicts the corresponding theoretical prediction [28]

Concentration variation across the jet revealed high concentrations at the jet boundary due to evaporation, as well as a concentration rise at the jet center within ~1 mm from the jet start (Fig. 2.13), in agreement with the model and simulation.

Evaporation becomes dominant when stretching is weaker [e.g. at lower electric field and/or higher flow rate – see (2.1) and the definition of k], reducing or canceling the concentration peaks measured at the jet center (Fig. 2.14). Such tuning of parameters demonstrates the balance between the effects of evaporation and stretching, which determines the polymer network non-equilibrium conformation during electrospinning, and explains the diversity of macrostructures and properties found in solid nanofibers (see examples in Fig. 2.2). Specifically, dominant stretching is expected to yield uniform structures with axially oriented molecules and better mechanical properties, whereas dominant evaporation may result in porous nonuniform structures.

The technique of X-ray imaging during electrospinning was specifically developed for this research, including the algorithms and methods for processing and analyzing the recorded data. These experiments provided information on internal flow and concentration variations unattainable by other in-situ measurement methods. Fast X-ray phase contrast imaging provides high penetrability at very short exposures, allowing absorption measurements of the unsteady jet, as well as
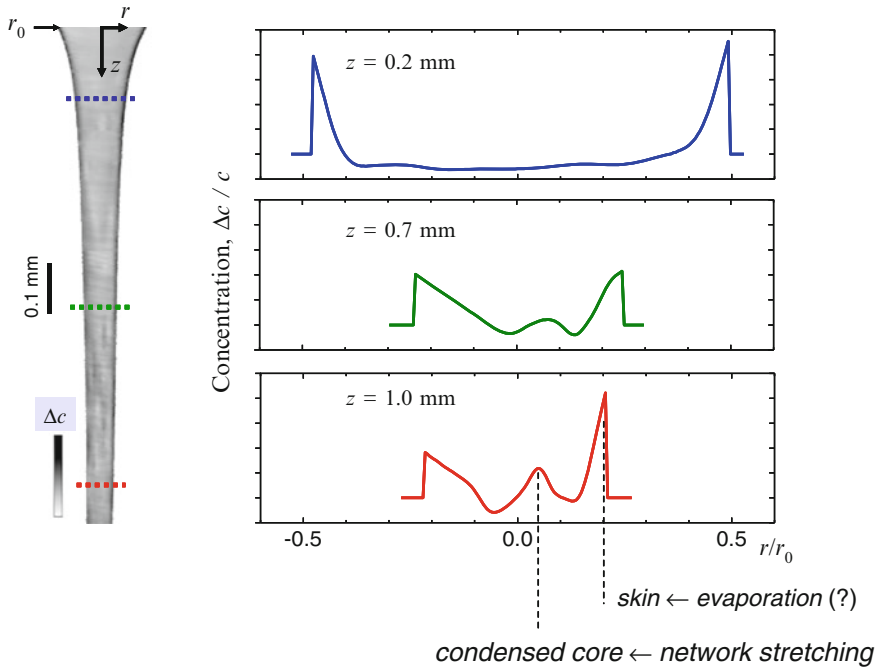
Fig. 2.13 Typical relative polymer concentration change across the jet, $\Delta c_p/c$, vs the relative radial distance from the jet center, r/r_0, for several axial positions z along the jet. The data are derived from X-ray absorption measurements of PEO 5 %, under an electric field of 2.8 kV/cm and flow rate of 1.9 mL/h [28]

enhanced phase boundary contrast, allowing high resolution viewing of the narrow jet and embedded particles.

2.4 Entanglement Loss and Short Nanofibers

As already pointed out, the validity of the network modeling is restricted to the initial stage of the jet, where elastic elongation is still possible and the network can be assumed to maintain its degree of entanglement. However, the effects of entanglement loss due to the high strain rate cannot be neglected when considering the final polymer conformation. When carrying out the electrospinning process to its extreme conditions, jet fragmentation (Fig. 2.15) was observed in the appearance of short nanofibers (Fig. 2.16), allowing quantification of the polymer entanglement loss under a high strain rate extensional flow.

Using PMMA of several molar masses, dissolved at different concentrations in solvent blends of varying quality, and tuning the electric field intensities and flow rates, the occurrence of short nanofibers, as well as of beads-on-string, was clearly
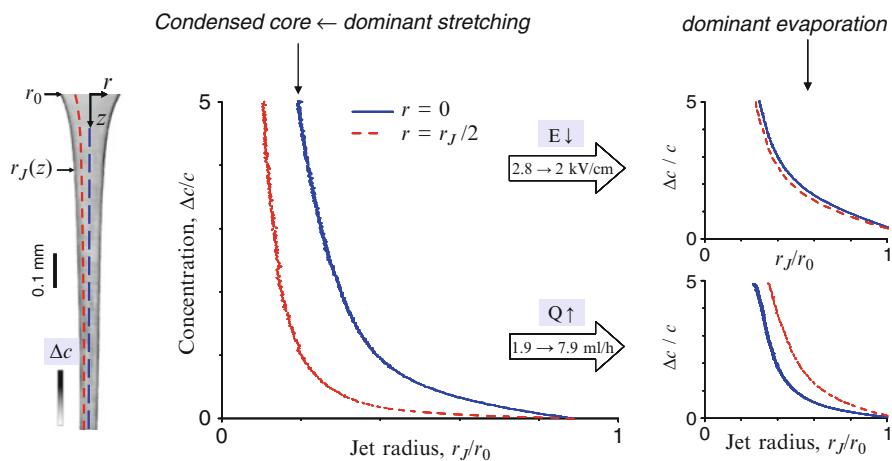
Fig. 2.14 Comparison of the relative concentration change, $\Delta c_p/c$, at the jet center ($r = 0$) to that measured at a radial offset from the center ($r = r_J/2$), presented vs. the relative jet radius r_J/r_0. The data were derived from X-ray absorption measurements of PEO 5 %, with modulation of the flow rate Q and electric field E [28]
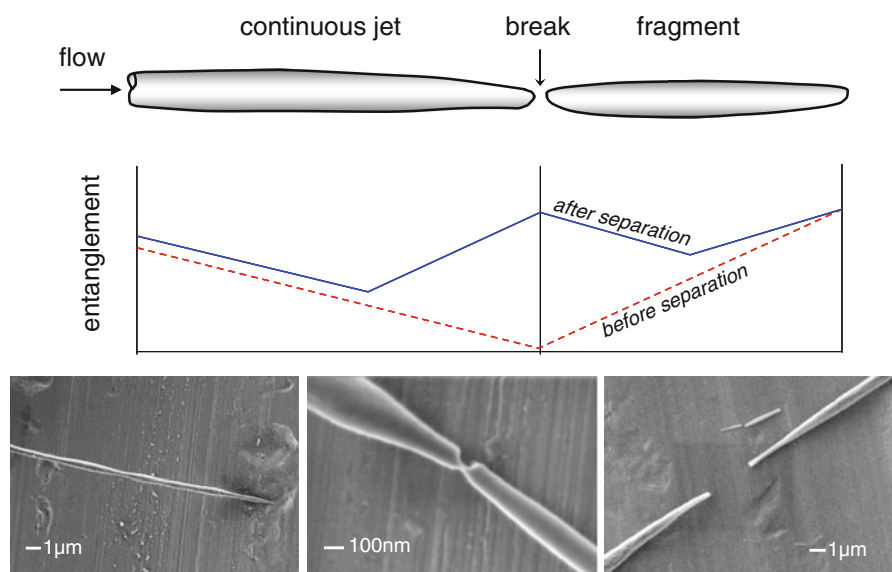
Fig. 2.15 (*top*) Illustration of jet fragmentation as a result of untangling of the polymer network in low-concentration solutions under high electric fields. (*bottom*) SEM micrographs of the fragmentation of PMMA fibers [29]
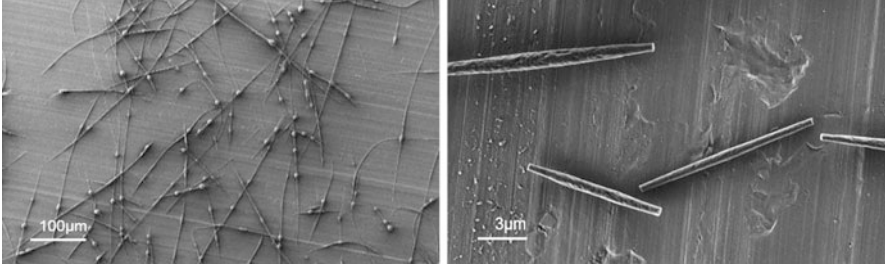
Fig. 2.16 SEM micrographs of electrospun short PMMA fibers [29]

identified and mapped (Fig. 2.17). Also, the dependence of the short nanofiber length and diameter on the material and process variables was characterized in the form of empirical scaling expressions. Short nanofibers appeared at solution concentrations slightly above the entanglement concentration ϕ_e, when the electric field intensity was high and the flow rate low. In other words, short nanofibers appeared, and their length was shorter, when the polymer molar mass, concentration, and solvent quality were lower and the flow strain rate was higher. Under such favorable low entanglement and high stretching conditions, the elastic extension of the polymer network accelerates the entanglement loss, eventually leading to separation of the network and fragmentation of the jet.

Using the known jet rheology and the premise of affine extension of the polymer network, a disentanglement model was developed. The underlying assumption is that the entanglement nodes are moving at the same velocity as the jet, while chains are allowed to disentangle but remain highly stretched (Fig. 2.18). Thus,

$$\frac{l}{l_0} \approx \frac{v}{v_0} \approx k^2 \left(\frac{z}{r_0}\right)^{2\beta}, \tag{2.13}$$

where the initial end-to-end distance of a chain section between two entanglements is given by $l_0 \approx b\phi^{-2/3}$ for a θ-solvent [39], and the jet parameter k depends on the material and process parameters (2.1) [29].

The short fibers modeled length for a θ-solvent is given by

$$\frac{L}{r_0} \approx \frac{z_s}{r_0} \approx k_0^{-2} N^{7/2} \phi^{41/9}$$

$$k_0 \cong \varepsilon_m^{1/6} r_0^{2/3} \sigma^{1/4} \eta_s^{-5/12} v_0^{-2/3} E^{5/6}, \tag{2.14}$$

where the semi-dilute solution viscosity was written explicitly [39] as $\eta \approx \eta_s N^3 \phi^{14/3}$ for a θ-solvent [29]. The modeled diameter of short and continuous fibers for a θ-solvent is
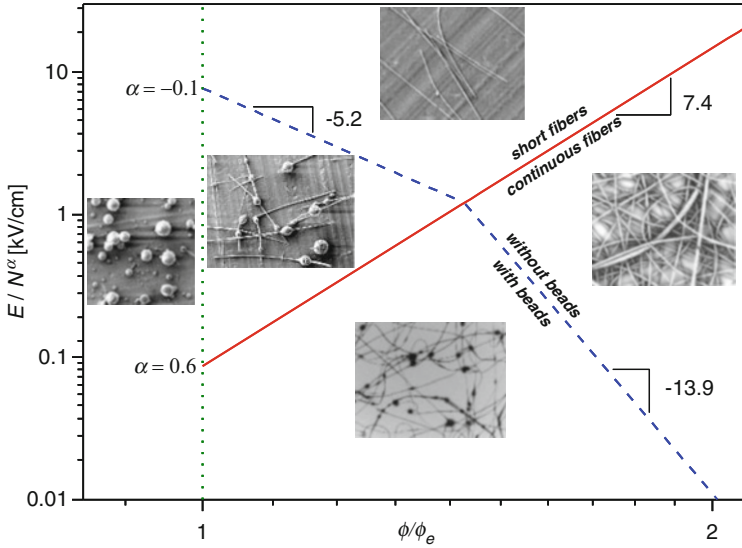
Fig. 2.17 Electrospun PMMA fibers, short fibers and beads, and measured conditions for their creation, mapped over the electric field E, the relative polymer concentration ϕ/ϕ_e, and the degree of polymerization N [29]

Fig. 2.18 Illustration of polymer untangling during electrospinning, and definition of the modeling parameters. Elastic stretching followed by relaxation of chains gradually disentangle chains from the network. The subscript s denotes the jet break point [29]
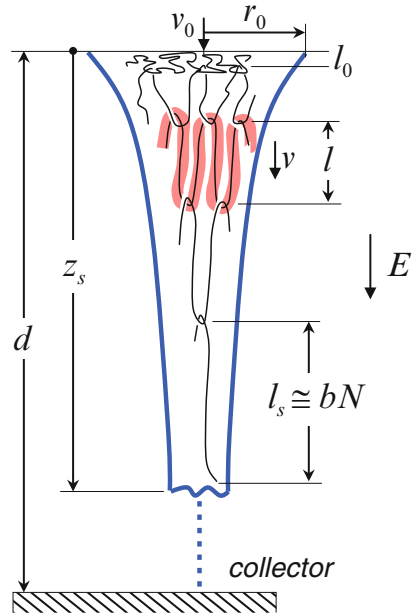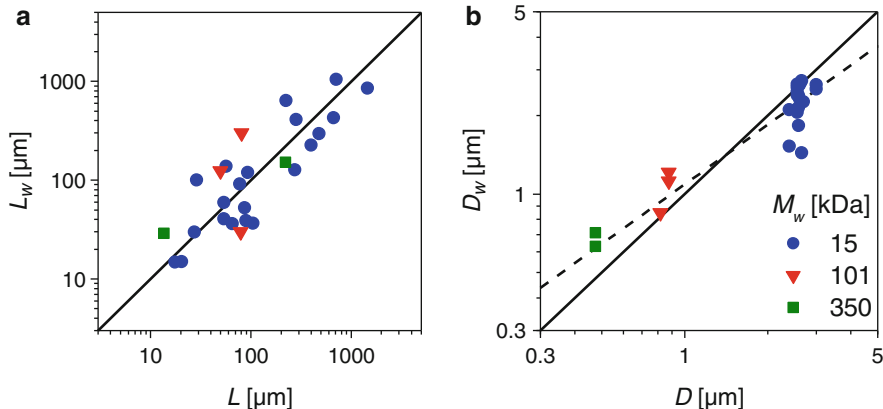
Fig. 2.19 Experimental and theoretical short nanofibers dimensions. (**a**) Measured length L_w versus the theoretical length L. (**b**) Measured diameter D_w versus the theoretical diameter D [29]

$$\frac{D}{r_0} \approx \sqrt{\phi \frac{l_0}{l}} \approx \begin{cases} \phi^{1/6}/N^{1/2} & \text{short fibers} \\ k_0^{-1}(d/r_0)^{-1/2}N^{5/4}\phi^{22/9} & \text{continuous fibers,} \end{cases} \tag{2.15}$$

where the local condensed polymer diameter is reduced by the extension factor $\sqrt{l/l_0}$ [29]. The experimental results and theoretical predictions for short nanofibers correlate well, confirming the proposed disentanglement mechanism (Fig. 2.19). Diameter measurements of continuous fibers [15, 40] also correlate well with the model.

An important outcome of the analysis is the dependence of the fiber diameter on the material and process parameters (Fig. 2.20). The diameter of short nanofibers grows weakly with increasing the relative concentration, while their length grows sharply. When the concentration is increased beyond a transition point, continuous nanofibers are created and the diameter's growth slope increases abruptly. The transition point identifies the conditions that lead to a minimal possible radius in continuous fibers.

While the diameter of a continuous nanofiber depends on the solution's relative concentration by a power of 2.4, the corresponding power in short nanofibers is only 0.17, marking a distinct difference between the two morphologies. The reason for these differences is that in continuous nanofibers, the process of disentanglement is not carried out until complete separation of the polymer network as in short nanofiber, since it is terminated at the collector, and therefore the amount of entanglement loss, and hence the diameter, depend on the flow dynamics and the electrodes gap size.

The high elastic stretching and entanglement loss required to create short nanofibers are likely to lead to an ordered, aligned solid nanostructure with improved mechanical properties. At the same time, since fragmentation occurs before full solidification, the polymer network may partially relax in solvent rich
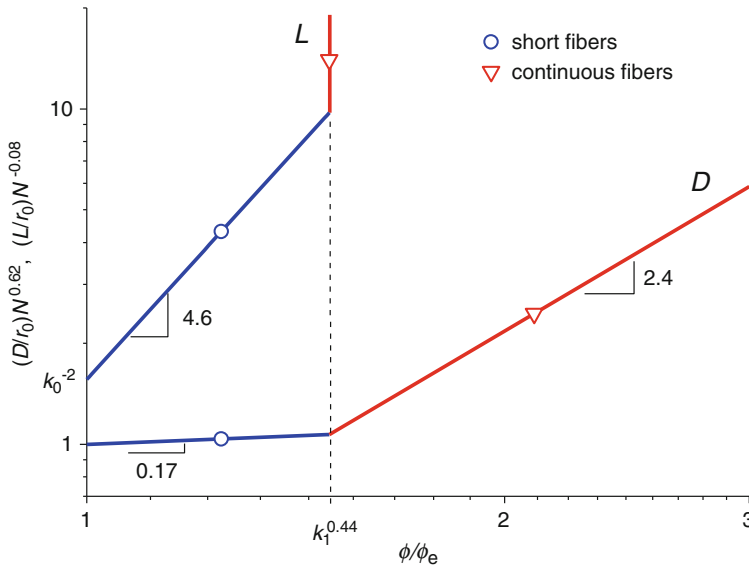
Fig. 2.20 Nanofiber length L/r_0 and diameter D/r_0 versus the relative concentration ϕ/ϕ_e. N is the degree of polymerization, $k_1 = k_0\sqrt{d/r_0}$, d is the gap distance between the electrodes, and r_0 is the jet initial radius [29]

areas and leave voids in the polymer matrix. Hence, a nonuniform structure can result in both the axial and radial directions, with regions of aligned rigid structure and regions of amorphous porous structure. The prospect of nanofiber size tuning, and hence their morphology, in accordance with the proposed model, can be exploited to improve their as-spun mechanical, optical and thermodynamic properties, such as the elastic modulus and light polarization. Combined with the possible biaxial nonuniform nanostructure, it may find interesting applications in tissue engineering, drug delivery, composites reinforcement, filtration, electrical and thermal conduction, and light amplification.

2.5 Fiber Nanostructure and Mechanical Properties

The gradual solidification of the jet during the advanced stage of electrospinning, which results in viscosity increase, crystal growth, and partial relaxation of chains from their non-equilibrium state back toward their coil state, raises a question whether the beneficial outcome of stretching and molecular packing remains in the solid fiber.

The opportunity presented itself in electrospinning of the conjugated polymer MEH-PPV. This optically active, electrically conductive polymer is of high interest because of its potential applications in semi-conducting devices such as field effect

Fig. 2.21 Simulated ideal chain conformations of a conjugated polymer. From *top*: polymer network at rest; a single chain with $N = 146$; strands (subchains) with different defects concentration, *left* $N_s = 14$ ($n = 5$ beads, 10 % defects), *right* $N_s = 67$ ($n = 3.4$ beads, 15 % defects); stretched subchains during electrospinning at distances of $z = 0.08$ mm and $z = z_s = 0.16$ mm from the jet exit, $N_s = 14$ [13]
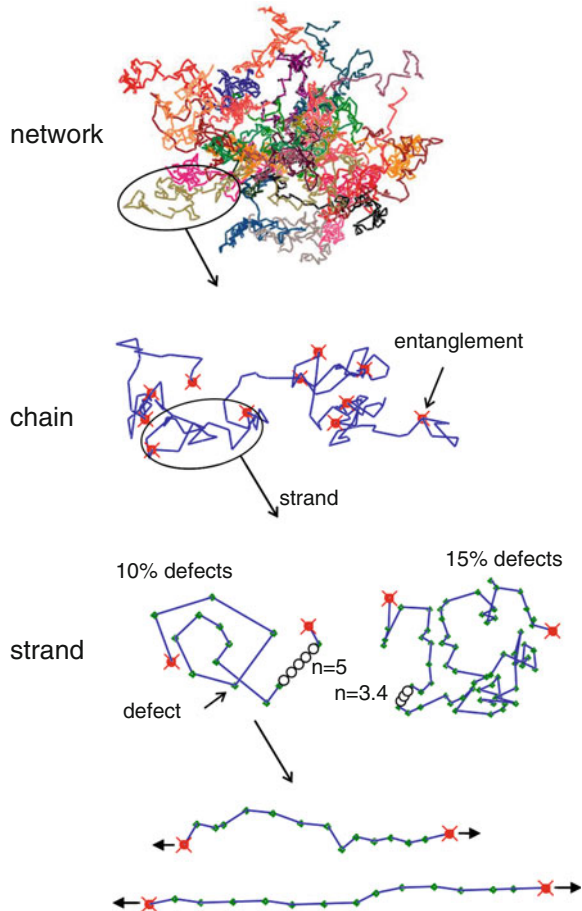
transistors, light emitting diodes, active layer in lasers, and sensors. Two properties make this polymer an excellent candidate for examining the posed question. First, MEH-PPV has high absorption in the visible waveband, specifically around the wavelength of the laser used for radiation, lending itself to optical probing. Second, unlike freely jointed chains, conjugated polymer chains are not flexible, but are rather semi-flexible as a result of the high bending rigidity of the chain backbone, which is composed of alternating single and double covalent bonds. Owing to inherent bonding defects, which substitute rigid conjugated links by flexible tetra-hedral links, the conjugated chains can be described as flexible chains having longer Kuhn (rigid) segments (Fig. 2.21). Consequently, as shown by our generalized modeling and simulation (more details later), the stretching and lateral contraction phenomena should be more pronounced in this class of polymers.
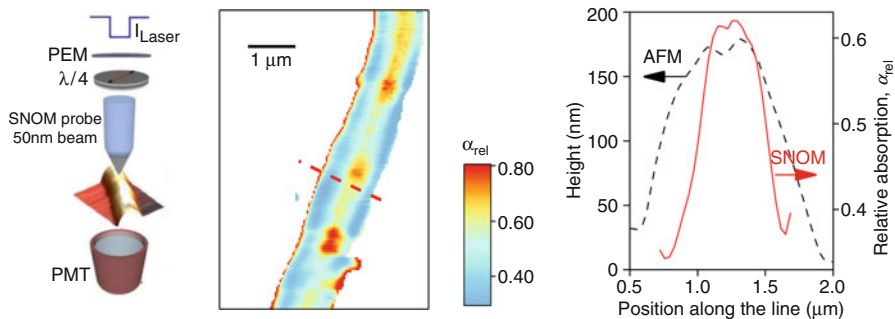
Fig. 2.22 SNOM scanning of a single fiber (*left*). SNOM map of the nanoscale variation of the relative optical absorption coefficient of an MEH-PPV electrospun fiber (*center*). Fiber topography (*dashed line*, measured by AFM) and the corresponding relative optical absorption, α/α_{max} (*continuous line*, measured by SNOM) along a transverse line (*right*). The polymer density is proportional to the absorption coefficient [12, 13]

Fig. 2.23 Young's modulus map measured by AFM indentation at the cross section of an MEH-PPV nanofiber embedded in UV-cured polymer (*red*). The modulus at the fiber core (*blue*) is more than twice the modulus at its boundary (*yellow*) [12]
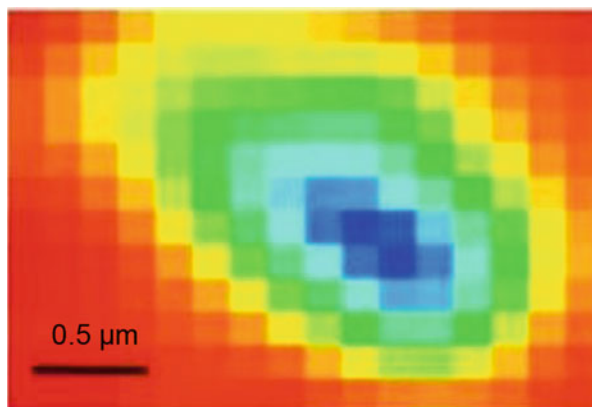
Measurements by high resolution, scanning near-field optical microscopy (SNOM) revealed a core-sheath structure, in which the fiber core has a higher density, whereas closer to the fiber boundary the density is lower (Fig. 2.22).

This observation was strengthened by force-indentation measurements of the elastic modulus at the cross-section of the fiber, using atomic force microscopy (AFM), which showed a higher modulus at the fiber center with respect to the boundary (Fig. 2.23), indicative of higher density and possibly molecular ordering at the core.

These results confirm that the close-packed molecular conformation of the polymer network in the liquid jet, demonstrated by the simulation of the semi-flexible conjugated polymer (Fig. 2.24), is essentially retained in the solid fiber.

In perspective, the found graded-density internal structure can possibly improve charge transport by the fiber core, whereas the lower density sheath can determine the amplification of light guided in the fiber. Similarly, for scaffold applications, the
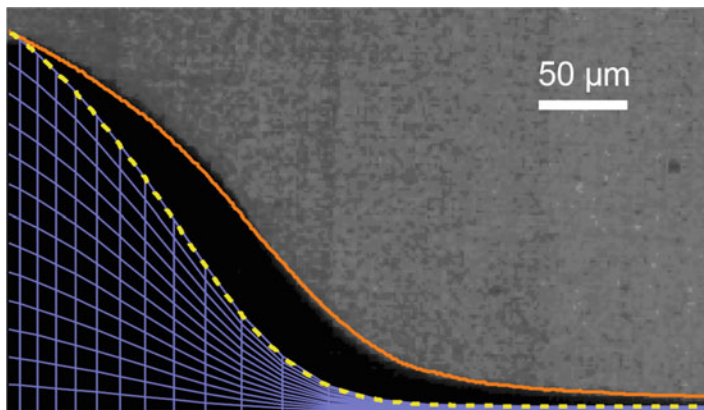
Fig. 2.24 Simulated polymer network mesh, superimposed on an MEH-PPV electrospinning jet (only the upper half is shown). Viewed mesh density is diluted × 300 in each direction. Conditions: electric field 1.8 kV/cm, flow rate 10 μL/min, polymer volume fraction 0.025 [12]

core can provide the needed strength, rigidity, and conductivity, while the boundary layer has enhanced material absorption and adhesion properties.

2.6 Chain Orientation in Fibers

A valid concern is whether the observed dense region at the fiber core consists of an ordered structure or an amorphous structure. In an ordered structure, the mechanical properties of the nanofiber should be improved with respect to bulk material. Moreover, in conjugated polymers such as MEH-PPV, ordering and orientation of chain sections results in a longer effective conjugation length, and consequently longer chromophores (chain parts responsible for color absorption or excitation) and improved optical and electrical properties. We exploited the unique optical properties of conjugated polymers to investigate this concern by measurements of optical absorption and polarization modulation.

The most common process used in producing conjugated polymer macrostructures is spincasting. Electrospinning of conjugated polymers is usually avoided due to their low miscibility, or carried out by mixing other polymers in the solution or by using the core-shell technique. However, while amorphous aggregation of the polymer is favored in films, the elongational dynamics of electrospinning leads to extended structures having interchain alignment. Measurements of the absorption spectra of nanofibers, compared to those of spincast films, showed a peak red shift, which indicates an increase of the effective conjugation length attributable to a more ordered molecular packing. Additionally, the absorption and photoluminescence linear dichroism spectrums, measured on uniaxially aligned MEH-PPV nanofibers, evidence a predominance for light polarized along the fiber longitudinal
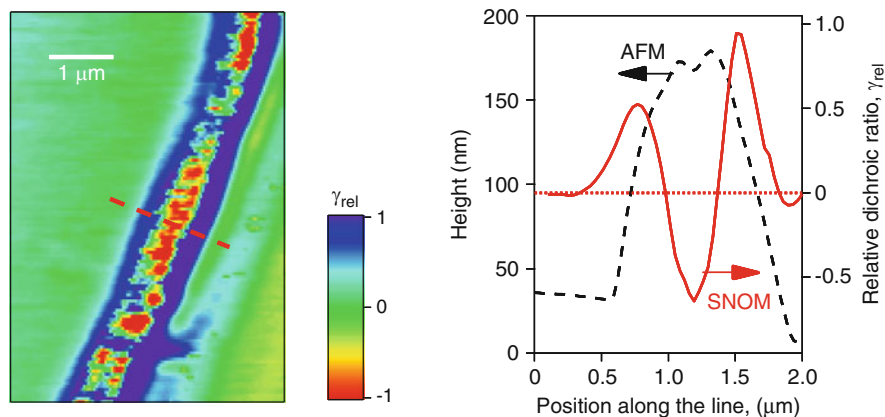
Fig. 2.25 SNOM map of the nanoscale variation of the relative dichroic ratio of an MEH-PPV electrospun fiber (*left*). Fiber topography (*dashed line*, measured by AFM) and the corresponding relative dichroic ratio, γ/γ_{max}, where $\gamma = (I_{//} - I_{\perp})/(I_{//} + I_{\perp})$ and I is the transmitted intensity (*continuous line*, measured by SNOM with polarization modulation), along a transverse line (*right*). The minimum indicates preferred molecular alignment in the axial direction, while the maxima indicate preferred radial alignment [13]

axis, a fingerprint of a preferential alignment of the polymer backbones along the fiber length.

The nanoscale mapping of the local dichroism of individual fibers, measured by polarized near-field optical microscopy (Fig. 2.25), unveiled for the first time the presence of an internal spatial variation of the molecular order. Specifically, these results confirm the presence of a core (of width ~40 % of fiber diameter) with axially aligned molecules, and a sheath (envelope) with almost radially oriented molecules. The unexpected radial orientational preference in the fiber sheath is attributed to relaxation of polymer chains in the lower density region, combined with crystallic growth in the radial direction.

A key question is how and to what extent the process can be controlled in order to achieve desired nanostructures within the fiber. For that purpose, the polymer network dynamic model and simulation, described in Sect. 2.2, were generalized by tuning the degree of chain flexibility with the segmental aspect ratio (i.e., the number of monomers in a rigid segment, inversely proportional to the bonding defects concentration). Thus, the generalized model applies to a wide range of linear flexible polymers, including conjugated polymers with different bonding defect concentrations, as well as fully flexible polymers that are a particular case of the model in which the segmental aspect ratio is 1.

Given the aspect ratio n, polymer volume fraction ϕ, and solution properties expressed by Flory's exponent ν and Flory's interaction parameter χ, the number of rigid segments in a single subchain in the polymer network, for a good solvent, is

$$N_s \approx \left(\frac{n}{1-2\chi}\right)^{3(2\nu-1)/(3\nu-1)} \left(n^2\phi\right)^{-1/(3\nu-1)}, \tag{2.16}$$

and the corresponding correlation length is $\xi \approx b[(1-2\chi)/n]^{2\nu-1}N_s^{\nu}$ [13]. The exponent ν is 0.5 for ideal chains, corresponding to θ-solvents, and ~0.6 for real chains, corresponding to good and athermal solvents. Note that when $n = 1$, the equation converges to the classic expression for fully flexible chains, corresponding to the polymer network mesh size.

When the aspect ratio is larger (lower defects concentration), the subchains become shorter and more rigid, in other words the network mesh size is smaller (Fig. 2.26a); specifically, the number of subchain segments is reduced by a power of 4 of the aspect ratio (ideal chain). At concentrations above the athermal limit at point B, the chain conformation is always ideal (θ-solvent condition). When the polymer volume fraction is sufficiently high, subchains start to interact within a single correlation volume, a condition not existing in fully flexible chains, thereby enhancing the likelihood of nematic ordering and molecular orientation (Fig. 2.26b).

The results of the model and simulation for a representative conjugated polymer (10 % defects concentration) are presented in Fig. 2.27, and typical free and extended chain conformations are depicted in Fig. 2.21, exhibiting a similar behavior as in fully flexible chains (Fig. 2.4), but with a strong dependence on the aspect ratio.

Full extension is approached when $\xi_\parallel \approx bN_s$, i.e. at the axial position z_S and a corresponding jet radius r_S. Using (2.8) and (2.16), the jet radius reduction ratio at full stretching is expressed for good solvents by [13]:

$$\frac{r_0}{r_S} \approx \left(\frac{bN_s}{\xi_0}\right)^{1/2} \approx \left(\frac{n}{1-2\chi}\right)^{(2\nu-1)/(3\nu-1)} \left(n^2\phi\right)^{-(1-\nu)/[2(3\nu-1)]}. \tag{2.17}$$

Thus, r_0/r_S is reduced as the chain is stiffer (larger n), and the exponent of n is -1 for a θ-solvent ($\nu = 0.5$) and -0.25 for good and athermal solvents ($\nu \cong 0.6$). Note that when $n = 1$ and $\nu = 0.5$, the equation converges to the expression for fully flexible chains in (2.8).

The axial position of full stretching can be obtained by substituting the radius reduction ratio into (2.1), and using the known viscosity expressions for semi-dilute solutions, $\eta \approx \eta_s N^3 \phi^{3/(3\nu-1)}$ for an athermal solvent and $\eta \approx \eta_s N^3 \phi^{14/3}$ for a θ-solvent. Omitting the effect of n, the position scales as [13]:

$$\frac{z_s}{r_0} \sim N^{3/2} \begin{cases} \phi^{\frac{\nu+2}{2(3\nu-1)}} & \text{athermal solvent} \\ \phi^{11/6} & \theta\text{-solvent.} \end{cases} \tag{2.18}$$

In this calculation the approximate value of k was used. The exponent of ϕ for the athermal solvent is approximately 13/8. Thus, the model predicts that full extension
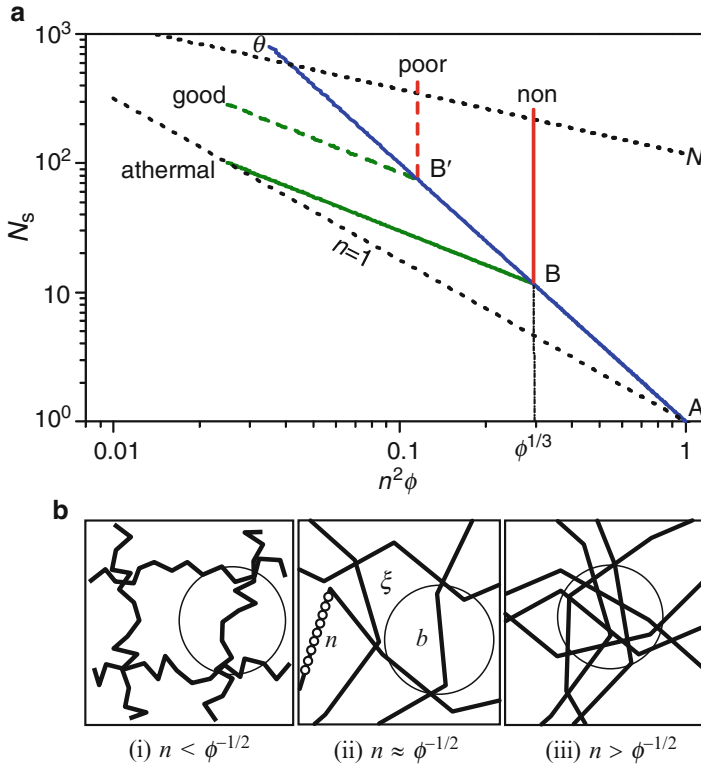
Fig. 2.26 Conjugated polymer conformation in a solution. (**a**) The number of subchain segments, N_s, versus the polymer volume fraction, ϕ, and the number of beads per segment, n, for different solvent quality grades. The *dotted lines* constitute the upper and lower limits for $\phi = 0.025$. Polymer molecular weight is 380 kDa, equivalent to $N_{beads} = 730$. Point B' is depicted for Flory's interaction parameter $\chi \cong 0.38$. (**b**) Crossover [Point A in (**a**)] of the polymer network conformation with respect to the scale of the correlation length ξ (*circles*) and the segment length b: (i) regular semi-dilute, $\xi > b$, (ii) crossover, $\xi \approx b$, and (iii) different chains intermix within a single correlation volume, $\xi \approx b$ [13]

of the network occurs at an earlier stage of the jet (closer to the orifice) when the concentration, molar mass, and solvent quality are lower, accounting for lower network entanglement (Fig. 2.28).

Under favorable stretching conditions that expedite full network extension, it is more likely that the extended conformation, and the associated axial molecular alignment, will partially remain in the polymer structure after solidification. Indeed, the measured far-field, macroscale emission from MEH-PPV nanofibers was found to be polarized along the longitudinal axis of the nanostructures, with a degree of polarization dependent on process variables. Specifically, the photoluminescence polarization ratio was raised up to five times that of amorphous polymer, by gradually decreasing the solution concentration down to a volume fraction of
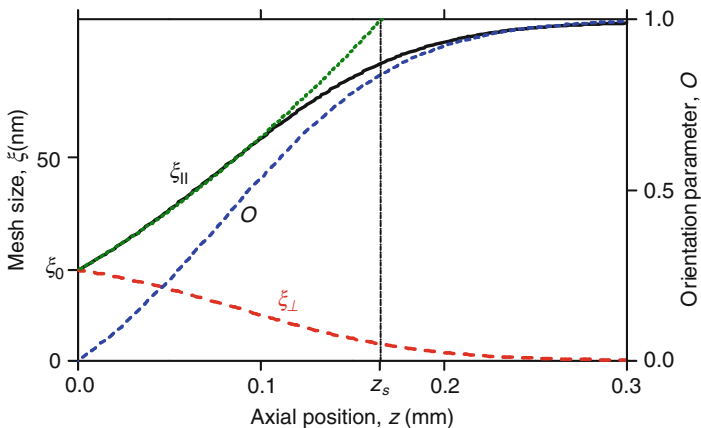
Fig. 2.27 Simulated subchain length during electrospinning. The axial mesh size $\xi_{\parallel}$, radial mesh size $\xi_{\perp}$, and orientation parameter O are plotted versus the axial position z along the jet. The simulated $\xi_{\parallel}$ (*solid line*) is compared with the theoretical model (*dotted line*). The position close to full subchain extension is designated by z_s. Parameters used: ideal chain, $\phi = 0.025$, $n = 5$ beads, bead size $d = 1.2$ nm, $\xi_0 \cong 20$ nm, $N_s = 14$ segments. Jet dynamics is derived from Fig. 2.24 [13]
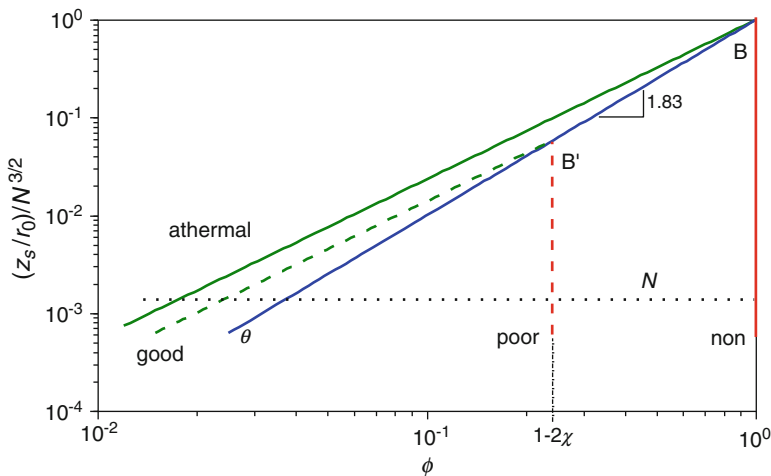
Fig. 2.28 Axial position where subchains approach full extension, z_s/r_0, normalized by $N^{3/2}$ (N is the chain's number of segments), versus the polymer volume fraction ϕ and solvent quality. Modeled for full chain flexibility ($n = 1$). The *dotted line* constitutes the lower limit imposed by $N_s < N$. Prefactors are omitted, and all other influencing parameters (e.g. electric field and flow rate) are assumed constant. Points B and B' are explained in Fig. 2.26 [13]

0.03 (Fig. 2.29), a clear indication for the inverse dependence of the longitudinal molecular alignment on concentration. Thus, the confirmed model provides tools for tailoring of the photophysical properties of the fibers.

Fig. 2.29 Polarization ratio of an MEH-PPV fiber versus the solution volume fraction, ϕ. An unpolarized sample (sprayed film) has a polarization ratio of 1, whereas values above 1 indicate a preferred molecular alignment along the axial direction [13]
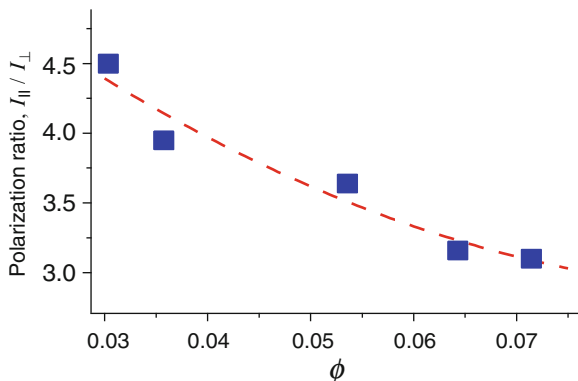
2.7 Controlling the Nanostructure

This research focused on the analysis of the polymer matrix evolution during a strong extensional flow of a polymer solution, using the technique of electrospinning as a test bed. When stretching is dominant, the structures revealed in electrospun nanofibers are dense, stiff and ordered, with a preference for molecular alignment along the fiber longitudinal axis. The observed structure is anisotropic, with a core-sheath conformation that can be utilized for improving charge transport, light amplification, and scaffolding (Fig. 2.30).

The study shows how the nanofiber diameter can be tuned by modifying the electrospinning conditions. The diameter can be decreased to the point just before fragmentation, resulting in the smallest achievable fiber diameter in given conditions, and potentially yielding the highest mechanical properties possible for these conditions, as well as enhanced electrical and optical properties.

The size dependence of these properties, well-documented by numerous experiments, is the consequence of the fiber nanostructure, namely the level of polymer entanglement and the degree of orientation in the solid structure, as well as the existence of super-molecular structures created by correlation between aligned molecules. It can be shown that these properties and the diameter are strongly related by

$$D \sim \left(\frac{n_{\text{ent}}}{\langle \cos \theta \rangle} \right)^{1/2}, \tag{2.19}$$

where n_{ent} is the number density of entanglements and $\langle \cos \theta \rangle$ is the average molecular orientation. This relationship is illustrated in Fig. 2.31.

In conclusion, the nanostructure of electrospun fibers can be controlled by tuning the material and process properties, such as the polymer type and molar mass, solvent quality, solution concentration, injection velocity and diameter, intensity of the electric potential, and the electrodes gap distance. Specific fiber properties can

dense, axially aligned structure
with improved strength, charge
transport, and light guidance

porous, radially aligned structure
with amplification of guided light, also
suitable as soft substrate for cell
adhesion, contaminant removal, or
drug delivery
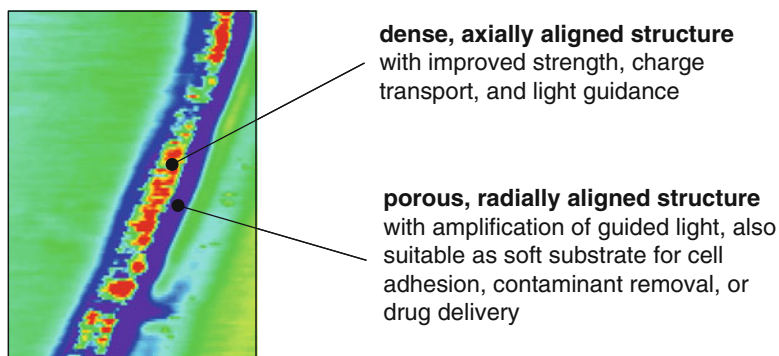
Fig. 2.30 Core-sheath anisotropic structure revealed in electrospun MEH-PPV fibers [13]
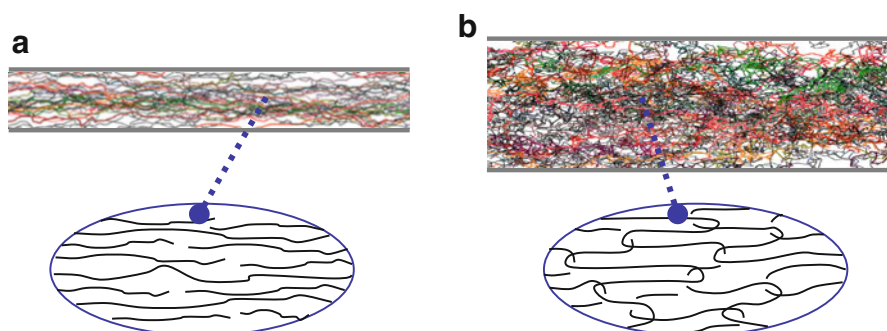
Fig. 2.31 Illustration of possible molecular structures in electrospun nanofibers. (**a**) Small fiber diameter with highly aligned untangled chains, typical of short nanofibers. (**b**) Large fiber diameter with partially aligned and partially entangled chains, typical of continuous nanofibers

be manipulated and tailored by making use of the trends learnt from the modeling and experimental characterization.

References

1. A.L. Andrady, *Science and Technology of Polymer Nanofibers* (Wiley, Hoboken, 2008)
2. J. Stanger, N. Tucker, M. Staiger, *Electrospinning*. Rapra Rev. Rep. **16**(10) (2005)
3. Z.M. Huang, Y.Z. Zhang, M. Kotaki, S. Ramakrishna, A review on polymer nanofibers by electrospinning and their applications in nanocomposites. Compos. Sci. Technol. **63**(15), 2223–2253 (2003). doi:10.1016/S0266-3538(03)00178-7

4. I.U.G. Gogotsi, *Nanotubes and Nanofibers*. Advanced materials series (CRC Taylor & Francis, Boca Raton, 2006)
5. M. Burman, A. Arinstein, E. Zussman, Do surface effects explain the unique elasticity of polymer nanofibers? Europhys. Lett. **96**, 16006 (2011)
6. Y. Liu, S. Chen, E. Zussman, C.S. Korach, W. Zhao, M. Rafailovich, Diameter-dependent modulus and melting behavior in electrospun semicrystalline polymer fibers. Macromolecules **44**(11), 4439–4444 (2011). doi:10.1021/ma200262z
7. Y. Ji, C. Li, G. Wang, J. Koo, S. Ge, B. Li, J. Jiang, B. Herzberg, T. Klein, S. Chen, J.C. Sokolov, M.H. Rafailovich, Confinement-induced super strong PS/MWNT composite nanofibers. Europhys. Lett. **84**(5), 56002 (2008). doi:Artn 56002 doi:10.1209/0295-5075/84/56002
8. M. Burman, A. Arinstein, E. Zussman, Free flight of an oscillated string pendulum as a tool for the mechanical characterization of an individual polymer nanofiber. Appl. Phys. Lett. **93**(19), 193118 (2008). doi:Artn 193118 doi:10.1063/1.3000016
9. A. Arinstein, M. Burman, O. Gendelman, E. Zussman, Effect of supramolecular structure on polymer nanofibre elasticity. Nat. Nanotechnol. **2**(1), 59–62 (2007). doi:10.1038/nnano.2006.172
10. X.M. Sui, H.D. Wagner, Tough nanocomposites: the role of carbon nanotube type. Nano Lett. **9**(4), 1423–1426 (2009). doi:10.1021/Nl803241y
11. X.M. Sui, E. Wiesel, H.D. Wagner, Enhanced mechanical properties of electrospun nanofibers through NaCl mediation. J. Nanosci. Nanotechnol. **11**(9), 7931–7936 (2011). doi:10.1166/jnn.2011.4760
12. A. Camposeo, I. Greenfeld, F. Tantussi, S. Pagliara, M. Moffa, F. Fuso, M. Allegrini, E. Zussman, D. Pisignano, Local mechanical properties of electrospun fibers correlate to their internal nanostructure. Nano Lett. **13**(11), 5056–5062 (2013). doi:10.1021/Nl4033439
13. A. Camposeo, I. Greenfeld, F. Tantussi, M. Moffa, F. Fuso, M. Allegrini, E. Zussman, D. Pisignano, Conformational evolution of elongated polymer solutions tailors the polarization of light-emission from organic nanofibers. Macromolecules **47**(14), 4704–4710 (2014). doi:http://dx.doi.org/10.1021/ma500390v
14. T. Han, A.L. Yarin, D.H. Reneker, Viscoelastic electrospun jets: initial stresses and elongational rheometry. Polymer **49**(6), 1651–1658 (2008). doi:10.1016/j.polymer.2008.01.035
15. P. Gupta, C. Elkins, T.E. Long, G.L. Wilkes, Electrospinning of linear homopolymers of poly (methyl methacrylate): exploring relationships between fiber formation, viscosity, molecular weight and concentration in a good solvent. Polymer **46**(13), 4799–4810 (2005). doi:10.1016/j.polymer.2005.04.021
16. D.H. Reneker, A.L. Yarin, E. Zussman, H. Xu, Electrospinning of nanofibers from polymer solutions and melts. Adv. Appl. Mech. **41**, 43–195 (2007). doi:10.1016/S0065-2156(06)41002-4
17. D.H. Reneker, A.L. Yarin, H. Fong, S. Koombhongse, Bending instability of electrically charged liquid jets of polymer solutions in electrospinning. J. Appl. Phys. **87**(9), 4531–4547 (2000)
18. L.M. Bellan, H.G. Craighead, J.P. Hinestroza, Direct measurement of fluid velocity in an electrospinning jet using particle image velocimetry. J. Appl. Phys. **102**(9), 094308 (2007). doi:Artn 094308 doi:10.1063/1.2799059
19. M.M. Hohman, M. Shin, G. Rutledge, M.P. Brenner, Electrospinning and electrically forced jets. I. Stability theory. Phys. Fluids **13**(8), 2201–2220 (2001)
20. Y.M. Shin, M.M. Hohman, M.P. Brenner, G.C. Rutledge, Experimental characterization of electrospinning: the electrically forced jet and instabilities. Polymer **42**(25), 9955–9967 (2001)
21. I. Greenfeld, A. Arinstein, K. Fezzaa, M.H. Rafailovich, E. Zussman, Polymer dynamics in semidilute solution during electrospinning: a simple model and experimental observations. Phys. Rev. E **84**(4), 041806 (2011). doi:Artn 041806 doi:10.1103/Physreve.84.041806

22. E. Zussman, A. Arinstein, Electrospun polymer nanofibers: mechanical and thermodynamic perspectives. J. Polym. Sci. Part B Polym. Phys. **49**(10), 691–707 (2011). doi:10.1002/polb.22247

23. A.J. Guenthner, S. Khombhongse, W.X. Liu, P. Dayal, D.H. Reneker, T. Kyu, Dynamics of hollow nanofiber formation during solidification subjected to solvent evaporation. Macromol. Theory Simul. **15**(1), 87–93 (2006). doi:10.1002/mats.200500034

24. P. Dayal, T. Kyu, Dynamics and morphology development in electrospun fibers driven by concentration sweeps. Phys. Fluids **19**(10), 107106 (2007). doi:Artn 107106 doi:10.1063/1.2800277

25. P. Dayal, J. Liu, S. Kumar, T. Kyu, Experimental and theoretical investigations of porous structure formation in electrospun fibers. Macromolecules **40**(21), 7689–7694 (2007). doi:10.1021/Ma0714181

26. S. Koombhongse, W.X. Liu, D.H. Reneker, Flat polymer ribbons and other shapes by electrospinning. J. Polym. Sci. Part B Polym. Phys. **39**(21), 2598–2606 (2001)

27. C.L. Casper, J.S. Stephens, N.G. Tassi, D.B. Chase, J.F. Rabolt, Controlling surface morphology of electrospun polystyrene fibers: effect of humidity and molecular weight in the electrospinning process. Macromolecules **37**(2), 573–578 (2004). doi:10.1021/Ma0351975

28. I. Greenfeld, K. Fezzaa, M.H. Rafailovich, E. Zussman, Fast X-ray phase-contrast imaging of electrospinning polymer jets: measurements of radius, velocity, and concentration. Macromolecules **45**(8), 3616–3626 (2012). doi:10.1021/Ma300237j

29. I. Greenfeld, E. Zussman, Polymer entanglement loss in extensional flow: evidence from electrospun short nanofibers. J. Polym. Sci. Part B Polym. Phys. **51**(18), 1377–1391 (2013). doi:10.1002/polb.23345

30. I. Greenfeld, Polymer network dynamics during electrospinning and its effect on the fibers nanostructure: Modeling, simulation and experiments. Mechanical Engineering. PhD thesis, Technion, Haifa, 2013

31. V.N. Kirichenko, I.V. Petrianovsokolov, N.N. Suprun, A.A. Shutov, Asymptotic radius of slightly conducting liquid jet in an electric-field. Dokl. Akad. Nauk SSSR **289**(4), 817–820 (1986)

32. A.F. Spivak, Y.A. Dzenis, Asymptotic decay of radius of a weakly conductive viscous jet in an external electric field. Appl. Phys. Lett. **73**(21), 3067–3069 (1998)

33. M.M. Hohman, M. Shin, G. Rutledge, M.P. Brenner, Electrospinning and electrically forced jets. II. Applications. Phys. Fluids **13**(8), 2221–2236 (2001)

34. F.J. Higuera, Stationary viscosity-dominated electrified capillary jets. J. Fluid Mech. **558**, 143–152 (2006). doi:10.1017/S0022112006000024

35. S.N. Reznik, E. Zussman, Capillary-dominated electrified jets of a viscous leaky dielectric liquid. Phys. Rev. E. **81**(2), 026313 (2010). doi:Artn 026313 doi:10.1103/Physreve.81.026313

36. P.G. de Gennes, Coil-stretch transition of dilute flexible polymers under ultrahigh velocity-gradients. J. Chem. Phys. **60**(12), 5030–5042 (1974)

37. P.G. de Gennes, *Scaling Concepts in Polymer Physics* (Cornell University Press, Ithaca, 1979)

38. R.J. Roe, *Methods of X-ray and Neutron Scattering in Polymer Science*. Topics in polymer science (Oxford University Press, New York, 2000)

39. M. Rubinstein, R.H. Colby, *Polymer Physics* (Oxford University Press, Oxford/New York, 2003)

40. M.G. McKee, G.L. Wilkes, R.H. Colby, T.E. Long, Correlations of solution rheology with electrospun fiber formation of linear and branched polyesters. Macromolecules **37**(5), 1760–1767 (2004). doi:10.1021/Ma035689h

Chapter 3
Graphene-Based Composite Materials for Chemical Sensor Application

Il-Doo Kim, Seon-Jin Choi, and Hee-Jin Cho

Abstract This book chapter reports a comprehensive review of graphene-based composite materials for application in chemical sensors. Recently, the attractive electrical and physical properties of graphene-based materials, i.e., graphite, graphene oxide, and reduced graphene oxide, have stimulated in-depth studies of chemical sensors which exhibit interesting sensing capabilities. For a further improvement in their chemical-sensing performances, graphene-based materials were functionalized with different types of nanostructured sensing layers, such as nanoparticles (NPs), nanorods (NRs), and nanofibers (NFs) prepared with various materials such as metals, metal oxides, and polymers. A number of synthetic methods to obtain graphene-based composite sensing layers were introduced, and they were categorized according to the materials and structures involved. In addition, we summarize recent promising progress in the area of chemical sensor applications with graphene-based composite materials, highlighting important sensing performance, such as those related to sensitivity (response), selectivity, response/recovery times, detection limits, and operating temperatures. Furthermore, potential sensing mechanisms are thoroughly analyzed in an effort to understand the characteristic sensing properties of graphene-based composite sensors. Finally, future perspectives on the development of graphene-based composite materials are discussed with regard to the realization of high-performance chemical sensors.

3.1 Chemical Sensors

Numerous sensing materials have been developed to detect chemical species in environments such as SO_2, NO_x, NH_3, and CO_x, as well as biomarkers from the exhaled breath such as acetone (CH_3COCH_3), toluene ($C_6H_5CH_3$), and H_2S. Sensitive and selective detection of low concentrations of ambient chemical

I.-D. Kim (✉) • S.-J. Choi • H.-J. Cho
Department of Materials Science and Engineering, Korea Advanced Institute of Science and Technology, 291 Daehak-ro, Yuseong-gu, Daejeon 305-701, Republic of Korea
e-mail: idkim@kaist.ac.kr

species is important for chemical sensors. In this regard, sensing layers with large surface area as well as high porosity are desirable considering that the sensing performance depends on the diffusion of gas molecules and surface reactions between the gas molecules and the sensing layers. For this reason, nanoparticle (NP), nanorod (NR), and nanofiber (NF) structures have been intensively researched in efforts to attain higher sensitivity compared to that of thin film structures. In addition, catalytic functionalization with metallic catalysts such as Pt, Pd, Au and Ag has been introduced to further enhance the gas sensing performance. Recently, graphene-based composite materials are receiving much attention due to their attractive electrical and physical properties. A number of composites with graphene-based materials have been proposed and their sensing properties have been demonstrated. In this chapter, we introduce several types of graphene-based composite sensing layers developed for application in environmental monitoring and exhaled breath analysis. In particular, we highlight the studies on the metal oxide nanofiber-graphene composite material as a new sensing layer for fast responding and highly sensitive chemical sensors.

3.2 Graphene-Based Sensing Layers

The gas sensing characteristics of graphene were first investigated by F. Schedin et al. in 2007 [1]. Since then, numerous studies have been carried out on highly sensitive chemical sensors using graphene sheets [2–5]. The attractive electrical and physical properties such as high carrier mobility (200,000 cm^2/V s) and large specific surface area (theoretically 2,630 m^2/g) of graphene have motivated in-depth studies in the field of chemical sensors. Table 3.1 summarizes recent publications related to chemical sensors using graphene-based sensing layers.

Reduced graphene oxide (RGO) sheets prepared by chemical and thermal reduction of graphene oxide (GO) have been widely investigated for gas sensing applications. For instance, hydrogen plasma treatment for the reduction of GO was performed and demonstrated high sensitivity to CO_2 at room temperature, where the response, i.e., $(R_{air} - R_x)/R_{air} \times 100\,(\%)$, was 71 % and 15 % at 1,500 ppm in N_2 (37 % RH) and air ambient (68 % RH), respectively [6]. In addition, ozone-treated graphene exhibited improved sensing properties such as better response (20 % response), limit of detection (1.3 ppb), and response time (<40 s) toward NO_2, which were attributed to optimized density of the oxygen functional groups by the ozone treatment [14].

RGO arrays prepared by thermal reduction demonstrated highly selective properties in the presence of different alcohols such as isopropanol, ethanol, methanol, and water [8]. Poor selective gas sensing properties of RGO are a major problem for practical applications. In this regard, optimized thermal reduction conditions were applied under vacuum ($p = 2 \times 10^{-5}$ torr) at 150 °C for 3 min to obtain only slightly reduced GO. The dimensions of GO flakes were in a range from hundreds of nm to 200 μm (Fig. 3.1a). The reduction proceeded with drop-casted GO flakes on a

Table 3.1 Recent publications for chemical sensors using graphene-based sensing layers

Composites	Sensing type	Response definition	Sensitivity (Response)	Detection limit	Testing ambient	Target gas	Response/ recovery time	Operating temp.	Ref.
Hydrogen plasma RGO	Resistivity change	$R_{N2\ or\ air} - R_x / R_{N2\ or\ air} \times 100$ (%)	15 % @ 1,500 ppm	2 % @ 300 ppm	68 % RH	CO_2	240 s/240 s	Room temp.	[6]
Chemically RGO	Resistivity change	$(R_{gas} - R_0) / R_0 \times 100$ (%)	23 % @ 50 ppm	2.4 % @ 1 ppb	Dry air ambient	NH_3	1.4 s/76 s[a]	Room temp.	[7]
Thermally RGO	Resistivity change	$\Delta R / R_0$	~7 % @ 1,500 ppm	>3.5 % @ 500 ppm	Dry air ambient	H_2O	–	Room temp.	[8]
GO	Resistivity change	$R_a - R_g / (R_a + R_G) \times 100$ (%)	–	20 ppb	Dry air ambient	NO_2	120 s/-	150 °C	[9]
Patterned RGO[b]	Resistivity change	$(R_0 - R) / R_0$	0.35 @ 38 %	10 ppm	N_2 ambient	NH_3	~550 s @ 100 °C/-	Room temp.	[10]
Few-layered graphene	Resistivity change	$|R_a - R_g| / R_a$	3.83 @ 200 ppm	0.081 @ 3 ppm	Air ambient	CO_2	11 s/14 s	Room temp.	[11]
CVD grown graphene	Resistivity change	% change in sheet resistance	90 % @ 1,000 ppm	~3 % @ 500 ppb	Air ambient	NH_3	<180 s @ 1,000 ppm/-	Room temp.	[12]
CVD grown graphene	Conductivity changes	$\Delta G / G_0$ (%)	~23 % @ 200 ppt	1.4 % 10 ppt	N_2 ambient	NO	-/-	Room temp.	[13]
Ozone treated graphene	Resistivity change	$(R_0 - R_g) / R_0 \times 100$ (%)	19.7 % @ 200 ppm	200 ppb	Dry air ambient	NO_2	~20 s/-	Room temp.	[14]
Defected bilayer graphene[c]	Conductivity changes	G / G_0 (%)	32 % @ 100 ppm	–	N_2 ambient	NO_2	328 s/-	Room temp.	[15]
partially RGO	Resistivity change	$(R_0 - R_g) / R_0 \times 100$ (%)	~4.5 % @ 160 ppm	30 ppm	Air ambient	H_2	~20 s/~10 s	Room temp.	[16]

(continued)

Table 3.1 (continued)

Composites	Sensing type	Response definition	Sensitivity (Response)	Detection limit	Testing ambient	Target gas	Response/ recovery time	Operating temp.	Ref.
Graphene nanomesh	Resistivity change	$\Delta R/R_0$ (%)	~4.5 % @ 1 ppm	15 ppb	Dry air ambient	NO_2	480 s/-	Room temp.	[17]
Sulfonated RGO.	Conductivity changes	G/G_0	24.7 @ 50 ppm	5 ppm	Air ambient	NO_2	-/-	Room temp.	[18]
Graphene sheet	Conductivity changes	$(G_a-G_g)/G_a$ (%)	~26 % @ 100 ppm	10 ppm	Air ambient	CO_2	<10 s/-	60 °C	[19]
Chemically derived graphene	Resistivity change	$\Delta R/R_0$ (%)	27 % @ 5 ppm	–	N_2 ambient	NO_2	-/-	Room temp.	[20]

[a]IR illumination during the recovery process maintaining the temperature less than 40 °C
[b]Highly oriented RGO microbelts
[c]Ga^+ ion irradiation to introduce controlled disorder into the graphene structure
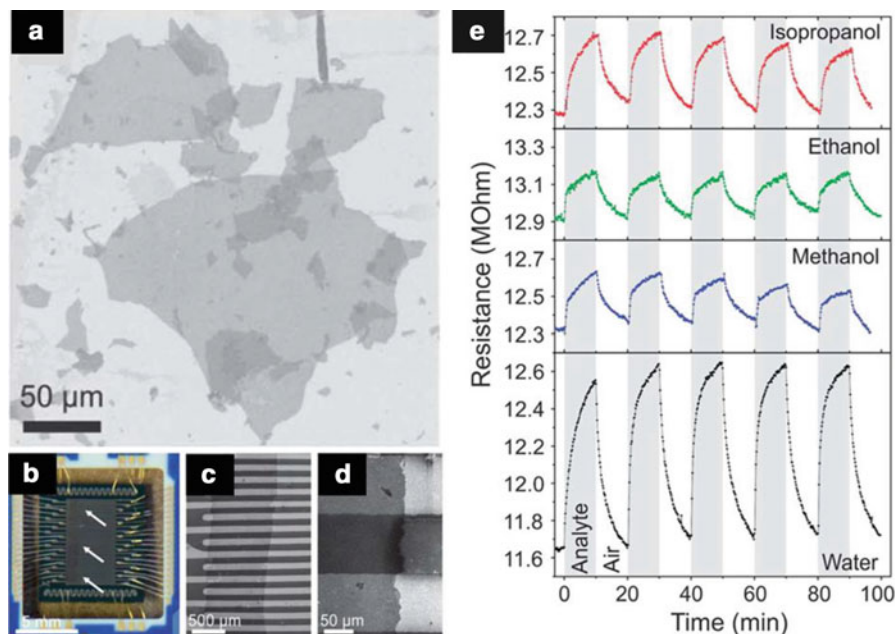
Fig. 3.1 (**a**) SEM image of prepared GO flakes, (**b**) optical microscopic image of the multielectrode KAMINA chip. (**c**) SEM image of the RGO coated sensor chip, (**d**) magnified SEM image of (**e**) and dynamic resistive transient characteristics of the RGO-based sensor array with multiple gas exposures such as isopropanol, ethanol, methanol and water with a concentration of 1,500 ppm (Reprinted with permission from Lipatov et al. [8]. Copyright (2013), The Royal Society of Chemistry)

modified KAMINA multisensor chip [21], as shown in Fig. 3.1b–d. Gas sensing characteristics using isopropanol, ethanol, methanol, and water with a concentration of 1,500 ppm were demonstrated at room temperature. Reproducible resistivity changes were observed, exhibiting responses to the injection of analyte gases and recovery by exposure to dry air (Fig. 3.1e). In particular, the response toward water was significantly improved compared to other analyte gases due to easy penetration of water molecules into the wide RGO interlayer ($d = 7.6$ Å), which was comparable to the GO layers in terms of width ($d = 8$ Å). Regarding the other alcohol sensing properties, only the top few layers participated in the reaction due to low penetration of the alcohol molecules, which resulted in relatively low sensitivity. For this reason, several parameters were involved in the sensitivity such as the size and geometry of RGO sheets as well as defects for different alcohol sensing. However, these parameters can promote selective detection of alcohol molecules if the different properties of RGO can be integrated by array type sensors. Hydrophilic GO and hydrophobic RGO sensor arrays were proposed as well for selective and sensitive detection of tetrahydrofuran (THF) and dichloromethane (MC), even at a highly humid ambient (90 % RH) with a gas concentration of 500 ppb at room temperature [22].

In general, functionalized graphene sheets exhibit improved sensing characteristics because the gas molecules can be adsorbed strongly on doped or defective graphene

sheets [15, 23, 24]. For this reason, highly oxidized and large flakes of GO were employed as effective NO sensing layers with a very low detection limit of 20 ppb at 150 °C [9]. Chemically modified graphene sheets such as sulfonated RGO (S-RGO) or ethylenediamine-modified RGO (EDA-RGO) were explored for high-performance NO_2 sensors [18]. The synthesized S-RGO and EDA-RGO exhibited 4–16 times higher responses compared to that of RGO. In particular, the NO_2 gas response of S-RGO sheets was evaluated with respect to the current or conductance changes (G/G_0, where G and G_0 are the conductance of the sensing layer in NO_2 and air ambient, respectively) and S-RGO showed a response of 24.7 toward 50 ppm NO_2, corresponding with a more than 16 times higher response compared to that ($G/G_0 = 1.5$) of pure RGO. The selective property of S-RGO was investigated and minor responses were observed toward interfering gases such as NH_3, H_2O, and toluene.

Flexible sensing devices are among the fascinating applications that exploit the flexible characteristics of graphene sheets. Several attempts to realize flexible gas sensors using graphene-based sensing layers have been reported [25–27]. G. Yang et al. reported graphene-based flexible NO_2 sensors on paper substrates [25]. First, graphene sheets were prepared by a chemical vapor deposition (CVD) method on a copper foil in a mixed gas ambient of methane and hydrogen at 1,000 °C. Polymethylmethacrylate (PMMA)-graphene-copper foil stacks were formed with size of 10 mm × 8 mm followed by O_2 plasma reactive-ion etching of the back-side graphene on the copper foil (Fig. 3.2a). PMMA-graphene was then obtained by chemically etching the copper foil using a 1 wt% solution of ammonium persulfate for 6–8 h (Fig. 3.2b). The PMMA-graphene structure was transferred to a commercialized cleanroom paper with a size of 2 cm × 2 cm (Fig. 3.2c). Finally, silver electrodes (1 mm × 3 mm in size and a 5 mm interval between the two electrodes) were patterned on the graphene layer to investigate gas sensing performance (Fig. 3.2d). Figure 3.2e shows camera images of the fabricated flexible gas sensor using CVD grown graphene sheets and the measurement setup. The gas response characteristics toward 200 ppm NO_2 simultaneously with the flexible property of the sensor following two different bending directions were confirmed at room temperature (Fig. 3.2f, g). The NO_2 response was evaluated as $R(\%) = [(R_{air} - R_{gas})/R_{air}] \times 100 \, (\%)$, where R_{air} and R_{gas} are the resistivity in air and NO_2, respectively. The results revealed that the fabricated graphene-based flexible sensor showed reproducible NO_2 sensing properties in strained (0.5 %) and relaxed states with minor response deviation (R = 32–39 %) (Fig. 3.2g).

Recently, graphene based materials with patterned structures such microbelts and a nanomesh were investigated for chemical sensors. R. K. Paul et al. proposed a graphene nanomesh as an effective NO_2 sensing layer using polymeric nanosphere lithography and reactive ion etching methods [17]. The graphene nanomesh exhibited a higher response ($I_{ON}/I_{OFF} = 6$) at room temperature compared to that of film type graphene sheets, which showed a minor response. J. Zhang et al. also reported highly oriented RGO microbelts array for the detection of NH_3 at an operating temperature range of 20–100 °C [10]. The RGO microbelts array was fabricated by a soft lithography technique using a PDMS stamp. The response
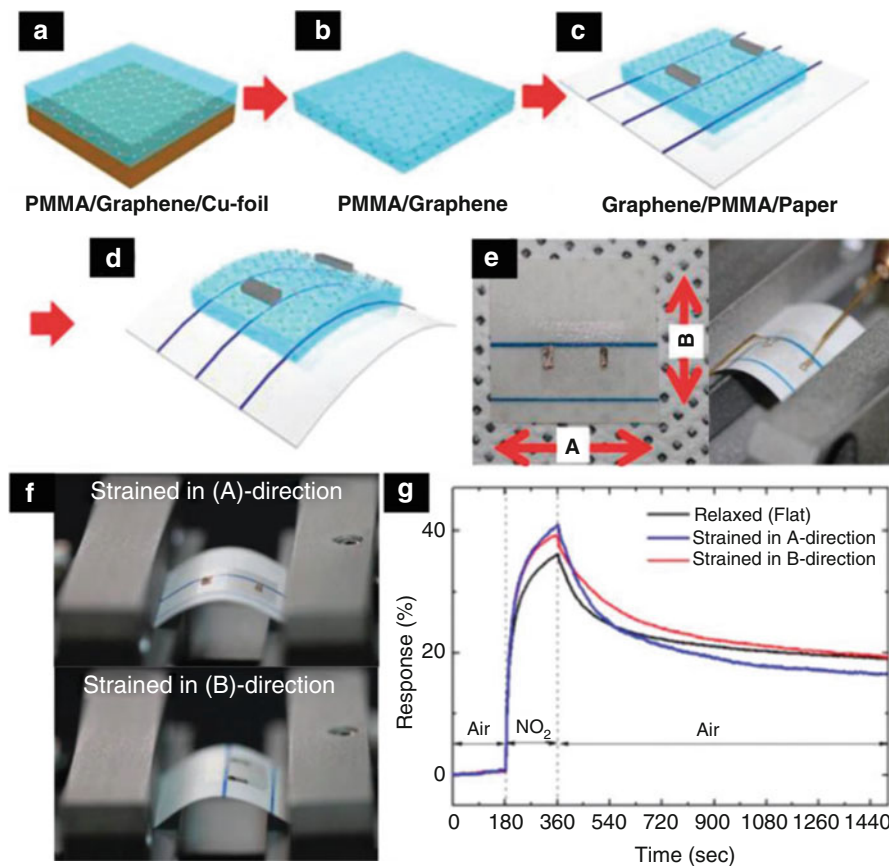
Fig. 3.2 Schematic illustration of the fabrication processes for the graphene-based flexible sensor: (**a**) formation of PMMA-graphene-Cu foil, (**b**) chemical etching of Cu foil, (**c**) transfer of PMMA-graphene to a cleanroom paper and formation of Ag electrodes, (**d**) concept of flexible gas sensors. (**e**) Device images of the fabricated graphene flexible sensor, (**f**) strained state in the two different directions and (**g**) NO$_2$ sensing characteristics in the strained and relaxed states (Reprinted with permission from Yang et al. [25]. Copyright (2013), The Royal Society of Chemistry)

$(R = (R_o - R)/R_o)$, where R_0 and R are resistivity of the sensor during the exposure of pure N_2 and the exposure of N_2 in NH_3 mixture, respectively) showed consistent values of around 0.19 toward 1 % NH_3 gas in a temperature range of 20–100 °C.

3.3 Nanoparticle-Graphene Composite Sensing Layers

Recently, many researchers have reported graphene functionalized novel metals or metal oxide NPs to enhance gas sensing performance, i.e., sensitivity, selectivity, or response/recovery times. Although metal/metal oxide NPs have good electron

transfer properties and large surface area, they suffer from degradation of sensitivity and long response/recovery times due to aggregation between particles, thereby reducing the effective surface area for the reaction with gas molecules. Therefore, combining NPs and graphene/RGO sheets to further increase the gas sensing performance by inhibiting aggregation of NPs and graphene sheets, respectively, is a powerful strategy. Thus far, several studies have reported that the sensing performances were dramatically increased when graphene-based materials were integrated with metal/metal oxide NPs. In this part, several examples of metal/metal oxide NP-graphene composites are introduced and the sensing mechanisms are discussed. Table 3.2 summarizes recent publications on chemical sensors using NPs-graphene composite sensing layers.

3.3.1   Metal NP-Graphene Gas Composite Sensing Layers

Metal NP-graphene composites are widely applied in many research fields including electronics, energy, and chemical sensors [42–45]. Various synthetic methods of novel metal NPs functionalized with graphene-based materials have been reported [46–48]. A well-known method to combine graphene based materials with metal NPs is the *in-situ* reduction synthesis of metallic salts and graphene/GO sheets using chemical agents. Briefly, defects or oxygen functionalities on the graphene/GO surface behave as nucleation sites for metal NP growth from the metallic salts (Fig. 3.3a). Another synthetic method is the *ex-situ* synthesis of metal NPs, assisted by chemical reduction of the metallic salts followed by decoration onto the graphene sheets (Fig. 3.3b) [29].

Decoration of metal NPs on graphene sheets or modified forms of this approach (e.g., GO and RGO) has also been intensively researched to enhance gas sensing performances. The gas sensing mechanisms of graphene-based sensors were investigated by measuring the resistivity changes, which were induced by adsorption or desorption of target molecules. Graphene is known as a p-type sensing material exhibiting a sensitive response to modulation of hole concentrations. Attaching metal NPs to graphene sheets results in lowering of the Fermi level of graphene due to the different work functions between metal NPs (e.g. Pt and Au) and graphene sheets and the transferring of electrons to metallic salts during the reduction process. Graphene is thus more likely to have p-type characteristics, i.e., it is more sensitive to hole concentration [30, 49]. In other words, NPs act as an electron transfer mediator between reducing gases and graphene when the hybrid structures are exposed to reducing gases. The electrons are injected from the adsorbed gas molecules to metal NPs, and this injection induces rearrangement of the Fermi level at the interface between the metal NPs and graphene. This phenomenon results in a reduction of hole concentrations and increased base line resistance. In contrast, the oxidizing gases take electrons from the NP-graphene composites, which resulted in hole doping, thereby reducing the base line resistance.

Table 3.2 Recent publications for chemical sensors using NPs-graphene composite sensing layers

Composites	Sensing type	Response definition	Sensitivity (Response)	Detection limit	Testing ambient	Target gas	Response/ recovery time	Operating temp.	Ref.
Pd-Pt alloy NP-RGO	Resistivity change	$\Delta R/R_0$ (%)	4.4 @ 2 %		Ar ambient	H_2	<2 s/8 s	40 °C	[28]
Pd NP-graphene	Resistivity change	$(R_g-R_o)/R_o \times 100$ (%)	32.9 % @ 1,000 ppm	20 ppm	N_2 ambient	H_2	~1 s/-	Room temp.	[29]
Au NP-RGO	Current change	$\Delta I/I_0 \times 100$ (%)	–	NO_2 68 ppb/H_2S 434 ppb	N_2 ambient	H_2S, NO_2	–	Room temp.	[30]
α-Fe$_2$O$_3$ NPs-RGO	Resistivity change	R_a/R_g	30 @ 1,000 ppm	–	50 % RH	ethanol	–	280 °C	[31]
WO$_3$ NP-RGO	Resistivity change	R_{NO2}/R_{AIR}	133 @ 5 ppm	1 ppm	Humid air ambient	NO_2	~20 s/-	250 °C	[32]
SnO$_2$ NP-RGO	Resistivity change	$(R_g-R_o)/R_o \times 100$ (%)	~800 @ 9 ppm	–	Dry air ambient	NO_2	–	150 °C	[33]
SnO$_2$ NP-RGO	Resistivity change	R_a/R_g	3.31 @ 5 ppm	0.5 ppm	25 % RH	NO_2	135 s/200 s	50 °C	[34]
SnO$_2$ NP-RGO	Impedance change	$(Z_{NH3}-Z_{carrier\ gas})/Z_{carrier\ gas} \times 100$ (%)	15.9 % @ 50 ppm	–	N_2 ambient	NH_3	<1 min	Room temp.	[35]
SnO$_2$ NC-RGO	Resistivity change	R_a/R_g	22 @ 1.12 ppm ethanol; 11 @ 1.12 ppm H$_2$S	–	Air ambient	Ethanol/H_2S	5 s/9 s	300 °C	[36]
Co$_3$O$_4$-RGO	Resistivity change	$(R_g-R_o)/R_o \times 100$ (%)	50 @ 60 ppm NO$_2$	–	N_2 ambient	NO_2/methanol	NO_2 ~20 min/ methanol 1–2 min	Room temp.	[37]

(continued)

Table 3.2 (continued)

Composites	Sensing type	Response definition	Sensitivity (Response)	Detection limit	Testing ambient	Target gas	Response/ recovery time	Operating temp.	Ref.
ZnO QDs-RGO	Conductance change	$(G_g - G_a)/G_a$	1.1 @ 100 ppm	–	Dry air ambient	Formaldehyde	30 s/40 s	Room temp.	[38]
SnO$_2$ NC-RGO	Current change	R_g/R_a	2.87 @ 100 ppm	1 ppm	Dry air ambient	NO$_2$	65 s/-	Room temp.	[39]
IDTO-RGO	Conductance change	$\Delta G/G_0$	11 @ 100 ppm	0.3 ppm	Air ambient	NO$_2$	–	Room temp.	[40]
Pd NP-TiO$_2$ NP-RGO	Resistivity change	$(R_g - R_o)/R_o$	92 % @ 500 ppm	–	Dry air ambient	H$_2$	18 s/29 s	180 °C	[41]
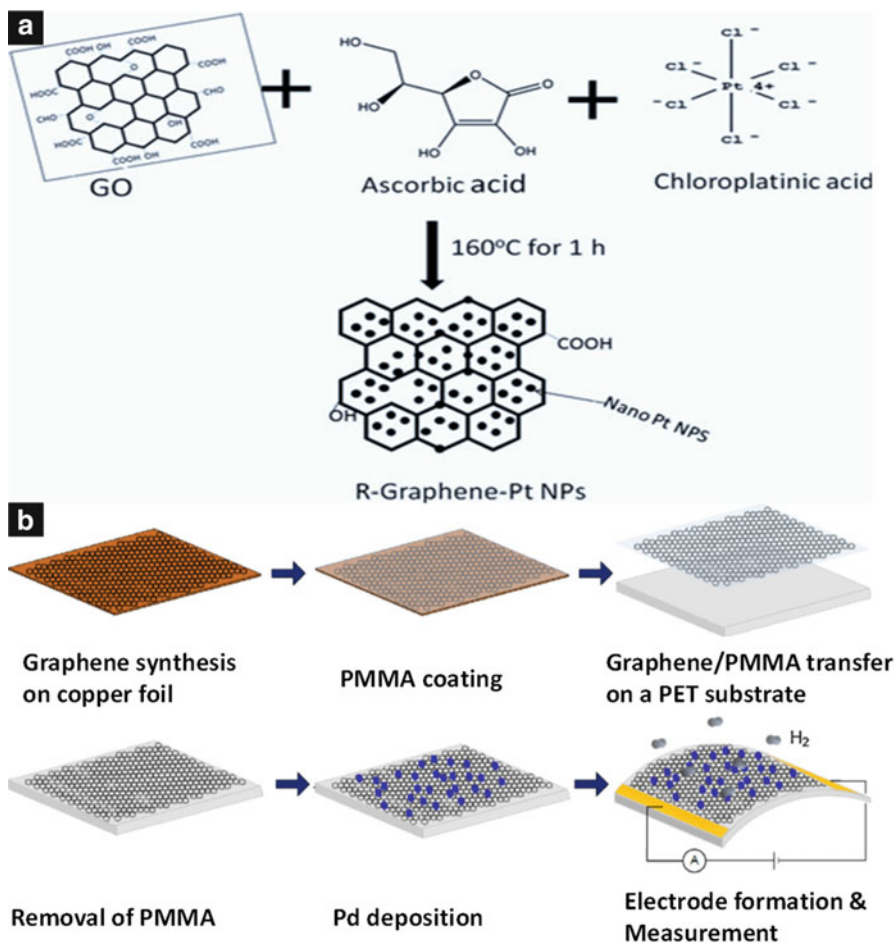
Fig. 3.3 Schematic images of the synthetic method of metal NP-graphene composite structures (**a**) *in-situ* reduction synthesis of Pt NPs on RGO (Reprinted with permission from Zhang et al. [42]. Copyright (2013), Springer) (**b**) Decoration of *ex-situ* synthesized Pd NPs onto graphene sheet (Reprinted with permission from Chung et al. [29]. Copyright (2012), Elsevier)

V. Tjoa et al. reported the behavior of Au NPs-RGO hybrid composites upon exposure to H_2S and NO_2, respectively [30]. Au NPs-RGO exhibited p-type sensing characteristics, resulting in a downward shifting Fermi level at the Au NP-RGO interface due to the hole doping to RGO (Fig. 3.4a). Although pure RGO exhibited minor resistivity changes during exposure to H_2S, the Au NPs-RGO showed improved sensing performance toward H_2S (Fig. 3.4c). The adsorption of H_2S onto Au NPs occurs especially by the high chemical affinity of sulfur to Au. This adsorption results in electron injection to Au, which readjusts the Fermi level at the interface between the Au NPs and graphene by reducing the hole current due to the recombination of electrons and holes (Fig. 3.4b). In contrast, the oxidizing gases
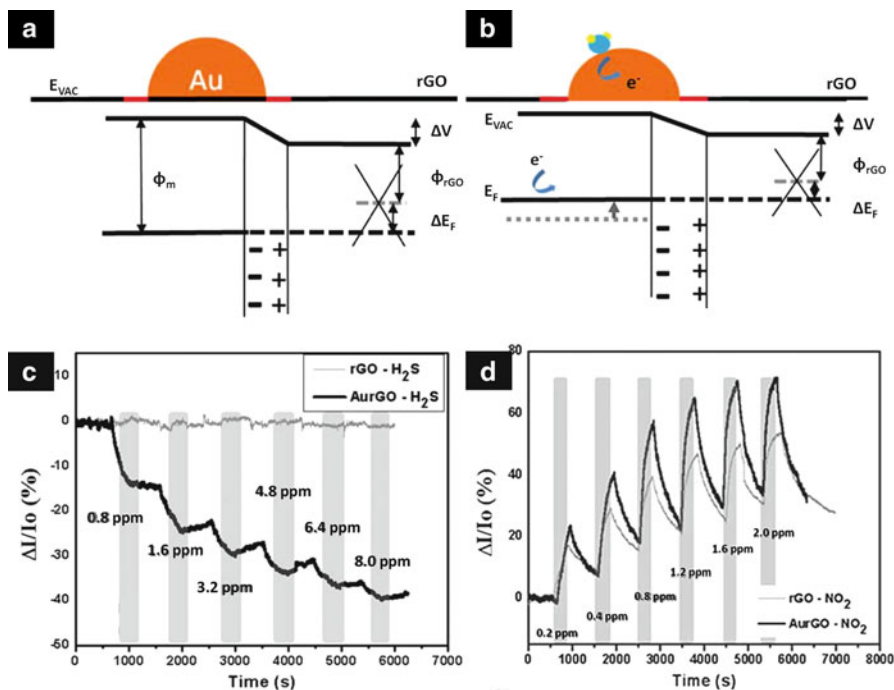
Fig. 3.4 Schematic illustrations of theoretical energy band diagram of Au NPs/RGO contact interface: (**a**) the equilibrium state when the RGO was combined with Au NPs, (**b**) the electronic interaction among gas molecules (e.g., H_2S), Au NPs and RGO. Injection of electrons to the Au NPs and transfer to graphene by the adsorption of gas molecules. The response characteristics toward (**c**) the reducing gas of H_2S and (**d**) oxidizing gas of NO_2, respectively (Reprinted with permission from Tjoa et al. [30]. Copyright (2011), The Royal Society of Chemistry)

withdraw electrons from the Au NP-RGO composite, which resulted in hole accumulations at the surface. Therefore, the hole current increased when Au NPs-RGO was exposed to oxidizing gases such as NO and NO_2 (Fig. 3.4d). Metallic alloys of Pd-Pt NPs were functionalized onto graphene sheets, as reported by R. Kumar et al. [28]. The metallic alloy-graphene composite showed a remarkably fast response (<2 s) and recovery (18 s) times to 2 % hydrogen at 40 °C. Pd and Pt are well-known catalytic materials exhibiting a catalytic sensing effect, i.e., electronic and chemical sensitization. These metals easily form hydrides (PdH_x, PtH_x) upon exposure to hydrogen, and in particular Pd-Pt alloys exhibit better hydrogenation compared to pure Pd or Pt. The H_2 molecules are adsorbed on the surface of Pd-Pt alloys followed by dissociation into atomic H forming MH_x and incorporation into interstitial sites of the Pd-Pt alloy. The incorporated MH_x acts as electron scattering centers, resulting in a decrease in carrier mobility. However, the formation of MH_x lowers the work function of Pd-Pt alloy, inducing resistivity changes with fast response and recovery times. As mentioned above, a number of studies on metal NP-graphene have been conducted in relation to sensing devices

because it affords better electronic and optic properties than pure graphene [50]. It is anticipated that metal NP-graphene hybrid composites will be further investigated with various metal NPs in efforts to attain better chemical sensing performances.

3.3.2 Metal Oxide NP-Graphene Composite Sensing Layers

Chemical sensors based on metal oxide NPs have attracted much attention due to their highly sensitive gas sensing characteristics [32, 51]. Metal oxides, which show significant resistance changes upon exposure to reducing or oxidizing gases, have been intensively researched for chemical sensing. However, pure metal oxide NPs are operated at an elevated temperature, which requires high power consumption. In the case of graphene, excellent gas detection capabilities are observed due to the defects or edges, where the gas molecules can be adsorbed and desorbed. However, its gas detection capabilities depend on the number of layers and their dispersion, and graphene/RGO sheets showed a tendency to aggregate, resulting in decreased sensitivity to gas molecules. Experimental studies have shown that the adsorption of gas molecules is too weak to effectively detect the gas molecules. For this reason, a combination of metal oxide NPs and graphene has been explored to enlarge the active area, resulting in enhancement of sensing properties by less agglomeration of graphene sheets and metal oxide NPs and uniformly decorated metal oxide NPs on graphene sheets (Fig. 3.5a and b) [38, 52, 53]. A number of reports on chemical sensors using metal oxide NP-graphene composites to improve the sensing performances have been reported. SnO_2 NP-RGO composites have been widely studied as sensing layers [34, 36, 39]. A typical method for incorporation of metal oxide NPs into RGO is hydrothermal reaction, where GO sheets were reduced to RGO while Sn^{2+} was oxidized to SnO_2 during the redox reaction. First, GO was prepared by a modified Hummers method [54, 55]. The prepared GO solution was then mixed with a Sn precursor ($SnCl_4 \cdot H_2O$) in deionized water. The mixture was stirred using sonication and then transferred into an autoclave and heated at 120 °C for 8 h [35]. By combing SnO_2 NPs and RGO, the active surface area of SnO_2 NPs was increased owing to their uniform dispersion. Generally, SnO_2 and RGO show n-type and p-type sensing characteristics, respectively. When the amount of SnO_2 is limited, SnO_2 NP-RGO showed p-type sensing characteristics, and a p-n junction is formed at the interface of SnO_2-RGO, exhibiting enhanced selectivity and sensitivity compared to those of pure RGO toward NO_2. S. Mao et al. explained the sensing characteristics of SnO_2-RGO [39]. The formation of a p-n junction at the interface between SnO_2 NPs and RGO sheets generated higher sensitivity to NO_2 gas while the sensitivity for NH_3 was suppressed compared to that of pure RGO (Fig. 3.5c and d). During the exposure of NO_2 to the composites, a large number of electrons were extracted from the RGO sheets toward SnO_2 due to the depletion region formed by the p-n junction. This electron transfer generated dominant hole current in RGO by modification of the Fermi level state. On the
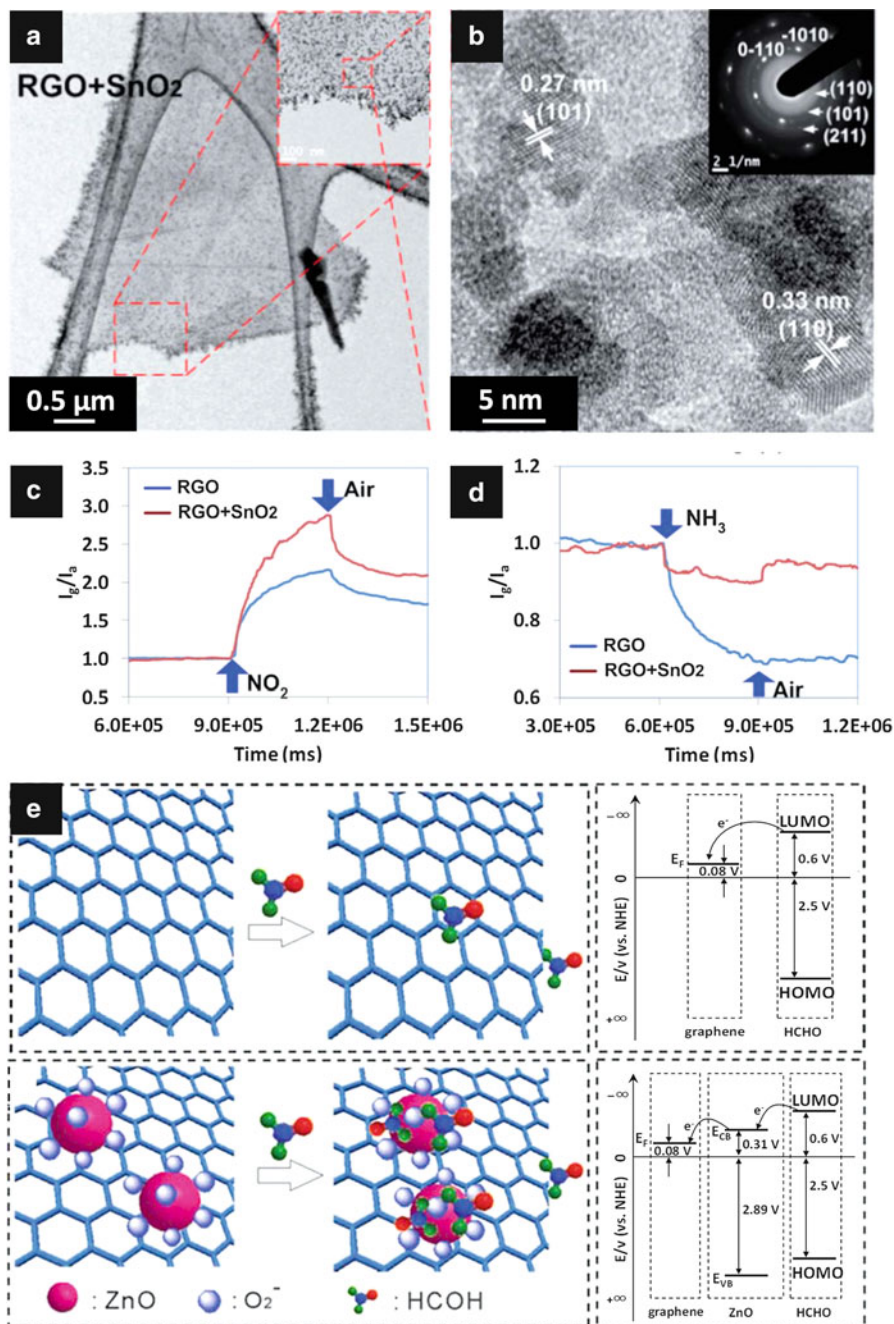
Fig. 3.5 (**a**) TEM and (**b**) HRTEM images of SnO_2 NP-RGO composite. The *inset* of (**b**) shows the SEAD pattern of SnO_2 NP-RGO; The response characteristics of pure RGO and the SnO_2 NP-RGO composite toward (**c**) NO_2 and (**d**) NH_3, respectively (Reprinted with permission from Mao et al. [39]. Copyright (2012), The Royal Society of Chemistry) (**e**) Schematic illustration of sensing mechanism: electron transfer process between the gas molecules and graphene (*upper*) and electron transfer process between gas molecules and ZnO QD-graphene composites (*lower*) (Reprinted with permission from Huang et al. [38]. Copyright (2012), The Royal Society of Chemistry)

other hand, a reducing gas such as NH_3 donated electrons to the SnO_2 NP-RGO composite, inducing decreased hole concentration and hole current in RGO due to fewer injected electrons to RGO. These reduced electron injection is attributed to the p-n junction and hole depletion zone. Another possible explanation of the decreased sensitivity to NH_3 is a shadowing effect of SnO_2 NPs covering the RGO functional groups, which can react with NH_3 [39]. G. Neri et al. also further evaluated the sensing behaviour of SnO_2 NP-RGO composites toward NO_2 at various RGO concentrations [33]. The RGO concentration was controlled by the amount of GO added to the solution. The SnO_2-RGO type and gas detection mechanism vary according to the SnO_2/RGO ratio. When the density of SnO_2 is low, SnO_2-RGO composites show p-type characteristics and the resistivity decreases upon exposure to oxidizing gas such as NO_2. However, when the density of SnO_2 is large, the SnO_2-RGO composite acts like an n-type sensing material and has more p-n junctions between SnO_2 and RGO. These p-n junctions are more dominant than the high electrical conductivity of RGO, and the surface of SnO_2, where the reaction takes place, increases. Thus, at a particular ratio of SnO_2/RGO (the GO content in solution is 0.1 g when the tin precursor is 1.0 g), enhanced sensitivity is observed for NO_2 owing to the effect on modification of the potential barrier by p-n junctions and an increase of effective reaction sites of SnO_2. The highest response is *ca.* 850 for 8 ppm NO_2 at 150 °C, (the response is defined as $(R_g - R_o)/R_o \times 100 \, (\%)$, where R_o and R_g are the sensor resistivity before and after target gas exposure, respectively).

In addition to SnO_2 NP-graphene, a number of different types of metal oxide NP-graphene composites have been proposed for chemical sensors. For example, Q. Hang et al. suggested ZnO quantum dot (QD)-graphene composites that showed outstanding gas sensing performance to formaldehyde (HCHO) and good stability after repeated exposure to 100 ppm of formaldehyde [38]. Here, the gas response is defined as $(G_g - G_a)/G_a$, where G_a and G_g are the conductivity in atmospheric ambient and during target gas exposure, respectively. In the case of pure graphene sensors, there are weak van der Waals interactions with the formaldehyde molecules and graphene, thereby transferring electrons and thereupon generating conductivity changes. In addition, the weak adsorption of formaldehyde was attributed to the fast response/recovery times. When ZnO QDs were decorated with graphene, ZnO promoted electron transfer from formaldehyde to graphene because the conduction band of ZnO is located between the LUMO of formaldehyde and the E_F of grapheme (Fig. 3.5e). Formaldehyde molecules showed stronger interaction with chemisorbed oxygen species (O^-, O^{2-}) on the surface of ZnO QDs compared to that with graphene. Therefore, stronger interactions took place between ZnO QDs and formaldehyde than interactions between pure graphene and formaldehyde. ZnO QD-graphene exhibited better sensitivity than pure graphene for formaldehyde sensing due to the synergistic effect of ZnO QDs and graphene; that is, ZnO QDs on graphene sheets act reactions sites for the adsorption of detecting gases, and the graphene provides conducting paths. At lower temperature (<100 °C), O_2^- was abundantly produced on the surface of ZnO QDs, which have lower oxidation

ability than other chemisorbed oxygen species (i.e., O^-, O^{2-}) that can be produced at higher temperatures. The metastable intermediate product (formate species) was formed as a result of the formaldehyde oxidation reaction with O_2^- on ZnO QD-graphene composites, as shown below (3.1):

$$3O_2^-(ad) + 4HCHO \leftrightarrow 4HCOO^-(intermediate\ product) + 2H_2O + 3e^- \quad (3.1)$$
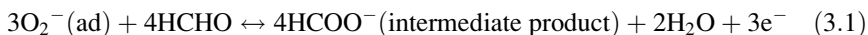
The electrons produced during the oxidation reaction change the conductivity and reduce the energy barrier between formaldehyde and graphene by transferring electrons to ZnO QDs and further transfer to graphene. When the baseline air was injected to the sensors, a reversible oxidation reaction occurred where the formate species was decomposed again to formaldehyde. The ZnO QDs act as reaction centers with target gas molecules, resulting in enhanced selectivity and sensitivity for formaldehyde relative to those of pure graphene.

Similarly, S. Liang et al. reported a α-Fe_2O_3 NP-graphene gas sensor for ethanol detection [31]. Hematite (α-Fe_2O_3) is an attractive sensing material due to its low cost, environment-friendliness, and corrosion resistance under ambient conditions. However, there have been many attempts to make composite based α-Fe_2O_3 NPs for further enhancement of gas sensing characteristics [56]. For further improvement in sensitivity and stability of hematite, S. Liang et al. combined α-Fe_2O_3 NPs with RGO sheets [31]. It was also confirmed that the sensing properties were affected by the concentration of RGO and the operating temperature. An optimized response ($R_a/R_g = 30$ for 1,000 ppm ethanol) was presented with RGO content of 2 wt% at 280 °C (Fig. 3.6a). High sensitivity was achieved by the high electrical
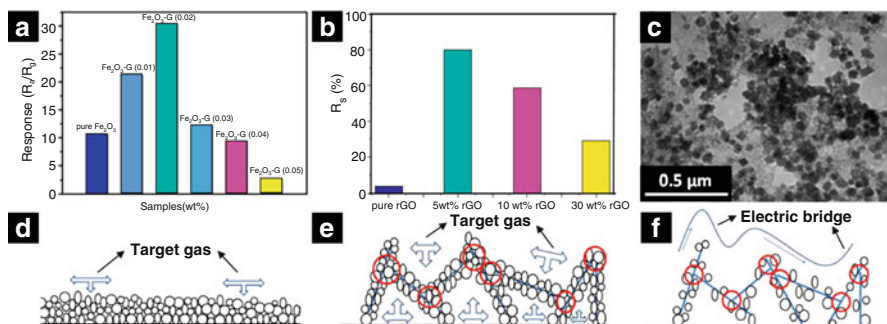
Fig. 3.6 The impact of graphene concentration of metal oxide NP-graphene nanocomposite; (**a**) the response to 1,000 ppm ethanol of α-Fe_2O_3 NP-graphene composite sensors at 280 °C (Reprinted with permission from Liang et al. [31]. Copyright (2014), Elsevier) (**b**) The response of Co_3O_4 NP-RGO hybrid sensors to 60 ppm NO_2 at room temperature (Reprinted with permission from Chen et al. [37]. Copyright (2013), Elsevier) (**c**) TEM image of α-Fe_2O_3 NP-graphene. Schematic illustrations of possible diffusion method of target gas into (**d**) pure α-Fe_2O_3 NP based sensor (**e**) combined with the optimal amount of graphene to α-Fe_2O_3 NPs (**f**) combined with excess graphene to α-Fe_2O_3 (Reprinted with permission from Liang et al. [31]. Copyright (2014), Elsevier)

conductivity of graphene and porous structures, which can facilitate the contact of gas by diffusion (Fig. 3.6e). Another parameter for obtaining high sensitivity is the junction state of the α-Fe$_2$O$_3$ NP-RGO composite. Schottky contact was formed between α-Fe$_2$O$_3$ NPs and RGO sheets, resulting in easy capture and transfer of electrons. However, there is the appropriate amount of RGO that can help electron transfer effectively (Fig. 3.6e). If the amount of RGO is too high, RGO sheets make bridges to each other via contacts surrounding α-Fe$_2$O$_3$ NPs. The RGO bridges hinder the adsorption of target gases to α-Fe$_2$O$_3$, resulting in decreased sensitivity (Fig. 3.6f). Therefore, optimized RGO concentration incorporated with α-Fe$_2$O$_3$ NPs is important for optimized sensing performance.

N. Chen et al. studied Co$_3$O$_4$ NP intercalated RGO composites showing enhanced sensitivity for the detection of NO$_2$ as well as fast response/recovery times for methanol sensing [37]. Co$_3$O$_4$ NPs exhibited p-type properties and catalytic properties when combined with RGO. The intercalated Co$_3$O$_4$ NPs in RGO generated large active reaction area of RGO, preventing stacking of graphene sheets and generating a coupling effect between the Co and RGO [57]. The coupling effect induced more ionic binding of Co-O, and consequently the Co^{3+} withdrew electrons indirectly from the RGO, thereby reducing the resistance in the presence of NO$_2$. There was also an optimum concentration of RGO when mixed with Co$_3$O$_4$ NPs where the highest sensitivity ($R_s = 80$, where $R_s = |R_g - R_0|/R_0 \times 100\%$) was exhibited (5 wt% RGO was incorporated (Fig. 3.6b)). On the other hand, methanol molecules reacted on the RGO sheets via weak interactions with sp^2 bonding of RGO without reacting with negatively charged oxygen defects, because negatively charged oxygen defects would be reluctant to receive electrons from a reducing gas such as methanol. For this reason, the methanol molecules are more likely to be adsorbed or desorbed by sp^2 bonding of the RGO surface due to the weak interactions, resulting in faster response/recovery times. The active surface of the RGO sheets was largely increased due to the intercalated Co$_3$O$_4$ NPs, which promoted a higher degree of exfoliation of the RGO with coupling effects, as discussed earlier.

A number of incorporated metal oxide NPs with graphene composites have been reported in the literature, including Ni and NiO NP-GO composites for photocatalysts in water splitting activity [58], SnO$_2$-graphene, MnO$_2$-graphene, RuO$_2$-graphene for supercapacitor electrodes [59], and ZnO-RGO optical gas sensors [60]. However, they still have not been extensively studied for chemical sensors and further characterization of the gas sensing performance with various metal oxide NP-graphene composites is necessary.

3.3.3 Metal-Metal Oxide NP Hybrid-Graphene Composite Sensing Layers

A few research groups have attempted to incorporate catalyst decorated metal oxide NPs with graphene sheets for chemical sensors to demonstrate the sensitivity and

response/recovery time characteristics. The addition of metallic NPs to metal oxide NP led to improved sensing properties due to the Schottky barrier formation between the metal NPs and metal oxide NPs as well as a catalytic effect in sensing of metallic NPs [61]. A. Esfandiar et al. reported a hydrogen gas sensor composed of Pd and Pt decorated TiO_2 NPs on RGO sheets [41]. The Pd-TiO_2 NP-RGO hybrid structure was synthesized by three steps. TiO_2 NPs were prepared by a sol-gel method and the dispersed GO suspension was prepared by a modified Hummer's method. UV radiation was illuminated to the mixture of the TiO_2 solution and dispersed GO suspension. The UV radiation generated photoreduction of GO as well as attachment of TiO_2 NPs on the RGO sheets. The TiO_2 NP-RGO suspension was coated on alumina substrates followed by calcination in an argon atmosphere for 3 h at 350 °C. A Pd precursor of 10^{-3} M Pd(OAc)$_2$ and a surfactant of 0.1 M CTAB were then added into TiO_2 NP-RGO samples and this was heated to 60 °C for decoration of Pd NPs on TiO_2 NP-RGO. A 0.01 M NaBH$_4$ solution was then added to samples for reduction of Pd NPs. Similarly, a Pt-TiO_2 NP-RGO composite was synthesized via the same steps except for using a metallic precursor of H$_2$PtCl$_6$ instead of Pd(OAc)$_2$. The sensitivity of different composites was tested with TiO_2, TiO_2 NP-RGO, Pt-TiO_2, Pd-TiO_2, Pt-TiO_2 NP-RGO, and Pd-TiO_2 NP-RGO to investigate the role of RGO and metallic NPs. Here, sensitivity was calculated as $S = |(R_{gas}-R_{air})/(R_{air})| \times 100$ (%), where R_{gas} and R_{air} are the resistivity upon exposure to target gas and baseline air, respectively. Response and recovery times were defined as the time required to reach 90 % of the maximum resistivity value and 90 % of the initial value, respectively. The optimum sensitivity towards 500 ppm hydrogen was achieved with Pd-TiO_2 NP-RGO, exhibiting sensitivity of 92 % and a response time of 18 s at operating temperature of 180 °C.

Figure 3.7a, b show TEM images of Pd-TiO_2 NP-RGO. The thin RGO sheet contained Pd NP-TiO_2 NPs (Fig. 3.7a). High magnifications of Fig. 3.7a shows Pd NPs with size of less than 10 nm, and they were decorated onto TiO_2 NPs fixed to RGO sheets (Fig. 3.7b). The RGO provided preferential pathways for electrons and generated electron transfer, which resulted in enhancement of the electrical conductivity. The RGO also hindered aggregation of NPs; the composite has a porous structure that facilitated diffusion of the hydrogen molecules. In addition, metallic NPs induced catalytic effects of chemical sensitization and electronic sensitization [62, 63]. During the chemical sensitization, gas molecules dissociated into active forms (here, the H$_2$ molecule was dissociated to H* or H$^+$) on the metallic NPs and the active forms (i.e., H*, H$^+$) were diffused to the metal oxide surface to react with chemisorbed oxygen species, leading to reduced resistance of the sensor. On the other hand, electronic sensitization induced direct electron transfer between the additive metal and metal oxide by dissolving hydrogen gas and changing the redox state of the additive metal NPs. In the case of the Pd-TiO_2 NP-RGO hybrid structures, Pd behaved as an electronic sensitizer due to the higher dissolution of hydrogen, resulting in direct donation of electrons to TiO_2 NP-RGO. In the case of Pt-TiO_2 NP-RGO hybrid structures, Pt acted as a chemical sensitizer at low hydrogen concentration (below 2,000 ppm), but become an electronic sensitizer at very high gas concentrations (over 2,000 ppm). This behavior of Pt is attributed
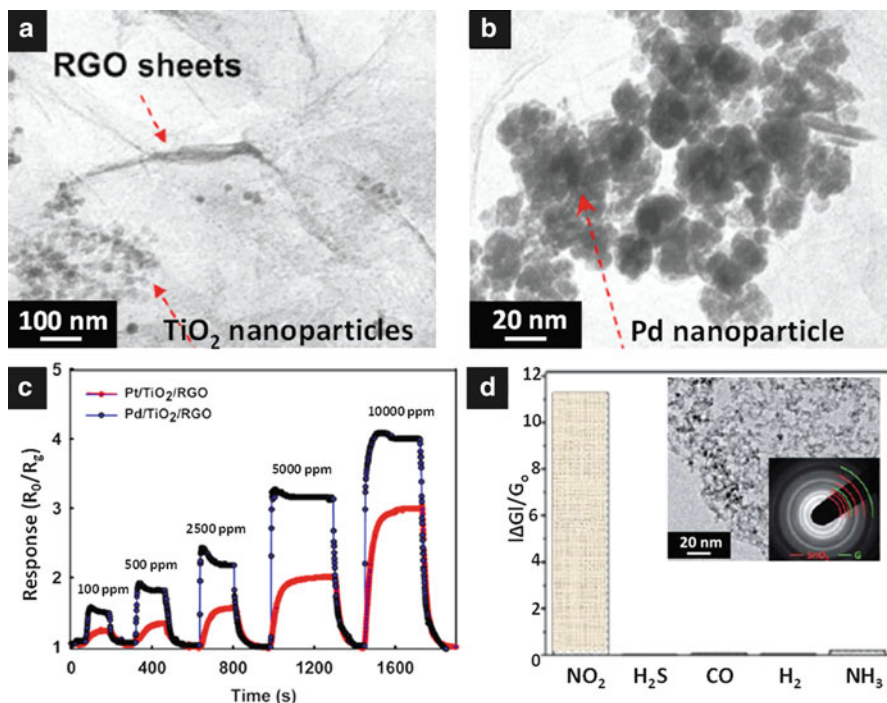
Fig. 3.7 (**a**) TEM (**b**) HRTEM images of Pd-TiO$_2$ NP-RGO; (**c**) the response characteristics of Pd-TiO$_2$ NP-rGO and Pt-TiO$_2$ NP-rGO to H$_2$ gas with a concentration range of 100–10,000 ppm at 180 ˚C (Reprinted with permission from Esfandiar et al [41]. Copyright (2012), Elsevier) (**d**) the selectivity characteristic for NO$_2$ of IDTO NPs-RGO compared to interfering gases; the inset is TEM images and the SEAD pattern of IDTO NPs-RGO (Reprinted with permission from Cui et al. [40]. Copyright (2013), The Royal Society of Chemistry)

to Pt being a better oxygen adsorbent and hydrogen dissolution to Pt being lower than Pd. At 500 ppm of H$_2$ gas, Pt acts as a chemical sensitizer, and an electronic sensitizer show a faster response than a chemical sensitizer. Therefore, the Pd-TiO$_2$ NP-RGO hybrid structures showed better sensitivity and response time compared to the Pt-TiO$_2$ NP-RGO hybrid structure (Fig. 3.7c).

Besides decoration metallic NPs onto metal oxide NPs, doping in metal oxide NPs also can enhance the sensing properties. A dopant can facilitate electron transfer during the interaction with gases by increasing the concentration of charge carriers in the metal oxide. Dopants also prevent the growth of metal oxide NPs in the hydrothermal method, and as a result metal oxide NPs become small and have a larger surface-to-volume ratio than pure metal oxide NPs. For example, in the case of SnO$_2$, many researchers have reported that the selectivity for a specific gas can be enhanced depending on the dopant materials in SnO$_2$ [64, 65]. In particular, it is well known that doping of indium and ruthenium into SnO$_2$ plays a crucial role in improvement of the response and selectivity and lowering the operating

temperatures for NO_2 gas sensing [66, 67]. Thus, S. Cui et al. reported that IDTO NP-graphene hybrid composites have better sensing characteristics than SnO_2-graphene composites [40]. Uniformly distributed IDTO NPs on RGO (IDTO NPs-RGO) were synthesized via a one-pot synthetic process. GO prepared by a modified Hummers method was dispersed into deionized water with sonication for 30 min. $InCl_3$ and $SnCl_4$ aqueous solutions were added into a GO solution with magnetic stirring at 400 rpm and sonication for 10 min for uniform adsorption of ions onto GO. For reduction of GO, an $NaBH_4$ aqueous solution was added and the resultant solution was kept at 50 °C on a hotplate for 1 h. The samples were then subjected to centrifugation. The TEM image of IDTO NPs-RGO revealed rutile SnO_2 (red arc in the inset of Fig. 3.7d) and reduced graphene oxide (green arc in the inset of Fig. 3.7d). The IDTO NPs were well-distributed onto the RGO, as seen from the TEM image. Through calculation of the difference in ionic sizes (<15 %), it was confirmed that In doped SnO_2 and Ru doped SnO_2 were uniformly stable solid solutions. The enhancement of sensitivity was seen from the increase of oxygen adsorbates (O^-, O^{2-}, and O_2^-) on SnO_2 by introducing in as a dopant.

$$NO_2(gas) + O^{\delta-}(oxygen\ adsorbates) = NO_3^{\delta-}(adsorption) \qquad (3.2)$$
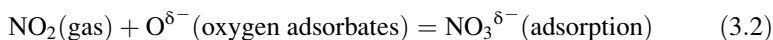
As shown in the (3.2), the NO_2 gas reacted with oxygen adsorbates on SnO_2, resulting in electron transfer from SnO_2 to NO_2. The large amount of adsorption of oxygen adsorbates (O^-, O^{2-}, and O_2^-) on IDTO resulted in higher sensitivity for NO_2 than in the case of pristine SnO_2. In addition, IDTO-graphene has high selectivity for NO_2 and a negligible response to other gases such as H_2S, CO, H_2, and NH_3 (Fig. 3.7d). Furthermore, a ZnO@ZnS hollow dumbbell-graphene composite shows outstanding selectivity and response rate to ethanol, as reported by X. Yu et al. [68]. Owing to the unique microstructure of hollow dumbbells and incorporation of the hetrostructured material ZnO@ZnS into graphene, the gas molecules easily approach the active surface, leading to enhanced sensing properties. Studies on the incorporation of catalyst decorated metal oxide NP-graphene composites are still at an early stage. These composites show possibility for various fields including gas sensors.

3.4   1D Structure-Graphene Composite Sensing Layers

Several types of 1D-structured materials have been incorporated with graphene based materials such as metal oxide NW-graphene and polymeric NF-graphene composites for chemical sensor applications, as summarized in Table 3.3. In this part, each type of graphene-1D structured sensing composite is introduced and the role of graphene based materials in the sensing performance is discussed.

Table 3.3 Recent publications for chemical sensors using 1D structure-graphene composite sensing layers

Composites	Sensing type	Response definition	Sensitivity (Response)	Detection limit	Testing ambient	Target gas	Response/ recovery time	Operating temp.	Ref.
SnO_2 NF-RGO	Resistivity change	R_a/R_g	14.2 @ 5 ppm	3.4 @ 1 ppm	Humid air ambient 95 % RH	Acetone	~60 s/~25 s	350 °C	[69]
ZnO NR-RGO	Resistivity change	R_a/R_g	~27 @ 50 ppm	5 ppm	Air ambient 37 % RH	Ethanol	<10 s/<10 s	260 °C	[70]
WO_3 NR-graphene	Resistivity change	R_g/R_a	202 @ 20 ppm	13 @ 25 ppb	Air ambient	NO_2	-/-	300 °C	[71]
Cu_2O NW-RGO	Conductivity change	$(I_{gas}-I_0)/I_0 \times 100$ (%)	1.7 @ 2 ppm	0.4 ppm	N_2 ambient	NO_2	-/-	Room temp.	[72]
SnO_2 NR-Graphene	Resistivity change	R_a/R_g	130 @ 50 ppm	1 ppm	Air ambient	H_2S	5 s/10 s	260 °C	[73]
ZnO NR-Graphene	Conductivity change	R_a/R_g	90 @ 50 ppm	9 @ 10 ppm	Air ambient	Ethanol	-/-	300 °C	[74]
Polypyrrole-RGO	Resistivity change	$(R_g-R_a)/R_a \times 100$ (%)	~35 % @ 50 ppm	1 ppm	N_2 ambient	NO_2	-/-	Room temp.	[75]
Polyaniline-graphene	Resistivity change	$|(R_{gas}-R_0)/(R_0)| \times 100$ (%)	16.57 % @ 1 %	0.06 %	Air ambient	H_2	-/-	Room temp.	[76]
CNT-RGO	Resistivity change	$(R-R_0)/R_0 \times 100$ (%)	20 % @ 10 ppm	0.5 ppm	N_2 ambient	NO_2	-/-	Room temp.	[77]

3.4.1 Metal Oxide-Graphene Composite Sensing Layers

A number of 1D-structured semiconductor metal oxides (SMOs) have been explored for application in gas sensing elements such as nanowires (NWs), nanorods (NRs), and nanofibers (NFs) due to the higher sensitivity compared to a thin film layer [78]. Numerous synthetic routes have been proposed to obtain 1D-structured SMO sensing materials, including hydrothermal growth, a vapour-liquid-solid reaction strategy, and an electrospinning approach. Recently, composite sensing layers of 1D-structured SMOs with graphene based materials are receiving much attention due to their improved sensitivity and selectivity as well as fast response/recovery characteristics.

A two-step synthetic route is a general method to obtain metal oxide NR-graphene composites, where the graphene sheets are first prepared and then the metal oxide NRs are grown on the graphene sheets hydrothermally. Zhang et al. reported highly aligned SnO_2 NRs on a graphene sheet using a nanocrystal-seeds-directing hydrothermal method [73]. Briefly, chemical vapour deposition (CVD) method was utilized to grow the graphene sheets [79]. The prepared graphene sheets were dispersed into a $SnCl_4$ aqueous solution using ultrasonication with a given concentration of 0.05 M. Hydrolysis was performed with the suspension for 12 h followed by calcination at 100 °C, which resulted in the formation of SnO_2 nanocrystal seeds by hydrolytic growth, i.e., $SnCl_4 + 2H_2O \rightarrow SnO_2 + 4HCl$, on the graphene sheets. The SnO_2 nanocrystal seeds anchored graphene sheets were then injected into a precursor solution, which consists of 0.1 M $SnCl_4$, 1 M NaOH, and 0.33 M SDS (sodium dodecyl sulphate), and stirred to obtain a homogeneous solution. Finally, hydrothermal growth of SnO_2 NRs on the graphene sheet was achieved with a reaction temperature at 220 °C for 20 h followed by washing the precipitates. The SEM image showed the obtained final product, which exhibited 3D array structures, i.e., vertically and densely aligned NRs on the substrate with length of 300–400 nm, as well as a square shaped cross section with a width of 50 nm (Fig. 3.8a).

Gas sensing performances were investigated at an operating temperature of 260 °C using the synthesized SnO_2 NR-graphene composite and pure SnO_2 NRs, which exhibited a radial flower structure without incorporation of graphene sheets (Fig. 3.8b inset). The results revealed that the SnO_2 NR-graphene composite showed almost a two-fold higher response compared to that of the pure SnO_2 NRs in the presence of 50 ppm analyte gases, i.e., hydrogen sulfide (H_2S) formaldehyde (HCHO), ethanol (C_2H_5OH), methanol (CH_3OH), acetone (CH_3COCH_3), and ammonia (NH_3) (Fig. 3.8b). In particular, the SnO_2 NR-graphene composite exhibited the highest response (R_{air}/R_{gas}) (more than 120) toward H_2S. The dynamic responses of the SnO_2 NR-graphene composite and the pure SnO_2 NR were investigated with different diameters and density of SnO_2 NRs (Fig. 3.8c–f). The optimum sensitivity toward H_2S at a concentration of 50 ppm was achieved with uniformly distributed SnO_2 NRs having 50 nm diameter and the highest density of $ca.$ 285 μm^{-2} of SnO_2 NRs (Fig. 3.8c), yielding a response value of
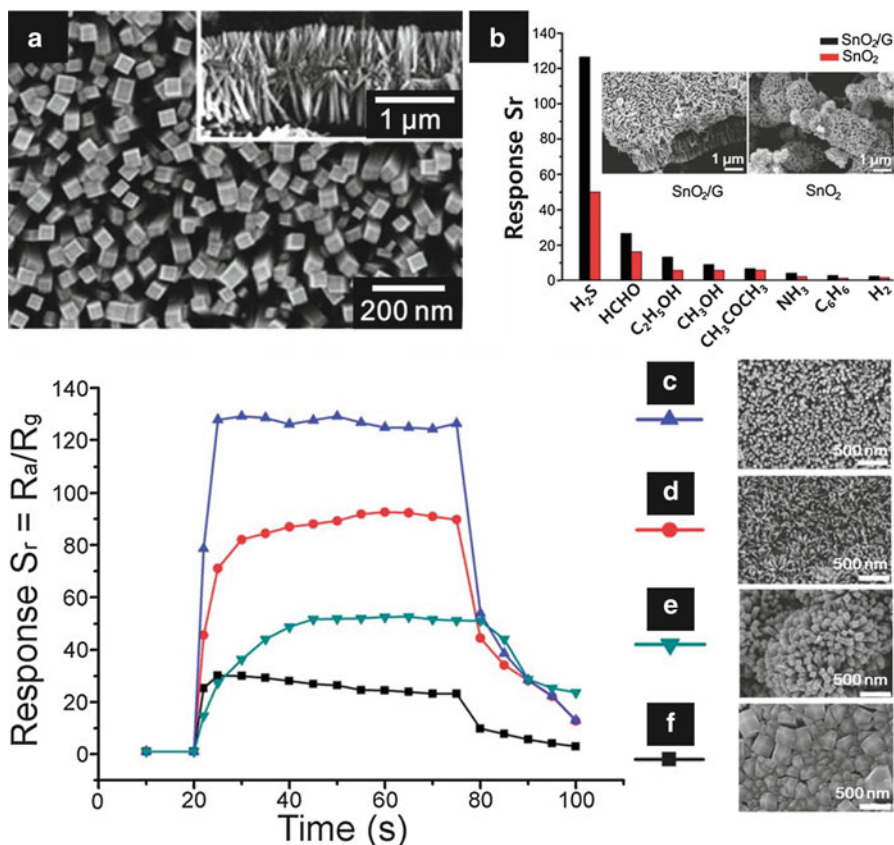
Fig. 3.8 (**a**) SEM image of the synthesized SnO_2 NR-graphene composites (*top view*) with the cross sectional view in the *inset*. (**b**) Gas sensing performances of the SnO_2 NR-graphene composite and the pure SnO_2 NRs at a gas concentration of 50 ppm with a working temperature at 260 ˚C in the presence of the analyte gases. Dynamic response transient characteristics of (**c**) optimized SnO_2 NR-graphene composite, (**d**) thin SnO_2 NRs (smaller than 20 nm in diameter with the density of ca. 241 μm^{-2})-graphene composite, (**e**) pure SnO_2 NRs with flower structure, (**f**) thick SnO_2 NRs (greater than 200 nm in diameter with a density of ca. 40 μm^{-2})-graphene composite (Reprinted with permission from Zhang et al. [73]. Copyright (2011), The Royal Society of Chemistry)

130 when forming a composite with graphene. Excessively thin SnO_2 NRs (smaller than 20 nm in diameter with a density of *ca.* 241 μm^{-2}) and thick SnO_2 NRs (greater than 200 nm in diameter with a density of *ca.* 40 μm^{-2}) with the composite of graphene showed relatively weak responses to H_2S, as presented in Fig. 3.8d, e, respectively. Very short response and recovery times were achieved with the optimized SnO_2 NR-graphene composites, exhibiting values of 7 s and 20 s, respectively. Even though the pure SnO_2 NRs showed better response characteristics compared to that of the thick SnO_2 NR-graphene composites (Fig. 3.8e and f), very slow response/recovery time characteristics were observed. The improved

sensing characteristics of the optimized SnO_2 NR-graphene composite were attributed to the high surface area (25.261 m^2g^{-1}) as well as to the open porosity (3.539 $cm^3g^{-1}nm^{-1}$). In addition, the high electrical conductive property and chemical sensing characteristics of graphene promoted the H_2S sensing performance. High carrier transport capability, which resulted from the high mobility of the graphene sheets, promoted rapid recognition of electrical changes during the H_2S exposure, thereby shortening the response/recovery times. Furthermore, electrons are easily captured and migrated from the conduction band due to the formation of a Schottky barrier at the interface of SnO_2 NRs and graphene, which improved the sensitivity of the SnO_2 NP-graphene composites.

Similar approaches to synthesize ZnO NR-graphene [80] and WO_3 NR-graphene [71] composites for H_2S and NO_2 sensing materials, respectively, were reported. The ZnO NR-graphene composites were fabricated by hydrothermal growth of ZnO NRs on a graphene sheet. The obtained ZnO NR-graphene composite exhibited improved sensitivity to H_2S in nitrogen ambient at $270\,°C$. X. An et al. also reported hydrothermal growth of WO_3 NRs on graphene oxide (GO) sheets [71]. WO_3 NRs with 3.5 wt% graphene composite exhibited highly sensitive NO_2 sensing characteristics with a response (R_{gas}/R_{air}) of 202 at 20 ppm with an operating temperature of $300\,°C$, which is 25 times higher than that ($R_{gas}/R_{air} = 8$) of pristine WO_3 NRs. The WO_3 NR-graphene composite showed sensing capability down to 25 ppb. Selective sensing characteristics were also investigated using a WO_3 NR-graphene composite for practical application and increased NO_2 sensing properties were demonstrated with suppressed detection capability toward interfering gases such as NH_3, H_2O, acetone, propanol, cyclohexane, methanol, SO_2, Cl_2, ethanol, toluene, and butanol. The possible explanations of the improved NO_2 sensing characteristics were discussed and the major reason was thought to be the highly conductive property of graphene contributing to the sensing performance, considering that the principle of the sensing composite is based on conductivity variation. In addition, the high specific surface area of graphene could facilitate gas adsorption and diffusion on the active surface, thereby increasing the sensitivity [43]. Furthermore, the formation of a Schottky barrier due to the contact of WO_3 NRs and graphene sheets generated specific capture and migration of electrons from WO_3 NR to the graphene sheet. This facilitates electron transfer from WO_3 NRs to NO_2 molecules, thereby inducing large electrical conductivity changes [60]. The role of graphene in selective sensing properties was also investigated and the composite of WO_3 NR-graphene exhibited a different sensing mechanism where electron transfer from graphene to WO_3 NR is not favorable. For this reason, locally accumulated electrons released from the desorption of chemisorbed oxygen ions on the graphene sheets had no effect on the conductivity changes of WO_3 NRs. Therefore, the WO_3 NR-graphene composites exhibited high sensitivity to oxidizing gases such as NO_2 with minor responses toward reducing gases such as ethanol, acetone, methanol, etc. A similar sensing role of reduced graphene oxide (RGO) was reported while forming composites with hydrothermally grown Cu_2O NWs for NO_2 detection [72]. The Cu_2O NW-RGO composite showed high sensitivity of 67.8 % with 2 ppm NO_2 at room temperature, which was higher than that of pristine

RGO (22.5 %) and Cu_2O NW (44.5 %) with the calculated limit of detection (LOD) of 64 ppb. The improved sensing performance was attributed to larger surface accessibility and increased conductivity of the Cu_2O NW-RGO composite.

An electrospinning approach is one of the facile strategies to synthesize 1D-structured SMOs. Almost unlimited material selection and composition can be achieved in the form of a 1D structure, making electrospinning a powerful tool for developing optimized sensing materials and composites. Several examples have been demonstrated using electrospun SMO sensors such as TiO_2 NFs [81], Pd doped WO_3 NFs [82], Pt functionalized SnO_2 NFs [83, 84], and Pd loaded SnO_2 NFs [85] as well as multicomposite sensing layers such as Zn_2SnO_4 NFs [86] and $SrTi_{0.65}Fe_{0.35}O_3$ NFs [87]. A 1D structure of hollow nanotubes can be easily achieved as well by using a sacrificial templating route assisted by electrospinning of polymeric NFs, which are selectively removed after coating the outer shell. Hollow WO_3 hemitubes [88], NiO tubes [89], and ZnO nanotubes [90] are examples of 1D structured nanotube structures, and they were fabricated by physical vapour deposition (PVD) of electrospun polymeric NFs followed by high temperature calcination to selectively eliminate the polymeric NFs.

Recently, Choi et al. reported electrospun SnO_2 NFs-RGO composites for selective detection of H_2S and acetone for application in diagnosis of halitosis and diabetes, respectively [69]. The schematic illustration shows the fabrication processes for the SnO_2 NFs-RGO composites (Fig. 3.9a). First, electrospun SnO_2 NFs were obtained by preparation of the electrospinning solution, which consisted of 0.2 g of polyvinylpyrrolidone (PVP, $M_w = 1,300,000$ $gmol^{-1}$) and 0.2 g of polymethylmethacrylate (PMMA, $M_w = 350,000$ $gmol^{-1}$) dissolved in 2.831 g of N,N-dimethylformamide (DMF). Subsequently, 0.4 g of tin(IV) acetate and 0.11 g of acetic acid were added to the electrospinning solution. As-spun polymer/Sn precursor NFs were obtained by electrospinning the solution by applying DC voltage of 15 kV between the needle (21 gauge) and a collector plate. The collected as-spun polymer/Sn precursor NFs were calcined at 500 °C to form SnO_2 NFs by decomposition of polymer components and oxidation of the Sn precursor. SnO_2 NFs were then homogeneously mixed with the GO dispersed solution followed by heat-treatment in a reducing ambient (20 % H_2 in N_2), which resulted in the formation of SnO_2 NFs-RGO composites. Different RGO concentrations were incorporated with SnO_2 NFs with RGO content of 0.01 wt% and 5 wt% with respect to the content of SnO_2 NFs to investigate the gas sensing performance depending on the RGO concentration.

Figure 3.9b shows the synthesized electrospun SnO_2 NFs with an average diameter of 370 nm. The SnO_2 NFs were integrated with the RGO sheets (white arrow in Fig. 3.9c) by homogeneously mixing them with GO followed by heat-treatment at 500 °C for 1 h in a reducing ambient (20 % H_2/N_2 gas mixture). A TEM analysis revealed that the composite of SnO_2 NF-RGO was formed with multiple SnO_2 NFs covered by graphene sheets. H_2S and acetone sensing characteristics were investigated in a highly humid atmosphere (90 % RH) to demonstrate the suitability for application in exhaled breath sensors (Fig. 3.9e and f). Interestingly, the H_2S sensing performance was optimized at low operating temperature (200 °C)
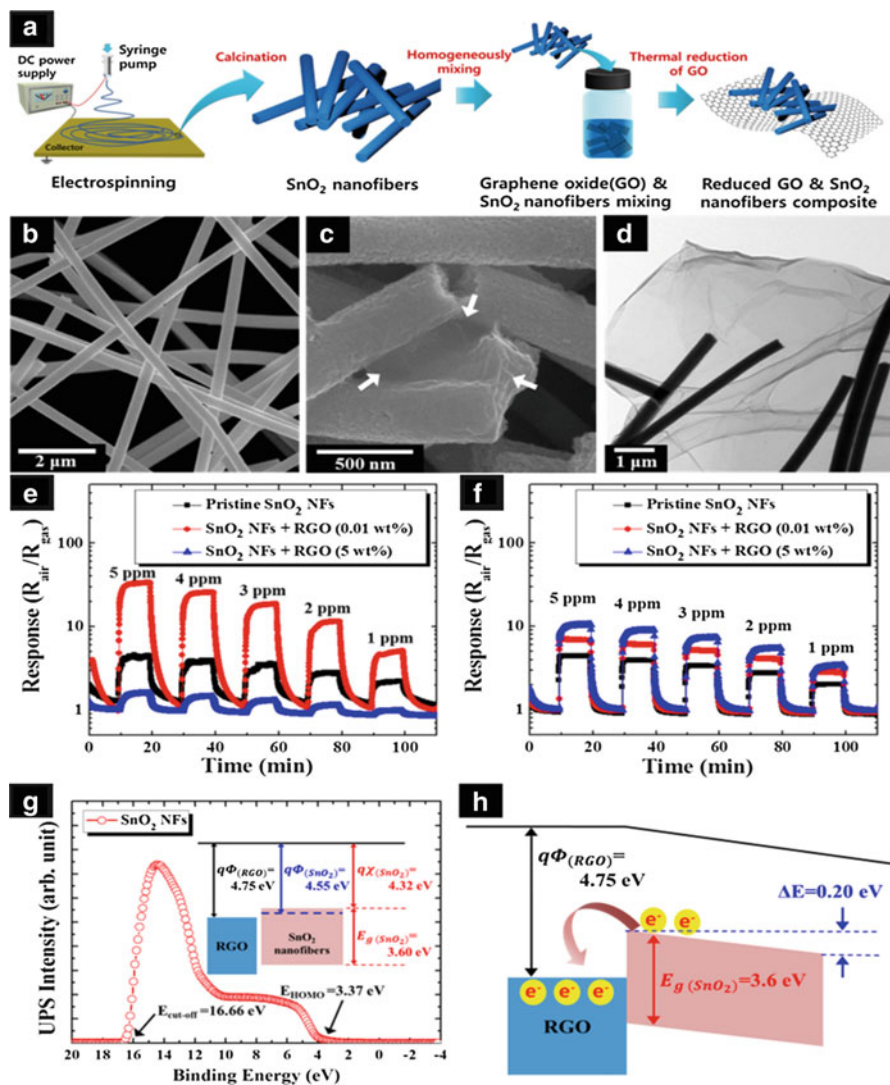
Fig. 3.9 (**a**) Schematic illustration of the fabrication process of electrospun SnO_2 NF-RGO composite sensing layers. SEM images of (**b**) as-spun SnO_2 NFs and (**c**) SnO_2 NF-RGO composite. (**d**) TEM image of SnO_2 NF-RGO composite. Dynamic sensing characteristics of pristine SnO_2 NF, SnO_2 NF-RGO (0.01 wt%) and SnO_2 NF-RGO (5 wt%) toward (**e**) H_2S at 200 °C and (**f**) acetone at 350 °C in a concentration range of 1–5 ppm. (**g**) Ultraviolet photoelectron spectroscopy (UPS) spectrum of SnO_2 NFs and the schematic energy band structure of RGO and SnO_2 NFs before forming the electrical junction in the inset and (**h**) schematic illustration of band bending after making a junction between RGO and SnO_2 NF (Reprinted with permission from Choi et al. [69]. Copyright (2014), American Chemical Society)

with the SnO NF-RGO (0.01 wt%) composite, which exhibited a 7.6 times higher response (R_{air}/R_{gas} = 32.9 at 5 ppm) compared to that (R_{air}/R_{gas} = 4.3 at 5 ppm) of pristine SnO_2 NFs. A suppressed H_2S response (R_{air}/R_{gas} = 1.6 at 5 ppm) characteristic was observed with SnO NF-RGO (5 wt%) (Fig. 3.9e). In contrast, SnO NF-RGO (5 wt%) showed the highest response (R_{air}/R_{gas} = 10.5 at 5 ppm) toward acetone at high operating temperature (350 °C) among the sensors (Fig. 3.9f). Based on the sensing characteristics of SnO_2 NF-RGO composites, highly sensitive and selective sensing properties toward H_2S and acetone were achieved by simply modulating the operating temperature and controlling the content of RGO in the composites.

To understand the sensing mechanism and the role of RGO in the SnO_2 NF-RGO composites, an ultraviolet photoelectron spectroscopy (UPS) analysis was performed to measure the work function of the SnO_2 NFs, thereby ascertaining the band alignment and electron transfer (Fig. 3.9g, h). The UPS spectrum of pristine SnO_2 NFs showed cut-off energy ($E_{cut-off}$) of 16.66 eV and a HOMO energy (E_{HOMO}) of 3.37 eV (Fig. 3.9g), indicating that the work function and electron affinity of the SnO_2 NFs are 4.55 and 4.32 eV, respectively. Considering that the work function of RGO is 4.75 eV, a Schottky barrier of 0.2 eV is formed at the junction of the SnO_2 NF-RGO composite while the electrons flow from the SnO_2 NF to the RGO (Fig. 3.2h). The electron transfer characteristic was also noted in a previous report where the electrons flow from TiO_2 NPs to RGO [91]. The electrons flow and are trapped in the discrete RGO sheets, resulting in increased base resistance (7.76 MΩ at 200 °C) of the SnO_2 NF-RGO (0.01 wt%) composite compared to that (66.49 kΩ at 200 °C) of the pristine SnO_2 NFs. However, a reverse trend in base resistance characteristics was observed: the base resistance of the SnO_2 NF-RGO (5 wt%) composite showed a much lower value (3.93 kΩ at 200 °C) compared to that of the pristine SnO_2 NFs, which is mainly attributed to the continuous percolation pathways of RGO at high RGO loading levels. The base resistance changes and the configuration of RGO contributed to the sensing performances significantly. When a small (0.01 wt%) amount of RGO was added to the SnO_2 NFs, enhanced H_2S sensitivity was observed, especially at low temperature (200 °C). This can be explained as follows: the released electrons that were trapped by the chemisorbed oxygen species (O^- and O^{2-}) induced large surface conductivity changes, i.e., gas-modulated surface conductivity changes by exposure to H_2S [92]. In contrast, a different charge transport mechanism and sensing characteristics were observed with a large (5 wt%) RGO loading level. In the SnO_2-RGO (5 wt%) composite, highly conductive RGO formed continuous percolation pathways, which dominated the electrical transport and gas sensing properties. In this case, the SnO_2 NFs sensitized the response of RGO to oxidizing analytes by donating electrons that can be trapped in the RGO and transported to electron acceptor species [93] such as acetone molecules [94]. Therefore, increased acetone sensitivity with the SnO_2-RGO (5 wt%) composite was achieved by the increased hole concentration in p-type RGO, which was attributed to the electron accepting characteristic of acetone from the RGO.

A number of graphene based materials with electrospun SMOs composites have been reported, such as Co_3O_4 NF-nonoxidized graphene nanoflakes for $Li-O_2$ batteries [95], NiO NF-GO for glucose sensor [96], SnO_2 NR-graphene for lithium storage [97], and TiO_2-graphene for photovoltaic applications [98], as well as Li-ion batteries [99]. With the emergence of SMO-graphene composites, there are plenty of opportunities to develop optimized sensing layers to detect specific analyte gases.

3.4.2   Polymer-Graphene Composite Sensing Layers

Polymeric fibers incorporated with graphene based materials have been developed as gas sensing layers especially for application in room temperature operating sensing devices. A polyaniline (PANI)-graphene composite was proposed as a sensing layer of H_2 at room temperature [76]. PANI-graphene composites were synthesized by chemical polymerization. First, GO sheets were prepared by oxidation of graphite with sulfuric acid and potassium permanganate (H_2SO_4-$KMnO_4$). The GO sheets were then reduced chemically to form graphene sheets using hydrazine in DMF. The prepared graphene sheets were sonicated for 1 h in ethylene glycol (10 mL) with a mixture of aniline (1 mmol) and N-phenyl-1,4-phenylenediamine (0.05 mmol). Finally, 0.25 mmol of APS in 10 mL of HCl (1.0 M) was added to the mixture and stirred for 24 h to form a graphene/PANI nanocomposite.

SEM and TEM analyses revealed that PANI having a fibrous morphology with diameters in a range of 25–50 nm was grown on the surface of the graphene sheets (Fig. 3.10a, b). The mechanism for the formation of PANI on the graphene sheets is as follows: electrostatic attractions induce adsorption of the aniline monomer onto the surface of the graphene sheets. The PANI-graphene composite is then produced during the oxidation of aniline by APS in the mixture of dimer and N-phenyl-1,4-phenylenediamine. Here, the graphene sheets act as a support material, contributing active nucleation sites for the growth of PANI [100].

H_2 sensing performances were investigated using pure graphene, pure PANI, and PANI-graphene composites at room temperature with different H_2 concentrations in a range of 0.06–1 % with baseline air. Here, the gas response was calculated as the sensor sensitivity (S), i.e., $S = |(R_{gas}-R_0)/(R_0)| \times 100\%$, where R_{gas} is the resistivity of the sensors during H_2 gas exposure and R_0 is the resistivity during the baseline air exposure. As shown in Fig. 3.10c, distinctive H_2 sensing characteristics were observed and the PANI-graphene composite showed the highest sensitivity (16.57 %) at 1 % H_2, compared to that of graphene (0.83 %) and PANI (9.38 %). However, almost the same sensitivities were observed with the sensors of PANI and the PANI-graphene composite at lower H_2 concentrations (0.06, 0.12, and 0.25 %). The two sensors exhibited the same sensitivity due to the same doping degree of PANI. In the case of higher H_2 concentration (0.5, 1 %), pure PANI showed saturated sensitivity, in contrast with the PANI-graphene composite, which is
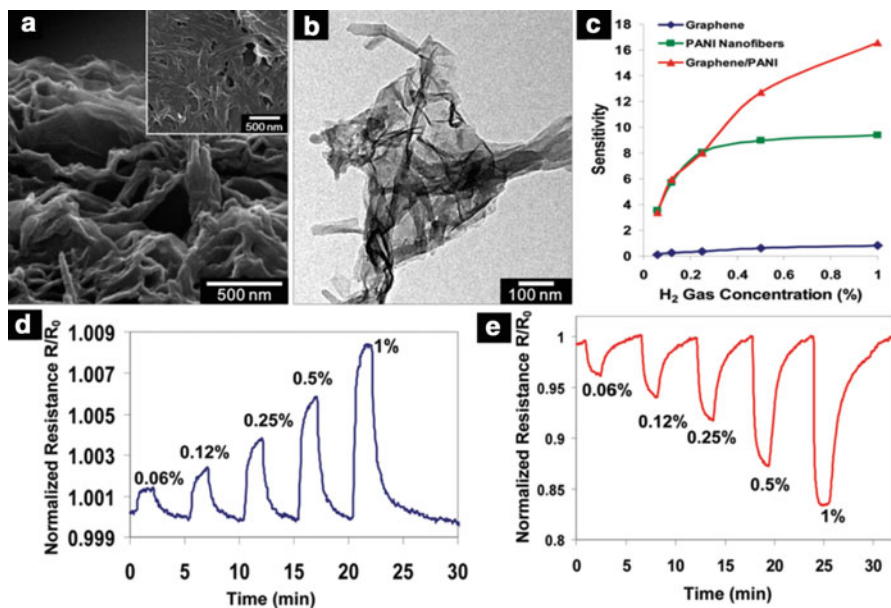
Fig. 3.10 (**a**) SEM and (**b**) TEM observation of the PANI-graphene composite. (**c**) H_2 sensing characteristics of pure graphene, pure PANI NFs and PANI-graphene composite with a gas concentration in a range of 0.06–1 % at room temperature. Dynamic resistivity transient of (**d**) pure graphene and (**e**) PANI-graphene composite with exposure to H_2 in a concentration range of 0.06–1 % (Reprinted with permission from Al-Mashat et al. [76]. Copyright (2010), American Chemical Society)

attributed to degradation of the sensitivity due to H_2O generated by the reaction of chemisorbed H_2 and oxygen in the atmosphere [101]. The sensitivity saturation characteristic disappeared in the case of the PANI-graphene composite sensor, which is ascribed to the high specific surface area of graphene and its highly porous nanostructure. The high porosity of the PANI-graphene composite was advantageous regarding the release of H_2O produced by exposure to H_2, which resulted in steadily increasing sensitivity at high concentrations of H_2 [102].

The resistivity changing mechanisms were discussed and are illustrated in Fig. 3.10d, e. For pure PANI NFs, H_2 gas molecules might be adsorbed at the charged amine nitrogen sites, forming N-H bonds by dissociation of H_2 on PANI chains. Subsequently, charge transfer between amine nitrogen generated a polaronic emeraldine salt state, which resulted in decreased resistivity of PANI NFs. When the gas source was eliminated and the baseline air was exposed to PANI NFs, the H_2 from the PANI chains was released, which resulted in increased resistivity. Reverse resistivity transition was observed with graphene exhibiting a p-type characteristic with exposure to a reducing gas such as H_2 and NH_3 [1, 20] (Fig. 3.10e). The composite of PANI-graphene showed decreased resistivity following H_2 exposure. This is attributed to the dominant sensing characteristic of

PANI NFs compared to graphene due to the large surface coverage with PANI NFs inducing high accessibility to H_2 molecules.

Similarly, a polypyrrole (PPY) NF-RGO composite was proposed as well for application in a NO_2 sensing layer [75]. The composite was synthesized by irradiation of UV to pyrrole and a GO mixture in DI water to form PPY and RGO, simultaneously. Gas sensing characteristics toward NO_2 were investigated using pure RGO and a PPY NF-RGO composite in a gas concentration range of 1–50 ppm at room temperature. The results revealed that the composite of PPY NF-RGO showed four times higher sensitivity $(R = (R_g - R_a)/R_a \times 100\ (\%))$ compared to that of pure RGO, even at a 1 ppm level.

Electrospun 1D polymeric NFs were integrated with graphene based materials for applications not only for gas sensing layers but also in many research fields. Several examples are nylon-6 NF-GO composite for air/water filtration [103] (Fig. 3.11a), polyvinyl alcohol (PVA) NF-RGO, GO for biocomposite scaffolds [104, 107] (Fig. 3.11b), polyamide 66 NF-graphene composite for a transparent conductive thin film [105] (Fig. 3.11c), and a carbon nanofiber (CNF)-graphene composite for supercapacitors [106] (Fig. 3.11d).
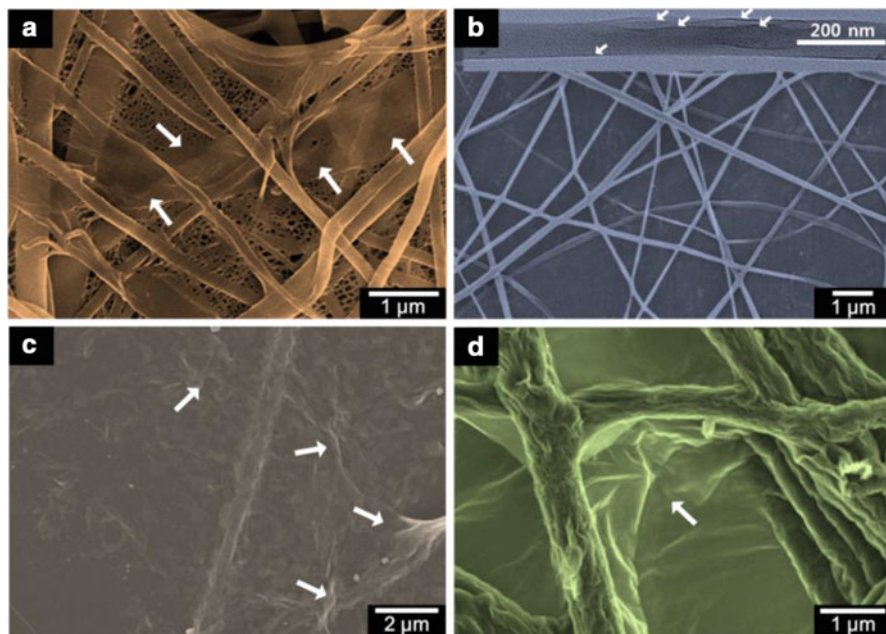
Fig. 3.11 A variety of electrospun 1D polymeric NFs-graphene composites: (**a**) Nylon-6 NF-GO (Reprinted with permission from Pant et al. [103]. Copyright (2012), Elsevier) (**b**) PVA NF-RGO (Reprinted with permission from Tan et al. [104]. Copyright (2012), The Royal Society of Chemistry) (**c**) Polyamide 66 NF-graphene composite (Reprinted with permission from Huang et al. [105]. Copyright (2011), IOP Publishing) (**d**) CNF-graphene composite (Reprinted with permission from Dong et al. [106]. Copyright (2013), Elsevier) *White arrows* indicate the graphene based materials

3.4.3 Carbon Nanotubes (CNTs)-Graphene Composite Sensing Layers

Carbon nanotubes (CNTs) show a one dimensional structure with a very high aspect ratio. The exceptionally high carrier mobility (100,000 cm^2/V s) of CNTs has driven intensive research on the application in chemical sensors. To obtain synergetic sensing capability using CNTs and graphene sheets, a CNT-graphene composite was proposed for NO$_2$ sensor by H. Y. Jeong et al. [77]. The composite structure showed a vertically aligned CNT array on a graphene film substrate, which was prepared on a polyimide flexible substrate containing a microheater. The main feature of the CNT-graphene hybrid composite is stable sensing properties under an extremely bent (15 mm bending radius) condition. Indeed, the NO$_2$ sensing performance was maintained without significant variation during the bent state. The optimum sensing response (S), where $S = (R - R_0)/R_0 \times 100\,(\%)$, was 20 % toward 10 ppm NO$_2$ at room temperature. To address the slow recovery process of the CNT-graphene composite, the operating temperature was controlled using a microheater up to 350 °C. This facilitates the desorption process of gas molecules on the CNT-graphene composite.

3.5 Summary and Future Prospects

The attractive electrical and physical properties of graphene have promoted intensive research on sensing layers in chemical sensors. Different types of graphene-based materials, i.e., RGO and GO, were prepared and their effects on chemical sensing performances have been investigated. In addition, different reduction methods of graphene oxide and post treatment to RGO sheets such as hydrogen plasma treatment and ozone treatment were performed to modify the gas sensing characteristics. Not only pure graphene-based sensing materials, but numerous composite sensing layers have been proposed to achieve synergetic effects and thereby optimize the sensing performance. Metals, metal oxides, and polymers have been integrated with graphene-based materials to form composites. Furthermore, various structures such as nanoparticles, nanorods, nanowires, and nanofibers have been synthesized and combined with graphene-based materials. With efforts to optimize the material properties and structures, highly sensitive and selective sensing performances have been achieved with graphene based composite sensing materials. Based on current reports, the development of high performance chemical sensing materials with graphene-based composites by optimizing the structures, materials, and relative composition of base materials holds great promise. In addition, new approaches for synthetic processes to obtain diverse graphene-based composite materials will be explored for optimized chemical sensors in specific applications such as environmental monitoring and exhaled breath gas detection.

References

1. F. Schedin, A.K. Geim, S.V. Morozov, E.W. Hill, P. Blake, M.I. Katsnelson, K.S. Novoselov, Detection of individual gas molecules adsorbed on graphene. Nat. Mater. **6**(9), 652–655 (2007)
2. Q.Y. He, S.X. Wu, Z.Y. Yin, H. Zhang, Graphene-based electronic sensors. Chem. Sci. **3**(6), 1764–1772 (2012)
3. F. Yavari, N. Koratkar, Graphene-based chemical sensors. J. Phys. Chem. Lett. **3**(13), 1746–1753 (2012)
4. S. Basu, P. Bhattacharyya, Recent developments on graphene and graphene oxide based solid state gas sensors. Sens. Actuators B **173**, 1–21 (2012)
5. W.J. Yuan, G.Q. Shi, Graphene-based gas sensors. J. Mater. Chem. A **1**(35), 10078–10091 (2013)
6. S.M. Hafiz, R. Ritikos, T.J. Whitcher, N.M. Razib, D.C.S. Bien, N. Chanlek, H. Nakajima, T. Saisopa, P. Songsiriritthigul, N.M. Huang, S.A. Rahman, A practical carbon dioxide gas sensor using room-temperature hydrogen plasma reduced graphene oxide. Sens. Actuators B **193**, 692–700 (2014)
7. N.T. Hu, Z. Yang, Y.Y. Wang, L.L. Zhang, Y. Wang, X.L. Huang, H. Wei, L.M. Wei, Y.F. Zhang, Ultrafast and sensitive room temperature NH_3 gas sensors based on chemically reduced graphene oxide. Nanotechnology **25**(2), 025502 (2014)
8. A. Lipatov, A. Varezhnikov, P. Wilson, V. Sysoev, A. Kolmakov, A. Sinitskii, Highly selective gas sensor arrays based on thermally reduced graphene oxide. Nanoscale **5**(12), 5426–5434 (2013)
9. S. Prezioso, F. Perrozzi, L. Giancaterini, C. Cantalini, E. Treossi, V. Palermo, M. Nardone, S. Santucci, L. Ottaviano, Graphene oxide as a practical solution to high sensitivity gas sensing. J. Phys. Chem. C **117**(20), 10683–10690 (2013)
10. J. Zhang, R.F. Zhang, X.N. Wang, W. Feng, P.A. Hu, W. O'Neill, Z.L. Wang, Fabrication of highly oriented reduced graphene oxide microbelts array for massive production of sensitive ammonia gas sensors. J. Micromech. Microeng. **23**(9), 095031 (2013)
11. K.R. Nemade, S.A. Waghuley, Chemiresistive gas sensing by few-layered graphene. J. Electron. Mater. **42**(10), 2857–2866 (2013)
12. F. Yavari, E. Castillo, H. Gullapalli, P.M. Ajayan, N. Koratkar, High sensitivity detection of NO_2 and NH_3 in air using chemical vapor deposition grown graphene. Appl. Phys. Lett. **100**(20), 203120 (2012)
13. G. Chen, T.M. Paronyan, A.R. Harutyunyan, Sub-ppt gas detection with pristine graphene. Appl. Phys. Lett. **101**(5), 053119 (2012)
14. M.G. Chung, D.H. Kim, H.M. Lee, T. Kim, J.H. Choi, D.K. Seo, J.B. Yoo, S.H. Hong, T.J. Kang, Y.H. Kim, Highly sensitive NO_2 gas sensor based on ozone treated graphene. Sens. Actuators B **166**, 172–176 (2012)
15. Y. Hajati, T. Blom, S.H.M. Jafri, S. Haldar, S. Bhandary, M.Z. Shoushtari, O. Eriksson, B. Sanyal, K. Leifer, Improved gas sensing activity in structurally defected bilayer graphene. Nanotechnology **23**(50), 505501 (2012)
16. J. Wang, Y. Kwak, I.Y. Lee, S. Maeng, G.H. Kim, Highly responsive hydrogen gas sensing by partially reduced graphite oxide thin films at room temperature. Carbon **50**(11), 4061–4067 (2012)
17. R.K. Paul, S. Badhulika, N.M. Saucedo, A. Mulchandani, Graphene nanomesh as highly sensitive chemiresistor gas sensor. Anal. Chem. **84**(19), 8171–8178 (2012)
18. W.J. Yuan, A.R. Liu, L. Huang, C. Li, G.Q. Shi, High-performance NO_2 sensors based on chemically modified graphene. Adv. Mater. **25**(5), 766–771 (2013)
19. H.J. Yoon, D.H. Jun, J.H. Yang, Z.X. Zhou, S.S. Yang, M.M.C. Cheng, Carbon dioxide gas sensor using a graphene sheet. Sens. Actuators B **157**(1), 310–313 (2011)
20. J.D. Fowler, M.J. Allen, V.C. Tung, Y. Yang, R.B. Kaner, B.H. Weiller, Practical chemical sensors from chemically derived graphene. ACS Nano **3**(2), 301–306 (2009)

21. P. Althainz, A. Dahlke, M. Frietschklarhof, J. Goschnick, H.J. Ache, Reception tuning of gas-sensor microsystems by selective coatings. Sens. Actuators B **25**(1–3), 366–369 (1995)
22. S. Some, Y. Xu, Y. Kim, Y. Yoon, A. Qin, A. Kulkarni, T. Kim, H. Lee, Highly sensitive and selective gas sensor using hydrophilic and hydrophobic graphenes. Sci. Rep. UK **3**, 1868 (2013)
23. Y.H. Zhang, Y.B. Chen, K.G. Zhou, C.H. Liu, J. Zeng, H.L. Zhang, Y. Peng, Improving gas sensing properties of graphene by introducing dopants and defects: a first-principles study. Nanotechnology **20**(18), 185504 (2009)
24. M. Chi, Y.P. Zhao, Adsorption of formaldehyde molecule on the intrinsic and Al-doped graphene: a first principle study. Comp. Mater. Sci. **46**(4), 1085–1090 (2009)
25. G. Yang, C. Lee, J. Kim, F. Ren, S.J. Pearton, Flexible graphene-based chemical sensors on paper substrates. Phys. Chem. Chem. Phys. **15**(6), 1798–1801 (2013)
26. C. Lee, J. Ahn, K.B. Lee, D. Kim, J. Kim, Graphene-based flexible NO_2 chemical sensors. Thin Solid Films **520**(16), 5459–5462 (2012)
27. V. Dua, S.P. Surwade, S. Ammu, S.R. Agnihotra, S. Jain, K.E. Roberts, S. Park, R.S. Ruoff, S.K. Manohar, All-organic vapor sensor using inkjet-printed reduced graphene oxide. Angew. Chem. Int. Edit. **49**(12), 2154–2157 (2010)
28. R. Kumar, D. Varandani, B.R. Mehta, V.N. Singh, Z. Wen, X. Feng, K. Mullen, Fast response and recovery of hydrogen sensing in Pd-Pt nanoparticle-graphene composite layers. Nanotechnology **22**(27), 275719 (2011)
29. M.G. Chung, D.-H. Kim, D.K. Seo, T. Kim, H.U. Im, H.M. Lee, J.-B. Yoo, S.-H. Hong, T.J. Kang, Y.H. Kim, Flexible hydrogen sensors using graphene with palladium nanoparticle decoration. Sens. Actuators B **169**, 387–392 (2012)
30. V. Tjoa, W. Jun, V. Dravid, S. Mhaisalkar, N. Mathews, Hybrid graphene–metal nanoparticle systems: electronic properties and gas interaction. J. Mater. Chem. **21**(39), 15593 (2011)
31. S. Liang, J. Zhu, C. Wang, S. Yu, H. Bi, X. Liu, X. Wang, Fabrication of α-Fe_2O_3@ graphene nanostructures for enhanced gas-sensing property to ethanol. Appl. Surf. Sci. **292**, 278–284 (2014)
32. S. Srivastava, K. Jain, V.N. Singh, S. Singh, N. Vijayan, N. Dilawar, G. Gupta, T.D. Senguttuvan, Faster response of NO_2 sensing in graphene-WO_3 nanocomposites. Nanotechnology **23**(20), 205501 (2012)
33. G. Neri, S.G. Leonardi, M. Latino, N. Donato, S. Baek, D.E. Conte, P.A. Russo, N. Pinna, Sensing behavior of SnO_2/reduced graphene oxide nanocomposites toward NO_2. Sens. Actuators B **179**, 61–68 (2013)
34. H. Zhang, J. Feng, T. Fei, S. Liu, T. Zhang, SnO_2 nanoparticles-reduced graphene oxide nanocomposites for NO2 sensing at low operating temperature. Sens. Actuators B **190**, 472–478 (2014)
35. Q. Lin, Y. Li, M. Yang, Tin oxide/graphene composite fabricated via a hydrothermal method for gas sensors working at room temperature. Sens. Actuators B **173**, 139–147 (2012)
36. Y. Chang, Y. Yao, B. Wang, H. Luo, T. Li, L. Zhi, Reduced graphene oxide mediated SnO_2 nanocrystals for enhanced gas-sensing properties. J. Mater. Sci. Technol. **29**(2), 157–160 (2013)
37. N. Chen, X. Li, X. Wang, J. Yu, J. Wang, Z. Tang, S.A. Akbar, Enhanced room temperature sensing of Co_3O_4-intercalated reduced graphene oxide based gas sensors. Sens. Actuators B **188**, 902–908 (2013)
38. Q. Huang, D. Zeng, H. Li, C. Xie, Room temperature formaldehyde sensors with enhanced performance, fast response and recovery based on zinc oxide quantum dots/graphene nanocomposites. Nanoscale **4**(18), 5651–5658 (2012)
39. S. Mao, S. Cui, G. Lu, K. Yu, Z. Wen, J. Chen, Tuning gas-sensing properties of reduced graphene oxide using tin oxide nanocrystals. J. Mater. Chem. **22**(22), 11009 (2012)
40. S.M. Cui, Z.H. Wen, E.C. Mattson, S. Mao, J.B. Chang, M. Weinert, C.J. Hirschmugl, M. Gajdardziska-Josifovska, J.H. Chen, Indium-doped SnO_2 nanoparticle-graphene nanohybrids: simple one-pot synthesis and their selective detection of NO2. J. Mater. Chem. A **1**(14), 4462–4467 (2013)

41. A. Esfandiar, S. Ghasemi, A. Irajizad, O. Akhavan, M.R. Gholami, The decoration of TiO$_2$/ reduced graphene oxide by Pd and Pt nanoparticles for hydrogen gas sensing. Int. J. Hydrog. Energy **37**(20), 15423–15432 (2012)

42. Y. Zhang, C. Liu, Y. Min, X. Qi, X. Ben, The simple preparation of graphene/Pt nanoparticles composites and their electrochemical performance. J. Mater. Sci. Mater. Electron **24**(9), 3244–3248 (2013)

43. M. Zhou, Y.H. Lu, Y.Q. Cai, C. Zhang, Y.P. Feng, Adsorption of gas molecules on transition metal embedded graphene: a search for high-performance graphene-based catalysts and gas sensors. Nanotechnology **22**(38), 385502 (2011)

44. U. Lange, T. Hirsch, V.M. Mirsky, O.S. Wolfbeis, Hydrogen sensor based on a graphene – palladium nanocomposite. Electrochim. Acta **56**(10), 3707–3712 (2011)

45. H. Yu, P. Xu, D.W. Lee, X. Li, Porous-layered stack of functionalized AuNP–rGO (gold nanoparticles–reduced graphene oxide) nanosheets as a sensing material for the micro-gravimetric detection of chemical vapor. J. Mater. Chem. A **1**(14), 4444 (2013)

46. P.T. Yin, T.H. Kim, J.W. Choi, K.B. Lee, Prospects for graphene-nanoparticle-based hybrid sensors. Phys. Chem. Chem. Phys. **15**(31), 12785–12799 (2013)

47. Q. Zhuo, Y. Ma, J. Gao, P. Zhang, Y. Xia, Y. Tian, X. Sun, J. Zhong, X. Sun, Facile synthesis of graphene/metal nanoparticle composites via self-catalysis reduction at room temperature. Inorg. Chem. **52**(6), 3141–3147 (2013)

48. S. Yang, J. Dong, Z. Yao, C. Shen, X. Shi, Y. Tian, S. Lin, X. Zhang, One-pot synthesis of graphene-supported monodisperse Pd nanoparticles as catalyst for formic acid electro-oxidation. Sci. Rep. **4**, 4501 (2014)

49. M. Shafiei, P.G. Spizzirri, R. Arsat, J. Yu, J. du Plessis, S. Dubin, R.B. Kaner, K. Kalantar-Zadeh, W. Wlodarski, Platinum/graphene nanosheet/SiC contacts and their application for hydrogen gas sensing. J. Phys. Chem. C **114**(32), 13796–13801 (2010)

50. A.M. Zaniewski, M. Schriver, J. Gloria Lee, M.F. Crommie, A. Zettl, Electronic and optical properties of metal-nanoparticle filled graphene sandwiches. Appl. Phys. Lett. **102**(2), 023108 (2013)

51. F.L. Meng, H.H. Li, L.T. Kong, J.Y. Liu, Z. Jin, W. Li, Y. Jia, J.H. Liu, X.J. Huang, Parts per billion-level detection of benzene using SnO2/graphene nanocomposite composed of sub-6 nm SnO$_2$ nanoparticles. Anal. Chim. Acta **736**, 100–107 (2012)

52. A. Cao, Z. Liu, S. Chu, M. Wu, Z. Ye, Z. Cai, Y. Chang, S. Wang, Q. Gong, Y. Liu, A facile one-step method to produce graphene-CdS quantum dot nanocomposites as promising opto-electronic materials. Adv. Mater. **22**(1), 103–106 (2010)

53. G. Williams, B. Seger, P.V. Kamat, TiO$_2$-graphene nanocomposites. UV-assisted photocatalytic reduction of graphene oxide. ACS Nano **2**(7), 1487–1491 (2008)

54. H. William, O. Richard, Preparation of graphitic oxide. J. Am. Chem. Soc. **80**, 1339 (1958)

55. S. Liu, J. Tian, L. Wang, X. Sun, A method for the production of reduced graphene oxide using benzylamine as a reducing and stabilizing agent and its subsequent decoration with Ag nanoparticles for enzymeless hydrogen peroxide detection. Carbon **49**(10), 3158–3164 (2011)

56. J. Zhang, X. Liu, L. Wang, T. Yang, X. Guo, S. Wu, S. Wang, S. Zhang, Synthesis and gas sensing properties of alpha-Fe$_2$O$_3$@ZnO core-shell nanospindles. Nanotechnology **22**(18), 185501 (2011)

57. Y.Y. Liang, Y.G. Li, H.L. Wang, J.G. Zhou, J. Wang, T. Regier, H.J. Dai, Co$_3$O$_4$ nanocrystals on graphene as a synergistic catalyst for oxygen reduction reaction. Nat. Mater. **10**(10), 780–786 (2011)

58. A.K. Agegnehu, C.-J. Pan, J. Rick, J.-F. Lee, W.-N. Su, B.-J. Hwang, Enhanced hydrogen generation by cocatalytic Ni and NiO nanoparticles loaded on graphene oxide sheets. J. Mater. Chem. **22**(27), 13849 (2012)

59. R.B. Rakhi, W. Chen, D. Cha, H.N. Alshareef, High performance supercapacitors using metal oxide anchored graphene nanosheet electrodes. J. Mater. Chem. **21**(40), 16197 (2011)

60. G. Singh, A. Choudhary, D. Haranath, A.G. Joshi, N. Singh, S. Singh, R. Pasricha, ZnO decorated luminescent graphene as a potential gas sensor at room temperature. Carbon **50**(2), 385–394 (2012)

61. C. Wang, L. Yin, L. Zhang, D. Xiang, R. Gao, Metal oxide gas sensors: sensitivity and influencing factors. Sensors **10**(3), 2088–2106 (2010)
62. S. Matsushima, Y. Teraoka, N. Miura, N. Yamazoe, Electronic interaction between metal additives and tin dioxide in tin dioxide-based gas sensors. Jpn. J. Appl. Phys. **27**(10), 1798–1802 (1988)
63. N. Yamazoe, New approaches for improving semiconductor gas sensors. Sens. Actuators B **5**(1–4), 7–19 (1991)
64. J.-K. Choi, I.-S. Hwang, S.-J. Kim, J.-S. Park, S.-S. Park, U. Jeong, Y.C. Kang, J.-H. Lee, Design of selective gas sensors using electrospun Pd-doped SnO2 hollow nanofibers. Sens. Actuators B **150**(1), 191–199 (2010)
65. F. Pourfayaz, A. Khodadadi, Y. Mortazavi, S.S. Mohajerzadeh, CeO_2 doped SnO_2 sensor selective to ethanol in presence of CO, LPG and CH_4. Sens. Actuators B **108**(1–2), 172–176 (2005)
66. J. Kaur, R. Kumar, M.C. Bhatnagar, Effect of indium-doped SnO_2 nanoparticles on NO_2 gas sensing properties. Sens. Actuators B **126**(2), 478–484 (2007)
67. N.S. Ramgir, I.S. Mulla, K.P. Vijayamohanan, A room temperature nitric oxide sensor actualized from Ru-doped SnO_2 nanowires. Sens. Actuators B **107**(2), 708–715 (2005)
68. X. Yu, G. Zhang, H. Cao, X. An, Y. Wang, Z. Shu, X. An, F. Hua, ZnO@ZnS hollow dumbbells–graphene composites as high-performance photocatalysts and alcohol sensors. New J. Chem. **36**(12), 2593 (2012)
69. S.J. Choi, B.H. Jang, S.J. Lee, B.K. Min, A. Rothschild, I.D. Kim, Selective detection of acetone and hydrogen sulfide for the diagnosis of diabetes and halitosis using SnO_2 nanofibers functionalized with reduced graphene oxide nanosheets. ACS Appl. Mater. Interfaces **6**(4), 2588–2597 (2014)
70. R.J. Zou, G.J. He, K.B. Xu, Q. Liu, Z.Y. Zhang, J.Q. Hu, ZnO nanorods on reduced graphene sheets with excellent field emission, gas sensor and photocatalytic properties. J. Mater. Chem. A **1**(29), 8445–8452 (2013)
71. X.Q. An, J.C. Yu, Y. Wang, Y.M. Hu, X.L. Yu, G.J. Zhang, WO_3 nanorods/graphene nanocomposites for high-efficiency visible-light-driven photocatalysis and NO2 gas sensing. J. Mater. Chem. **22**(17), 8525–8531 (2012)
72. S. Deng, V. Tjoa, H.M. Fan, H.R. Tan, D.C. Sayle, M. Olivo, S. Mhaisalkar, J. Wei, C.H. Sow, Reduced graphene oxide conjugated Cu_2O nanowire mesocrystals for high-performance NO_2 gas sensor. J. Am. Chem. Soc. **134**(10), 4905–4917 (2012)
73. Z.Y. Zhang, R.J. Zou, G.S. Song, L. Yu, Z.G. Chen, J.Q. Hu, Highly aligned SnO_2 nanorods on graphene sheets for gas sensors. J. Mater. Chem. **21**(43), 17360–17365 (2011)
74. J. Yi, J.M. Lee, W. Il Park, Vertically aligned ZnO nanorods and graphene hybrid architectures for high-sensitive flexible gas sensors. Sens. Actuators B **155**(1), 264–269 (2011)
75. H.N. Tien, S.H. Hur, One-step synthesis of a highly conductive graphene-polypyrrole nanofiber composite using a redox reaction and its use in gas sensors. Phys. Status Solidi R **6**(9–10), 379–381 (2012)
76. L. Al-Mashat, K. Shin, K. Kalantar-Zadeh, J.D. Plessis, S.H. Han, R.W. Kojima, R.B. Kaner, D. Li, X.L. Gou, S.J. Ippolito, W. Wlodarski, Graphene/polyaniline nanocomposite for hydrogen sensing. J. Phys. Chem. C **114**(39), 16168–16173 (2010)
77. H.Y. Jeong, D.S. Lee, H.K. Choi, D.H. Lee, J.E. Kim, J.Y. Lee, W.J. Lee, S.O. Kim, S.Y. Choi, Flexible room-temperature NO_2 gas sensors based on carbon nanotubes/reduced graphene hybrid films. Appl. Phys. Lett. **96**(21), 213105 (2010)
78. I.D. Kim, A. Rothschild, H.L. Tuller, Advances and new directions in gas-sensing devices. Acta Mater. **61**(3), 974–1000 (2013)
79. K.S. Kim, Y. Zhao, H. Jang, S.Y. Lee, J.M. Kim, K.S. Kim, J.H. Ahn, P. Kim, J.Y. Choi, B.H. Hong, Large-scale pattern growth of graphene films for stretchable transparent electrodes. Nature **457**(7230), 706–710 (2009)
80. T.V. Cuong, V.H. Pham, J.S. Chung, E.W. Shin, D.H. Yoo, S.H. Hahn, J.S. Huh, G.H. Rue, E.J. Kim, S.H. Hur, P.A. Kohl, Solution-processed ZnO-chemically converted graphene gas sensor. Mater. Lett. **64**(22), 2479–2482 (2010)

81. I.D. Kim, A. Rothschild, B.H. Lee, D.Y. Kim, S.M. Jo, H.L. Tuller, Ultrasensitive chemiresistors based on electrospun TiO_2 nanofibers. Nano Lett. **6**(9), 2009–2013 (2006)

82. N.H. Kim, S.J. Choi, D.J. Yang, J. Bae, J. Park, I.D. Kim, Highly sensitive and selective hydrogen sulfide and toluene sensors using Pd functionalized WO_3 nanofibers for potential diagnosis of halitosis and lung cancer. Sens. Actuators B **193**, 574–581 (2014)

83. J. Shin, S.J. Choi, I. Lee, D.Y. Youn, C.O. Park, J.H. Lee, H.L. Tuller, I.D. Kim, Thin-wall assembled SnO_2 fibers functionalized by catalytic Pt nanoparticles and their superior exhaled-breath-sensing properties for the diagnosis of diabetes. Adv. Funct. Mater. **23**(19), 2357–2367 (2013)

84. B.H. Jang, O. Landau, S.J. Choi, J. Shin, A. Rothschild, I.D. Kim, Selectivity enhancement of SnO_2 nanofiber gas sensors by functionalization with Pt nanocatalysts and manipulation of the operation temperature. Sens. Actuators B **188**, 156–168 (2013)

85. D.J. Yang, I. Kamienchick, D.Y. Youn, A. Rothschild, I.D. Kim, Ultrasensitive and highly selective gas sensors based on electrospun SnO_2 nanofibers modified by Pd loading. Adv. Funct. Mater. **20**(24), 4258–4264 (2010)

86. S.H. Choi, I.S. Hwang, J.H. Lee, S.G. Oh, I.D. Kim, Microstructural control and selective C_2H_5OH sensing properties of Zn2SnO4 nanofibers prepared by electrospinning. Chem. Commun. **47**(33), 9315–9317 (2011)

87. S.H. Choi, S.J. Choi, B.K. Min, W.Y. Lee, J.S. Park, I.D. Kim, Facile synthesis of p-type perovskite $SrTi_{0.65}Fe_{0.35}O_3$ nanofibers prepared by electrospinning and their oxygen-sensing properties. Macromol. Mater. Eng. **298**(5), 521–527 (2013)

88. S.J. Choi, I. Lee, B.H. Jang, D.Y. Youn, W.H. Ryu, C.O. Park, I.D. Kim, Selective diagnosis of diabetes using Pt-functionalized WO_3 hemitube networks as a sensing layer of acetone in exhaled breath. Anal. Chem. **85**(3), 1792–1796 (2013)

89. N.G. Cho, H.S. Woo, J.H. Lee, I.D. Kim, Thin-walled NiO tubes functionalized with catalytic Pt for highly selective C_2H_5OH sensors using electrospun fibers as a sacrificial template. Chem. Commun. **47**(40), 11300–11302 (2011)

90. S.H. Choi, G. Ankonina, D.Y. Youn, S.G. Oh, J.M. Hong, A. Rothschild, I.D. Kim, Hollow ZnO nanofibers fabricated using electrospun polymer templates and their electronic transport properties. ACS Nano **3**(9), 2623–2631 (2009)

91. I.V. Lightcap, T.H. Kosel, P.V. Kamat, Anchoring semiconductor and metal nanoparticles on a two-dimensional catalyst mat. Storing and shuttling electrons with reduced graphene oxide. Nano Lett. **10**(2), 577–583 (2010)

92. A. Rothschild, H.L. Tuller, Gas sensors: new materials and processing approaches. J. Electroceram **17**(2–4), 1005–1012 (2006)

93. A. Rothschild, Y. Komem, On the relationship between the grain size and gas-sensitivity of chemo-resistive metal-oxide gas sensors with nanosized grains. J. Electroceram **13**(1–3), 697–701 (2004)

94. C.E. Kehayias, S. MacNaughton, S. Sonkusale, C. Staii, Kelvin probe microscopy and electronic transport measurements in reduced graphene oxide chemical sensors. Nanotechnology **24**(24), 245502 (2013)

95. W.H. Ryu, T.H. Yoon, S.H. Song, S. Jeon, Y.J. Park, I.D. Kim, Bifunctional composite catalysts using Co_3O_4 nanofibers immobilized on nonoxidized graphene nanoflakes for high-capacity and long-cycle Li-O-2 batteries. Nano Lett. **13**(9), 4190–4197 (2013)

96. Y.Q. Zhang, Y.Z. Wang, J.B. Jia, J.G. Wang, Nonenzymatic glucose sensor based on graphene oxide and electrospun NiO nanofibers. Sens. Actuators B **171**, 580–587 (2012)

97. S.M. Jiang, B.T. Zhao, R. Ran, R. Cai, M.O. Tade, Z.P. Shao, A freestanding composite film electrode stacked from hierarchical electrospun SnO_2 nanorods and graphene sheets for reversible lithium storage. RSC Adv. **4**(18), 9367–9371 (2014)

98. P.N. Zhu, A.S. Nair, S.J. Peng, S.Y. Yang, S. Ramakrishna, Facile fabrication of TiO_2-graphene composite with enhanced photovoltaic and photocatalytic properties by electrospinning. ACS Appl. Mater. Interfaces **4**(2), 581–585 (2012)

99. X. Zhang, P.S. Kumar, V. Aravindan, H.H. Liu, J. Sundaramurthy, S.G. Mhaisalkar, H.M. Duong, S. Ramakrishna, S. Madhavi, Electrospun TiO_2-graphene composite nanofibers

as a highly durable insertion anode for lithium ion batteries. J. Phys. Chem. C **116**(28), 14780–14788 (2012)

100. J. Yan, T. Wei, B. Shao, Z.J. Fan, W.Z. Qian, M.L. Zhang, F. Wei, Preparation of a graphene nanosheet/polyaniline composite with high specific capacitance. Carbon **48**(2), 487–493 (2010)

101. J.D. Fowler, S. Virji, R.B. Kaner, B.H. Weiller, Hydrogen detection by polyaniline nanofibers on gold and platinum electrodes. J. Phys. Chem. C **113**(16), 6444–6449 (2009)

102. A.Z. Sadek, C.O. Baker, D.A. Powell, W. Wlodarski, R.B. Kaner, K. Kalantar-zadeh, Polyaniline nanofiber based surface acoustic wave gas sensors-effect of nanofiber diameter on H_2 response. IEEE Sens. J. **7**(1–2), 213–218 (2007)

103. H.R. Pant, C.H. Park, L.D. Tijing, A. Amarjargal, D.H. Lee, C.S. Kim, Bimodal fiber diameter distributed graphene oxide/nylon-6 composite nanofibrous mats via electrospinning. Colloid Surf. A **407**, 121–125 (2012)

104. Y.Q. Tan, Y.H. Song, Q. Zheng, Hydrogen bonding-driven rheological modulation of chemically reduced graphene oxide/poly(vinyl alcohol) suspensions and its application in electrospinning. Nanoscale **4**(22), 6997–7005 (2012)

105. Y.L. Huang, A. Baji, H.W. Tien, Y.K. Yang, S.Y. Yang, C.C.M. Ma, H.Y. Liu, Y.W. Mai, N.H. Wang, Self-assembly of graphene onto electrospun polyamide 66 nanofibers as transparent conductive thin films. Nanotechnology **22**(47), 475603 (2011)

106. Q. Dong, G. Wang, H. Hu, J. Yang, B.Q. Qian, Z. Ling, J.S. Qiu, Ultrasound-assisted preparation of electrospun carbon nanofiber/graphene composite electrode for supercapacitors. J. Power Sources **243**, 350–353 (2013)

107. Y.Y. Qi, Z.X. Tai, D.F. Sun, J.T. Chen, H.B. Ma, X.B. Yan, B. Liu, Q.J. Xue, Fabrication and characterization of poly(vinyl alcohol)/graphene oxide nanofibrous biocomposite scaffolds. J. Appl. Polym. Sci. **127**(3), 1885–1894 (2013)

Chapter 4
Electrospinning of Electro-Active Materials: Devices Based on Individual and Crossed Nanofibers

Nicholas J. Pinto

Abstract Electrospinning is a simple, cheap and rapid technique to fabricate fibers of a variety of materials in air, under ordinary laboratory conditions. The diameters of these fibers lie in the range of a few nm to several μm. The thinner the fiber, the greater is the surface area to volume ratio making it an ideal candidate for use in sensors and low power devices. Fibers of electro-active polymers formed via this technique are typically very long (~cm) and hence can be manipulated with relative ease. The present work has focused on electrospinning polyaniline doped with camphor sulfonic acid (PANiCSA), poly(3,4-ethylenedioxythiophene) doped with (poly styrene sulfonic acid)-(PEDOT-PSSA) and a tin oxide (SnO_2) precursor for use in diodes and gas sensors. Individual PANiCSA fibers were used in gas sensors and compared to sensors made with multiple fibers, while crossed SnO_2/PEDOT-PSSA fibers were used in the fabrication of diodes. For the sensor, exposure to methanol vapors increased its resistance with a response time of 32 s while exposure of the diode to UV radiation increased the current and made it possible to rectify low frequency ac signals. Electrospinning is thus proposed as an inexpensive method of fabricating devices and sensors.

4.1 Introduction

Electro-active polymers and ceramic oxides are used in various applications ranging from metallic interconnects to electronic devices and sensors. Such versatility, combined with the ease of synthesis, high yield, and good environmental stability have motivated scientists and engineers to explore new horizons in this field of study. Polyaniline is one such polymer that has been investigated the most. It can be doped during the chemical synthesis to directly yield the conducting emeraldine salt

N.J. Pinto (✉)
Department of Physics and Electronics, University of Puerto Rico at Humacao,
Humacao 00792, Puerto Rico
e-mail: nicholas.pinto@upr.edu

or it can be doped *after* synthesis by protonation of the insulating emeraldine base [1]. The ability to process polyaniline in the conducting form has led to a significant increase in its bulk conductivity with signatures of true metallicity down to 5 K [2]. While most studies have focused on the use of polyaniline in the form of thin films, recent advances in the fabrication of nanofibers have opened up new methods to construct low power consumption devices and sensors based on these nanofibers. The large surface area to volume ratio of nanofibers makes them ideal candidates for use as ultrasensitive chemical sensors with the additional advantage of having a faster response time compared to thin film sensors. Several methods have been used in the past to obtain polyaniline nanofibers that include the use of a template [3] or without a template [4], interfacial polymerization [5] and electrospinning [6]. Of the aforementioned techniques, electrospinning is the easiest method of obtaining *isolated* and relatively *long* polymer nanofibers. Tin oxide (SnO_2) nanostructures are also of considerable scientific interest as new ways are being sought to use them in sensors and electronic devices. This material possesses two vital characteristics that make it technologically attractive viz. it is optically transparent and semiconducting [7, 8]. Tin oxide is a non-stoichiometric semiconducting material (oxygen vacancies turns it *n*-type) with a large band gap (~3.6 eV) at room temperature and hence can be used in transparent conducting electrodes for organic light emitting diodes and solar cells.

In this work, we present results of the electrical response of *individual* electrospun polyaniline nanofibers to methanol vapor and compare it to the response obtained from multiple fibers and thin films. Methanol is an extremely toxic alcohol that can result in blindness and even death in small concentrations in humans. Because it is similar in appearance and odor to ethanol which is a common alcohol in beverages, it is therefore important to be able to detect methanol in small concentrations prior to consumption. Due to the small size, uniform diameter and large surface area of the electrospun fiber, true saturation is seen in the resistance changes upon exposure and removal of the alcohol vapor making them useful as reliable sensors. Our results also show that the response of a single electrospun polyaniline nanofiber is faster with bigger changes in the sensing current than for a sensor made up of several fibers. In addition, we also present results on the fabrication and testing of a Schottky diode via crossing an electrospun SnO_2 nanoribbon with a PEDOT-PSSA nanoribbon. Diodes are the main electronic components used in converting AC signals to DC which is commonly used in consumer electronics like cell phones and computers. Making diodes with nanofibers have the additional benefit of space reduction and higher operating frequencies due to the associated lower capacitance of the fibers. The diode characteristics were analyzed using the thermionic emission model appropriate for Schottky junction. Exposure to UV radiation increased the diode on state current making is possible to demonstrate proof of concept rectification of low frequency ac signals for this simple device.

4.2   Experimental

4.2.1   Electrospinning

Electrospinning is a simple, cheap and quick method of fabricating polymer nanofibers with practically zero energy consumption [9]. The basic elements in the electrospinning (or electrostatic) process are shown in Fig. 4.1. The experimental setup consists of a high voltage low current voltage source, a hypodermic needle (anode) and a metal cathode. The polymer to be electrospun is dissolved in an appropriate solvent (that does not have too high a boiling point) and filled into a hypodermic syringe. The syringe is then mounted onto a syringe pump and the flow controlled to have a flow rate of about one drop per 30 s flowing out of the syringe. Typical distances for the cathode are 20–30 cm from the anode. The voltage to the anode is then increased and the droplet at the end of the pipette deforms into a shape of a cone called the Taylor cone. When the electric field reaches a critical value (about 15 kV at separations of 20 cm) the charged polymer solution overcomes the surface tension and a jet issued forth. This jet is seen to have a spiral shape after emerging from the needle and is observed to get thinner, and as the solvent evaporates fibers of ultrafine diameters are collected on the cathode as a non-woven mat. This process can be controlled so that relatively long fibers (anywhere from a few microns to a few centimeters) can be collected on the cathode with average fiber diameters ranging from tens of nanometers to a few micrometers depending on the electrospinning conditions. The fiber diameter was found to depend on many factors like solution viscosity, molecular weight of the polymer, electric field gradient and method of fiber collection. In order to capture isolated nanofibers, the substrate is quickly put in the path of the electrospun jet in a downward sweeping action. This results in a few fibers sticking to the substrate.
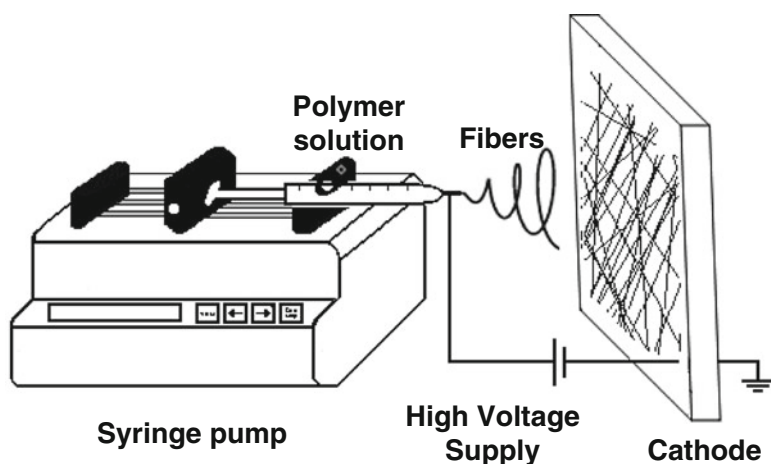
Fig. 4.1   Basic components of the electrospinning apparatus

4.2.2 Gas Sensor

100 mg of commercially available emeraldine base polyaniline was mixed with
129 mg of CSA and dissolved in 10 ml CHCl$_3$ for a period of 4 h. The resulting deep
green solution (doped polyaniline – PANiCSA) was filtered and 3.2 mg of poly-
ethylene oxide (PEO) having a molecular weight 2,000,000 was added to the
solution and stirred for an additional 2 h. PEO was added to assist in fiber formation
by acting as a plasticizer and the solution was then filtered again using a 0.45 μm
PTFE syringe filter. Part of this solution was filled into a hypodermic needle and
electrospun at a voltage of 8 kV. Individual fibers and several fibers were captured
on pre-patterned doped Si/SiO$_2$ wafers. In addition, a thin film of the above solution
before and after the addition of PEO was also prepared by drop casting on two
separate pre-patterned doped Si/SiO$_2$ wafers. The purpose of these films was to
compare the sensor results to that of the electrospun fiber to determine what role if
any the PEO had on the nanofiber sensor. Figure 4.2 shows an SEM image of a
typical PANiCSA nanofiber captured on a pre-patterned substrate.

4.2.3 Diode

Crossed nanoribbons of SnO$_2$ and PEDOT-PSSA were fabricated via the
electrospinning technique using sols that were prepared as follows: 2 ml of com-
mercially available tin(IV) isopropoxide, 10 % w/v in isopropanol/toluene (Alfa-
Aesar) was thoroughly mixed with 0.5 ml of a 0.7 wt% polyethylene oxide
(PEO-Aldrich) in chloroform. PEDOT-PSSA was purchased from Baytron
(Baytron P) and used as received. Since PEO is water soluble, a second sol of a
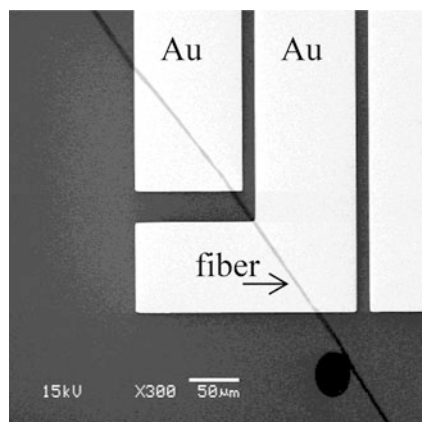
Fig. 4.2 SEM image of an isolated PANi-CSA nanofiber contacting pre-patterned gold
(Au) electrodes. For sensing measurements, the current passing through a single fiber was
monitored at a fixed voltage as a function of time while the sensing gas was allowed to flow
over the fiber in a closed chamber fitted with input and output openings for gas flow

1 wt% PEO in PEDOT-PSSA which is an aqueous dispersion of the polymer was prepared. The tin isopropoxide sol was first electrospun and ribbons of this were captured in doped Si/SiO$_2$ wafers. The substrates were then annealed in air at 700 °C for 2 h to yield SnO$_2$ nanoribbons that were seen to firmly adhere to it. The PEDOT-PSSA/PEO sol was then electrospun using the same electrospinning parameters, and the substrates containing the annealed SnO$_2$ nanoribbons were used to intercept PEDOT-PSSA nanoribbons by quickly passing the substrate in the path of the electrospun jet in a downward sweeping motion, some of which were seen to intersect the SnO$_2$ ribbons, each such intersection resulting in four "integrated" Schottky diodes. They are Schottky diodes because SnO$_2$ is *n*-type and PEDOT-PSSA is *p*-type (metal). The flexible and charged polymer ensured permanent bonding with the SnO$_2$ nanoribbon and the substrate and which are then placed in an oven at 70 °C for a few hours before being characterized. Figure 4.3 shows an optical microscope image of one such device after the evaporation of contact pads on each fiber, with an inset depicting the schematic external electrical connections that could be made to the hetero-junction (SnO$_2$/PEDOT-PSSA), the continuous SnO$_2$ branch or the continuous PEDOT-PSSA branch. The advantage of using a doped Si/SiO$_2$ substrate is the convenience of using a back gate bias as is done in a field effect transistor (FET) configuration to see what effect if any it had on the diode performance.
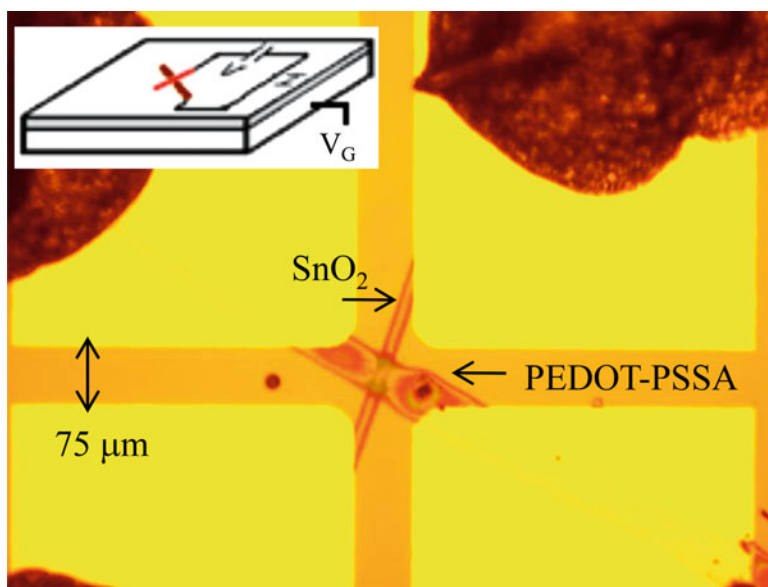
Fig. 4.3 Optical microscope image of a typical device, showing an electrospun SnO$_2$ nanoribbon crossed with a PEDOT-PSSA nanoribbon captured on a doped Si/SiO$_2$ wafer. Gold contact pads were made using a TEM grid as a shadow mask. The inset is a schematic of the external circuit used to electrically characterize the device. V$_G$ is the back gate terminal. Current-voltage (I-V) curves were asymmetric across a hetero-junction but symmetric otherwise

4.2.4   Electrical Characterization

The sensor was electrically characterized by measuring the two lead resistance as a function of time. The current voltage characteristic curves of the sensors in air are linear indicating Ohmic contacts with the external metal leads. In all of the sensor measurements, the resistance of the sensor was monitored while a constant flow of dry N_2 gas (control) was passed over it in a homebuilt gas chamber. Once the resistance stabilized then the control gas was bubbled at the same rate (930 ± 10 ml/min) into the alcohol at room temperature and allowed to flow into the gas chamber. After the sample stabilized in the presence of the alcohol vapor, the gas flow was then switched between pure N_2 and alcohol vapor in time intervals of 200 s for several cycles after which the experiment was terminated.

The currents through the fibers (for the sensor and the diode) were measured using a Keithley Model 6517A electrometer in air and in a vacuum of ~2×10^{-2} Torr. For the diode, ultraviolet illumination was obtained by a UVP model UVGL-25 source, a SRS model DS335 synthesized function generator was used for AC signal excitation and that was recorded on a Tektronix model TDS 3012B digital storage oscilloscope.

4.3   Discussion

4.3.1   Gas Sensor

Figure 4.4 shows the time dependence of the change in the normalized resistance for an individual isolated electrospun PANiCSA nanofibers (as seen in Fig. 4.2) and for multiple PANiCSA nanofibers upon exposure to vapors of methanol, where R_{N2} is the resistance of the fiber under a flow of dry N_2 gas [10]. The flow of N_2 decreases the resistance while the flow of alcohol vapor increases the resistance. Due to the larger surface area to volume ratio of a single nanofiber compared to multiple fibers, the response time is seen to be slighter faster and the change in the resistance is much larger for an individual fiber compared to many fibers. Since a trace amount of PEO was used in the fabrication of electrospun fibers, a thin film of the same polymer with and without the PEO was tested to see what effect if any the PEO had on the fiber response. The inset to Fig. 4.4 shows the response of these two sensors to methanol vapor. Although the response times were slower compared to the fiber primarily due to a reduced exposed surface area of the thin film, nevertheless the response was qualitatively similar i.e. a decrease and an increase in the resistance upon to exposure to N_2 gas and methanol vapor respectively. The film with PEO had a slightly faster response time implying that while the PEO could have enhanced the sensor speed by facilitating vapor diffusion into the polymer the general response to methanol vapor was similar. From Fig. 4.4 we calculate the response time of the fiber to methanol gas to be 32 s and the recovery time 20s.
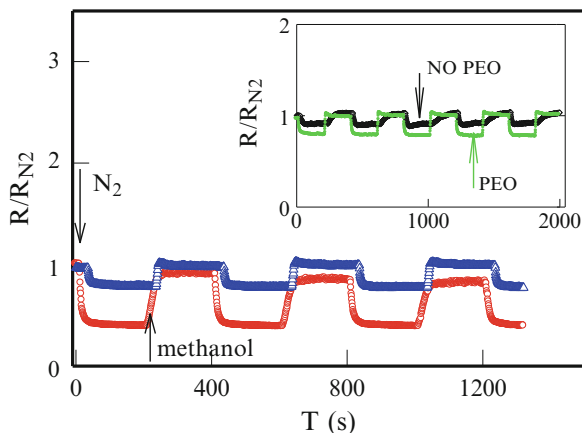
Fig. 4.4 Normalized resistance of individual (*red*) and multiple (*blue*) electrospun PANiCSA doped polyaniline nanofibers to methanol vapors. The *inset* shows the normalized resistance of a cast film of the same polymer with (*green*) and without (*black*) the addition of PEO. The films have a slower response time but similar overall behavior compared to that of the nanofiber indicating that PEO has no negative effect on the response to methanol

The percentage fractional change in the fiber resistance was 94 % in the presence of methanol vapors.

The response of the electrospun nanofiber to methanol can be explained as follows: The initial flow of N_2 gas for several minutes leaves the fiber relatively free of absorbed moisture. The moment methanol vapor is introduced into the chamber, the immediate increase of the resistance could be related to polymer swelling due to adsorbed moisture (physisorption) leading to reduced crystallinity followed immediately by the diffusion of the alcohol into the polymer and its subsequent interaction with the nitrogen atoms of polyaniline resulting in an extended chain formation facilitating charge transport and reducing the resistance. The trace amounts of PEO in the nanofiber would be to enhance the speed of this effect by facilitating vapor diffusion into the polymer and in addition, being a polar polymer it would assist in trapping some water molecules. Once equilibrium with the alcohol vapor is established, subsequent flow of N_2 gas will tend to remove the trapped moisture (without affecting the chain conformation) increasing the crystallinity and bringing the polymer chains closer together reducing the resistance and the addition of alcohol vapor would be to reintroduce the moisture level. Such an assumption is consistent since the resistance changes follow the general trend set by the equilibrium value reached after the first exposure to the alcohol vapor.

4.3.2 Diode

Figure 4.5 shows the current-voltage (I-V) characteristics of the device shown in Fig. 4.3 with different back gate biases. In this experiment for external electrical

Fig. 4.5 Device characteristic curves measured across a hetero-junction for different back gate biases. +40 V (*blue*), 0 V (*green*) and −40 V (*red*)
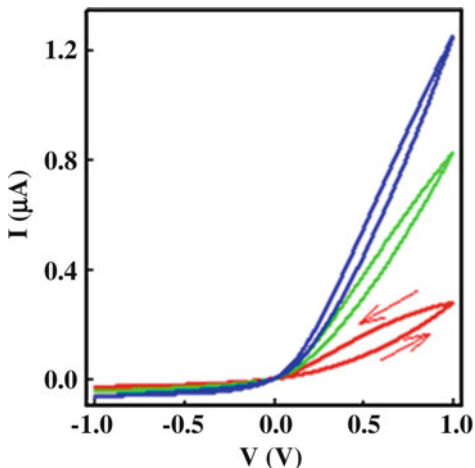
characterization, the external contacts were made across a heterojunction and involved a SnO$_2$ arm and a PEDOT-PSSA arm. Several devices were studied, and for each heterojunction, in general, the I-V characteristic curves were asymmetrical with a turn-on voltage in the range 0.1–0.4 V and a much reduced reverse bias current [11]. A hysteresis is observed when characterized in air, with the current on the downward voltage sweep being higher than the upward voltage sweep. The observed hysteresis was smaller under reverse bias and is primarily due to the SnO$_2$ arm of the device. This effect could be related to adsorbed moisture species that increase the surface charge density lowering the nanoribbon resistance. This hysteresis effect is much reduced in vacuum confirming our hypothesis for the observed hysteresis in air resulting from adsorbed moisture species. The device rectification ratio (I$_{ON}$/I$_{OFF}$), defined as the ratio of the forward to reverse bias current at ±1 V and diode turn-on voltage (V$_{ON}$) obtained by extrapolating the linear portion of the I-V curve in the first quadrant to intersect the voltage axis at zero current are 17 and 0.31 respectively when the gate bias is zero volts. Since the rectification ratio is higher in air, further characterization was carried out under these conditions. Low values of V$_{ON}$ are beneficial for polymer based devices that typically operate at much higher voltages. By increasing V$_G$, the conductance of the SnO$_2$ arm increases raising the rectification ratio and lowering V$_{ON}$ in air.

In order to quantitatively analyze the diode characteristics, we assume the standard thermionic emission model of a Schottky junction as follows [12]:

$$J = J_s \left[\exp\left(\frac{qV}{nkT}\right) - 1 \right] \tag{4.1}$$

$$J_s = A^* T^2 \exp\left(-\frac{q\phi_B}{kT}\right) \tag{4.2}$$

where J is the current density, J_s is the saturation current density, q is the electron charge, k is the Boltzmann constant, T is the absolute temperature, ϕ_B is the barrier height and n is the ideality factor which takes into account corrections to the original simple model e.g. image-force barrier lowering. The Richardson's constant $\left(A* = \frac{4\pi q m * k^2}{h^3} \right)$ is calculated to be 120 A/K^2-cm^2 assuming m* is the bare electron mass. By extrapolating the linear portion of the semi-log plot of current vs. voltage (in Fig. 4.5) in the forward bias regime to zero bias, the saturation current density of the diode can be determined, and the ideality factor can be calculated from the slope of the linear portion of the plot as follows:

$$n = \frac{q}{kT}\left(\frac{\partial V}{\partial \ln J} \right) \tag{4.3}$$

Using these equations, we can also calculate the barrier height ϕ_B. These values for the diode in air and with zero back gate voltage are 1.2 and 0.63 for n and ϕ_B respectively. Values of n > 1 have been attributed to several factors that include the recombination of holes and electrons in the depletion layer, the presence of an interfacial layer and interface states at the polymer-semiconductor interface or even a tunneling process.

Being transparent, the SnO$_2$ and PEDOT-PSSA nanoribbons conductance is insensitive to visible light, the diode was therefore tested in the presence of a UV light source ($\lambda = 365$ nm) and its response is shown in Fig. 4.6 in air, without a back gate bias. The diode was first characterized in the absence of UV light (in the dark) and had I-V characteristics similar to that reported earlier with a rectification ratio of ~20. In the presence of UV light however, there is a noticeable increase in the on state current. The rectification ratio increased to ~30. The increase in the on state current of the diode in the presence of UV is dominated by the change in conductance of the SnO$_2$ arm of the device. The lower diode resistance in the on state in the presence of UV light is related to the removal of adsorbed oxygen species that release the surface bound electrons on the SnO$_2$ nanoribbon that contribute to the observed current, and due to photoexcitation of electrons from the valence to the conduction band. Since the bandgap is direct in rutile structures of SnO$_2$ and was reported to be ~3.4 eV, it is not surprising that the UV light of wavelength 365 nm with photon energies of ~3.4 eV is large enough to cause direct excitation of electrons from the valence to the conduction band leading to enhanced carrier concentration and hence higher conduction. We also found that there is an increased charge mobility in the presence of UV that could be due to acquired photoenergy that assist the charge carriers overcome scattering due to defects and the presence of trap sites, features that hinder charge transport. Turning the UV lamp off resulted in the device slowly returning to its original value thereby making it reusable as a diode and as a light sensor (multifunctional). The increase of the diode on state current under UV light exposure motivated us to test it as a rectifier by connecting a 2 MΩ resistor in series with it, as shown in the upper inset to Fig. 4.6. A 10 Hz ac signal was applied across the input terminals and the output voltage that developed
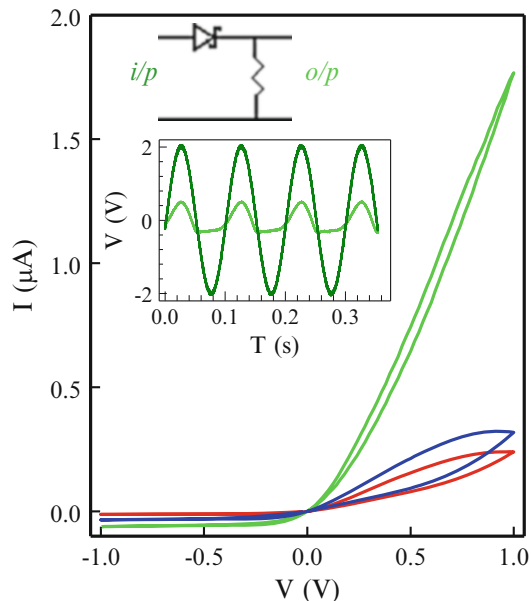
Fig. 4.6 Current-voltage characteristics (measured in air and zero back gate bias) across a hetero-junction of the device, in the presence of UV light. (**a**) No UV light-red (**b**) UV light present-green (**c**) UV light turned off (measured after several hours).-*blue*. The device is reusable. *Top inset*: External connections to the device when exposed to UV light. *Bottom Inset*: Oscilloscope trace of the input 10 Hz signal (*dark green*) and the output rectified signal taken across a 2 MΩ series resistor (*green*)

across the resistor was monitored with an oscilloscope. The lower inset to Fig. 4.6 shows the oscilloscope traces of the input and the output waveforms. There is clear evidence of waveform clipping in the negative cycle of the ac signal consistent with the device output characteristics and shows that these simple devices are indeed capable of low frequency rectification.

The two applications using isolated polymer nanofibers show why the electrospinning technique is more attractive compared to other fiber fabrication techniques like using templates or interfacial polymerization which only produce fibers in bulk. By controlling the rate of fiber formation and its subsequent capture on a rolling cathode, it should be possible to fabricate long fibers for continuous processing.

4.4 Conclusions

Sensors fabricated from isolated electrospun PANiCSA nanofibers, multiple nanofibers and cast films were tested in the presence of methanol vapor. Due to the large surface area, uniform diameter and small quantity of active material used

in the construction of electrospun sensors, they are comparable to or faster than those prepared from multiple nanofibers or from thin films. In addition, Schottky diodes were fabricated in air using the electrospinning process by simply crossing individual SnO_2 and PEDOT-PSSA nanoribbons. The diodes operate in air with low turn-on voltages and device parameters that are tunable via a back gate bias or a UV light source. Higher rectification ratios are predicted if the back gate bias and UV light are used simultaneously. The increase in the diode on state current in the presence of UV light made it possible to test it as a half wave rectifier with noticeable waveform clipping in the negative cycle at low frequencies. Connecting such diodes in tandem expands the possibility of their use in more complex circuits. Electrospinning is proposed as a cheap and easy technique to fabricate low power consumption devices and sensors.

References

1. J.C. MacDiarmid, A.G. Polyaniline, Protonic acid doping of the emeraldine form to the metallic regime – Chiang. Synth. Met. **13**, 193 (1986)
2. K. Lee, S. Cho, S.H. Park, A.J. Heeger, C.-W. Lee, S.-H. Lee, Metallic transport in polyaniline. Nature **441**, 65 (2006)
3. C.R. Martin, Nanomaterials: a membrane-based synthetic approach. Science **266**, 1961 (1994)
4. L. Zhang, M. Wan, Synthesis and characterization of self-assembled polyaniline nanotubes doped with D-10-camphorsulfonic acid. Nanotechnology **13**, 750 (2002)
5. J. Huang, S. Virji, B.H. Weiller, R.B. Kaner, Polyaniline nanofibers: facile synthesis and chemical sensors. J. Am. Chem. Soc. **125**, 314 (2003)
6. A.G. MacDiarmid, W.E. Jones, I.D. Norris, J. Gao, A.T. Johnson, N.J. Pinto, J. Hone, B. Han, F.K. Ho, H. Okuzaki, M. Llaguno, Electrostatically-generated nanofibers of electronic polymers. Synth. Met. **119**, 27 (2001)
7. Z. Liu, D. Zhang, S. Han, C. Li, T. Tang, W. Jin, X. Liu, B. Lei, C. Zhou, Laser ablation synthesis and electron transport studies of tin oxide nanowires. Adv. Mater. **15**, 1754 (2003)
8. S. Mathur, S. Barth, H. Shen, J.C. Pyun, U. Werner, Size-dependent photoconductance in SnO2 nanowires. Small **1**, 713 (2005)
9. D.H. Reneker, L.Y. Yarin, Electrospinning jets and polymer nanofibers. Polymer **49**, 2387 (2008)
10. N.J. Pinto, I. Ramos, R. Rojas, P.-C. Wang, A.T. Johnson Jr., Electric response of isolated electrospun polyaniline nanofibers to vapors of aliphatic alcohols. Sens. Actuators B **129**, 621 (2008)
11. K.V. Carrasquillo, N.J. Pinto, Tunable Schottky diodes fabricated from crossed electrospun SnO2/PEDOT-PSSA nanoribbons. Mater. Sci. Eng. B **177**, 805 (2012)
12. S. Scheinert, G.P. Paasch, Fabrication and analysis of polymer field-effect transistors. Phys. Status Solidi A **201**, 1263 (2004)

Chapter 5
Photoconductive Electrospun Titania Nanofibres to Develop Gas Sensors Operating at Room Temperature

Emiliano Zampetti, Antonella Macagnano, and A. Bearzotti

Abstract The use of nanostructured materials, such as those based on metal or metal oxides, has opened a new way to enhance the performances of chemical sensors making them able to detect gases at ppb level. In this type of sensors, the conductance is modulated by the presence of analytes that interact through physical-chemical processes of absorption and desorption, inducing changes in mobility or carriers density. The nano-scale dimensions of these materials enhance the interaction phenomena in terms of time and responses. In order to activate the physical/chemical interaction processes of the sensors based on oxide materials, an high operating temperature (200–400 °C) is required, resulting in significant power consumption. In this chapter, we report our recent studies on the possibility to exploit the titania photoconduction to develop gas sensor devices working at room temperature. We present the characterization of two different photoconductive Electrospun sensing layers: the first one is composed of titania nanofibres (TiO_2 NFs) and the second of TiO_2 NFs decorated with Pt nanoparticles (PtNPs) ranging from 5 to 10 nm.

5.1 Introduction

Monitoring low concentrations of toxic gases and VOCs are desired for environmental [1, 2] or biomedical applications [3]. Therefore this has led researchers to focus their attention on materials that could improve the detection performance of the sensors involved in such systems. In the last few years, many studies have shown that one of the possible ways to enhance sensor performance is the use of chemically reactive nanostructured materials able to detect gases at ppb level [4–8].

E. Zampetti (✉) • A. Macagnano • A. Bearzotti
Institute of Atmospheric Pollution Research of the National Research Council of Italy,
Via Salaria km 29,300, Monterotondo (RM), Italy
e-mail: e.zampetti@iia.cnr.it

These materials may vary significantly their physico-chemical properties when it interacts with the analyte through adsorption/desorption phenomena. Several kind of transducers [9–11] can be used to detect these interactions, providing an electrical signal correlated to the analyte concentration. An important category of materials used in gas sensing devices are metal oxides [12], however, most of the sensors based on these materials must work at high temperature (200–500 °C) to activate the physical/chemical interaction processes, resulting in significant power consumption. To reach these temperatures the sensor devices require the implementation of microheaters [13]. High temperature confined in a small volume (e.g. in sensor package or in test chamber) reduces the possible applications, especially in environments where there are flammable or explosive substances in particular at high concentration level.

To detect gases at ambient temperature, many research groups have proposed to use the photoconductivity of selected nanostructured metal oxides to develop highly sensitive chemical sensors. When a photoconductive material absorbs photons with energies larger than its band-gap, the charge carriers are generated [14]. Depending on the semiconducting material, its dimensions and stoichiometry, these carriers can either diffuse into the bulk of materials or affect the surface. As reported by Comini et al. [15], the experimental results have shown that the employment of light (UV) in the development of gas sensors, based on tin oxide thin films, is quite promising for the detection of nitrogen dioxide also at low temperatures. Law et al. [16], have found that the strong photo-conducting response of individual single-crystalline SnO_2 nano-ribbons makes it possible to achieve good results, if compared with high temperature performances, in the detection of NO_2 at room temperature by illuminating the devices with ultraviolet. Yang et al. [17], described the possibility to develop an oxygen gas sensor based on Co doped ZnO nanofibres working at room temperature under the illumination of a Xe lamp. Gui et al. [18], have tested TiO_2 and TiO_2-doped ZnO based sensors under UV irradiation to detect ethanol at room temperature. Peng et al. [19], discussed about the response of the copper-doped ZnO versus ethanol and acetone concentrations with and without the illumination of 355 nm light. They have found that the ultraviolet light irradiation could enhance the gas response. A hybrid (GaN nanowire)/(SnO_2 nanocrystals) sensor for selective alcohol sensing at room temperature and under UV irradiation has been presented by Bajpai et al. [20].

5.2 Electrospun Titania Based Gas Sensors

Titanium oxide is a material which can easily structure at nanoscale level in order to use it in applications such catalytic devices, solar cells and sensors [21–26]. This material can be synthesised in various shapes, as nanoporous material, nanoparticles, nanowires, nanorods, nanotubes and nanofibres, by different preparation methods such as sol–gel, hydrothermal synthesis, solvo-thermal synthesis, micro-emulsion, anodization, vapour deposition and electrospinning [27–32].

The electrospinning is a versatile technique capable of developing nanofibres from a wide variety of organic and even inorganic materials [33–35], allowing the fabrication of TiO_2 nanofibres by exploiting the sol–gel technique, as was first reported in 2003 [36].

There are several scientific papers concerning the fabrication of gas sensors based on Titania nanofibres deposited by electrospinning technique. As reported by Ying Wang et al. in 2009 [37], highly porous polypyrrole (PPy)-coated TiO_2/ZnO nanofibrous was tested in presence of NH_3 concentrations, the material has exhibited a fast response over a wide dynamic range and high sensitivity with a detection limit of 60 ppb. A detection limit of 0.268 ppm of ethanol was reached using titania-doped chromium oxide operating at 400 °C, as reported by Zheng, Y et al. [38], the device has shown also a long term stability. A comparison of ethanol measurements performed at two relative humidity levels (15 and 50 %) put in evidence the influence of moisture on resistance behaviour. Il-Doo Kim et al. in 2006 [39], have presented a TiO_2 nanofibre sensors that showed a limit of detection below 1 ppb for NO_2 at 300 °C. The fibres were hot pressed at 120 °C and then calcinated at 450 °C. The hot pressing procedure was able to improve the adhesion between the TiO_2 fibre mats. Comparable results at ppb levels for NO_2 and CO concentrations were found by Landau O. et al. in 2008 [40] developing a sensor based on electrospun titania operating at high temperature (300–400 °C). The sensors showed fast and opposite responses (in terms of resistivity variations) for the two tested gases. Titania nanofibres are also been used in composite materials to detect oxygen concentrations at moderate temperatures (hundreds of degrees) as recently reported in Frontera P. et al. in 2014 [41]. In particular the authors have investigated about the sensing properties of multi-walled-carbon-nanotubes/polyvinylacetate/titanium oxide (MWCNTs/PVAc/TiO_2) composite fibres with different MWCNT loadings. Highly sensitive gas sensor based on non-woven mats of Pd-doped TiO_2 nanofibres has been reported in Jaehyun Moon et al. [42]. The Pd doped TiO_2 nanofibres showed enhanced capability to detect nitrogen dioxide compared to pristine material. The sensor exhibited exceptional sensitivity to NO_2 gas concentrations as low as 0.16 ppm working at 180 °C. Heterostructure based on Titania nanofibres has been investigated as material for developing gas sensors. In fact, as recently discussed by Jianan Deng et al. in 2014 [43], they presents a new type of quasi-1D nanofibre architecture with a heterostructure of CuO–TiO_2, prepared via a combination of electrospinning and hydrothermal strategies and showed a high response and excellent selectivity to formaldehyde and ethanol gases. Furthermore, S.S. Batool et al. in 2013 [44] have investigated about the importance and the effect of metal (Ti, Ni, and Au) electrodes on humidity sensing properties of electrospun TiO_2 nanofibres. The results have shown that Ti-electrode sensor is found to have linear response, fast response and recovery time and higher sensitivity as compared with those of Ni- and Au-electrode sensors. Titania nanofibres are also often used as scaffold material in hybrid structures employed in sensors developing. In fact as reported in our previous work, Zampetti et al. [45], we have developed a NO_2 gas sensor based on hybrid material consisting in TiO_2 nanofibres coated with an organic conducting

polymer, PEDOT–PSS. In this case, the titanium nanofibres play two important roles, the first relating to the increase of the surface to volume ratio and the second related to the possible catalysis of the analyte.

5.3 Photoconductive Electrospun TiO_2 Nanofibres Based Gas Sensors

We present a summary of a recently published results regarding the developing and the study of a chemoresistor, based on titania nanofibres assisted by UV irradiation and working at room temperature [46, 47]. Specifically, we report some detail concerning the fabrication and the characterization of two type of chemoresistors the first based on TiO_2 nanofibres (TiO_2 NF) and the second based on TiO_2 NF decorated with Platinum nanoparticles (TiO_2 NF-PtNP).

5.3.1 Photoconductive Chemoresistor Based on TiO_2 Nanofibres

In this section we presents some details concerning the fabrication of a photoconductive chemoresistor, based on electrospun titania nanofibres. The developed sensor consisted of an interdigitated electrodes (IDEs) transducer, where a TiO_2 nanofibrous layer was deposited by electrospinning technique as reported in Fig. 5.1. The sensor is a chemiresistor, where the photoconductive TiO_2 nanofibrous layer acted as a chemically interactive material to detect analytes. The photoconductive effect of the nanomaterial was revealed by the IDE acting as transducer. IDE consisted of 40 pairs of platinum electrodes with a gap of 20 μm, 100 nm thick and 20 μm width, implemented on a passivated silicon wafer (SiO_2/Si) using a standard photolithographic process. A 20 nm thick sputtered titanium was
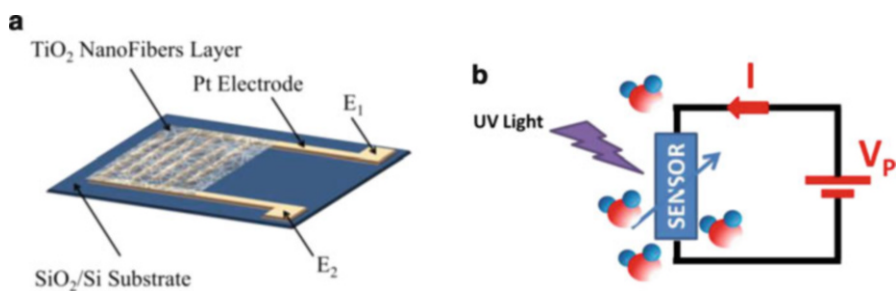
Fig. 5.1 (**a**) Sensor sketch where E_1, E_2 are the sensor electrodes. (**b**) Sketch of the sensor working principle

previously deposited in order to enhance the platinum adhesion. The overall active sensor area was about 1 cm^2.

Electrospinning is one of the most useful techniques to produce titania nanofibrous scaffold directly on the transducer, decreasing the number of steps due to the sensor fabrication process. The fabrication requires two main steps: the first one consists of the deposition of the nanofibrous layer composed of a TiO$_2$ precursor polymer and the second one of a thermal treatment capable of removing the organic material and allowing the materials crystallization. The TiO$_2$ precursor solution (Tiip/PVP) was obtained by mixing a solution of polyvinylpyrrolidone (PVP, Mw ~1,300,000) in anhydrous ethanol (EtOHa) with a 1:4 (w/v) solution of titanium isopropoxide (TiiP, Aldrich) in a 1:1 (v/v) mixture of glacial acetic acid (AcAcg) and EtOH. In order to deposit the precursor nanofibres, a 2-mL glass syringe, with a stainless steel needle having an inner tip diameter of 480 μm was filled with the previously prepared solution. In our electrospinning apparatus it is possible to control the feeding rate by a syringe pump controller (KDS 200, KD Scientific) to optimize the deposition process. A set of the IDE transducers were fixed on the surface of the rotating grounded metal collector in order to coat them with a layer of the precursor nanofibres. To draw the nanofibres from polymer solution, the syringe tip, 15 cm away from the collector, was connected to a high DC voltage power source. The parameters process was a: 100 μL/h of feed rate, 6 kV of high voltage and a collector speed of 500 rpm. The deposition, lasting 20 min, was carried out in a controlled chamber at 24 °C and at 45 % RH.

After the deposition of Tiip/PVP nanofibres, a thermal curing was carried out to remove the organic material and to obtain TiO$_2$ nanofibres having nanocrystalline form [46]. The calcination was carried out in air using a furnace, where the temperature was increased from 25 to 550 °C with a rate of 1 °C/min. The crystallization processes was completed maintaining the material at 550 °C for 4 h.

The morphology of the titania nanofibres was investigated by scanning electron microscopy (SEM – Jeol JSM 5200), transmission electron microscopy (TEM–Jeol JEM 2010 equipped with LaB$_6$ gun operating at 200 keV) and atomic force microscopy (AFM–PSIA XE 100 NC-HR) techniques. In Fig. 5.2, SEM micrograph highlights that fibres lie both on the substrate of oxidised silicon and on the platinum electrodes (20 μm wide and 100 nm thick).

The inset of Fig. 5.2 shows the AFM micrograph of the Titania nanofibres as deposited. The gas permeation, during the adsorption/desorption processes, is made easier by the presence of structured layer with a high surface to volume ratio and a large amount of pores between nanofibres. Electron diffraction (SAED) analysis of TiO$_2$ nanofibres revealed a poly-crystalline structure with grains size ranging from 5 to 40 nm and anatase form, known for the desirable properties of being chemically stable, readily available and active as a photocatalyst for oxidation processes [48].

In order to investigate the absorption spectrum of the TiO$_2$ nanofibrous layer and select the UV stimulus wavelength, a UV–Vis spectrometer (PerkinElmer Lambda 35 UV/Vis) has been used. The results have shown a broad absorbance near ultraviolet range and a prominent peak at 340 nm Fig. 5.3a.
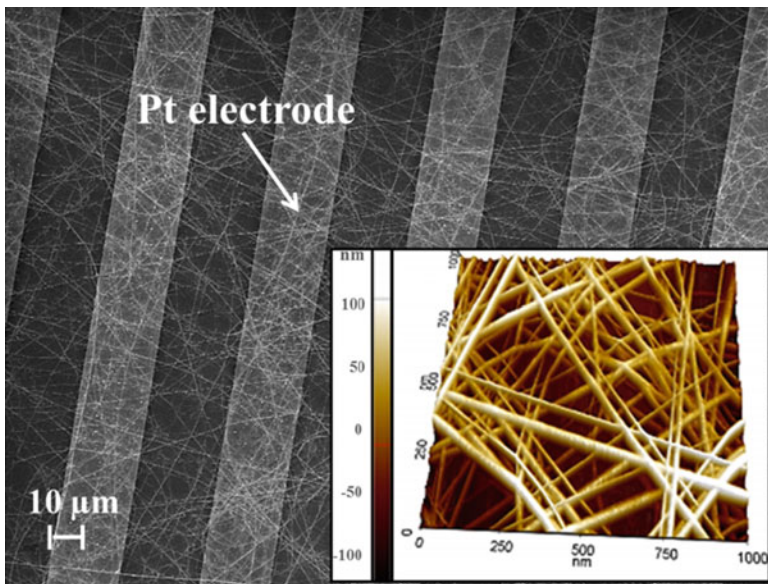
Fig. 5.2 SEM image of nanofibres on IDE. The *inset* reports the AFM micrograph of the Titania nanofibres as deposited
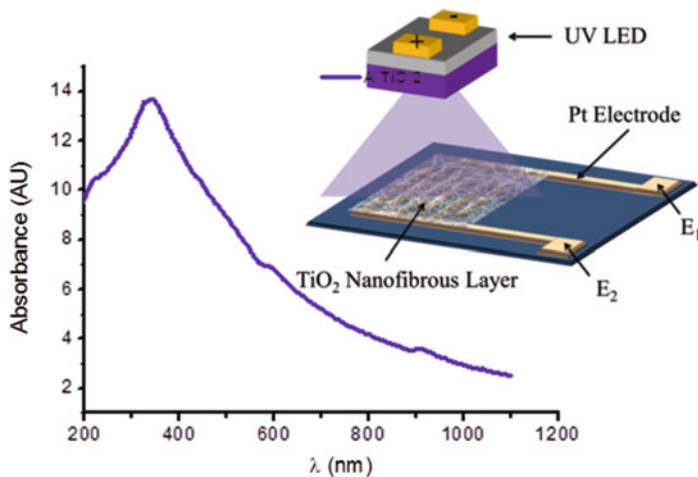
Fig. 5.3 Absorption spectrum of the TiO₂ nanofibrous layer

5.3.1.1 Sensor Responses Towards Humidity, Ammonia and Nitrogen Dioxide

The sensors were placed in a test chamber made of stainless steel. On the top of the chamber, a hole houses a low cost UV LED used during all the measures presented in this experiment. The device was tested at increasing percentage of RH, ranging
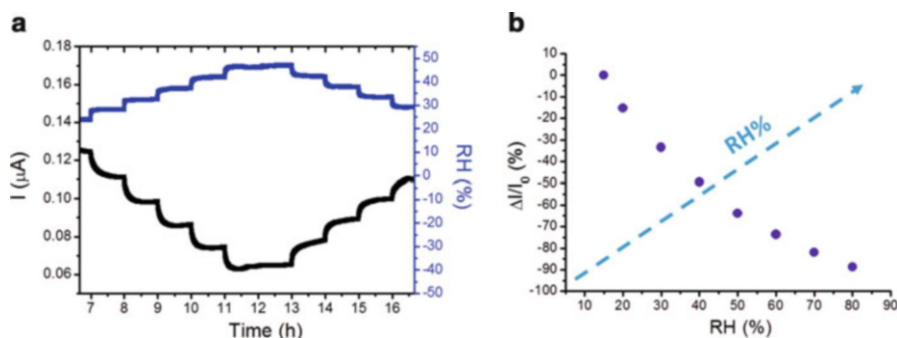
Fig. 5.4 Current variations stimulated by changes of relative humidity

from 5 to 80 % (Fig. 5.4). The relative change of the current, in terms of $(I-I_0)/I_0$ where I_0 was the current in dry nitrogen atmosphere, showed a decreasing trend for increasing values of humidity. This effect could be attributed to the ability of water to act as an electron scavenger to trap the conduction band electrons. The current variations due to changes in RH were quite rapid and reversible, also due to the fact that the dissociation of water on the surface of titania was completely reversible according with literature [49, 50].

The device was also tested in presence of ammonia and nitrogen dioxide concentration diluted in a flow (200 sccm) of dried nitrogen (@RT, under UV). The behaviour of current variation in correspondence of one step of ammonia concentration was characterized by a first segment, with high slope, which was exhausted in a few seconds and then followed by a phenomenon with a higher time constant. This trend could be associated to the ammonia adsorption on the nanofibres surface, the second one to a deeper diffusion through in the material having a high percolation coefficient due to its peculiar texture. The removal of ammonia by flowing dry nitrogen in the test chamber, is a phenomenon slower than the previous one [51]. The sensor response showed a drift of about 2 % after several measuring cycles of ammonia and for a total measuring time of about 2 h. In order to avoid damaging due to the doping effect when the gases concentrations were larger than 1 ppm, the exposure time, both of NH_3 than NO_2 gases, were fixed at 5 min. Figure 5.5 shows the comparison of sensor responses towards NO_2 and NH_3 concentrations, in terms of relative current variations.

5.3.2 Photoconductive Chemiresistor Based on TiO_2 Nanofibres Decorated with Pt Nanoparticles

Metallic nanoparticles as gold, silver, platinum and palladium, deposited on the surface of oxide materials, through their catalytic activity can split the hydrogen molecules promoting the sensing mechanism [52–55]. The activity of Platinum

Fig. 5.5 Comparison of
sensor responses towards
NO_2 and NH_3
concentrations
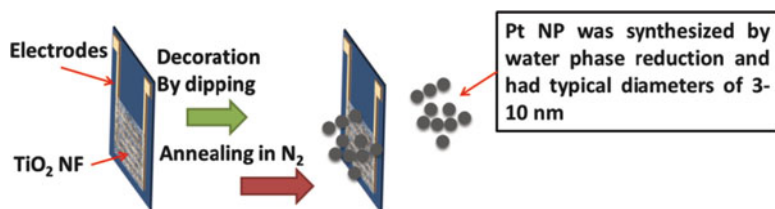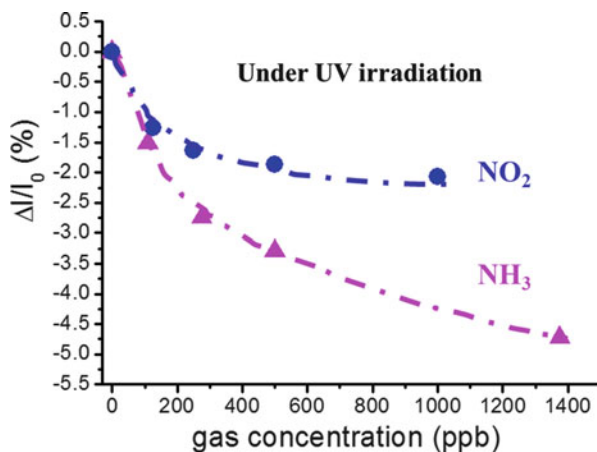
Fig. 5.6 Sketch of the decoration process performed by dip-coating

toward H_2 is a topic of interest for the development of hydrogen sensors and has
been investigated by Lewis in 1967 [56, 57] and recently in nanotechnology [58]. In
agreement with the literature previously reported, we have used Pt nanoparticles to
enhance the sensitivity of photo-conducting gas sensors based Titania nanofibres
versus hydrogen at room temperature. In particular Platinum nanoparticles (PtNPs),
with diameters of 3–10 nm, were synthesized by water phase reduction, using
3-mercapto-1-propanesulfonate (3MPS) as hydrophilic capping agent. As depicted
in Fig. 5.6, the titania nanofibres (TiO_2NFs) deposited on the IDE were decorated
with PtNPs by dip-coating [59]. In order to investigate the role of the amount of Pt
nanoparticles on the sensor performances, two water suspensions of Pt-3MPS-4
have been used to be absorbed on titania nanofibres: 400 μg/mL and 800 μg/mL.
The withdrawal speed of the IDE (covered by nanofibres) from the solution was
10 mm/min and the deposition was performed in a closed chamber where the
humidity and temperature were maintained at 40 % RH and 23 °C respectively.
After the decoration the samples were placed in a controlled oven at 37 °C
overnight to stabilize the material. Three different devices were prepared: the first
one with TiO_2 nanofibres dipped in 400 μg/mL (D1), the second dipped in 800 μg/
mL (D2) and the last one with TiO_2 nanofibres alone (D0).
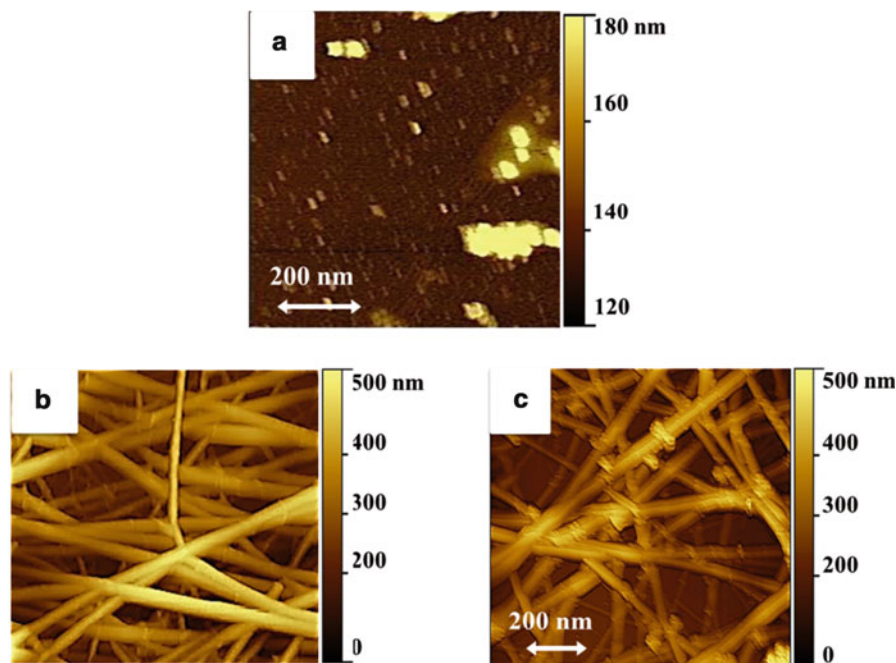
Fig. 5.7 AFM images of (**a**) Pt NPs, (**b**) TiO$_2$-NF and (**c**) Pt-TiO$_2$ hybrid system (D2)

Figure 5.7a depicts the AFM image analysis of PtNPs on silicon dioxide surface deposited by dip-coating. AFM analysis of TiO$_2$-NF and hybrid TiO$_2$-NF decorated with PtNPs (D2) was reported in Fig. 5.7b and in Fig. 5.7c respectively. TiO$_2$-NF (Fig. 5.7b) exhibits an average diameter of 80 nm and the AFM of PtTiO$_2$ hybrids points out the presence of PtNPs on the nanofibres surface (Fig. 5.7c).

Before moving on to the characterization of the material in presence of hydrogen, electrical measurements have been performed to determine the I versus V curves (I/V). These measures were carried out to change the voltage (V_D) across the IDE electrodes and to measure the current (I_D) in a stream of dry nitrogen and in presence of UV irradiation. As shown in Fig. 5.8, the I/V curve presents a non-linear trend due to the presence of a Schottky barrier potential of about 0.6 V, probably due to the contact between the titania and electrodes (IDE/TiO$_2$/IDE).

The I/V curves point out that the presence of Pt nanoparticles on the nanofibres surface play an important role in the conduction phenomena under UV irradiation. In fact the conductance of the devices D1, D2 was greater than that D0. Anyway, the presence of nanoparticles, without UV, did not produce measurable rise of the nanofibres conductance. Furthermore, as might be expected, the conductance of the devices (D1, D2) increase with increasing particle concentration (D2 curve is upper than D1 and D0 curves).

Fig. 5.8 I/V curve in dry
nitrogen and under UV
irradiation
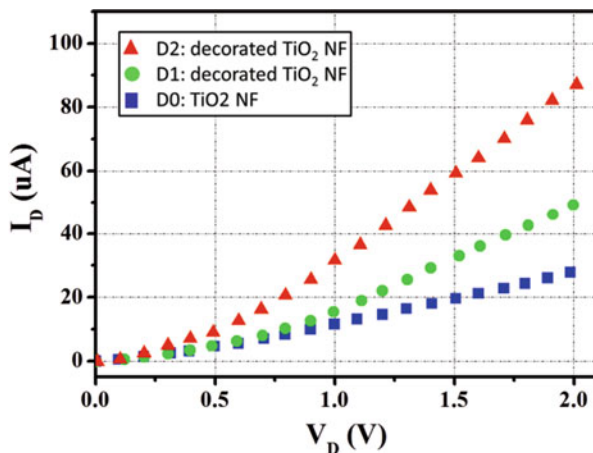
5.3.2.1   Sensor Responses Towards Hydrogen at Room Temperature

After the morphological and electrical characterizations, the improvement offered
by the presence of PtNPs in the interaction of TiO_2-NFs hybrid material with
hydrogen has been studied. As previously described in the Sect. 3.1 the devices
were placed in a suitable measurement chamber containing a UV light emitting
diode ($\lambda = 365$ nm). Sensor responses were recorded measuring the I_D current
(by Keithley 595) at a fixed voltage $V_D = 1$ V. During the experiment to generate
controlled hydrogen concentration diluted in nitrogen carrier a gas delivery system
has been employed. All the measurements were carried out at 25 °C, with 200 sccm
of total gas flow and in dry condition. In order to preserve the sensor functioning,
we have fixed at 2 min the exposure to hydrogen while the exposure time in
recovery phase (cleaning), performed in nitrogen, was 6 min.

   The sensor responses versus hydrogen concentrations (150, 400, 650, 900,
1,150 ppm) are reported in Fig. 5.9. The inset in Fig. 5.9 shows an example of
the devices (D2, D1, and D0) dynamic response during the exposure to 700 ppm of
hydrogen. These results highlight that the presence of Platinum nanoparticles on the
titania nanofibres increases the response towards hydrogen gas, under UV irradia-
tion and at room temperature. Moreover, devices show an increasing sensitivity
towards hydrogen increasing the PtNPs quantity (Device D2 exhibits a response at
least two times higher than D1 and four times higher than D0). As reported in
literature titania shows n-type semiconducting properties due to presence of donor-
type defects (e.g. oxygen vacancies) [60, 61]. Several supported metals, and among
others Pt, have been studied in order to understand the spilt-over hydrogen [62]. For
these reason, it is possible to assume that a synergic role of titania and Pt allows the
hybrid Pt TiO_2 system to be able to dissociate gaseous hydrogen in to atomic form,
contributing to the n-type conductivity enhancement. Finally, defining the limit of
detection (LOD) as three times of the noise value with a response noise value of
0.2 %, we have obtained 75 ppm of LOD for hydrogen @RT.
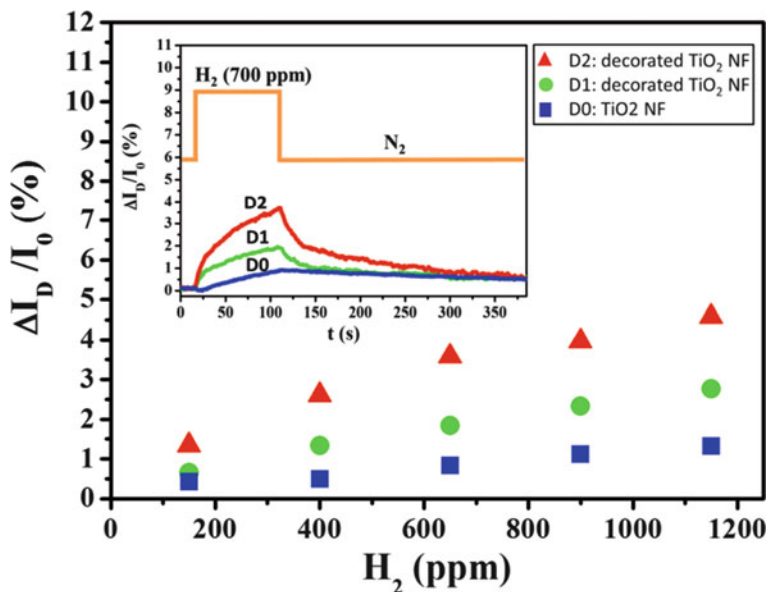
Fig. 5.9 Device responses towards increasing hydrogen concentrations. The device response has been reported as percentage of relative current variation calculated as: $(I - I_0) \times 100/I_0 = \Delta I/I_0$ (%) where I_0 was the current in nitrogen atmosphere

References

1. N. Pirrone, W. Aas, S. Cinnirella, R. Ebinghaus, I.M. Hedgecock, J. Pacyna, F. Sprovieri, E. Sunderland, Toward the next generation of air quality monitoring: mercury. Atmos. Environ. (2013). doi:10.1016/j.atmosenv.2013.06.053
2. S. Nativi, P. Mazzetti, M. Craglia, N. Pirrone, The GEOSS solution for enabling data interoperability and integrative research. Environ. Sci. Pollut. Res. **21**(6), 4177–4192 (2014). ISSN: 1614-7499
3. D. Kohl, Function and applications of gas sensors. J. Phys. D Appl. Phys. **34**, R125 (2001)
4. E. Traversa, Y. Sadaoka, M.C. Carotta, G. Martinelli, Environmental monitoring field tests using screen-printed thick-film sensors based on semiconducting oxides. Sens. Actuators B **65**, 181–185 (2000)
5. M.C. Carotta, G. Martinelli, L. Crema, C. Malagu', M. Merli, G. Ghiotti, E. Traversa, Nanostructured thick film gas sensors for atmospheric pollutant monitoring: quantitative analysis on field tests. Sens. Actuators B **76**, 336–342 (2001)

6. X.J. Huang, Y.K. Choi, Chemical sensors based on nanostructured materials. Sens. Actuators B **122**, 659–671 (2007)
7. M. Breedon, P. Spizzirri, M. Taylor, J. Du Plessis, D. McCulloch, J. Zhu, L. Yu, Z. Hu, C. Rix, W. Wlodarski, K. Kalantar-zadeh, Synthesis of nanostructured tungsten oxide thin films: a simple, controllable, inexpensive, aqueous sol–gel method. Cryst. Growth Des. **10**, 430–439 (2010)
8. T.A. Rajesh, D. Kumar, Recent progress in the development of nano-structured conducting polymers/nanocomposites for sensor applications. Sens. Actuators B **136**(1), 275–286 (2009)
9. H. Jane, R.P. Tatam, Optical gas sensing: a review. Meas. Sci. Technol. **24**, 012004 (2013)
10. Hua Bai, Gaoquan Shi, Gas sensors based on conducting polymers. Sensors **7**(3), 267–307 (2007)
11. G. Korotcenkov, Metal oxides for solid-state gas sensors: what determines our choice? Mater. Sci. Eng. B **139**, 1–23 (2007)
12. N. Barsan, D. Koziej, U. Weimar, Metal oxide-based gas sensor research: how to? Sens. Actuators B **121**(1), 18–35 (2007)
13. Y. Mo, Y. Okawa, M. Tajima, T. Nakai, N. Yoshiike, K. Natukawa, Micro-machined gas sensor array based on metal film micro-heater. Sens. Actuators B **79**, 175–181 (2001)
14. T. Zhai, Z. Fang, M. Liao, X. Xu, H. Zeng, B. Yoshio, D. Golberg, A comprehensive review of one-dimensional metaloxide nanostructure photodetectors. Sensors **9**, 6504–6529 (2009)
15. E. Comini, G. Faglia, G. Sberveglieri, UV activation of tin oxide thin films for NO_2 sensing at low temperatures. Sens. Actuators B **78**, 73–77 (2001)
16. M. Law, H. Kind, B. Messer, F. Kim, P. Yang, Photochemical sensing of NO_2 with SnO_2 nanoribbon nanosensors at room temperature. Angew. Chem. Int. Ed. **41**, 2405–2408 (2002)
17. M. Yang, T.F. Xie, L. Peng, Y. Zhao, D. Wang, Fabrication and photoelectric oxygen sensing characteristics of electrospun Co doped ZnO nanofibres. Appl. Phys. A **89**, 427–430 (2007)
18. Y. Gui, S. Li, J. Xu, C. Li, Study on TiO_2-doped ZnO thick film gas sensors enhanced by UV light at room temperature. Microelectron. J. **39**, 1120–1125 (2008)
19. L. Peng, T.F. Xie, M. Yang, P. Wang, S. Pang, D.J. Wang, Light induced enhancing gas sensitivity of copper-doped zinc oxide at room temperature. Sens. Actuators B **131**, 660–664 (2008)
20. R. Bajpai, A. Motayed, A.V. Davydov, V.P. Oleshko, G.S. Aluri, K.A. Bertness, M.V. Rao, M.E. Zaghloul, UV-assisted alcohol sensing using SnO_2 functionalized GaN nanowire devices. Sens. Actuators B **171–172**, 499–507 (2012)
21. A. Fujishima, T.N. Rao, D.A. Tryk, Titanium dioxide photocatalysis. J. Photochem. Photobiol. C **1**, 1–21 (2000)
22. T.Y. Yang, H.M. Lin, B.Y. Wei, C.Y. Wu, C.K. Lin, UV enhancement of the gas sensing properties of nano-TiO_2. Rev. Adv. Mater. Sci. **4**, 48–54 (2003). ISSN 1605-8127
23. M. Hirano, K. Matsushima, Effect of niobium on the structure and photoactivity of anatase (TiO_2) nanoparticles. J. Nanosci. Nanotechnol. **6**, 762–770 (2006)
24. G.K. Mor, K. Shankar, M. Paulose, O.K. Varghese, C.A. Grimes, Use of highly-ordered TiO_2 nanotube arrays in dyesensitized solar cells. Nano Lett. **6**, 215–218 (2006)
25. N.L. Lala, R. Jose, M.M. Yusoff, S. Ramakrishna, Continuous tubular nanofibres of vanadium pentoxide by electrospinning for energy storage devices. J. Nanopart. Res. **14**, 1201–1210 (2012)
26. Renyuan Zhang, A.A. Elzatahry, S.S. Al-Deyab, Dongyuan Zhao, Mesoporous titania: from synthesis to application. Nano Today **7**(4), 344–366 (2012)
27. E. Stathatos, P. Lianos, F.D. Monte, D. Levy, D. Tsiourvas, Formation of TiO_2 nanoparticles in reverse micelles and their deposition as thin films on glass substrates. Langmuir **13**, 4295–4300 (1997)
28. Y. Yue, Z. Gao, Synthesis of mesoporous TiO_2 with a crystalline framework. Chem. Commun. **18**, 1755–1756 (2000)
29. X. Chen, S.S. Mao, Synthesis of titanium dioxide (TiO_2) nanomaterials. J. Nanosci. Nanotechnol. **6**, 906–925 (2006)

30. K.M. Sawicka, P. Gouma, Electrospun composite nanofibres for functional applications. J. Nanopart. Res. **8**, 769–778 (2006)
31. S. Ramakrishna, K. Fujihara, W.E. Teo, T. Yong, Zuwei Ma, R. Ramakrishna, Electrospun nanofibres: solving global issues. Mater. Today **9**, 40–50 (2006)
32. A.Z. Sadek, H. Zheng, K. Latham, W. Wlodarski, K. Kalantar-zadeh, Anodization of Ti thin film deposited on ITO. Langmuir **25**, 509–514 (2009)
33. P. Lu, B. Ding, Applications of electrospun fibres. Recent Pat. Nanotechnol. **2**, 169–182 (2008)
34. E. Zampetti, A. Muzyczuk, A. Macagnano, S. Pantalei, S. Scalese, C. Spinella, A. Bearzotti, Effects of temperature and humidity on electrospun conductive nanofibres based on polyaniline blends. J. Nanopart. Res. **13**, 6193–6200 (2011)
35. Bin Ding, Moran Wang, Xianfeng Wang, Jianyong Yub, Gang Suna, Electrospun nanomaterials for ultrasensitive sensors. Mater. Today **13**(11), 16–27 (2010)
36. D. Li, Y. Xia, Fabrication of titania nanofibres by electrospinning. Nano Lett. **3**, 555–560 (2003)
37. Ying Wang, Wenzehao Jia, Timothy Strout, Ashely Schempf, Heng Zhang, Baikun Li, Junhong Cui, Yu Lei, Ammonia gas sensor using polypyrrole-coated TiO_2/ZnO nanofibres. Electroanalysis **21**(12), 1432–1438 (2009)
38. Y. Zheng, J. Wang, P. Chen, C. Li, X. Li, Structure and gas-sensing behavior of electrospun titania-doped chromium oxide fibres. Int. J. Appl. Ceram. Technol. **10**, E304–E309 (2013)
39. Il-Doo Kim, Avner Rothschild, Byong Hong Lee, Dong Young Kim, Seong Mu Jo, H.L. Tuller, Ultrasensitive chemiresistors based on electrospun TiO_2 nanofibres. Nano Lett. **6**(9), 2009–2013 (2006)
40. O. Landau, A. Rothschild, E. Zussman, Electrospun nanostructured TiO_2 gas sensors. IEEE Sensors Conference 2008, 863–865 (2008)
41. P. Frontera, S. Trocino, A. Donato, P.L. Antonucci, M. Lo Faro, G. Squadrito, G. Neri, Oxygen-sensing properties of electrospun CNTs/PVAc/TiO_2 composites. Electron. Mater. Lett. **10**(1), 305–313 (2014)
42. Jaehyun Moon, Jin-Ah Park, Su-Jae Lee, Taehyoung Zyung, Il-Doo Kim, Pd-doped TiO_2 nanofibre networks for gas sensor applications. Sens. Actuators B Chem. **149**(1), 301–305 (2010)
43. Jianan Deng, Lili Wang, Zheng Lou, Tong Zha, Design of CuO–TiO_2 heterostructure nano fibres and their sensing performance. J. Mater. Chem. A **2**, 9030 (2014)
44. S.S. Batool, Z. Imran, M. Israr Qadir, M. Usman, H. Jamil, M.A. Ra, M.M. Hassan, M. Willander, Comparative analysis of Ti, Ni, and Au electrodes on characteristics of TiO_2 nano fibres for humidity sensor application. J. Mater. Sci. Technol. **29**(5), 411–e414 (2013)
45. E. Zampetti, S. Pantalei, A. Muzyczuk, A. Bearzotti, F. De Cesare, C. Spinella, A. Macagnano, A high sensitive NO_2 gas sensor based on PEDOT–PSS/TiO_2 nanofibres. Sens. Actuators B **176**, 390–398 (2013)
46. E. Zampetti, A. Macagnano, A. Bearzotti, Gas sensor based on photoconductive electrospun titania nanofibres operating at room temperature. J. Nanopart. Res. **15**(4), (2013), art. no. 1566
47. I. Fratoddi, A. Macagnano, C. Battocchio, E. Zampetti, I. Venditti, M.V. Russo, A. Bearzotti, Platinum nanoparticles on electrospun titania nanofibres as hydrogen sensing materials working at room temperature. Nanoscale **6**, 9177–9184 (2014). doi:10.1039/C4NR01400F
48. D. Chatterjee, S. Dasgupta, Visible light induced photocatalytic degradation of organic pollutants. J Photochem. Photobiol. C **6**, 186–205 (2005)
49. U. Diebold, The surface science of titanium dioxide. Surf. Sci. Rep. **48**, 53–229 (2003)
50. M.A. Henderson, The interaction of water with solid surfaces: fundamental aspects revisited. Surf. Sci. Rep. **46**, 1–308 (2002)
51. E. Comini, A. Cristalli, G. Faglia, G. Sberveglieri, Light enhanced gas sensing properties of indium oxide and tin dioxide sensors. Sens. Actuators B **65**, 260–263 (2000)
52. Q. Xiang, G. Meng, Y. Zhang, J. Xu, P. Xu, Q. Pan, W. Yu, Ag nanoparticle embedded-ZnO nanorods synthesized via a photochemical method and its gas-sensing properties. Sens. Actuators B **143**, 635 (2010)

53. X. Liu, J. Zhang, X. Guo, S. Wu, S. Wang, Amino acid-assisted one-pot assembly of Au, Pt nanoparticles onto one-dimensional ZnO microrods. Nanoscale **2**, 1178 (2010)
54. Y.H. Lin, Y.C. Hsueh, P.S. Lee, C.C. Wang, J.M. Wu, T.P. Perng, H.C. Shih, Fabrication of tin dioxide nanowires with ultrahigh gas sensitivity by atomic layer deposition of platinum. J. Mater. Chem. **21**, 10552 (2011)
55. X. Xue, Z. Chen, C. Ma, L. Xing, Y. Chen, Y. Wang, T. Wang, One-step synthesis and gas-sensing characteristics of uniformly loaded Pt@SnO_2 nanorods. J. Phys. Chem. C **114**, 3968 (2010)
56. F.A. Lewis, *The Palladium-Hydrogen System* (Academic, London/New York, 1967)
57. A. Abburi, W.J. Yeh, Temperature and pore size dependence on the sensitivity of a hydrogen sensor based on nanoporous platinum thin films. IEEE Sens. J. **12**, 2625 (2012)
58. A. Kaniyoor, R. Imran Jafri, T. Arockiadoss, S. Ramaprabhu, Nanostructured Pt decorated graphene and multi walled carbon nanotube based room temperature hydrogen gas sensor. Nanoscale **1**, 382 (2009)
59. C.J. Brinker, G.C. Frye, A.J. Hurd, C.S. Ashley, Preparation and characterization fundamentals of sol-gel dip coating. Thin Solid Films **201**, 97–108 (1991)
60. R.N. Blumenthal, J. Baukus, W.M. Hirthe, Defect structure of nonstoichiometric rutile, TiO_{2-x}. J. Electrochem. Soc. **114**, 172 (1967)
61. J. Nowotny, T. Bak, M.K. Nowotny, L.R. Sheppard, Titanium dioxide for solar-hydrogen II. Defect chemistry. Int. J. Hydrogen Energy **32**, 2630 (2007)
62. U. Roland, T. Braunschweig, F. Roessner, On the nature of spilt-over hydrogen. J. Mol. Catal. A: Chem. **127**, 61–84 (1997)

Chapter 6
Electrospun Fluorescent Nanofibers and Their Application in Optical Sensing

A. Camposeo, M. Moffa, and L. Persano

Abstract Electrospun light-emitting nanofibers are attracting an increasing interest for their potential exploitation in photonic applications, as miniaturized light sources, detectors, waveguides and optical sensors. Fluorescent electrospun fibers can be realized by embedding emissive systems (quantum dots, dyes and bio-chromophores) in optically inert polymer matrices, and by using light-emitting conjugated polymers. The peculiar properties of the electrospinning process allows for obtaining fluorescent fibers featuring typically improved optical properties compared to flat thin films, such as enhanced photoluminescence quantum yield and radiative rates, polarized emission and self-waveguiding of the emitted light. These properties, combined with a high surface area to volume ratio, make these nanostructured materials suitable for high performance optical sensing. This Chapter provides an introductory overview of the properties of fluorescent electrospun nanofibers and presents illustrative examples of their application as optical sensors for the detection of heavy metal ions, explosive compounds and bio-molecules.

6.1 Introduction

Electrospun nanofibers are a class of materials currently exploited in many applications, some of which are nowadays close to industrial production and commercialization [1]. In this framework, the use of electrospun nanofibers in photonics is emerging as a promising research field aimed at developing novel microscale light sources and detectors, lasers and optical sensors. This field is growing very fast, since optically-active electrospun nanofibers with specific and tailored optical properties can be produced by various approaches exploiting the unique properties

---

A. Camposeo (✉) • L. Persano
Istituto Nanoscienze-CNR, via Arnesano, I-73100 Lecce, Italy

Soft Materials and Technologies S.r.l., I-73100 Lecce, Italy
e-mail: andrea.camposeo@nano.cnr.it

M. Moffa
Istituto Nanoscienze-CNR, via Arnesano, I-73100 Lecce, Italy

of organic light-emitting materials (tunability of the emission, strong absorbance, high quantum yield, large Stokes shift, etc.). The resulting fluorescent nanostructures combine remarkable optical performances with high exposed surface (orders of magnitude larger than flat thin films), a property that is particularly appealing for sensing applications, where surface-interactions with the system to be detected are especially relevant. Indeed, the increase of exposed surface in nanofibers may strongly enhance the sensitivity of devices. The demonstration of the possibility of using the quenching of the photoluminescence intensity of electrospun fibers for sensing heavy metal ions and nitroaromatic compounds by Wang et al. [2] has stimulated a lot of research efforts aimed at improving the sensing performances of fluorescent nanofibrous systems and at enriching the class of detectable species, as well as at investigating more in depth the optical and photoluminescence properties of electrospun nanofibers at a fundamental level.

This Chapter provides background information and an overview of state of art progress in the field of light-emitting and fluorescent electrospun nanofibers, and of their use in optical sensing. The Chapter is organized in three main Sections: in Sect. 6.2 some fluorescent electrospun nanofiber systems will be introduced, with particular emphasis on the used active components. Section 6.3 introduces some basic properties of fluorescent electrospun fibers. In Sect. 6.4, some applications of photoluminescent fibers for optical sensing of metal ions, explosive molecules and bio-compounds are presented.

6.2 Nanofiber-Based Light-Emitting Systems

The high flexibility of the electrospinning (ES) process, in terms of number and typology of processable materials, is corroborated by the large variety of luminescent nanofibers developed in the last 10 years. The number of demonstrated fiber classes is continuously growing, with novel systems featuring emission of light both by optical and electrical excitation [3]. Electrospun fluorescent nanofibers can be realized by essentially two approaches: the first involves the use of transparent or optically inert polymers which can be doped with luminescent systems (inorganic quantum dots, organic chromophores and polymers, and bio-chromophores), whereas the second is based on conjugated polymers, which are intrinsically luminescent. The solubility, rheological and optical properties of these materials feature a very broad variability, which requires the development of specific approaches for obtaining electrospun nanofibers with uniform morphology and fluorescence. In the following paragraphs, a brief overview of some relevant examples of fluorescent electrospun fibers is presented, without entering into the details of the ES process of the different presented systems. The reader can refer to the original papers for more technical information.

6.2.1   Quantum Dot- and Dye-Doped Electrospun Nanofibers

A very effective approach to obtain luminescent electrospun nanofibers uses transparent thermoplastic polymers or polymeric photoresists as matrix, and inorganic quantum dots (QD) or nanowires as fluorescent components (Fig. 6.1a–b) [4–6]. In this way, composite fibers with diameters of few hundreds of nanometers can be easily obtained starting from the well established procedures developed for the matrix polymers, whereas the photoluminescence properties can be tailored by means of the inorganic nanoparticles which feature emission in a broad spectral range, from visible to near infrared. These nanoparticles, most often composed by group II-VI elements such as CdS, CdSe, CdTe, have diameters of few nanometers and, more importantly, electronic band gaps and photoluminescence wavelengths tunable upon changing their size [7]. Indeed, in these inorganic systems, quantum confinement effects can be appreciated for particle size approaching the exciton Bohr radius, a_b, which is typically of few nanometer ($a_b \cong 3$ nm for CdS) [8]. A blue-shift of the emission can be also observed by decreasing the particle size below the Bohr radius. Fluorescent composite nanofibers can be produced through two principal approaches: *i*) by adding colloidal QDs and nanowires, which are synthesized *ex-situ*, to the ES solution or (*ii*) by embedding suitable molecular precursors in the polymer matrix, which enables the *in-situ* synthesis of the QDs in electrospun fibers by precursor decomposition through thermal treatment [9], gas reaction [10], or optical and electron beam exposures [11]. In the former approach, the use of colloidal QDs allows for a precise control of the particles diameter and size distribution, even though the presence of these particles may somewhat alter the rheological properties of the ES solution [9, 12]. The varied rheology may even lead to clogging of the ES spinneret and failure of the process. These problems may be overcome by the *in-situ* synthesis, since the physical and chemical properties of the polymer solution are minimally altered by the presence of molecular precursors. Another advantage of *in-situ* synthesis is the possibility to spatially control the formation of the QDs, by using patterning methods based on laser writing or electron beam lithography [11, 13]. The main difficulty of QDs *in-situ* synthesis is represented by the frequently limited control on the particle diameter and size distribution. This is made complex by effects that characterize the molecular precursors decomposition, including the diffusion of the produced atomic elements and their aggregation.

Alternatively to QDs, organic luminescent chromophores can be embedded in polymer matrices in order to obtain light-emitting electrospun nanofibers (Fig. 6.1c–d). Fluorescent organic molecules have emission from the ultra-violet to the near infrared and can be easily added in polymers such as poly(methyl methacrylate) (PMMA), polystyrene (PS), poly(vinyl pyrrolidone) (PVP) and poly(ethylene oxide) (PEO) [14]. Particular care must be paid in preparing solutions, since the emission properties of these organic molecules are very sensitive to the used solvents and to their own resulting micro-environment. By this approach a broad range of luminescent fibers have been realized, which are used for optical
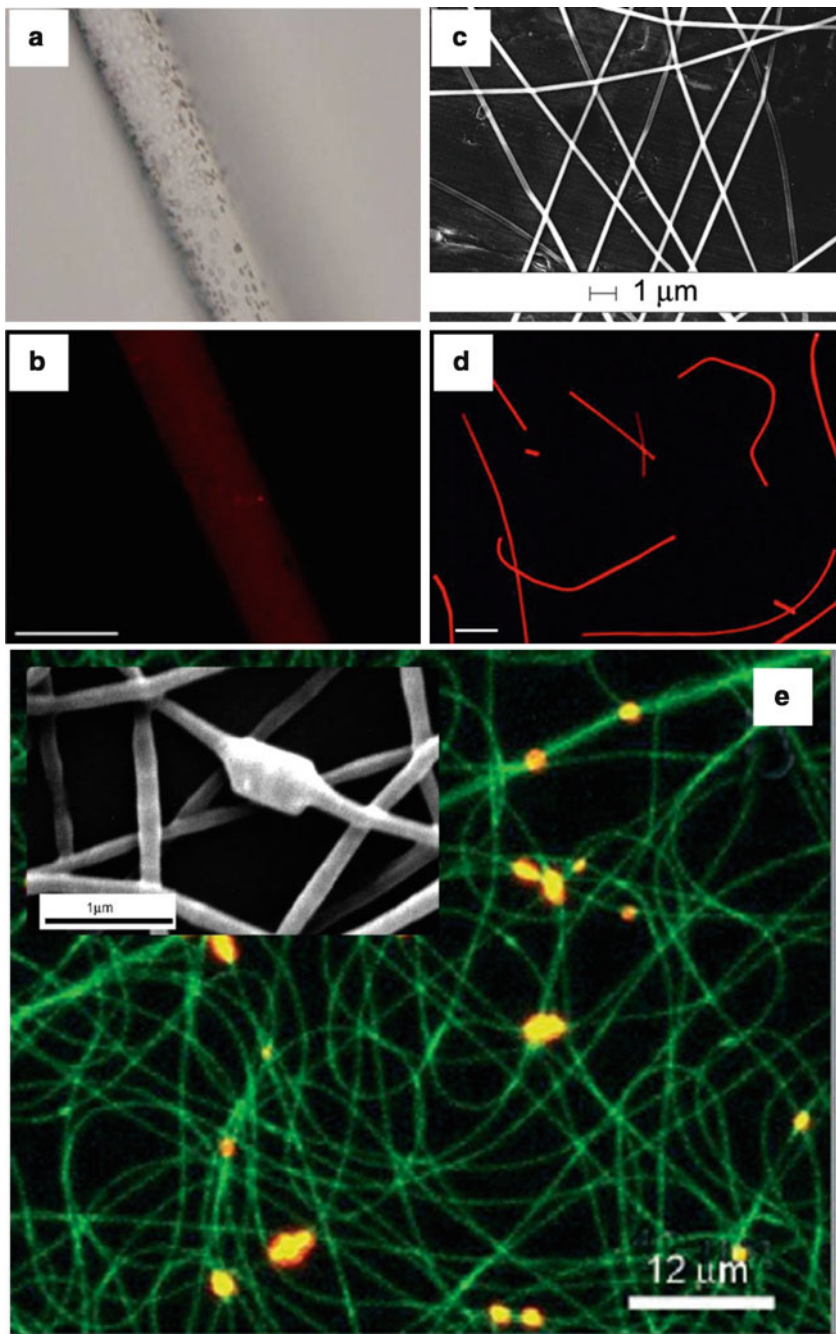
Fig. 6.1 Fluorescence microscopy images in bright (**a**) and dark (**b**) field, respectively, of a PMMA electrospun nanofiber embedding core-shell CdSe/ZnS QDs. *Scale bar*: 5 μm (Adapted from [6], Copyright © 2011, with permission from Elsevier). Scanning electron microscopy image (**c**) and fluorescence micrograph (**d**) of PMMA nanofibers doped with laser dyes. *Scale bar* in (**d**): 10 μm (Adapted with permission from [16], Copyright © 2009 of Wiley-VCH Verlag GmbH & Co. KGaA). (**e**) Confocal microscopy image of luminescent nanofibers containing zeolites loaded with a red light-emitting system. The *inset* shows a scanning electron micrograph of these fibers. *Scale bar*: 1 μm (Adapted with permission from [18], Copyright © 2007 of WILEY-VCH Verlag GmbH & Co. KGaA)

sensing and in other photonic applications such as light sources [15] and microlasers [16, 17].

Figure 6.1e shows an interesting example of hybrid luminescent system, where organic luminescent dyes are loaded in inorganic zeolite L crystals, whose orientation and assembly is controlled by their inclusion in polymer electrospun nanofibers with diameters as low as 150 nm [18]. The hybrid nanofibers feature bright localized emission, that is polarized due to the orientation of the zeolite crystals induced by the ES process.

6.2.2   Nanofibers Embedding Bio-chromophores

Among the various systems that can be embedded in electrospun nanofibers, bioluminescent chromophores deserve particular attention, due to their potential applications in optical biosensing. One of the most studied luminescent bio-molecules is the green fluorescent protein (GFP) from the jellyfish *Aequorea victoria* [19, 20]. Unlike the most of fluorescent proteins which contain fluorophores distinct from the amino acid sequence, the chromophore of the GFP is internally generated by a reaction involving three amino acid residues. In addition, GFP displays a correlation between its fluorescence properties and conformation changes [20], a property that has paved the way for the exploitation of GFP in a variety of sensing applications [20, 21].

The use of bio-chromophores for the realization of fluorescent fibers requires some particular care for engineering both the ES process and the fiber structure. In general charges generated in the ES polymer jet may alter the functionality of bio-macromolecules and of biological objects such as proteins, viruses and bacteria [22]. The inclusion of GFP in electrospun fibers made by PEO dissolved in water leads, in fact, to structures with diameters of several hundreds of nanometers which do not show any fluorescence due to the denaturation of the GFP in the solid matrix. The exploitation of co-electrospinning and the inclusion of GFP proteins in core-shell structures [22, 23] is instead effective in preserving the functionality of the protein and its fluorescence (Fig. 6.2). In the co-electrospinning process the electrical charges are mainly located on the outer surface, whereas the inner solution and the embedded systems are not charged, a condition that allows one to better preserve the properties of the objects embedded in the core [22]. Moreover, a more favorable micro-environment can be created in the core in order to maintain active the fluorescence of the used bio-chromophores.

6.2.3   Nanofibers Made by Conjugated Polymers

Conjugated polymers are a class of organic materials, featuring many optoelectronic properties typical of semiconductors [24]. In particular, their electronic band
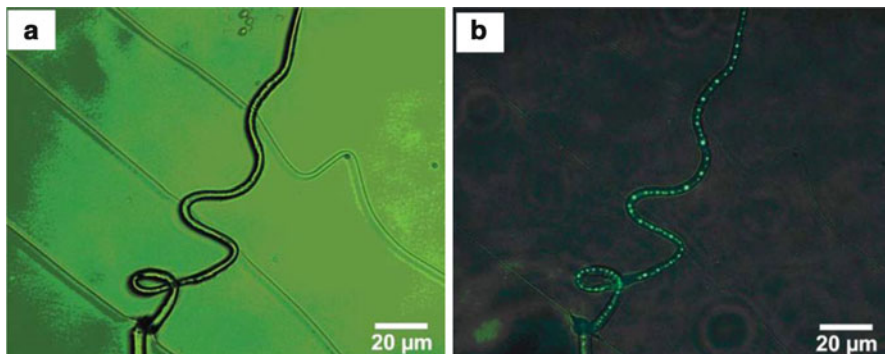
Fig. 6.2 Microscope image (**a**) and corresponding fluorescence micrograph (**b**) of core-shell fibers embedding GFP in the core (Adapted from [22], Copyright © 2007, with permission of The Royal Society of Chemistry)

gap structure can be finely controlled by chemical synthesis, a property that has opened interesting scenarios for the realization of flexible systems with emission from the UV to the near-infrared. Other properties of conjugated polymers include high emission efficiency and large stimulated emission cross sections, and the possibility to be processed by solution-based approaches [24]. The literature is rich of examples developed for ES of light-emitting conjugated polymers [3]. The main challenges arise from the frequently low molar mass, significant chain rigidity and limited solubility of these polymers, which have stimulated the development of specific ES methodologies. Similarly to QDs and organic chromophores, conjugated polymers can be blended with optically-transparent matrices such as PMMA and PS, which can easily form fibers by ES. Figure 6.3a shows an example of electrospun fibers made by a blend of PMMA and poly(9,9-dioctylfluoreny-2,7-diyl) (PFO) [25], a blue-emitting conjugated polymer. The fibers display bright and uniform fluorescence along their length, and phase separation between the two polymer components, as evidenced by high resolution transmission electron microscopy. Instead, pristine conjugated polymer nanofibers can be obtained by using mixtures of different solvents (Fig. 6.3b) for the ES solution [26, 27]. In particular adding of a non solvent such as dimethyl sulfoxide (DMSO), which is less volatile and displays improved electrical properties with respect to the solvents typically used for conjugated polymers (such as chloroform, toluene, tetrahydrofuran) is effective for obtaining pristine conjugated polymer fibers.

Recently, blue-emitting fibers with mean diameters as low as 180 nm [28] have been realized by ES, with a solution of a conjugated polymer dissolved in a good solvent (chloroform) and the addition of organic salts (Fig. 6.4). The spectroscopic investigation of the optical properties of the resulting fibers evidences that the presence of the organic salt does not significantly alter the emission properties (emission wavelength, efficiency and characteristic decay times) of the used conjugated polymer.
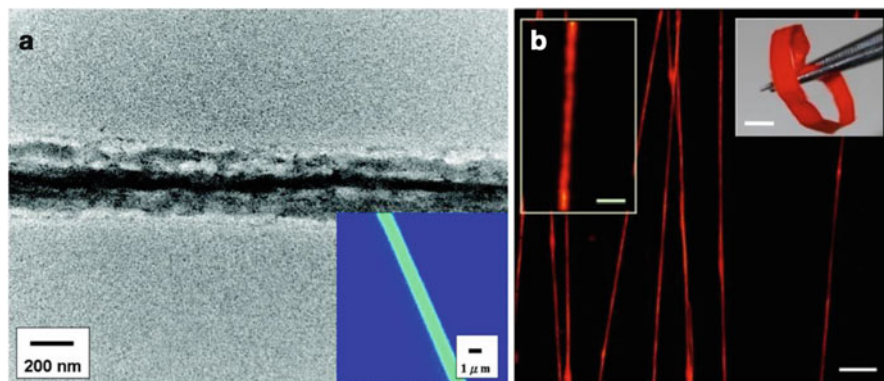
Fig. 6.3 (**a**) Transmission electron microscopy image of a PMMA/PFO electrospun fiber. *Inset*: confocal fluorescence microscopy image of the PMMA/PFO fiber. *Scale bar*: 1 μm. PMMA:PFO weight ratio 2:1 (Adapted with permission from [25]. Copyright © 2007 American Chemical Society). (**b**) Confocal fluorescence microscopy image of pristine poly[2-methoxy-5-(2-ethylhexyl-oxy)-1,4-phenylene-vinylene] (MEH-PPV) electrospun nanofibers. *Scale bar*: 10 μm. *Left inset*: fluorescence image of an individual nanofiber. *Scale bar*: 2 μm. *Right inset*: photograph of a MEH-PPV nanofiber mat realized by a rotating collector. *Scale bar*: 4 mm (Adapted with permission from [27]. Copyright © 2013 American Chemical Society)

Finally, it is worth mentioning an approach that, similarly to the one used for the inclusion of GFP in polymer fibers, exploits co-electrospinning to obtain fibers made by conjugated polymers [29]. In this case core shell structures are electrospun by using a PVP solution as the shell and a solution of conjugated polymers as the core. Pristine fibers of conjugated polymers are than realized by dissolving the PVP shell layer by ethanol extraction.

6.2.4 Luminescent Nanofiber Arrays

An important issue when dealing with luminescent fibers is represented by the capability of producing ordered macroscopic arrays. This is becoming increasingly relevant, since most of the emerging applications of electrospun nanofibers, including optical sensing (see Sect. 6.5), need a precise control of both the fiber morphology (in particular the diameter uniformity) and of the fiber positioning, essential in order to connect the active fiber element to excitation sources and detectors. An elegant approach developed for the control of fiber positioning and for realizing ordered arrays exploits a patterned metallic system as collector [30, 31]. The simplest patterned collector is composed by two parallel metallic stripes, a system which allows for collecting nanofibers uniaxially aligned perpendicularly to the metallic stripes. More complex geometries have been also demonstrated, by a proper design of the metal-covered regions of the collector [31].
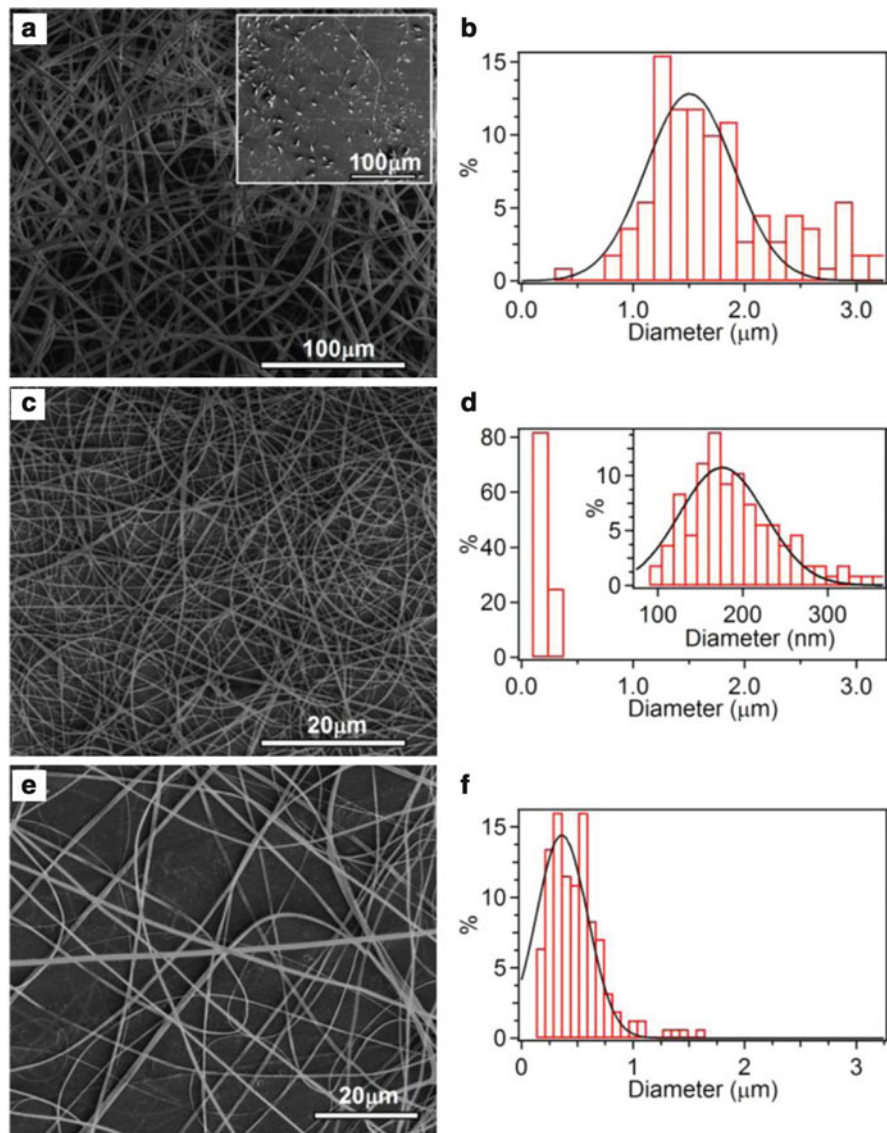
Fig. 6.4 Analysis of the size distribution of electrospun conjugated polymer nanofibers by scanning electron microscopy (SEM). (**a**)–(**b**) SEM image and corresponding fiber diameter distribution of nanofibers made of poly[(9,9-dioctylfluorenyl-2,7-diyl)-co-(N,N′-diphenyl)-N, N′di(p-butyl-oxy-phenyl)-1,4-diaminobenzene)] (PFO-PBAB) dissolved in a THF:DMSO mixture. *Scale bar*: 100 μm. In the *inset* a SEM image of PFO-PBAB fibers obtained by using a single solvent (CHCl₃) is shown. *Scale bar* = 100 μm. SEM micrographs, (**c**) and (**e**), and fiber diameter distribution, (**d**) and (**f**), of PFO-PBAB nanofibers produced by dissolving the conjugated polymer in CHCl₃ with the addition of tetrabutylammonium iodide and tetrabutylammonium bromide, respectively. *Scale bar* = 20 μm. *Continuous lines* in (**b**), (**d**) and (**f**) are Gaussian fits to the data (Reprinted with permission from [28]. Copyright 2013 American Chemical Society)
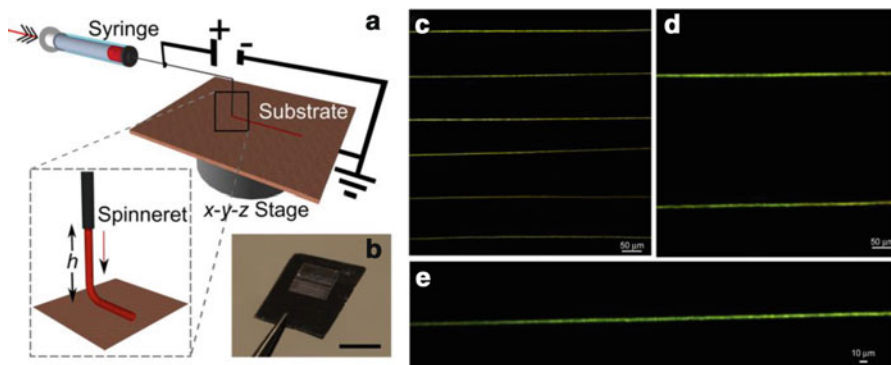
Fig. 6.5 (**a**) Scheme of the NF-ES set-up used for the controlled deposition of light-emitting nanofibers. $h = 500$ μm. (**b**) Photograph of an array of nanofibers made by a blend of PEO and MEH-PPV. *Scale bar*: 5 mm. (**c**)–(**e**) Confocal fluorescence microscopy images of parallel nanofibers made by MEH-PPV, deposited by NF-ES. *Scale bars*: (**c**)–(**d**) 50 μm, (**e**) 10 μm (Adapted with permission from [36]. Published by The Royal Society of Chemistry)

The main drawback of the ES process for obtaining ordered arrays of nanofibers are the instabilities that characterize the jet propagation from the needle to the collector. Recently, near-field electrospinning (NF-ES) [32] has emerged has an alternative approach for precise positioning of individual nanofibers and for realizing arrays of nanofibers with almost arbitrary geometries [33]. This method exploits the stable region of the ES jet, by positioning the substrate few mm or less far from the needle, before the onset of the jet instabilities. This allows one to precisely deposit individual nanofibers and to realize arrays of ordered nanofibers by moving the substrate in a plane perpendicular to the jet propagation axis [32, 34]. The technique has been applied to different materials such as PEO, polyvinylidene fluoride, polycaprolactone, TiO_2, SnO_2 [35] and also to light-emitting conjugated polymers [36]. Arrays of parallel and crossed luminescent fibers composed by a blend of PEO and poly[2-methoxy-5-(2-ethylhexyloxy)-1,4-phenylenevinylene] (MEH-PPV) have been deposited on Si/SiO$_2$ substrate with micrometric spatial resolution (Fig. 6.5).

6.3 Emission Properties of Electrospun Nanofibers

The study of the emission properties of electrospun nanofibers and the comparison with bulk and thin film properties is especially relevant for the development of new applications. Most of organics used for the fabrication of light-emitting nanofibers display emission properties which are very sensitive to the local microenvironment and to the resulting conformation of molecules [37]. In fact, the photo-physics of organic molecules and polymers in solution is rich of examples of changes of the spectral properties (peak wavelength shifts, increase or decrease of the emission efficiency and of the radiative rates, etc.) induced by the specific used solvents

[38]. When dealing with solid-state samples such effects are complicated by the influence of the processing conditions, which may induce particular conformations in molecules and polymers [39]. In ES, such conditions are especially related to the strength of the applied electric field, the used solvents, and the ambient humidity.

6.3.1 Spectral Properties of Photoluminescence of Electrospun Fibers

Figure 6.6 shows a comparison between the absorption and photoluminescence spectra of electrospun nanofibers and spincast films made of poly [(9,9-dioctylfluorenyl-2,7-diyl)-co-(1,4-benzo-{2,10-3}-thiadiazole)] (F8BT), which is a conjugated polymer with emission at about 570 nm [40]. The main difference between films and fibers is the blue-shift of the emission, by 10 nm. Similar shifts of the photoluminescence peak wavelengths of nanofibers compared to reference films have been reported also for other conjugated polymers and
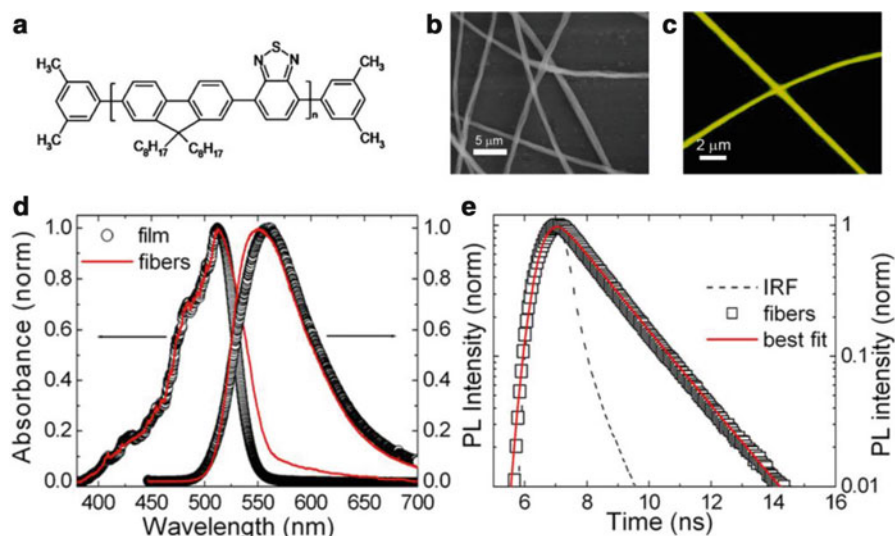
Fig. 6.6 (**a**) Chemical structure of the poly[(9,9-dioctylfluorenyl-2,7-diyl)-co-(1,4-benzo-{2,10-3}-thiadiazole)] conjugated polymer. SEM (**b**) and confocal microscopy (**c**) images of F8BT electrospun fibers. (**d**) Normalized absorbance (*left vertical scale*) and photoluminescence (*right vertical scale*) spectra of F8BT fibers (*red continuous lines*) and films (*black open symbols*). (**e**) Photoluminescence time decay of F8BT fibers (*black open symbols*). The *red continuous line* is a best fit to the data by an exponential function convoluted with the Instrumental Response Function (IRF, *dashed line*) (Adapted with permission from [40]. Copyright © 2013, AIP Publishing LLC) (color figure online)

chromophores [29, 41, 42], both toward lower energies (red-shift) and toward higher energies (blue-shift). It is worth mentioning that the variety of data available in literature is also influenced by scattering and self-absorption effects, which may cause broadening of the absorption and emission spectra as well as red-shifts of photoluminescence, that are not related to the intrinsic optical transitions of the used materials [43]. Therefore, special care must be paid to the optical characterization of absorption and emission properties of electrospun nanofibers. Approaches include, for instance, the use of an integrating sphere which may reduce the contribution of scattering and waveguiding [44], and of thin samples in order to keep the self-absorption contribution as low as possible [41, 43]. In general, the observed emission shifts can be rationalized by considering conjugated polymer molecules as multi-chromophore systems, because the presence of twists and kinks along the polymer chain breaks the conjugation length and form an ensemble of conformational sub-units, which emit light [45]. Absorption of light excites this ensemble of chromophores, and energy transfer mechanisms funnel the excitation toward sub-units at lower energy (exciton migration), which determine the wavelength and shape of the ultimate photoluminescence spectrum [45]. Such energy transfer may be affected by the peculiar conformation of macromolecules in the fibers, induced as a consequence of the high stretching rate of the polymer jet in typical ES processes [46]. As shown in the following Paragraph 6.3.3, the ES process can induce an alignment of the polymer molecules along the fiber axis. This configuration, depending on the structure of the chain of the used polymer, can enhance or decrease the electronic energy transfer toward lower energy emissive subunits [47]. Other effects that influence the emission spectra of fibers compared to films are the generally reduced chain aggregation and increased conjugation length [29].

6.3.2 Emission Quantum Yield and Lifetime

For some applications in photonics and for optical sensing based on fluorescent systems, the control of the photoluminescence quantum yield (PLQY) is a crucial issue. Typically QDs, low molar mass organic molecules, and conjugated polymers can show very high PLQY in solution, whereas their inclusion in solid-state systems can adversely affect the yield by activating nonradiative channels through bulk and surface defects and related trap states [8, 48]. Given the peculiar processing conditions of the ES process [46], the measurement of the PLQY of polymer electrospun nanofibers is relevant for determining the optimal parameters allowing to preserve or enhance the number of emitted photons. Few reports have investigated this issue in depth [25, 40, 49], demonstrating that PLQY can be significantly enhanced in electrospun nanofibers compared to other solid state systems, such as thin films. Kuo and co-workers [25] have measured the PLQY for electrospun nanofibers made by PMMA, blended with different conjugated polymers, finding an increase up to a factor 3 for poly[2,7-(9,9-dihexylfluorene)-alt-5,8-quinoxaline] compared to spin-coated films. G. Morello et al. [40] have reported an increase of

the PLQY of about 50 % in electrospun fibers of pristine F8BT compared to thin films. The concomitant measure of the PLQY and of the photoluminescence lifetime allows also to determine to what extent the radiative and nonradiative lifetimes are influenced by the ES process. A typical time-resolved photoluminescence decay profile for pristine F8BT electrospun fibers is shown in Fig. 6.6e. The decays typically follow an exponential trend, with a characteristic lifetime, τ_{PL}, that is related to the intrinsic radiative (τ_r) and nonradiative (τ_{nr}) lifetimes:

$$\frac{1}{\tau_{PL}} = \frac{1}{\tau_r} + \frac{1}{\tau_{nr}} \tag{6.1}$$

Given the PLQY, $\Phi = \frac{\tau_{PL}}{\tau_r}$, the measurement of Φ and τ_{PL} allows the radiative and nonradiative lifetimes to be determined. Interestingly, this analysis has evidenced an increase of the radiative rate by 22.5 % in F8BT electrospun fibers compared to spin-coated films. Therefore, ES provides a method for producing solid state photoluminescent structures, featuring enhanced emission efficiency.

6.3.3 Polarization of the Emission

Many reports have evidenced that the strong stretching forces that characterize the ES process may induce orientation of the polymer chains along the fiber axis [50] and generate a complex internal nanostructure [27, 51]. These peculiar characteristics of the ES process compared to other fabrication methods (spincoating, casting) are also responsible of interesting anisotropic optical properties observed in electrospun nanofibers. In particular, when dealing with electrospun nanofibers containing conjugated polymers as the optically-active component, polarized emission is often observed (Fig. 6.7a). In conjugated polymers the emission dipole transitions are mostly aligned along the polymer chain and, therefore, the chain alignment in the electrospun fibers produce an overall photoluminescence polarized along the fiber length [42, 52, 53].

Polarized emission has been observed both in ensemble of macroscopically aligned electrospun fibers and in individual fibers, with a polarization ratio (the ratio between the intensity of the photoluminescence with polarization parallel and perpendicular to the long fiber axis) in the range 2–5 [15, 52, 53]. Post-processing mechanical stretching has been demonstrated to increase the polarization ratio, up to values around 25 [42].

The microscopic alignment of polymer chains in electrospun fibers has been studied by different methods, including small-area electron diffraction, infrared, and Raman spectroscopies [50, 53].

Transmission electron microscopy of nanofibers made by PMMA and poly {[9,9-di(3,30-N,N0-trimethylammonium) propylfluorenyl-2,7-diyl]-alt-(9,9
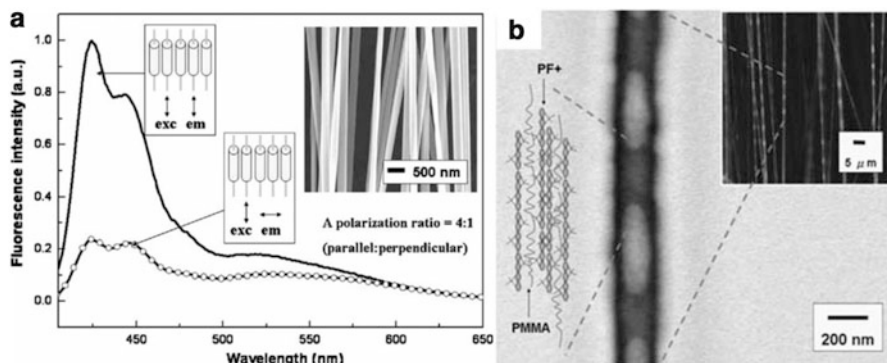
Fig. 6.7 (**a**) Polarized photoluminescence spectra of uniaxially aligned fibers made by blending PMMA and the poly{[9,9-di(3,30-N,N0-trimethylammonium) propylfluorenyl-2,7-diyl]-alt-(9,9-dioctylfluorenyl-2,7-diyl)} diiodide salt (PF$^+$). Fibers are excited with a polarization parallel to the fiber axis, whereas emission is collected with polarization either parallel (*continuous line*) or perpendicular (*open circles*) to the fiber axis. *Inset*: SEM image of uniaxially aligned PMMA/PF$^+$ fibers. *Scale bar*: 500 nm. (**b**) Transmission electron microscopy image of an individual electrospun fiber made of PMMA/PF$^+$. *Inset*: laser confocal microscopy image of the PMMA/PF$^+$ electrospun fibers. *Scale bar*: 5 μm (Adapted with permission from [52], Copyright © 2008 of WILEY-VCH Verlag GmbH & Co. KGaA)

dioctylfluorenyl-2,7-diyl)} diiodide salt (PF$^+$) has evidenced the formation of nanoscale domains composed by the active conjugated polymer, with well aligned polymer chains (Fig. 6.7b) [52].

A recent study [53] has made use of polarized micro-Raman spectroscopy to investigate the degree of chain alignment in pristine F8BT electrospun nanofibers made by using different solvents (Fig. 6.8). In particular, fibers made by either tetrahydrofuran (THF, good solvent for F8BT) solutions or mixtures of THF and a non solvent (DMSO) have been investigated and compared. The fibers made by THF feature a higher degree of polymer chain alignment, even though they are often not continuous but show the presence of beads with a linear density around 10 mm^{-1}. Interestingly, fibers made by THF display an increase of polarization ratio of about a factor two compared to fibers made by the solvent mixture.

6.4 Optical Sensing by Modulating Emission Intensity

The availability of various fluorescent electrospun nanofibers shown above, with emission properties in many cases improved compared to thin films and increased surface area, is stimulating a lot of research for the development of high-performance optical sensors [54]. Optical sensors are generally preferred for their high sensitivity, fast response time and low power consumption [55]. The most of reported optical sensing systems are based on the analyte-induced quenching of the
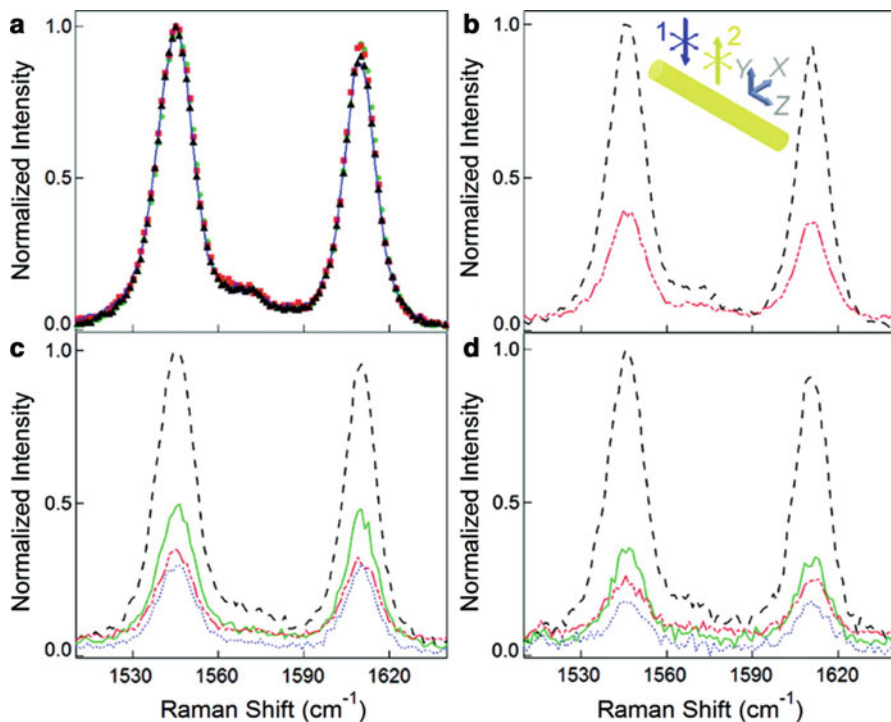
Fig. 6.8 Micro-Raman analysis of individual F8BT electrospun nanofibers. (**a**) Examples of normalized Raman scattering spectra of fibers made by using THF (*circles*) and THF/DMSO (*squares*) solvents, and of the corresponding reference films (*solid line* and *triangles*), respectively. (**b**) Polarized Raman spectra of F8BT films, measured in the Z|Z (*dashed line*) and Z|X (*dashed-dotted line*) configurations. Here the notation "incident polarization|analyzed polarization" is used. *Inset*: schematic representation of the experimental geometry. X, direction perpendicular to the fiber axis in the sample plane; Y, propagation direction of incident laser light (*arrow 1*) and of backscattered light (*arrow 2*); Z, fiber axis. (**c–d**) Polarized Raman spectra from individual F8BT fibers obtained by using THF/DMSO (**c**) and THF (**d**) measured in the Z|Z (*dashed lines*), Z|X (*solid lines*), X|Z (*dashed-dotted lines*), and X|X (*dotted lines*) configurations (Reprinted with permission from [53]. Copyright © 2011, American Chemical Society)

fluorescence of electrospun nanofibers, an effect that may be induced either by energy or electron transfer between the fluorescent molecules and the detected element [2]. As reviewed in the following, this approach has been mainly applied to metal ions, explosive molecules and bio-molecules, with remarkable results in terms of detection limit and time response.

6.4.1 Metal Ions

The sensing and detection of cations, in particular of heavy metals, is extremely important for the enormous potential impact on environmental and health-related issues. These ions can strongly quench the emission of conjugated compounds, providing an efficient mechanism for optical detection [2, 56–59]. To this aim, mats of electrospun fibers doped with fluorescent compounds, such as pyrene [2] and 1,4-dihydroxyanthraquinone [56], have been exposed to metal ions.

An elegant approach has been reported recently [57], developing methods for the synthesis of ultra-small amounts of products (down to 10^{-21} mol, zeptomol volumes) in the junctions of crossed polymer nanofibers [60]. Crossed electrospun fibers containing the different reagents for the synthesis of fluorescent molecules are deposited on a substrate, in a configuration that enables the synthesis of the active chromophores only at the nanofiber junctions which have typical volumes of the order of attoliters (Fig. 6.9a–c). In particular, the use of reagents for the synthesis of fluorophore-polyamines, whose fluorescence is quenched upon binding of metal ions, has been exploited for the realization of an array of nanoscale sensors [57]. Optical sensing of a benchmark of ten metal ions (Al^{3+}, Fe^{3+}, Co^{2+}, Ni^{2+}, Cu^{2+}, Zn^{2+}, Hg^{2+}, Cd^{2+}, Ca^{2+}, Mg^{2+}) has been reported by this approach, with a detection limit down to 2.0 ppm for Co^{2+} in water (pH 5).

Such approach is also very powerful due to its reversibility (up to four cycles demonstrated) and allows one to synthesize fluorophores with different emission wavelength in the same mat, for parallel processing of multi-analytes. Moreover, such mats exhibit good mechanical strength and are suitable for the deposition of the sensor on a nitrile glove (Fig. 6.9d–g).

F. J. Orriach-Fernández et al. have recently developed a highly selective optical sensor for Hg^{2+} in water [58]. Their system relies on electrospun nonwoven mats doped with a spirocyclic phenylthiosemicarbazide Rhodamine 6G derivative (FC1), showing a turn-on of fluorescence in presence of Hg^{2+} ions. The realized nanofiber optical sensor exhibit response time and detection limit improved compared to solid state films.

6.4.2 Explosive Compounds

Another issue in the field of optical sensing is the detection of explosive compounds [61]. In this case, sensing should possibly occur without contact with the explosive, most of which are very sensitive to friction, impact and shock.

Optical detection of explosive compounds exploits the quenching of the emission of fluorescent conjugated systems, induced by the interaction with the explosive molecule [62]. Similarly to metal cations, nitroaromatic and similar explosive compounds are electron-deficient systems, thus inducing quenching through photo-
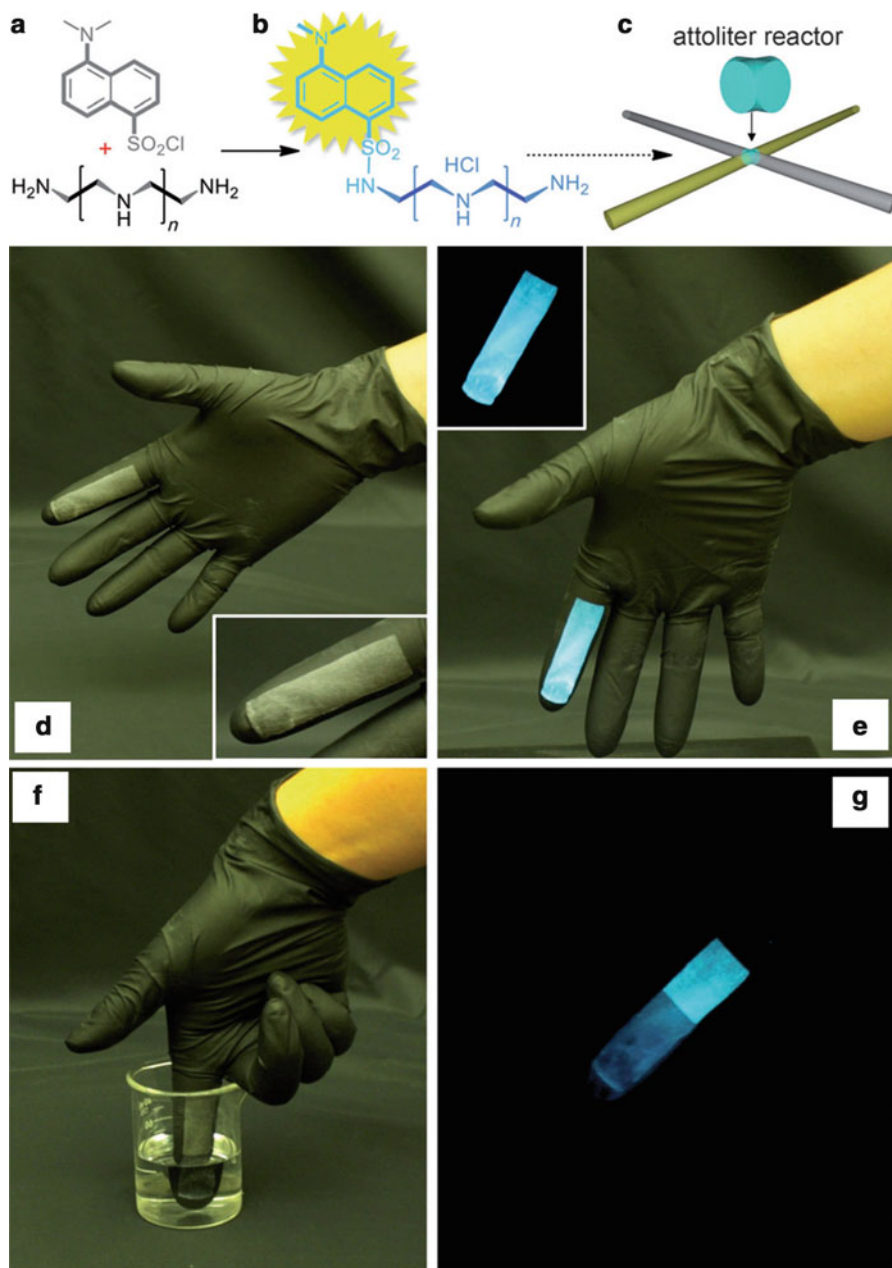
Fig. 6.9 (**a**)–(**c**) Schematic representation of the operational principle of the attoliter reactor. The reactor is realized in the overlap volume of two crossed electrospun fibers, each embedding a different reagent, such as dansyl chloride and polyamine (**a**), to produce fluorescent products (**b**) in the fiber junctions (**c**). (**d**)–(**g**) Example of a wearable sensor made of an attoliter reactor mat. (**d**) Fiber mat deposited through a shadow mask on a glove. (**e**) Image of fiber fluorescence excited at 365 nm. (**f**) Exposure of the wearable fiber sensor to a solution of Co^{2+} ions. (**g**) Photograph of the fiber fluorescence upon UV excitation after exposure to Co^{2+} ions, evidencing the fiber emission quenching in the region exposed to the metal ions (Adapted with permission from [57]. Copyright © 2012 of WILEY-VCH Verlag GmbH & Co. KGaA)

induced electron transfer from the excited state of the conjugated systems to the lowest unoccupied molecular orbital of the explosive molecules [2, 63].

Different reports have demonstrated the potentialities of using electrospun nanofibers doped with conjugated small molecules and polymers [64–66], leading to improved sensing performances compared to thin films. In particular, Y. Long et al. [64] have developed a reversible sensor based on PS electrospun nanofibers doped with a conjugated polymer, whose photoluminescence intensity is efficiently quenched by 2,4-dinitrotoluene (2,4-DNT), and recovered after immersion in ammonia for 20 min. After 5 cycles of quenching/regeneration, a loss of 25 % of the fluorescence intensity has been observed.

An interesting low cost system based on fluorescent electrospun nanofibers has been proposed by Y. Wang and co-workers [63]. In this work the sensing element is composed by a mat of electrospun fibers (thickness 1–15 μm) made by PS doped with pyrene, an organic molecule showing bright cyan emission upon UV excitation. The nanofibers have been electrospun by adding an organic salt (tetrabutylammonium hexafluorophosphate, TBAH) to the solution, in order to obtain fibers with uniform diameters of (120 ± 20) nm. For optical sensing the use of thin fibers is especially useful, since studies on films of conjugated polymers exposed to 2,4,6-trinitrotoluene (TNT) have evidenced that fluorescence quenching occurs within the first few tens of nm, hence films with thickness >25 nm have shown a drop of the fluorescence quenching, probably related to the limited TNT diffusion [67]. The emission of the pyrene/PS nanofibers is characterized by two main bands. The band in the range 370–400 nm has been attributed to the singlet exciton emission, whereas another, broad band at about 470 nm has been attributed to the excimer emission due to possible π-π stacking. When fibers are exposed to equilibrium vapors (about 193 ppb) of 2,4-DNT, a 90 % quenching of the emission is achieved within 6 min, with a minimal dependence on the mat thickness. Interestingly, this system can detect other nitroaromatic compounds (for instance 2,6-DNT and 1,2-dinitrobenzene), as well as non saturated vapors of nitramines and nitrate esters. The authors have also demonstrated the possibility to detect buried 2,4-DNT (Fig. 6.10a–d) in an open environment, and explosive particulate contaminated handprint through direct contact (Fig. 6.10e). Overall, the sensing performances of this simple and low-cost detection system are attributed to an amplification of the quenching mechanism, due to the particular conformation of the pyrene molecule and the PS phenyl pendants, allowing long range exciton migration [63].

6.4.3 Optical Biosensing

A biosensor can be defined as a device for the detection of analytes, combining a biological recognition system with a physicochemical detecting component. Enhanced biosensors have been developed using ES and incorporating a biological or biomimetic sensing element [54]. Moreover, the optical detection in biosensors
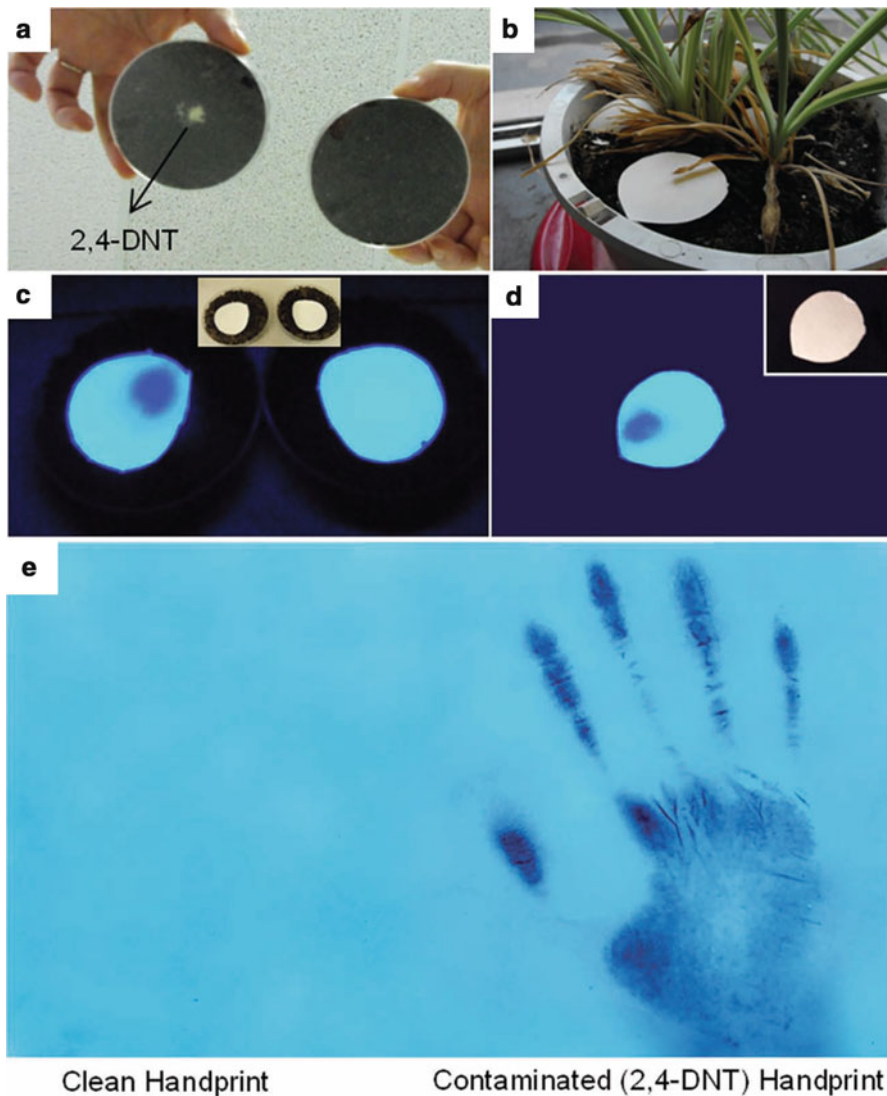
Fig. 6.10 (**a**)–(**d**) Above-ground detection of buried 2,4-DNT using electrospun pyrene-doped PS mats. (**a**)–(**b**) Images of soil with (*left*) and without (*right*) buried 2,4-DNT in Petri dishes (**a**) and of soil with buried DNT in a flower pot (**b**), respectively. (**c**) Image of the fluorescence of the sensing system after 30 min exposure to buried DNT, highlighting emission quenching due to the leaked explosive molecules from the buried sample. The fluorescence is excited by UV light with $\lambda = 275$ nm. (**d**) Image obtained from the pyrene-doped PS nanofiber sensing sample on 2,4-DNT buried in the flower pot (**b**) after 30 min exposure. *Insets* in (**c**) and (**d**) are the bright-field images of the nanofiber samples after exposure. (**e**) Example of detection of explosive-contaminated hand using the electrospun pyrene-doped PS nanofiber samples. The image shows the UV-excited fluorescence of a pyrene/PS mat, after the contact with a clean (*left*) and contaminated (*right*) handprint, respectively (Reprinted with permission from [63]. Copyright © 2012 of WILEY-VCH Verlag GmbH & Co. KGaA)

may offer different advantages including enhanced and fast response, immunity of the signal to electrical or magnetic interference and potential for higher information integration and processing [68]. In the following, some examples of biosensors based on electrospun nanofibers are presented.

C. Zhou et al. [69] have proposed a nanofiber optical biosensor for glucose. A transition metal complex, iridium(III) bis(2-phenylbenzothiozolato-N,C$^{2\prime}$) acetylacetonate, whose emission is efficiently quenched by oxygen, has been embedded as fluorescent probe in mats of randomly oriented electrospun PS nanofibers, which are functionalized with glucose oxidases (GOD) (Fig. 6.11a). When glucose is added to the solution, the oxygen present in the PS fibers is consumed more efficiently than the oxygen dissolved out of the fibrous mat, because of the fiber surface functionalization with GOD (Fig. 6.11a). The decrease of the oxygen content in the fibers produces an increase of Ir complex fluorescence (Fig. 6.11b–c), with a response time of about 1 s. The nanofiber mats feature about 70 % increase of photoluminescence intensity, much higher than the values measured in reference thin-films (about 15 %) (Fig. 6.11b–c). The increase of photoluminescence intensity is directly related to the concentration of glucose, as shown in Fig. 6.11d, and the developed system features a detection limit as low as 1.0×10^{-10} M [69].

Core-shell nanofibers embedding GFP have been used for optical detection of urea [22]. Immersion of a mat of these nanofibers in a solution containing urea leads to a decrease of the GFP photoluminescence intensity, which is reversibly recovered upon immersion of the nanofiber sensing mat in water. This reversible change in presence of a denaturing agent is due to the switching properties of the GFP between native and denatured conformations.

Solid-state optical biosensors based on electrospun fluorescent fibers have been also developed for the detection of proteins. B. W. Davis et al. [70] have realized cellulose acetate nanofibers by ES, which emit light at about 475 nm due to the inclusion of an anionic fluorescent dendrimer. Cytochrome c and hemoglobin have been detected in solution through the decrease of the dendrimer emission intensity, whereas bovine serum albumin induces an increase of the photoluminescence intensity. This different response of the fluorescent fiber sensor to proteins has been attributed to the interaction of proteins with the fluorophores, occurring primarily by energy transfer, even though electron transfer has not been ruled out. In particular, the quenching of the emission is suggested to be a consequence of a static adsorption of proteins to the dendrimer molecules [71]. Interestingly, sensing performances have been improved by creating evenly distributed secondary pores through the backbone of the nanofibers, utilizing a deacetylation treatment [72]. The authors demonstrated also the reusability of the nanofiber sensor, with a decrease of the fluorescence intensity of 15 % over 5 sensing cycles.

Other examples of optical biosensors based on fluorescent nanofibers include the detection of DNA plasmid by PFO-doped PMMA fibers [52], and of nucleic acids by DNA-functionalized gold nanoparticles on electrospun nanofibers [73].
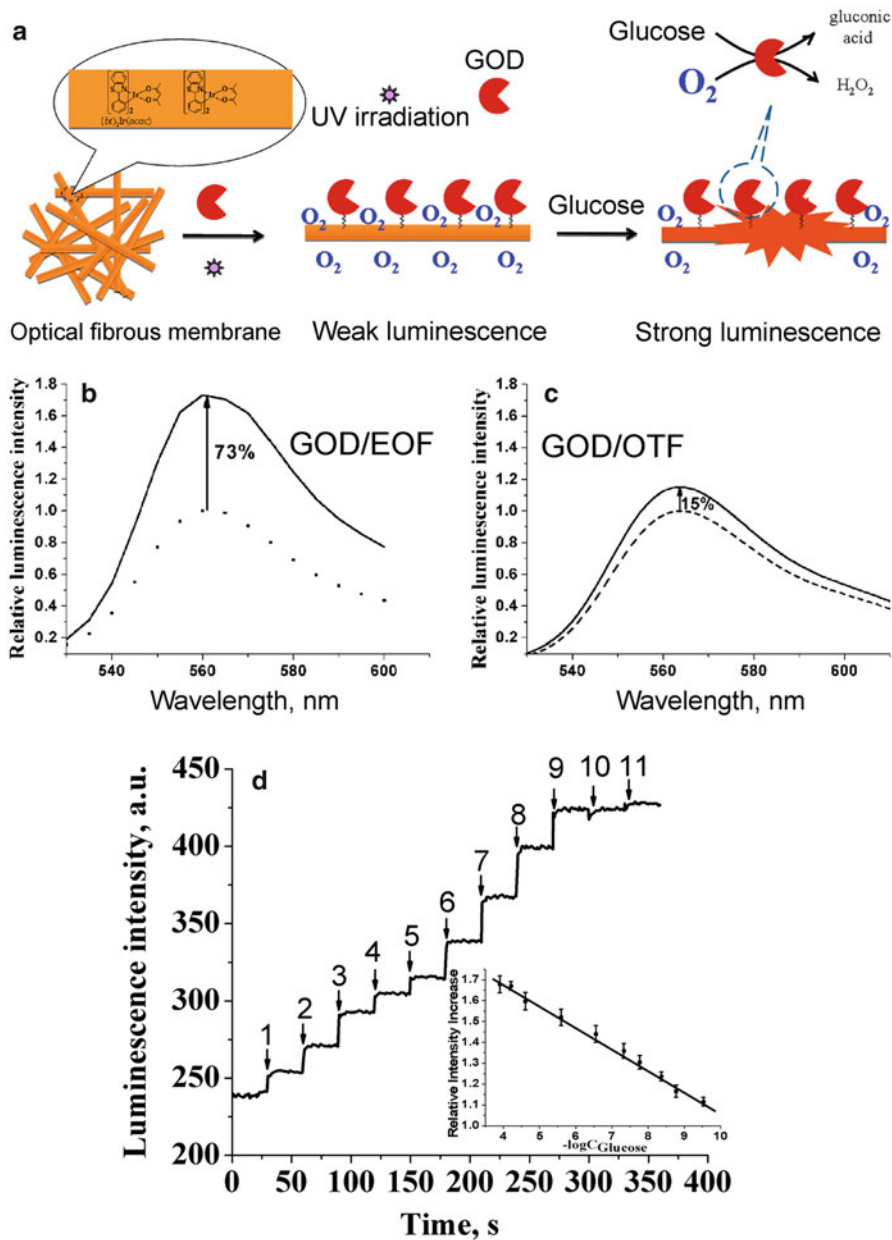
Fig. 6.11 (**a**) Schematics of the glucose sensor based on fluorescent electrospun nanofibers. (**b**)–(**c**) Comparison of the different sensing performance of the electrospun optical fibrous (EOF) membrane (**b**) and optical thin-film (OTF) (**c**) functionalized with GOD. The emission spectra of samples soaked in PBS buffer solution with (*solid line*) or without (*dotted line*) 1.0 mM glucose are shown. (**d**) Typical response curves of the GOD/EOF sensing membrane to various glucose solutions in PBS buffer (pH 7). Glucose concentration: (1): 3×10^{-10} M; (2): 1.7×10^{-9} M; (3): 4.4×10^{-9} M; (4): 1.7×10^{-8} M; (5): 4.8×10^{-8} M; (6): 2.8×10^{-7} M; (7): 2.6×10^{-6} M; (8): 2.5×10^{-5} M; (9): 6.2×10^{-5} M; (10): 1.3×10^{-4} M; (11): 2.6×10^{-4} M. *Inset*: plot of the relative fluorescence intensity increase *vs.* the logarithm of the glucose concentration ($C_{Glucose}$) (Adapted with permission from [69]. Copyright © 2012, American Chemical Society)

6.5 Other Optical Sensing Mechanisms: Waveguiding

An optical waveguide is essentially a microscale elongated material (known as the fiber *core*) able to guide and trap light by total internal reflection, provided by the refractive index contrast between the core and the surrounding material. Light can be confined and guided in a polymer nanofiber (with refractive index n_f) surrounded by a medium with refractive index $n_m < n_f$ (for example air or water), because of the internal reflections occurring at the interface between the polymer and the surrounding medium. Among the different applications of electrospun fibers, waveguiding has been extensively studied in the last 5 years [3]. The refractive index of most of the polymers used for the production of electrospun fibers are >1.5, quite larger than air ($n = 1$) and water ($n = 1.33$), a condition that allows one to observe efficient waveguiding in suspended or immersed electrospun fibers. Waveguiding of light has also been found for fibers deposited on suitable substrates, i.e. on substrates having a refractive index typically lower than 1.5, such as quartz ($n = 1.46$) and magnesium fluoride ($n = 1.37$). In order to investigate optical waveguiding, nanofibers can be doped with fluorescent systems (typically organic chromophores or inorganic quantum dots), whose emission is excited by a tightly focused laser beam, as schematized in Fig. 6.12a [4, 28, 74]. Part of the fluorescence emitted by the active system embedded into the polymer fiber is coupled and waveguided along the fiber and diffused by the fiber tip, appearing as a bright
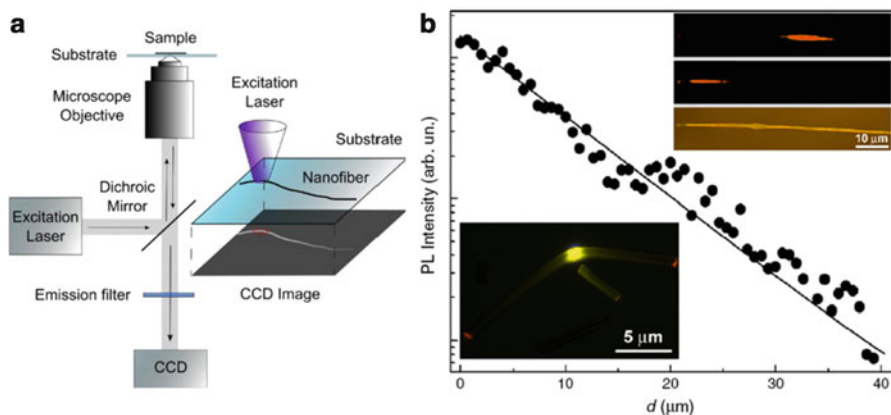
Fig. 6.12 (**a**) Schematics of the experimental setup used for the characterization of the waveguiding properties of individual electrospun fiber (Adapted with permission from [28]. Copyright © 2013, American Chemical Society). (**b**) Emission intensity guided inside a single polymer fiber *vs.* the distance, *d*, between the fiber tip and the exciting laser spot. The superimposed *continuous line* is the best fit of the data to an exponential decay. *Top-right inset*: bright-field micrograph of a single light-emitting fiber (*bottom image*) and corresponding fluorescence images evidencing the bright spots corresponding to the fiber tip and the excitation spot for $d = 50 \mu m$ (*middle image*) and 200 μm (*top image*), respectively. *Bottom-left inset*: Fluorescence micrograph of a fiber excited by a focused laser beam (Adapted from [74], Copyright © 2010, with permission from Elsevier)

spot in fluorescence images (inset of Fig. 6.12b). The measure of the intensity diffused by the fiber tip as a function of the distance, d, between the excitation spot and the tip, allows the waveguiding losses to be estimated.

Alternatively, waveguiding losses can be measured by the intensity of fluorescence emitted by the fiber surface, at variable distances from the excitation spot [28]. Such analysis is exemplified in Fig. 6.12b, for a PMMA fiber doped with Rhodamine 6G [74]. Typical fiber losses are in the range $10–10^3$ cm^{-1}, depending on the losses mechanisms. For electrospun nanofibers, the main losses effects are attributable to self-absorption, scattering and coupling of the guided light to the substrate. The former can be reduced by using polymers transparent at the wavelength of interest, whereas decreasing the scattering effects requires a precise control of the ES process in order to reduce instabilities of the polymer jets which can cause the formation of morphological defects, variation of polymer density and of fiber diameter, etc.. The choice of substrates with refractive index lower than that of electrospun fibers allows one to significantly reduce the losses associated to the partial coupling of the guided light into the substrate, as recently reported for conjugated polymer nanofibers [26](a).

The waveguiding of light with wavelength λ can occur in nanofibers having a diameter, d_f, larger than a cut-off value, d_c, which can be smaller than λ [75]. Therefore, waveguiding can also occur in fibers with sub-wavelength size. In this case a fraction of the injected light power couples in the surrounding medium as evanescent waves, having a sub-wavelength spatial extension and an intensity highly-sensitive to the variations of the local refractive indexes. For a cylindrical waveguide operating at a wavelength, λ, with diameter d_f, the fraction, p, of power confined in the nanofiber is given by [75]:

$$p = 1 - \left[\left(2.4 e^{-1/V} \right)^2 / V^3 \right], \tag{6.2}$$

where $V = \left(\pi d_f / \lambda \right) \sqrt{n_f^2 - n_m^2}$. A molecule at the fiber surface or diffusing into the fiber can therefore induce a variation of the local refractive index properties, in turn determining a change of the fraction of power confined in the fiber. In principle, this effect can be exploited for sensing applications, by monitoring the intensity of the guided light. The advantages of sub-wavelength nanofiber optical sensors rely basically on the high spatial resolution combined with high sensitivity and fast response time [76]. Moreover, compared to inorganic nanowires, polymer nanofibers inherit the advantages of polymer in terms of biocompatibility, permeability to small molecules and the possibility of hosting functional molecules, which can be exploited to selectively tailor the properties of the sensing component. This approach has been poorly investigated for electrospun nanofibers, even though their waveguiding properties are well established. Some examples of optical sensors have been reported for fibers which are physically drawn from solutions [76]. In particular, a humidity sensor allowing for real time monitoring of relative humidity with a time response faster than 90 ms has been realized by using a PS nanofiber doped with CdSe/ZnS core-shell QDs [76].

6.6   Conclusions and Perspectives

In summary, optically-active electrospun nanofibers constitute a novel class of nanomaterials with intriguing properties. Currently, fluorescent mats made of electrospun nanofibers can be realized by many approaches, which basically include doping with fluorescent QDs, organic π-conjugated molecules and bio-chromophores, or the use of conjugated polymers. In general, these nanofibers are characterized by enhanced optical properties compared to bulk system or thin films, and are also suitable for developing optical sensors for heavy metal ions, explosives, and biomolecules. The systems developed so far have demonstrated great potentialities in terms of detection limit, time response and associated low production costs. In many cases the developed devices are very simple, they do not need complex analytical systems and show performances comparable to other well established technologies.

More research efforts are needed to improve the sensor specificity and to assess interference issues with are typical of sensing components. In perspective, the improved control of fiber composition, morphology and optical properties can open new optical sensing paradigms and extend the number and typology of detected systems. The photophysics of electrospun nanofibers is rich of interesting phenomena, still poorly exploited, and may open new avenues in the growing field of optical sensing.

References

1. L. Persano, A. Camposeo, C. Tekmen, D. Pisignano. Industrial upscaling of electrospinning and applications of polymer nanofibers: a review. Macromol. Mater. Eng. **298**, 504–520 (2013)
2. X. Wang, C. Drew, S.-H. Lee, K.J. Senecal, J. Kumar, L.A. Samuelson, Electrospun nanofibrous membranes for highly sensitive optical sensors. Nano Lett. **2**, 1273–1275 (2002)
3. A. Camposeo, L. Persano, D. Pisignano, Light-emitting electrospun nanofibers for nanophotonics and optoelectronics. Macromol. Mater. Eng. **298**, 487–503 (2013)
4. H. Liu, J.B. Edel, L.M. Bellan, H.G. Craighead, Electrospun polymer nanofibers as subwavelength optical waveguides incorporating quantum dots. Small **2**, 495–499 (2006)
5. X. Lu, C. Wang, Y. Wei, One-dimensional composite nanomaterials: synthesis by electrospinning and their applications. Small **5**, 2349–2370 (2009)
6. S. Wei, J. Sampathi, Z. Guo, N. Anumandla, D. Rutman, A. Kucknoor, L. James, A. Wang, Nanoporous poly(methyl methacrylate)-quantum dots nanocomposite fibers toward biomedical applications. Polymer **52**, 5817–5829 (2011)
7. Y. Shirasaki, G.J. Supran, M.G. Bawendi, V. Bulović, Emergence of colloidal quantum-dot light-emitting technologies. Nat. Photonics. **7**, 13–23 (2013)

8. T. Vossmeyer, L. Katsikas, M. Giersig, I.G. Popovic, K. Diesner, A. Chemseddine, A. Eychmüller, H. Weller, CdS nanoclusters: synthesis, characterization, size dependent oscillator strength, temperature shift of the excitonic transition energy, and reversible absorbance shift. J. Phys. Chem. **98**, 7665–7673 (1994)

9. F. Di Benedetto, A. Camposeo, L. Persano, A.M. Laera, E. Piscopiello, R. Cingolani, L. Tapfer, D. Pisignano, Light-emitting nanocomposite CdS-polymer electrospun fibres via in situ nanoparticle generation. Nanoscale **3**, 4234–4239 (2011)

10. X. Lu, Y. Zhao, C. Wang, Fabrication of PbS nanoparticles in polymer-fiber matrices by electrospinning. Adv. Mater. **17**, 2485–2488 (2005)

11. L. Persano, A. Camposeo, F. Di Benedetto, R. Stabile, A.M. Laera, E. Piscopiello, L. Tapfer, D. Pisignano, CdS-polymer nanocomposites and light-emitting fibers by in situ electron-beam synthesis and lithography. Adv. Mater. **24**, 5320–5326 (2012)

12. L. Persano, S. Molle, S. Girardo, A.A.R. Neves, A. Camposeo, R. Stabile, R. Cingolani, D. Pisignano, Soft nanopatterning on light-emitting inorganic–organic composites. Adv. Funct. Mater. **18**, 2692–2698 (2008)

13. A. Camposeo, M. Polo, A.A.R. Neves, D. Fragouli, L. Persano, S. Molle, A.M. Laera, E. Piscopiello, V. Resta, A. Athanassiou, R. Cingolani, L. Tapfer, D. Pisignano, Multi-photon in situ synthesis and patterning of polymer-embedded nanocrystals. J. Mater. Chem. **22**, 9787–9793 (2012)

14. (a) A. Camposeo, F. Di Benedetto, R. Stabile, R. Cingolani, D. Pisignano, Electrospun dye-doped polymer nanofibers emitting in the near infrared. Appl. Phys. Lett. **90**, 143115 (2007); (b) Y. Ner, J.G. Grote, J.A. Stuart, G.A. Sotzing, Enhanced fluorescence in electrospun dye-doped DNA nanofibers. Soft Matter **4**, 1448–1453 (2008)

15. S. Pagliara, A. Camposeo, S. Polini, R. Cingolani, D. Pisignano, Electrospun light-emitting nanofibers as excitation source in microfluidic devices. Lab Chip **9**, 2851–2856 (2009)

16. A. Camposeo, F. Di Benedetto, R. Stabile, A.A.R. Neves, R. Cingolani, D. Pisignano, Laser emission from electrospun polymer nanofibers. Small **5**, 562–566 (2009)

17. A.J. Das, C. Lafargue, M. Lebental, J. Zyss, K.S. Narayan, Three-dimensional microlasers based on polymer fibers fabricated by electrospinning. Appl. Phys. Lett. **99**, 263303 (2011)

18. I. Cucchi, F. Spano, U. Giovanella, M. Catellani, A. Varesano, G. Calzaferri, C. Botta, Fluorescent electrospun nanofibers embedding dye-loaded zeolite crystals. Small **3**, 305–309 (2007)

19. J.S. Sparks, R.C. Schelly, W.L. Smith, M.P. Davis, D. Tchernov, V.A. Pieribone, D.F. Gruber, The covert world of fish biofluorescence: a phylogenetically widespread and phenotypically variable phenomenon. PLoS One **9**, e83259 (2014)

20. R.Y. Tsien, The green fluorescent protein. Annu. Rev. Biochem. **67**, 509–544 (1998)

21. R. Bizzarri, M. Serresi, S. Luin, F. Beltram, Green fluorescent protein based pH indicators for in vivo use: a review. Anal. Bioanal. Chem. **393**, 1107–1122 (2009)

22. A.L. Yarin, E. Zussman, J.H. Wendorff, A. Greiner, Material encapsulation and transport in core–shell micro/nanofibers, polymer and carbon nanotubes and micro/nanochannels. J. Mater. Chem. **17**, 2585–2599 (2012)

23. Y. Dror, W. Salalha, R. Avrahami, E. Zussman, A.L. Yarin, R. Dersch, A. Greiner, J.H. Wendorff, One-step production of polymeric microtubes by co-electrospinning. Small **3**, 1064–1073 (2007)

24. M.D. McGehee, A.J. Hegeer, Semiconducting (Conjugated) polymers as materials for solid-state lasers. Adv. Mater. **12**, 1655–1668 (2000)

25. C.-C. Kuo, C.-H. Lin, W.-C. Chen, Morphology and photophysical properties of light-emitting electrospun nanofibers prepared from poly(fluorene) derivative/PMMA blends. Macromolecules **40**, 6959–6966 (2007)

26. (a) F. Di Benedetto, A. Camposeo, S. Pagliara, E. Mele, L. Persano, R. Stabile, R. Cingolani, D. Pisignano, Patterning of light-emitting conjugated polymer nanofibres. Nat. Nanotechnol. **3**, 614–619 (2008); (b) W. Zhong, F. Li, L. Chen, Y. Chen, Y. Wei, A novel approach to electrospinning of pristine and aligned MEH-PPV using binary solvents. J. Mater. Chem. **22**, 5523–5530 (2012)

27. A. Camposeo, I. Greenfeld, F. Tantussi, S. Pagliara, M. Moffa, F. Fuso, M. Allegrini, E. Zussman, D. Pisignano, Local mechanical properties of electrospun fibers correlate to their internal nanostructure. Nano Lett. **13**, 5056–5062 (2013)
28. V. Fasano, A. Polini, G. Morello, M. Moffa, A. Camposeo, D. Pisignano, Bright light emission and waveguiding in conjugated polymer nanofibers electrospun from organic salt added solutions. Macromolecules **46**, 5935–5942 (2013)
29. D. Li, A. Babel, S.A. Jenekhe, Y. Xia, Nanofibers of conjugated polymers prepared by electrospinning with a two-capillary spinneret. Adv. Mater. **16**, 2062–2066 (2004)
30. D. Li, Y. Xia, Electrospinning of nanofibers: reinventing the wheel? Adv. Mater. **16**, 1151–1170 (2004)
31. D. Li, G. Ouyang, J.T. McCann, Y. Xia, Collecting electrospun nanofibers with patterned electrodes. Nano Lett. **5**, 913–916 (2005)
32. D. Sun, C. Chang, S. Li, L. Lin, Near-field electrospinning. Nano Lett. **6**, 839–842 (2006)
33. (a) G.S. Bisht, G. Canton, A. Mirsepassi, L. Kulinsky, S. Oh, D. Dunn-Rankin, M.J. Madou, Controlled continuous patterning of polymeric nanofibers on three-dimensional substrates using low-voltage near-field electrospinning. Nano Lett. **11**, 1831–1837 (2011); (b) H. Wang, G. Zheng, W. Li, X. Wang, D. Sun, Direct-writing organic three-dimensional nanofibrous structure. Appl. Phys. A **102**, 457–461 (2011)
34. C. Chang, K. Limkrailassiri, L. Lin, Continuous near-field electrospinning for large area deposition of orderly nanofiber patterns. Appl. Phys. Lett. **93**, 123111 (2008)
35. (a) C. Chang, Van H. Tran, J. Wang, Y.-K. Fuh, L. Lin, Direct-write piezoelectric polymeric nanogenerator with high energy conversion efficiency. Nano Lett. **10**, 726–731 (2010); (b) F.-L. Zhou, P.L. Hubbard, S.J. Eichhorn, G.J.M. Parker, Jet deposition in near-field electrospinning of patterned polycaprolactone and sugar-polycaprolactone core–shell fibres. Polymer **52**, 3603–3610 (2011); (c) Y. Zhang, X. He, J. Li, Z. Miao, F. Huang, Fabrication and ethanol-sensing properties of micro gas sensor based on electrospun SnO$_2$ nanofibers. Sens. Actuatators B-Chem. **132**, 67–73 (2008); (d) M. Rinaldo, F. Ruggieri, L. Lozzi, S. Santucci, Well-aligned TiO2 nanofibers grown by near-field-electrospinning. J. Vac. Sci. Technol. B **27**, 1829–1833 (2009)
36. D. Di Camillo, V. Fasano, F. Ruggieri, S. Santucci, L. Lozzi, A. Camposeo, D. Pisignano, Near-field electrospinning of light-emitting conjugated polymer nanofibers. Nanoscale **5**, 11637–11642 (2013)
37. J.C. Bolinger, M.C. Traub, J. Brazard, T. Adachi, P.F. Barbara, D.A. Vanden Bout, Conformation and energy transfer in single conjugated polymers. Acc. Chem. Res. **45**, 1992–2001 (2012)
38. (a) T.-Q. Nguyen, V. Doan, B.J. Schwartz, Conjugated polymer aggregates in solution: control of interchain interactions. J. Chem. Phys. **110**:4068–4078 (1999); (b) T.-Q. Nguyen, I.B. Martini, J. Liu, B.J. Schwartz, Controlling interchain interactions in conjugated polymers: the effects of chain morphologyon exciton-exciton annihilation and aggregation in MEH-PPV films. J. Phys. Chem. B **104**:237–255 (2000)
39. M. Richard-Lacroix, C. Pellerin, Molecular orientation in electrospun fibers: from mats to single fibers. Macromolecules **46**, 9473–9493 (2013)
40. G. Morello, A. Polini, S. Girardo, A. Camposeo, D. Pisignano, Enhanced emission efficiency in electrospun polyfluorene copolymer fibers. Appl. Phys. Lett. **102**, 211911 (2013)
41. S. Pagliara, A. Camposeo, R. Cingolani, D. Pisignano, Hierarchical assembly of light-emitting polymer nanofibers in helical morphologies. Appl. Phys. Lett. **95**, 263301 (2009)
42. M. Campoy-Quiles, Y. Ishii, H. Sakai, H. Murata, Highly polarized luminescence from aligned conjugated polymer electrospun nanofibers. Appl. Phys. Lett. **92**, 213305 (2008)
43. Y. Ishii, H. Murata, True photoluminescence spectra revealed in electrospun light-emitting single nanofibers. J. Mater. Chem. **22**, 4695–4703 (2012)
44. N.C. Greenham, I.D.W. Samuel, G.R. Hayes, R.T. Phillips, Y.A.R.R. Kessener, S.C. Moratti, A.B. Holmes, R.H. Friend, Measurement of absolute photoluminescence quantum efficiencies in conjugated polymers. Chem. Phys. Lett. **241**, 89–96 (1995)

45. I. Hwang, G.D. Scholes, Electronic energy transfer and quantum-coherence in π-conjugated polymers. Chem. Mater. **23**, 610–620 (2011)
46. D. Pisignano, *Polymer Nanofibers* (Royal Society of Chemistry, Cambridge, 2013), pp. 50–119
47. T.-Q. Nguyen, J. Wu, V. Doan, B.J. Schwartz, S.H. Tolbert, Control of energy transfer in oriented conjugated polymer-mesoporous silica composites. Science **288**, 652–656 (2000)
48. A.C.-A. Chen, J.U. Wallace, S.K.-H. Wei, L. Zeng, S.H. Chen, T.N. Blanton, Light-emitting organic materials with variable charge injection and transport properties. Chem. Mater. **18**, 204–213 (2006)
49. C.-C. Lee, S.-Y. Lai, W.-B. Su, H.-L. Chen, C.-L. Chung, J.-H. Chen, Relationship between the microstructure development and the photoluminescence efficiency of electrospun poly(9,9-dioctylfluorene-2,7-diyl) fibers. J. Phys. Chem. C **117**, 20387–20396 (2013)
50. (a) R. Dersch, T. Liu, A. K. Schaper, A. Greiner, J.H. Wendorff, Electrospun nanofibers: Internal structure and intrinsic orientation. J. Polym. Sci. Pol. Chem. **41**, 545–553 (2003); (b) L.M. Bellan, H. G. Craighead, Molecular orientation in individual electrospun nanofibers measured via polarized Raman spectroscopy. Polymer **49**, 3125–3129 (2008)
51. (a) A. Arinstein, E. Zussman, Postprocesses in tubular electrospun nanofibers. Phys. Rev. E **76**, 056303 (2007); (b) C.-L. Pai, M. C. Boyce, G.C. Rutledge, Morphology of porous and wrinkled fibers of polystyrene electrospun from dimethylformamide. Macromolecules **42**, 2102–2114 (2009); (c) U. Stachewicz, R.J. Bailey, W. Wang, A.H. Barber, Size dependent mechanical properties of electrospun polymer fibers from a composite structure. Polymer **53**, 5132–5137 (2012)
52. C.-C. Kuo, C.-T. Wang, W.-C. Chen, Highly-aligned electrospun luminescent nanofibers prepared from polyfluorene/PMMA blends: fabrication, morphology, photophysical properties and sensory applications. Macromol. Mater. Eng. **293**, 999–1008 (2008)
53. S. Pagliara, M.S. Vitiello, A. Camposeo, A. Polini, R. Cingolani, G. Scamarcio, D. Pisignano, Optical anisotropy in single light-emitting polymer nanofibers. J. Phys. Chem. C **115**, 20399–20405 (2011)
54. B. Ding, M. Wang, X. Wang, J. Yu, G. Sun, Electrospun nanomaterials for ultrasensitive sensors. Mater. Today **13**, 16–27 (2010)
55. (a) J.R. Askim, M. Mahmoudi, Kenneth S. Suslick, Optical sensor arrays for chemical sensing: the optoelectronic nose. Chem. Soc. Rev. **42**, 8649–8682 (2013); (b) X. Guo, Y. Ying, L. Tong, Photonic nanowires: from subwavelength waveguides to optical sensors. Acc. Chem. Res. **47**, 656–666 (2014)
56. M. Wang, G. Meng, Q. Huang, Y. Qian, Electrospun 1,4-DHAQ-doped cellulose nanofiber films for reusable fluorescence detection of trace Cu^{2+} and further for Cr^{3+}. Environ. Sci. Technol. **46**, 367–373 (2012)
57. P. Anzenbacher Jr., F. Li, M.A. Palacios, Toward wearable sensors: fluorescent attoreactor mats as optically encoded cross-reactive sensor arrays. Angew. Chem. **124**, 2395–2398 (2012)
58. F.J. Orriach-Fernández, A.L. Medina-Castillo, J.E. Díaz-Gómez, A. Muñoz de la Pena, J.F. Fernández-Sánchez, A. Fernández-Gutiérrez, A sensing microfibre mat produced by electrospinning for the turn-on luminescence determination of Hg^{2+} in water samples. Sens. Actuators B **195**, 8–14 (2014)
59. (a) Y. Cai, L. Yan, G. Liu, H. Yuan, D. Xiao, In-situ synthesis of fluorescent gold nanoclusters with electrospun fibrous membrane and application on Hg (II) sensing. Biosens. Bioelectron. **41**, 875–879 (2013); (b) L. Heng, B. Wang, Y. Zhang, L. Zhang, B.Z. Tang, L. Jiang, Sensing mechanism of nanofibrous membranes for fluorescent detection of metal ion. J. Nanosci. Nanotechnol. **12**, 8443–8447 (2012)
60. P. Anzenbacher Jr., M.A. Palacios, Polymer nanofibre junctions of attolitre volume serve as zeptomole-scale chemical reactors. Nat. Chem. **1**, 80–86 (2009)
61. B. Zu, Y. Guo, X. Dou, Nanostructure-based optoelectronic sensing of vapor phase explosives – a promising but challenging method. Nanoscale **5**, 10693–10701 (2013)

62. (a) T.M. Swager, The molecular wire approach to sensory signal amplification. Acc. Chem. Res. **31**, 201–207 (1998); (b) D.T. Mc Quade, A.E. Pullen, T.M. Swager, Conjugated polymer-based chemical sensors. Chem. Rev. **100**, 2537–2574 (2000)
63. Y. Wang, A. La, Y. Ding, Y. Liu, Y. Lei, Novel signal-amplifying fluorescent nanofibers for naked-eye-based ultrasensitive detection of buried explosives and explosive vapors. Adv. Funct. Mater. **22**, 3547–3555 (2012)
64. Y. Long, H. Chen, Y. Yang, H. Wang, Y. Yang, N. Li, K. Li, J. Pei, F. Liu, Electrospun nanofibrous film doped with a conjugated polymer for DNT fluorescence sensor. Macromolecules **42**, 6501–6509 (2009)
65. W.-E. Lee, C.-J. Oh, I.-K. Kang, G. Kwak, Diphenylacetylene polymer nanofiber mats fabricated by freeze drying: preparation and application for explosive sensors. Macromol. Chem. Phys. **211**, 1900–1908 (2010)
66. L. Guo, B. Zu, Z. Yang, H. Cao, X. Zheng, X. Dou, APTS and rGO co-functionalized pyrenated fluorescent nanonets for representative vapor phase nitroaromatic explosive detection. Nanoscale **6**, 1467–1473 (2014)
67. J.S. Yang, T.M. Swager, Porous shape persistent fluorescent polymer films: an approach to TNT sensory materials. J. Am. Chem. Soc. **120**, 5321–5322 (1998)
68. M.N. Velasco-Garcia, Optical biosensors for probing at the cellular level: a review of recent progress and future prospects. Semin. Cell Dev. Biol. **20**, 27–33 (2009)
69. C. Zhou, Y. Shi, X. Ding, M. Li, J. Luo, Z. Lu, D. Xiao, Development of a fast and sensitive glucose biosensor using iridium complex-doped electrospun optical fibrous membrane. Anal. Chem. **85**, 1171–1176 (2013)
70. B.W. Davis, N. Niamnont, C.D. Hare, M. Sukwattanasinitt, Q. Cheng, Nanofibers doped with dendritic fluorophores for protein detection. ACS Appl. Mater. Interfaces **2**, 1798–1803 (2010)
71. B.W. Davis, N. Niamnont, R. Dillon, C.J. Bardeen, M. Sukwattanasinitt, Q. Cheng, FRET detection of proteins using fluorescently doped electrospun nanofibers and pattern recognition. Langmuir **27**, 6401–6408 (2011)
72. S.O. Han, W.K. Son, J.H. Youk, W.H. Park, Electrospinning of ultrafine cellulose fibers and fabrication of poly(butylene succinate) biocomposites reinforced by them. J. Appl. Polym. Sci. **107**, 1954–1959 (2008)
73. H. Wang, D. Wang, Z. Peng, W. Tang, N. Li, F. Liu, Assembly of DNA-functionalized gold nanoparticles on electrospun nanofibers as a fluorescent sensor for nucleic acids. Chem. Commun. **49**, 5568–5570 (2013)
74. S. Pagliara, A. Camposeo, F. Di Benedetto, A. Polini, E. Mele, L. Persano, R. Cingolani, D. Pisignano, Study of optical properties of electrospun light-emitting polymer fibers. Superlattice. Microstr. **47**, 145–149 (2012)
75. D. O'Carroll, I. Lieberwirth, G. Redmond, Melt-processed polyfluorene nanowires as active waveguides. Small **3**, 1178–1183 (2007)
76. C. Meng, Y. Xiao, P. Wang, L. Zhang, Y. Liu, L. Tong, Quantum-dot-doped polymer nanofibers for optical sensing. Adv. Mater. **23**, 3770–3774 (2011)

Chapter 7
Nanofibre-Based Sensors for Visual and Optical Monitoring

Iline Steyaert, Hubert Rahier, and Karen De Clerck

Abstract Sensors supplying a change in optical properties, easily detectable with the naked eye (visual) or inexpensive equipment such as compact spectrometers (optical), are a very powerful tool to visualise a wide range of parameters, including temperature, light, pH and concentration of chemical substances. Most of these sensors rely on indicator compounds showing a change in optical absorbance (colour) or fluorescence under the influence of a certain parameter. Halochromic dyes, for instance, change colour with pH. Since the use of nanofibres improves sensor sensitivity and response time due to their large surface area to volume ratio, the incorporation of indicator compounds into nanofibres is one of the current challenges in sensor design. This chapter discusses the production of colorimetric and fluorescent nanofibrous membranes for visual and optical monitoring (Sects. 7.3 and 7.4), supplemented by some fundamental information on those sensing systems (Sect. 7.2) and some interesting applications (Sect. 7.5).

I. Steyaert
Fibre and Colouration Technology Research Group, Department of Textiles,
Faculty of Engineering and Architecture, Ghent University, Technologiepark 907,
Ghent 9052, Belgium

Research Unit of Physical Chemistry and Polymer Science (FYSC), Department of Materials
and Chemistry, Faculty of Engineering, Vrije Universiteit Brussel, Pleinlaan 2,
Brussels 1050, Belgium

H. Rahier
Research Unit of Physical Chemistry and Polymer Science (FYSC), Department of Materials
and Chemistry, Faculty of Engineering, Vrije Universiteit Brussel, Pleinlaan 2,
Brussels 1050, Belgium

K. De Clerck (✉)
Fibre and Colouration Technology Research Group, Department of Textiles,
Faculty of Engineering and Architecture, Ghent University, Technologiepark 907,
Ghent 9052, Belgium
e-mail: karen.declerck@ugent.be

7.1 Introduction

It is clear that nanofibres can be used for several sensor applications due to the inherent properties linked to their nanoscale diameters. Nanofibrous nonwovens are characterized by small pore sizes, large specific surface area, high porosity and good inter-pore connectivity. They have improved sensor sensitivity mainly due to the large surface area to volume ratio, providing an increased number of sites for analyte interaction or signal transduction. An increasing demand for highly sensitive sensors in many sectors, including environmental monitoring, food inspection and the biomedical field, has stimulated the research into nanostructured materials for sensor applications. Among several types of nanofibre-based sensors, optical sensors are gaining interest due to some advantages, such as absence of electromagnetic interference [1, 2]. In general, optical sensors yield information on analytes through optical absorption/luminescence, other spectroscopic techniques such as FTIR, or optical parameters including refractive index and reflectivity. Since most analytes do not have measurable intrinsic optical properties making direct optical sensing possible, most of the optical sensors are reagent-mediated. This means that a change in optical response of an intermediate agent, usually an analyte-sensitive dye molecule, is used to monitor analyte concentrations. The interaction between the analyte and the sensing molecule is thus paramount and can be optimized using a porous nanofibrous substrate with increased sensitivity and response time [1, 3]. A wide variety of indicator dyes are available, resulting in a colour change or luminescence under the influence of pH, O_2, CO_2, a wide range of volatile organic compounds (VOC's), metal ions, peptides, etc. [4–11] Luminescence is intrinsically more sensitive than absorption [7]; within a certain window, not only the presence but also the concentration of an analyte can be measured, and measuring is possible at lower concentrations. Despite this advantage of luminescence over absorbance-based sensing, a significant change in absorbance results in a colour change visible to the naked eye. This could be particularly interesting for several applications, wound management or protective clothing for instance, since no additional (electronic) equipment is necessary to measure parameters. This addresses the need for cheap, fast and easy to operate products, especially in the health sector [12]. Moreover, colorimetric nanofibrous membranes are flexible sensor systems that can supply local information while monitoring a large area, not only making them interesting for biomedical applications but also for technical ones such as agricultural monitoring [13]. This chapter discusses the production of colorimetric and fluorescent nanofibrous membranes for visual and optical monitoring (Sects. 7.3 and 7.4), supplemented by some fundamental information on those sensing systems (Sect. 7.2) and some interesting applications (Sect. 7.5).

7.2   Principles of Colorimetric and Fluorescence Sensing Mechanisms

A colour change of a substance, whether it is due to absorbance or fluorescence, can easily be detected by the human eye or by using simple spectrophotometric instruments, resulting in visual and optical monitoring respectively. Below, it is briefly explained how absorbance and fluorescence can be used in sensing mechanisms. For a more detailed description on colour chemistry and chromic phenomena, the reader is referred to extensive works by Zollinger and Bamfield [14, 15].

7.2.1   Absorbance-Based Sensing

In general, a molecule will absorb electromagnetic energy if the energy of the light is equal to the energy difference between the occupied and unoccupied molecular orbitals. Molecules showing absorbance in the visual part of the electromagnetic spectrum, are characterised by a linear or cyclic system of conjugated double bonds, since the excitation of electrons from π to π^* orbitals in a conjugated system does not demand a lot of energy. This means that light of lower energy, *i.e.* light of longer wavelength corresponding to the visual part of the electromagnetic spectrum, is absorbed. Every impulse causing significant changes to the energy levels of this conjugated system, can be seen as a colour change since the absorbed wavelength are changing too. These colour change phenomena are classified according to the stimulus that causes the change: photochromism (light), electrochromism (oxidation/reduction), thermochromism (heat), solvatochromism (solvent polarity), ionochromism (ions), halochromism (pH), etc. In the electrospinning community, pH-sensitive nanofibres are gaining attention. These fibres are mostly based on halochromic dyes, characterized by a change in electron configuration upon protonation/deprotonation. The clearly visible colour change of halochromic dyes is mostly based on a ring opening (Fig. 7.1) or a tautomerism (Fig. 7.2), illustrating the significant changes of the conjugated systems.
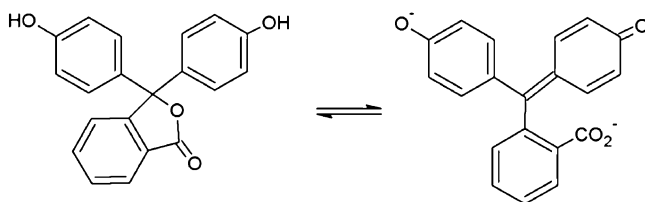
Fig. 7.1   Ring opening upon deprotonation of phenolphthalein halochromic dye (*left: colourless*, *right: red*)
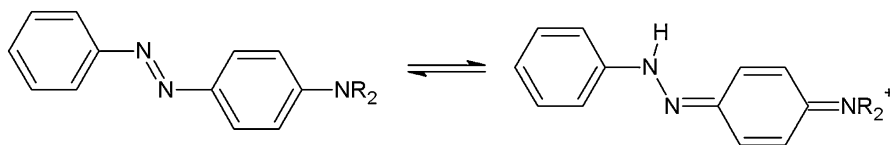
Fig. 7.2 Shift from the ammonium to the azonium tautomer upon protonation of aminoazo dyes resulting in a colour change

7.2.2 Fluorescence-Based Sensing

When a molecule absorbs energy and is brought to an excited state, one of the possible ways to lose that energy is fluorescence, *i.e.* emission of visible radiation from the lowest vibrational level of the excited state to any of the vibrational levels of the ground state. The emitted light has lower energy and thus longer wavelengths than the absorbed radiation due to a loss of vibrational energy in the excited state. The difference in wavelengths between the absorption and the fluorescence spectral peaks is called the Stokes shift. It is very important for a sensor system that this Stokes shift is as large as possible to minimize the interference of the excitation light with the fluorescence emission [16].

Unlike colorimetric sensors, most fluorescent sensors do not register a shift in colour, but an increase or decrease in fluorescence intensity caused by an external stimulus. A fluorophore can show increased/decreased fluorescence upon (i) collision with the analyte, (ii) reversible binding with the analyte or (iii) analyte recognition of a linked receptor group (Fig. 7.3a) [17]. The latter sensing mechanism depends mainly on photoinduced processes, such as photoinduced electron transfer (PET), and Förster resonance energy transfer (FRET) [18]. PET describes processes that prevent the relaxation of the excited state electron due to the coupling of an electron donor or acceptor moiety. The fluorescence that normally follows the relaxation is therefore quenched. In first instance, PET can be used for sensing of analytes efficiently quenching fluorescence via the PET process. Most explosives and several biological materials (peptides, proteins, etc.), for instance, are electron-deficient compounds preventing relaxation of excited state electrons of fluorescent probes [19, 20]. A second way of using the PET process as sensing mechanism consists of coupling a fluorophore and an electron donor/acceptor. When an analyte prevents the exchange of electrons between the two, PET is cancelled and the fluorescence is regained, also making analyte sensing possible (Fig. 7.3b). FRET energy transfer occurs between two fluorophores with spectral overlap. Fluorescence of the donor fluorophore is quenched since it emits at wavelengths that overlap with the absorption spectrum of the acceptor fluorophore, resulting in acceptor emission. When the energy transfer is hindered in the presence of an analyte, the fluorescence of the donor is restored (Fig. 7.3c).

Although the changes in fluorescence often can be seen with the naked eye, most fluorescent sensors are not used for visual detection because of the need for a specific illuminating source (at the exciting wavelengths) and possible spectral
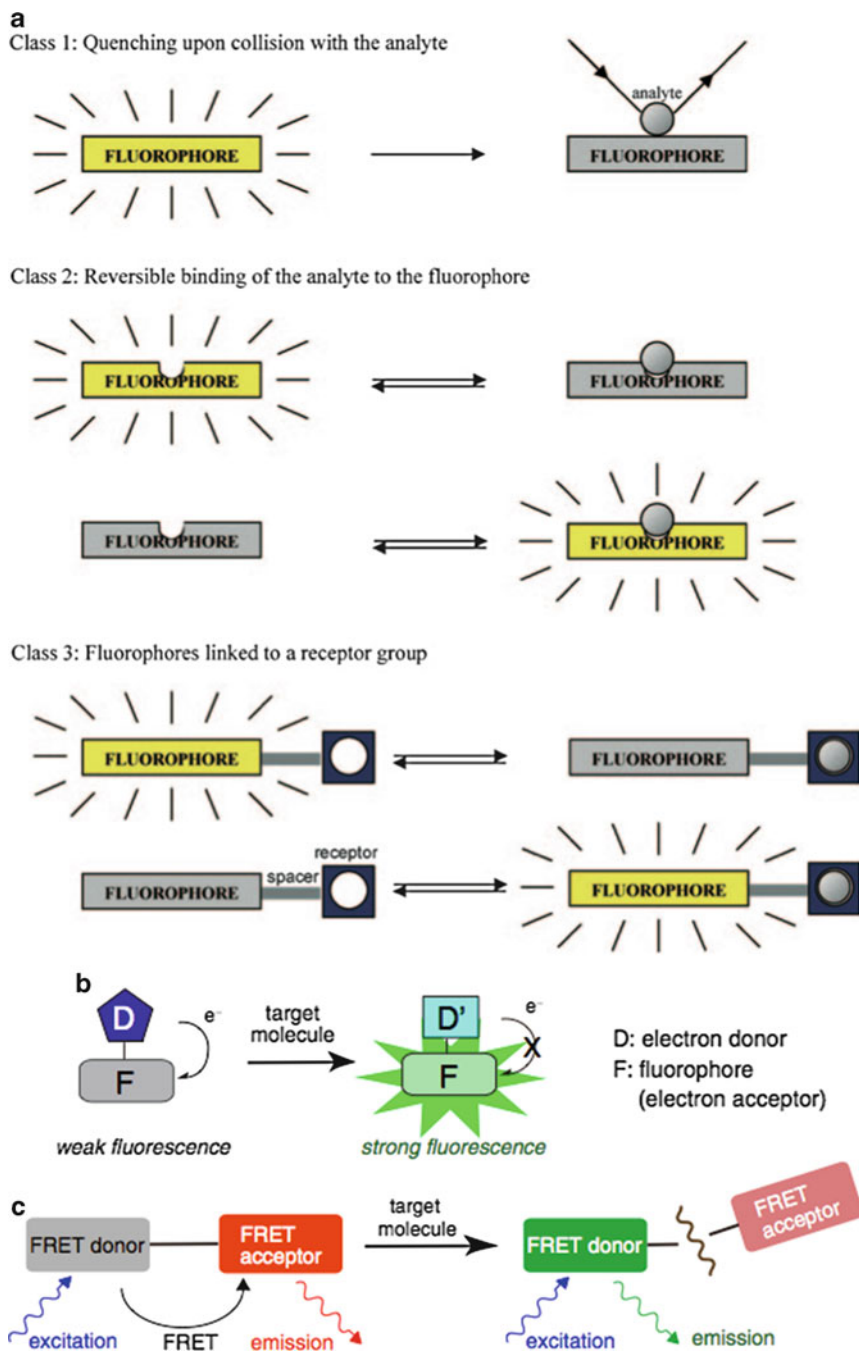
Fig. 7.3 Sensing mechanisms based on fluorophore-analyte interactions (**a**), with a focus on photoinduced electron transfer or PET (**b**) and Förster resonance energy transfer or FRET (**c**) (Sources: (**a**) [17] (**b**, **c**) [18])
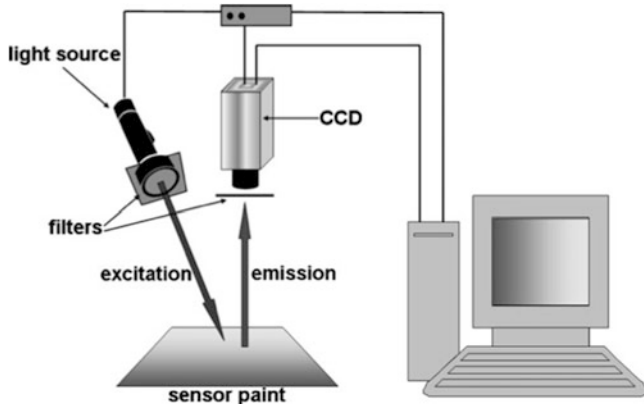
Fig. 7.4 Setup for optical monitoring of solid fluorescent sensors (Source [21])

overlaps. However, optical monitoring using solid fluorescent materials is possible using relatively simple equipment such as LED light sources and CCD cameras or compact inexpensive spectrometers (Fig. 7.4) [10, 21, 22]. Additionally, optical monitoring of sites inaccessible to conventional setups or over longer distances and several spots is possible using fibre optics [16, 23]. In order to compensate for varying conditions, such as illumination intensity or presence of oxygen, ratiometric detection of analytes can be applied [17, 24, 25]. This implies using an indicator dye and a dye inert for the analyte, allowing a referenced measurement.

7.2.3 Materials for Colorimetric and Fluorescence Sensing

Dyes supplying a colorimetric or fluorescent signal are widely used in biochemistry, biology, medicine and analytical chemistry for biological staining, identification of chemical structures and reactions, titration, ion detection, solvent characterization, etc. [14] For sensor applications, the indicator molecules need to be immobilized, either in liquid or in solid phase, to facilitate a measurable interaction with an analyte. A lot of effort has been done to immobilize indicator dyes on solid substrates for use in optical sensor systems, since a solid matrix encapsulates the indicator while it remains accessible to the analytes [7]. Think of the use of pH-indicator paper; rather than adding the dye itself to the solution, the solid substrate provides information on the solution without contaminating it.

As mentioned in the introduction, electrospun nanofibres have received great attention for their benefits in sensor applications due to their improved sensitivity and response time in comparison to other solid substrates. Solvent electrospinning is a relatively simple process to produce nanofibres from polymer solutions and is therefore the most commonly applied [26, 27]. There are several ways to obtain usable optical properties of nanofibres produced through solvent electrospinning,

resulting in a material suitable for absorbance- or fluorescence-based sensing. These include dye-doping, covalent bonding of dyes and use of conjugated polymers. These methods are addressed in the following sections of this chapter. Within this discussion, the use of nanoparticles is omitted.

7.3 Nanofibrous Sensors Based on Dye-Doping

7.3.1 Dye-Doping: A Fast and Easy Procedure for the Production of Colorimetric and Fluorescent Nanofibres

A lot of research has been focussing on the development of new and improved dye molecules for sensor applications. Mohr, for instance, reviews developments in the use of (reversible) covalent bonding to detect neutral and ionic analyte molecules such as cyanide, formaldehyde, amino acids, peptides, proteins, etc. [8] supplementing indicator dyes primarily based on hydrogen bonding, Coulomb, Van der Waals and hydrophobic interactions. Incorporation of specific dyes into nanofibrous structures allows us to combine the extensive knowledge on indicator dyes with the advantages of the nanoscale diameters, leading to new and improved sensors with extraordinary properties. Fantini et al. have studied dye, fluorophore and pigment colouration of nanofibres through addition of powders to the polymer electrospinning solution, *i.e.* doping of the solution. They have found that addition of organic dyes and fluorophores does not significantly affect the electrospinning process or the nanofibre morphology [28]. However, great alterations were observed when pigments are used. Van der Schueren et al. concluded that this is due to an insufficient solubility in the electrospinning solution, since the same behaviour is observed for dyes that are not well dissolved in the solvent system [29]. Functionalization of a wide variety of nanofibres with indicator dyes is thus easily achieved by dye-doping when taking into account the solubility of the dye in the electrospinning solution.

A major part of the research on nanofibres for visual and optical monitoring is focussed on developing pH-sensitive membranes. pH plays an important role in a diverse set of applications, including protective clothing and safety, environmental pollution, agriculture and the biomedical field [13, 30, 31]. Moreover, a wide variety of halochromic indicator dyes is available. Van der Schueren et al. explored the feasibility of using commercial pH-indicator dyes for dye-doping polyamide 6.6 (PA66) nanofibres [29]. This resulted in a wide range of nanofibrous membranes showing halochromic behaviour, which could differ from the indicator dyes in solution. The pH-range of the colour change shifts and/or broadens and even the colour itself can be influenced, all depending on the strength and mode of interaction between the polymer matrix and the dye. Two follow-up studies, incorporating the commercial azo indicator Nitrazine Yellow

(NY) in polyamide (PA) or in polycaprolactone (PCL) and PCL/chitosan nanofibres, study the influence of a polymer nanofibrous matrix on the halochromic behaviour of an indicator dye in more detail [32, 33]. From these studies, it can be concluded that the changing microenvironment of an indicator dye due to incorporation into nanofibres influences the halochromic behaviour on three levels: (i) the absorbance spectrum (*i.e.* the colours), (ii) the dynamic pH-range (pK$_a$, broadening) and (iii) the response time. For instance, NY-doping of PA6 and PA66 nanofibres resulted in a slight shift of the acidic and alkaline wavelength maxima, and a shift and broadening of the dynamic pH-range. When using PCL as the matrix polymer, the halochromic behaviour of NY is even completely suppressed. Addition of chitosan to this system restores the halochromic behaviour again. Moreover, the PCL/chitosan nanofibres have superior wetting behaviour in comparison with the PCL nanofibres, effectively lowering the response time from 3 h to 5 min. These studies thus show that a well-considered choice of nanofibrous matrix is crucial. Additionally, the dye systems can be studied. Agarwal et al. for instance, describe the use of a combination of five commercially available indicator dyes in a specific ratio for dye-doping of PA6 nanofibres, resulting in pH-sensitive nanofibrous membranes capable of detecting pH values in de range of 1–10 by indicating a unique colour code for each pH [34]. Also the design of new indicator dyes opens up many possibilities. Trupp et al. for example, report on the development of functional hydroxyazobenzene dyes with pK$_a$ values tailored by appropriate choice of substituents for the para substituted phenols [35]. Kim et al. used an in-house synthesized halochromic dye for doping polyacrylonitrile (PAN) nanofibres.

Also fluorophores, capable of sensing a wide variety of analytes, have been incorporated into nanofibres by a simple doping technique. However, fluorophore dye-doping is less straightforward since undesirable quenching phenomena can complicate the process [28]. Liang et al. doped poly(diallyldimethylammonium chloride) (PDAC) with fluorescein and three other fluorescein derivatives, producing nanofibrous membranes suitable for detection of pH variations and biomolecules. They found that the dye concentration was characterized by an optimum, since the fluorescence signal increases in intensity with increasing concentration only when self-quenching is not significant [36]. Not only the dye concentration was found to affect the sensor performance, but also the fibre diameter and the pore structure. Tao et al. found that porphyrin-doped silica nanofibres for detection of TNT-vapours showed enhanced sensitivity when the fibre diameter is reduced and/or pores are introduced [37]. They ascribed this to improved analyte diffusion and a larger relative amount of quenched porphyrin molecules. Also Yang et al. reported on improved sensor performance by introducing secondary porous structures into nanofibres [38]. It should be noted, however, that fluorescent dye molecules are sensitive to quenching by oxygen and that nanofibres with smaller sizes are quenched more rapidly due to a higher oxygen diffusion, effectively reducing the emission lifetime of the nanofibrous sensors [39]. Ner et al. report on a different strategy for enhancing the fluorescence of dye-doped nanofibres, namely the exploitation of a preferential interaction of the fluorophore with the nanofibrous matrix minimizing quenching effects [40]. They dye-doped deoxyribonucleic acid (DNA) nanofibres, since many fluorescent dyes are known

for their ability to bind to or intercalate with DNA. When comparing DNA and poly (methyl methacrylate) (PMMA) nanofibres and films containing such a dye, the effect of both the nanofibrous structure and the preferential interaction could be compared. The fibre morphology was responsible for a 5–6 fold amplification, whereas the specific interactions between the fluorophore and DNA resulted in an 18–21 fold amplification. This result highlights the importance of dye-fibre interactions, not only for colorimetric sensors but also for fluorescent sensors.

7.3.2 The Power of Molecular Modelling of a Dye and a Dye-Doped System

The previous section clearly illustrates the importance of understanding dye-fibre interactions and how they affect the sensing performance of dye-doped nanofibres. A very powerful tool, supporting experimental results, is molecular modelling of the dye and the dye-doped system. A combination of theory and experiment is, in first instance, very promising to gain a detailed understanding of the nature of the sensing properties of dye molecules. It is for instance paramount to understand the mechanism causing a colour change in halochromic dyes, to be able to assess whether incorporation into a nanofibrous matrix could affect this mechanism. De Meyer et al. developed a theoretical procedure, based on molecular dynamic (MD) simulations combined with time-dependent density functional theory (TD-DFT), which can be applied to predict the properties of (azo) dyes in aqueous environment [41]. It is thus possible to understand the structural differences at the molecular scale on the origin of halochromism. Additionally, De Meyer et al. demonstrated in a recent study that a computational study can provide crucial information on the effects of substituents of a chromophore on its halochromic behaviour [42]. This makes predictions possible for hypothetical dyes with the same chromophore and for existing dyes in another environment, such as a nanofibrous polymer matrix. Eventually, this opens up the possibility of future design of tailor-made dyes for specific application or incorporation in a specific matrix.

Molecular modelling was used to explain the difference in halochromic behaviour of Nitrazine Yellow (NY) in aqueous solution and the three nanofibrous polymer matrices described in Sect. 7.3.1 [32, 33]. Ab initio calculations of the neutral and deprotonated dye molecules were used to confirm that the suspected azo-hydrazone tautomerism (Fig. 7.5) is responsible for the halochromic behaviour. These results indicate that changes at the azo group (N=N) induce the colour change. Subsequently, model systems for PA, PCL and chitosan were constructed, allowing the evaluation of the interactions of NY with the polymer matrices. This revealed that the ester groups of PCL interact with the chromophore via long-range interactions, shielding the NY azo group from any interaction with water molecules, effectively prohibiting any halochromic behaviour. Interaction with chitosan, however, is very different, showing hydrogen bonding and electrostatic interactions between the sulphate groups of NY and the amino groups of chitosan. These
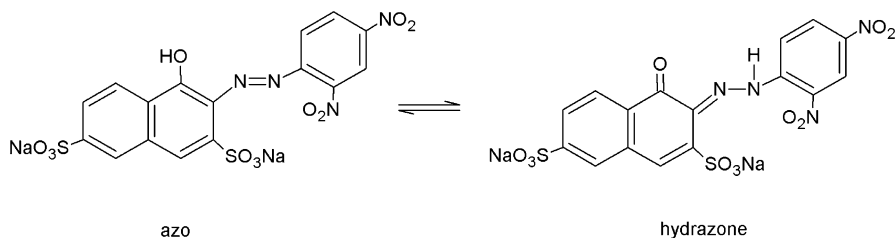
Fig. 7.5 Azo-hydrazone tautomerism of Nitrazine Yellow (*left: blue*, *right: yellow*)

interactions do not shield the halochromic azo group and deprotonation in alkaline environment is possible. Additionally, theoretical modelling allows for an estimation of the Gibbs free energy of the interactions, resulting in a value of -35.6 kJ/mol for PCL and -132.3 kJ/mol for chitosan. NY therefore preferentially interacts with chitosan, explaining the restored halochromic behaviour of NY upon chitosan addition to the PCL nanofibrous matrix. This example illustrates the power of molecular modelling to supplement the experimental results, gain understanding in sensor mechanisms and predict the behaviour of future dye-doped systems.

7.3.3 The Main Problem of the Dye-Doping Technique: Dye-Migration

Although the dye-doping technique results in easy-to-produce nanofibrous sensor membranes, dye leaching is a major problem [29, 32, 34]. This not only affects the long-term sensitivity and stability of the sensor, but the toxicity of the leaching dye may be of significant concern. Van der Schueren et al. showed that leaching could be countered by adding a polycationic complexing agent (PDAC) to the electrospinning solution, so that diffusion of the complexed dye molecule is hindered [29, 33]. However, this does not always eliminate leaching effects completely and for some dye molecules complexation is not possible. Covalent linkage of the dye to a suitable matrix appears to be the most efficient immobilization method, resulting in materials with negligible leaching [4, 9, 16, 17, 35, 43]. Since dye leaching is not a problem specific to nanofibrous sensors [7], research into new dyes suitable for covalent bonding is quite extensive [4, 9, 16, 35, 44, 45]. For instance, Mohr et al. report on the development of indicator dyes for biomedical sensing applications, covalently linked through an ether bond that is also stable in the presence of enzymes [4]. Today, the major challenge in the development of nanofibrous colorimetric and fluorescent sensors is to apply the present knowledge on dye immobilization to nanofibres, without compromising the processability in the electrospinning process or the resulting nanofibre morphology. It is also clear that, similar to incorporation through dye-doping, covalent bonding of an indicator dye can cause significant changes in the sensing behaviour compared to the free dye, since both the molecular composition and the microenvironment of

the dye are changed [9, 35]. Even though it requires a more rigorous design than dye-doping with commercially available dyes, some nanofibrous colorimetric and fluorescent sensors based on covalently bonded dyes are reported in literature, which will be reviewed in the next section.

7.4   Nanofibrous Sensors Based on Functional Polymers

As discussed in the previous section, leaching of the functional component providing the colorimetric or fluorescent properties of the nanofibres can be a significant problem. Using functional polymers, unable to leach out of the nanofibrous membranes, is a valuable approach to this problem. In general, there are two types of functional polymers suitable for the production of nanofibrous sensors for visual and optical monitoring: (i) functionalized polymers containing a sensing molecule covalently bonded to the backbone and (ii) polymer with a backbone consisting of a conjugated system of π-bonds, showing inherent colorimetric or fluorescent properties.

7.4.1   Functionalized Polymers

Although the research on covalent immobilization of indicator dyes has resulted in many applicable solutions to the dye leaching problem (Sect. 7.3.3), there are not many studies reporting on the use of this technology to produce colorimetric and fluorescent nanofibres. Wang et al. describe the use of pyrene methanol (PM), a fluorescent indicator showing a large Stokes shift, high quantum yield, strong absorbance, and excellent photostability and lifetime. PM was covalently attached to a polyacrylic acid (PAA) backbone, which was subsequently used to electrospin together with a cross-linkable polymer [46, 47]. The use of the functionalized polymer resulted in nanofibrous membranes showing good sensitivity towards electron-deficient metal cations (Fe^{2+}, Hg^{2+}) or nitroaromatic compounds (DNT, TNT) by fluorescence quenching, with a minimized self-quenching effect. Zhang et al. postulate that functionalization after the electrospinning process would be beneficial, since the indicator dye is then located on the surface of the nanofibres, resulting in a shorter diffusion path of the analyte to the dye [48]. They produced pH-sensitive colorimetric nanofibres with a response time of a few seconds by covalently bonding phenolphthalein to polyacrylonitrile (PAN) nanofibres after the electrospinning process by first aminating with ethylenediamine and a Mannich reaction. Ondigo et al. used a similar approach for the production of Fe^{2+}-sensitive colorimetric nanofibres [49]. They applied a surface modification of electrospun poly(vinylbenzyl chloride) (PVBC) with an imidazole derivative. The derivative acts as a ligand for Fe^{2+} cations and induces a clearly visible colour change. It can thus be concluded that both the use of a functionalized polymer in the electrospinning process and the modification of electrospun polymers can be of interest for the production of colorimetric and fluorescent sensors, but the true potential of both methods has yet to be exploited.

7.4.2   Conjugated Polymers

Polymers with conjugated double bonds in the main chain are characterized by several peculiar properties. They are semiconductors or conductors and interact with light [50], meaning that they can also be exploited for their optical properties. In literature, only a few reports on the use of conjugated polymers for optical monitoring can be found, probably due to the difficulties of processing the polymers in the electrospinning process. Researchers of the Beijing National Laboratory for Molecular Sciences have published a few paper on the use of novel polycyclic conjugated polymers for the production of nanofibrous sensing membranes [19, 51, 52]. They are, however, not electrospinnable in pure form and are electrospun using a mixture with polystyrene (PS). PS was chosen as a carrier polymer since it has appropriate hydrophobicity leading to a well-dispersed phase of the conjugated polymer, has negligible fluorescence emission in the measured wavelengths, and is soluble in a common solvent. Through this blend electrospinning process, a nanofibrous membrane showing excellent fluorescence quenching by explosive vapours was produced. Similar to the effects of fibre morphology reported for fluorophore-doped membranes (Sect. 7.3.1), both lowering the fibre diameter and introducing secondary pores by adding a surfactant to the electrospinning solution improved the fluorescence quenching significantly [19, 51]. Additionally, the membrane showed good sensitivity towards some haemproteins due to a FRET mechanism; the absorption maximum of the haemproteins is close to the emission maximum of the conjugated polymer [52].

Another interesting approach, resulting in the use of nanofibres containing conjugated polymers for sensing applications, comprises of using photopolymerizable monomers such as diacetylene (DA) in the electrospinning process. An electrospinning solution containing DA monomers and a carrier polymer was electrospun and irradiated after fibre formation, creating polydiacetylene (PDA) with a conjugated backbone within the nanofibres. Several types of DA monomers are commercially available, leading to PDA-containing nanofibres with a colorimetric response (blue to red) to several organic solvents [53]. Also PDA-containing nanofibrous membranes showing strong red fluorescence when in contact with α-cyclodextrin and weak fluorescence for β- and γ-cyclodextrins are reported using this technique [54]. Functionalization of commercially available DA monomers can lead to even more possibilities, such as colorimetric nanofibrous CO_2 sensors [55].

A third and final strategy reported in literature, is based on coating nanofibres with conjugated polymers. Wang et al. report on a layer-by-layer coating technique for immobilizing a sensing layer on the surface of electrospun cellulose acetate nanofibres [20]. This way, the high specific surface area of the nanofibres are combined with localizing small quantities of the conjugated polymer on the surface, which means the accessibility of the sensing element to the quencher is optimal and a higher sensitivity can be obtained.

Although the synthetic routes for the production of conjugated polymers are often difficult or time-consuming and the processability in the electrospinning

process is often poor, the use of conjugated polymers can offer some advantages. Foremost, no leaching of an indicator dye is possible, not even due to cleavage of a covalent bond. Also, conjugated polymers can exhibit collective properties that are sensitive to very minor perturbations [20], which could make them very interesting depending on the application.

7.5 The Potential of Colorimetric and Fluorescent Sensors for Visual and Optical Monitoring: Applications

In order to properly illustrate the potential of colorimetric and fluorescent nanofibres, some applications are discussed in the following sections. For this, also non-nanofibrous sensor systems showing interesting features are addressed. In several cases, the approach can be translated to nanofibrous membranes, which could show improved sensor sensitivity and response time due to the high specific surface. Wolfbeis, for instance, reviews the extensive possibilities of sensor paints [21]. He defines a sensor paint as a material that consists of a solvent, a polymeric support and an indicator dye. This mixture can be sprayed onto a surface to produce a thin film with sensing abilities. It is not hard to imagine that, if there is a similar electrospinnable mixture, improved sensing performances could be obtained in most cases. Also within the field of electronic noses, for example, there is a growing interest in optical systems based on absorbance and fluorescence with enhanced sensitivity [56]. Consequently, some broader applications of colorimetric and fluorescent sensors for visual and optical monitoring are covered in this section. Additionally, a short recapitulation of the application domains of the nanofibrous sensors discussed in previous sections is given in Table 7.1.

7.5.1 Environmental Monitoring and Safety

Colorimetric and fluorescent sensors are more and more applied for environmental monitoring and safety since they can visualize several harmful gases, volatile organic compounds (VOCs), heavy metal ions and explosives. Especially highly sensitive colorimetric and/or fluorescent sensor arrays, capable of identifying closely related gases or organic compounds by creating a 'fingerprint' pattern (Fig. 7.6) are of interest [5, 56]. Janzen et al. postulate that few technologies are as advanced or as inexpensive as visual imaging (digital cameras and scanners), making cheap and portable sensor arrays possible [5]. Moreover, they state that the demand for increasingly sensitive systems can only be met in an economical way by using disposable sensors that are not integrated in the readout device. For this, colorimetric and fluorescent nanofibres could offer a great solution since they are

Table 7.1 Overview of colorimetric and fluorescent nanofibrous membranes for visual and optical monitoring reported in literature

Dye-doped nanofibres	Sensing mechanism[a]	Sensing of . . .	Ref
Silica + porphyrin	F	TNT vapour	[37]
PDAC + fluorescein derivatives	F	pH, biological material such as peptides, proteins, etc.	[36]
DNA/CTMA + hemicyanine dye	F	Not specified	[40]
CA + 9-chloromethylantracene	F	Not specified (model quencher)	[38]
PA6, PA66 + commercial pH indicators	C	pH	[29, 32, 34]
PAN + pyran-based dye	C	pH	[30]
PCL, PCL/chitosan + commercial pH indicators	C	pH	[33]
Nanofibres containing functionalized polymers			
PAA functionalized with pyrene derivative	F	Fe^{2+}, Hg^{2+}, DNT and TNT vapour	[46, 47]
PAN functionalized with phenolphthalein	C	pH	[48]
PVBC functionalized with imidazole derivative	C	Fe^{2+}	[49]
Nanofibres containing conjugated polymers			
PDA	C	VOCs, CO_2, cyclodextrins	[53–55]
H-PURET	F	Methyl viologen, cytochrome c	[20]
In-house designed conjugated polymer	F	DNT vapour, haemproteins	[19, 51, 52]

[a]*C* colorimetric, through visual colour change, *F* fluorescent, through quenching of emission

highly sensitive and have no need for electronic coupling to the readout systems. Yoon et al. illustrated the use of a colorimetric nanofibrous sensor array by developing PDA-containing nanofibres based on four types of commercial diacetylene (DA) monomers, showing a different response to several organic solvents (Fig. 7.7). This type of material, *i.e.* colorimetric sensors for detection of chemical gases and vapours, can also make a difference in protective clothing. Table 7.1 illustrates that a major part of the research on colorimetric nanofibres is focused on pH-sensitivity, making visual detection of acid or alkaline vapours possible.

Another popular research topic within environmental monitoring and safety, is the detection of explosives. It is possible to detect certain explosive vapours containing electron-deficient nitroaromatic compounds able to quench
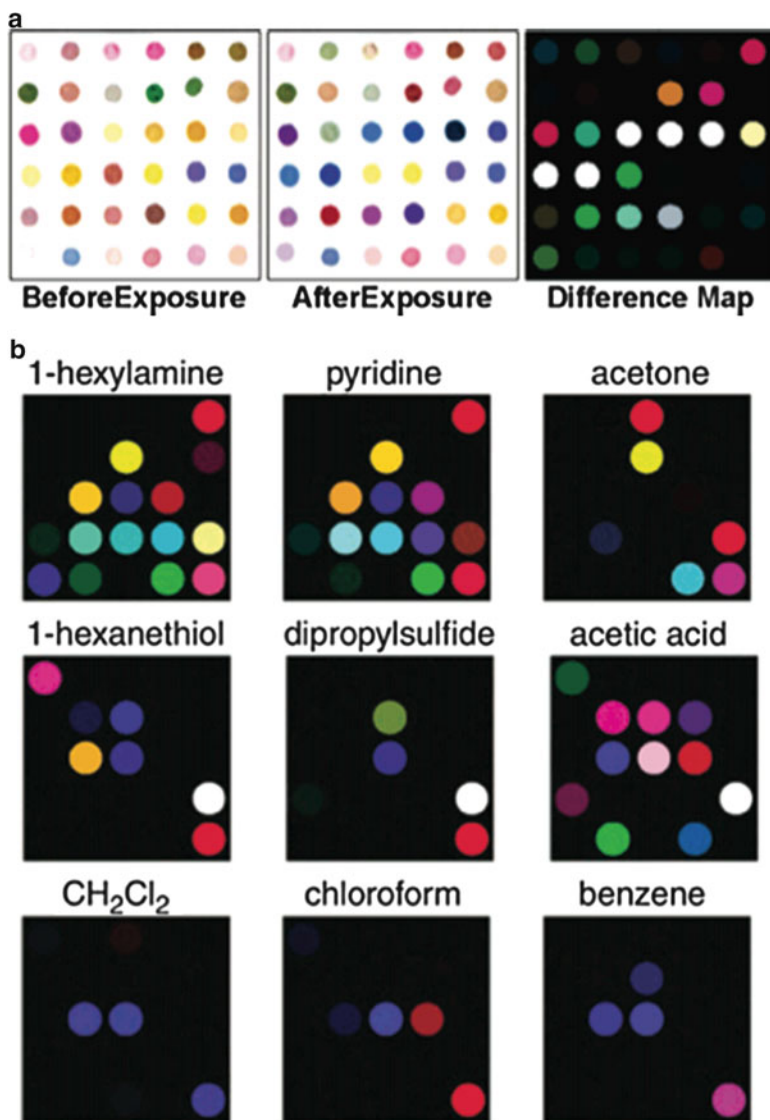
Fig. 7.6 (**a**) Creation of a 'fingerprint' pattern of decylamine using a 36-dye colorimetric sensor array, showing the colour pattern before and after exposure (*left* and *middle* resp.) and the subtraction (*right*) yielding a difference vector in 108 dimensions (*i.e.* 36 changes in *red*, *green* and *blue colour* values) (**b**) Illustration of the identification of several chemical substances using a 25-dye colorimetric sensor array (Sources: (**a**) [5] (**b**) [56])

Fig. 7.7 Colour pattern of four polydiacetylene-containing nanofibrous membranes in response organic solvents. The nanofibrous samples were created with four different commercial diacetylene monomers with different responses to the investigated solvents, resulting in a 'fingerprint' pattern (Source [53])

Fig. 7.8 Fluorescence quenching in response to exposure to DNT vapour for 30 min of nanofibres (**a** vs. **b**) and a dense spin-cast film (**c** vs. **d**) containing a fluorescent conjugated polymer. Nanofibres show good quenching behaviour whereas the spin-cast film does not, indicating a higher sensitivity (Source [51])

fluorescence. Long et al. demonstrated the large difference in sensitivity towards explosive vapours between electrospun nanofibres and spin-cast films (Fig. 7.8), illustrating the potential of nanofibrous sensors for this application.

7.5.2 Biomedical Sciences

The amount of measurable parameters in biomedical sciences through visual and optical monitoring is enormous. It is, for instance, possible to detect volatiles or gases related to infections, intoxications, metabolic diseases, etc. [56] Also measuring compounds of biological importance, such as haemoglobin [52], bacteria [25], metabolites [57], ions [49] and proteases [58], has already been reported. A major parameter being researched for biomedical purposes is pH, this because it is a biological marker for processes such as wound healing and infection [31, 59, 60] (illustrated in Fig. 7.9) and tumour metabolism [25]. In a recent review by Dagarville et al. the importance of sensors and imaging for wound healing is discussed [31]. They conclude that a sensor system monitoring wound parameters such as pH can significantly aid wound management. For example, often wound dressings are changed prematurely out of precaution, whereas the wound itself would benefit from fewer disturbances. A nanofibrous wound dressing containing an indicator molecule could give an indication of the condition of the wound, adding some objectivity to wound management. Additionally, nanofibres are known to aid wound healing. Indeed, nanofibrous nonwovens mimic the natural structure of the native extracellular matrix (ECM) providing structural support for cells in human tissue, making them ideal for fast and scar-free healing [61, 62]. They also allow for oxygen permeation, drainage of wound exudate, protection against infection and dehydration, good wound covering, etc. [63, 64]. The use of nanofibres could therefore give rise to dressings both stimulating and monitoring wound healing.
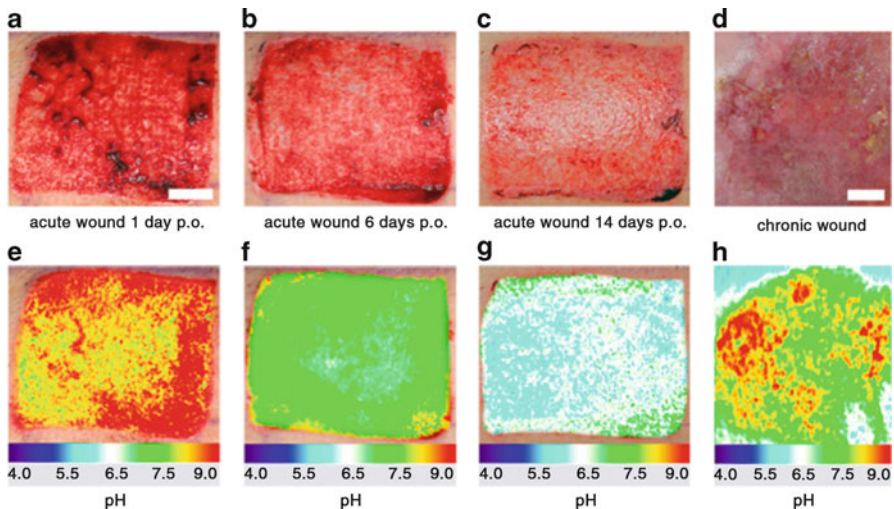
Fig. 7.9 Healing phases and pH during cutaneous wound healing (**A/E**: inflammation, **B/F**: granulation, **C/G**: reepithelialisation, **D/H**: chronic venous ulcer). Decreasing pH values reflect wound healing (Source [25])

7.5.3 Others

There are several other domains in which sensing mechanisms could benefit from a nanofibrous structure, including food technology, agricultural monitoring, monitoring of industrial processes and marine research [21]. Vu et al. report on a UV-activated oxygen indicator for intelligent food packaging, enabling consumers to evaluate the food quality through a visual signal [65]. The indicators are brightly coloured until they are irradiated with UV-light, after which they only regain their colour in the presence of oxygen. The recovery time of the spin-coated materials was 4 h, which is significantly lower than other reported systems. It is feasible that the recovery time would be even more reduced when using this indicator in electrospun material, optimizing the use of sensor for food spoilage. An interesting example of a more technical application of a fluorescent sensor is reported by Nguyen et al. [16]. They describe the use of a fluorophore covalently attached to a polymer network by copolymerization for the monitoring of pH in steel-reinforced concrete structures. The embedded steels are only passivated at pH values higher than 10, making monitoring of the pH in the alkaline region important. The response time was sufficiently fast since the sensor was only used over longer periods of time. However, the reported slow diffusion and response time could be significantly improved using nanofibres, possibly making this a material suitable for a wider range of application demanding pH-monitoring in the alkaline region. The possibilities of colorimetric and fluorescent sensors are thus endless, taking into account all the applications already using these types of sensors but that could benefit from the nanofibrous structure.

References

1. B. Ding, M. Wang, J. Yu, G. Sun, Gas sensors based on electrospun nanofibers. Sensors **9**, 1609–1624 (2009)
2. B. Ding, M. Wang, X. Wang, J. Yu, G. Sun, Electrospun nanomaterials for ultrasensitive sensors. Mater. Today **13**(11), 16–27 (2010)
3. L. Matlock-Colangelo, A.J. Baeumner, Recent progress in the design of nanofiber-based biosensing devices. Lab Chip **12**, 2612–2620 (2012)
4. G.J. Mohr, H. Müller, B. Bussemer, A. Stark, T. Carofiglio, S. Trupp, R. Heuermann, T. Henkel, D. Escudero, L. Gonzalez, Design of acidochrmic dyes for facile preparation of pH sensor layers. Anal. Bioanal. Chem. **392**, 1411–1418 (2008)
5. M.C. Janzen, J.B. Ponder, D.P. Bailey, C.K. Ingison, K.S. Suslick, Colorimetric sensor arrays for volatile organic compounds. Anal. Chem. **78**, 3591–3600 (2006)
6. E. Moczko, I.V. Meglinski, C. Bessant, S.A. Piletsky, Dyes assay for measuring physicochemical parameters. Anal. Chem. **81**, 2311–2316 (2009)
7. C. McDonagh, C.S. Burke, B.D. MacCraith, Optical chemical sensors. Chem. Rev. **108**, 400–422 (2008)

8. G.J. Mohr, New chromogenic and fluorogenic reagents and sensors for neutral and ionic analytes based on covalent bond formation – a review on recent developments. Anal. Bioanal. Chem. **386**, 1201–1214 (2006)
9. P. Makedonski, M. Brandes, W. Grahn, W. Kowalsky, J. Wihern, S. Wiese, H.-H. Johannes, Synthesis of new kinds of reactive azo dyes and their application for fibre-optical pH-measurements. Dyes Pigments **61**, 109–119 (2004)
10. M. Schäferling, The art of fluorescence imaging with chemical sensors. Angew. Chem. Int. Ed. **51**, 3532–3554 (2012)
11. G.J. Mohr, D. Citterio, C. Demuth, M. Fehlmann, L. Jenny, C. Lohse, A. Moradian, T. Nezel, M. Rothmaier, U.E. Spichiger, Reversible chemical reactions as the basis for optical sensors used to detect amines, alcohols and humidity. J. Mater. Chem. **9**, 2259–2264 (1999)
12. S. Chigome, N. Torto, A review of opportunities for electrospun nanofibers in analytical chemistry. Anal. Chim. Acta. **706**, 25–36 (2011)
13. L. Van der Schueren, K. De Clerck, Coloration and application of pH-sensitive dyes on textile materials. Color. Technol. **128**, 82–90 (2012)
14. H. Zollinger, *Color Chemistry: Syntheses, Properties and Applications of Organic Dyes and Pigments* (Wiley-VCH, Weinheim, 1991)
15. P. Bamfield, *Chromic Phenomena: Technological Applications of Colour Chemistry* (The Royal Society of Chemistry, Cambridge, 2001)
16. T.H. Nguyen, T. Venugopala, S. Chen, T. Sun, K.T.V. Grattan, S.E. Taylor, P.A.M. Basheer, A.E. Long, Fluorescence based fibre optic pH sensor of the pH 10–13 range suitable for corrosion monitoring in concrete structures. Sensors Actuators B Chem. **191**, 498–507 (2014)
17. T. Doussineau, A. Schulz, A. Lapresta-Fernandez, A. Moro, S. Körsten, S. Trupp, G.J. Mohr, On the design of fluorescent ratiometric nanosensors. Chem. Eur. J. **16**, 10290–10299 (2010)
18. T. Terai, T. Nagano, Small-molecule fluorophores and fluorescent probes for bioimaging. Pflugers Arch. Eur. J. Physiol. **465**, 347–359 (2013)
19. H. Long, H. Chen, H. Wang, Z. Peng, Y. Yang, G. Zhang, N. Li, F. Liu, J. Pei, Highly sensitive detection of nitroaromatic explosives using an electrospun nanofibrous sensor based on a novel fluorescent conjugated polymer. Anal. Chim. Acta. **744**, 82–91 (2012)
20. X. Wang, Y.-G. Kim, C. Drew, B.-C. Ku, J. Kumar, L.A. Samuelson, Electrostatic assembly of conjugated polymer thin layers on electrospun nanofibrous membranes for biosensors. Nano Lett. **4**(2), 331–334 (2004)
21. O.S. Wolfbeis, Sensor paints. Adv. Mater. **20**, 3759–3763 (2008)
22. H. Guillemain, M. Rajarajan, Y.-C. Lin, C.-T. Chen, T. Sun, K.T.V. Grattan, Feasibility studies using thin sol-gel films doped with a novel lead-selective fluorophore for optical fibre sensing applications. Measurement **46**, 2971–2977 (2013)
23. O.S. Wolfbeis, Fiber-optic chemical sensors and biosensors. Anal. Chem. **80**, 4269–4283 (2008)
24. S. Hornig, C. Biskup, A. Gräfe, J. Wotschadlo, T. Liebert, G.J. Mohr, T. Heinze, Biocompatible fluorescent nanoparticles for pH-sensing. Soft Matter **4**, 1169–1172 (2008)
25. S. Schreml, R.J. Meier, O.S. Wolfbeis, M. Landthaler, R.-M. Szeimies, P. Babilas, 2D luminescence imaging of pH in vivo. Proc. Natl. Acad. Sci. **108**(6), 2432–2437 (2011)
26. S. Ramakrishna, K. Fujihara, W.-E. Teo, T.-C. Lim, Z. Ma, *An Introduction to Electrospinning and Nanofibers* (World Scientific Publishing Co. Pte. Ltd., Singapore, 2005)
27. J.H. Wendorff, S. Agarwal, A. Greiner, *Electrospinning: Materials, Processing and Applications* (Wiley-VCH Verlag & Co., Weinheim, 2012)
28. D. Fantini, L. Costa, Dye, fluorophores and pigment coloration of nanofibers produced by electrospinning. Polym. Adv. Technol. **20**, 111–121 (2009)
29. L. Van der Schueren, T. Mollet, O. Ceylan, K. De Clerck, The development of polyamide 6.6 nanofibres with a pH-sensitive function by electrospinning. Eur. Polym. J. **46**, 2229–2239 (2010)
30. S.-H. Kim, J.-S. Bae, Halochromic chemosensor prepared by pyran-based nanofibers. Fibers Polym. **14**(12), 1981–1984 (2013)

31. T.R. Dargaville, B.L. Farrugia, J.A. Broadbent, S. Pace, Z. Upton, N.H. Voelcker, Sensors and imaging for wound healing: a review. Biosens. Bioelectron. **41**, 30–42 (2013)
32. L. Van der Schueren, K. Hemelsoet, V. Van Speybroeck, K. De Clerck, The influence of a polyamide matrix on the halochromic behaviour of the pH-sensitive azo dye Nitrazine Yellow. Dyes Pigments **94**, 443–451 (2012)
33. L. Van der Schueren, T. De Meyer, I. Steyaert, O. Ceylan, K. Hemelsoet, V. Van Speybroeck, K. De Clerck, Polycaprolactone and polycaprolactone/chitosan nanofibres functionalised with the pH-sensitive dye Nitrazine Yellow. Carbohydr. Polym. **91**, 284–293 (2013)
34. A. Agarwal, A. Raheja, T.S. Natarajan, T.S. Chandra, Development of universal pH sensing electrospun nanofibers. Sensors Actuators B Chem. **161**, 1097–1101 (2012)
35. S. Trupp, M. Alberti, T. Carofiglio, E. Lubian, H. Lehmann, R. Heuermann, E. Yacoub-George, K. Bock, G.J. Mohr, Development of pH-sensitive indicator dyes for the preparation of micro-patterned optical sensor layers. Sensors Actuators B Chem. **150**, 206–210 (2010)
36. X. Liang, Y. Li, W. Peng, J. Bai, C. Zhang, Q. Yang, Efficient method for fabrication of fluorescein derivative/PDAC composite nanofibers and characteristics of their photoluminescent properties. Eur. Polym. J. **44**, 3156–3162 (2008)
37. S. Tao, G. Li, J. Yin, Fluorescent nanofibrous membranes for trace detection of TNT vapor. J. Mater. Chem. **17**, 2730–2736 (2007)
38. Y. Yang, X. Fan, Y. Long, K. Su, D. Zou, N. Li, J. Shou, K. Li, F. Liu, A simple fabrication of electrospun nanofiber sensing materials based on fluorophore-doped polymer. J. Mater. Chem. **19**, 7290–7295 (2009)
39. A. Camposeo, F. Di Benedetto, R. Stabile, R. Cingolani, D. Pisignano, Electrospun dye-doped polymer nanofibers emitting in the near infrared. Appl. Phys. Lett. **90**, 143115 (2007)
40. Y. Ner, J.G. Grote, J.A. Stuart, G.A. Sotzing, Enhanced fluorescence in electrospun dye-doped DNA nanofibers. Soft Matter **4**, 1448–1453 (2008)
41. T. De Meyer, K. Hemelsoet, L. Van der Schueren, P. Ewald, K. De Clerck, V. Van Speybroeck, Investigating the halochromic properties of azo dyes in an aqueous environment by using a combined experimental and theoretical approach. Chem. Eur. J. **18**, 8120–8129 (2012)
42. T. De Meyer, K. Hemelsoet, V. Van Speybroeck, K. De Clerck, Substituent effects on absorption spectra of pH indicators: an experimental and computational study of sulfonphthalene dyes. Dyes Pigments **102**, 241–250 (2014)
43. A. Lobnik, I. Oehme, I. Murkovic, O.S. Wolfbeis, pH optical sensors based on sol-gels: chemical doping versus covalent immobilization. Anal. Chim. Acta. **367**, 159–165 (1998)
44. C. Munkholm, D.R. Walt, A fiber-optic sensor for CO2 measurement. Talanta **35**(2), 109–112 (1988)
45. T. Carofiglio, C. Fregonese, G.J. Mohr, F. Rastrelli, U. Tonellato, Optical sensor arrays: one-pot, multiparallel synthesis and cellulose immobilization of pH and metal ion sensitive azo-dyes. Tetrahedron **62**, 1502–1507 (2006)
46. X. Wang, C. Drew, S.-H. Lee, K.J. Senecal, J. Kumar, L.A. Samuelson, Electrospinning technology: a novel approach to sensor application. J. Macromol. Sci. **A39**, 1251–1258 (2002)
47. X. Wang, C. Drew, S.-H. Lee, K.J. Senecal, J. Kumar, L.A. Samuelson, Electrospun nanofibrous membranes for highly sensitive optical sensors. Nano Lett. **2**(11), 1273–1275 (2002)
48. C. Zhang, Y. Li, W. Wang, N. Zhan, N. Xiao, S. Wang, Y. Li, Q. Yang, A novel two-nozzle electrospinning process for preparing microfiber reinforced pH-sensitive nano-membrane with enhanced mechanical property. Eur. Polym. J. **47**, 2228–2233 (2011)
49. D.A. Ondigo, Z.R. Tshentu, N. Torto, Electrospun nanofiber based colorimetric probe for rapid detection of Fe^{2+} in water. Anal. Chim. Acta. **804**, 228–234 (2013)
50. G.R. Strobl, *The Physics of Polymers: Concepts for Understanding Their Structure and Behavior* (Springer, Berlin/Heidelberg, 2007)

51. Y. Long, H. Chen, Y. Yang, H. Wang, Y. Yang, N. Li, K. Li, J. Pei, F. Liu, Electrospun nanofibrous film doped with a conjugated polymer for DNT fluorescence sensor. Macromolecules **42**, 6501–6509 (2009)
52. H. Wang, Z. Peng, Y. Long, H. Chen, Y. Yang, N. Li, F. Liu, A simple and reusable fluorescent sensor for heme proteins based on a conjugated polymer-doped electrospun nanofibrous membrane. Talanta **94**, 216–222 (2012)
53. J. Yoon, S.K. Chae, J.-M. Kim, Colorimetric sensors for volatile organic compounds (VOCs) based on conjugated polymer-embedded electrospun fibers. J. Am. Chem. Soc. **129**, 3038–3039 (2007)
54. S.K. Chae, H. Park, J. Yoon, C.H. Lee, D.J. Ahn, J.-M. Kim, Polydiacetylene supramolecules in electrospun microfibers: fabrication, micropatterning, and sensor applications. Adv. Mater. **19**, 521–524 (2007)
55. Q. Xu, S. Lee, Y. Cho, M.H. Kim, J. Bouffard, J. Yoon, Polydiacetylene-based colorimetric and fluorescent chemosensor for the detection of carbon dioxide. J. Am. Chem. Soc. **135**, 17751–17754 (2013)
56. R. Röck, N. Barsan, U. Weimar, Electronic nose: current status and future trends. Chem. Rev. **108**, 705–725 (2008)
57. L.I. Kazakova, L.I. Shabarchina, S. Anastasova, A.M. Pavlov, P. Vadgama, A.G. Skirtach, G.B. Sukhorukov, Chemosensors and biosensors based on polyelectrolyte microcapsules containing fluorescent dyes and enzymes. Anal. Bioanal. Chem. **405**, 1559–1568 (2013)
58. J.V. Edwards, N. Prevost, K. Sethumadhavan, A. Ullah, B. Condon, Peptide conjugated cellulose nanocrystals with sensitive human neutrophil elastase sensor activity. Cellulose **20**, 1223–1235 (2013)
59. E. Osti, Skin pH variations from the acute phase to re-epithelialization in burn patients treated with new materials (Burnshield®, semipermeable adhesive film, Dermasilk®, and Hyalomatrix®). Non-invasive preliminary experimental clinical trial. Ann. Burns Fire Disaster **21**(2), 73–77 (2008)
60. Fraunhofer-Gesellschaft, *Research News Nov 02 2010*. Consulted on the 7th of September 2013, http://www.fraunhofer.de/en/press/research-news/2010/11/dressing-indicates-infections.html (2010)
61. N. Bhardwaj, S.C. Kundu, Electrospinning: a fascinating fiber fabrication technique. Biotechnol. Adv. **28**, 325–347 (2010)
62. Y.-F. Goh, I. Shakir, R. Hussain, Electrospun fibers for tissue engineering, drug delivery, and wound dressing. J. Mater. Sci. **48**, 3027–3054 (2013)
63. P. Zahedi, I. Rezaeian, S.-O. Ranaei-Siadat, S.-H. Jafari, P. Supaphol, A review on wound dressings with an emphasis on electrospun nanofibrous polymeric bandages. Polym. Adv. Technol. **21**, 77–95 (2010)
64. S. Agarwal, J.H. Wendorff, A. Greiner, Use of electrospinning technique for biomedical applications. Polymer **49**, 5603–5621 (2008)
65. C.H.T. Vu, K. Won, Novel water-resistant UV-activated oxygen indicator for intelligent food packaging. Food Chem. **140**, 52–56 (2013)

Chapter 8
Electrospun Fluorescent Nanofibers for Explosive Detection

Anitha Senthamizhan and Tamer Uyar

Abstract Development of an instant on-site visual detection method for 2,4,6 trinitrotoluene (TNT) has become a significant requirement of the hour towards a secured society and a greener environment. Despite momentous advances in the respective field, a portable and reliable method for quick and selective detection of TNT still poses a challenge to many reasons attributing to inappropriate usage in subordinate areas and untrained personnel. The recent effort on the fluorescent based detection represents as one of easy method in terms of fast response time and simple on/off detection. Therefore, this chapter provides a consolidation of information relating to recent advances in fluorescence based TNT detection. Further, the main focus will be towards advances in the nanofibers based TNT detection and their reason to improving the sensitivity.

8.1 Introduction

The last few decades has experienced extensive urbanization and industrialization, resulting in the extraordinary mobilization of natural resources, ultimately causing environmental pollution. The pollution caused by the harmful explosives 2,4,6 trinitrotoluene (TNT) has been regarded as a ruinous element, looked upon as a security threat. TNT has been listed on the United States Environmental Protection Agency (US EPA) priority pollutants: a known mutagen, causing pancytopenia as a result of bone marrow failure [1]. One of the striking features of these aromatic nitro compounds has been their resistance to chemical or biological oxidation and hydrolysis attributed to the presence of electron-withdrawing nitro groups present in them [2–4].

A. Senthamizhan
UNAM-National Nanotechnology Research Centre, Bilkent University, Ankara 06800, Turkey

T. Uyar (✉)
UNAM-National Nanotechnology Research Centre, Bilkent University, Ankara 06800, Turkey

Institute of Materials Science & Nanotechnology, Bilkent University, Ankara 06800, Turkey
e-mail: uyar@unam.bilkent.edu.tr

Subsequently, owing to their resistance, their treatment and remediation techniques pose a serious threat. In addition, TNT has a very low mobility once adsorbed into the soil. As set by the US EPA, the maximum allowable concentration of these compounds in drinking water are about 2 parts-per-billion (ppb) and a resident soil screening level of 19 milligrams per kilogram (mg/kg) and an industrial soil screening level of 79 mg/kg [5]. Keeping in mind the security and safety of the public and the environment, investigations of arson, post-blast residues and locating the buried land mines is the need of the hour. This has grabbed the attention and interest for the detection of nitroaromatic explosives in the recent years [6, 7]. Following the speculation and the need, numerous methods have been devised for the detection of TNT, namely gas and liquid chromatography, mass spectrometry, surface plasmon resonance (SPR), surface enhanced Raman scattering (SERS), field-effect transistors, electrochemical methods and fluorescent and colorimetric methods [8–12]. These techniques, however, suppose to be time consuming, requiring bulky equipment with a tedious way of preparing the sample and usually require an expert operator. Apart from these methods, biological methods such as bioreactors, bioslurry treatment, and passive subsurface biobarriers have been put into use for developing efficacious method in reducing TNT concentrations [3–6].

Further, most of the methods and systems have the disadvantage of not being able to be downsized, lacking the ability to be performed in an automated high-throughput analysis. This calls in for some improvement in the sensing techniques, attracting considerable research efforts in recent years. Among the various techniques, fluorescence-based sensors appear simple, cost-effective, and highly sensitive detection modalities [13–17]. Adding to the list, miniaturized smart sensors based on one-dimensional (1D) nanostructures have gained much attention owing to their fast and high sensitivity towards enhanced adsorption. The large surface-to-volume ratio and the high dispersivity of the nanostructured materials essentially provide a large surface area for the adsorption and thus the enrichment of the analyte. This also contributes to the stable immobilization of a large amount of molecular recognition elements, resulting in the excellent improvement of the sensitivity and selectivity of the sensor. Some such one-dimensional (1D) nanomaterials are, silicon nanowires, metal oxide nanowires and carbon nanotubes have been utilized to fabricate TNT sensors [18–23]. This chapter will oversee the recent advances in the development of various techniques and approaches designed for TNT sensors. Furthermore, we will concentrate on the usage of electrospun nanofibers for the improved TNT sensing performance.

8.2 Colorimetric Detection

Colorimetric technique has received much attention due to its short response time, excellent sensitivity, simplicity and most convenient to execute which highly suitable for real time application. Until now, there have been a variety of quantum
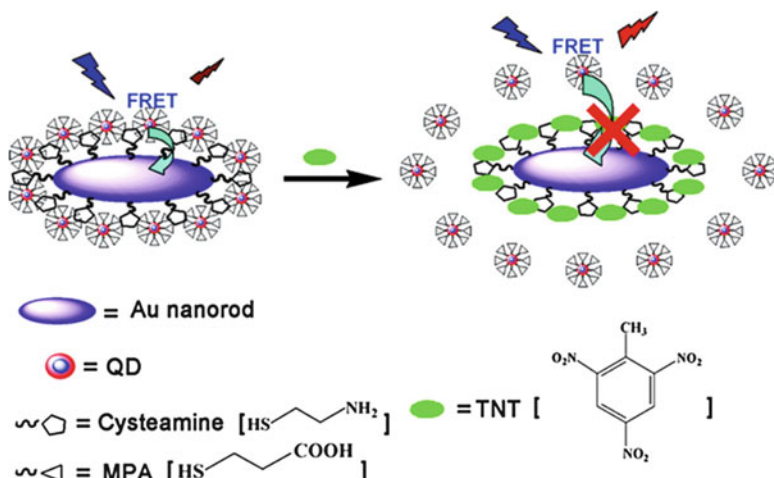
Fig. 8.1 Structure of the hybrid AuNR–QDs assembly and schematic illustration of FRET-based operating principle [24a]

dots used because of its size tunable emission spectrum and apparent improvement fluorescent dye molecules that they do not photobleach [15, 17, 19, 20]. The quenching processes are believed to occur via analyte induced aggregation or reversible electron transfer mechanism or chemical oxidation [21–23]. Recently Yunsheng Xia et al. designed turn-on fluorescent TNT sensor, consisting of gold nanorod (AuNR) and QDs for turn-on fluorescent sensing of TNT in near-infrared region [24a]. Further, they have modified with short thiol-molecules such as cysteamine and 3-mercaptopropionic acid (MPA), respectively to form hybrid assembly through amine-carboxyl attractive interaction. The reported design is shown in Fig. 8.1. In the presence of TNT, the preformed assembly gets broken because they can replace the QDs around AuNRs, based on the specific reaction of forming meisenheimer complexes between TNT and primary amines.

Thus, the forster resonance energy transfer (FRET) is switched off, and a more than 10 times fluorescent enhancement is obtained. The fluorescence turn-on is immediate, and the limit of detection for TNT is as low as 0.1 nM. Importantly, TNT can be well distinguished from its analogues due to their electron deficiency difference. Ellen R. Goldman demonstrated the self-assembled QD-based FRET sensor for the specific detection of the explosive TNT in aqueous environments [22]. The sensor consists of anti-TNT specific antibody fragments, appended with an oligohistidine sequence, specifically immobilized on the surface of Cadmium selenide- zinc sulfide (CdSe-ZnS) QDs. The use of an antibody fragment instead of a full antibody provides a more compact QD conjugate and is better suited for FRET, as distances between donor and antibody-bound acceptor are substantially reduced. The assembled conjugate produced a substantial rate of FRET when pre-assembled with a quencher-labeled TNT analogue. The unique optical properties of noble metal nanostructures have placed a vital role in the field of biological

Fig. 8.2 (**a**) Colorimetric visualization of TNT by using Au NPs (containing 500 nM cysteamine). TNT concentrations varied from 5×10^{-13} (2) to 5×10^{-9} M (6). (**b**) UV/Vis spectra of the Au NPs suspension (10 nM) containing 500 nM cysteamine in the presence of different concentrations of TNT: *red*, 0 M; *dark yellow*, 5×10^{-13} M; *yellow*, 5×10^{-12} M; *magenta*, 5×10^{-11} M; *cyan*, 5×10^{-10} M; *blue*, 5×10^{-9} M. *Inset*: plot of A_{650}/A_{520} against $\log C_{TNT}$ for TNT assay [21]
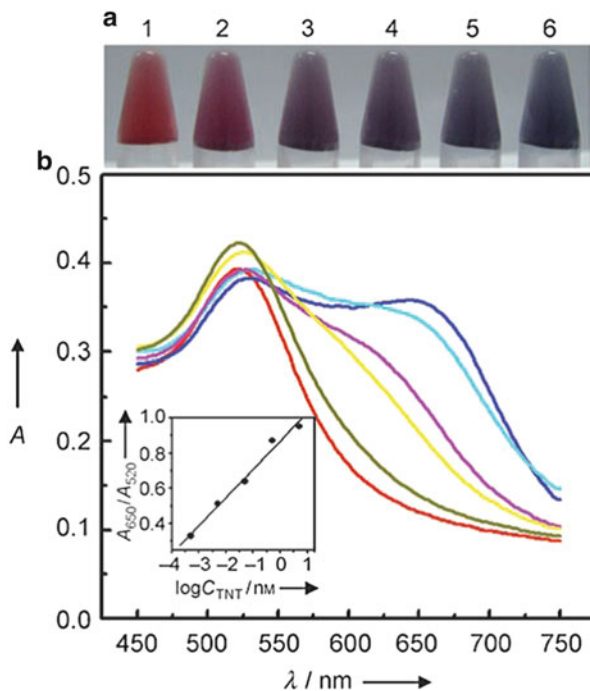
and chemical sensors and this has been known for long time [11, 22]. Ying Jiang reported a simple and sensitive method for the colorimetric visualization of TNT at picomolar levels by using gold nanoparticles [21]. In this study, cysteamine was used both as the primary amine and as the stabilizer for Au NPs to facilitate the Donor–Acceptor interaction between TNT and the primary amine at the Au NP solution interface for direct visualization of TNT, based on the TNT-induced colorimetric nano-gold aggregation phenomenon.

Figure 8.2 demonstrated the colorimetric visualization of TNT by using Au NPs. Initially, the cysteamine-stabilized Au NPs were well dispersed in distilled water and the color of the uniform suspension was wine red, because of the strong surface plasmon resonance of the Au NPs. The addition of TNT to the dispersion essentially leads to the aggregation of the cysteamine-stabilized Au NPs as a result of the Donor-Acceptor (D–A) interaction between TNT and cysteamine, and the color of the suspension is accordingly changed to violet blue. The clear change in the color of the suspension could be used for the direct colorimetric visualization of TNT. As such a color change can be readily seen by the naked eye.

Zhang K et al. prepared ratiometric fluorescence probe comprising dual-emission QDs and the establishment of its utility for instant, on-site, and visual identification of TNT particulates deposited on various package surfaces such as manila envelopes, synthetic fabric bags, and rubber materials [24b]. They have prepared two different sized Cadmium telluride (CdTe) QDs emitting red and green

fluorescence's, respectively; have been hybridized by embedding the red-emitting one in silica nanoparticles and covalently linking the green-emitting one to the silica surface, respectively, to form a dual-emissive fluorescent hybrid nanoparticle. The fluorescence of red QDs in the silica nanoparticles stays constant, whereas the green QDs functionalized with polyamine can selectively bind TNT by the formation of Meisenheimer complex, leading to the green fluorescence quenching due to resonance energy transfer. The variations of the two fluorescence intensity ratios display continuous color changes from yellow-green to red upon exposure to different amounts of TNT.

The response of the dual-wavelength fluorescence intensity of the green emission from the reactive small QDs is gradually decreased by the addition of TNT, whereas the intensity of the red emission from the encapsulated large QDs still remains constant (Fig. 8.3a). The changes in the intensity ratio of the two emission wavelengths result in a continuous fluorescence color evolution (Fig. 8.3, bottom panel). Clearly, even a slight decrease of the green emission intensity leads to an obviously distinguishable color from the original background with the naked eye. The advantages of the ratiometric fluorescence for visual detection can be confirmed by the comparison with the single fluorescence quenching experiments which are employed in most of the current fluorometry for TNT detection (Fig. 8.3b). It can be seen that, unlike the ratiometric probe, the fluorescence images of the pure green QDs are hard to distinguish among the other images by the naked
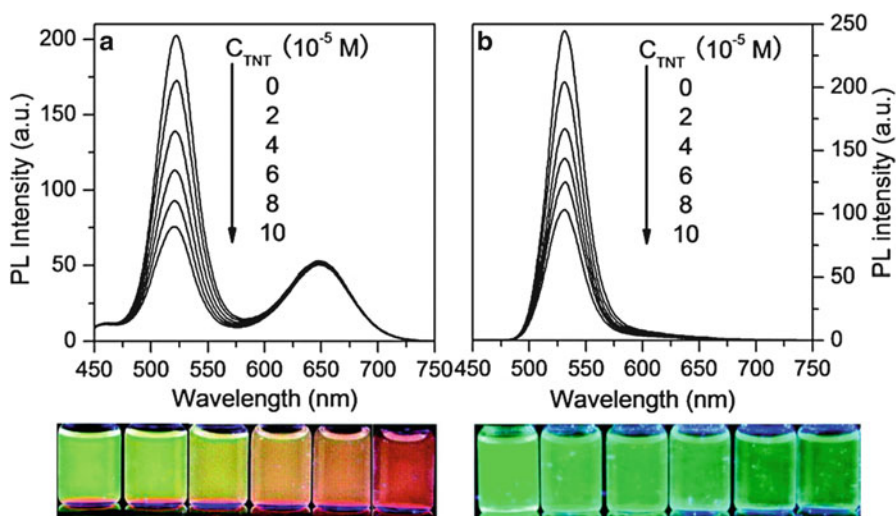
Fig. 8.3 Dependence of the fluorescence spectra ($\lambda_{ex} = 365$ nm) of (**a**) the ratiometric probe and (**b**) the *pure green* QDs modified with polyallylamine upon the exposure to different amount of TNT. (*Bottom panel*) Comparison between the fluorescence colors of the ratiometric probe solutions (*left*) and the *pure green* QDs solutions (*right*) after exposure to TNT. The concentrations of TNT from *left* to *right* are 0, 2×10^{-5}, 4×10^{-5}, 6×10^{-5}, 8×10^{-5}, and 10×10^{-5} mol/L, respectively. All the photos were taken under a 365 nm UV lamp [24b]

eye. The comparison clearly shows that the ratiometric fluorescence method is more sensitive and reliable for visual detection of TNT than a single fluorescence quenching method, although the intensity of the green emission decreases at the same level.

The collective oscillation of surface electrons on metal nanostructured materials has been leveraged for the amplification of optical processes in Raman scattering. The phenomenon of surface enhanced Raman scattering (SERS) is generally explained by a combination of an electromagnetic (EM) mechanism describing the surface electron movement in the substrate and a chemical mechanism related to charge transfer (CT) between the substrate and the analyte molecules. The possibility of observing raman signals, which are normally very weak, with enhancements of the order of and the unique ability to obtain molecular recognition of an analyte at very low concentrations in aqueous environment allow SERS to be unique for ultrasensitive biological and chemical analysis and environmental sensing. Based on unique SERS properties of cysteine modified gold nanoparticle, Samuel S. R. Dasary reported cysteine modified gold nanoparticle based miniaturized, inexpensive ultrasensitive SERS probe, for highly sensitive and selective screening of TNT from aqueous solution in 2 picomolar (pM) level [25]. Due to the formation of meisenheimer complex between TNT and cysteine, gold nanoparticles undergo aggregation in the presence of TNT via electrostatic interaction between meisenheimer complex bound gold nanoparticle and cysteine modified gold nanoparticle illustrated in Fig. 8.4. The reported SERS assay is rapid and takes less than 10 min from TNT binding to detection and analysis.

8.3 Smart Hybrid Sensor

The reported successful techniques being mostly solution-based have resulted in stability problems, limiting their potential ability and practical applications. Moreover, the response towards analyte predominantly monitored in situ, with respect to optical responses (color changes, intensity variation, shift in the emission spectra) making the sensor inefficient. This necessitates a need to develop a novel and modernistic method to fabricate a solid template-based sensor on a large scale for technological applications. A very few methods effectively demonstrated the sensing permanence of TNT in real time application [16, 26–36]. For example Daming Gao reported a resonance energy transfer-amplifying fluorescence quenching at the surface of silica nanoparticles for the ultrasensitive detection of TNT in solution and vapor environments [17]. They have modified the surface of silica nanoparticles with fluorescent dye and amine ligands. The formed hybrid can specifically bind TNT species by the charge-transfer complexing interaction between electron-rich amine ligands and electron-deficient aromatic rings.

The resultant TNT–amine complexes bound at the silica surface can strongly suppress the fluorescence emission of the chosen dye by the FRET from dye donor to the irradiative TNT–amine acceptor through intermolecular polar–polar
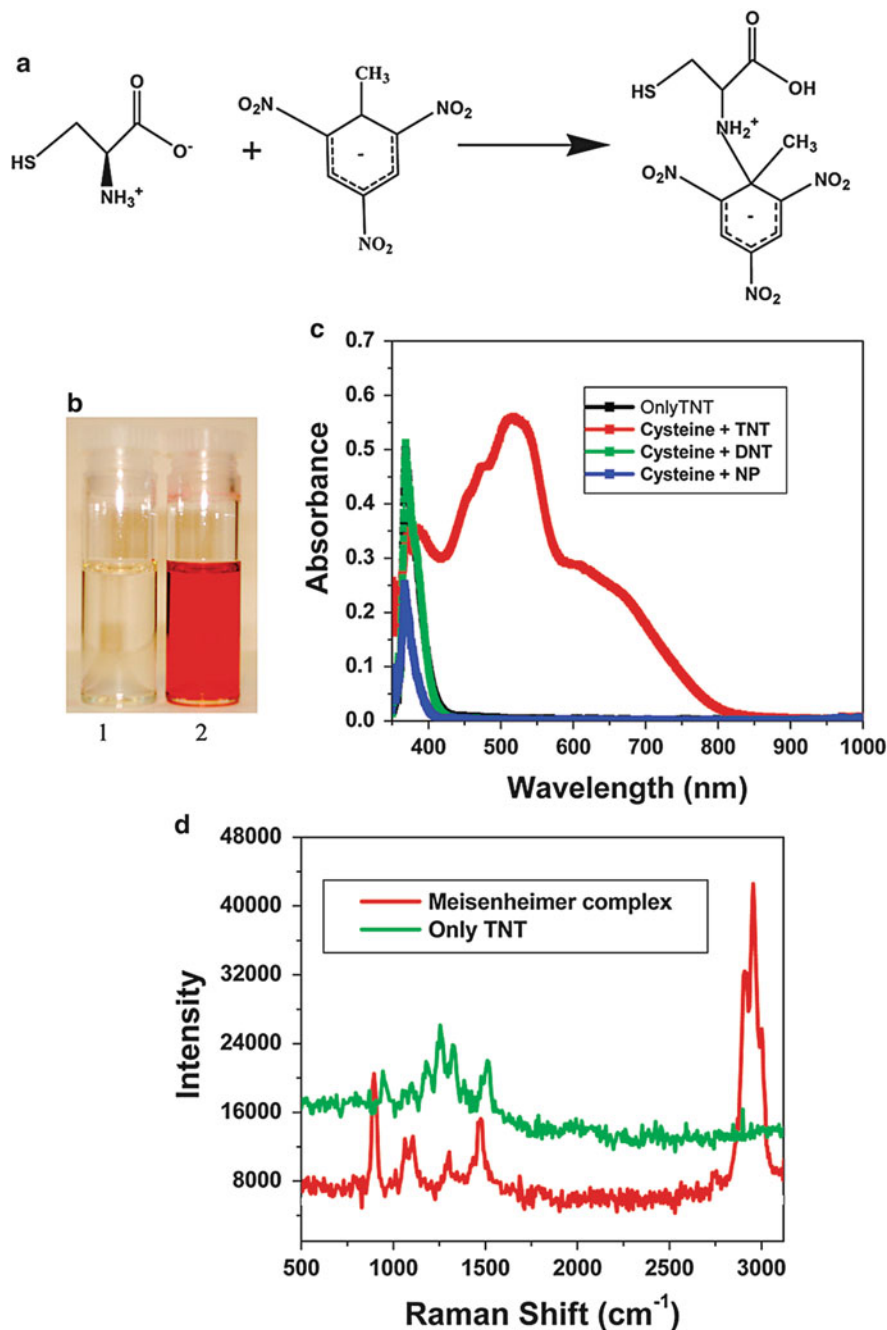
Fig. 8.4 (**a**) Schematic representation of the formation of Meisenheimer complex between cysteine and TNT, (**b**) Photograph showing how TNT changes the color when it forms Meisenheimer complex with cysteine (10 mM cysteine + 1 mM TNT), (1) 1 mM only TNT, (2) Meisenheimer complex after addition of 10 mM cysteine in 1 mM TNT. (**c**) absorption spectra demonstrating new peaks at 520 and 630 nm due to the formation of Meisenheimer complex in presence of 1 mM TNT. (**d**) Normal Raman spectra from 10 mM TNT and Meisenheimer complex
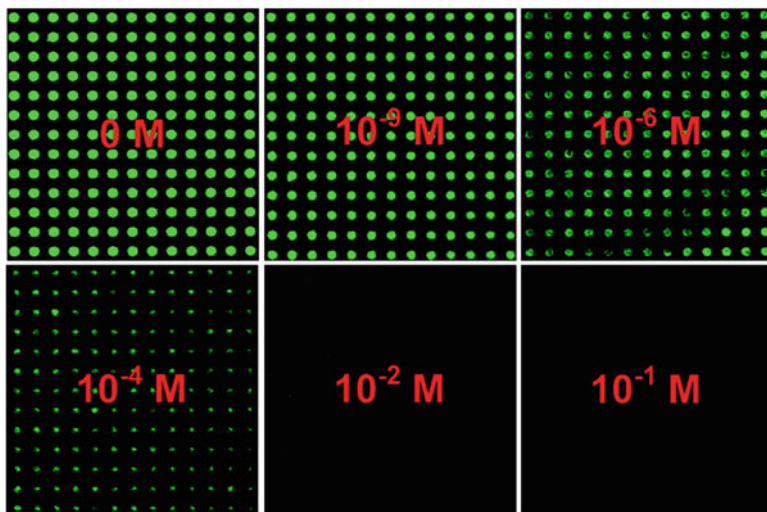
Fig. 8.5 Regular array assembly of fluorescein isothiocyanate (FITC) -NH$_2$-silica nanoparticles on the silicon wafer with etched microwells. Confocal fluorescence images show the evolution of the brightness and size of fluorescent dots on dropping 10 μL of TNT solution of different concentrations [17]

interactions at spatial proximity. Figure 8.5 shows the colorful fluorescence images under laser excitation on a confocal microscope. The fluorescent dot array is highly regular and extremely bright, and all microwells are completely filled with the fluorescent silica particles. The evolution of the brightness and size of fluorescent dots is clearly observed by dropping only 10 μL of TNT solution of different concentrations onto the 1×1 cm^2 sized chip. The brightness and size of fluorescent dots become smaller and smaller and ultimately disappear with the increase of concentration from 1×10^{-9} to 10^{-1} M. However, the nanoparticle chip seems to have a more sensitive response to the ultratrace amount of TNT than the nanoparticle suspensions. As shown in the Fig. 8.5, 10 μL of 1 nM TNT can result in a surprising reduction of the brightness and size of fluorescent dots under confocal microscope. It is thus estimated that 2 pg of TNT can clearly be detected using the nanoparticle-assembled chip. Moreover, one of the main advantages of the detection chips is that less amount of sample is needed for an ultratrace-level detection, due to the collective effect of particle assembly in the microwells. Therefore, the microchips can be used as a convenient indicator of TNT residues.

Kalathil K. Kartha reported that a fluorescent organogelator exhibits superior detection capability for TNT in the gel form when compared to that in the solution state [37]. The gel when coated on disposable paper strips detects TNT at a record attogram (ag, 10^{-18} g) level (12 ag/cm^2) with a detection limit of 0.23 ppq. The contact-mode response to TNT by the filter paper strips was tested by placing TNT
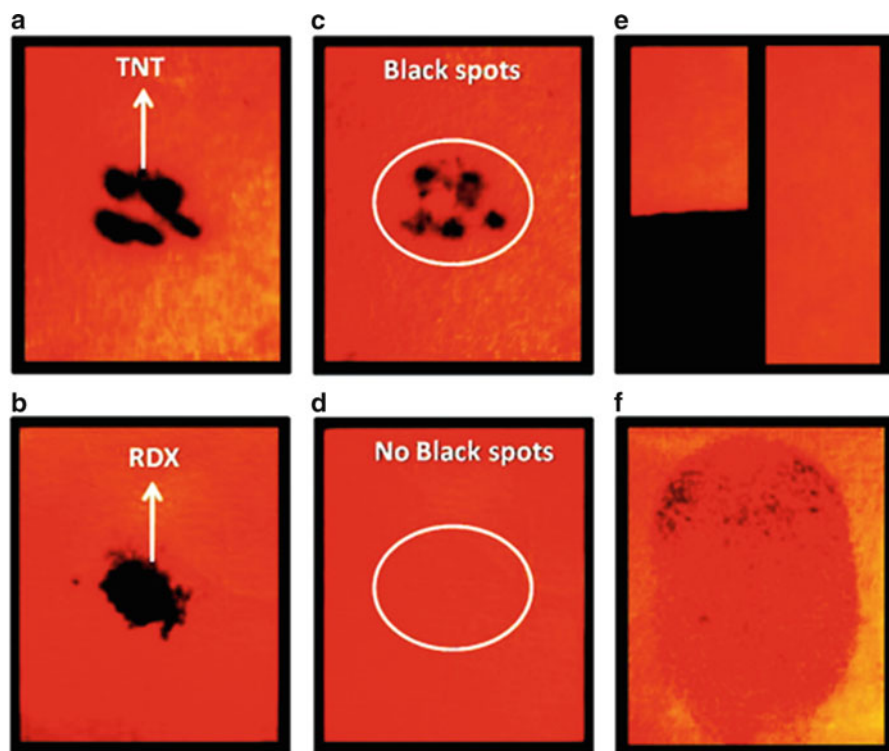
Fig. 8.6 Photographs of perfluoroarene-based gelator coated test strips under different experimental conditions. (**a**) TNT and (**b**) RDX crystals on *top*. (**c, d**) Corresponding photographs upon removal of the crystals after 5 s. (**e**) After dipping into solutions of TNT (*left*) and RDX (*right*) in acetonitrile (1×10^{-3} M). (**f**) Thumb impression after rubbing with TNT crystals (All photographs were taken under 365 nm UV illumination [37])

crystals over a test strip for 5 s, resulting in black spots upon illumination with a UV lamp (Fig. 8.6a, c). The same experiment was repeated with 1,3,5-trinitro-1,3,5-triazinane (RDX), and no spots corresponding to fluorescence quenching were found (Fig. 8.6b, d).

In addition, the test strips were dipped into acetonitrile solutions of TNT and RDX, and fluorescence quenching was observed only in the case of TNT (Fig. 8.6e). In another experiment, a human thumb was rubbed with TNT, and then all visible TNT particles were brushed off, followed by pressing the thumb against a test strip. The fingerprint of the thumb could be seen as quenched luminescence when illuminated with UV light (Fig. 8.6f). As a control experiment, the thumb (gloved) which was not contaminated with TNT was pressed on the test strip, and no fingerprint was seen. These images illustrate the utility of the gel-coated test strips for the on-site instant visualization of trace residues of TNT present on a specimen. Christina M. Gonzalez also reported the dodecyl groups
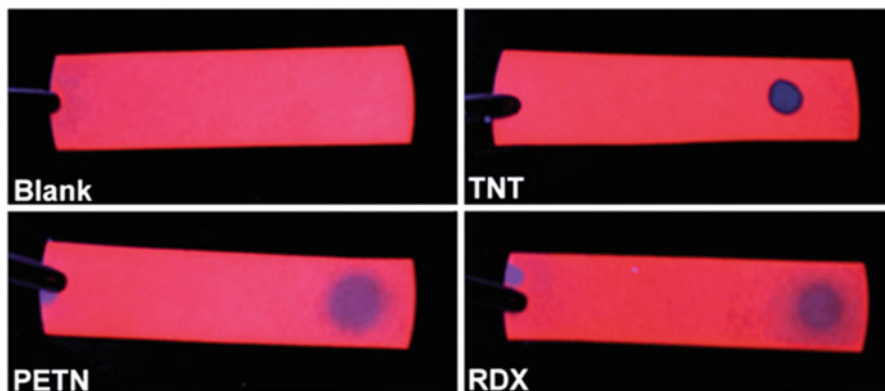
Fig. 8.7 Images of Si-NC coated filter paper under a handheld UV-lamp without the presence of nitrocompounds and in the presence of solutions of TNT, PETN, and RDX, as indicated [38]

functionalized luminescent silicon nanocrystals (Si-NCs) for nitroexplosive detection [38]. They found that Si-NC luminescence was quenched upon exposure to nitroaromatics via an electron transfer mechanism and a straightforward paper-based Si-NC sensor was developed which is found to be sensitive to solution, vapor, and solid phase nitroaromatics, as well as solution borne RDX and pentaerythritol tetranitrate (PETN) as illustrated in Fig. 8.7.

The meticulous animals changes their skin color to communicate, to express mood, for camouflage, or to respond to environmental changes due to their various nano and microscale components in their tissues [39–41]. Inspired by nature, sensors are being developed that change color in response to target chemicals by employing biomimetic structures and mechanisms. Jin-Woo Oh reported the self-assembly of genetically engineered viruses (M13 phage) into target-specific color-imetric biosensors [42]. The sensors are composed of phage-bundle nanostructures and exhibit viewing-angle independent color, similar to collagen structures in turkey skin.

On exposure to various volatile organic chemicals, the structures rapidly swell and undergo distinct color changes. Furthermore, sensors composed of phage displaying TNT binding peptide motifs identified from a phage display selectively distinguish TNT down to 300 ppb. As the concentration of applied TNT vapor increased, the TNT–Phage litmus showed pronounced color changes due to structural changes induced by TNT binding illustrated in Fig. 8.8. Moreover they confirmed that TNT binding to TNT–Phage litmus through Fourier transform–infrared spectroscopy analyses. They analyzed the specificity of the phage matrices, by comparing the sensing performance of DNT and MNT. On exposure to TNT (20 ppm), DNT (20 ppm) and MNT (300 ppm) vapor, the TNT–Phage litmus showed selective response to the TNT molecules, more than three and five times higher compared with DNT and MNT, respectively (Fig. 8.8c).
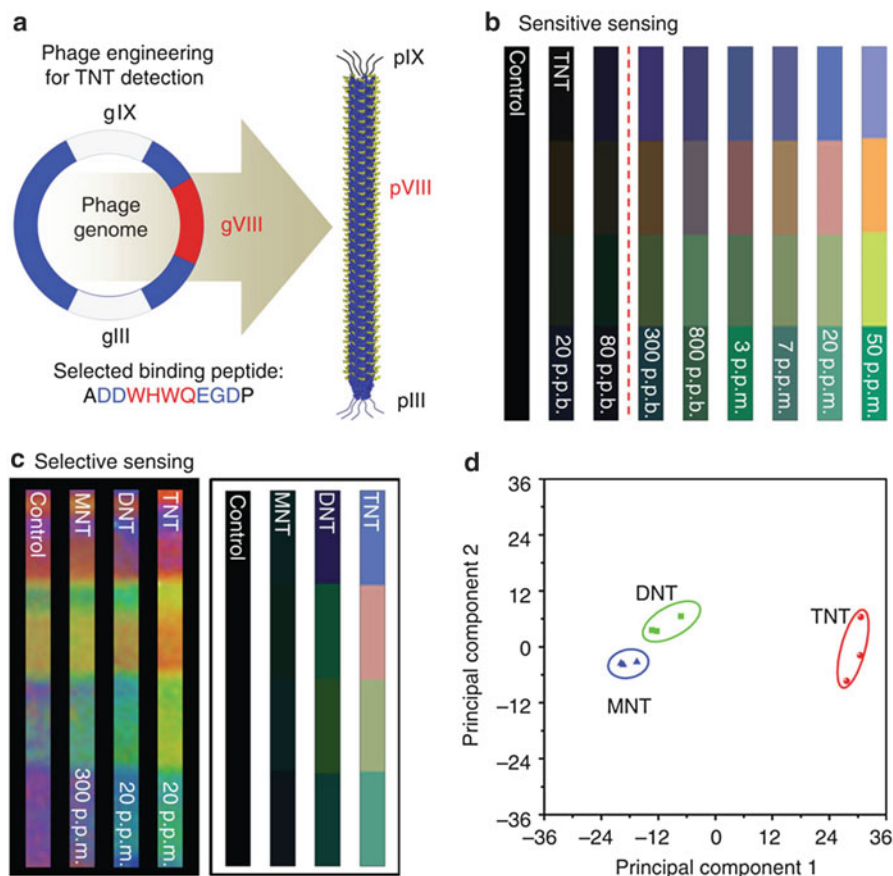
Fig. 8.8 (**a**) Two thousand and seven hundred copies of the TNT-binding receptor identified by directed evolution are genetically engineered onto the surface of M13 phage (TNT phage). (**b**) Using the iPhone-based analysis system, TNT is detectable down to 300 ppb in the gas phase. The *dashed redline* indicates the sensitivity limit of the TNT–Phage litmus against TNT. (**c**) Photos and processed color fingerprints from the TNT–Phage litmus after TNT, DNT and MNT exposure. The TNT–Phage litmus selectively detects the target TNT (20 ppm) over other molecules with similar chemical structures, such as DNT (20 ppm) and MNT (300 ppm). (**d**) Principal component analysis plot of the color changes resulting from the exposure of the Phage litmus to TNT, DNT and MNT [42]

8.3.1 Fluorescent Electrospun Nanofibers for Explosive Detection

Recently, much attention has been paid to the development of novel sensing materials for explosives in terms of improved sensitivity and selectivity [43]. However, it should be notable that multiple procedures are still required to fabricate such fascinating materials with controlled one dimensional structure. Compared with various chemical and physical methods have been developed so far, fluorescence-

based sensing performance attracts much consideration due to its high sensitivity and simplicity. However, the required multi-step processes restrict their practical applications in somewhat. To overcome this limitation, the researchers were adopted electrospinning technique to prepare one dimensional nanofiber and extended to incorporate various kinds of active materials in to them [44–51]. Yanke Che reported that nanoporous nanofibers fabricated from carbazole-based tetracycles allow for slow diffusion and strong encapsulation of TNT molecules within the nanopores, thus resulting in postexposure fluorescence quenching behavior, which enables selective detection of TNT among other common nitroaromatic explosives and oxidizing reagents [52].

Feng Wang demonstrates a new electrochemical method for the detection of ultratrace amount of TNT with synthetic copolypeptide-doped polyaniline nanofibers [53]. The copolypeptide, comprising of glutamic acid (Glu) and lysine (Lys) units, is in situ doped into polyaniline through the protonation of the imine nitrogen atoms of polyaniline by the free carboxylic groups of Glu segments, resulting in the formation of polyaniline nanofibers of emeraldine salt. The free amino groups of Lys segments at the surface of nanofibers provide the receptor sites of TNT through the formation of charge–transfer complex between the electron-rich amino groups and the electron-deficient aromatic rings.

The schematic representation of the structure of poly(Glu-Lys)-doped Polyaniline (PANI) nanofibers and their specific interaction with TNT molecules is illustrated in Fig. 8.9. Adsorptive stripping voltammetry results demonstrate that
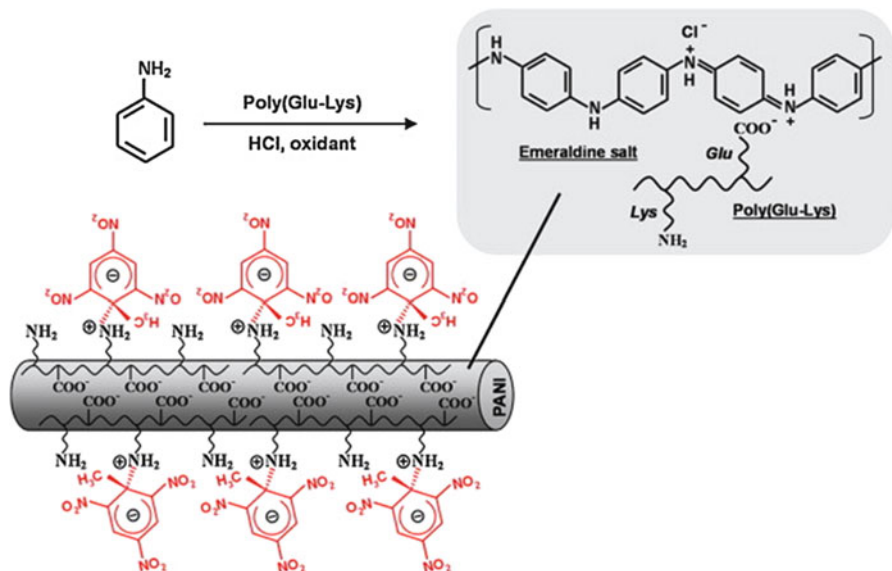
Fig. 8.9 Schematic illustrations for synthesis and structure of poly(Glu-Lys)-doped PANI nanofibers. The *bottom-left inset* shows the specific interaction between the doped nanofiber and TNT molecules through the formation of charge–transfer complex [53]

the poly(Glu-Lys)-doped nanofibers confined onto glassy carbon electrodes exhibit a remarkable enriching effect and thus sensitive electrochemical response to TNT with a linear dynamic range of 0.5–10 μM and a detection limit down to 100 nM.

It is well known that solid state sensing material for highly desired for vapor detection. In most cases, the performance is readily depends on the film thickness, which might be due to the slow diffusion of analyte vapors into the films. To reduce the dependence of sensing performance on film thickness, a highly porous nanostructure could be a solution, mainly attributed to their large surface to volume ratio, inherently high porosity, and easy accessibility of sensing materials. In this regard, electrospinning has emerged in recent years as a simple and cost-effective approach to fabricate nonwoven nanofibrous polymer composite films with high porosity and flexibility, which has great potential for enhanced explosives detection.

Ying Wang developed the electrospun fluorescent nanofibrous membrane of pyrene/polystyrene/tetrabutylammonium hexafluorophosphate (pyrene/PS/TBAH) via electrospinning for the detection of ultra-trace nitro explosive vapors and buried explosives by naked eye under UV excitation [54]. The schematic illustration of experimental setup for evolution of electrospun pyrene/PS/TBAH films towards nitro-explosive vapors is presented in Fig. 8.10. Under UV light, the fluorescence quenching upon the exposure of the as-electrospun film to various sub-equilibrium vapors could be observed by naked eye (Fig. 8.10c). The dark spots on the luminescent sensing films indicate the quenching of the as-electrospun pyrene/PS/TBAH by analyte vapors. Clearly, all nitramine and nitrate ester explosives could be discriminated by their sub-equilibrium vapors generated from nanogram residues. The sub-equilibrium vapors from 10 ng of RDX and PETN could produce acceptable dark quenching circles and visualized by naked eye after 20 min, and down to 1 ng of RDX and PETN could be visualized with an extended exposure time of 2 h. The time for octahydro-1,3,5,7-tetranitro-1,3,5,7-tetrazocine (HMX) detection took considerably longer time (2 h for 1 μg, and 12 h for 1 ng) due to its extremely low volatility.

The performance of the developed sensor is very impressive, considering the fact that the tested vapors were generated from freshly spotted explosive residues in an open environment with concentrations much lower than their equilibrium or saturated vapor concentration (e.g. 0.1 ppt for HMX, 5 ppt for RDX, 7 ppt for PETN, and 74 ppt for Tetryl) and the detection was conducted without the use of any piece of advanced instruments. The observed dramatic quenching in its fluorescence emission is due to the high binding affinity between the electron-deficient nitro explosives and the sensing film.

To clean up the unexploded landmines, direct detection of buried explosives has emerged as a promising need. In this regard, they extended the application of as-electrospun pyrene/PS/TBAH nanofibrous membrane for buried explosives (2,4-DNT). Figure 8.11a–d shows the detection of explosives buried in soil using electrospun pyrene/PS/TBAH nanofibrous film coated filter paper. Due to the leaked explosive molecules from buried explosives, a strong fluorescence quenching can be observed in 10 min by naked eye under UV light.
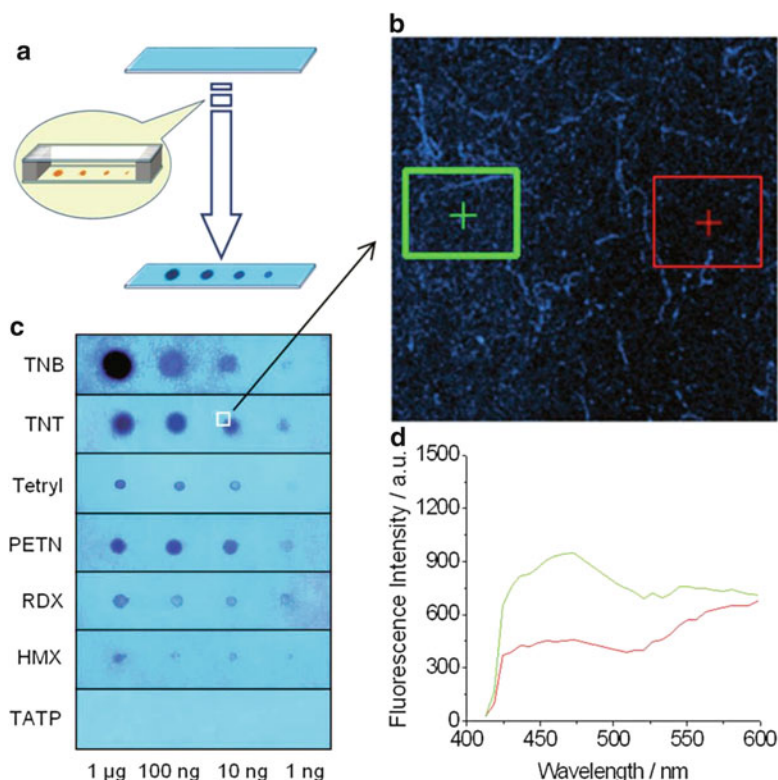
Fig. 8.10 (**a**) Schematic illustration of experimental setup for electrospun pyrene/PS/TBAH films towards sub-equilibrium nitro-explosive vapors; (**b**) the fluorescence microscopy image (λ ex 343 nm, λ em 470 nm) at the edge of the quenching spot in (**c**); (**c**) UV excited (λ ex 275 nm) images of 3- μ m thick films after exposure to sub-equilibrium vapors generated from 1 μ g, 100 ng, 10 ng, and 1 ng solid analytes; (**d**) emission profile (λ ex 343 nm) of the square area outside (*green*) and inside (*red*) the quenching spot in (**b**) [54]

The quenching spots indicated the position of buried explosives, while other parts without explosives are still glowing. It is worth noting that the electrospun sensing film on filter paper does not directly contact with soil samples. Therefore, the quencher is solely the leaked 2,4-DNT vapor that penetrates through the soil and filter paper. In recent past, Metal-organic frameworks (MOFs) have been gained enormous attention due to their distinct features including high porosity, large surface area, and flexible skeleton [55, 56]. Moreover, considerable attention also paid to produce MOF membranes by growing continuous MOF crystals on porous substrates. Thereby, the development of chemical sensors based on MOFs has drawn considerable attention due to their flexible structures responsive to external stimulation. Yunxia Xu reported the example of using electrospun nanofibrous mats as skeletons to produce MOF membranes, and demonstrated the great potentials of
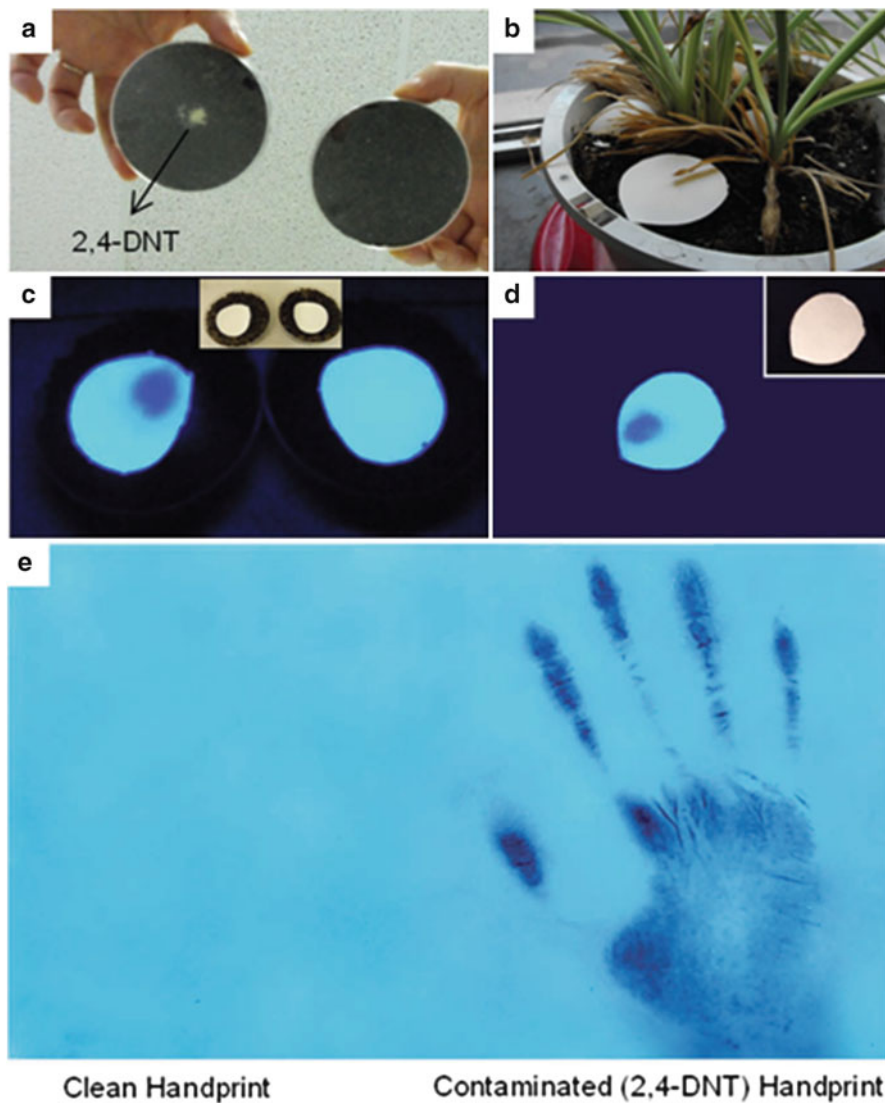
Fig. 8.11 (**a–d**) Above-ground detection of buried 2,4-DNT using the electrospun pyrene/PS/ TBAH films (3- μ m thick, figures are taken at 30 min exposure time for a better visibility): (**a**) Optical images of soil with (*left*) and without (*right*) buried 2,4-DNT in Petri dishes; (**b**) optical images of soil with buried DNT in a flower pot; (**c**) UV (λ ex 275 nm) excited image of electrospun sensing films on buried DNT in a Petri dish after 30 min exposure time; (**d**) UV (λ_{ex} 275 nm) excited image obtained from the test of electrospun sensing film on 2,4-DNT buried in a flower pot after 30 min. Insets in (**c**) and (**d**) are the bright-field images of same membranes after detection; (**e**) detection of particulate explosives contaminated hand using the electrospun pyrene/PS/TBAH films [54]

such nonwoven fiber mats as a new kind of porous supports in MOF research field [57]. Macroporous network structure of Zn-MOF/PST-1 thin films prepared by using electrospinning technique.

The secondary growth technique was further developed to strongly anchor Zn-MOF seed crystals on porous supports Zn-MOF/PST-1 to form Zn-MOF/PST-2 thin films. Figure 8.12 illustrates characterization of Zn-MOF/PST-1 and Zn-MOF/PST-2. Following this, they were performed the fluorescence quenching experiments to demonstrate the ability of Zn-MOF/PST-2 thin films for detection of
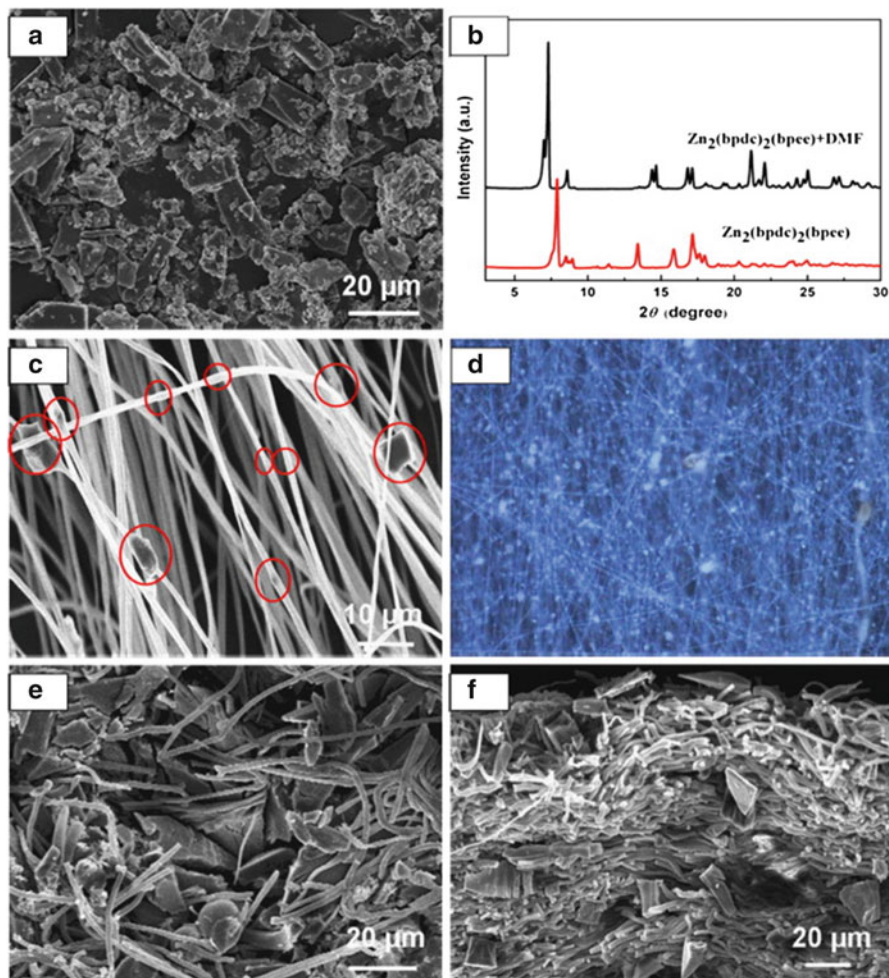
Fig. 8.12 (**a**) SEM image and (**b**) XRD pattern of the [Zn$_2$(bpdc)2(bpee)] crystals; (**c**) SEM image and (**d**) fluorescent image of Zn-MOF/PST-1 thin film; (**e**) *top* view and (**f**) cross-sectional SEM image of Zn-MOF/PST-2 thin film by secondary growth [57]
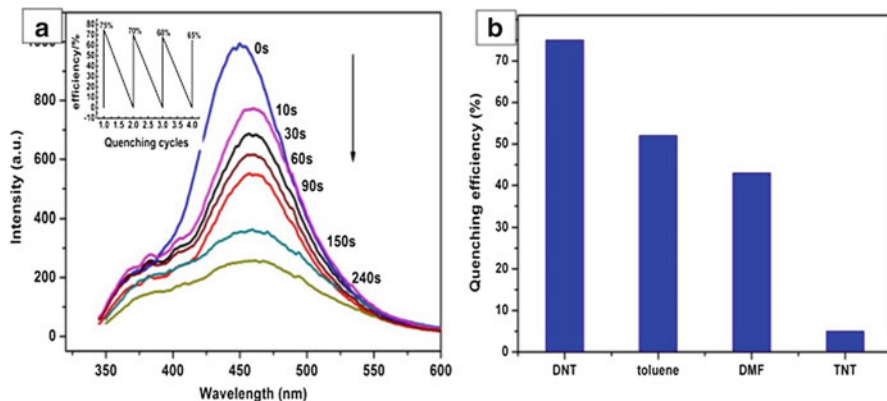
Fig. 8.13 (**a**) Fluorescence quenching of Zn-MOF/PST-2 films upon exposure to DNT vapor from 0 to 240 s, and (**b**) the percentage of fluorescence quenching of Zn-MOF/PST-2 films with four different vapors: DNT, toluene, DMF, TNT [57]

nitroaromatic explosives. Fluorescence response to vapors of DNT and TNT was certained by inserting the prepared films into glass vials (10 mL) which containing 1.5 g solids DNT and TNT powder and cotton gauze. Figure 8.13a shows the fluorescence intensity evolution of Zn-MOF/PST-1 film upon exposure to saturated DNT vapor for 60 s. About 5 % fluorescence quenching happened in the first 10 s, and finally 24 % quenched after 60 s. According to fluorescence quenching data shown in Fig. 8.13b, the quenching intensity of Zn-MOF/PST-2 film was increased to 42 % after exposure for 60 s. The higher quenching efficiency attributes to more particles on the surface and inside of Zn-MOF/PST-2 film, compared with particles only inside of the Zn-MOF/PST-1 film.

Yang et al. developed a tetrakis(4-methoxylphenyl)porphyrin (TMOPP) and polystyrene based electrospun nanofibrous film sensor for detection four nitroaromatic explosives [58]. Porphyrins as an obvious class of electron-donating dyes are very attractive for sensing devices. The sensing of explosive vapors were performed by keeping the 3 mg/3 μL of explosives at saturation vapor pressure in a 1 cm quartz cell with the fabricated sensing film.

Time-dependent fluorescence quenching was measured over 2 h of exposure towards the saturated explosive vapors in air. At room temperature the vapor pressures of DNT, TNT and picric acid (PA) are 280 ppb, 4 ppb, and 0.0077 ppb, respectively. After 40 min, the percentage of fluorescence quenching was 38 %, 17 %, 4 %, and 2 % for DNT, DNP, TNT and PA vapors, respectively. Because the vapor pressure of DNT is about 70-fold and 4×10^4 fold that of TNT and PA, respectively, the quenching percentage with TNT or PA vapor is thus surprisingly larger than that expected from the relative vapor pressure of these explosives. That means TMOPP-based electrospun nanofibrous films have the potential to

sensitively detect down to several parts-per-billion of TNT vapor or several parts-per-trillion of PA vapor in the atmosphere. The ultra sensitive detection of TNT is demonstrated by using porphyrinated polyimide nanofibers by Lv YY [59]. The covalent bonding of porphyrin fluorophores with polyimide main chains reduces the aggregation-caused fluorescence self-quenching of porphyrin and improved the physicochemical stability of the polyimide nanofibers.

Besides TNT, 2,4-dinitrotoluene (DNT), 2,4,6-trinitrophenol (PA) and nitrobenzene (NB) could also quench the fluorescence of the porphyrinated nanofibers, but the quenching efficiency is much lower than that of TNT. The time-dependent fluorescence quenching efficiency of the porphyrinated nanofibers exposed to different analytes is presented in Fig. 8.14. For those explosive vapors, TNT, DNT, NB and PA, the quenching efficiencies are in the order of TNT > DNT > NB > PA. Conjugated polymers (CP) have been recognized as one of the high-performance sensing probes due to their excellent molar absorptivity and fluorescence quantum. The fluorescence self-quenching behavior by self aggregation nature of CPs is a major disadvantage counteracting their application in chemical sensors.

Therefore, the combination of electrospinning with fluorescent CPs offers the potential application as a new and universal fabrication approach for chemosensory devices. Long Y et al. prepared electrospun nanofibrous film doped with a fluorescent conjugated polymer P as a sensory device for detection of the explosive
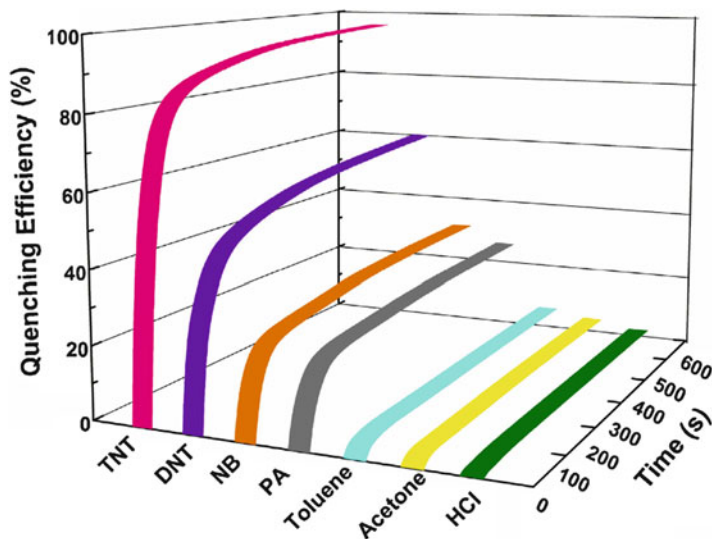
Fig. 8.14 Time-dependent fluorescence quenching efficiency of the porphyrinated nanofibers for different analytes (saturated vapors, except 30 ppm for HCl) [59]
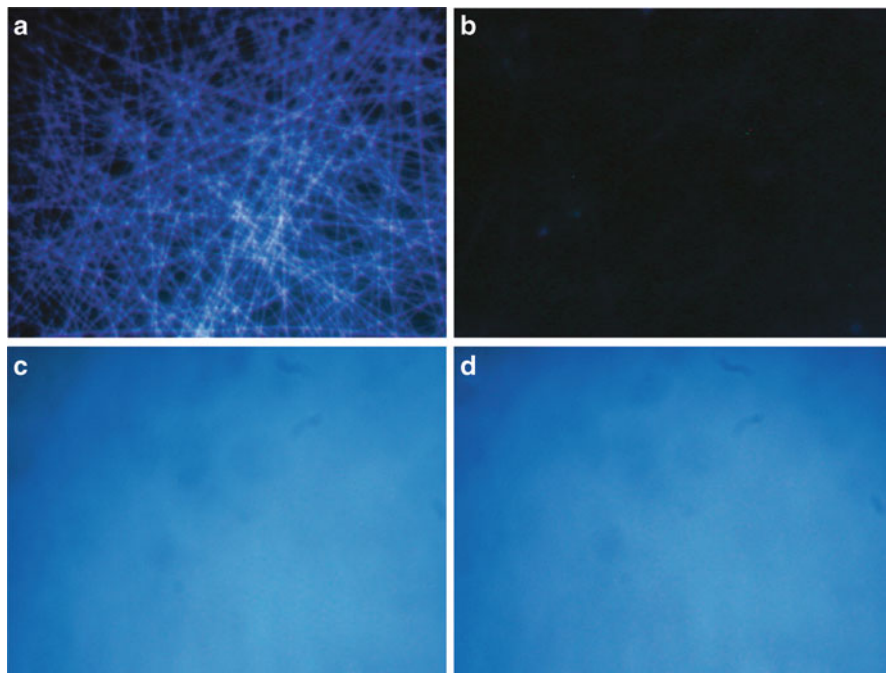
Fig. 8.15 Fluorescence images of electrospun nanofibers with porogen (**a**) before and (**b**) after being exposed to DNT vapor for 30 min and dense spin casting film (**c**) before and (**d**) after being exposed to DNT vapor for 30 min [60]

2,4-dinitrotoluene (DNT) [60]. Polymer P obtained through a sonogashira cross-coupling polymerization. The electrospinning technique effectively reduced aggregation and fluorescence self-quenching of the conjugated polymers. The efficient quenching towards DNT was clearly observed by visible using fluorescence microscopy (Fig. 8.15). In a control experiment, the fluorescence images of spin-casting film before and after the DNT exposure were taken and shown in Fig. 8.15. There was hardly any difference observed from this densely packed sensing film. And also Liao et al. prepared the blue light-emitting oligotriphenylene nanofibers by oxidizing triphenylene using ferric chloride, as fluorescent sensors for detecting traces of nitro-based explosives including nitromethane, nitrobenzene, and 2,4,6-trinitrophenol [61]. Shengyang Tao adopted a simple sol–gel chemistry and the electrospinning technique for the production of nanocomposite fibers [62]. Bridged organosilane was used as a cross-linker to form a viscous gel solution, and without the addition or help of polymer, generally used in the literature, nanocomposite fibers were conveniently fabricated at room temperature and were demonstrated as
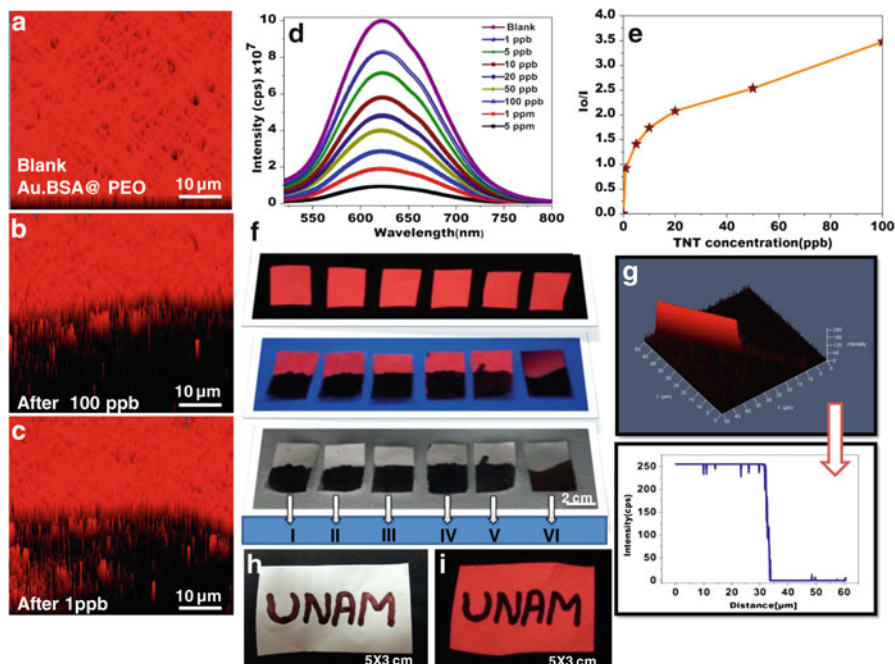
Fig. 8.16 (**a–c**) CLSM images of the Au.BSA@PEO-NFM on glass slides before (**a**) and after (**b–c**) exposure to TNT (λext $=488$ nm, $20\times$ magnification) (**d**) Fluorescence spectra of Au. BSA@PEO-NFM upon treatment of various concentration of TNT (**e**) The relative fluorescence intensity (I_0/I, where I and I_0 are the fluorescence intensity in the presence and absence of TNT, respectively) versus the TNT concentration (**f**) Photograph of the fluorescence quenching of Au. BSA@PEO-NFM strips by different concentration of TNT on contact mode when viewed under UV and white light (*I*-1 ppm, *II*-100 ppb, *III*-50 ppb, *IV*-20 ppb, *V*-10 ppb, *VI*-1 ppb). (**g**) TNT treated Au.BSA@PEO-SNF and their fluorescence intensity profile. (**h–i**) Au.BSA@PEO-NFM based TNT sensor for visual detection by hand writing on the Au.BSA@PEO-NFM using TNT solution as ink [63]

novel fluorescence-based chemosensors for the rapid detection of trace vapor (10 ppb) of explosive.

Anitha et al. demonstrated selective, on-the-spot detection of TNT at sub ppt level using a single nanofiber embedded fluorescent gold clusters hybrid system [63]. They have incorporated red fluorescent BSA-capped gold clusters into the PEO nanofibers termed as Au.BSA@PEO-NFM using a simple and straightforward electrospinning method. The use of polymeric matrix and the adopted method has allowed to attain a uniform dispersion of gold clusters in the nanofibers while at the same time maintaining its morphology. The sensing performance of Au.BSA@PEO NFM has been tested upon exposure to different concentration of TNT is presented in Fig. 8.16. The fluorescence intensity is clearly decreased as a function of increasing concentration of TNT which is demonstrated by CLSM images

(Fig. 8.16a–c). The fluorescence spectral changes of the Au.BSA@PEO-NFM for a wide range of TNT concentration has been picturised in Fig. 8.16d.

The relative fluorescence intensity (I_0/I, where I and I_0 are the fluorescence intensity in the presence and absence of TNT, respectively) versus the TNT concentration has been presented in Fig. 8.16e.

The visual fluorescence responses of Au.BSA@PEO-NFM at different concentrations of TNT by contact mode method have been tested by placing the nanofibrous membrane in the TNT solution for a second has been displayed in Fig. 8.16f. Immediately, the color of the Au.BSA@PEO-NFM changed from white to either deep red or blue depending on the concentration and time in normal light condition which clearly illustrates their utility for the onsite instant visualization of TNT. The ocular noticeable response of the hybrid nanofibrous membrane towards the TNT solution has been found to be at one parts per billion (1 ppb). Further, the known factor in sensing performance in their bulk state has been known to be limited by their cross linked nature. Moreover, the complete decrease in the fluorescence intensity at 1 ppb level of TNT in bulk state further projected to investigate their sensing performance on even lower concentrations using single nanofiber (SNF), due to which it will further reduce the outlay of the devices. As predicted, a SNF could sensitively detect the TNT molecules and showed enhanced detection limit of TNT that reaches a level up to sub ppt (0.1 ppt). The gradual decrease in the intensity, upon increasing the concentration is clearly observed at SNF level as presented in Fig. 8.17. The decrease in the luminescence intensity occurred consistently throughout the SNF and such admirable characteristics of uniformity are significant in the development of a trustworthy method. Fluorescent organic polymers also successfully made into the nanofibers and further used as a sensory probe for TNT detection [64–66].

8.4   Conclusions

In this chapter, we summarized initially the major advancement in the field of fluorescent nanohybrids from challenging synthesis to the promise application in TNT sensor. Despite substantial progress have been made, a diversity of challenges remains restricts their sensing performance in outdoor application. On the basis of the outlined achievements over the past few years, the electrospun nanofibers have been successfully adopted as a support for fluorescent probes and in some cases as a probe for improved sensitivity. The growing number of electrospun hybrid nanofiber systems might open a new venture in addressing important issues for detection of TNT in environmental application and we believe that the creation of new hybrid nanofiber for improved sensing performance will persistently grow over coming years.
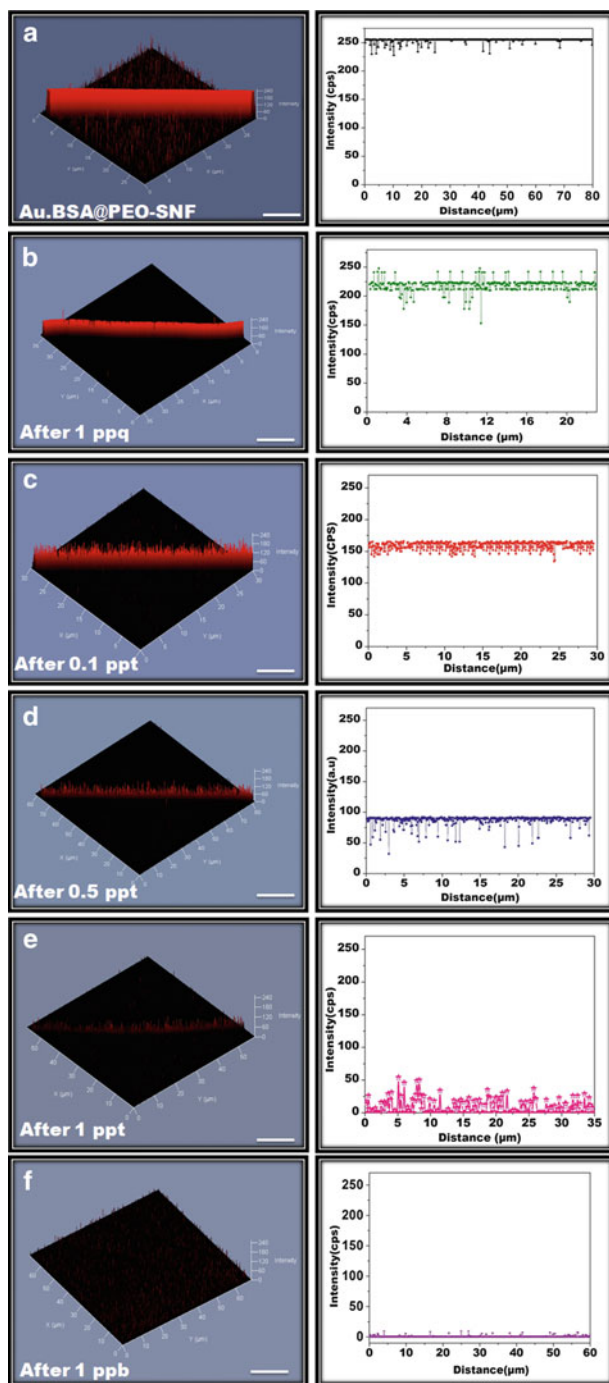
Fig. 8.17 CLSM images of Au.BSA@PEO-SNF upon exposure to different concentration of TNT and their intensity profile collected from the surface of the nanofiber (*scale bar* 10 μm) [63]

References

1. R. Freeman, T. Finder, L. Bahshi, R. Gill, I. Willner, Functionalized CdSe/ZnS QDs for the detection of nitroaromatic or RDX explosives. Adv. Mater. **24**, 6416–6421 (2012)
2. Z.C. Symons, N.C. Bruce, Bacterial pathways for degradation of nitroaromatics. Nat. Prod. Rep. **23**, 845–850 (2006)
3. M. Kulkarni, A. Chaudhari, Microbial remediation of nitro-aromatic compounds: an overview. J. Environ. Manag. **85**, 496–512 (2007)
4. M.E. Honeycutt, A.S. Jarvis, V.A. McFarland, Cytotoxicity and mutagenicity of 2,4,6-TNT and its metabolites. Ecotoxicol. Environ. Saf. **35**(3), 282–287 (1996)
5. R. Martel, M. Mailloux, U. Gabriel et al., Behavior of energetic materials in ground water at an anti-tank range. J. Environ. Qual. **38**, 75–92 (2009)
6. J.D. Rodgers, N.J. Bunce, Treatment methods for the remediation of nitroaromatic explosives. Wat. Res. **35**(9), 2101–2111 (2001)
7. K. Ayoub, E.D. van Hullebusch, M. Cassir et al., Application of advanced oxidation processes for TNT removal: a review. J. Hazard. Mater. **178**, 10–28 (2010)
8. S.J. Toal, W.C. Trogler, Polymer sensors for nitroaromatic explosives detection. J. Mater. Chem. **16**, 2871–2883 (2006)
9. M.B. Pushkarsky, I.G. Dunayevskiy, M. Prasanna et al., High-sensitivity detection of TNT. PNAS **103**(52), 19630–19634 (2006)
10. L.A. Pinnaduwage, A. Gehl, D.L. Hedden et al., A microsensor for trinitrotoluene vapour. Nature **425**, 474 (2003)
11. M. Riskin, R. Tel-Vered, O. Lioubashevski et al., Ultrasensitive surface plasmon resonance detection of trinitrotoluene by a bis-aniline-cross-linked Au nanoparticles composite. J. Am. Chem. Soc. **131**, 7368–7378 (2009)
12. S. Kumar, N. Venkatramaiah, S. Patil, Fluoranthene based derivatives for detection of trace explosive nitroaromatics. J. Phys. Chem. C **117**, 7236–7245 (2013)
13. R. Tu, B. Liu, Z. Wang et al., Amine-capped ZnS-Mn^{2+} nanocrystals for fluorescence detection of trace TNT explosive. Anal. Chem. **80**, 3458–3465 (2008)
14. S.W.I.I.I. Thomas, G.D. Joly, T.M. Swager, Chemical sensors based on amplifying fluorescent conjugated polymers. Chem. Rev. **107**(4), 1339–1386 (2007)
15. G.H. Shi, Z.B. Shang, Y. Wang et al., Fluorescence quenching of CdSe quantum dots by nitroaromatic explosives and their relative compounds. Spectrochim. Acta Mol. Biomol. Spectrosc. **70**(2), 247–252 (2008)
16. J.S. Yang, T.M. Swager, Fluorescent porous polymer films as TNT chemosensors: electronic and structural effects. J. Am. Chem. Soc. **120**, 11864–11873 (1998)
17. D. Gao, Z. Wang, B. Liu et al., Resonance energy transfer-amplifying fluorescence quenching at the surface of silica nanoparticles toward ultrasensitive detection of TNT. Anal. Chem. **80**, 8545–8553 (2008)
18. Y. Engel, R. Elnathan, A. Pevzner et al., Supersensitive detection of explosives by silicon nanowire arrays. Angew. Chem. Int. Ed. **49**, 6830–6835 (2010)
19. G.B. Demirel, B. Daglara, M. Bayindir, Extremely fast and highly selective detection of nitroaromatic explosive vapours using fluorescent polymer thin films. Chem. Commun. **49**, 6140–6142 (2013)

20. Y. Chen, Z. Chen, Y. He et al., L-Cysteine-capped CdTe QS-based sensor for simple and selective detection of trinitrotoluene. Nanotechnology **21**, 125502 (2010)
21. Y. Jiang, H. Zhao, N. Zhu et al., A simple assay for direct colorimetric visualization of trinitrotoluene at picomolar levels using gold nanoparticles. Angew. Chem. Int. Ed. **47**, 8601–8604 (2008)
22. E.R. Goldman, I.L. Medintz, J.L. Whitley et al., A hybrid quantum dot-antibody fragment fluorescence resonance energy transfer-based TNT sensor. J. Am. Chem. Soc. **127**, 6744–6751 (2005)
23. M. Alcaniz, J.L. Vivancos, R. Masot et al., Design of an electronic system and its application to electronic tongues using variable amplitude pulse voltammetry and impedance spectroscopy. J. Food Eng. **111**, 122–128 (2012)
24. (a) Yunsheng Xia, Lei Song, and Changqing Zhu, Turn-on and near-infrared fluorescent sensing for 2,4,6-trinitrotoluene based on hybrid (gold nanorod)−(quantum dots) Assembly. Anal. Chem. **83**(4), 1401–1407 (2011); (b) K. Zhang, H. Zhou, Q. Mei et al., Instant visual detection of trinitrotoluene particulates on various surfaces by ratiometric fluorescence of dual-emission quantum dots hybrid. J. Am. Chem. Soc. **133**(22), 8424–8427 (2011)
25. S.S.R. Dasary, A.K. Singh, D. Senapati et al., Gold nanoparticle based label-free SERS probe for ultrasensitive and selective detection of trinitrotoluene. J. Am. Chem. Soc. **131**, 13806–13812 (2009)
26. Q. Fang, J. Geng, B. Liu et al., Inverted opal fluorescent film chemosensor for the detection of explosive nitroaromatic vapors through fluorescence resonance energy transfer. Chem. Eur. J. **15**, 11507–11514 (2009)
27. H. Sohn, R.M. Calhoun, M.J. Sailor et al., Detection of TNT and picric acid on surfaces and in seawater by using photoluminescent polysiloles. Angew. Chem. **40**(11), 2104–2105 (2001)
28. P.C. Chen, S. Sukcharoenchoke, K. Ryu et al., 2,4,6-Trinitrotoluene (TNT) chemical sensing based on aligned single-walled carbon nanotubes and ZnO nanowires. Adv. Mater. **22**, 1900–1904 (2010)
29. A.D. Aguilar, E.S. Forzani, M. Leright et al., A hybrid nanosensor for TNT vapor detection. Nano Lett. **10**, 380–384 (2010)
30. A. Rose, Z. Zhu, C.F. Madigan et al., Sensitivity gains in chemosensing by lasing action in organic polymers. Nature **434**, 876–879 (2005)
31. A. Lan, K. Li, H. Wu et al., A luminescent microporous metal–organic framework for the fast and reversible detection of high explosives. Angew. Chem. Int. Ed. **48**, 2334–2338 (2009)
32. K. Cizek, C. Prior, C. Thammakhet et al., Integrated explosive preconcentrator and electrochemical detection system for 2,4,6-trinitrotoluene (TNT) vapor. Anal. Chim. Acta. **661**, 117–121 (2010)
33. C.X. Guo, Z.S. Lu, Y. Lei et al., Ionic liquid–graphene composite for ultratrace explosive trinitrotoluene detection. Electrochem. Commun. **12**, 1237–1240 (2010)
34. H.X. Zhang, A.M. Cao, J.S. Hu et al., Electrochemical sensor for detecting ultratrace nitroaromatic compounds using mesoporous SiO_2-modified electrode. Anal. Chem. **78**, 1967–1971 (2006)
35. M. Riskin, R. Tel-Vered, T. Bourenko et al., Imprinting of molecular recognition sites through electropolymerization of functionalized Au nanoparticles: development of an electrochemical TNT sensor based on π-donor-acceptor interactions. J. Am. Chem. Soc. **130**, 9726–9733 (2008)
36. S. Hrapovic, E. Majid, Y. Liu et al., Metallic nanoparticle-carbon nanotube composites for electrochemical determination of explosive nitroaromatic compounds. Anal. Chem. **78**, 5504–5512 (2006)
37. K.K. Kartha, S.S. Babu, S. Srinivasan et al., Attogram sensing of trinitrotoluene with a self-assembled molecular gelator. J. Am. Chem. Soc. **134**, 4834–4841 (2012)
38. C.M. Gonzalez, M. Iqbal, M. Dasog et al., Detection of high-energy compounds using photoluminescent silicon nanocrystal paper based sensors. Nanoscale **6**, 2608–2612 (2014)

39. J.P. Vigneron, J.M. Pasteels, D.M. Windsor et al., Switchable reflector in the Panamanian tortoise beetle Charidotella egregia (Chrysomelidae: Cassidinae). Phys. Rev. E Stat. Nonlinear Soft Matter Phys. **76**, 031907 (2007)
40. R.E. Young, F.M. Mencher, Bioluminescence in mesopelagic squid: diel color change during counterillumination. Science **208**, 1286–1288 (1980)
41. K.S. Bejoymohandas, T.M. George, S. Bhattacharya et al., AIPE-active green phosphorescent iridium(III) complex impregnated test strips for the vapor-phase detection of 2,4,6-trinitrotoluene (TNT). J. Mater. Chem. C **2**, 515–523 (2014)
42. J.W. Oh, W.J. Chung, K. Heo et al., Biomimetic virus-based colourimetric sensors. Nat. Commun. (2014). doi:10.1038/ncomms4043
43. H. Sohn, M.J. Sailor, D. Magde et al., Detection of nitroaromatic explosives based on photoluminescent polymers containing metalloles. J. Am. Chem. Soc. **125**, 3821–3830 (2003)
44. S. Anitha, B. Brabu, T.D. John et al., Optical, bactericidal and water repellent properties of electrospun nano-composite membranes of cellulose acetate and ZnO. Carbohydr. Polym. **87**, 1065–1072 (2012)
45. S. Anitha, T.S. Natarajan, Fabrication of hierarchical ZnO enriched fibrous PVA membrane. J. Nanosci. Nanotechnol. **12**, 1–9 (2012)
46. S. Anitha, B. Brabu, T.D. John et al., Preparation of free-standing electrospun composite ZnO membrane for antibacterial applications. Adv. Sci. Lett. **4**, 1–7 (2012)
47. T. Uyar, J. Hacaloglu, F. Besenbacher, Electrospun polyethylene oxide (PEO) nanofibers containing cyclodextrin inclusion complex. J. Nanosci. Nanotechnol. **11**(5), 3949–3958 (2011)
48. T. Uyar, R. Havelund, J. Hacaloglu et al., Functional electrospun polystyrene nanofibers incorporating alpha, beta and gamma cyclodextrins: comparison of molecular filter performance. ACS Nano **4**(9), 5121–5130 (2010)
49. F. Kayaci, T. Uyar, Electrospun zein nanofibers incorporating cyclodextrins. Carbohydr. Polym. **90**, 558–568 (2012)
50. A. Celebioglu, T. Uyar, Green and one-step synthesis of gold nanoparticles incorporated in electrospun cyclodextrin nanofibers. RSC Adv. **3**, 10197–10201 (2013)
51. A. Celebioglu, O.C.O. Umu, T. Tekinay et al., Antibacterial electrospun nanofibers from triclosan/cyclodextrin inclusion complexes. Colloids Surf. B **116**, 612–619 (2014)
52. Y. Che, D.E. Gross, H. Huang et al., Diffusion-controlled detection of trinitrotoluene: interior nanoporous structure and low highest occupied molecular orbital level of building blocks enhance selectivity and sensitivity. J. Am. Chem. Soc. **134**, 4978–4982 (2012)
53. F. Wang, W. Wang, B. Liu et al., Copolypeptide-doped polyaniline nanofibers for electrochemical detection of ultra trace trinitrotoluene. Talanta **79**, 376–382 (2009)
54. Y. Wang, A. La, Y. Ding et al., Novel signal-amplifying fluorescent nanofibers for naked-eye-based ultrasensitive detection of buried explosives and explosive vapors. Adv. Funct. Mater. **22**, 3547–355 (2012)
55. J.H. Lee, S. Kang, J.Y. Lee et al., Instant visual detection of picogram levels of trinitrotoluene by using luminescent metal–organic framework gel-coated filter paper. Chem. Eur. J. **19**, 16665–16671 (2013)
56. H. Xu, F. Liu, Y. Cui et al., A luminescent nanoscale metal–organic framework for sensing of nitroaromatic explosives. Chem. Commun. **47**, 3153–3155 (2011)
57. Y. Xu, Y. Wen, W. Zhu et al., Electrospun nanofibrous mats as skeletons to produce MOF membranes for the detection of explosives. Mater. Lett. **87**, 20–23 (2012)
58. Y. Yang, H. Wang, K. Su et al., A facile and sensitive fluorescent sensor using electrospun nanofibrous film for nitroaromatic explosive detection. J. Mater. Chem. **21**, 11895 (2011)
59. Y.Y. Lv, W. Xu, F.W. Lin et al., Electrospun nanofibers of porphyrinated polyimide for the ultra-sensitive detection of trace TNT. Sensor Actuators B Chem. **184**, 205–211 (2013)
60. Y. Long, H. Chen, Y. Yang et al., Electrospun nanofibrous film doped with a conjugated polymer for DNT fluorescence sensor. Macromolecules **42**, 6501–6509 (2009)
61. Y.Z. Liao, V. Strong, Y. Wang et al., Oligotriphenylene nanofiber sensors for detection of nitro-based explosives. Adv. Funct. Mater. **22**, 726–735 (2012)

62. S. Tao, G. Li, J. Yin, Fluorescent nanofibrous membranes for trace detection of TNT vapor. J. Mater. Chem. **17**, 2730–2736 (2007)
63. S. Anitha, C. Asli, U. Tamer, Ultrafast on-site selective visual detection of TNT at sub ppt level using fluorescent gold cluster incorporated single nanofiber. Chem. Commun. (2014). doi:10.1039/C4CC01190B
64. W. Li, N.D. Ho, Y. Cho et al., Nanofibers of conducting polyaniline for aromatic organic compound sensor. Sensor Actuators B-Chem. **143**, 132–138 (2009)
65. C. Deng, P. Gong, Q. He et al., Highly fluorescent TPA-PBPV nanofibers with amplified sensory response to TNT. Chem. Phys. Lett. **483**, 219–223 (2009)
66. W.E. Lee, C.J. Oh, I.K. Kang et al., Diphenylacetylene polymer nanofiber mats fabricated by freeze drying: preparation and application for explosive sensors. Macromol. Chem. Phys. **211**, 1900–1908 (2010)

Chapter 9
Nanoparticle/Nanochannels-Based Electrochemical Biosensors

Marisol Espinoza-Castañeda, Alfredo de la Escosura-Muñiz, and Arben Merkoçi

Abstract The purpose of this chapter is to provide a general comprehensive overview on the latest trends in the development of nanoparticle/nanochannels-based electrochemical biosensors. Given the importance of nanoparticles, some general considerations about their use in biosensors are given before focusing on nanochannels-based electrochemical biosensing systems. A detailed description of representative and recent works covering the main nanochannel arrays fabrication techniques and their application in electrochemical biosensing systems is also given. The combination of nanochannel array sensing capability with the known advantages of nanoparticles in immunosensing is shown as an ideal approach for the diagnostic of proteins and DNA. As conclusion, the integration of nanochannel arrays with electrochemical transducers (ex. screen-printed electrode) seems to be one of the most important challenges in the development of robust sensing devices that may bring electrochemical/nanochannel-based biosensing technology to the market.

9.1   Electrochemical Biosensors and Nanomaterials

Biosensing represents the recognition of an analyte (chemical or biochemical) through the use of an immobilized bioreceptor (e.g. enzyme, antibody, cell etc.). The possible change during the recognition event (occurring at the transducer) can be optical, electrical, mass etc. (Fig. 9.1a). Between various kinds of the generated signals the electrical/electrochemical one shows advantages of related instruments

M. Espinoza-Castañeda • A. de la Escosura-Muñiz
ICN2-Nanobioelectronics & Biosensors Group, Institut Catala de Nanociencia y
Nanotecnologia, Campus UAB, 08193 Bellaterra, Barcelona, Spain

A. Merkoçi (✉)
ICN2-Nanobioelectronics & Biosensors Group, Institut Catala de Nanociencia y
Nanotecnologia, Campus UAB, 08193 Bellaterra, Barcelona, Spain

ICREA – Institucio Catalana de Recerca i Estudis Avançats, 08010 Barcelona, Spain
e-mail: arben.merkoci@icn.cat
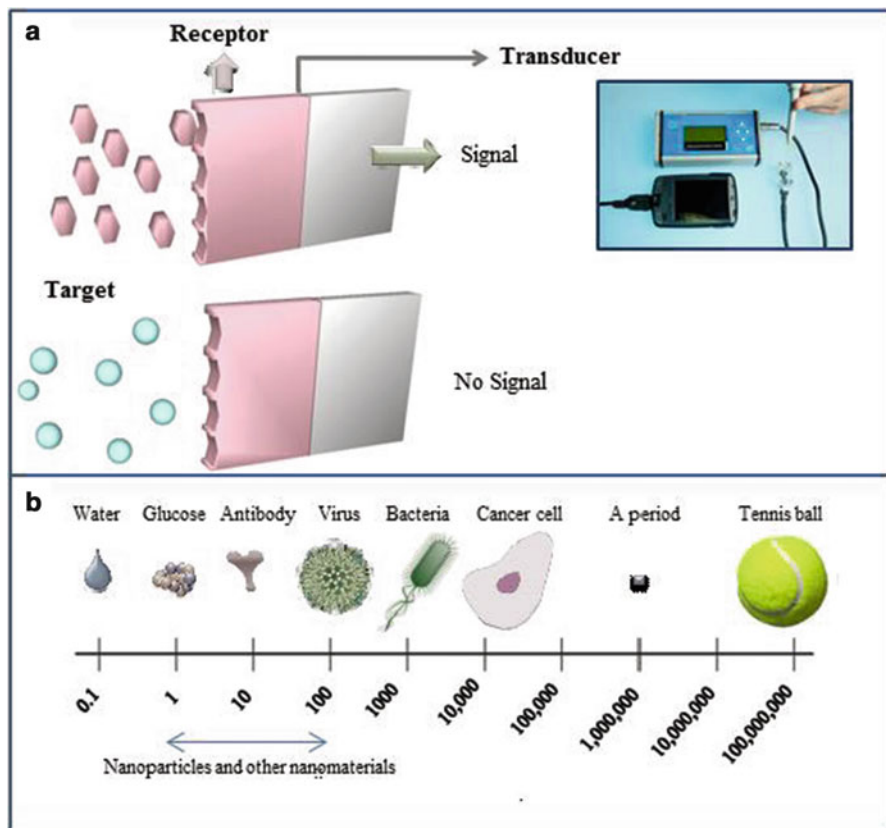
Fig. 9.1 (**a**) Schematic representation of the main components of a biosensor. Inset picture correspond to the set-up of a portable electrochemical biosensor. (**b**) Size-scale of various materials including nanoparticles and other nanomaterials

simplicity, moderate cost and portability. The purpose of the electrochemical transducer is to convert the biological recognition event between the analyte and the receptor into a useful electrical signal that can be easily transformed to a quantitative or qualitative analytical one [1].

Electrochemical devices have traditionally received the major share of the attention in biosensor development [2] and recently are getting an increased attention with the advances in nanoscience and nanotechnologies in general and especially recent development in nanomaterials (NMs) field.

A wide variety of NMs, especially nanoparticles (normally in the range of 1–100 nm, Fig. 9.1b) with different properties have found broad application in analytical methods [3]. NMs are being increasingly used for the development of electrochemical biosensors, due to their interesting qualities ranging from unique electrocatalytic properties shown in nanoscale, capability to be easily linked with various polymers and bioactive molecules (e.g., antibodies, DNA and other receptors). In addition, NMs can interface biological recognition events with electronic signal transduction while being used as labels [4].

Due to their high specificity, speed, portability, and low cost, NM-based electrochemical biosensors offer exciting opportunities for numerous applications in biomedical field [5].

Given the importance of nanoparticles, between various NMs, some general considerations about their use in biosensors will be given in the following sections before focusing on nanochannels based biosensing systems.

9.1.1 Use of Nanoparticles in Electrochemical Biosensors: Gold Nanoparticles

The application of nanoparticles (NPs) in biosensors strongly relates to their properties that derive to a certain extent from their synthesis and later modifications (chemical and biological) [6]. NP characterization and quantification play a crucial role in the final biosensing applications [7]. The size and the composition of a NP seems to be advantageous over the corresponding bulk structure, because a target binding event (i.e. DNA hybridization or immunoreaction [8–10]) involving NPs have a significant effect in optical (change of the light absorption or emission) or electrochemical properties (oxidation or reduction current onto a transducing platform), offering novel options for bioanalysis.

Given their special properties, a special attention is given in this chapter to gold nanoparticles (AuNPs). AuNPs are the most stable metal nanoparticles. They have size-related electronic, magnetic and optical properties with interest for applications in catalysis and biology as well as other fields [11, 12].

Among the conventional methods of synthesis of AuNPs by reduction of gold (III) derivatives, the most popular one for a long time has been through the citrate reduction of $HAuCl_4.3H_2O$ using trisodium citrate as both the reducer and the stabilizer which was introduced by Turkevich in 1951 [13]. AuNPs shapes can be tuned through specifically devised synthetic procedures and later chemical and biological modifications of their surfaces.

Different methodologies for AuNPs detection such as optical (through UV-Vis or lateral flow devices) or electrical/electrochemical methods have been applied through various sensing technologies [7, 9, 10].

One of the most important applications of AuNPs has been its use as labels in various biosensing technologies. Recently the use of AuNPs as electroactive labels for the detection of analytes of clinical interest such as proteins in human serum [14] and cancer cells [15–17] has been reported. A special role in the biosensing performance plays the size of AuNPs. For example the electrochemical properties of AuNPs suspensions are found to be strongly dependent on the size and the hydrodynamic properties of the solvent, while working in a bioassay systems [18]. All these advantageous properties of AuNPs have been recently approached in nanochannels-based sensing systems, as will be detailed in the following sections.

9.1.2   Nanochannels

9.1.2.1   Sensing Using Nanochannels: From the Coulter Counter to the Stochastic Sensing

The fundament of sensing using nanochannels [19] is based on the concept of the Coulter counter [20, 21] a device that consists of two electrolyte-filled chambers separated by one or few more microchannels. When a microscopic particle enters through the microchannel, a change in the electrical conductance is recorded as electric current or voltage pulse, which can be correlated to size, mobility, surface charge, and concentration of the microparticle. The Coulter counter was designed to measure particles in the micrometric scale, but for biosensing purposes, devices able to detect molecules in the nanometric scale (e.g. proteins and ssDNA) are needed and for this reason the research in this field was focused in the last years on the development of channels of nanometric size [22–24], inspired by the natural ion channels. The pioneer approach to build these biomimetic nanochannels consisted in the insertion of the α-hemolysin bacterial protein pore (Fig. 9.2a) [25] in artificial lipid bilayers. The as-prepared biological single nanochannels work in a similar way as the Coulter counter, being able to detect nanosized molecules.

The resistive-pulse process, called stochastic sensing, entails mounting the membrane containing the nanochannel between two electrolyte solutions, applying a transmembrane potential difference, and measuring the resultant ion current flowing across the electrolyte – filled nanochannel (Fig. 9.2b) [26]. The selectivity of the system is given by specific receptors that can be inserted inside the nanochannel by using genetic engineering techniques.

Stochastic sensing using biological ion channels has been widely applied for the detection of different analytes, such as DNA [27], proteins [28] and others [29]. Of special relevance are the exciting perspectives related to the potential ability of the α-hemolysin nanochannel for DNA sequencing. DNA single strands could be electrophoretically driven through the α-hemolysin channel [30] and pass in an elongated conformation generating a "fingerprint"-like blocking of the ionic current, which would be specific for each strand. The transit time and extent of the current could reveal information about the length of the nucleic acid and its base composition [31–33].

However, in spite of the advantages of the biological ion channels in terms of sensitivity, selectivity, and ability for the analysis of a variety of analytes, limitations related to their low stability, time consuming analysis and the need of genetic engineering techniques for the insertion of specific receptors have directed the research in this field to the preparation and application of more robust systems based on solid-state nanochannels. This opened the way to a broad research area, where not only single nanochannels but also nanochannel arrays can be prepared. These nanochannel arrays bring novel sensing possibilities, both optical [34–37] and electrochemical, totally different from those based on the stochastic sensing.

Next section will be focused on some representative methods of preparation of solid-state nanochannel arrays and their application in electrochemical biosensing.
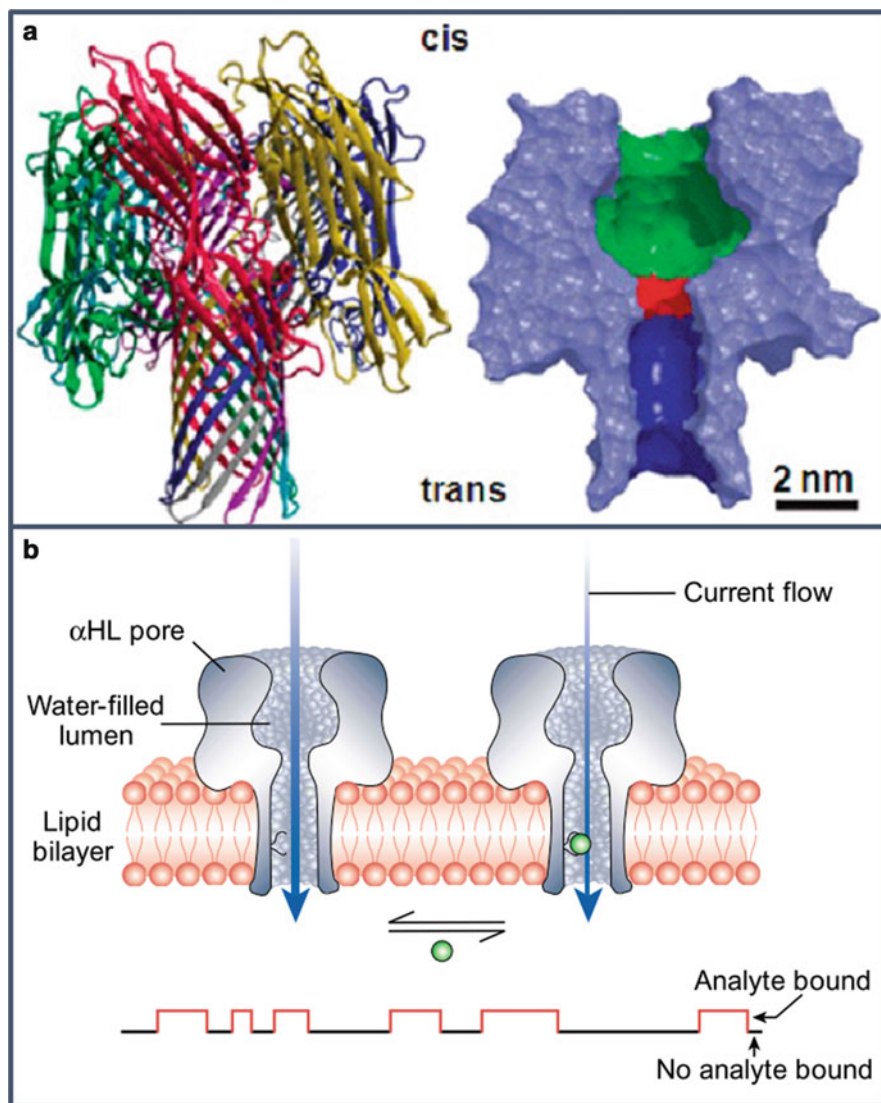
Fig. 9.2 (**a**) Detailed structure of the heptameric α-hemolysin channel. The cross-sectional view on the *right* displays the inner cavity (*green*), inner constriction (*red*), and β-barrel (*blue*) [25] (**b**) Stochastic Sensing: schematic representation of the sensing using an engineered α-hemolysin protein nanochannel inserted in a lipid bilayer membrane. The change in conductance between the two sides of the membrane in the absence (*left*) and presence (*right*) of an analyte in the sample allows its detection and quantification [26]

9.1.2.2 Solid-State Nanochannel Arrays Preparation

Different methods for the preparation of solid-state nanochannels like anodization [38], ion sputtering [39], quantum lithography [40], nanosphere lithography [41], microchannel compression [42], electron-beam lithography [43], block polymer self-assembly [44], microcontact printing [45], micromolding [46], water-assisted self-assembly [47], nanoimprint lithography [48] and high ordered mesoporous thin films formation [49, 50] have been reported.

In this chapter, special emphasis will be given to the main methods used for the preparation of arrays of these solid-state nanochannels such as highly ordered mesoporous thin film formation by nanoparticle assembling, micro-/nanomolding techniques and metallic substrates anodization.

9.2 Highly Ordered Mesoporous Thin Film Formation by Nanoparticle Assembling

Monodisperse polymer nanospheres have been used to fabricate monolayer nanopore arrays. The surface of polymer particles can be modified by proteins or biopolymers via physical adsorption [51]. These monolayers have a high specific surface area and an ordered arrangement of pores. These structures have already been applied in catalysis, separations, sensors [52], bioscience, photonics and optoelectronic devices. Polymer nanospheres modified with functional surface groups provide strong chemical bonds for immunoreagents. Carboxylic groups with the capacity to form amide bonds with the amino groups of bioligands are the most used. These monolayers have been deposited onto transparent conductive oxides (TCO) and used for photovoltaic applications (for example nanostructured solar cells). Guérin and co-workers [53] reported the use of polystyrene microsphere to modify the surface of the transparent fluorine doped tin oxide (FTO) with interest for solar cells. These monolayers could be used as templates for the fabrication of nanocavities by the inverse opal technique [54] for different applications as the fabrication of large-scale ZnO ordered pore arrays for gas sensors [55]. An example of the process steps for the fabrication of these monolayers is described in Fig. 9.3, where the fabrication of a monolayer of microparticles on indium tin oxide (ITO) glass substrate as well as the cavities formation is illustrated. A substrate of ITO was treated with UV light to obtain hydrophilic surfaces, and put into a Petri dish adding deionized water; a polystyrene (PS) colloid solution was dropped onto the surface of the dispersion substrate, after a surfactant was dropped into the Petri dish. After that, the support substrate was removed from the Petri dish and treated on a hot plate to fix the array on the surface of the substrate. To obtain the nanocavities, a mixed solution was added onto the surface of the arrays by spin coating technique. Then, the PS nanosphere array template was removed using a solvent and ultrasonication [56].

The holes formed between the nanospheres can be used as nanochannels and FTO serving then as a working electrode.
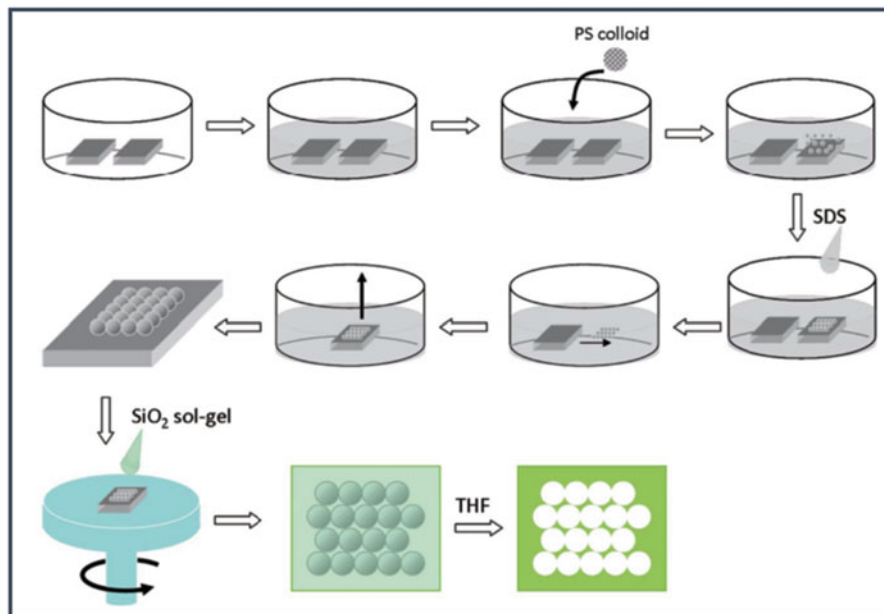
Fig. 9.3 Highly ordered mesoporous thin film formation by nanoparticle assembling. Detailed preparation procedure for an inversed opal mask of SiO_2 on a substrate [56]

9.3 Micro-/Nanomolding Techniques: Nanoimprint Lithography

Nanoimprint lithography (NIL) was first developed in 1995 as a low-cost and high throughput alternative for researchers who need high-resolution patterning [57]. NIL depends on direct mechanical deformation of the resist and can therefore achieve resolutions beyond the limitations set by light diffraction or beam scattering that are encountered in conventional lithographic techniques [58]. NIL provides the ability to pattern materials into small structures with interest for various applications ranging from the production of integrated circuits, information storage devices, sensors, actuators, biochips, microfluidic devices, and micro-optical components [59, 60].

Figure 9.4 describes the basic process steps to print a large-area of nanostructures.

Depending on the application, the requirements for a successful lithographic process can vary substantially. The minimum feature size of a test pattern is usually the most obvious issue one must consider when selecting a proper lithographic technique.
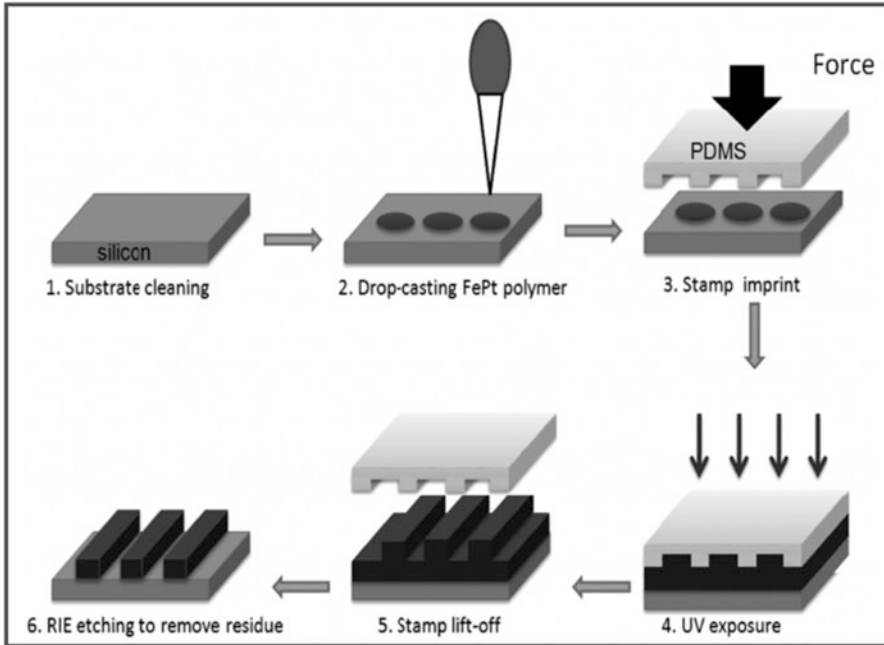
Fig. 9.4 Micro/Nanomolding techniques: Nanoimprint lithography. Schematic illustration of the fabrication of large-area nanostructures by nanoimprint lithography. *1*, a silicon substrate is cleaned with acetone and deionized water together with sonication. *2*, a polymer is drop-casted onto the silicon substrate with a dropper. *3*, the PDMS stamp is pressed onto the sample with a uniform force. *4*, the whole sample and the stamp is irradiated with UV light to induce cross-linking. *5*, the stamp is then lifted off. *6*, the residue is removed by reactive-ion etching (RIE) [61]

9.4 Metallic Substrates Anodization: Anodic Aluminum Oxide Nanoporous Membranes Preparation

Anodic aluminum oxide (AAO) is a rigid and dense porous material and is chemically and thermally stable. The principal characteristics of AAO are the perfectly ordered and size controlled nanopores [62]. The fabrication process is based on facile and inexpensive electrochemical anodization, wide accessibility, the capability of top-bottom fabrication with nanoscale precision and access to high aspect ratio structures. Figure 9.5 shows the two-step anodization process under hard conditions [63]. The structure of AAO can be described as a close-packed hexagonal array of parallel cylindrical nanopore perpendicular to the surface on top of the underlying Al substrates [64].

The rich content of hydroxyl groups on the alumina membrane surface allow them to be easily modified via modification with organic molecules with the desired functionality [65].
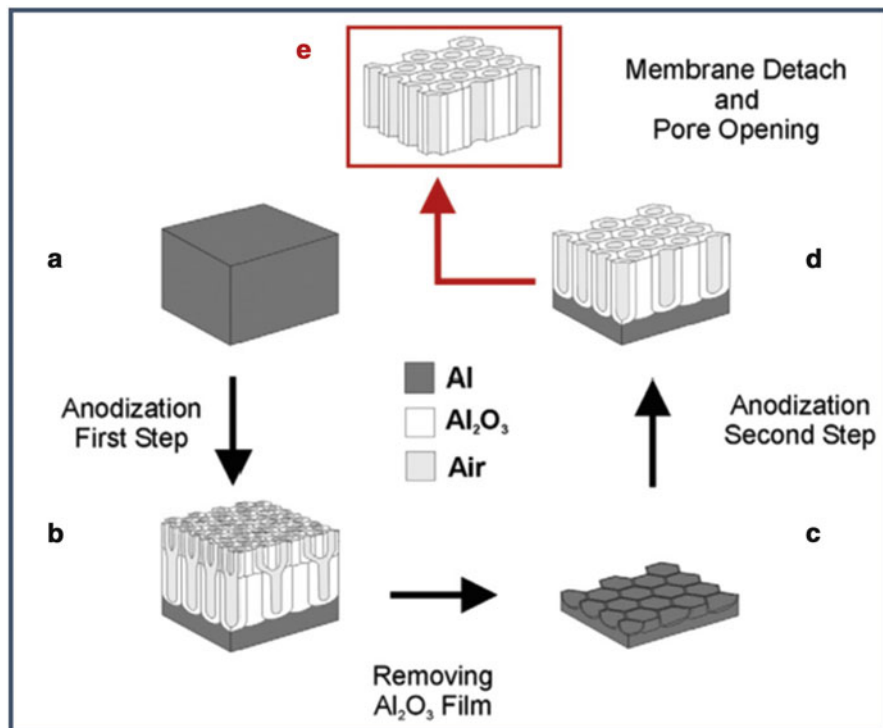
Fig. 9.5 Metallic substrates anodization: Anodic aluminum oxide (AAO) nanoporous membranes preparation. The two-step anodization process under hard conditions. (*a*) Annealed and electropolished aluminium substrate. (*b*) nanoporous anodic aluminum with a protective layer on the *top* and ordered pores on the *bottom*. (*c*) Patterned Al substrate after removing the oxide film. (*d*) nanoporous anodic aluminum membrane with straight and closed pores. (*e*) nanoporous anodic aluminum membrane with straight and open pores after performing the membrane detach and the pore opening at the same time [63]

9.5   Solid-State Nanochannel Arrays Functionalization

Binding ligands are commonly used to modify the inner nanochannel walls to provide recognition sites for analytes; these ligands play a crucial role in achieving the desired sensing performance [66]. One of the common surface modification techniques is by wet chemical approach as: silanes, organic acids, and layer-by-layer deposition. Subsequent modifications of the thus introduced functionality with biomolecules or nanoparticles can be carried out. The chemical modification mainly refers to the chemical reactions between the inner wall of the nanochannel and functional molecules in a solution to create new covalent bonds. One method is based on the formation of functional groups as -COOH inside the nanochannels able to react with molecules to form covalent bonds (for example, -C(O)-NH-). Another method for chemical modification of nanochannels is based on functional thiol molecules to form Au–S covalent bonds after the gold electrodes deposition
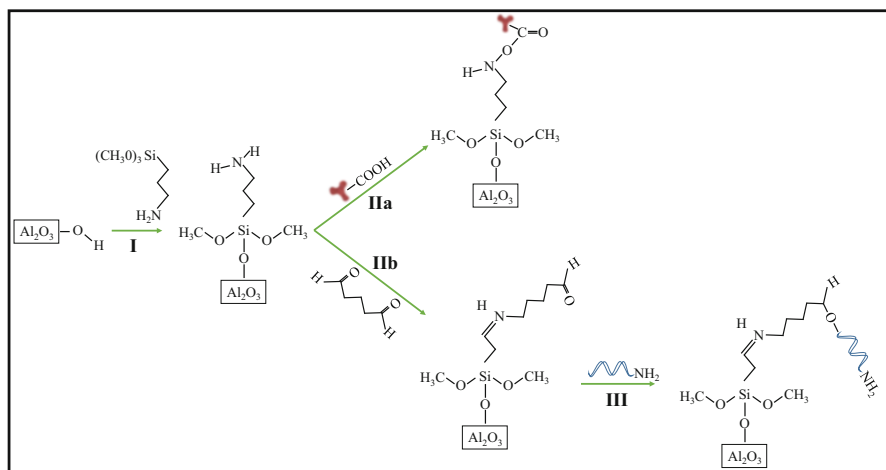
Fig. 9.6 Solid-state nanochannels functionalization. Scheme of the biofunctionalization procedure for antibodies immobilization in AAO nanoporous membranes: generation of amino groups by silanization process (*I*) followed by covalent binding of antibodies using EDC/sulfo-NHS cross-linker (*IIa*). In the case of ssDNA, carboxyl groups by reaction with glutaraldehyde (*IIb*) are generated after the silanization, followed by the immobilization of the amino-modified probe ssDNA by the peptide bond (*III*) [68–70]

onto the inner surface of the nanochannel. It is obvious that by reducing the diameter of the orifice to the nm range, the size of the detectable species can be extended down to the molecular level.

Layer-by-layer (LBL) assembly is a very versatile method for incorporating functional groups into nanochannels. This method avoids the need for complex chemical steps in the process [67].

Nanoporous membranes modified with various functional groups can be functionalized with antibodies or ssDNA for later biosensing applications, as shown in Fig. 9.6 [68–70].

The efficient antibody immobilization inside nanochannels can be checked by using antibodies labelled with a fluorescent tag (i.e. FITC), observing in the confocal microscope the presence of fluorescence not only on the external surface of the membranes but also in the inner walls (Fig. 9.7) [70].

9.6 Electrochemical Biosensing Systems Based on Solid-State Nanochannel Arrays

9.6.1 Detection Principle

The most recent and representative approaches are focused on the use of arrays of solid-state nanochannels as modifiers of conventional electrotransducer surfaces,
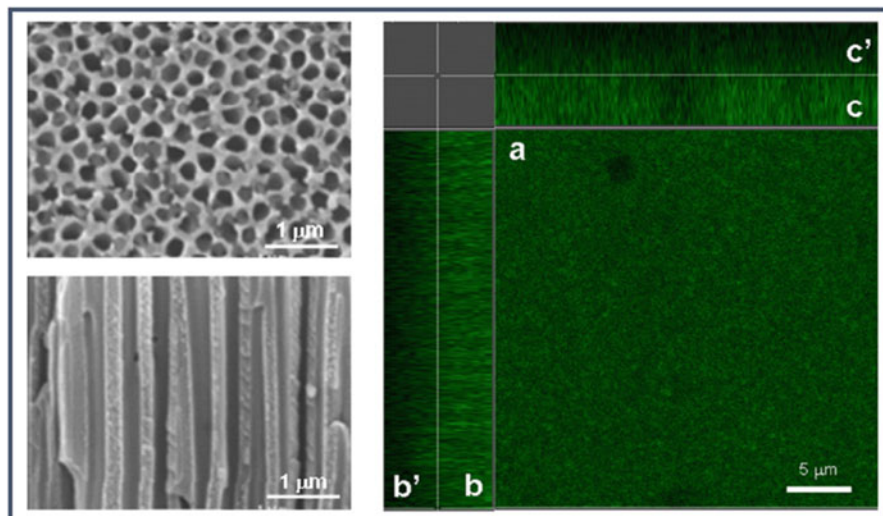
Fig. 9.7 (*Left*) SEM images of a plan (*top*) and cross-sectional view (*bottom*) of a 200 nm pore AAO nanoporous membrane. (*Right*) Confocal image of a 200 nm pore AAO membrane with antibody-FITC immobilized. Plan view (*a*) and planes until 5 μm in depth from the *top* surface (*b*, *c*) and from the *bottom* surface (*b′*, *c′*) [70]

measuring the changes of the electrochemical response of an electroactive species in solution due to the presence of the analyte inside the channels. AAO membranes prepared by anodization have a high pore density ($1 \times 10^9/cm^2$) and small pore diameters, which results in a substrate with high surface area that can be easily functionalized (as stated before) being very advantageous for biosensing. These characteristics, together with their commercial availability, have made them one of the preferred nanoporous substrates for biosensing applications. The sensing principle for the detection of proteins and DNA is explained in Fig. 9.8. In the case of proteins, the formation of the immunocomplex inside the nanochannels produces a partial blockage in the diffusion of electroactive species through the nanoporous membranes to the electrochemical transducer surface (working electrode) leading to a decrease of the electrochemical signal related to $[Fe(CN)_6]^{4-}$ oxidation to $[Fe(CN)_6]^{3-}$. Differential pulse voltammetry (DPV) oxidation peak is selected as analytical signal. The blockage of the pores due to the formation of DNA hybridization complexes is also detected following the same principle. Furthermore, nanoporous membranes can act as filters of e.g. cells present in real samples (as illustrated in the figure), allowing to minimize matrix effects [70].

This system is consistent with the relation between the pore size of the nanopore membrane used (typically 200 nm) and the length of both antibody and antigen, that is, 14.5 nm × 8.5 nm × 4 nm in the case of human immunoglobulin G (HIgG) and also with the size of a i.e. 21-mer ssDNA (approximately diameter of 1.84 nm and length of 0.38 nm).
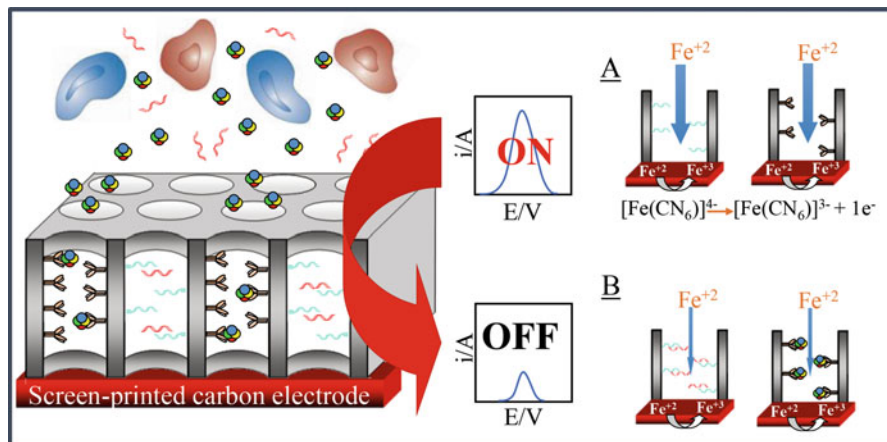
Fig. 9.8 Principle of electrochemical biosensing using AAO nanoporous membranes. *Left*: cells in the sample remain outside the pores while the proteins (or ssDNA) enter inside and are recognized by specific antibodies (or complementary ssDNA). *Right*: sensing principle in the absence (**A**) and presence (**B**) of the specific biomolecule in the sample [70]

9.6.2 Application for Protein Biomarkers Detection

The above explained sensing principle has been applied for the detection of protein biomarkers in whole human blood samples, without any sample preparation, taking advantage of the dual ability of the membranes to act not only as sensing platforms but also as filter of complex components such as red and blood cells. That is the case of the detection of CA15-3 breast cancer marker spiked in whole human blood [70]. The sensitivity of the system is here improved thanks to the use of AuNPs tags in sandwich assay approaches. The presence of such AuNPs inside the channels increase in a high extent the blockage of the diffusion of the electroactive species achieving in this way lower detection limits. Moreover, the catalytic activity of the AuNPs toward the silver deposition is approached for the selective formation of silver crystals around the AuNPs, increasing in this way the AuNP size and consequently the blockage of the channels and the limit of detection of proteins.

Figure 9.9 (top), shows a schematic representation about how the differential pulse voltammograms decrease due to the blockage effect occurring inside the nanochannels, and its effect on the limit of detection of HIgG (chosen as model protein), starting with the label-free assay, antibody labeled with 20 nm AuNPs, 80 nm AuNPs and finally 80 nm AuNPs after silver deposition.

With this methodology, a new system for detection of CA15-3 cancer marker spiked in whole blood was developed capable to detect 52 U mL^{-1} of CA15-3 with very low matrix effects, as shown in Fig. 9.9 (bottom). In addition, the developed device presents the advantage of the quantitative analysis that can be performed with the low-cost electrochemical analyzers using a simple and low-cost detection technology. Another interesting application recently reported is the rapid
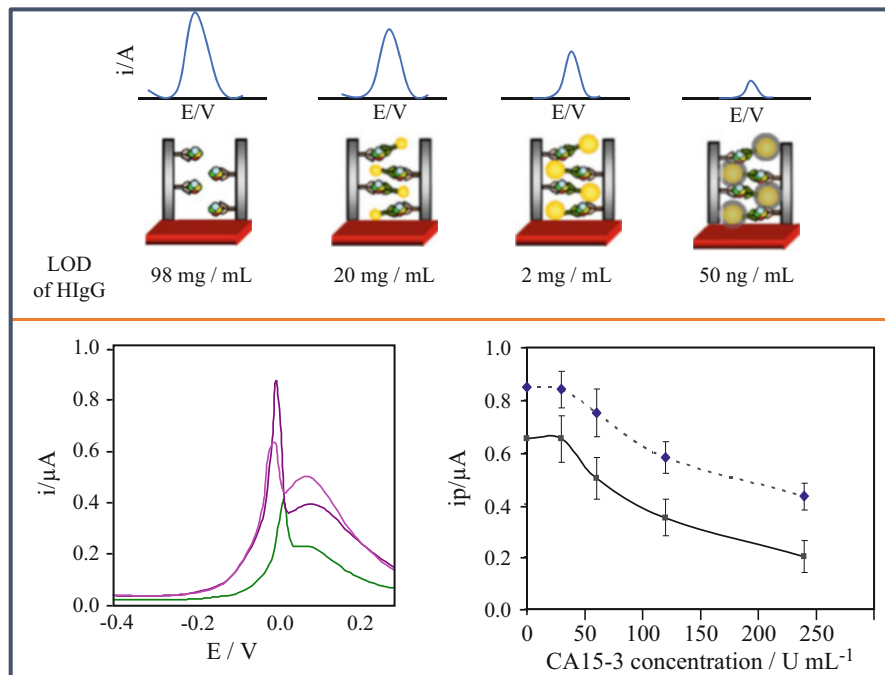
Fig. 9.9 *Top*; Schematic representation of the differential pulse voltammograms response and the detection limits of HIgG obtained depending on the blockage degree inside the nanochannels. *Bottom left*; DPV results for blood samples containing different concentrations of added CA15-3: 60, 120 and 240 U m^{-1} (from *top* to *bottom*). DPV parameters Pre-concentration potential: -550 m V; preconcentration time: 30 s; step potential: 10 mV; modulation amplitude: 50 mV; scan rate: 33.5 mV s^{-1}. *Bottom right*; Comparison of the effect of the concentration of CA15-3 on the voltammetric peak current obtained in PBS buffer (*dotted line*) and in the blood sample (*solid line*) [70]

determination of thrombin spiked in whole blood [71], taking advantage of both aptamer-based recognition and the use of a nanoporous membrane. The protocol involves sandwich format (aptamer/thrombin/antibody-AuNP) and silver amplification in the inner walls of an AAO membrane. The effect of the electrostatic interactions between the aptamer/thrombin/antibody-AuNP complex and the redox indicator, in addition to the steric effects were also investigated here. The resulted biosensing system allows detecting thrombin spiked in whole blood at very low levels, which are within the range of clinical interest for the diagnostic of coagulation abnormalities as well as pulmonary metastasis.

Figure 9.10a left, is a schematic representation of the blockage occurring inside the nanochannels after a sandwich assay and silver deposition onto AuNP tags. In Fig. 9.10a right, the filtering ability of the AAO membranes in the analysis of whole human blood is illustrated by the SEM image showing white and red blood cells that remain out of the nanochannels. This image also shows that the solution containing the blood cells doesn't block the entire pores so thrombin biomarker can pass
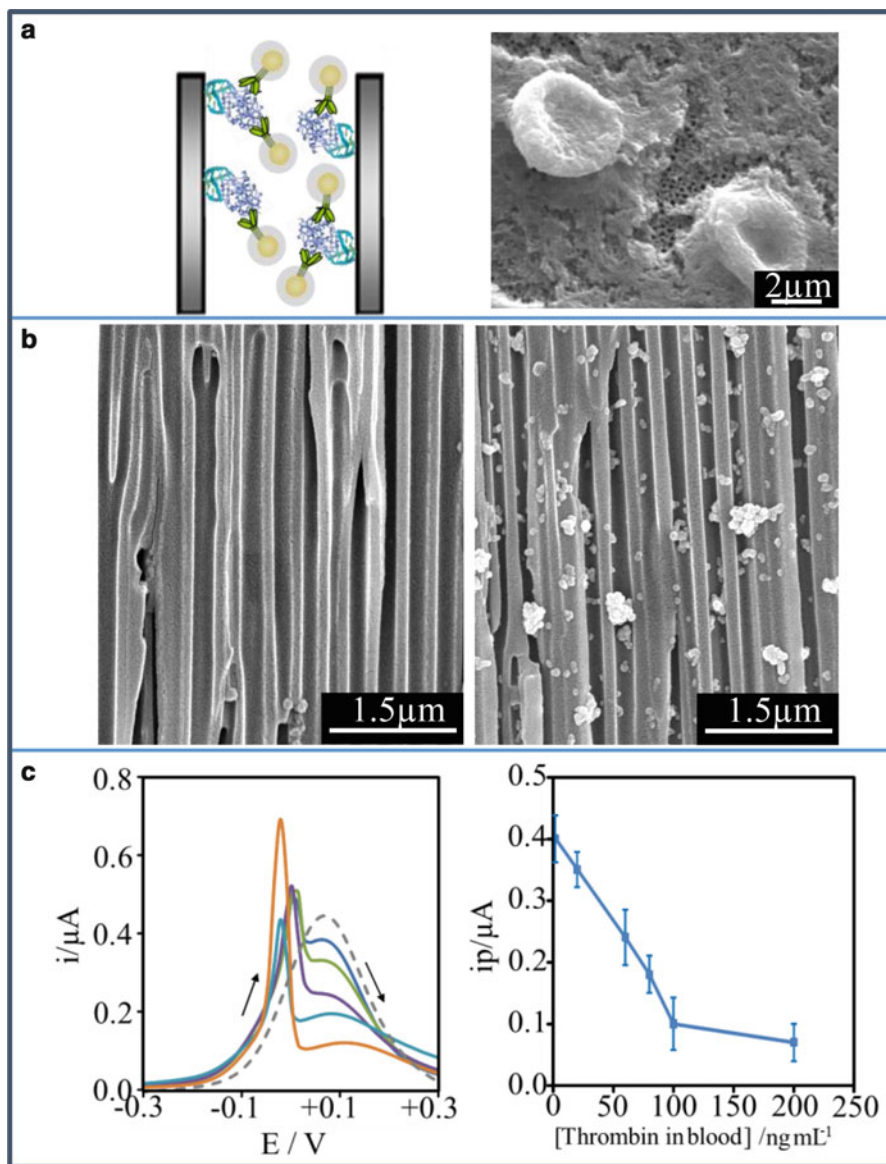
Fig. 9.10 (**a**) *Left*; schematic representation (not in scale) of a sandwich assay (aptamer/thrombin/antibody) with AuNP labeled antibodies and silver deposition. *Right*; SEM *top* view image of an AAO membrane of 200 nm pore size on which a 30 μL drop of blood was deposited. White and red blood cells as well as the nanochannels are observed. (**b**) SEM (cross-sectional view) images of AAO membranes of 200 nm pore size modified with the aptamer and *left* to react with a blood sample containing 100 ng mL^{-1} of spiked thrombin (*Right*) and a blood sample without spiked thrombin (*Left*). The sandwich assay is then completed with anti-thrombin/AuNPs followed by silver enhancement (white silver crystals are observed). (**c**) *Left*; DPVs registered 1 mM K$_3$[Fe(CN)$_6$]/0.1 M NaNO$_3$ for blood samples containing spiked thrombin at concentrations of (*up* to *down*): 0 (*dashed line*), 2, 20, 60, 80 and 100 ng/mL. DPV parameters: pre-concentration potential: −0.3 V; pre-concentration time: 30 s; step potential: 10 mV; modulation amplitude: 50 mV; scan rate: 33.5 mV s^{-1}. *Right*; Effect of the concentration of thrombin spiked in blood on the voltammetric peak current of oxidation of [Fe(CN)$_6$]$^{4-}$ to [Fe(CN)$_6$]$^{3-}$ (approx. +0.1 V) chosen as analytical signal [71]

through the nanochannels to be in contact with the working electrode surface. Figure 9.10b shows SEM images, cross-sectional view, of AAO membranes of 200 nm nanochannels size modified with the aptamer and left to react with a blood sample containing 100 ng mL^{-1} of spiked thrombin (right) and a blood sample without spiked thrombin (left). The sandwich assay is then completed with anti-thrombin/AuNPs followed by silver enhancement (silver crystals are observed; B right). The DPV signals and the quantitative analysis for different quantities of spiked thrombin are shown in Fig. 9.10c, which allow to obtain a detection limit of 1.8 ng of thrombin per mL of human blood [71].

9.6.3   Application for DNA Detection

Following the sensing principle described above, a novel methodology for the detection of ssDNA using nanoporous alumina filter membranes have also been reported. The blockage of the pores due to the hybridization is detected by measuring the decrease in the differential pulse voltammetric response of the $[Fe(CN)_6]^{4-/3-}$ redox indicator using screen printed carbon electrodes [69]. AuNPs tags are used again in order to increase the sensitivity of the assay (Fig. 9.11).

The effect of the concentration of target ssDNA labeled with AuNPs on the DPV peak current used as analytical signal was evaluated (Fig. 9.11 left), obtaining a linear correlation in the range 50–250 ng mL^{-1}. The limit of detection (calculated as the concentration of target ssDNA corresponding to three times the standard deviation of the estimate) was 42 ng mL^{-1} for a 21-mer ssDNA (Fig. 9.11 right).

9.7   Conclusions

A wide variety of NMs, such as nanoparticles and nanochannels have found broad application in analytical methods. Of special relevance are the exciting perspectives of the sensing systems based on nanochannels.

Since the first *in vitro* use of biological channels the appearance of novel technologies able to fabricate synthetic/solid nanochannels has significantly improve the biosensing systems based on such platforms. Nanopores in both synthetic and biological membranes are used as resistive-pulse sensors for molecular and macro-molecular analyte detection. The nanoporous membranes have been shown not only to act as platform for the protein and DNA recognition but also as filter of the micrometric components.

The most reported nanochannel array platform is the anodic aluminum oxide (AAO) membrane due to the homogeneity and precision in the distribution in the pore diameter. AAO membranes can be manufactured with high feasibility and easily reach the specific requirements of the detection systems. As demonstrated in several reports, by reducing the pore diameter it is possible to reduce the biosensing
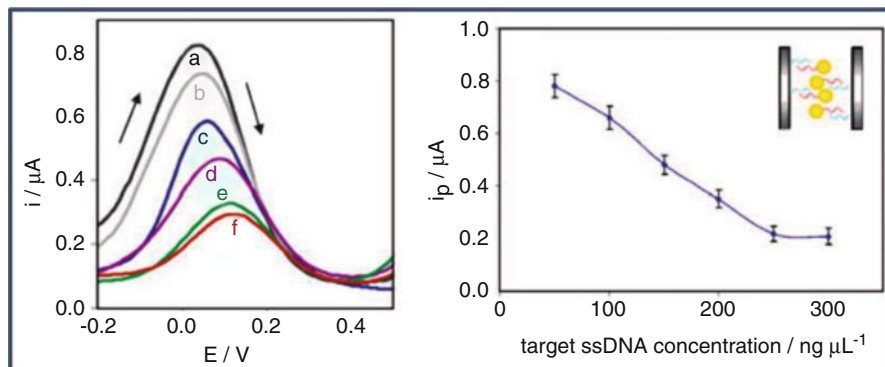
Fig. 9.11 *Left*: differential pulse voltammograms obtained for solutions with different concentrations of target ssDNA labeled with 20 nm AuNPs: (*a*) 50, (*b*) 100, (*c*) 150, (*d*) 200, (*e*) 250 and (*f*) 300 ng mL^{-1}. Pre-concentration potential: -0.55 V; pre-concentration time: 30 s; step potential: 10 mV; modulation amplitude: 50 mV; scan rate: 33.5 mV s^{-1}. *Right*: effect of the concentration of the target ssDNA labeled with 20 nm AuNPs on the analytical signal [69]

detection limits. Further enhancements also can be achieved by amplification by using bigger size nanoparticles including enlargement by catalytic reactions (e.g. Ag deposition onto AuNPs). The combinations of nanochannel sensing capability with the known advantages of NPs in immunosensing bring new benefits in the diagnostic of proteins.

The integration of nanochannel/nanoporous membrane with electrochemical transducer (ex. screen-printed electrode) seems to be one of the most important challenges in the development of robust sensing devices that may bring electrochemical/nanochannel-based biosensing technology to the market.

References

1. N.J. Ronkainen, H.B. Halsall, W.R. Heineman, Electrochemical biosensors. Chem. Soc. Rev. **39**, 1747–1763 (2010)
2. A.P.F. Turner, Biosensor: sense and sensibility. Chem. Soc. Rev. **42**, 3175–3648 (2013)
3. F. Valentini, G. Palleschi, Nanomaterials and analytical chemistry. Anal. Lett. **41**, 479–520 (2008)
4. A. Merkoci, M. Aldabert, S. Marón, S. Alegret, New materials for electrochemical sensing V: nanoparticles for DNA labeling. Anal. Chem. **24**, 341–349 (2005)
5. J.R. Windmiller, J. Wang, Wearable electrochemical sensors and biosensors: a review. Electroanalysis **25**, 29–46 (2013)

6. B. Pérez-López, A. Merkoçi, Nanoparticles for the development of improved (bio)sensing systems. Anal. Bioanal. Chem. **399**, 1577–1590 (2011)
7. A. De la Escosura-Muñiz, A. Ambrosi, A. Merkoçi, Electrochemical analysis with nanoparticle-based biosystems. Anal. Chem. **27**, 568–584 (2008)
8. A. De la Escosura-Muñiz, A. Mekoçi, Electrochemical detection of proteins using nanoparticles: applications to diagnostics. Expert. Opin. Med. Diagn. **4**, 21–37 (2010)
9. A. De la Escosura-Muñiz, C. Parolo, A. Merkoçi, Immunosensing using nanoparticles. Mater. Today **13**, 24–34 (2010)
10. A. Merkoçi, Nanoparticles-based strategies for DNA, protein and cell sensors. Biosens. Bioelectron. **26**, 1164–1177 (2010)
11. H. Jans, Q. Huo, Gold nanoparticle-enabled biological and chemical detection and analysis. Chem. Soc. Rev. **41**, 2849–2866 (2012)
12. M.-C. Daniel, D. Astruc, Gold nanoparticles: assembly, supramolecular chemistry, quantum-size-related properties, and applications toward biology, catalysis, and nanotechnology. Chem. Rev. **104**, 293–346 (2004)
13. J. Turkevich, P. Cooper Stevenson, J. Hillier, A study of the nucleation and growth processes in the synthesis of colloidal gold. Discuss. Faraday Soc. **11**, 55–75 (1951)
14. A. De la Escosura-Muñiz, M. Maltez-da Costa, C. Sánchez-Espinel et al., Gold nanoparticle-based electrochemical magnetoimmunosensor for rapid detection of anti-hepatitis B virus antibodies in human serum. Biosens. Bioelectron. **26**, 1710–1714 (2010)
15. A. De la Escosura-Muñiz, C. Sánchez-Espinel, B. Díaz-Freitas et al., Rapid identification and quantification of tumor cells using an electrocatalytic method based on gold nanoparticles. J. Anal. Chem. **81**, 10268–10274 (2009)
16. M. Maltez-da Costa, A. de la Escosura-Muñiz, C. Nogués et al., Simple monitoring of cancer cells using nanoparticles. Nano Lett. **12**, 4164–4171 (2012)
17. M. Maltez-da Costa, A. de la Escosura-Muñiz, C. Nogués et al., Detection of circulating cancer cells using electrocatalytic gold nanoparticles. Small **8**, 3605–3612 (2012)
18. A. De la Escosura-Muñiz, C. Parolo, F. Maran, A. Mekoçi, Size-dependent direct electrochemical detection of gold nanoparticles: application in magnetoimmunoassays. Nanoscale **3**, 3350–3356 (2011)
19. A. De la Escosura-Muñiz, A. Merkoci, Nanochannels preparation and application in biosensing. ACS Nano **6**, 7556–7583 (2012)
20. W.H. Coulter, Means for Counting Particles Suspended in a Fluid. (1953)
21. W.H. Coulter, J. Coulter, High speed automatic blood cell counter and cell size analyzer. Proc. Natl. Electron. Conf. **12**, 1034–1040 (1956)
22. T. Albrecht, J.B. Edel, M. Winterhalter, New developments in nanopore research-from fundamentals to applications. J. Phys. Condens. Matter. **22**, 450301 (1pp) (2010)
23. S. Bezrukov, I. Vodyanoy, A. Parsegian, Counting polymers moving through a single ion channel. Nature **370**, 279–281 (1994)
24. W. Vercoutere, S. Winter-Hilt, V. DeGuzman et al., Discrimination among individual Watson-Crick base pairs at the termini of single DNA hairpin molecules. Nucleic Acids Res. **31**, 1311–1318 (2003)
25. S. Howorka, Z. Siwy, Nanopore analytics: sensing of single molecules. Chem. Soc. Rev. **38**, 2360–2384 (2009)
26. H. Bayley, P.S. Cremer, Stochastic sensors inspired by biology. Nature **413**, 226–230 (2001)
27. R.F. Purnell, J.J. Schmidt, Discrimination of single base substitutions in a DNA strand immobilized in a biological nanopore. ACS Nano **3**, 2533–2538 (2009)
28. D. Rotem, L. Jayasinghe, M. Salichou, H. Bayley, Protein detection by nanopores equipped with aptamers. J. Am. Chem. Soc. **134**, 2781–2787 (2012)
29. G. Oukhaled, J. Mathé, A.-L. Biance et al., Unfolding of proteins and long transient conformations detected by single nanopore recording. Phys. Rev. Lett. **98**, 158101–158104 (2007)
30. J. Kasianowicz, E. Brandin, D. Branton, D. Deamer, Characterization of individual polynucleotide molecules using a membrane channel. Proc. Natl. Acad. Sci. U. S. A. **93**, 13770–13773 (1996)

31. D. Branton, D.W. Deamer, A. Marziali et al., The potential and challenges of nanopore sequencing. Nat. Biotechnol. **26**, 1146–1153 (2008)
32. J.J. Kasianowicz, J.W.F. Robertson, E.R. Chan et al., Nanoscopic porous sensors. Anal. Chem. **1**, 737–766 (2008)
33. B.M. Venkatesan, R. Bashir, Nanopore sensors for nucleic acid analysis. Nat. Nanotechnol. **6**, 615–624 (2011)
34. J.O. Arroyo, J. Andrecka, K.M. Spillane et al., Label-free, All-optical detection, imaging, and tracking of a single protein. Nano Lett. **14**, 2065–2070 (2014)
35. T. Kumeria, A. Santos, D. Losic, Ultrasensitive nanoporous interferometric sensor for label-free detection of gold(III) ions. ACS Appl. Mater. Interfaces **5**, 11783–11790 (2013)
36. A. Santos, G. Macías, J. Ferré-Borrull et al., Photoluminescent enzymatic sensor based on nanoporous anodic alumina. ACS Appl. Mater. Interfaces **4**, 3584–3588 (2012)
37. A. Santos, T. Kumeria, D. Losic, Optically optimized photoluminescent and interferometric biosensors based on nanoporous anodic alumina: a comparison. Anal. Chem. **85**, 7904–7911 (2013)
38. K. Wang, G. Liu, N. Hoivik et al., Electrochemical engineering of hollow nanoarchitectures: pulse/step anodization (Si, Al, Ti) and their applications. Chem. Soc. Rev. **43**, 1476–1500 (2014)
39. Y. Tian, X. Hou, L. Jiang, Biomimetic ionic rectifier systems: asymmetric modification of single nanochannels by ion sputtering technology. J. Electroanal. Chem. **656**, 231–236 (2011)
40. S.Y. Chou, W.-D. Li, X. Liang, Quantized patterning using nanoimprinted blanks. Nanotechnology **20**, 155303 (2009)
41. M.J.K. Klein, F. Montagne, N. Blondiaux et al., SiN membranes with submicrometer hole arrays patterned by wafer-scale nanosphere lithography. J. Vac. Sci. Technol. B **29**, 0210121–0210125 (2011)
42. J.-M. Li, C. Liu, X. Ke et al., Fabrication of 1D nanochannels on thermoplastic substrates using microchannel compression. Microsyst. Technol. **19**, 1845–1850 (2013)
43. N.R. Devlin, D.K. Brown, P.A. Kohl, Patterning decomposable polynorbornene with electron beam lithography to create nanochannels. J. Vac. Sci. Technol. B **27**, 2508–2511 (2009)
44. J.Y. Cheng, C.A. Ross, H.I. Smith, E.L. Thomas, Templated self-assembly of block copolymers: top-down helps bottom-up. Adv. Mater. **18**, 2505–2521 (2006)
45. A.P. Quist, E. Pavlovic, S. Oscarsson, Recent advances in microcontact printing. Anal. Bioanal. Chem. **381**, 591–600 (2005)
46. P. Wang, S. Paik, S. Chen et al., Fabrication and characterization of polymer hollow microneedle array using UV lithography into micromolds. J. Microelectromech. Syst. **22**, 1041–1053 (2013)
47. W. Zhang, Z. Meng, J. Zhai, L. Heng, Ion current behaviors of mesoporous zeolite-polymer composite nanochannels prepared by water-assisted self-assembly. Chem. Commun. **50**, 3552–3555 (2014)
48. X. Li, H. You, H. Jiang et al., Fabrication of size controllable SU-8 nanochannels using nanoimprint lithography and low-pressure thermal bonding methods. Micro Nano Lett. **9**, 105–108 (2014)
49. A. Yamaguchi, N. Teramae, Fabrication and analytical applications of hybrid mesoporous membranes. Anal. Sci. **24**, 25–30 (2008)
50. B. Cao, W. Cai, F. Sun et al., Fabrication of large-scale zinc oxide ordered pore arrays with controllable morphology. Chem. Commun. **14**, 1604–4605 (2004)
51. A.Y. Menshikova, T.G. Evseeva, Y.O. Skurkis et al., Monodisperse carboxylated polystyrene particles: synthesis, electrokinetic and adsorptive properties. Polymer **46**, 1417–1425 (2005)
52. A. Walcarius, Electrocatalysis, sensors and biosensors in analytical chemistry based on ordered mesoporous and macroporous carbon-modified electrodes. Trends Anal. Chem. **38**, 79–97 (2012)
53. V.-M. Guérin, J. Elias, T.T. Nguyen et al., Ordered networks of ZnO-nanowire hierarchical urchin-like structures for improved dye-sensitized solar cells. Phys. Chem. Chem. Phys. **14**, 12948–12955 (2012)

54. L.K. Teh, K.H. Yeo, C.C. Wong, Isotropic photonic pseudogap in electrodeposited ZnO inverse opal. Appl. Phys. Lett. **89**, 051105 (2006)
55. R.W.J. Scott, S.M. Yang, G. Chabanis et al., Tin dioxide opals and inverted opals: near-ideal microstructures for gas sensors. Adv. Mater. **13**, 1468–1472 (2001)
56. L.-Y. Chen, K.-H. Yang, H.-C. Chen et al., Innovative fabrication of a Au nanoparticle-decorated SiO2 mask and its activity on surface-enhanced Raman scattering. Analyst **139**, 1929–1937 (2014)
57. M. Bender, A. Fuchs, U. Plachetka, H. Kurz, Status and prospects of UV-nanoimprint technology. Microelectron. Eng. **83**, 827–830 (2006)
58. H. Lan, Y. Ding, Nanoimprint Lithography, in *Lithography*, ed. by M. Wang (In Tech, Croatia, 2010), pp. 458–494
59. Y. Shen, L. Yao, Z. Li et al., Double transfer UV-curing nanoimprint lithography. Nanotechnology **24**, 465304 (2013)
60. C. Simao, W. Khunsin, N. Kehagias et al., Order quantification of hexagonal periodic arrays fabricated by in situ solvent-assisted nanoimprint lithography of block copolymers. Nanotechnology **25**, 175703 (2014)
61. Q. Dong, G. Li, C.-L. Ho et al., A polyferroplatinyne precursor for the rapid fabrication of L1o -FePt-type bit patterned media by nanoimprint lithography. Adv. Mater. **24**, 1034–1040 (2012)
62. A.K. Kasi, J.K. Kasi, N. Afzulpurkar et al., Bending and branching of anodic aluminum oxide nanochannels and their applications. J. Vac. Sci. Technol. B **30**(031805), 1–6 (2012)
63. A. Santos, P. Formentín, J. Ferré-Borrull et al., Nanoporous anodic alumina obtained without protective oxide layer by hard anodization. Mater. Lett. **67**, 296–299 (2012)
64. A. Santos, T. Kumeria, D. Losic, Nanoporous anodic aluminum oxide for chemical sensing and biosensors. Anal. Chem. **44**, 25–38 (2013)
65. G. Koh, S. Agarwal, P.-S. Cheow, C.-S. Toh, Development of a membrane-based electrochemical immunosensor. Electrochim. Acta **53**, 803–810 (2007)
66. A. Debrassi, A. Ribbera, W.M. De Vos et al., Stability of (bio)functionalized porous aluminum oxide. Langmuir **30**, 1311–1320 (2014)
67. L. Wen, Z. Sun, C. Han et al., Fabrication of layer-by-layer assembled biomimetic nanochannels for highly sensitive acetylcholine sensing. Chem. Eur. J. **19**, 7686–7690 (2013)
68. A. De la Escosura-Muñiz, A. Mekoçi, Label-free voltammetric immunosensor using a nanoporous membrane based platform. Electrochem. Commun. **12**, 859–863 (2010)
69. A. De la Escosura-Muñiz, A. Mekoçi, Nanoparticle based enhancement of electrochemical DNA hybridization signal using nanoporous electrodes. Chem. Commun. **46**, 9007–9009 (2010)
70. A. De la Escosura-Muñiz, A. Merkoçi, A nanochannel/nanoparticle-based filtering and sensing platform for direct detection of a cancer biomarker in blood. Small **7**, 675–682 (2011)
71. A. De la Escosura-Muñiz, W. Chunglok, W. Surareungchai, A. Merkoçi, Nanochannels for diagnostic of thrombin-related diseases in human blood. Biosens. Bioelectron. **40**, 24–31 (2013)

Chapter 10
Electrospinning-Based Nanobiosensors

Fabrizio De Cesare and Antonella Macagnano

Abstract Biological interactions in biosensors occur through different mechanisms, on the basis of the type of biological receptor elements employed therein that confer the biological specificity to the biosensors themselves (biocatalytic, biocomplexing or bioaffinity biosensors). The use of different transduction systems (amperometric, potentiometric, field-effect transistors, piezometric and conductometric) defines the mode of detection. The interest and relevance of nanomaterials in the fabrication of nanobiosensors lie in their extraordinary properties that make them ideally suited and very promising for sensing applications. The resulting nanobiosensors are capable of sensing analytes in traces with fast, precise and accurate biological identification through miniaturised and easy to use systems. These advanced sensors are also characterised by lower detection limits, higher sensitivity values and high stability, and can further offer multi-detection possibilities. These exceptional features make nanobiosensors as the favourite tools in quality control, food safety, and traceability for their capacity of revealing and warning people against the presence of pathogens, toxins and pollutants, as well as bioterrorism agents. Despite the outstanding properties of these nanobiosensors, however, the efficiency of the biorecognition agent and the number of biorecognition sites available for interacting with target analytes can limit the sensitivity of this kind of sensors. The number of available biorecognition sites is directly related to the surface area of the sensor. Electrospinning technology can significantly increase the sensitivity of biosensors by replacing the typical planar interactive surface of conventional biosensors with a mat of electrospun nonwoven nanofibres, thereby taking advantage of the ultrahigh surface area offered by electrospun nanofibres. Moreover, adjusting the electrospinning process to produce

F. De Cesare (✉)
Department for Innovation in Biological, Agro-food and Forest Systems, University of Tuscia, Via S. Camillo De Lellis, 01100 Viterbo, Italy

Institute of Atmospheric Pollution Research-National Research Council, Research Area of Rome 1, Via Salaria km 29,300, 00016 Monterotondo, Rome, Italy
e-mail: decesare@unitus.it

A. Macagnano
Institute of Atmospheric Pollution Research-National Research Council, Research Area of Rome 1, Via Salaria km 29,300, 00016 Monterotondo, Rome, Italy
e-mail: a.macagnano@iia.cnr.it

hollow nanofibres can further increase the surface area of electrospun nanofibres. The immobilisation of bioreceptors into or onto electrospun nanofibres remarkably increases the number of recognition sites for biosensing, i.e. available for capturing the analytes through specific binding mechanisms. Furthermore, electrospinning technology can provide the deposition onto transducers of 3D frameworks of electrospun nanofibrous mat, with a tunable interconnected porosity, predictable pore geometries and sizes, and large global pore volumes. Such feature can supply further properties to the resulting nanobiosensor suitable for the detection of analytes in particular environments, where an efficient transport of the analytes through the membrane toward the electrode surface is required. Due to such an extreme versatility, electrospinning is expected to have several strategic advantages over other nanotechnologies as concerns nanobiosensing.

In the present chapter, a brief overview of the main recent studies on electrospun nanobiosensor and applications is proposed. Attention is focused on enzyme-based nanobiosensors, and the advantages and drawbacks of enzyme immobilisation as well as improvements due to employment of electrospinning in these biosensors are presented. Specifically, the application of nanobiosensors in glucose detection and the contribution of electrospinning to these sensing systems are reported. Furthermore, the use of bioaffinity mechanisms in recognition processes of nanobiosensors is considered by focusing on nanobiosensors employing hybridisation probes and functional nucleic acids (aptamers, peptide nucleic acids, Rybozymes, DNAzymes and Aptazymes) and their outstanding sensitivities are described. The improvements of electrospinning in these sensing systems are highlighted, when applicable. Similarly, electrospun-based immunobiosensors (antibody-based nanobiosensors) and their applications are described.

10.1 Introduction

According to the most recent definition released by IUPAC and reported by Thévenot et al. (2001) [1], a biosensor (electrochemical) is classified as a "self-contained integrated device, which is capable of providing specific quantitative or semi-quantitative analytical information using a biological recognition element (biochemical receptor) which is retained in direct spatial contact with an electro-chemical transduction element." As stated, this definition includes those devices that are both disposable after one measurement and unable to control the analyte concentration continuously or after rapid and reproducible regeneration, i.e. a single use biosensor, but excludes bioanalytical systems, which requires additional processing steps, such as reagent addition [1]. According to that classification, biosensors are distinguished on the basis of the type of biological receptor element and the mechanism conferring the biological specificity into (i) biocatalytic bio-sensors, i.e. containing enzyme, whole cells and tissues; (ii) biocomplexing or

bioaffinity biosensors, e.g. antibody-antigen based, agonist/antagonist-based and DNA-based. Biosensors can be also classified on the basis of the mode of detection as amperometric, potentiometric, piezometric, using field-effect transistors sensitive to surface charges, and conductometric. Finally on the basis of the analytes or reactions they monitor, biosensors can be distinguished into: direct or indirect monitoring biosensors. Operatively then, biosensors can be defined as analytical devices able to convert a biological interaction into a readable electrical/optical signal. Usually, the steps required to fabricate a biosensor are: (i) choosing a proper bioreceptor useful for the biological identification of interest; (ii) immobilising the receptor on a transducer; (iii) selecting the transduction mechanism and (iv) linking the sensing unit to a reliable detector to get reproducible responses. A transducer converts a biochemical signal generated by the interaction of a target analyte with the bioreceptor immobilised onto the matrix into an electronic signal. Depending on the nature of the biochemical interaction with the species of interest, suitable transducing systems can be adapted in a sensor assembly. The physical transducers vary from electrochemical, potentiometric, optical, calorimetric, conductometric/impedimetric, piezoelectric and ion charge/field effect; the most commonly used are potentiometric and amperometric [1].

Nanobiosensors are biosensors comprising nanomaterials. The reason for the involvement of these materials in the fabrication of nanobiosensors lies in the extraordinary properties of nanomaterials [2]. According to the definition used by the U.S. Environmental Protection Agency (EPA) and developed by the National Nanotechnology Initiative (NNI) of U.S., "nanotechnology" is basically "the science of manipulating matter at the atomic or molecular scale" and involves: (i) research and technology development at the atomic, molecular, or macromolecular levels, in the length scale of approximately 1–100 nanometer (nm) range in any direction; (ii) creation and use of structures, devices, and systems that have novel properties and functions as a result of their small and/or intermediate size; (iii) ability to control or manipulate on the atomic scale. The rational behind the employment of nanotechnology in sensors lies in the outstanding properties that materials at nanoscale often express. Materials in the nanoscale range (i.e., with at least one dimension in the size range of approximately 1–100 nm) can in effect exhibit different chemical or physical properties, or biological effects compared to larger-scale materials with the same chemical composition. These unexpected changes are called quantum effects. These effects may derive from altered chemical, biological, or magnetic properties, altered electrical conductivity, optical activity or elasticity, increased structural integrity and strength, different colour and greater reactivity, or other unique characteristics of materials at the nanoscale range that they do not possess at the micro or macro scales. Then, nanomaterials have number of features that make them ideally suited and very promising for sensing applications [3].

The possibility to control the matter on the nanometer length scale is providing a chance to design and create an entirely new generation of biological sensors. These new systems will be capable of sensing at the single-molecule level with fast, precise and accurate biological identification through miniaturized and easy to use systems [4]. Several nanomaterials can be employed in the generation of

nanobiosensors: nanotubes (NTs), nanowires, nanorods (NRs), nanoparticles (NPs) and thin films made up of nanocrystalline matter [5]. Nanomaterials such as (magnetic) nanoparticles ((M)NPs), carbon nanotubes (CNTs), nanorods (NRs), quantum dots (QDs), nanowires (NWs), and nanochannels (NCs) have very high capacity for charge transfer, so that they can enable the resulting nanobiosensors to achieve lower detection limits and higher sensitivity values. Additionally, the possibility to manipulate the materials at nanoscale is highly remarkable in biology, since biomolecules, biomacromolecule and their structures are in the range 1–1,000 nm, and also biochemical reactions and molecular interactions occur at nanosize. The improved electrical sensitivity and chemical reactivity of nanomaterials, combined with an extraordinary increase in the interacting surface area, can permit nanobiosensors to achieve very low detection limits (down to single molecule or cell) and a high stability (i.e., NPs such as QDs are more stable than enzymes or fluorescence dyes). In addition, they offer multi-detection possibilities. Such outstanding features of nanobiosensors have spread the doors to a plethora of possible applications in any field and context and to the generation of a multitude of different biosensing tools employing nanomaterials. The decision about the use of a particular kind of nanomaterial for a certain biosensing application depends on a multitude of factors ascribable to their physical and chemical properties along with their energy, as well as their sensitive and selective responses.

Nanostructured biosensors with a high degree of precision and accuracy are then considered as the most innovative and advanced tools to reveal analytes in traces, whatever their nature (organic or inorganic). They are capable of detecting molecules naturally occurring in biological fluids of organisms, entire cells such as microorganisms present in other organisms or in various environments, metals and other inorganic ions and organic pollutants in cells, tissues, organism and environments. The innate worry of humans to preserve their health and survive to adverse agents, combined with the exceptional features of these detectors, make nanobiosensors as the favourite tools in quality control, food safety, and traceability for their capacity of revealing and warning people against the presence of pathogens, toxins, pollutants and bioterrorism agents. The use of nanobiosensors, then, includes mostly biomedical, diagnostic and environmental applications, plus some particular involvements in limited industrial processes, e.g. in bioreactors and separations.

The efficiency of the biorecognition agent and the number of biorecognition sites interacting with target analytes can limit the sensitivity of these biosensors. The number of sites available for biorecognition is directly related to the specific surface area of sensors. Electrospinning technology can significantly increase the sensitivity of biosensors by replacing the typical planar interactive surface of conventional biosensors with a mat of electrospun nanofibres, thereby taking advantage of the ultrahigh surface area offered by electrospun nanofibres. The surface area of electrospun nanofibres can be further increased using modifications in the electrospinning process to produce hollow nanofibres [6]. The immobilisation of bioreceptors into or onto electrospun nanofibres remarkably increases the number
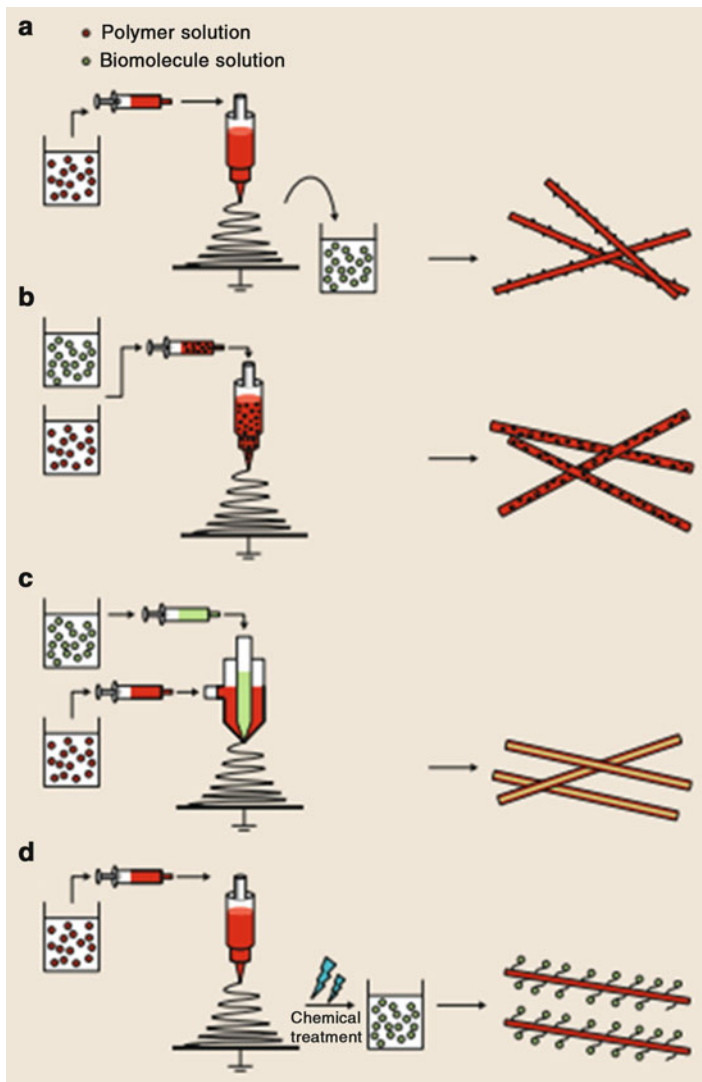
Fig. 10.1 Fabrication techniques for bioactive electrospun scaffolds. (**a**) Physical adsorption, (**b**) blend electrospinning, (**c**) coaxial electrospinning, (**d**) covalent immobilisation [7] (Copyright Springer)

of biorecognition sites for biosensing, i.e. available for capturing the analytes through specific binding mechanisms (Fig. 10.1) [7].

Immobilisation of bioreceptors can be achieved in three different ways: (i) by solving such molecules directly into the electrospinning solution in order to obtain nanofibres where bioreceptors are embedded into the electrospun polymer [8]; (ii) by binding bioreceptors to electrospun nanofibres through physical, chemical

or physicochemical interactions [9]; (iii) by functionalising the nanofibre surface after electrospinning with suitable ligands, covalently attached to surface through proper reactions to prevent their leaching, and then immobilising bioreceptors by fixing them to ligands, mostly through chemical or physicochemical bonds [10].

An additional feature of the electrospinning technology in nanobiosensors is to deposit electrospun sensitive mats onto transducers characterised by 3D structures or scaffolds, with a tunable porosity, achieved through adjustments in the electrospinning process. Such feature can supply further properties to the resulting nanobiosensor suitable for the detection of analytes in particular environments. These porous scaffolds are necessary elements to achieve an efficient transport of the analytes through the membrane toward the electrode surface.

Summing up, electrospinning technology provides the following opportunities in the development of advanced nanobiosensors: (i) to generate membranes designed with excellent (or tuned on purpose) interconnected porosity, predictable pore geometries and sizes, large global pore volumes; (ii) to obtain nanofibres with desired diameters, then extending specific surface area; (iii) to regulate, in a single electrospinning deposition step, the desired thickness of the applied membrane, from tens of nanometres to several micro-meters; (iv) to use a large variety of materials (organic and inorganic polymers, composites, polymer-blends, hybrids, ceramics, metallic nanoparticles) exhibiting a great deal of different interacting properties [11]. All these features make electrospinning as an outstanding technology in the fabrication of nanobiosensors suitable for the detection of a multitude of analytes. Some of these advantages and potentials will be featured below, through a brief overview of the main recent electrospun nanobiosensor studies and applications. Due to such an extreme versatility, electrospinning is expected to have several strategic advantages over other nanotechnologies as concerns nanobiosensing.

10.2 Enzyme-Based Nanobiosensors

10.2.1 Enzyme Immobilisation

In recent decades enzyme immobilisation onto one-dimensional nanostructured materials has attracted continuous attention due to the resulting assemblies unique features. Enzymes are well-known for their high degree of specificity that provides them with a high efficiency for applications in industry, medicines and environment, such as fine-chemical/pharmaceutical synthesis, food processing, cosmetics, biosensors fabrication, bioremediation of polluted sites and materials and protein digestion in proteomic analysis [12–16]. Conversely, their instability and dependence of catalytic activity on environmental conditions, ease inactivation, inhibition, denaturation and even degradation, as well as their non-reusability are parameters that limit the use of enzymes in biosensors. Enzyme immobilisation is a process that can be

performed on different matrices [17–20], and following different procedures [21], and which can positively overcome these limitations. The multiple-point adhesion to any matrix, for example, can hinder, limit or prevent undesired conformational changes of the enzyme structure in adverse and extreme environments (e.g. strongly acidic or alkaline, high temperature, solvents), inhibition by compounds such as heavy metals [22], and degradation by biological agents (e.g. proteases) [23]. Additionally, the use of insoluble matrices in immobilisation allows ease recovering and recycling, much more than soluble enzymes. Multipoint fixation to supports, however, can also have some drawbacks, due to the possible reduction in the catalytic performances (kinetics) of enzymes (lower V_{max} and higher K_m). These inconveniences are the consequence of several factors mostly related to the surface chemistry of fabrics, as follows: (i) induced modifications of the overall conformation of enzymes that can induce denaturation of enzymes or hinder the access of substrates to the catalytic sites; (ii) limitations in conformational changes of enzymes necessary for the catalysis of reactions; (iii) restriction, decline or slowing down in diffusion of both substrates towards and products off enzymes (mass transfer); (iv) delay in electron transfer involved in the catalysis process, especially for redox enzymes, and induced by the support. However, these drawbacks may be considered the price to pay for a greater stability and longer retention of the catalytic activity. The performance of immobilised enzymes, strongly depend on the properties of scaffolds, such as material types, compositions and structures [24]. Until now, several nanostructured materials, such as mesoporous silica, nanotubes, nanoparticles and nanofibres, have been used as matrices due to their extremely high surface area-to-volume ratios. Large specific surface areas, in effect, provide highly efficient immobilisation and stabilises enzymes. One-dimensional materials may be usually arranged in the forms of rods, belts, tubes, fibres, spirals and wires, generated by several techniques. However, the disadvantages of some of the nanostructured materials are difficult to overcome. For example, mesoporous silica usually confines enzyme molecules on its inner surface, which limits the diffusion of substrate towards the enzymes and of products off of them, then resulting in lower catalytic performances and global enzyme activities [25]. Nanoparticles and nanotubes are known to decrease remarkably mass transfer limitation, but their dispersion and recycling are more difficult than the films. On the contrary, electrospun nanofibres have a great potential to overcome these problems, and then may be promising mats for enzyme immobilisation. Briefly, the qualification of nanofibres as excellent fabric for this purpose is attributed to (i) a variety of electrospinnable polymers to meet different requirements, (ii) the high porosity and the interconnectivity of electrospun frames endowing nanofibres with a small hindrance in mass transfer, and (iii) the modifiable nanofibre surfaces to benefit enzyme activity [26]. The potentialities of electrospun nanofibres in the mass transfer have been extensively studied in several applications, where the collection of randomly arrayed nanofibres, often forming a non-woven mesh (or membrane) with reusability, has been employed as filters [27–29]. In the study of Ye et al. (2006) [30], the nanofibrous membranes obtained from poly (acrylonitrile-co-maleic acid) (PANCMA) and containing carboxylic reactive groups, which can be used to immobilise covalently biomacromolecules, were tethered with

two natural macromolecules, chitosan and gelatin, using 1-ethyl-3-(dimethyl-aminopropyl) carbodiimide hydrochloride (EDC)/N-hydroxyl succinimide (NHS), in order to fabricate dual-layer biomimetic supports for enzyme immobilisation. Lipase was then immobilised on these dual-layer biomimetic supports using glutar-aldehyde (GA) or EDC/NHS on the original PANCMA. Such nanofibrous mats, when hosting immobilised enzymes, combine simultaneously the biocatalytic func-tion of enzymes and their separation from end products, performed with the help of a selective membrane, which is a typical mode for running continuous catalytic processes in enzymatic membrane-bioreactors [31–33]. Similarly, electrospun nanofibrous membrane have been involved recently in the fabrication of enzymatic membrane-bioreactors [34–36].

Immobilisation of enzymes onto electrospun nanofibres has been examined in a good deal of studies in the last years [37]. The possibility to use a multitude of polymers, organic and inorganic, singly or in combinations (composites or blends) to fabricate electrospun mats and the wide number of procedures available for enzyme immobilisation permit a flexible tailoring of the surface chemistry of nanofibres to generate nanofibrous catalytic mats through several ways. Wang et al. (2009) described some approaches followed in the immobilisation of enzymes onto electrospun nanofibrous mats, which are reported in Table 10.1 [38].

In the same review, some strategies followed to overcome the drawbacks affecting the enzymatic activity and inherent to the immobilisation processes, previously listed, have also been described, and are reported in Fig. 10.2.

The first study about this issue is that of Jia et al. (2002), where α-chymotrypsin was covalently immobilised [39] onto fibres of hydroxyl-functionalised polysty-rene, thus increasing both the specific activity of the native enzyme in aqueous solution over 65 % and its stability to several organic solvents (e.g. isooctane and hexane). Although nanofibres have large surface area-to-volume ratio, the immobilised enzymes only formed, in that case, a monolayer on each fibre that largely limits the enzyme loading. Therefore, Kim et al. [48] developed enzyme-aggregate coatings on the electrospun polymer nanofibres. In their work, seed molecules of α-chymotrypsin were covalently attached to electrospun nanofibres consisting of a mixture of polystyrene and poly(styrene-co-maleic anhydride). Then, additional enzyme molecules and aggregates from the solution were cross-linked to the seed enzyme molecules through a glutaraldehyde (GA) treatment. The results showed that this method increased the amount of enzyme loading up to eight times and that the initial apparent activity of the enzyme-aggregate-coated nanofibres was nine times higher than that of nanofibres with just one layer of covalently attached enzyme molecules. The enzyme stability of the resulting enzyme-aggregate-coated nanofibres was greatly improved, since after a month of observation under vigorous shaking conditions no significantly measurable loss of activity was observed. Such a property was mainly due to the high stability of the pre-organised superstructure of cross-linked enzyme aggregates covalently attached to the nanofibres. Several other enzymes have been used in immobilisation studies: lipase (the most tested), trypsin, lysozyme, esterase, acetylcholinesterase, catalase, cellulase, etc. [49–55].

Table 10.1 Some typical cases of enzyme immobilisation on electrospun nanofibres

Nanofibrous scaffold	Enzymes	Activity maintenance (%)	Loading (mg/g fibres)	Immobilisation strategy	References
PS	α-Chymotrypsin	65	14.0	Chemical	Jia (2002) [39]
SF	α-Chymotrypsin	66.78	56.6	Chemical	Lee (2005) [40]
PANCMA	Lipase	37.6	21.2	Chemical	Ye (2006) [30]
PAN	Lipase	81.3	21.2	Chemical	Li (2007) [41]
PS/PSMA	Lipase	16.5	5.6	Chemical	Nair (2007) [42]
Dispersed/PS/PSMA	Lipase	16.5	42.4	Chemical	Nair (2007) [42]
Chitosan-tethered PANCMA	Lipase	45.6	22.5	Chemical	Ye (2006) [30]
Gelatin-tethered PANCMA	Lipase	49.7	20.7	Chemical	Ye (2006) [30]
PAN	Lipase	56.4	23.2	Physical	Huang (2006) [43]
PANCMPC	Lipase	76.8	22.9	Physical	Huang (2006) [43]
PSF	Lipase	6.2	0.8	Physical	Wang (2006) [44]
PSF/PVP	Lipase	26.7	0.59	Physical	Wang (2006) [44]
PSF/PEG-200	Lipase	18.7	1.24	Physical	Wang (2006) [44]
PANCAA	Catalase	33.11	23.9	Chemical	Xie (2003) [45]
PANCAA/MWCNT	Catalase	47.90	31.1	Chemical	Xie (2003) [45]
PANAACoPP	Catalase	39.3	18.9	Chemical	Wang (2008) [46]
PANCAACoPP/MWCNT	Catalase	48.5	22.81	Chemical	Wang (2008) [46]
PANCAA NF	Horseradish peroxidase	14.02	21.8	Chemical	Wu (2005) [47]
PANCAA/MWCNT	Horseradish peroxidase	23.56	25.1	Chemical	Wu (2005) [47]

Wang et al. [38]. Copyright Elsevier Ltd. 2009

PS polystyrene nanofibres

SF Regenerated silk fibroin nanofibres

PANCMA poly(acrylonitrile-co-maleic acid) nanofibres

PS/PSMA pristine polystyrene/poly(styrene-co-maleic anhydride) composite nanofibres

Dispersed PS/PSMA aqueous alcohol solution treated polystyrene/poly(styrene-co-maleic anhydride) composite nanofibres

PANCMPC poly(acrylonitrile-co-(2-methacryloyloxyethyl phosphorylcholine))

PEG-200 PEG with average molecular weight of 200 g/mol

PANCAA poly(acrylonitrile-co-acrylic acid).

PANAACoPP terpolymer from acrylonitrile, acrylic acid and metalloporphyrin with Co^{2+}
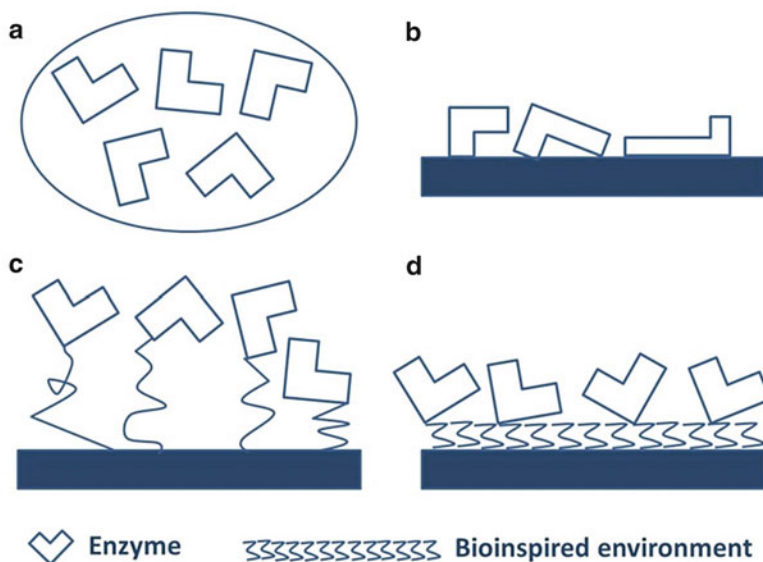
Fig. 10.2 Effect of the surrounding environment on the enzymatic activity: (**a**) native state; (**b**) undesired conformational change upon the adhesion onto the support surface; (**c**) increased mobility by the flexible spacer; (**d**) decreased nonspecific interactions by the bioinspired layer

One of the most common tailoring approaches in the development of advanced biosensors involves the use of biomaterials and polymers with high grade of biocompatibility, in order to mimic natural systems, which succeeds in both stabilising enzymes and retaining their activities. Chitosan is a natural polyaminosaccharide and is the N-deacetylated derivative of chitin. Chitosan is recommended as suitable functional materials because it has excellent properties, extensively described in the literature, such as biocompatibility, biodegradability with ecological safety and low toxicity, adsorption properties, ability to form films and polyoxysalts, and to chelate metal ions. Other interesting features are optical structural characteristics, versatile biological activities such as antimicrobial activity and low immunogenicity, physiological inertness, remarkable affinity toward proteins, good gel forming properties. The application of chitosan and chitosan-based materials for enzyme immobilisation has been discussed in detail by Sun et al. (2011) and Krajewska (2004, 2005) [56–58], while Agboh and Qin (1997) and Wang et al. (2013) reviewed its features as a biocompatible material [59, 60]. Gelatin is derived from collagen and shares with it the biological properties. The binding of these two biomacromolecules to the nanofibres may be used to combine their biocompatibility characteristics with the mechanical strength of nanofibres and to increase a number of reactive groups for enzyme immobilisation [30]. As biocompatible and biodegradable materials, nanofibres of poly(e-caprolactone) and poly(D, L-lactic-co-glycolic acid)-b-poly(ethylene glycol)-NH$_2$ (PLGA-b-PEG-NH$_2$) block copolymer were also used as supports for covalent immobilisation of lysozyme [51].

Another strategy for immobilisation of enzymes is the incorporation of phospholipid moieties into the backbones or side chains of polymers to fabricate biomimetic surfaces. Researches have shown that membranes, modified with phospholipid moieties, bind enzymes due to the increase in hydrophobicity derived by the introduction of alkoxyl groups, and also exhibited excellent biocompatibility [61, 62]. One of the advantages of phospholipid and phospholipid analogues modifications of polymers is the interaction with proteins without inducing three-dimensional conformational changes even when the proteins were adsorbed onto the polymer surface [43, 62, 63]. Their studies used phospholipids integration into electrospun nanofibrous biomimetic layer from the phospholipid moieties, which provided a stable, highly hydrophilic and biocompatible external environment, leading to an effective interfacial activation of the immobilised lipase.

Polymer blending is another effective strategy to enhance the surface biocompatibility of synthetic polymeric materials and then their potential in the generation of enzyme-based electrospun nanofibrous mats. Polysulfone is engineering plastic with high mechanical strength and ductility and limited biocompatibility. However, its blends with hydrophilic and biocompatible components, such as poly(N-vinyl-2-pyrrolidone) (PVP), show significantly enhanced biocompatibility [64]. Immobilisation of lipase onto the polysulfone-based electrospun nanofibres through physical adsorption was achieved using PVP or PEG as additives [44]. The results showed that the activity of immobilised lipase as compared with free lipase showed an increased in the optimum temperature while pH value decreased, and thermal stability increased. Furthermore, kinetic parameters showed lower V_{max} and higher K_m values for immobilised preparations, as it often happens in immobilised enzymes. Noteworthy, enzyme activity increased dependently on the content of PVP or PEG in the nanofibres, though the adsorption amount of lipase was not influenced. This effect was due to weakened adsorption strength at fibre surface induced by these hydrophilic biocompatible additives, which presumably provided a compatible microenvironment for the protein to retain its natural conformation. Compared with other nanofibres used in the lipase immobilisation, the composite nanofibres showed much lower adsorption capacity of enzyme protein and retention of its activity. Nevertheless, upon proper modification, the electrospun polysulfone nanofibres are still possible supports for lipase immobilisation.

In order to reduce non-specific interactions between immobilised enzymes and supports and to increase, at the same time, the movement of bound enzymes during catalysis, spacer arms are often used as linkers between the support surface and enzymes [65]. Wang et al. (2004) introduced PEG as a spacer arm onto the alkali-hydrolysed cellulose nanofibres in the covalent immobilisation of lipase [66]. The fibre-bound lipase exhibited significantly higher catalytic activity at elevated temperatures and possessed much superior retention of catalytic activity after exposure to organic solvents than the free form. These results suggested the effects on lipase catalytic activity were mainly due to the molecular structure of PEG rather than to its chain length.

10.2.2   Enzyme Nanobiosensors

Based on the previously reported features of enzyme-linked electrospun nanofibrous mats, the consequent intuitive and prospective application of enzyme immobilised electrospun nanofibres is in the development of biosensors [8, 67, 68]. The high specificity of enzymes provides them with a great potential for applications in efficient biosensors. However, although electrospun nanofibres have large surface area-to-volume ratio, the tendency of immobilised enzymes to form a monolayer on each fibre can limit the enzyme loading and then the biosensor response. The solution proposed by Kim et al. (2005) [48], previously described to create enzyme-aggregation coatings, after cross-linking of additional enzyme molecules, to seed enzyme molecules firstly fixed on polymers, deals with this problem. It greatly enhances, in effect, enzyme loading and the overall enzymatic activity, although the cross-linking reaction can damage the enzyme activity. Such a suggestion is very promising in the manufacturing of enzyme-based nanobiosensors.

In the so-manufactured biosensors, enzymes can be electrospun together with several polymers, thus resulting embedded into the nanofibres, or it can be somehow linked to the surface after electrospinning through the methodologies previously summarised. One of the advantages of such nanobiosensors is that peeling away the nanofibrous mesh can facilely regenerate the electrode. These biosensors share some common features such as a low detection limit and fast response, as reported in the literature [8, 67, 69]. However, because most of the enzyme molecules are confined inside the nonporous fibres, the accessibility of the substrate to the enzyme can be sometimes inhibited. Co-electrospinning [70], i.e. an electrospinning procedure generating core-shell structures, can overcome this drawback simultaneously providing a favourable microenvironment for the enzyme catalytic activity and the stability of the nanofibrous layer in aqueous solutions.

In reactions catalysed by redox enzymes, the transformation of substrates into products involves the transfer of electrons, and the reactions are sustained until electron transfer is guaranteed. Then, the use of electrically conductive polymers in the immobilisation of enzymes is of particular concern in the generation of electrochemical biosensors [71–74]. Conducting polymers have different electronic structures, compared to saturated polymers. The chemical bonding therein provides one unpaired electron (π electron) per carbon atom in the backbone of the polymer, and since carbon atoms are in sp^2p_z configuration in π bonding, orbitals of successive carbon atoms overlap providing delocalization of electrons along the backbone of the polymer [73, 75]. Due to such electronic delocalization generated by single and double bonds alternating along the polymer chain and forming an extended π-conjugated system, this kind of polymers are characterised by high charge mobility along the backbone of the polymer chain. Such feature provides them typical properties, such as high electrical conductivity, low ionization potential, low energy optical transitions and high electron affinity, which are very promising in biosensor manufacturing [75, 76]. The flexibility in chemical structures of conducting polymers, i.e. the possibility to modulate the required electronic and mechanical properties as required through chemical modelling and synthesis, make these polymers

extremely appealing in the creation of several types of biosensors [73, 77]. Additionally, several different parameters, such as polymer layer thickness, electrical properties and bio-reagent loading, provide control of these molecular electronic materials. Several biomolecules can be linked through a number of mechanisms to these polymers (physical adsorption, cross-linking, gel entrapment, covalent coupling etc.), thus greatly enlarging their applicability in biosensing [73, 75, 77, 78]. The changes in physical properties when materials are at nanoscale, such as electrical, electronic, magnetic, optic and thermodynamic properties, and their large surface to volume ratio, make the involvement of nanomaterials in the synthesis of electrically conductive polymers an important candidate for technological development of nanobiosensors. Therefore, conducting polymer-based biosensors can fulfil the pressing requirements due in various biosensing applications, such as the possibility of in vivo sensing, continuous monitoring (of drugs or metabolites), biocompatibility, multi-parametric assays, miniaturisation and high information density. Consequently, several types of electrically conductive nanostructured polymers have been used to fabricate nanobiosensors, till now. In this context, blending of insulating polymers and electrically conductive nanomaterials may be an additional approach to fabricating suitable supports for enzyme immobilisation [79, 80].

Wang et al. (2007) [81] filled the poly(acrylonitrile-co-acrylic acid) nanofibres with multiwalled carbon nanotubes (MWCNTs) in order to covalently immobilise catalase and donate/accept electrons during the catalysis of the redox enzyme. They observed that, by increasing MWCNTs concentration, the activity of the immobilised catalase was enhanced by 42 %. This result was partly attributed to the exceptional electrical conductivity of MWCNTs and presumably to the electron-transfer path that could be formed through charge-transfer complexes and MWCNTs. Catalase immobilised on the composite nanofibres also showed higher storage stability than that on the pristine nanofibres, which is associated with the hydrophilization and biocompatibility from MWCNTs.

10.2.2.1 Glucose Nanobiosensors

Biomedicine, health care and diagnostics represent fields of application of sensors. The incorporation of nanomaterials into sensors has significantly improved the performances of sensors such as sensitivity, which is of great concern in diagnostic analyses. Most of the studied and effectual involvements of nanosensors from a clinical point of view include numerous clinical applications such as the detection of glucose in diabetic patients, detection of urinary tract bacterial infections, detection of HIV-AIDS, and the diagnosis of cancer. Although several nanosensors have employed a non-enzymatic approach in the detection of analytes [82, 83], most of the sensing tools are nanobiosensors. The main analytes tested in biomedicine comprise glucose, urea, pesticides, cholesterol, DNA and lactate [73, 84] and the development of nanobiosensors specific for these compounds have mostly involved the tethering of enzyme to various nanomaterials. For example, a great deal of nanosensors has been developed to detect glucose. Several of them are enzyme-free sensing systems [85, 86] and some can involve the use of electrospinning technology [87–89]. However, major

efforts have been devoted to fabricating different amperometric glucose biosensors based on glucose oxidase (GOD), because of its importance in food production, fermentation, and clinical diagnostics [90, 91]. Many GOD-based glucose biosensors involve hydrogen peroxide (H_2O_2) quantification, but since the responses of oxygen/hydrogen peroxide-based sensors are affected by fluctuations in the concentration of dissolved oxygen, electron mediators, such as quinones, ferrocenes, viologens and Ru, and Os complexes have been used to eliminate this effect [92, 93], decrease the applied potential with which to follow the enzyme catalysed reaction and achieve effective electrical interaction at the redox-active sites with electrodes at low potentials. Mediated electrocatalysis is a powerful tool for electron transfer measurements of redox-active biomolecules. Such biosensors exhibit fast response, amplify the analytical signal and largely diminish interference from other reduction species [94, 95]. However, the rate at which the mediator exchanges electrons with an enzyme is a critical factor in designing biosensors. Furthermore, all mediators used in bioelectrochemistry and biosensors are also general electrocatalysts and therefore compromise the selectivity of these devices. However, for most amperometric biosensors, the need for an electron transfer mediator has hindered their development and use in continuous, real-time in vivo monitoring because they are leached easily out of the electrode surface, then compromising sensor performances [91, 93, 96]. Several artificial electron mediators have been reported. Prussian blue (PB) also known as "artificial peroxidase" has been widely employed in fabricating amperometric glucose biosensors because of its good biocompatibility, well-known capabilities for enhancing electron transport and excellent catalytic activity toward H_2O_2 reduction at low over-potential. The first application of electrospinning technology to enzyme-based biosensors is dated to 2006, when Ren et al. immobilized GOD onto electrospun poly (vinyl alcohol) (PVA) fibrous membranes [67]. In the context of enzyme-based nanobiosensors for glucose detection using electron mediators, Wu and Yin (2013) [97] designed and fabricated a simple, novel glucose biosensor using PB as electron transfer mediator through a two steps-procedure including electrodeposition of PB film on indium tin oxide (ITO)-coated glass plate and subsequent electrospinning of chitosan-polyvinyl alcohol composite (CS–PVA) nanofibres. CS-PVA was used as a protective film to improve PB stability through its abundant amino groups for its excellent bioaffinity and porous morphology suitable to create a substrate with a high surface area to support GOD immobilisation, and finally to prevent that PB film leached out from the surface. In such a structured electrospun nanobiosensor, the electrocatalytic activity occurred because the porous and high-surface area of the nanomaterial enabled the diffusion of glucose to GOD. When the reaction product, i.e. H_2O_2, reached the PB surface, the PB film rapidly catalysed H_2O_2 and substantially enhanced the electron transfer rate between GOD and the electrode.

Figure 10.3 depicts the relationship between amperometric responses at the GOD/CS–PVA/PB/ITO electrode and glucose at increasing concentrations [97]. The electrode exhibited a rapid and sensitive current–time response to successive step changes in glucose concentration in optimised experimental conditions, which indicates the proper electrocatalytic behaviour of the modified electrode. An excellent linear relationship was observed for a wider concentration range, from 3.30×10^{-6} M to 5.56×10^{-2} M, with low detection limit (3.61×10^{-7} M)
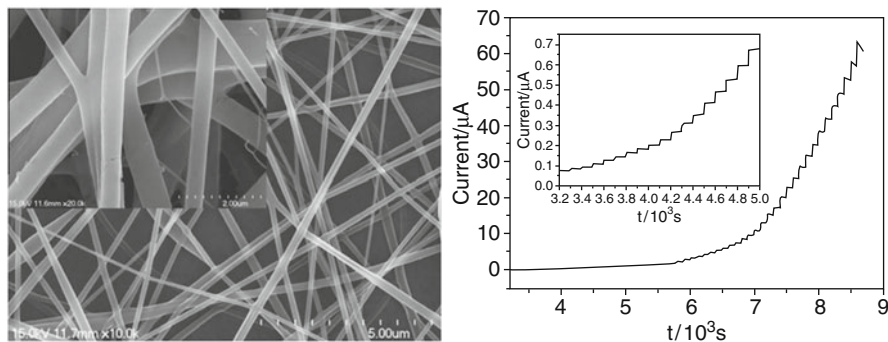
Fig. 10.3 SEM image of CS–PVA composite nanofibres (on the *left*) and amperometric response of the GOD/CS–PVA/PB/ITO electrode to successive injection of glucose into constantly stirred PBS (pH 7.0, applied potential −0.3 V) (on the *right*) [97] (Copyright Elsevier Ltd. 2013)

at high signal-to-noise ratio (S/N = 3). These concentrations encompassed both normal (3.6–6.1 mM) and abnormal (20 mM) glucose levels in human blood. The obtained detection limit was lower than that of other enzymatic glucose sensors based on different modified nanomaterials, while affinity of GOD was remarkably good (1.06 mM) [67, 90, 98–104].

Furthermore, Wang et al. (2013) investigated the potentials of a miniaturised amperometric glucose biosensor completely embedded within an electrospun PU (polyurethane) membrane in order to withstand implantation [105]. It is known that the first generation of implantable glucose biosensors suffers for factors including (i) sensitivity drift, due to susceptibility of GOD to degradation or inactivation that can further be accelerated by the accumulation of H_2O_2 in the enzyme layer during inherent delays between measurements, (ii) interference from other electroactive agents in complex biological media, (iii) O_2 dependence and (iv) failure upon implantation in the body resulting by the long-term performance of the biosensors. In that study, an electrospun coating of the whole sensor was used to overcome these problems, and the sensor coated with all electrospun membrane configurations resulted in a long-term stability (84-days study period). Advantages in the use of electrospun membranes over traditional solvent-cast membranes are related to achieving a well-controlled interconnecting porous structure, thickness and permeability of the coating in a single electrospinning setup. Electrospinning technology is also capable of withstanding the tremendous pressures exerted by the swelling of the inner enzyme (taking into account the possible mass transport limiting layers). Overall, this study demonstrated that fibro-porous membranes with suitable properties (glucose detection range of 2–30 mM) could be electrospun to coat miniature biosensors, a result difficult to achieve with traditional solvent-cast membranes. In the electrospinning procedure here used, the sensor was placed parallel to the auxiliary flat-plate collector and rotated at about 660–690 rpm in the electrospinning field (position, distance and rotation speed parameters were defined by FEA-Finite Element Analysis simulation results). Figure 10.4 describes the resulting bio-device.

Then, single or multiple electrospun layers are able to address mass-transport limiting and needs for multiple membranes for improving biocompatibility of
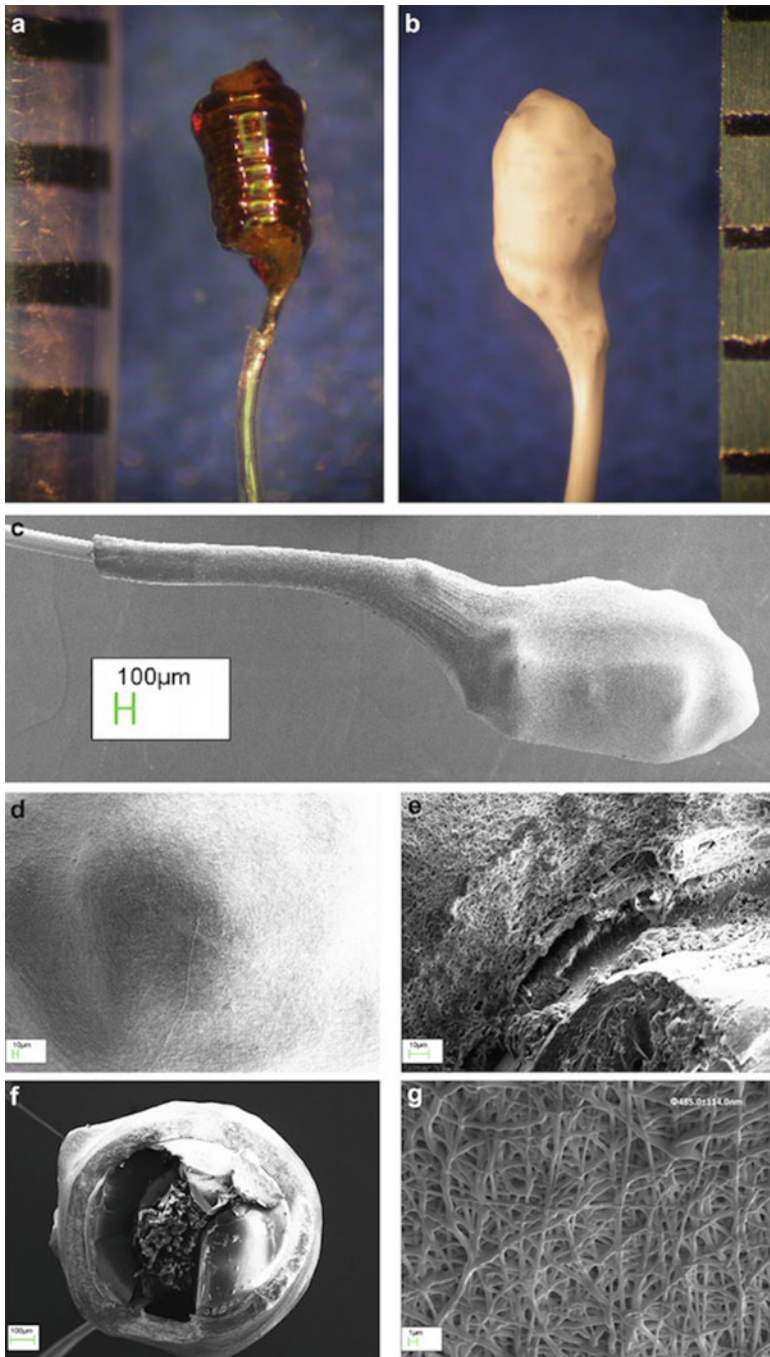
Fig. 10.4 Optical microscope (**a** and **b**) and SEM (**c**, **e** and **g**) images showing the morphology of a coil-type biosensor without (**a**) and with (beg) electrospun 8PU coating spun using a dynamic collector, showing the uniform covering of the miniature coil-type sensor including at its convex tip (**d**), while a closer look at its cross-section and surface revealed a uniform porosity (**e** and **f**) and random orientation of the electrospun fibres (**g**) respectively. Scale in **a** and **b** is in mm [105] (Copyright 2012 Elsevier Ltd.)

implantable biosensors or other biomedical devices requiring analyte transport, especially those belonging to the first generation of implantable glucose biosensors.

Electrodes can also be modified by electrospinning technique in order to improve the biosensing performances. In the study of Marx et al. (2011) [106] a new form of high surface area bioelectrode, based on nanofibres of electrospun gold with immobilised fructose dehydrogenase, was developed. A solution containing PAN and $HAuCl_4$ in DMF were electrospun and nanofibres collected on a rotating cylinder, then reduced by immersion in a suitable $NaBH_4$ solution until no H_2 evolution was apparent, and following washed with dilute HCl and then H_2O. Therefore, gold was electroless deposited on the fibres by dipping the fibres in an aqueous solution containing hydroxylamine hydrochloride and $HAuCl_4$. Figure 10.5 illustrates the morphological aspect of the functionalised bio-fibre and its electrical biosensing signals.

The electrochemical surface area of the gold microfibres was 0.32 ± 0.04 m^2/g. Fructose dehydrogenase (FDH) was immobilised on the gold fibres via glutaraldehyde crosslinking to a self-assembled monolayer of cystamine, which served as the chemical anchor to the gold, to obtain 0.36 ± 0.03 molecules of enzymes/nm^2 fibre coverage. Oppositely, 1.8 ± 0.14 molecules of enzymes/nm^2 were detected, instead, on a polished gold disc electrode (2 mm diameter) (control). The enzyme exhibited electron transfer mediated directly to the gold electrode. In this case, the density of the enzyme on the fibre electrode might be lower than theoretically expected, due to the inaccessibility of the enzyme to the inner layers of the nanofibrous mat. Notwithstanding, the residual activity of FDH on gold fibres after immobilisation was 14.4 % of the immobilised enzyme, while immobilisation on the flat gold disc surface resulted in less than 4 % activity of the immobilised enzyme. A possible explanation of this improved retention of activity might lie in the micro-structure of the gold fibres as previously explained. The limit of detection of fructose was 11.7 mM, and the K_m of the immobilised enzyme was 5 mM (50 % less than the K_m of FDH in solution). The microfibre electrode was stable over 20 cycles with a 3.05 % standard deviation. The response time of the sensor was less than 2.2 s and reached half maximum value within 3.6 s. The sensor was proven to be accurate and precise in both serum and traditional beverages sweetened with high fructose corn syrup. Finally, the addition of glucose isomerase enabled the sensor to detect glucose, thus expanding the available analyte selection for the sensor.

Therefore, these recent results confirm the effectiveness of the electrospinning in successfully immobilising enzymes and designing novel and highly performing biosensors for numerous applications.

10.3 (Bio)Affinity Nanobiosensors

10.3.1 DNA-Based Nanobiosensors

DNA-based biosensors are among the most specific sensing systems. There are different types of DNA-based recognition systems, dependently on the type of
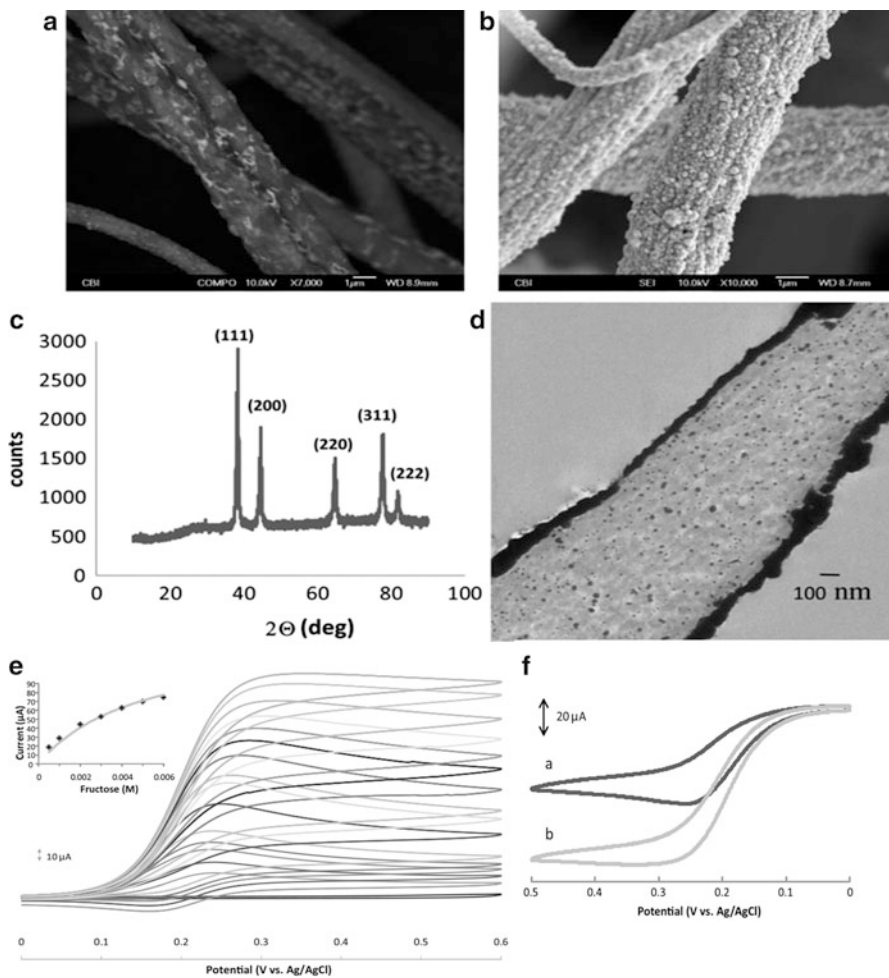
Fig. 10.5 (**a**) SEM of as-spun PAN-HAuCl$_4$ polymer; (**b**) SEM of the same polymer after electroless deposition of gold; (**c**) XRD of the fibre after electroless deposition; (**d**) TEM of a cross section of the fibre through its length; (**e**) Cyclic voltammetry of FDH immobilised on gold fibre electrode, in McIlvaine buffer pH 4.5, containing $5 \times 10 - 4$ M ferrocene methanol. Scan rate $= 20$ mV/s. Fructose concentrations are 0.1–1.5 mM. *Inset*: Michalies–Menten kinetics of electrochemical activity of FDH as a function of fructose concentration; (**f**) Cyclic voltammetry of FDH immobilised on gold fibre electrode, *a* – after addition of 100 mg glucose isomerase and 11 mM glucose; *b* – after addition of 10 mM fructose. Measured in McIlvaine buffer pH 4.5 with $5 \times 10 - 4$ M ferrocene methanol. Scan rate $= 20$ mV/s [106] (Copyright Elsevier BV 2011)

nucleotide molecular structure involved, whose functions are beyond the conventional genetic roles of nucleic acids: nucleotide sequence hybridisation systems, aptamers, DNAzymes, ribozymes, aptazymes and peptide nucleic acids. DNAzymes and ribozymes (usually grouped as nucleic acid enzymes NAEs), aptamers and aptazymes (deriving from the combination of aptamers and NAEs)

are collectively classified as "functional nucleic acids" – FNAs. Functional nucleic acids can act as catalytic and ligand binding elements, differently. FNAs are broadly classified in two categories: (a) catalytic FNAs (DNAzyme and RNAzyme) and (b) non-catalytic FNAs (aptamers and spiegelmers – L-nucleic acids).

10.3.1.1 Recognition Systems

DNA Hybridisation

DNA hybridisation is among the most specific recognition systems since the variation of even a single nucleotide along the sequence of oligomers or probes can generate different signals in biosensors. DNA is a unique biomolecule, since it acts as a storehouse of genetic information in living species. Nowadays, the detection of appropriate DNA sequences is essential for diagnosis of genetic or infectious diseases, environmental testing for bacterial contamination, and rapid detection of biological warfare agents. Additionally, chemical compounds can interact with specific portions of the DNA helicoidal structure in genomes, then resulting extremely dangerous to health of organisms upon modifications of DNA functions. Because of such interactions, specific DNA sequences are also able to detect these compounds in environments [107].

Aptamers

Aptamers are synthetic single strand DNA or RNA molecules that fold up into secondary and tertiary structures with a high affinity for their target molecules; then, they are mostly a chemical equivalent of antibodies. Aptamers (from the Latin, *apto*, meaning "to fit") are molecules that are randomly generated through a combinatorial method developed in 1990 called "in vitro selection" [108] or "systematic evolution of ligands by exponential enrichment" (SELEX) [109, 110] Then, they are screened from the resulting population of DNA/RNA sequences for their ability to bind with desired molecular targets, such as simple ions, small molecules (nucleotides and nucleobases, amino acids, organic dyes, cofactors, toxins and antibiotics), peptides, proteins, nucleic acids, organelles, viruses and even entire cells, tissues and organisms, with high affinity and specificity [111–113]. Wilson and Szostak (1999) [113] reported that about one out of every 1,010 RNA molecules could fold in such a way as to form a specific binding site for these rather arbitrarily chosen compounds. In the case of complex targets like cells, the emerging aptamers will recognize the most abundant or easily recognizable molecular targets, which will not necessarily be the desired ones [113]. They also commented that it is surprising that only four chemically similar subunits can create so many distinct structures from polymers. They also raised questions about the minimal chemical requirements for the generation of stable structures. The screening process mimics natural selection and therefore it is possible, theoretically, to

obtain aptamers that can recognize virtually any target molecules with high affinity and specificity, similarly to antibodies [111, 112]. In addition to their discriminate recognition, aptamers offer advantages over antibodies, as they can be selected mostly to bind any target of choice, while antibodies cannot be obtained for molecules too small to stimulate an immunogenic reaction (e.g., Mg^{2+} or Pb^{2+} without any chelator addition) or with high toxicity. Furthermore, aptamers can be engineered entirely and synthetically isolated in a test tube, and they have the advantage over antibodies of being not only highly specific, but also relatively small in size. They also possess desirable storage properties and elicit little or no immunogenicity in therapeutic applications. Moreover, they also retain their binding and inhibitory behaviour after immobilisation, with binding performances comparable or even better than those of antibodies against the same targets, demonstrating at the same time high specificity and even stereospecificity (isomers) [114–116]. Finally, since aptamers are chemically synthesised, chemical modifications can be introduced mostly at any position of choice, and it is also possible to design sensors based largely on aptamers secondary structures with minimal knowledge of their tertiary structures. For these reasons altogether, aptamers can be reasonably considered as extremely useful alternative to antibodies in the development of sensors and as a promising tool in environmental monitoring and diagnostics.

Nucleic Acid Enzymes (NAEs) (Ribozymes + DNAzymes)

In the early 1980s the research groups of Tom Cech (1981) and Sidney Altman (1983) [117a, b] independently found out that not all biological catalytic reactions are mediated by proteins (enzymes), but that also RNA molecules can have catalytic functions. This class of catalytic RNAs are known as ribozymes. These ribozymes consisting of naturally occurring RNA sequences with catalytic activity, are localised in the nucleus, mitochondria, and chloroplasts of eukaryotic organisms, but also in some viruses. Natural ribozymes are hammered ribozymes, the VS ribozyme, the lead-dependent ribozyme (leadzyme) and the hairpin ribozyme. One of the most powerful properties of RNA as a biopolymer, is its high negative charge (one charge per nucleotide). The presence of positively charged cations is then essential for the catalytic activity of all ribozymes and among them the cation of choice is Mg^{2+}, as it has a high affinity for the negatively charged phosphate backbone of RNA and is the most abundant divalent metal ion. Additionally, its double charge enables bridging of two phosphates from distant RNA regions, facilitating long-range structure formation and inducing intricate three-dimensional RNA catalysts structures. These tertiary structural motifs rival in complexity those of protein enzymes, allowing for the precise positioning of a substrate in a catalytic core.

Although the first ribozymes discovered are natural, most ribozymes known today are chemically synthesised through in vitro selection (or SELEX). Several reactions are catalysed by ribozymes, such as RNA cleavage, ligation,

polymerization, capping, phosphorylation, peptide bond formation, as well as compound synthesis (e.g. urea) [118–121]. Similarly, many DNAzymes are ssDNA molecules with catalytic activity isolated from random sequence DNA libraries by in vitro selection (or SELEX). They catalyse several reactions (despite the lack of the 2′-hydroxyl group and their discovery more than a decade later than ribozymes) such as RNA or DNA cleavage and RNA or DNA ligation [122–126]. Typically, since the rate enhancement of NAEs can be as high as 10^{10} over uncatalysed reactions and the catalytic efficiency (k_{cat}/K_m) can reach 10^9 M^{-1} min^{-1}, they can rival that of protein enzymes. Additionally, they are characterised by excellent stability and cost-effective chemical synthesis so that they can easily match the requirements in biotechnological applications like biosensors. In the case of NAE-based sensors, the target molecule is usually a cofactor that can accelerate the catalytic reaction or an inhibitor of the reaction. Then, a selection process can be performed so that the desired reaction happens only in the presence of a target analyte, while negative selections can be carried out towards sequences that are also active with competing analytes. Since the stoichiometry of the NAE-catalysed reactions involves metal ions as cofactors and some NAEs even show metal specificity, NAE sensors are promising in metal detection and sensing, and ultimately in monitoring heavy metals in polluted environments [127–130].

Aptazymes

A combination of the catalytic activity of NAEs along with the sequence-specific binding ability of aptamers has given rise to the most advanced form of functional nucleic acid-based sensors called aptazymes.

Allosteric DNAzymes can be coupled to aptamers to bind a broad range of molecules. A combination of these FNAs has generated a new class of functional nucleic acids known as allosteric ribozyme/deoxyribozyme, or aptazymes. This hybrid strategy of aptazymes combines the aspect of both the effector-binding (receptor site) and activity-based (the catalytic active site) selection approaches. The result is a system that undergoes modulation of catalytic activity in the presence of an effector molecule binding to a receptor site: upon analytes binding to the aptamer motif, the tertiary structure of an aptazyme is activated and can cleave the corresponding substrate. Aptazymes can be fabricated integrating aptamers with hammerhead ribozyme, hairpin ribozyme, or ligase ribozyme. In several studies, enzymes contain a replaceable stem-loop or hairpin structure where aptamers can be incorporated easily. Hammerhead ribozyme can also be replaced by many other nucleic acid enzymes as scaffolds for aptazymes, such as ligase ribozyme. Then, aptazymes are allosteric ribozymes that have been selected (via in vitro selection) or engineered so that their activity is modulated by the presence of a particular analyte. Allosteric ribozyme can present an activity of not only self-cleavage, but also ligase, as some authors reported [131, 132]. Therefore, the analyte-dependent activity of engineered "aptazymes", wherein aptamers are fused with hammerhead or ligase ribozymes, has enabled their use in intelligent

biosensing, through ligand-induced conformational rearrangement and activation mechanisms, using a number of different detection schemes.

Peptide Nucleic Acids (PNAs)

Peptide nucleic acids (PNAs) are synthetic molecules mimicking the DNA structure and behaviour, which binds complementary nucleic acid strands. PNAs, then, are powerful new biomolecular tools with a wide range of relevant applications. In PNAs, the deoxyribose phosphate backbone of the Hoogsteen strand was removed, and a pseudo peptide backbone was built in its place, following computer model building to obtain a backbone homomorphic with the DNA one. However, the four natural nucleobases have been retained, as well as the specificity and the reversible nature of the hydrogen bonding between complementary nucleobases, properties. These features are remarkable because they allow the strands of the double helix to be unwound and then rewound in exactly the same configuration [133–136]. Nielsen et al. (1991) [133] first described this kind of molecule, which was originally designed and developed as a reagent for sequence-specific recognition of double-stranded (ds) DNA, using a conventional triple helix type (TAT) as a scaffold, but they also realised that it would be a mimic of single-stranded nucleic acids by default. The structure of PNA is relatively simple, consisting of repeating N-(2-aminoethyl)-glycine units linked by amide bonds, and the purine (A, G) and pyrimidine (C, T) bases are attached, instead, to the backbone through methylene carbonyl linkages, then providing a DNA mimic with remarkable properties and benefits. Firstly, to obtain a neutral DNA mimic (the charges at the C- and N-terminals are easily modified to give neutral groups) is advantageous, since electrostatic repulsion between this mimic and negatively charged DNA and RNA are avoided. It results, then, in a stronger binding between complementary PNA/DNA strands than that between complementary DNA/DNA strands at low to medium ionic strength. Interestingly, the specificity was also found to be higher in addition to the affinity for PNA/DNA duplexes. Watson-Crick base pairing rules were strictly preserved in hybrids of PNA and nucleic acids. Interestingly, a mismatch in a PNA/DNA duplex resulted to be more destabilising than a mismatch in a DNA/DNA duplex, with decreases in T_m of 8–20 °C for single mismatches in the middle of a pentadecamer PNA/DNA duplex. The lowest measured ΔT_m for the DNA/DNA duplex, in effect, is 4 °C vs. 8 °C for the PNA/DNA duplex: the PNA is "twice" as discriminating in the case of the least discriminating base pair. This thermal stability of PNA-DNA duplexes relative to the corresponding DNA-DNA duplexes (ca. 1 °C per base pair) was mainly ascribed to lack of electrostatic repulsion between the two strands. Such specificity appears to be an important property of PNA/nucleic acid duplexes in hybridisation experiments, and can be exploited in many applications.

Other remarkable features of PNA/nucleic acid duplexes are: (i) reporter groups, intercalators, metal binders, and other biofunctional derivatives can be attached through either the N-terminal amino group or the C-terminal carboxylic acid;

(ii) high biostability of these duplexes because oligomers are neither degraded by nucleases nor proteases; (iii) PNA achirality avoiding problems of enantiomeric purity. Early interest in PNA was referred to antisense research and strand invasion by homopyrimidine PNA oligomers. However, the main interest has come from the potential use of PNA as a molecular hybridisation probe in the same applications as traditional synthetic DNA or DNA analogues (e.g. molecular biology, diagnostics and gene therapy) [137, 138]. PNAs can be labelled with biotin, fluorescein, or reporter enzymes or various types of nanomaterials (e.g. metal nanoparticles, graphene, CNTs, magnetic particles) as powerful probes in most hybridisation based assay formats, where oligonucleotide probes are commonly used [134, 139]. The ability to bind to both DNA and RNA is a key feature of PNA, as compared to other analogues that tend to have a higher preference for binding to RNA. The neutral backbone also increases significantly the rate of hybridisation in assays where either the target or the probe is immobilised. All these features of PNAs suggest a great potential in the use of these molecules in the fabrication of biosensors and nanobiosensors.

10.3.1.2   DNA Nanobiosensors

The widespread distribution of contaminants in all environments throughout the planet is increasing the awareness of the threat they pose to human health. Then, the monitoring of pollutants and toxins, as well as the early detection of emerging toxicants, in natural and anthropic environments and the assessment of the exposure risks of people are urgent requests arising in the society from both common people and decision makers. In an effort to monitor these environmental hazards, the ideal sensing technology should be capable of reacting to and diagnose the type of exposure within seconds. DNA-based sensors are proposed as a promising solution to such challenge.

Both electrochemical, gravimetric and optical sensors have been developed employing FNAs as receptors [130, 140–147].

DNA Hybridisation Nanobiosensors

Most studies carried out till now have concerned the identification of nucleotide sequences in various environments using nucleotide probes holding complementary sequences to that of the target of interest. Several studies have then been carried out to detect and identify microorganism, cells and genomic alterations, using several strategies, approaches and transducers (e.g. piezoelectric, electrochemical and optical sensors). Exceptional results have often been achieved in terms of sensitivity of signals and specificity of recognition (e.g. single nucleotide discrimination between the target sequence and a population of nucleotide sequences), with very remarkable consequences especially in diagnostics [148–154]. To enhance the signals of responses and improve sensitivity of biosensors several strategies

involving nanomaterials have been performed: nanoparticles (metals, magnetic particles), fluorescent probes; carbon nanotubes, graphene, biotin/avidin interactions, amplification systems (e.g. rolling circle amplification-RCA and branched DNA) [155–166].

Electrospinning technology has been introduced in some studies aimed to generate DNA-based nanobiosensors. Typically, in a few studies DNA molecules were not used as probes for hybridisation with oligomers, but to contribute to the global nanofibre features. In the study of Liu et al. (2008) [167], ultrafine fibres with diameters ranging from 50 to 300 nm were prepared from DNA/single-walled carbon nanotubes (SWNTs)/poly(ethylene oxide) blended dispersion, and well-defined electrospun fibres were obtained, with good interaction between DNA and SWNTs. The resulting fibres also exhibited electroactive behaviour and could be used as an immobilisation matrix for a glucose oxidase enzyme biosensor. Ner et al. (2008) [168] fabricated nanoscale fibres and non-woven meshes composed of DNA complexed with a cationic surfactant (cetyltrimethylammonium chloride, or CTMA) through electrospinning to make easier DNA electrospinning. They then incorporated a hemicyanine chromophore in the material, thus resulting in an amplified emission, as compared to thin films of identical composition, and they further evaluated the mechanical properties of freestanding electrospun non-woven fibre meshes. Li et al. (2006) [169] incorporated biotin into polylactic acid (PLA) nanofibres through electrospinning to prepare membrane substrates for biosensors based on biotin–streptavidin specific binding. They observed that streptavidin immobilised on the membrane surface could capture a biotinylated DNA probe for the detection of a synthetic *Escherichia coli* DNA where streptavidin had been deposited. In the study of Wang et al. (2013) [170] both electrospinning and nanoparticles (i.e. MWCNTs) were included in the sensing process, and sophisticated strategies were used. Specifically, they developed a novel electrochemical biosensor based on functional composite nanofibres for the sensitive hybridisation detection of p53 tumor suppressor using methylene blue (MB) as an electrochemical indicator. They used electrospinning to prepare composite nanofibres comprised of carboxylated multi-walled carbon nanotubes (MWNTs) doped with nylon 6 (PA6) (MWNTs–PA6) that served as nanosized backbone for pyrrole (Py) electropolymerisation. The functional composite nanofibres (MWNTs–PA6–PPy) were used as supporting scaffolds for ssDNA immobilisation to dramatically increase the amount of DNA attachment and the hybridisation sensitivity. The resulting biosensor, in effect, displayed good sensitivity and specificity: the target wild-type p53 sequence (wtp53) could be detected as low as 50 fM and the discrimination was up to 57.5 % between the wtp53 and the mutant type p53 sequence (mtp53). Such findings are a promising support for the early diagnosis of cancer development and monitoring of patient therapy. Ramanathan et al. (2005) [171] reported another simple, single-step method for fabricating biologically (avidin) functionalised conducting-polymer (polypyrrole) nanofibres on pre-patterned electrodes and its application to label-free bioaffinity sensing. When a biologically functionalised streptavidin – polypyrrole nanowires kept in contact with a solution containing biotin – DNA, a rapid change in resistance of the

polymer as low as 1 nM was generated, demonstrating the usefulness of the conducting biomolecule-functionalised nanofibres in biosensing. The method showed advantages of direct incorporation of functional biological molecules into conducting-polymer nanowires during its deposition and their site-specific positioning.

Our Development of a Nanofibrous DNA-Based Biosensor

In order to fabricate a DNA-based biosensor involving nanofibrous frameworks functionalised with oligonucleotide probes, a water-insoluble polymer (poly (methyl methacrylate) – PMMA) was used to create nanofibrous scaffold structures through electrospinning technique. The scaffold frameworks were properly designed and implemented in order to coat quartz crystal microbalances (QCMs) as transducers and then to create a potential DNA-based biosensor.

Since PMMA is an organic polymer that cannot bind DNA directly, it needs to be chemically modified on purpose. In past years, several chemical procedures have been developed to bind DNA molecules to the surface of materials with distinct chemistry [172–176]. In this study, the method reported by Fixe et al. (2004) and Vasudev et al. (2008) was used, with slight modifications [177, 178]. Two cross-linking chemistries were used for *in situ* modifications of PMMA nanofibres to bind DNA oligomers. Firstly, amination of PMMA was carried out (with slight operative modifications according to the distinct supports) incubating PMMA nanofibres with 10 % putrescine in 100 mM borate buffer pH 9.5, for 2 h, which converts the end groups of PMMA into terminal amine groups, then followed by 3×10 min washings. Secondly, 30 mers single-stranded and double-stranded DNA, modified with $5'$-phosphate (ssDNAP and dsDNAP, respectively) or without modification (ssDNA), were immobilised onto the amine-derivatised PMMA nanostructured scaffold. Immobilisation was obtained through incubation with 0.1 M 1-Ethyl-3-(3-dimethylaminopropyl)carbodiimide (EDAC) and 0.1 M 1- N-methylimidazole buffered at pH 6, both acting as activator reagents of the $5'$-end phosphate groups of DNA oligomers. This reaction converted phosphates into phosphoramidates, thus anchoring DNA probes onto PMMA mats. All steps of the process, i.e. polymer deposition and covalent binding of DNA probes-PMMA nanofibres electrospun to different suitable supports (silicon wafers, grids, cover slips, quartzes, QCMs), were investigated through image (stereomicroscope and SEM), colorimetric (transmission electron microscope-TEM, confocal laser scanning microscope-CLSM and UV transilluminator), and gravimetric (frequency readout) analyses (Fig. 10.6). In this study, the sensing performance (sensitivity) of a DNA-based nanobiosensors, comprising QCMs coated with a PMMA nanofibrous layer, were studied under various ambient conditions. Such nanobiosensor showed better performances than its thin film counterparts, as well as PMMA fibrous sensors reported better sensitivities than the compact ones for gas/VOCs detection (Fig. 10.7) [179].

According to the QCM theory, the sorption of analytes onto the quartz surface, or any sensitive layer used to coat it, results in a mass change that induces a shift in the fundamental resonance frequency of the QCM. When small mass changes
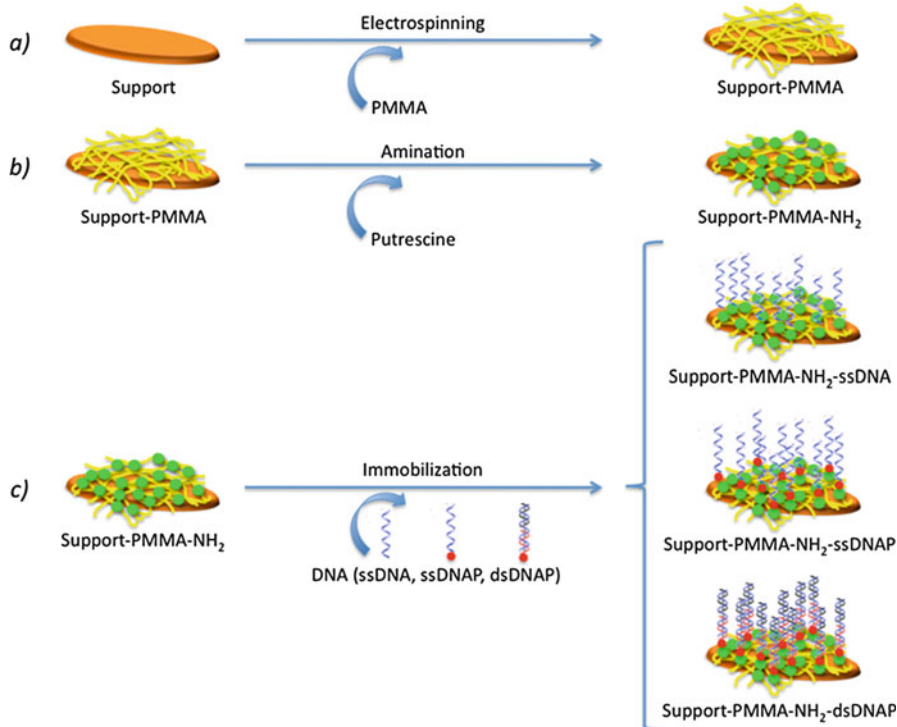
Fig. 10.6 Diagram of steps in fabricating sensing coatings for a potential electrospun DNA-based nanobiosensor: deposition of PMMA onto supports through electrospinning (*a*); amination of electrospun PMMA fibres (*b*); immobilisation of different DNA oligomers (ssDNA, ssDNAP and dsDNAP) onto aminated PMMA fibres (*c*)

occur, this relationship is linear and is described by Sauerbrey's law [180]. According to this law, the QCM connected to a proper oscillator circuit (Colpitts oscillator), owing to the quartz piezoelectricity, drives its frequency, and the frequency value of the oscillator output signal results to be then a measure of the quantity of mass ad/absorbed onto the sensing layer coating the QCM. Nanofibrous films can be used as either a sensing interface or a scaffold hosting biomolecules for the piezoelectric sensors or both. PMMA was chosen for its great adhesiveness to a good deal of materials and its plastic features.

PMMA nanofibrous mats were analysed upon several treatments using different supports to afford the detection with distinct optical techniques, and nanofibrous samples were processed accordingly. For UV detection (300 nm) (through a transilluminator), PMMA-coated transparent quartzes and relative control quartzes (i.e. without DNA) were treated with 127 μM Ethidium Bromide (EtBr). EtBr is a DNA-dye more specific for DNA in gels, i.e. in a physical form rather approximating to DNA linked to nanofibres, and incubated for 10 min to let chromophore bind to ssDNA and dsDNA oligomers. For the confocal microscope detection, aliquots
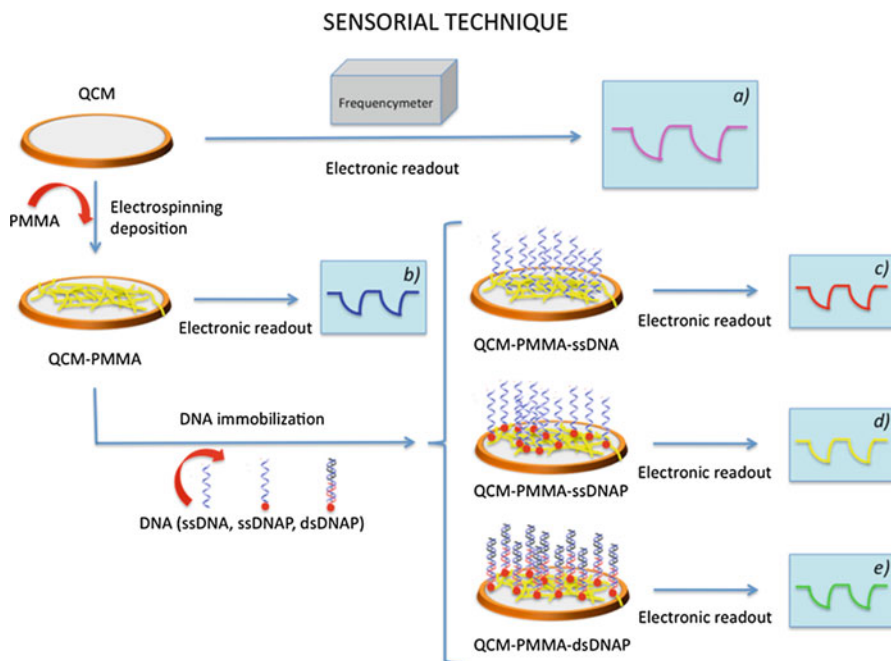
Fig. 10.7 Diagram of the utilisation of the oscillation frequency responses of QCMs, with respect to the fundamental resonance frequency (not deposited QCM) (*a*), to detect the different steps in the fabrication of sensing coatings for the development of a potential electrospun DNA-based nanobiosensor; electrospun deposited PMMA fibres (*b*); ssDNA anchoring (*c*), ssDNAP linkage (*d*) and dsDNAP anchoring (*e*) oligomers immobilised onto PMMA fibres

of PMMA-coated cover slips were treated with 1:200 (v/v) diluted PicoGreen®, a fluorochrome specific for DNA in solution described as an ultrasensitive fluorescent nucleic acid stain. DNA-bound PMMA nanofibres were incubated 5 min in the darkness to let the fluorochrome bind to both single and double-stranded DNA oligomers, and the resulting fluorescent signals were detected using 488 excitation and 530 emission wavelengths. For TEM detection, PMMA-coated nickel grids underwent two steps negative-staining (10 s + 90 s) with 2 % uranyl acetate and were then analysed through TEM. For piezoelectric measurements, QCMs (AT-cut, 10 MHz), 13.5 mm diameter and 150 μm thickness, consisted of two Cr-Au electrodes evaporated on each side (8 mm diameter, 1,500 Å thick). QCM frequency variations related to the mass of electrospun-deposited PMMA nanofibres and to the covalent binding of both ssDNA and dsDNA were recorded after drying and under N_2 flow (5 sccm). The frequency shifts were converted into an index of DNA binding efficiency, consisting in the mass of DNA immobilised per unit of PMMA mass deposited onto quartz, normalised to the fundamental frequency of oscillation of the same PMMA-coated QCM. Deposition of PMMA through electrospinning resulted in fairly uniaxially aligned nanofibres at stereomicroscope (Fig. 10.8a), which appeared as originating from spindle structures in SEM micrographs (Fig. 10.8b), and ranging between 140 and 560 nm.
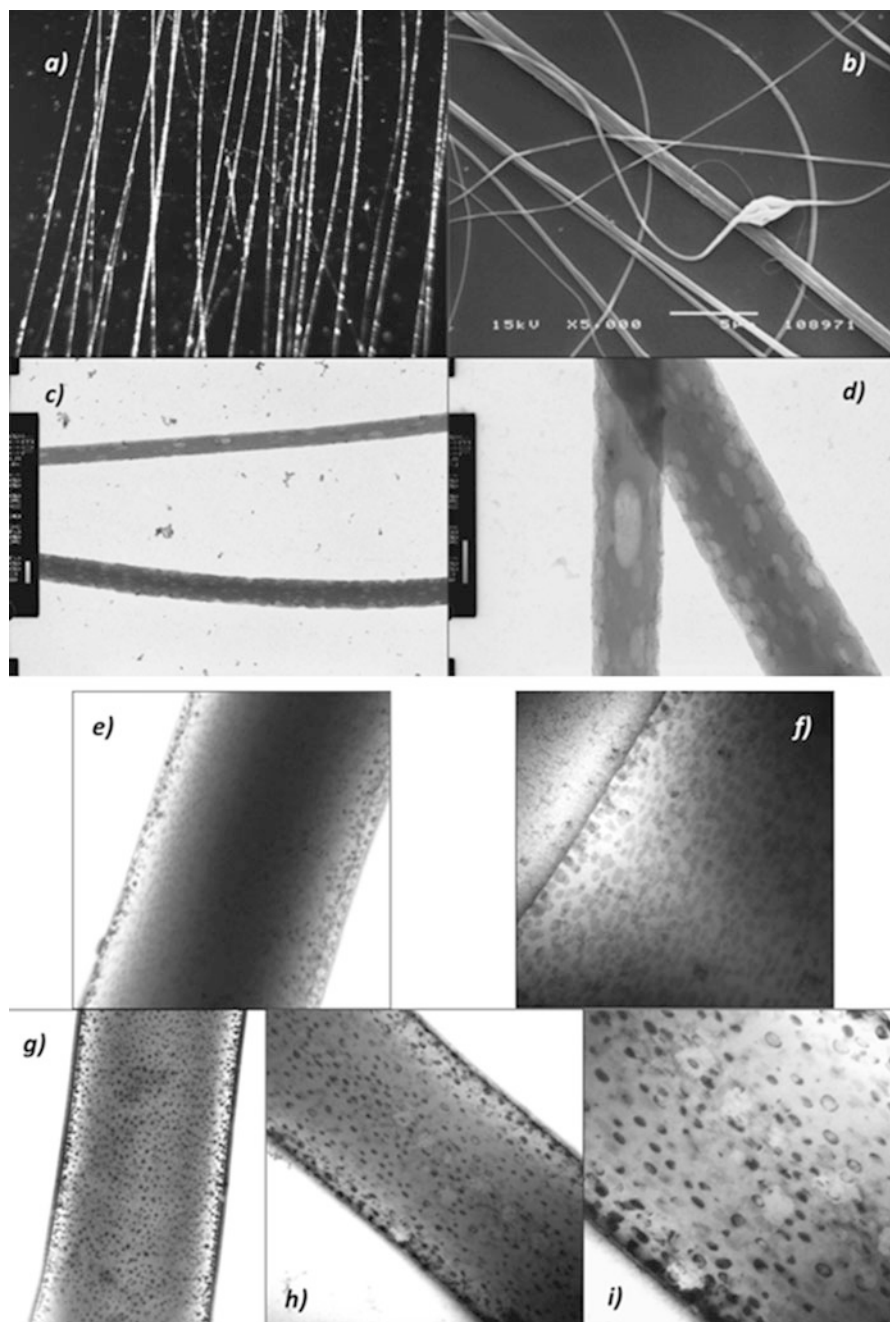
Fig. 10.8 Morphological features of electrospun PMMA fibres detected through micrographs obtained with different optical techniques: stereomicroscopy (**a**); scanning electron microscopy (**b**); transmission electron microscopy (**c–i**). (**a–f**) pristine PMMA electrospun nanofibres; (**g**) PMMA electrospun nanofibres after ssDNA binding; (**h** and **i**) PMMA electrospun nanofibres after dsDNA binding. All micrographs were captured from samples after 7×5 min washings. Further details are reported in the text.

TEM micrographs of control samples showed that two different structures are observed in PMMA nanofibres. The first structure was observed in micrographs obtained with perfectly perpendicular transmission of the electron beam, relative to nanofibre disposition, where several dark grey spots due to more electron-dense material were detected throughout the nanofibres. These spots showed a fairly high density distribution (Fig. 10.8e, f), dimensions around a few nanometres, oval- or ellipse-shaped and with major axis coaxially arranged along the nanofibre. A possible explanation of this structural organisation was a spatial aggregation of polymer molecules in the nanofibres forming a sort of clusters. A fairly equivalent distribution of spots was observed in PMMA nanofibres after covalent binding of ssDNA and ssDNA, where a multitude of electron-dense spots similar to that of controls were detected all along the nanofibres, whatever the type of oligomer used (Fig. 10.8g–i). This finding seems to confirm that the spotted image of PMMA nanofibres is related to the specific cluster-like structure of this material after electrospinning. The second structure was observed, instead, in micrographs obtained when the nanofibrous fabrics were slightly tilted relative to the transmission of the electron beam direction, the surface conformation of PMMA nanofibres was displayed. Specifically, the nanofibre surface appeared as very porous, showing empty concavities or holes (Fig. 10.8d) with oval or elliptic shape and dimensions in the range 10×50 nm–20×150 nm and major axis coaxial to the nanofibres. It is reported that when a miscible solvent is used with a miscible polymer solution, highly porous fibres are formed due to phase separation between polymer-rich and polymer-poor regions. Owing to fast evaporation of the solvent and the cooling effect on the fibre surface during the electrospinning process, causing the so-called thermally induced phase separation (TIPS), there would be a high probability for pores to be formed in the solidified poor region [181–183]. The extent of pore formation can depend on the solvent used so that the quantity, distribution and shape of pores can be modulated by choosing the appropriate solvent or solvent mixture and adjusting the relative proportions of both phases, in order to create different nanofibre topologies. It is known that also humidity can affect the generation, extent, morphology and diameter of nanopores onto nanofibres [184–186]. Condensation processes during electrospinning can occur upon spinning jet cooling consequent to solvent evaporation in a very humid environment so that tiny droplets of water precipitate onto the jet and then create pores in the solidified nanofibre. Pore formation can then be tuned by varying the humidity during electrospinning. In the present study, 30 % RH did not greatly affect nanofibre porosity. The importance of this nanoporosity in nanofibres lies in the further increase in specific surface area they determine, thus generating further opportunities for anchoring points or molecular binding sites, but also of unspecific adsorption. In general, the PMMA nanofibres electrospun from the chloroform solution are characterised by a range of different sized nanopores along the fibre surface. Similar distribution of pores was also observed in the present study. Their dimensions were in agreement with the sizes reported in other studies where similar or different polymers were tested [181, 185, 186], but fairly smaller than the size reported by Megelski et al. (2002) [187]. According to the classification of pores
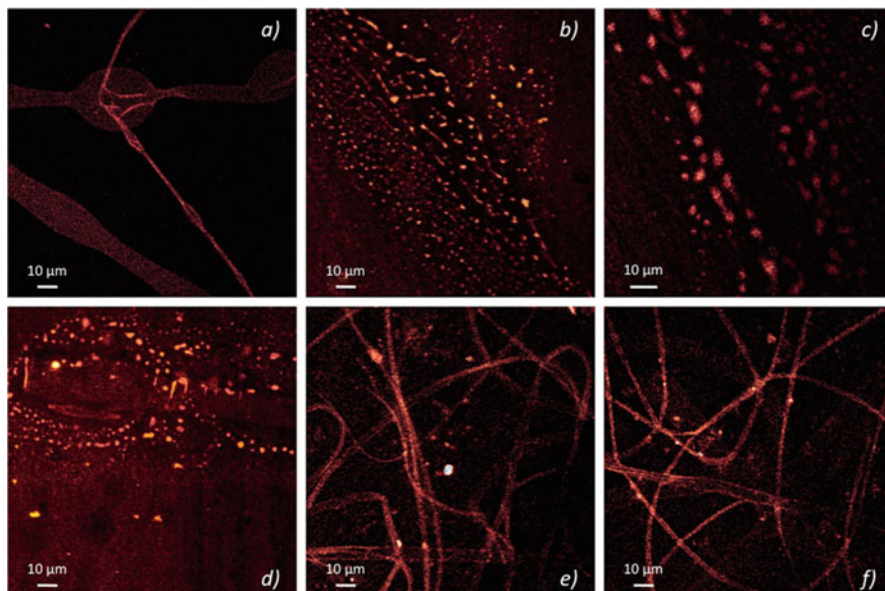
Fig. 10.9 Fluorescence emission of electrospun PMMA nanofibres captured with CLSM after deposition onto cover slips (**a**) and after amination (upon EDAC reaction with putrescine) plus covalent binding of ssDNA (**b**, **c**) and dsDNAP (**d**); non-aminated PMMA nanofibres in the absence (**e**) or in the presence (**f**) of dsDNAP oligomers. All micrographs were captured from samples after 3×5 min washings for comparison at the same conditions, since after 7×5 min washings samples (**e** and **f**) gave black micrographs

suggested by Casper et al. (2004) the pores we observed on electrospun PMMA nanofibres could be both classified as "nanopores" and "micropores".

CLSM analyses showed a very slight and uniform fluorescence all along the pristine PMMA nanofibres, after 3×5 min washing (Fig. 10.9a) (only observable after great enhancement of the picture exposure). This slight fluorescence was completely removed after 7×5 min washings (not shown because completely dark), similarly to what reported by Wei et al. (2011) [181]. CLSM analyses of samples also pointed out the crucial importance of amination in DNA binding onto the PMMA mat that was demonstrated by comparing two sets of QCMs, one where putrescine was bound to the surface of PMMA nanofibres and the other without amination. After repeated washings (7×5 min) of PMMA mats to completely remove any unspecific fluorescence, PMMA nanofibres observed after reaction with DNA oligomers in absence of amination did not show any DNA binding when treated with PicoGreen®, i.e. similarly to samples not incubated with DNA oligomers (Fig. 10.9e, f). Upon the DNA anchoring procedure, fluorescent spots were observed on PMMA nanofibres binding ssDNA (Fig. 10.9b, c) and dsDNA (Fig. 10.9d); these spots appeared clearly distributed as along lines (maybe the nanofibre axes) and remembering the pores along PMMA nanofibres observed in TEM micrographs.
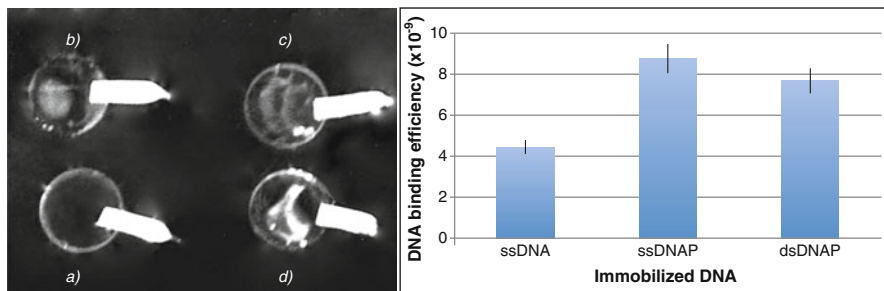
Fig. 10.10 *Left*: UV absorbance detected through transilluminator of PMMA fibres deposited by electrospinning onto transparent quartzes, aminated and subdued to binding reaction in the absence (*a*) or in the presence of ssDNA (*b*), ssDNAP (*c*) and dsDNAP (*d*) oligomers. Photograph was captured from samples after 3×5 min washings

Right: DNA binding efficiency for ssDNA, ssDNAP and dsDNAP oligomers. The efficiency was calculated on the basis of the different QCM frequency shifts. *Bars* represent standard deviation of the index, as calculated from frequency readouts of 3 replicates for each treatment

When pristine PMMA nanofibres deposited through electrospinning onto transparent quartzes were irradiated with UV light at 300 nm after EtBr binding to DNA molecules and observed with transilluminator, no spots were observed (Fig. 10.10a). Differently, electrospun PMMA nanofibres with anchored ssDNA and dsDNA showed emitting (white) area, then confirming the presence of DNA bound to samples (Fig. 10.10b–d).

Oscillation frequencies of QCMs before and after deposition of pristine electrospun PMMA nanofibres ($8.51 \times 103 \pm 1.62 \times 103$ Hz) or coated with PMMA nanofibres binding different DNA probes, i.e. ssDNA and dsDNA, showed different values. The DNA binding efficiency for various DNA oligomers used was different. As shown in Fig. 10.10, on the right, the index of efficiency in DNA immobilisation related to the amount of PMMA deposited was lower for ssDNA while it was more than doubled in dsDNA. The spot-like aspect of DNA bound to PMMA nanofibres observed in CLSM micrographs, instead of the expected uniformly distributed fluorescence onto PMMA nanofibres might arise some doubts about the cause of these spots. However, the correspondence of these fluorescent spots with pores on PMMA nanofibres observed in TEM micrographs suggests that fluorescent spots might derive from unspecific accumulation of DNA oligomers inside the pores, instead of specific DNA link to nanofibres. However, due to the particular procedure used in DNA anchorage (covalent binding) and following the comparison between DNA treated and suitable untreated controls tested, it was induced to exclude the occurrence of any unspecific accumulation. Such an event, in effect, could only happen upon an unreasonable accumulation of amine groups into the pores. On the contrary, the suggested hypothesis is that the spot-like aspect was the mere consequence of an introflexed surface. Any fluorescent point somehow associated to both the vertical and horizontal surfaces would then contribute to the overall emission projected onto to the corresponding flat area as appears from above. The resulting fluorescent emission would be the sum of the colour points

along the whole surfaces inside the pores and would apparently result as greater per surface unit relative to the rest of the nanofibrous surface.

The different techniques used to assess DNA probe binding to electrospun PMMA nanofibres highlighted a different capacity of single and double strand DNA to bind to nanofibres. Specifically, dsDNA seemed to be more efficient (more than doubled) in anchoring to the nanofibrous mats, when assessed through variations in QCM oscillation frequency. The halved binding efficiency observed for ssDNA could be related to possible higher specific binding for dsDNA oligomers due to the presence of phosphate at the 5′-end of DNA responsible for binding. Such a chemical feature would result in a standing spatial conformation of dsDNA probes bound to PMMA and then in a more efficient anchorage that would tend to use all available binding sites. Conversely, the binding of ssDNA oligomers would occur through both 3′-end phosphate and the phosphate backbone of DNA molecules, so that bound DNA probes would occupy several binding sites per PMMA nanofibre, then resulting less efficient.

Finally, the involvement of electrospinning technology to create a bio-inspired and biofunctionalised nanofibrous layer to use as a sensing fabric for nanobiosensors was effective. The procedure used resulted to be reliable in generating sensing supports for nanobiosensors, i.e. preventing unspecific binding of the molecules to use as probes. QCMs were reliable tools to employ in the fabrication of biosensors since the measures obtained were more sensitive in quantification of ligand binding than specific detectors (dyes). The following research will obviously include the test of this nanobiosensor in hybridization experiments with suitable probes for the identification of specific nucleotidic sequences of interest (e.g. pathogens).

FNAs Nanobiosensors

The capacity of FNAs to recognise analytes and express activity remind to that of antibodies. Although nucleic acid oligomers have reduced complexity, and chemical functionalities compared to proteins, binding affinity toward the target molecule of the FNAs can rival that of the antibody, which is produced *in vivo* instead. However, amino acids have greater torsional freedom and conformational flexibility than nucleic acids, but modification with additional chemical groups or internal structure dynamics increases the conformational freedom and binding capacity of FNAs with their targets. Furthermore, structure chemical groups can be varied to improve FNA-target contact in complexes of traditionally known nucleoside. The altered structure of modified nucleosides offers greater conformational diversity of FNAs, thus increasing the potential of the library. Modifications in FNA structures can induce more stable conformations or increase the affinity for a target to generate custom-made FNAs or FNAs more resistant to hydrolysis, nuclease resistant, and thermally stable, then expanding their applicability in the field of sensor technology [128]. Finally, functional nucleic-acid-based sensors (FNASs) can be conjugated with metallic nanoparticles, fluorescent molecules, or quantum dots to obtain fast

detection of a multitude of target molecules [188]. Therefore, the durability, sensitivity, and cost-effectiveness of FNA-based biosensors have been proposing them as an extraordinary and promising tool to face the ever-increasing threats arising from industrialisation, such as pathogens, toxic heavy metals and organic pollutants, bioterrorism agents and other biological toxins. An excellent extended description of FNAs and FNAs biosensors is reported in the recent review of Liu et al. (2009) [126]. To our knowledge, no study has been published till now, instead, where electrospinning has been used in combination with FNAs to detect any target.

Aptamers Biosensors

Non-catalytic FNAs like aptamers have been widely exploited in sensor technology. The possibility for DNA or RNA aptamers to be custom-made, tagged with different fluorophores, quenchers, or metallic nanoparticles provide them high sensitivity and precision in detecting environmental pollutants. Specific adsorption of nucleic acids to transducers can be adjusted by using different surface immobilisation strategies, i.e. physical (adsorption) or chemical (covalent-binding): (i) the gold–thiol bond is the typical solution used to get easy and stable immobilisation of the DNA strand; (ii) binding between –COOH and –NH$_2$ groups to generate carbodiimide bond can also be used to link DNA probes; (iii) biotin-avidin interactions are finally used to tether biotinylated single-stranded DNA (ssDNA) aptamers to a streptavidin modified support electrode. Some examples of aptasensors are the followings [189, 190]. Yao et al. 2010 [144] developed a QCM biosensor with aptamers as recognition element. They compared immuno-globulin E detection using an antibody-based and an aptamer-based biosensor in human serum. They found that the linear range of the antibody was 10–240 μg/L while it was 2.5–200 μg/L with the aptamer. The aptamer-based biosensor resulted in tolerating repeated regeneration while the antibody-based could not. Xiao et al. (2005) developed a redox-labelled anti-thrombin aptamer that spatially arranged, upon binding of thrombin, into a tertiary configuration where the redox-label is electrically contacted with the electrode, and they used it for the ampero-metric detection of thrombin [191, 192]. Similarly, Baker et al. (2006) reported that the redox-labelled aptamer they set up to analyse a small substrate (cocaine) self-organised in the presence of cocaine, and that the resulting amperometric response of the rearranged nucleic acid showed a sensitivity limit corresponding to 1×10^{-5} M [193]. Finally, Au-nanoparticle labelled aptamers were used in the creation of a highly sensitive quartz crystal microbalance with dissipation monitoring (QCM-D) biosensor for protein detection using a sandwich aptamer/thrombin/Apt-GNPs tertiary configuration, where gold nanoparticles were used for signal amplification. This biosensor resulted improved in sensitivity, selectivity and repeatability [194, 195]. Several other studies have also been performed and published on aptamer-based biosensors [196]. Despite the wide literature on the use of aptamers in biosensors, it seems that most of publications are reviews [197] while the
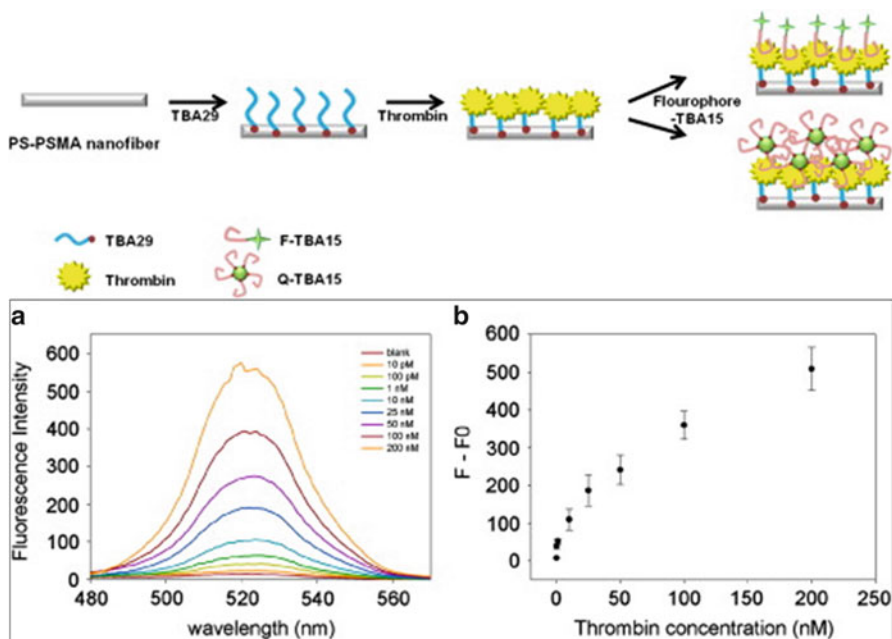
Fig. 10.11 Scheme (*top*) of aptamers-on-nanofibre based biosensors for thrombin detection: aptamers (TBA29) are immobilised on polymer nanofibres; thrombin binds to TBA29 aptamers immobilised on nanofibres; sandwich type thrombin detection using fluorescein-labeled or quantum dot (QD)-labeled TBA15 for fluorescence signals

Optical signals (*bottom*) of thrombin binding assays using human serum samples. (**a**) Fluorescence spectra obtained from concentration–response assays using aptamers-on-nanofibre biosensors with Q-TBA15 as the signaling probe and (**b**) relative fluorescence signal intensities (F − F0) of thrombin detection [204] (Copyright ©2012 Elsevier B.V.)

experimental studies are still quite few. These latter studies can be grouped on the basis of aptamers associated to quantum dots (QDs) [142, 198], nanoparticles [195, 199, 200], carbon nanotubes [201], or label-free [202] as compared with antibodies-based studies [203].

Lee et al. (2012) [204] were the only ones, to the best of our knowledge, who described the use of an aptamer-immobilised electrospun polystyrene–poly(styrene-co-maleicanhydride) (PS–PSMA) nanofibre as a new cost-effective aptasensor platform for protein detection (Fig. 10.11).

The ability of oligonucleotides-on-nanofibre based aptasensors to capture thrombin in biologically complex matrices was evaluated, using tenfold diluted human serum spiked with exogenous thrombin. High sensitivity for thrombin (up to 10 pM) in both buffer and diluted human serum samples could be obtained by using QDs with high fluorescence intensities. The fibres functionalisation occurred by incubation with streptavidin in PBS buffer solution for 1 h at room temperature and could be stored at 4 °C. Streptavidin-coated nanofibres, after washing, were immersed in 1 nmol biotin-aptamer B&W buffer solution (Tris-HCl, EDTA,

NaCl, pH 7.5) under mild rotation at RT for 1 h to allow the aptamer immobilisation. Such a scaffold worked as an excellent capturing fluorescent probe for the thrombin detection.

Aptazyme, DNAzyme and Ribozyme Biosensors

Optical aptazymes-based sensors [205] have been developed for the determination of adenosine: in the presence of adenosine, the anti-adenosine sequence formed a rigid structure with its ligand. Such a rigid structure produced a spatial hindrance and inhibited the formation of hemin-contained DNAzyme, changing the detectable optical signal [206]. Similar work was reported for the detection of lysozyme [207]. In another colorimetric design, by combination of anti-adenosine aptamer with DNAzyme with phosphodiester cleavage activity, the presence of adenosine could be characterized through the dispersal of aggregated AuNPs linked by the substrate strand of DNAzyme, which was inactive in the absence of adenosine [208]. Liu et al. (2009), Cho et al. (2009) and Wang et al. (2010) [126, 209, 210] reviewed other studies on aptazymes for sensing applications. Recently, aptazymes are revealing as a promising candidate, custom-made, allosteric molecule for sensing environmental pollutants. Frequent applications of DNAzymes, ribozymes and aptazymes (mostly DNAzymes) biosensors concern the detection of pollutants (heavy metals) [127, 130].

No study has been published till now, so far as we know, where electrospinning has been used in combination with ribozymes, DNAzymes and aptazymes to detect any target.

Peptide Nucleic Acids (PNAs) Biosensors

In solution studies, surface-attached peptide nucleic acids (PNA) have been reported to retain their unique and efficient hybridisation properties. Compared to their DNA counterparts, then, PNA recognition layers can offer significant advantages for sequence-specific DNA biosensors. As previously reported, higher sensitivity and specificity (including greater discrimination against single-base mismatches), faster hybridisation at room and elevated temperatures, minimal dependence on ionic strength, and use of shorter (10–15-mer) probes are all characteristics that sounds promising for their possible employment in the fabrication of biosensors and nanobiosensors for various applications. As a consequence, PNAs have stimulated several studies to test such capabilities in different contexts. Different strategies have been used to detect hybridised molecules on the surface and in solution [211, 212]. Some of them are here described. Wang et al. (1996) [213] were the first to use these molecules in the development of biosensor. They highlighted the unique properties and advantages in connection with electrochemical detection of the hybridisation event, as well as the new capabilities and opportunities afforded by the use of PNA surface probes. Mateo-Martì

et al. (2007) [214] set up a DNA biosensor based on self-assembled monolayers (SAMs) of thiol-derivatived PNA molecules adsorbed on gold surfaces so that in such structural configuration BioSAMs of PNAs maintained their capability for recognizing complementary DNA. Infrared spectroscopy X-ray photoemission spectroscopy were then used for the detection and spectroscopic characterization of PNA–DNA hybridisation process on gold surfaces to obtain an unambiguous signature of the PNA–DNA heteroduplex formation. Endo et al. (2005) [215] developed a localised surface plasmon resonance (LSPR) based label-free optical biosensor based on a gold-capped nanoparticle layer substrate immobilised with peptide nucleic acids (PNAs). A PNA probe was designed to recognize the target DNA related to tumour necrosis factor.

Hejazi et al. (2010) [216] developed an electrochemical DNA biosensor, using a gold electrode modified with a self-assembled monolayer composed of a PNA probe and 6-mercapto-1-hexanol. They covalently attached first the 14-mer PNA probe related to the hepatitis C virus genotype 3a (pHCV3a) core/E1 region on the electrode. Then, they selectively hybridised it with a complementary sequence in solution to form double-stranded PNA-DNA on the surface. As a result, an increase in the peak current of methylene blue (MB) was recorded and used to detect the target DNA sequence. A similar strategy was used by Ozkan et al. (2002a, b) [217, 218] on diverse types of electrodes in their works. They tested even a mixture that contained one-base mismatched. In the presence of a DNA oligonucleotide containing a one-base mismatch, a slight difference between the signal of the DNA probe-target hybridisation and the one of DNA probe-mismatch hybridisation could be observed. Potentiality in discrimination of single-base mismatches was confirmed in the study and a review of Wang (1998) [219]. Nanomaterials have been introduced in the creation of PNA-based nanobiosensors in order to improve their sensitivity. Examples of such studies are those of Zhang et al. (2006), whose DNA sensor could detect as low as femtomolar (zeptomoles) DNA targets and exhibited excellent selectivity against even a single base mismatch, additionally to a fairly good reproducibility, stability, and reusability [220]. Pita et al. (2008) used magnetic nanoparticles functionalised with a mixture of amino and thiol groups that facilitated the electrostatic attraction and further chemisorption of gold nanoparticles. Then, they immobilised biomolecules via thiol chemistry, which is exemplified by the immobilisation of peptide nucleic acid (PNA) oligomers that specifically hybridised with complementary DNA molecules in solution, resulting in an increase in response [221].

As far as we knows, no biosensing application to detect any target has been published till now, where electrospinning has been used in combination with Peptide Nucleic Acids. By the way, US Patent (2006) reported the instructions to design biosensors based on thermoplastic polymers (for example cellulose acetate, polyacrylonitrile, polyethylene oxide, polyamides, polyesters) and a system of biomolecules binders (e.g. PNA) [222]. The patented rational design is expected to be a kind of a universal approach to design and fabricate electrospinning-based biosensors, also based on PNA biosensors. The first binder could be, for example,

a multifunctional molecule of molecular weight ranging from 200 to 500 such as biotin, fluorescein or digoxygenin. It can be normally combined with the electrospun thermoplastic polymer nanofibre in an amount ranging from 1 to 20 % by weight of the thermoplastic polymer. A preferred first binder is biotin. For solution electrospinning, the biotin is readily associated with polymer by dissolving biotin and polymer in solution. A solvent for biotin and PLA is chloroform/acetone solvent (3:1 volume ratio), and the mixture is ultrasonicated for 60 min to obtain uniform dispersion. The second binder is usually joined to nanofibre incorporating first binder, for example, through simple incubation with the fibre, incubation at varying temperatures (e.g. from 0 to 98 °C.) or shaking or mixing during an incubation period. The second binder could be, for example, avidin/streptavidin, antibody, receptor, protein A, protein G, other protein, DNA and RNA molecules, PNA (peptide nucleic acid), enzyme or lectin. The association constant between biotin and avidin is $10–15 \ M^{-1}$. The association constant for streptavidin binding to biotin is $10–16 \ M^{-1}$. The following step concerns the potential to join a third binder (as antibody, antigen, DNA or other molecule, including reporter probe, e.g., the oligonucleotide probe or antivirus or DNA or RNA sequences) that hybridizes with the target.

10.3.2 Immunosensors

Immunosensors are a kind of biosensor planned to detect the formation of antigen-antibody complexes and convert it into electrical signals by means of a suitable transducer [223]. Antibodies are proteins produced by the immune system to recognise bacteria, viruses, parasites and all those microorganisms or macromolecules considered extraneous to the hosting living system.

Because of significant differences in affinity constants, antibodies may confer an incredibly high sensitivity to immunosensors in comparison to enzyme sensors. They are particularly appreciated for point of care diagnosis of diseases or wherever carrying out immunoassays, such as ELISA (Enzyme-Linked Immunosorbent Assay), is not an alternative. Indeed they are aimed mainly to the detection of the presence of certain antibodies or antigens in body fluids, especially in serum. However, there is also a significant concern in developing immunosensors using antibodies for the detection of different analytes in the environment (e.g. TNT contamination in groundwater via the formation of antibody-TNT complexes), once provided the match of analytes with the requirements that let them work as antigens [224]. Mainly electrochemical, optical and piezoelectric transducers have been investigated to develop immunobiosensor, taking advantage of the changes of properties occurring during the formation of antigen-antibody complexes. Briefly, in electrochemical sensors the antigen-antibody complex is converted into an electrical signal (amperometric, potentiometric or conductometric sensors), due to the cooperation with redox enzymes. In order to allow the immunosensor to work properly, it is necessary for the enzyme used as a label to be very close to the

electrode surface. In optical biosensors, the biological sensing element responds to the interaction with the target analyte either by generating an optical signal (e.g. fluorescence) or by undergoing changes in optical properties (i.e. absorption, reflectance, emission, refractive index, and optical path) [225], where the conjugate antibody is labelled with an optically detectable probe, (e.g. a fluorophore). Differently, microcantilevers and QCMs are especially attractive for immunosensors because of the potential to microfabricate immunosensors at low cost: antigen-antibody complex can be detected as mass change causing a vibration frequency shift, without using additional labels [226, 227].

If the antigen is immobilised onto the electrode surface, this requisite is complied. The immobilisation of the biological recognition element onto the surface of the transducer is by far the most common configuration employed in biosensors.

10.3.2.1 Immunosensors Through Electrospinning

The high surface area of electrospun nanofibres, the possible use of several polymeric materials and nanomaterials and combinations of them, including the use of biomimetic, biocompatible and biodegradable (nano)materials, have recently induced the test of nanofibres for biomedical applications as well as for fabrication of nanofibre-based immunosensors. The tailoring on the surface of nanofibres of molecules with specific recognition capabilities such as antibodies, and the possibility to attach more than one type of antibody on the nanofibrous mats can reasonably support the development of sensing systems with multianalyte detection capability. Consequently, several studies have been published about the use of electrospinning in the fabrication of various types of immunosensors. Hereinafter, only a few examples are reported.

Luo et al. (2010, 2012) designed and optimised a novel electrospun based biosensor able to detect suspensions of bacteria and virus [228, 229]. It comprised immunochromatography, nanoparticle-based magnetic separation and an immuno-assay for rapid and sensitive detection of microbial and viral pathogens. A scheme of the biosensing capturing strategy is presented in Fig. 10.12. The electrospun material, deposited on a polyvinylidene chloride substrate, was fabricated using nitrocellulose polymer due to its excellent biocompatibility and solubility in common solvents (8%wt). They used a CLF (conductometric lateral flow) biosensor as a device. It consisted of application pad, capture pad, absorption pad and a pair of electrodes capable of measuring the conductance of the adsorbed pathogens linked with conductive and magnetic nanoparticles. The fibre surface was bio-modified for polyclonal antibodies (affinity purified goat anti-*E. coli* O157:H7 polyclonal antibody or purified swine anti-BVDV polyclonal antibody) attachment using glutaraldehyde as cross-linker. Due to the unique nanostructure and biocompatibility of electrospun nitrocellulose membranes, the biosensor had linear detection response for *E. coli* O157:H7 and BVDV virus samples. Eight minute's detection process showed that the sensitivity of the portable and low-cost biosensor were 61 CFU/mL and 103 CCID/mL for *E. coli* O157:H7 and BVDV, respectively.
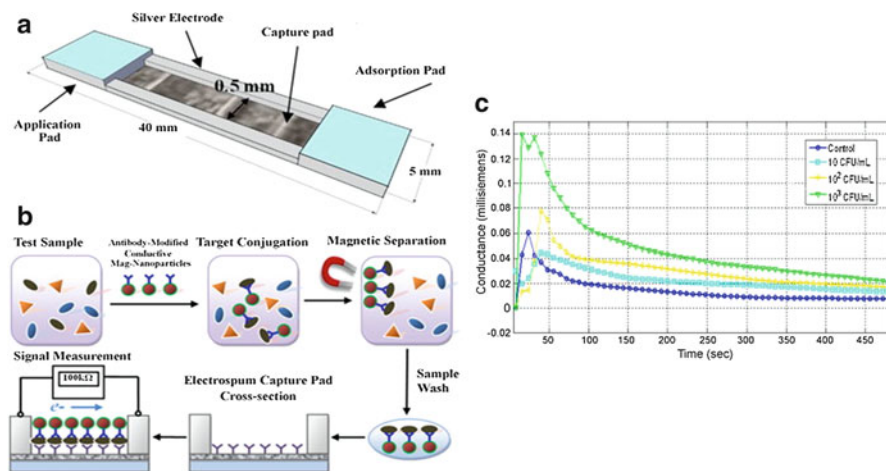
Fig. 10.12 (**a**) Diagram of the biosensor structure and membrane assembly consisting of cellulose application and absorption pads and electrospun cellulose nitrate capture pad. (**b**) Detection scheme of the lateral flow immunosensor based on the antibody functionalised electrospun capture membrane. (**c**) Biosensor conductance versus test time for different target concentrations of *E. coli* O157:H7 bacteria samples [228] (Copyright 2010 Elsevier)

More recently, Reinholt et al. developed a biosensor based on paper (lateral flow assay, LFA) [230] using electrospun nanofibres of polylactic acid (PLA) with poly (ethylene glycol) (PEG) and a functionalised polystyrene (PS). Specifically, anti-streptavidin antibodies adsorbed on the nanofibres captured streptavidin-conjugated sulforhodamine B (SRB)-encapsulating liposomes. Varying the functional polymer concentration within the PLA base allowed the creation of separate capture zones. Also, a sandwich assay for the detection of *E. coli* O157:H7 was developed using anti-*E. coli* antibodies as capture and reporter species with horseradish peroxidase for signal generation (LOD: 1.9×104 cells).

On the basis of economic criteria and the need for ultrasensitive assays, Dai et al. (2014) [231] developed very recently a novel 3D-biosensing platform based on electrospun carbon nanotubes/poly(methyl methacrylate) nanofibres composite bio-functionalised with α-fetoprotein (α-AFP) antibody, via electrostatic interaction. This platform was used to fabricate label-free electrochemiluminescent (ECL) immunosensor to detect α-AFP. A sketch of this biosensing platform is depicted in Fig. 10.13. CNTs were incorporated at first in the PMMA to form nanofibres through electrospinning. A three-dimensional network structure composed of chitosan, peroxydisulfate and CNTs/PMMA nanofibres was deposited on a disk glassy carbon electrode (GCE) for sensing, benefited from the unique properties of this netlike interface (i.e. strong ECL emission of peroxydisulfate nearly 35-folds higher than GCE alone). When the reaction between antibody and AFP happened, the ECL response of peroxydisulfate dramatically decreased. Such design offered a suitable carrier for immobilising biological recognition elements with low-toxicity and eco-friendliness, thus opening a promising approach to developing further

Fig. 10.13 Schematic routine of the label-free ECL sensing platform for APF [231] (Copyright 2014 Elsevier)
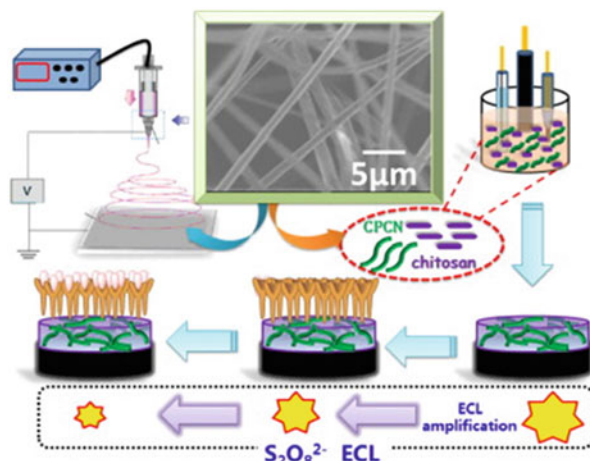
electrospun nanofibres based on amplified ECL biosensors with remarkable analytical performances.

Sun et al. (2011) fabricated a 3D immunosensor consisting in a chloramphenicol (CAP) biosensor composed of antibodies immobilised on electrospun polystyrene (PS) membranes and quartz crystal microbalances (QCMs). Three-dimensional fibrous PS membranes comprising porous PS fibres were deposited on the electrode of QCM via electrospinning and then functionalised with sensing antibody on the membranes. The functionality of the immobilised antibodies was tested with CAP using the 3-mercaptopropionic acid (MPA) method. The antibody-functionalised MPA biosensor sensitivity increased concurrently with increasing the PS loading and the specific surface area on the QCM, and its responses showed good linearity in the 5–100 ppb concentration range. The authors also observed fast response (2–3 s) to CAP, detection limit of 5 ppb, and sound capturing selectivity to CAP when tested with other antibiotics at a concentration between 5 and 200 ppb [232].

In an interesting study, Lee et al. (2011) [233] fabricated nanofibre-based protein microarrays through a combination of electrospinning and hydrogel lithography. Clearly defined hydrogel microstructures with incorporated nanofibres were created through electrospinning of polystyrene (PS)/poly(styrene-alt-maleic anhydride) (PSMA) fibres with diameters ranging from 0.5 to 1.0 μm followed by photopatterning of poly(ethylene glycol) (PEG) hydrogel on the electrospun fibres. Because of the protein-repellent nature of PEG hydrogels, they selectively immobilised IgG only within the nanofibrous region, creating an IgG microarray. Due to increased surface area, they recorded as much as six times IgG loading in nanofibrous substrates greater than on planar substrates and a consequent higher fluorescence signal and faster reaction rate in immunoassays. Furthermore, they exploited the capability of encapsulating enzymes in PEG hydrogels to be also used for additional biosensor elements, resulting in a micropatterned nanofibrous substrate consisting of IgG-immobilised nanofibres and enzyme-entrapping PEG hydrogels that might simultaneously carry out both immunoassays and enzyme-based assays.

The use of electrospun sensing membrane was described in the study of Senecal et al. (2008) [234], who developed two types of electrospun capture membranes containing either carboxyl (COOH) or amine (NH$_2$) functional groups for covalent attachment of antibodies. The carboxyl functional membrane was produced by electrospinning polyvinyl chloride (PVC) formulated to be 1.8 % carboxylated, while the amine functional membrane was made through co-electrospinning of two polymers, water-soluble polyamine and water insoluble polyurethane. Antibodies were covalently attached to the functional groups on the membranes, and the assay was developed for detecting *Staphylococcus* enterotoxin B (SEB) and resulted in effective recognition.

The potential of electrospun fibres for long-range surface plasmon resonance (LR-SPR) immunosensors applications was reported by Netsuwan et al. (2014) [235] for the detection of human immunoglobulin G. Water-stable poly(acrylic acid) (PAA) fibres were fabricated on flat gold thin films via an electrospinning technique by adding ß-cyclodextrin as a crosslinker, followed by thermal treatment at 150 °C for 40 min. The obtained fibres were then used to construct LR-SPR biosensors. The layer-by-layer deposition of poly(diallyldimethylammonium chloride) and PAA ultrathin films on the electrospun PAA fibres functionalised their surfaces and further increased their water-stability by increasing the number of active carboxylic acid groups, which were then successfully activated for the construction of immunosensors.

10.3.2.2   Our Development of an Electrospun Nanofibrous Immunosensor

A functionalised nanofibrous scaffold of titania grown on GaPO4 crystal microbalances was developed in our laboratories and used in the creation and arrangement of a biomolecule-binding sensor to implement further as immunosensor in diagnostics. The advantage in the use of nanostructured fibres of titania is in the combination of features typical of nanostructured fabrics with those of this nanocrystalline metal oxide: (i) high surface area, and then potential increase in binding sites density, in capture efficiency and sensitivity; (ii) low-toxicity; (iii) ease of fabrication; (iv) chemical and photochemical stability; (v) electrochemical and catalytic activity; (vi) capacity of binding an assortment of macromolecules (proteins) and (vii) biocompatibility. GaPO$_4$ microbalances were chosen as gravimetric transducers for their thermal resistance as requested by the oxidization process of the electrospun web. This piezo-material (stable up to 900 °C), in effect, is 100 times less sensitive to temperature than conventional AT-cut quartz crystals. As a consequence, it is capable of functioning as a resonator according to Sauerbrey's law even after the calcination process. The TiO$_2$ nanofibres after the electrospinning deposition were described through, scanning electron microscopy (SEM), transmission electron microscopy (TEM), electron diffraction pattern (EDP) and atomic force microscopy (AFM) analyses [236]. The creation of TiO$_2$ (anatase) nanofibres ranging from 50 to 200 nm (Fig. 10.14A) significantly improved the ability of a
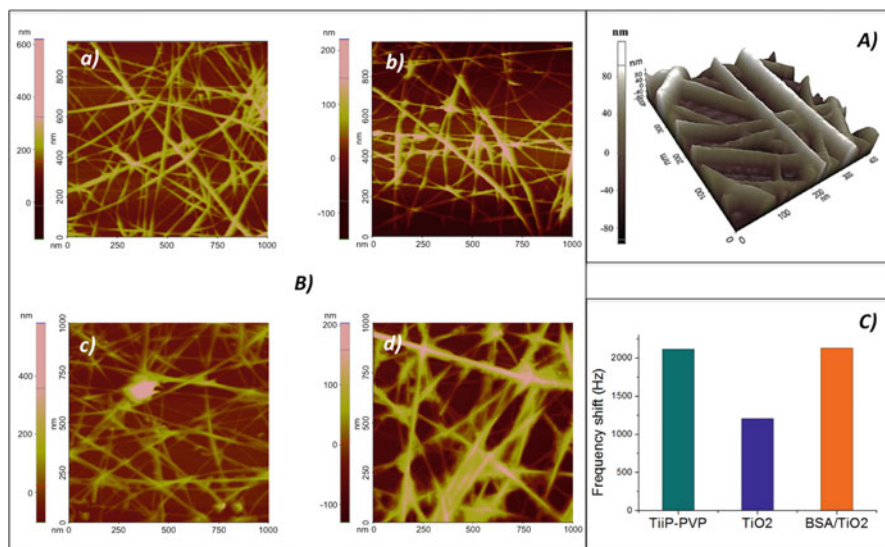
Fig. 10.14 (**A**) Pristine titania nanofibres electrospun onto silicon wafer (3D AFM micrograph), (**B**) BSA binding to TiO₂ nanofibres analysed through AFM of Si wafers coated with an electrospun TiO₂ scaffold after both incubation for 40 min at pH 3.5 and pH 8 (*a, b*) and for 40 min and 2 h with protein solution at pH 6.5 (*c, d*). (**C**) BSA binding to TiO₂ nanofibres quantified as global frequency shift in the oscillations of a GaPO₄ microbalance incubated for 2 h at pH 6.5

TiO₂-based potential biosensor to bind biomolecules. Both direct and mediated IgG binding to electrospun titania nanofibres were tested. Biomolecule immobilisation was carried out by incubating different proteins at distinct pHs and increasing incubation periods. Protein binding capacity of the electrospun nanofibrous mat was tested using bovine serum albumin (BSA), mouse immunoglobulin G (specifically IgG2a: for its greatest affinity vs. Protein A) and Protein A as macromolecular models. Immobilisation pHs were chosen according to features of the different proteins (isoelectric point – PI: BSA-PI = 4.7; IgG2a-PI = ~7; Protein A-PI = 5.16). Immobilisation of proteins was proved through recording changes in the frequency oscillation of microbalances (at 6 MHz) and observations through AFM and confocal laser scanning microscopy (CLSM). The greatest binding of BSA onto TiO₂ nanofibres occurred after 2 h pH 6.5 incubation (i.e. negatively charged) (Fig. 10.14 Bd), where ample coating of fibres was observed. Such immobilisation also generated a deflection in the frequency of GaPO4 microbalance oscillations (Fig. 10.14 C). The broadest IgG2a immobilisation onto TiO₂ nanofibres was observed in AFM and CLSM micrographs when incubation was performed at pH 7 for 40 min (i.e. about zero charge) (Fig. 10.15Ab, Ba). Differently, at pH 6 IgG2a (i.e. positively charged) seemed to aggregate in more sparse agglomerates onto nanofibres in AFM micrographs (Fig. 10.15Aa). At pH 8 (i.e. negatively charged) IgG2a rarely was linked to the scaffold (CLSM micrographs)
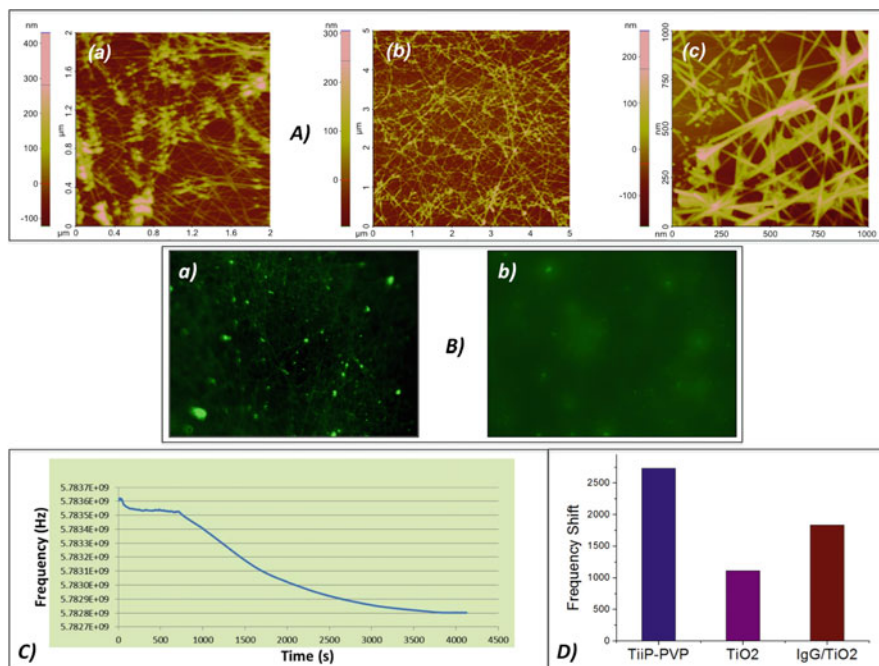
Fig. 10.15 (**A**) AFM micrographs of IgG2a anchored to TiO_2 nanofibres electrospun on Si wafers and incubated at pH 6 (*a*) and 7 (*b*, *c*: different optical magnification) for 40 min. (**B**) CLSM micrographs of IgG2a binding to TiO_2 nanofibres electrospun on SiO_2 disks and incubated at pH 7 (*a*) and 8 (*b*) for 2 h. (**C**) IgG2a binding to TiO_2 fibres at pH 7 analysed through the frequency decrease in the oscillation of GaPO4 microbalance up to equilibrium achievement. (**D**) Quantification of the global frequency shift on the basis of the frequency measurements reported in (**C**)

(Fig. 10.15Bb). The attachment of IgG2a to TiO_2 (IgG/TiO_2) resulted in about 930 Hz frequency shift in the transducer oscillation, with respect to the pristine calcined nanofibres (TiO_2) and the precursor nanofibrous layer before calcination (TiiP-PVP) (Fig. 10.15c, d). Anchoring of Protein A was higher along TiO_2 nanofibres at pH 4 incubations (i.e. positively charged) (Fig. 10.17a), while diffused aggregation among protein macromolecules occurred at increased pH (Fig. 10.16a, b). The further binding of IgG2a to Protein A performed at pH 7 showed a wide distribution of fluorescence along electrospun titania nanofibres (Fig. 10.17b). The results observed with different immobilisation procedures (pH) compared with PIs typical of both proteins and TiO_2 indicate that electrostatic interactions might be responsible for BSA and IgG2a binding onto TiO_2 nanofibres. The evidence of protein binding onto TiO_2 nanofibres and the effect of this attachment on the frequency responses of the selected resonator suggest the possible use of such functionalised nanofibrous scaffold to construct highly sensitive biosensors. Furthermore, the high grade of biocompatibility of TiO_2 may also indicate the use of such biosensors for medical applications and diagnostics.
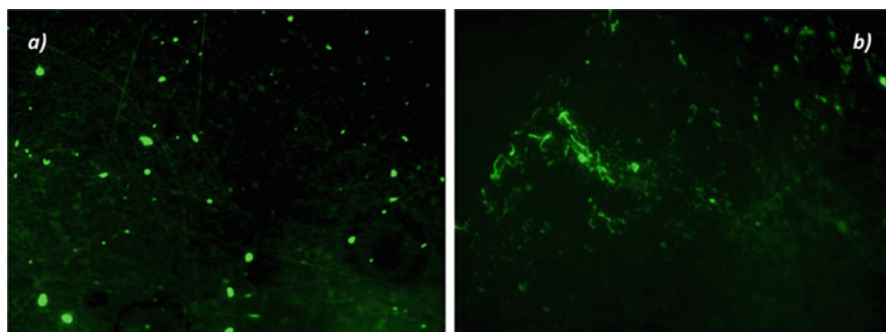
Fig. 10.16 CLSM micrographs of Protein A linked to SiO_2 disks coated with TiO_2 electrospun nanofibres and incubated for 2 h at pH 5 (**a**) and 6 (**b**)
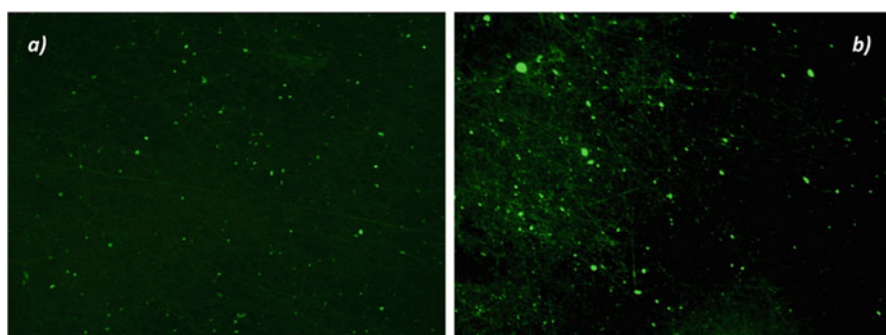
Fig. 10.17 CLSM micrographs of Protein A linked to SiO_2 disks coated with TiO_2 electrospun nanofibres and incubated for 2 h at pH 4 (**a**) and after IgG2a binding to Protein A (**b**) at pH 7

10.4 Outlooks

This chapter gives a brief description of the recent results related to electrospun biosensors. Nanofibres have been confirmed to be an excellent support for these detecting tools for several reasons: easy immobilisation of biomolecules, large surface-area-to-volume ratios, pore sizes tailoring towards various biomolecule sizes (e.g. oligonucleotides, proteins and antigens), a plethora of sites for interaction or attachment, functional surfaces, and a low mass-transfer limitation. These studies reported that biosensors exhibited high sensitivity and their activity was efficiently maintained, as well as their stability. However, the studies of this issue are still limited as there are still problems in their large-scale application for sensors manufacturing (Chap. 13). Nevertheless, based on their unique advantages, here it has been highlighted that the nanofibrous materials have a great potential in sensor applications.

References

1. D.R. Thévenot, K. Toth, R.A. Durst, G.S. Wilson, Electrochemical biosensors: recommended definitions and classification. Biosens. Bioelectron. **16**, 121–131 (2001)
2. R. Vajtai, *Springer Handbook of Nanomaterials* (Springer, Berlin, 2013). ISBN 978-3-642-20594-1
3. B. Ding, M. Wang, X. Wang, J. Yu, G. Sun, Electrospun nanomaterials for ultrasensitive sensors. Mater. Today **13**, 16–27 (2010)
4. A. Merkoci, *Biosensing Using Nanomaterials* (Wiley, Hoboken, 2009). ISBN 978-0-470-44772-7
5. P. Malik, V. Katyal, V. Malik, A. Asatkar, G. Inwati, T.K. Mukherje, Nanobiosensors: concepts and variations. ISRN Nanomaterials, **2013**, 9 (2013). doi:10.1155/2013/327435
6. J.H. Wendorff, S. Agarwal, A. Greiner, *Electrospinning: Materials, Processing, and Applications* (Wiley-VCH, Hoboken, 2012). ISBN 978-3-527-32080-6
7. R.N. Palchesko, Y. Sun, L. Zhang, J.M. Szymanski, Q. Jallerat, A.W. Feinberg, *Nanofiber Biomaterials, Springer Handbook of Nanomaterials*, ed. by R. Vajtai, (Springer, Berlin, 2013), pp. 977–1010. ISBN 978-3-642-20594-1
8. K. Sawicka, P. Gouma, S. Simon, Electrospun biocomposite nanofibers for urea biosensing. Sensor Actuat. B-Chem. **108**, 585–588 (2005)
9. S.D. Uzun, F. Kayaci, T. Uyar, S. Timur, L. Toppare, Bioactive surface design based on functional composite electrospun nanofibers for biomolecule immobilization and biosensor applications. ACS Appl. Mater. Interfaces **6**(7), 5235–5243 (2014)
10. W. Mattanavee, O. Suwantong, S. Puthong, T. Bunaprasert, V.P. Hoven, P. Supaphol, Immobilization of biomolecules on the surface of electrospun polycaprolactone fibrous scaffolds for tissue engineering. ACS Appl. Mater. Interfaces **1**(5), 1076–1085 (2009)
11. X. Chen, Z. Guo, G.-M. Yang, J. Li, M.-Q. Li, J.-H. Liu, X.-J. Huang, Electrical nanogap devices for biosensing. Mater. Today **13**, 28–41 (2010)
12. T. Polat, H.G. Bazin, R.J. Linhardt, Enzyme catalyzed regioselective synthesis of sucrose fatty acid ester surfactants. J. Carbohydr. Chem. **16**, 1319–1325 (1997)
13. F. Hasan, A.A. Shah, A. Hameed, Industrial applications of microbial lipases. Enzyme Microb. Technol. **39**, 235–251 (2006)
14. G. Choudhary, S.L. Wu, P. Shieh, W.S. Hancock, Multiple enzymatic digestion for enhanced sequence coverage of proteins in complex proteomic mixtures using capillary LC with ion trap MS/MS. J. Proteome Res. **2**, 59–67 (2003)
15. S. Akgol, E. Dinckaya, A novel biosensor for specific determination of hydrogen peroxide: catalase enzyme electrode based on dissolved oxygen probe. Talanta **48**, 363–367 (1999)
16. T.D. Sutherland, I. Horne, K.M. Weir, C.W. Coppin, M.R. Williams, M. Selleck, R.J. Russell, J.G. Oakeshott, Enzymatic bioremediation: from enzyme discovery to applications. Clin. Exp. Pharmacol. Physiol. **31**, 817–821 (2004)
17. L. Gianfreda, J.-M. Bollag, Effect of soils on the behavior of immobilized enzymes. Soil Sci. Soc. Am. J. **58**, 1672–1681 (1994)
18. A.K. Bajpai, S. Bhanu, Immobilization of α-amylase in vinylpolymer-based interpenetrating polymer networks. Colloid Polym. Sci. **282**, 76–83 (2003)
19. L. Mojovic, Z. Knezevic, R. Popadic, S. Jovanovic, Immobilization of lipase from *Candida rugosa* on a polymer support. Appl. Microbiol. Biot. **50**(6), 676–681 (1998)
20. S. Datta, L.R. Christena, Y.R. Sriramulu Rajaram, Enzyme immobilization: an overview on techniques and support materials. 3 Biotech **3**(1), 1–9 (2013)
21. J.M. Guisan, *Methods in Biotechnology: Immobilisation of Enzymes and Cells* (Humana Press Inc, Totowa, 2006). ISBN 978-1-58829-290-2

22. Q. Huanga, H. Shindo, Effects of copper on the activity and kinetics of free and immobilized acid phosphatase. Soil Biol. Biochem. **32**, 1885–1892 (2000)

23. R.G. Burns, R.P. Dick, *Enzymes in the Environment: Activity, Ecology and Applications* (Marcel Dekker, New York, 2005). ISBN 0-8247-0614-51996

24. S.E. Létant, B.R. Hart, S.R. Kane, M.Z. Hadi, S.J. Shields, J.G. Reynolds, Enzyme immobilization on porous silicon surfaces. Adv. Mater. **16**, 689–693 (2004)

25. A. Popat, S.B. Hartono, F. Stahr, J. Liu, S.Z. Qiao, G. Qing (Max) Lu, Mesoporous silica nanoparticles for bioadsorption, enzyme immobilisation, and delivery carriers. Nanoscale **3** (7), 2801–2818 (2011)

26. D. Yunrong, N. Junfeng, Y. Lifeng, L. Jia, J. Guoxiang, Electrospun nanofiber membranes as supports for enzyme immobilization and its application. Prog. Chem. **22**(09), 1808–1818 (2010)

27. K. Yoon, K. Kim, X.F. Wang, D.F. Fang, B.S. Hsiao, B. Chu, High flux ultrafiltration membranes based on electrospun nanofibrous PAN scaffolds and chitosan coating. Polymer **47**, 2434–2441 (2006)

28. R.S. Barhate, C.K. Loong, S. Ramakrishna, Preparation and characterization of nanofibrous filtering media. J. Membr. Sci. **283**, 209–218 (2006)

29. R. Gopal, S. Kaur, Z.W. Ma, C. Chan, S. Ramakrishna, T. Matsuura, Electrospun nanofibrous filtration membrane. J. Membr. Sci. **281**, 581–586 (2006)

30. P. Ye, Z.K. Xu, J. Wu, C. Innocent, P. Seta, Nanofibrous poly(acrylonitrile-co-maleic acid) membranes functionalized with gelatin and chitosan for lipase immobilization. Biomaterials **27**(22), 4169–4176 (2006)

31. H.T. Deng, Z.K. Xu, Z.W. Dai, J. Wu, P. Seta, Immobilization of *Candida rugosa* lipase on polypropylene microfiltration membrane modified by glycopolymer: hydrolysis of olive oil in biphasic bioreactor. Enzyme. Microb. Technol. **36**, 996–1002 (2005)

32. E.G. Diaz, R. Catana, B.S. Ferreira, S. Luque, P. Fernandes, J.M.S. Cabral, Towards the development of a membrane reactor for enzymatic inulin hydrolysis. J. Membr. Sci. **273**, 152–158 (2006)

33. M.M. El-Masry, A. De Maio, S. Di Martino, N. Diano, U. Bencivenga, S. Rossi, V. Grano, P. Canciglia, M. Portaccio, F.S. Gaeta, D.G. Mita, Modulation of immobilized enzyme activity by altering the hydrophobicity of nylon-grafted membranes – part 1. Isothermal conditions. J. Mol. Catal. B-Enzym. **9**, 219–230 (2000)

34. X.-J. Huang, A.-G. Yu, Z.-K. Xu, Covalent immobilization of lipase from *Candida rugosa* onto poly(acrylonitrile-co-2-hydroxyethyl methacrylate) electrospun fibrous membranes for potential bioreactor application. Bioresource Technol. **99**, 5459–5465 (2008)

35. P.-C. Chen, X.-J. Huang, F. Huang, Y. Ou, M.-R. Chen, Z.-K. Xu, Immobilization of lipase onto cellulose ultrafine fiber membrane for oil hydrolysis in high performance bioreactor. Cellulose **18**, 1563–1571 (2011)

36. X.-H. Chu, X.-L. Shi, Z.-Q. Feng, J.-Y. Gu, H.-Y. Xu, Y. Zhang, Z.-Z. Gu, In vitro evaluation of a multi-layer radial-flow bioreactor based on galactosylated chitosan nanofiber scaffolds. Biomaterials **30**(27), 4533–4538 (2014)

37. S. Gupta, A. Bhattachary, C.N. Murthy, Tune to immobilize lipases on polymer membranes: techniques, factors and prospects. Biocatal. Agric. Biotechnol. **2**(3), 171–190 (2013)

38. Z.-G. Wang, L.-S. Wan, Z.-M. Liu, X.-J. Huang, Z.-K. Xu, Enzyme immobilization on electrospun polymer nanofibers: an overview. J. Mol. Catal. B-Enzym. **56**, 189–195 (2009)

39. H.F. Jia, G.Y. Zhu, B. Vugrinovich, W. Kataphinan, D.H. Reneker, P. Wang, Enzyme-carrying polymeric nanofibers prepared via electrospinning for use as unique biocatalysts. Biotechnol. Prog. **18**, 1027–1032 (2002)

40. K.H. Lee, C.S. Ki, D.H. Baek, G.D. Kang, D.W. Ihm, Y.H. Park, Application of electrospun silk fibroin nanofibers as an immobilization support of enzyme. Fiber Polym. **6**, 181–185 (2005)

41. S.F. Li, J.P. Chen, W.T. Wu, Electrospun polyacrylonitrile nanofibrous membranes for lipase immobilization. J. Mol. Catal. B-Enzym. **47**, 117–124 (2007)

42. S. Nair, J. Kim, B. Crawford, S.H. Kim, Improving biocatalytic activity of enzyme-loaded nanofibers by dispersing entangled nanofiber structure. Biomacromolecules **8**, 1266–1270 (2007)

43. X.J. Huang, Z.K. Xu, L.S. Wan, C. Innocent, P. Seta, Electrospun nanofibers modified with phospholipid moieties for enzyme immobilization. Macromol. Rapid Commun. **27**, 1341–1345 (2006)

44. Z.G. Wang, J.Q. Wang, Z.K. Xu, Immobilization of lipase from *Candida rugosa* on electrospun polysulfone nanofibrous membranes by adsorption. J. Mol. Catal. B-Enzym. **42**, 45–51 (2006)

45. J.B. Xie, Y.L. Hsieh, Ultra-high surface fibrous membranes from electrospinning of natural proteins: casein and lipase enzyme. J. Mater. Sci. **38**, 2125–2133 (2003)

46. Y.H. Wang, Y.L. Hsieh, Immobilization of lipase enzyme in polyvinyl alcohol (PVA) nanofibrous membranes. J. Membr. Sci. **309**, 73–81 (2008)

47. L.L. Wu, X.Y. Yuan, J. Sheng, Immobilization of cellulase in nanofibrous PVA membranes by electrospinning. J. Membr. Sci. **250**, 167–173 (2005)

48. B.C. Kim, S. Nair, J. Kim, J.H. Kwak, J.W. Grate, S.H. Kim, M.B. Gu, Preparation of biocatalytic nanofibres with high activity and stability via enzyme aggregate coating on polymer nanofibres. Nanotechnology **16**, S382–S388 (2005)

49. X.-J. Huang, Z.-K. Xu, Preparation and characterization of stable chitosan nanofibrous membrane for lipase immobilization. Eur. Polym. J. **43**, 3710–3718 (2007)

50. H.K. Ahn, B.C. Kim, S.H. Jun, M.S. Chang, D. Lopez-Ferrer, R.D. Smith, M.B. Gu, S.W. Lee, B.S. Kim, J. Kim, Robust trypsin coating on electrospun polymer nanofibers in rigorous conditions and its uses for protein digestion. Biotechnol. Bioeng. **107**(6), 917–923 (2010)

51. T.G. Kim, T.G. Park, Surface functionalized electrospun biodegradable nanofibers for immobilization of bioactive molecules. Biotechnol. Prog. **22**(4), 1108–1113 (2006)

52. S.S. Sekhon, J.-M. Park, J.-Y. Ahn, T.S. Park, S.-D. Kwon, Y.-C. Kim, J. Min, Y.-H. Kim, Immobilization of paranitrobenzyl esterase-CLEA on electrospun polymer nanofibers for potential use in the synthesis of cephalosporinderived antibiotics. Mol. Cell. Toxicol. **10**(2), 215–221 (2014)

53. A. Moradzadegan, S.-O. Ranaei-Siadat, A. Ebrahim-Habibi, M. Barshan-Tashnizi, R. Jalili, S.-F. Torabi, K. Khajeh, Immobilization of acetylcholinesterase in nanofibrous PVA/BSA membranes by electrospinning. Eng. Life Sci. **10**, 57–64 (2010)

54. R. Huang, H. Deng, T. Cai, Y. Zhan, X. Wang, X. Chen, A. Ji, X. Lil, Layer-by-layer immobilized catalase on electrospun nanofibrous mats protects against oxidative stress induced by hydrogen peroxide. J. Biomed. Nanotechnol. **10**(7), 1346–1358 (2014)

55. T.C. Hung, C.C. Fu, C.H. Su, J.Y. Chen, W.T. Wu, Y.S. Lin, Immobilization of cellulase onto electrospun polyacrylonitrile (PAN) nanofibrous membranes and its application to the reducing sugar production from microalgae. Enzyme Microb. Tech. **49**(1), 30–37 (2011)

56. K. Sun, Z.H. Li, Preparations, properties and applications of chitosan based nanofibers fabricated by electrospinning. Expr. Polym. Lett. **5**(4), 342–361 (2011)

57. B. Krajewska, Application of chitin- and chitosan-based materials for enzyme immobilizations: a review. Enzyme Microb. Tech. **35**, 126–139 (2004)

58. B. Krajewska, Membrane-based processes performed with use of chitin/chitosan materials. Sep. Purif. Technol. **41**, 305–312 (2005)

59. O.C. Agboh, Y. Qin, Polym. Chitin and chitosan fibers. Adv. Technol. **8**, 355–365 (1997)

60. P. Wang, J. Liu, T. Zhang, In vitro biocompatibility of electrospun chitosan/collagen scaffold. J. Nanomater. **2013**, 8 (2013). doi:10.1155/2013/958172

61. S.-G. Wang, X. Jiang, P.-C. Chen, A.-G. Yu, X.-J. Huang, Preparation of coaxial-electrospun poly[bis(pmethylphenoxy)] phosphazene nanofiber membrane for enzyme immobilization. Int. J. Mol. Sci. **13**(11), 14136–14148 (2012)

62. H.T. Deng, Z.K. Xu, X.J. Huang, J. Wu, P. Seta, Adsorption and activity of *Candida rugosa* lipase on polypropylene hollow fiber membrane modified with phospholipid analogous polymers. Langmuir **20**, 10168–10173 (2004)

63. Y. Iwasaki, K. Ishihara, Phosphorylcholine-containing polymers for biomedical applications. Anal. Bioanal. Chem. **381**, 534–546 (2005)

64. M. Hayama, K. Yamamoto, F. Kohori, K. Sakai, How polysulfone dialysis membranes containing polyvinylpyrrolidone achieve excellent biocompatibility? J. Membr. Sci. **234**, 41–49 (2004)

65. A. De Maio, M.M. El-Masry, P. De Luca, V. Grano, S. Rossi, N. Pagliuca, F.S. Gaeta, M. Portaccio, D.G. Mita, Influence of the spacer length on the activity of enzymes immobilised on nylon/polyGMA membranes Part 2: Non-isothermal conditions. J. Mol. Catal. B-Enzym. **21**, 253–265 (2003)

66. Y.H. Wang, Y.L. Hsieh, Enzyme immobilization to ultra-fine cellulose fibers via amphiphilic polyethylene glycol spacers. J. Polym. Sci. Pol. Chem. **42**, 4289–4299 (2004)

67. G.L. Ren, X.H. Xu, Q. Liu, J. Cheng, X.Y. Yuan, L.L. Wu, Y.Z. Wan, Electrospun poly(vinyl alcohol)/glucose oxidase biocomposite membranes for biosensor applications. React. Funct. Polym. **66**, 1559–1564 (2006)

68. S. Ramakrishna, N.L. Lala, H. Garudadhwaj, R. Ramaseshan, V.K. Ganesh, Polymer nanofibers for biosensor applications, in *Molecular Building Blocks for Nanotechnology*, ed. by G.A. Mansoori, Th.F. George, L. Assoufid, G. Zhang. Topics in Applied Physics, vol. 109 (Springer, New York, 2007), pp. 377–392. ISBN 978-0-387-39938-6

69. D. Li, Z. Pang, X. Chen, L. Luo, Y. Cai, Q. Wei, A catechol biosensor based on electrospun carbon nanofibers. Beilstein J. Nanotechnol. **5**, 346–354 (2014)

70. Y.Z. Zhang, X. Wang, Y. Feng, J. Li, C.T. Lim, S. Ramakrishna, Coaxial electrospinning of (fluorescein isothiocyanate conjugated bovine serum albumin)-encapsulated poly(e-caprolactone) nanofibers for sustained release. Biomacromolecules **7**, 1049–1057 (2006)

71. K.F. Fernandes, C.S. Lima, H. Pinho, C.H. Collins, Immobilization of horseradish peroxidase onto polyaniline polymers. Process Biochem. **38**, 1379–1384 (2003)

72. C. Vedrine, S. Fabiano, C. Tran-Minh, Amperometric tyrosinase based biosensor using an electrogenerated polythiophene film as an entrapment support. Talanta **59**, 535–544 (2003)

73. M. Gerard, A. Chaubey, B.D. Malhotra, Application of conducting polymers to biosensors. Biosens. Bioelectron. **17**(5), 345–359 (2002)

74. A. Chaubey, K.K. Pande, V.S. Singh, B.D. Malhotra, Co-immobilization of lactate oxidase and lactate dehydrogenase on conducting polyaniline films. Anal. Chim. Acta **407**, 97–103 (2000)

75. B.D. Malhotra, A. Chaubey, S.P. Singh, Prospects of conducting polymers in biosensors. Anal. Chim. Acta **578**(1), 59–74 (2006)

76. R. Janmanee, S. Chuekachang, S. Sriwichai, A. Baba, S. Phanichphant, Functional conducting polymers in the application of SPR biosensors. J. Nanotechnol. **2012**, Article ID 620309, p. 7 (2012) doi:10.1155/2012/620309

77. N.K. Guimard, N. Gomez, C.E. Schmidt, Conducting polymers in biomedical engineering. Prog. Polym. Sci. **32**(8–9), 876–921 (2007)

78. T. Ahujaa, I.A. Mira, D.K. Rajesh, Biomolecular immobilization on conducting polymers for biosensing applications. Biomaterials **28**(5), 791–805 (2007)

79. A. Merkoci, M. Pumera, X. Llopis, B. Perez, M. del Valle, S. Alegret, New materials for electrochemical sensing VI: carbon nanotubes. TRAC-Trend Anal. Chem. **24**, 826–838 (2005)

80. J. Tkac, J.W. Whittaker, T. Ruzgas, The use of single walled carbon nanotubes dispersed in a chitosan matrix for preparation of a galactose biosensor. Biosens. Bioelectron. **22**, 1820–1824 (2007)

81. Z.G. Wang, B.B. Ke, Z.K. Xu, Covalent immobilization of redox enzyme on electrospun nonwoven poly(acrylonitrile-coacrylic acid) nanofiber mesh filled with carbon nanotubes: a comprehensive study. Biotechnol. Bioeng. **97**(4), 708–720 (2007)

82. S. Liu, B. Yu, F. Li, Y. Ji, T. Zhang, Coaxial electrospinning route to prepare Au-loading SnO2 hollow microtubes for nonenzymatic detection of H_2O_2. Electrochim. Acta **141**, 161–166 (2014)

83. E. Omidinia, N. Shadjou, M. Hasanzadeh, (Fe_3O_4)-graphene oxide as a novel magnetic nanomaterial for nonenzymatic determination of phenylalanine. Mater. Sci. Eng. C **33**, 4624–4632 (2013)

84. M.J. Ruedas-Rama, E.A.H. Hall, Analytical nanosphere sensors using quantum dot-enzyme conjugates for urea and creatinine. Anal. Chem. **82**, 9043–9049 (2010)

85. X. Wang, C. Hua, H. Liu, G. Du, X. He, Y. Xi, Synthesis of CuO nanostructures and their application for nonenzymatic glucose sensing. Sensor Actuat. B-Chem. **144**, 220–225 (2010)

86. S. Park, H. Boo, T. Dong Chung, Electrochemical non-enzymatic glucose sensors. Anal. Chim. Acta **556**, 46–57 (2006)

87. Y. Liu, Y. Ding, Y. Zhang, Y. Lei, Pt–Au nanocorals, Pt nanofibers and Au microparticles prepared by electrospinning and calcination for nonenzymatic glucose sensing in neutral and alkaline environment. Sensor Actuat. B-Chem. **171–172**, 954–961 (2012)

88. Y. Zhang, Y. Wang, J. Jia, J. Wang, Nonenzymatic glucose sensor based on graphene oxide and electrospun NiO nanofibers. Sensor Actuat. B-Chem. **171–172**, 580–587 (2012)

89. B. Zhang, G. Liu, A. Yao, Y. Xiao, J. Du, Y. Guo, D. Xiao, Q. Hu, M.M.F. Choi, A sensitive AgNPs/CuO nanofibers nonenzymatic glucose sensor based on electrospinning technology. Sensor Actuat. B-Chem. **195**, 431–438 (2014)

90. M.H. Yang, Y.H. Yang, B. Liu, G.L. Shen, R.Q. Yu, Amperometric glucose biosensor based on chitosan with improved selectivity and stability. Sensor Actuat. B-Chem. **101**, 269–276 (2004)

91. J. Wang, Electrochemical glucose biosensors. Chem. Rev. **108**, 814–825 (2008)

92. L.X. Wang, J. Bai, X.J. Bo, X.L. Zhang, L.P. Guo, A novel glucose sensor based on ordered mesoporous carbon–Au nanoparticles nanocomposites. Talanta **83**, 1386–1391 (2011)

93. A. Chaubey, B.D. Malhotra, Mediated biosensors. Biosens. Bioelectron. **17**, 441–456 (2002)

94. S. Warren, T. McCormac, E. Dempsey, Investigation of novel mediators for a glucose biosensor based on metal picolinate complexes. Bioelectrochemistry **67**(1), 23–35 (2005)

95. K. Yamamoto, H.S. Zeng, Y. Shen, M.M. Ahmed, T. Kato, Evaluation of an amperometric glucose biosensor based on a ruthenium complex mediator of low redox potential. Talanta **66**, 1175–1180 (2005)

96. F. Ricci, F. Caprio, A. Poscia, F. Valgimigli, D. Messeri, E. Lepori, G. Dall'Oglio, G. Palleschi, D. Moscone, Toward continuous glucose monitoring with planar modified biosensors and microdialysis: study of temperature, oxygen dependence and in vivo experiment. Biosens. Bioelectron. **22**, 2032–2039 (2007)

97. J. Wu, F. Yin, Sensitive enzymatic glucose biosensor fabricated by electrospinning composite nanofibers and electrodepositing Prussian blue film. J. Electroanal. Chem. **694**, 1–5 (2013)

98. X.Y. Wang, H.F. Gu, F. Yin, Y.F. Tu, A glucose biosensor based on Prussian blue/chitosan hybrid film. Biosens. Bioelectron. **24**, 1527–1530 (2009)

99. D. Pradhan, F. Niroui, K.T. Leung, High-performance, flexible enzymatic glucose biosensor based on ZnO nanowires supported on a gold-coated polyester substrate. Appl. Mater. **2**, 2409–2412 (2010)

100. K. Yang, G.-W. She, H. Wang, X.-M. Ou, X.-H. Zhang, C.-S. Lee, S.-T. Lee, ZnO nanotube arrays as biosensors for glucose. J. Phys. Chem. C **113**, 20169–20172 (2009)

101. Y.T. Wang, L. Yu, Z.Q. Zhu, Improved enzyme immobilization for enhanced bioelectrocatalytic activity of glucose sensor. Sensor Actuat. B-Chem. **136**, 332–337 (2009)

102. J.D. Qiu, W.M. Zhou, J. Guo, Amperometric sensor based on ferrocene-modified multiwalled carbon nanotube nanocomposites as electron mediator for the determination of glucose. J. Anal. Biochem. **385**, 264–269 (2009)

103. X.H. Kang, Z.B. Mai, X.Y. Zou, P.X. Cai, J.Y. Mo, Glucose biosensors based on platinum nanoparticles-deposited carbon nanotubes in sol–gel chitosan/silica hybrid. Talanta **74**, 879–886 (2008)

104. X.L. Chen, J.H. Chen, C.Y. Deng, Amperometric glucose biosensor based on boron-doped carbon nanotubes modified electrode. Talanta **76**, 763–767 (2008)

105. N. Wang, K. Burugapall, W. Song, J. Halls, F. Moussy, A. Ray, Y. Zheng, Electrospun fibroporous polyurethane coatings for implantable glucose biosensors. Biomaterials **34**, 888–901 (2013)

106. S. Marx, M.V. Jose, J.D. Andersen, A.J. Russell, Electrospun gold nanofiber electrodes for biosensors. Biosens. Bioelectron. **26**, 2981–2986 (2011)

107. V. Vyskočil, M. Blašková, A. Hájková, E. Horáková, Z. Krejčová, K. Stávková, J. Wang, Electrochemical DNA biosensors – useful diagnostic tools for the detection of damage to DNA caused by organic xenobiotics (A review). Sens. Electroanal. **7**, 141–162 (2012)
108. A.D. Ellington, J.W. Szostak, In vitro selection of RNA molecules that bind specific ligands. Nature **346**(6287), 818–822 (1990)
109. L. Gold, N. Janjic, T. Jarvis, D. Schneider, J.J. Walker, SK. Wilcox, D. Zichi, Aptamers and the RNA world, past and present, Cold Spring Harb. Perspect. Biol. **4**, a003582, 1–9 (2012)
110. C. Tuerk, L. Gold, Systematic evolution of ligands by exponential enrichment: RNA ligands to bacteriophage T4 DNA polymerase. Science **249**, 505–510 (1990)
111. G. Liu, X. Mao, J.A. Phillips, H. Xu, W. Tan, L. Zeng, Aptamer-nanoparticle strip biosensor for sensitive detection of cancer cells. Anal. Chem. **81**(24), 10013–10018 (2009)
112. J.J. Li, X. Fang, W. Tan, Molecular aptamer beacons for real-time protein recognition. Biochem. Biophys. Res. Commun. **292**, 31–40 (2002)
113. D.S. Wilson, J.W. Szostak, In vitro selection of functional nucleic acids. Annu. Rev. Biochem. **68**, 611–647 (1999)
114. Y. Wang, J. Killian, K. Hamasaki, R.R. Rando, RNA molecules that specifically and stoichiometrically bind aminoglycoside antibiotics with high affinities. Biochemistry **35**(38), 12338–12346 (1996)
115. D.W. Drolet, L. Moon-McDermott, T.S. Romig, An enzyme-linked oligonucleotide assay. Nat. Biotechnol. **14**, 1021–1025 (1996)
116. M. Michaud, E. Jourdan, A. Villet, A. Ravel, C. Grosset, E. Peyrin, A DNA aptamer as a new target-specific chiral selector for HPLC. J. Am. Chem. Soc. **125**(28), 8672–8679 (2003)
117. T.R. Cech, A.J. Zaug, P.J. Grabowski, In vitro splicing of the ribosomal RNA precursor of Tetrahymena: involvement of a guanosine nucleotide in the excision of the intervening sequence. Cell **27**, 487–496 (1981) (a); C. Guerrier-Takada, K. Gardiner, T. Marsh, N. Pace, S. Altman, The RNA moiety of ribonuclease P is the catalytic subunit of the enzyme. Cell **35**, 849–857 (1983) (b)
118. W.G. Scott, Ribozymes. Curr. Opin. Struc. Biol. **17**(3), 280–286 (2007)
119. D.M.J. Lilley, The origins of RNA catalysis in ribozymes. Trends Biochem. Sci. **28**(9), 495–501 (2003)
120. D.M.J. Lilley, Structure, folding and mechanisms of ribozymes. Curr. Opin. Struc. Biol. **15**(3), 313–323 (2005)
121. L. Liu, J.W. Cottrell, L.G. Scott, M.J. Fedor, Direct measurement of the ionization state of an essential guanine in the hairpin ribozyme. Nat. Chem. Biol. **5**, 351–357 (2009)
122. R.R. Breaker, DNA enzymes. Nat. Biotechnol. **15**, 427–431 (1997)
123. Y. Li, R.R. Breaker, Deoxyribozymes: new players in the ancient game of biocatalysis. Curr. Opin. Struc. Biol. **9**(3), 315–323 (1999)
124. D. Sen, C.R. Geyer, DNA enzymes. Curr. Opin. Struct. Biol. **2**(6), 680–687 (1998)
125. G.M. Emilsson, R.R. Breaker, Deoxyribozymes: new activities and new applications. Cell. Mol. Life Sci. **59**(4), 596–607 (2002)
126. J. Liu, Z. Cao, Y. Lu, Functional nucleic acid sensors. Chem. Rev. **109**(5), 1948–1998 (2009)
127. I. Palchetti, M. Mascini, Nucleic acid biosensors for environmental pollution monitoring. Analyst **133**(7), 846–854 (2008)
128. A. Sett, S. Das, U. Bora, Functional nucleic-acid-based sensors for environmental monitoring. Appl. Biochem. Biotechnol. **174**(3), 1073–1091 (2014)
129. L. Shen, Z. Chen, Y. Li, S. He, S. Xie, X. Xu, Z. Liang, X. Meng, Q. Li, Z. Zhu, M. Li, X.C. Le, Y. Shao, Electrochemical DNAzyme sensor for lead based on amplification of DNA-Au bio-bar codes. Anal. Chem. **80**(16), 6323–6328 (2008)
130. Y. Lu, J. Liu, J. Li, P.J. Bruesehoff, C.M.-B. Pavot, A.K. Brown, New highly sensitive and selective catalytic DNA biosensors for metal ions. Biosens. Bioelectron. **18**(5–6), 529–540 (2003)
131. M.P. Robertson, A.D. Ellington, In vitro selection of nucleoprotein enzymes. Nat. Biotechnol. **19**, 650–655 (2001)

132. M.P. Robertson, A.D. Ellington, In vitro selection of an allosteric ribozyme that transduces analytes to amplicons. Nat. Biotechnol. **17**, 62–66 (1999)
133. P.E. Nielsen, M. Egholm, R.H. Berg, O. Buchardt, Sequence-selective recognition of DNA by strand displacement with a thymine-substituted polyamide. Science **254**(5037), 1497–1500 (1991)
134. P.E. Nielsen, Peptide nucleic acid: a molecule with two identities. Acc. Chem. Res. **32**(7), 624–630 (1999)
135. B. Hyrup, P.E. Nielsen, Peptide nucleic acids (PNA): synthesis, properties and potential applications. Bioorg. Med. Chem. **4**, 5–23 (1996)
136. P.E. Nielsen, M. Egholm, *Peptide Nucleic Acids: Protocols and Applications* (Horizon Scientific Press, Norfolk, 1999). ISBN 978-1-898486-16-6
137. P.E. Nielsen, Peptide nucleic acid: a versatile tool in genetic diagnostics and molecular biology. Curr. Opin. Biotechnol. **12**, 16–20 (2001)
138. D.A. Dean, Peptide nucleic acids: versatile tools for gene therapy strategies. Adv. Drug Deliver. Rev. **44**, 81–95 (2000)
139. D.R. Corey, Peptide nucleic acids: expanding the scope of nucleic acid recognition. Trends Biotechnol. **15**, 224–229 (1997)
140. A.K.H. Cheng, D. Sen, H.-Z. Yu, Design and testing of aptamer-based electrochemical biosensors for proteins and small molecules. Bioelectrochemistry **77**(1), 1–12 (2009)
141. R.-Z. Hao, H.-B. Song, G.-M. Zuo, R.-F. Yang, H.-P. Wei, D.-B. Wang, Z.-Q. Cui, Z.-P. Zhang, Z.-X. Cheng, X.-E. Zhang, DNA probe functionalized QCM biosensor based on gold nanoparticle amplification for *Bacillus anthracis* detection. Biosens. Bioelectron. **26**(8), 3398–3404 (2011)
142. J.A. Hansen, J. Wang, A.-N. Kawde, Y. Xiang, K.V. Gothelf, G. Collins, Quantum-dot/aptamer-based ultrasensitive multi-analyte electrochemical biosensor. J. Am. Chem. Soc. **128**(7), 2228–2229 (2006)
143. H. Huang, J.-J. Zhu, Biosens. DNA aptamer-based QDs electrochemiluminescence biosensor for the detection of thrombin. Bioelectron. **25**(4), 927–930 (2009)
144. C. Yao, T. Zhu, Y. Qi, Y. Zhao, H. Xia, W. Fu, Development of a quartz crystal microbalance biosensor with aptamers as bio-recognition element. Sensors **10**(6), 5859–5871 (2010)
145. T. Liu, J. Tang, M. Han, L. Jiang, A novel microgravimetric DNA sensor with high sensitivity. Biochem. Bioph. Res. Co. **304**(1), 98–100 (2003)
146. E. Luzi, M. Minunni, S. Tombelli, M. Mascini, New trends in affinity sensing: aptamers for ligand binding. TRAC-Trend Anal. Chem. **22**(11), 810–818 (2003)
147. C.-W. Liu, C.-C. Huang, H.-T. Chang, Highly selective DNA-based sensor for lead(II) and mercury(II) ions. Anal. Chem. **81**(6), 2383–2387 (2009)
148. F. Wei, P.B. Lillehoj, C.-M. Ho, DNA diagnostics: nanotechnology-enhanced electrochemical detection of nucleic acids. Pediatr. Res. **67**(5), 458–468 (2010)
149. J. Wang, From DNA biosensors to gene chips. Nucleic Acids Res. **28**(16), 3011–3016 (2000)
150. L. Authier, C. Grossiord, P. Brossier, Gold nanoparticle-based quantitative electrochemical detection of amplified human cytomegalovirus DNA using disposable microband electrodes. Anal. Chem. **73**(18), 4450–4456 (2001)
151. A. Bonanni, M.I. Pividori, M. del Valle, Impedimetric detection of influenza A (H1N1) DNA sequence using carbon nanotubes platform and gold nanoparticles amplification. Analyst **135**, 1765–1772 (2010)
152. C. Yao, T. Zhu, J. Tang, R. Wu, Q. Chen, M. Chen, B. Zhang, J. Huang, W. Fu, Hybridization assay of hepatitis B virus by QCM peptide nucleic acid biosensor. Biosens. Bioelectron. **23**(6), 879–885 (2008)
153. J.B. Raoof, R. Ojani, S.M. Golabi, E. Hamidi-Asla, M.S. Hejazic, Preparation of an electrochemical PNA biosensor for detection of target DNA sequence and single nucleotide mutation on p53 tumor suppressor gene corresponding oligonucleotide. Sensor Actuat. B-Chem. **157**(1), 195–201 (2011)
154. X. Liu, R. Zhang, X. Yuan, L. Liu, Y. Zhou, Q. Gao, Highly sensitive voltammetric detection of DNA hybridization in sandwich format using thionine-capped gold nanoparticle/reporter DNA conjugates as signal tags. Gold Bull. **47**(1–2), 119–125 (2014)

155. A.M. Mohammed, R.A. Rahim, I.J. Ibraheem, F.K. Loong, H. Hisham, U. Hashim, Y. Al-Douri, Application of gold nanoparticles for electrochemical DNA biosensor. J. Nanomater, Article ID 683460, 7 (2014) doi:10.1155/2014/683460

156. S. Yang, Y. Liu, H. Tan, C. Wu, Z. Wu, G. Shena, R. Yu, Gold nanoparticle based signal enhancement liquid crystal biosensors for DNA hybridization assays. Chem. Commun. **48**, 2861–2863 (2012)

157. R. Bashir, DNA nanobiostructures. Mater. Today **4**(6), 30–39 (2001)

158. J. Wang, Nanoparticle-based electrochemical DNA detection. Anal. Chim. Acta **500**(1–2), 247–257 (2003)

159. J. Wang, Nanomaterial-based amplified transduction of biomolecular interactions. Small **1** (11), 1036–1043 (2005)

160. A. Erdem, Nanomaterial-based electrochemical DNA sensing strategies. Talanta **74**(3), 318–325 (2007)

161. Z. Chang, H. Fan, K. Zhao, M. Chen, P. He, Y. Fang, Electrochemical DNA biosensors based on Palladium nanoparticles combined with carbon nanotubes. Electroanalysis **20**(2), 131–136 (2008)

162. N.L. Rosi, C.A. Mirkin, Nanostructures in biodiagnostics. Chem. Rev. **105**(4), 1547–1562 (2005)

163. Y. Feng, T. Yang, W. Zhang, C. Jiang, K. Jiao, Enhanced sensitivity for deoxyribonucleic acid electrochemical impedance sensor: gold nanoparticle/polyaniline nanotube membranes. Anal. Chim. Acta **616**(2), 144–151 (2008)

164. W.M. Hassen, C. Chaix, A. Abdelghani, F. Bessueille, D. Leonard, N. Jaffrezic-Renault, An impedimetric DNA sensor based on functionalized magnetic nanoparticles for HIV and HBV detection. Sensor Actuat. B-Chem. **134**(2), 755–760 (2008)

165. K. Xu, J. Huang, Z. Ye, Y. Ying, Y. Li, Recent development of nano-materials used in DNA biosensors. Sensors **9**(7), 5534–5557 (2009)

166. A. Merkoci, M. Aldavert, G. Tarrason, R. Eritja, S. Alegret, Recent development of nano-materials used in DNA biosensors. Anal. Chem. **77**, 6500–6503 (2005)

167. Y. Liu, J. Chen, T. Nguyen, C.O. Too, V. Misoska, G.G. Wallace, Nanofiber mats from DNA, SWNTs, and poly(ethylene oxide) and their application in glucose biosensors. J. Electrochem. Soc. **155**(5), K100–K103 (2008)

168. Y. Ner, J.G. Grote, J.A. Stuart, G.A. Sotzing, Enhanced fluorescence in electrospun dye-doped DNA nanofibers. Soft Matter **4**, 1448–1453 (2008)

169. D. Li, M.W. Freya, A.J. Baeumner, Electrospun polylactic acid nanofiber membranes as substrates for biosensor assemblies. J. Membr. Sci. **279**(1–2), 354–363 (2006)

170. X. Wang, X. Wang, X. Wang, F. Chen, K. Zhu, Q. Xu, M. Tang, Novel electrochemical biosensor based on functional composite nanofibers for sensitive detection of p53 tumor suppressor gene. Anal. Chim. Acta **765**, 63–69 (2013)

171. K. Ramanathan, M.A. Bangar, M. Yun, W. Chen, N.V. Myung, A. Mulchandani, Bioaffinity sensing using biologically functionalized conducting-polymer nanowire. J. Am. Chem. Soc. **127**(2), 496–497 (2005)

172. S. Cosnier, P. Mailley, Recent advances in DNA sensors. Analyst **133**, 984–991 (2008)

173. H.-A. Ho, M. Leclerc, Biosensors based on conjugated polymers, in *Semiconducting Polymers: Chemistry, Physics and Engineering*, ed. by G. Hadziioannou, G.G. Malliaras, 2nd edn. (Wiley-VCH, Weinheim, 2007), pp. 643–665. ISBN 978-3-527-31271-9

174. N. Prabhakar, K. Arora, H. Singh, B.D. Malhora, Polyaniline based nucleic acid sensor. J. Phys. Chem. B **112**, 4808–4816 (2008)

175. N. Prabhakar, G. Sumana, K. Arora, H. Singh, B.D. Malhora, Improved electrochemical nucleic acid biosensor based on polyaniline-polyvinyl sulphonate. Electrochim. Acta **53**, 4344–4350 (2008)

176. X. Sun, P. He, S. Liu, J. Ye, Y. Fang, Immobilization of single-stranded deoxyribonucleic acid on gold electrode with self-assembled aminoethanethiol monolayer for DNA electrochemical sensor applications. Talanta **47**, 487–495 (1998)

177. F. Fixe, M. Dufva, P. Telleman, C.B.V. Christensen, Functionalization of poly(methyl methacrylate) (PMMA) as a substrate for DNA microarrays. Nucleic Acids Res. **32**(1), e9 (2004)

178. S.C. Vasudev, T. Chandy, Effects of double cross-linking technique on the enzymatic degradation and calcification of bovine pericardia. J. Biomater. Appl. **14**(3), 273–295 (2000)

179. S.J. Kwoun, R.M. Lec, B. Han, F.K. Ko, A novel polymer nanofiber interface for chemical sensor applications, in *Proceedings of the 2000 IEEE/EIA International Frequency Control Symposium and Exhibition* (IEEE, Piscataway, 2000), pp. 52–57

180. G. Sauerbrey, Verwendung von Schwingquarzen zur Wägung dünner Schichten und zur Mikrowägung. Z. Phys. **155**(2), 206–222 (1959)

181. S. Wei, J. Sampathi, A. Kucknoor, L. James, Z. Guo, N. Anumandla, D. Rutman, A. Kucknoor, L. James, A. Wang, Nanoporous poly(methyl methacrylate)-quantum dots nanocomposite fibers toward biomedical applications. Polymer **52**, 5817–5829 (2011)

182. Y.-F. Qian, Y. Su, X.-Q. Li, H.-S. Wang, C.-L. He, Electrospinning of polymethyl methacrylate nanofibres in different solvents. Iran. Polym. J. **19**(2), 123–129 (2010)

183. H.-S. Bae, A. Haider, K.M.K. Selim, D.-Y. Kang, E.-J. Kim, I.-K. Kang, Fabrication of highly porous PMMA electrospun fibers and their application in the removal of phenol and iodine. J. Polym. Res. **20**, Article 158, 7 (2013)

184. A. Greiner, J.H. Wendorff, Electrospinning: a fascinating method for the preparation of ultrathin fibers. Angew. Chem. Int. Ed. **46**, 5670–5703 (2007)

185. C.L. Casper, J.S. Stephens, N.G. Tassi, D.B. Chase, J.F. Rabolt, Controlling surface morphology of electrospun polystyrene fibers: effect of humidity and molecular weight in the electrospinning process. Macromolecules **37**, 573–578 (2004)

186. J. Huang, T. You, Electrospun nanofibers: from rational design, fabrication to electrochemical sensing applications, in *Advances in Nanofibres*, ed. by R. Maguire, (InTech, 2013), pp. 35–83. doi:10.5772/57099. ISBN: 978-953-51-1209-9

187. S. Megelski, J.S. Stephens, D.B. Chase, J.F. Rabolt, Micro- and nanostructured surface morphology on electrospun polymer fibers. Macromolecules **35**, 8456–8466 (2002)

188. J. Liu, Y. Lu, Colorimetric biosensors based on DNAzyme-assembled gold nanoparticles. J. Fluoresc. **14**(4), 343–354 (2004)

189. S. Song, L. Wang, J. Li, J. Zhao, C. Fan, Aptamer-based biosensors. TRAC-Trend Anal. Chem. **27**(2), 108–117 (2008)

190. T.-C. Chiu, C.-C. Huang, Aptamer-functionalized nano-biosensors. Sensors **9**, 10356–10388 (2009)

191. Y. Xiao, B.D. Piorek, K.W. Plaxco, A.J. Heeger, A reagentless signal-on architecture for electronic, aptamer-based sensors via target-induced strand displacement. J. Am. Chem. Soc. Commun. **127**, 17990–17991 (2005). doi:10.1021/ja056555h

192. Y. Xiao, A.A. Lubin, A.J. Heeger, K.W. Plaxco, Label-free electronic detection on thrombin in blood serum by using an aptamer-based sensor. Angew. Chem. **44**, 5456 (2005)

193. B.R. Baker, R.Y. Lai, M.C.S. Wood, E.H. Doctor, A.J. Heeger, K.W. Plaxco, An electronic, aptamer-based small molecule sensor for the rapid, label-free detection of cocaine in adulterated samples and biological fluids. J. Am. Chem. Soc. **128**(10), 3138–3139 (2006)

194. V. Pavlov, B. Shlyahovsky, I. Willner, Fluorescence detection of DNA by the catalytic activation of an aptamer/thrombin complex. J. Am. Chem. Soc. **127**(18), 6522–6523 (2005)

195. Q. Chen, W. Tang, D. Wang, X. Wu, N. Li, F. Liu, Amplified QCM-D biosensor for protein based on aptamer-functionalized gold nanoparticles. Biosens. Bioelectron. **26**, 575–579 (2010)

196. G.S. Bang, S. Cho, B.-G. Kim, A novel electrochemical detection method for aptamer biosensors. Biosens. Bioelectron. **21**, 863–870 (2005)

197. H. Pei, J. Li, M. Lv, J. Wang, J. Gao, J. Lu, Y. Li, Q. Huang, J. Hu, C. Fan, A graphene-based sensor array for high-precision and adaptive target identification with ensemble aptamers. J. Am. Chem. Soc. **134**, 13843–13849 (2012)

198. H. Huang, G. Jie, R. Cui, J.-J. Zhu, DNA aptamer-based detection of lysozyme by an electrochemiluminescence assay coupled to quantum dots. Electrochem. Commun. **11**, 816–818 (2009)

199. W. Zhao, W. Chiuman, J.C.F. Lam, S.A. McManus, W. Chen, Y. Cui, R. Pelton, M.A. Brook, Y. Li, DNA aptamer folding on gold nanoparticles: from colloid chemistry to biosensors. J. Am. Chem. Soc. **130**, 3610–3618 (2008)

200. W. Wang, C. Chen, M. Qian, X. Sheng Zhao, Aptamer biosensor for protein detection using gold nanoparticles. Anal. Biochem. **373**, 213–219 (2008)

201. K. Maehashi, K. Matsumoto, Y. Takamura, E. Tamiya, Aptamer-based label-free immunosensors. Using carbon nanotube field- effect transistors. Electroanalysis **21**(11), 1285–1290 (2009)

202. W. Wang, C. Chen, M.X. Qian, X.S. Zhao, Aptamer biosensor for protein detection based on guanine-quenching. Sensor Actuat. B-Chem. **129**, 211–217 (2008)

203. M.C. Rodríguez, G.A. Rivas, Label-free electrochemical aptasensor for the detection of lysozyme. Talanta **78**, 212–216 (2009)

204. S.J. Lee, R. Tatavarty, M.B. Gu, Electrospun polystyrene–poly(styrene-co-maleic anhydride) nanofiber as a new aptasensor platform. Biosens. Bioelectron. **38**, 302–307 (2012)

205. S.M. Knudsen, A.D. Ellington, Aptazymes: allosteric ribozymes and deoxyribozymes as biosensors, in *The Aptamer Handbook: Functional Oligonucleotides and Their Applications*, ed. by S. Klussmann (Wiley-VCH, Weinheim, 2006), pp. 290–310. doi:10.1002/3527608192.ch13. ISBN 978-3-527-31059-3

206. N. Lu, C. Shao, Z. Deng, Rational design of an optical adenosine sensor by conjugating a DNA aptamer with split DNAzyme halves. Chem. Commun. **46**, 6161–6163 (2008)

207. D. Li, B. Shlyahovsky, J. Elbaz, I. Willner, Amplified analysis of low-molecular-weight substrates or proteins by the self-assembly of DNAzyme-aptamer conjugates. J. Am. Chem. Soc. **129**, 5804–5805 (2007)

208. J. Liu, Y. Lu, Adenosine-dependent assembly of aptazyme-functionalized gold nanoparticles and its application as a colorimetric biosensor. Anal. Chem. **76**, 1627–1632 (2004)

209. E.J. Cho, J.-W. Lee, A.D. Ellington, Applications of aptamers as sensors. Annu. Rev. Anal. Chem. **2**, 241–264 (2009)

210. G. Wang, Y. Wang, L. Chena, J. Choo, Nanomaterial-assisted aptamers for optical sensing. Biosens. Bioelectron. **25**(8), 1859–1868 (2010)

211. O. Brandt, J.D. Hoheisel, Peptide nucleic acids on microarrays and other biosensors. Trends Biotechnol. **22**(12), 617–622 (2004)

212. R.P. Singh, B.-K. Oh, J.-W. Choi, Application of peptide nucleic acid towards development of nanobiosensor arrays. Bioelectrochemistry **79**(2), 153–161 (2010)

213. J. Wang, E. Palecek, P.E. Nielsen, G. Rivas, X. Cai, H. Shiraishi, N. Dontha, D. Luo, P.A.M. Farias, Peptide nucleic acid probes for sequence-specific DNA biosensors. J. Am. Chem. Soc. **118**(33), 7667–7670 (1996)

214. E. Mateo-Martì, C. Briones, C.M. Pradier, J.A. Martìn-Gago, A DNA biosensor based on peptide nucleic acids on gold surfaces. Biosens. Bioelectron. **22**, 1926–1932 (2007)

215. T. Endo, K. Kerman, N. Nagatani, Y. Takamura, E. Tamiya, Label-free detection of peptide nucleic acid-DNA hybridization using localized surface plasmon resonance based optical biosensor. Anal. Chem. **77**(21), 6976–6984 (2005)

216. M.S. Hejazi, M.H. Pournaghi-Azar, F. Ahour, Electrochemical detection of short sequences of hepatitis C 3a virus using a peptide nucleic acid-assembled gold electrode. Anal. Biochem. **399**, 118–124 (2010)

217. D. Ozkan, A. Erdem, P. Kara, P.E. Nielsen, K. Kerman, M. Ozsoz, Electrochemical detection of hybridization using peptide nucleic acids and methylene blue on self-assembled alkanethiol monolayer modified gold electrodes. Electrochem. Commun. **4**, 796–802 (2002)

218. D. Ozkan, A. Erdem, P. Kara, P.E. Nielsen, K. Kerman, M. Ozsoz, DNA and PNA sensing on mercury and carbon electrodes by using methylene blue as an electrochemical label. Bioelectrochemistry **58**, 119–126 (2002)

219. J. Wang, DNA biosensors based on peptide nucleic acid (PNA) recognition layers. A review. Biosens. Bioelectron. **13**, 757–762 (1998)

220. J. Zhang, S. Song, L. Zhang, L. Wang, H. Wu, D. Pan, C. Fan, Sequence-specific detection of femtomolar DNA via a chronocoulometric DNA sensor (CDS): effects of nanoparticle-mediated amplification and nanoscale control of DNA assembly at electrodes. J. Am. Chem. Soc. **128**(26), 8575–8580 (2006)

221. M. Pita, J.M. Abad, J.A. Martín-Gago, C. Vaz-Dominguez, M. del Puerto Morales, C. Briones, V.M. Fernández, E. Mateo-Martí, Synthesis of cobalt ferrite core/metallic shell nanoparticles for the development of a specific PNA/DNA biosensor. J. Colloid Interface Sci. **321**, 484–492 (2008)

222. M. Frey, A. Baeumner, D. Li, *Electrospun nanofibre-based biosensor assemblies*. Patent N. US20060260707 A1, 2006

223. C. Moina, G. Ybarra, Fundamentals and applications of immunosensors, in *Advances in Immunoassay Technology*, ed. by N.H.L. Chiu, Th.K. Christopoulos, (InTech, 2012). doi:10.5772/36947. ISBN: 978-953-51-0440-7

224. E.S. Bromage, G.G. Vadas, E. Harvey, M.A. Unger, S.L. Kaattari, Validation of an antibody-based biosensor for the rapid quantification of 2,4,6-trinitrotoluene (TNT) contamination in ground water and river water. Environ. Sci. Technol. **41**, 7067–7072 (2007)

225. S.M. Borisov, O.S. Wolfbeis, Optical biosensors. Chem. Rev. **108**, 423–461 (2008)

226. S. Kurosawa, J.W. Park, H. Aizawa, S. Wakida, H. Tao, K. Ishihara, Quartz crystal micro-balance immunosensors for environmental monitoring. Biosens. Bioelectron. **22**(4), 473–481 (2006)

227. Y. Montagut, J.V. García, Y. Jiménez, C. March, A. Montoya, A. Arnau, *QCM Technology in Biosensors in Biosensors- Emerging Materials and Applications*, ed. by A. Serra (InTech, 2011), pp. 153–173. doi:10.5772/17991. ISBN: 978-953-307-328-6

228. Y. Luo, S. Nartker, H. Miller, D. Hochhalter, M. Wiederoder, S. Wiederoder, E. Setteringtona, L.T. Drzal, E.C. Alocilj, Surface functionalization of electrospun nanofibers for detecting *E. coli* O157: H7 and BVDV cells in a direct-charge transfer biosensor. Biosens. Bioelectron. **26**, 1612–1617 (2010)

229. Y. Luo, S. Nartker, M. Wiederoder, H. Miller, D. Hochhalter, L.T. Drzal, E.C. Alocilj, Novel biosensor based on electrospun nanofiber and magnetic nanoparticles for the detection of *E. coli* O157:H7. IEEE Trans. Nanotechnol. **11**(4), 676–681 (2012)

230. S.J. Reinholt, A. Sonnenfeldt, A. Naik, M.W. Frey, A.J. Baeumner, Developing new materials for paper-based diagnostics using electrospun nanofibers. Anal. Bioanal. Chem. **406**, 3297–3304 (2014)

231. H. Dai, G. Xu, S. Zhang, L. Gong, X. Li, C. Yang, Y. Lin, J. Chen, G. Chen, Carbon nanotubes functionalized electrospun nanofibers formed 3D electrode enables highly strong ECL of peroxydisulfate and its application in immunoassay. Biosens. Bioelectron. **61**, 575–578 (2014)

232. M. Sun, B. Ding, J. Lin, J. Yu, G. Sun, Three-dimensional sensing membrane functionalized quartz crystal microbalance biosensor for chloramphenicol detection in real time. Sensor Actuat. B-Chem. **160**(1), 428–434 (2011)

233. Y. Lee, H.J. Lee, K.J. Son, W.-G. Koh, Fabrication of hydrogel-micropatterned nanofibers for highly sensitive microarray-based immunosensors having additional enzyme-based sensing capability. J. Mater. Chem. **21**, 4476–4483 (2011). doi:10.1039/C0JM03881D

234. A. Senecal, J. Magnone, P. Marek, K. Senecal, Development of functional nanofibrous membrane assemblies towards biological sensing. React. Funct. Polym. **68**, 1429–1434 (2008)

235. P. Netsuwan, H. Mimiya, A. Baba, S. Sriwichai, K. Shinbo, K. Kato, F. Kaneko, S. Phanichphant, Long-range surface plasmon resonance immunosensor based on water-stable electrospun poly(acrylic acid) fibers. Sensor Actuat. B-Chem. **204**, 770–776 (2014)

236. E. Zampetti, S. Pantalei, A. Muzyczuc, A. Bearzotti, F. De Cesare, C. Spinella, A. Macagnano, A high sensitive NO$_2$ gas sensor based on PEDOT–PSS/TiO2 nanofibres. Sensor Actuat. B-Chem. **176**, 390–398 (2013)

Chapter 11
Development by Electrohydrodynamic Processing of Heat Storage Materials for Multisectorial Applications

R. Pérez-Masiá, M.J. Fabra, W. Chalco-Sandoval, A. López-Rubio, and J.M. Lagaron

Abstract Phase change materials (PCM's) are substances that undergo a phase transition at a specific temperature and, as a result, they are able to absorb and release the latent heat when isothermal conditions are altered. PCM's could be used during transport or storage, for the protection of solid foods, beverages, pharmaceutical products, textile industry, blood derivatives, electronic circuits, cooked food, biomedical products and many others.

Direct application of PCM's is difficult since they have weak thermal stability, low thermal conductivity and some of them are liquid at ambient temperature and, thus, are not easy to handle or to be directly incorporated into packaging structures and refrigeration equipments. Therefore, the encapsulation of the PCM in a shell material is a plausible solution to avoid all these problems. The capsules protect the PCM against the influences of the outside environment, increasing the heat-transfer area, and permitting the core material to withstand changes in volume of the PCM, as the phase change occurs allowing small and portable thermal energy storage systems.

One proprietary methodology used for the encapsulation of PCM materials is electrohydrodynamic processing. This processing technique has proven to be a suitable method for encapsulation of several components, including biomedical substances, functional food ingredients, PCM's and others substances within polymer matrices. The electrohydrodynamic processing including electrospinning and electrospraying processes, is a technology whereby ultrafine structures, typically with diameters of several tens to several hundreds of nanometers, may be formed by applying a high-voltage electric field to a solution of polymers.

R. Pérez-Masiá • M.J. Fabra • W. Chalco-Sandoval • A. López-Rubio • J.M. Lagaron (✉)
Novel Materials and Nanotechnology Group, IATA-CSIC, Av.
Agusting Escardino 7, Paterna, Valencia 46980, Spain
e-mail: lagaron@iata.csic.es

11.1 Introduction

11.1.1 *Electrospinning for Energy Applications*

Electrospinning is a versatile process that is used to create long-length-scale fibers with micro- and nanoscale diameters from a wide range of polymer materials. These fibers present very high surface to volume ratios, which make them very attractive in a wide range of energy applications, such as solar cells, batteries, capacitors, fuel cells, hydrogen storage or thermal energy storage technologies. Normally, these systems use electrospun fibers to obtain high specific surfaces which generally improve the conversion energy efficiency and the conductivity of these materials [9]. Nevertheless, electrospun fibers can also be used to encapsulate and store energy sources, such as phase change materials (PCMs). PCMs are substances which can absorb and release a large amount of latent heat during their phase transition process over a narrow temperature range, and thus, they can be used to enhance the energy storage capability of different materials. Thus, they have been applied in multiple areas, such as building materials, packaging of temperature-sensitive products, air conditioning, greenhouses, temperature regulating textiles, electronics devices and biomedical systems [13]. PCMs are generally classified into two categories: inorganic materials, such as salt hydrates, and organic materials, such as paraffins or fatty acids. A large number of compounds can be identified as PCMs from their melting temperature; however, they should also present suitable physical, chemical and kinetic properties in order to be used in energy storage systems [6].

11.1.2 *Use of Electrospinning for PCM'S Encapsulation*

As it was commented before, PCMs can be used to enhance the energy storage capability of different materials. However, the use of these materials in thermal energy storage applications presents some drawbacks, such as weak thermal stability, low thermal conductivity and the fact that some of them are liquid at ambient temperature, and thus, they are not easy to handle [6]. The encapsulation of the PCM is a plausible solution to avoid these problems. Some of the advantages of introducing these materials inside a shell material are: (i) the PCM is protected against the influences of the outside environment; (ii) the heat transfer area is increased; (iii) the changes in volume of the PCM, as the phase transition occurs, are withstood; (iv) a solid matrix which allows an easier handling of the materials is provided, and; (v) small and portable energy storage systems can be designed. Among all the technologies available for the PCMs' encapsulation, electrospinning is one of the most interesting techniques. This technology provides proper encapsulation efficiency and also produces micro/nanocapsules which could increase the efficiency of the heat transfer, due to their high specific surface. Moreover,

electrospinning can encapsulate materials from the melt as well as from polymer solutions, enhancing even further the number of encapsulation matrices that can be used. Another significant advantage of the technique is the suitable use of biomass-derived materials and of biodegradable polymers as encapsulating elements, with the corresponding environmental benefits associated with their use. Biomass-derived materials not only present encapsulation flexibility and efficiency but can also help reduce the environmentally meaningful parameter, the so-called carbon footprint.

11.1.2.1 PCMs for the Protection of Thermo-sensitive Products

One of the potential applications of the micro/nanoencapsulated PCMs is the protection of thermo-sensitive products. In this field, heat management materials can be developed through the incorporation of encapsulated PCMs into the packaging structures, into refrigeration equipment, smart labels, sensors, etc. These structures could buffer thermal variations along the cold chain and improve and preserve the quality of products. Recently, heat management materials with potential applications in this area have been developed by means of electrospinning. Specifically, different PCMs with phase transitions at refrigeration temperatures were microencapsulated into various polymer matrices through electrospinning.

Regarding the matrices for encapsulation, different polymers and biopolymers are currently being tested. Initially, zein, the major storage protein of corn, was researched in our group as a shell material, since it is readily soluble, renewable and biodegradable and this protein has the ability to form fibers using electrospinning, and it has good thermal and stability properties. Biopolyesters such as polycaprolactone (PCL) or polylactic acid (PLA) have lately attracted great industrial interest because their characteristics. They present good physical properties (when compared to other biodegradable and renewable polymers), processability, water resistance, excellent biocompatibility and commercial availability. Futhermore, the encapsulation systems based on these biodegradable materials were compared with others obtained with polystyrene (PS), since this petro-based polymers is currently used in refrigerating equipments and food packaging.

Figure 11.1 shows some selected SEM images of the PCM microcapsules obtained from zein/PCM (Fig. 11.1a), PCL/PCM (Fig. 11.1b), PS/PCM (Fig. 11.1c) and PLA/PCM (Fig. 11.1d). The thermal characteristics and encapsulation efficiency of these capsules varied with the matrix material and the morphology of the encapsulation structures. Generally it was seen that fiber capsules were able to encapsulate greater amount of PCM than spherical capsules (beads) [11, 12]. Furthermore, among all the polymers tested, PCL was the most efficient matrix, probably because this polymer produced thicker structures than other matrices. It was observed that PCL/PCM fibers showed the ability of temperature buffering at the phase transition temperature of the PCM for some time [12].
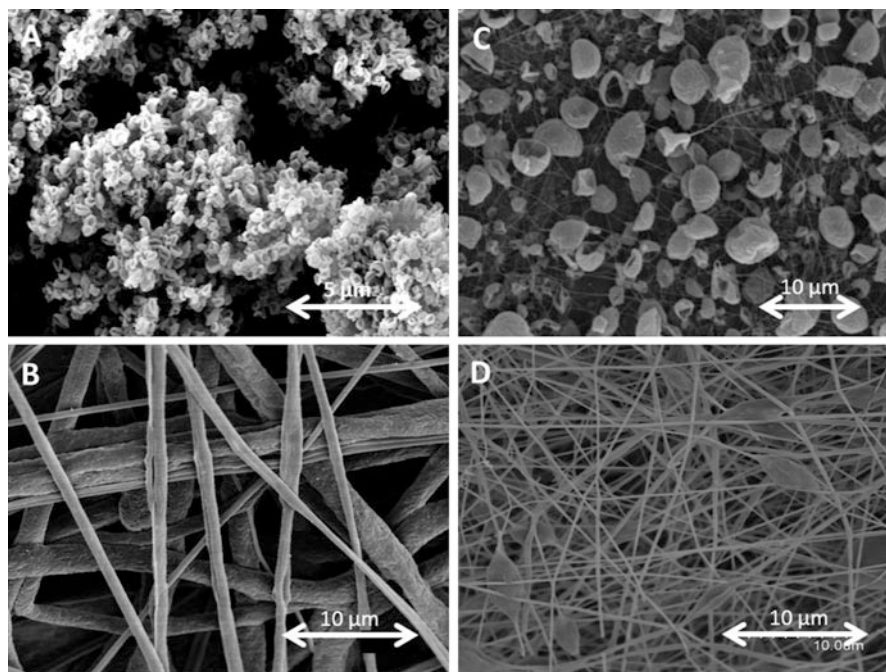
Fig. 11.1 Selected SEM images of different polymers/PCM capsules: (**a**) Zein/PCM; (**b**) PCL/PCM; (**c**) PS/PCM; (**d**) PLA/PCM (scale marker correspond to 10 μm)

As it was commented above, PCMs can be also applied in refrigeration equipment. The micro/nanoencapsulation of PCMs within a shell material through the electrospinning technology is a plausible strategy to introduce the PCM into the equipments. Specifically, encapsulated PCMs have been recently used to achieve thick slabs with a phase transition of ~5 °C, which is the most common temperature found in household refrigerators or in retail and display cabinets at supermarkets [2]. Figure 11.2 shows the morphology of the electrospun slabs obtained from PCL/PCM and PS/PCM. It is observed that PCL/PCM fibers were thicker than PS/PCM fibers, which explained the greater encapsulation efficiency of these structures.

The thermal behavior of these slabs along time was also studied and it was seen that no significant changes occurred during aging when they were stored at refrigerating temperatures, i.e. 4 °C. Additionally, the energy storage ability has been also evaluated and it was seen that slabs were able to slow down the rate of temperature rise locally (cf. Fig. 11.3).

Thus, the incorporation of these hybrid fibers or slabs within the packaging or in the walls of refrigeration equipment can be a suitable strategy to buffer the thermal fluctuations with the aim of improving the quality and safety of thermo-sensitive products. Moreover, these materials could also reduce the energy consumption of
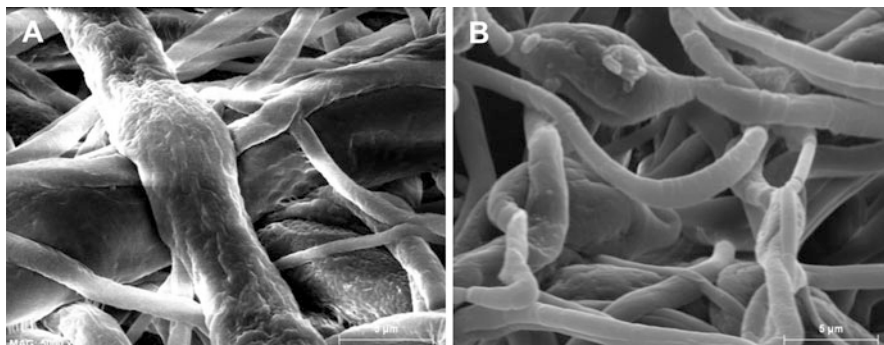
Fig. 11.2 SEM images of electrospun polymers/PCM: (**a**) PCL/PCM; (**b**) PS/PCM
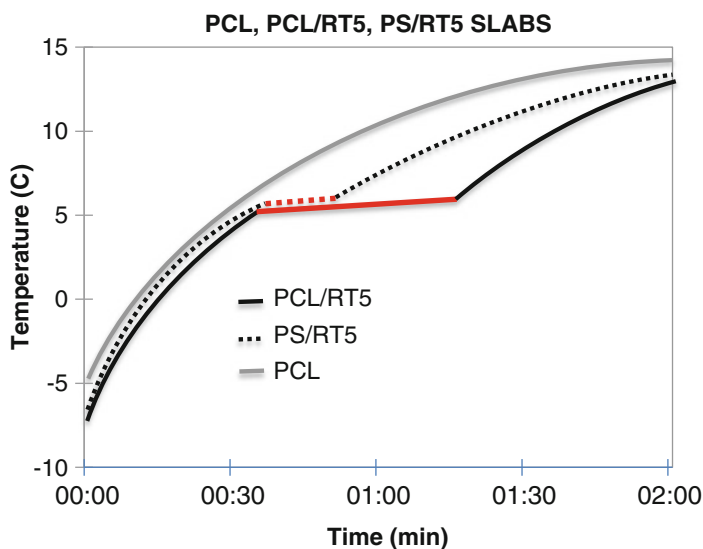
Fig. 11.3 Surface temperature as a function of time for PCL electrospun fibers and the PCL/RT5 and PCL/RT5 slabs

the refrigeration equipment, since they could buffer thermal variations of the surrounding environment.

11.1.2.2 PCMs for Textile Applications

Other recent application of encapsulated PCMs is the thermoregulating fibers area. In this case, PCMs present phase transitions at human comfort temperatures, usually form 15 to 35 °C, in order to keep constant body temperature and buffer surrounding temperature variations. The technology for incorporating PCMs into

textile structures was developed in early 1980s under NASA research programme to use fabrics in the astronauts' space suits and thus protect them against the extreme temperature in outer space [10]. Nevertheless, nowadays PCMs are already applied and commercialized in multiple textile materials (www.textileworld.com; www.schoeller-textiles.com; http://www.outlast.com). However, before applying PCMs into textile structure, the PCM should be microencapsulated in order to favor its thermal conductivity. Among other microencapsulation methods and techniques for the PCMs incorporation into the textiles, electrospinning has recently emerged as a very promising technology in this area, since this technique allows the microencapsulation and textile fiber production in only one step. Moreover, fibers attained through electrospinning showed suitable mechanical properties and also revealed good thermal properties (i.e., efficiency of enthalpy and thermal stability and reliability) after repeated thermal cycles' treatment [3, 4].

11.1.2.3   PCMs for Building Materials

Heating and air conditioning represent the majority of the total energy consumption and are still increasing. This fact, not only consumes valuable fossil fuel resources, but also emits a huge amount of CO_2 and other pollutants into the atmosphere. Therefore, research related to building energy efficiency is becoming more and more important nowadays. In this field, PCMs can be applied in building materials, usually under roofs and/or floor boards [7], in order to mitigate temperature variations inside flats and consequently reduce the energy consumption of heating/refrigeration equipments. Ideal characteristics of PCMs used for building energy conservation include (1) proper phase-change temperature (18–30 °C); (2) large heat of fusion because the space of the building envelope is limited and it should have good heat transfer ability in order to store and release the heat effectively; and (3) the PCMs' stable thermal performance for a long period with no or a small degree of supercooling [5]. Moroever, PCMs should be encapsulated in order to be stable during multiple thermal cycles and decrease the leakage risk, so that it does not adversely affect the function of the construction material. Previous experiments with large volume containment or macro-encapsulation failed due to the poor conductivity of the PCM. However, microencapsulation allows the PCM to be incorporated simply and economically into conventional construction and also avoids the poor conductivity problem [8]. Therefore, electrospinning has emerged as a very promising technology in this area, since this technique produces innovative form-stable ultrathin fibers containing PCMs which present suitable properties to be included into building materials [1,4].

11.2 Conclusions

The electrospinning technique is proving to be a very useful processing technique for enabling efficient energy storage applications related to temperature buffering. This technology is currently finding applications in areas as diverse as smart packaging, refrigeration, thermal insulation textiles and construction and should also be valuable in other less explored application areas such as sensors to for instance avoid overheating or supercoiling of these avoiding temperature driven signal variations or alterations of temperature sensitive biological materials resulting in wrong signaling.

References

1. Y. Cai, H. Ke, L. Lin, X. Fei, Q. Wei, L. Song, Y. Hu, H. Fong, Preparation, morphology and thermal properties of electrospun fatty acid eutectics/polyethylene terephthalate form-stable phase change ultrafine composite fibers for thermal energy storage. Energy Convers. Manag. **64**, 245–255 (2012)
2. W. Chalco-Sandoval, M.J. Fabra, A. López-Rubio, J.M. Lagaron, Electrospun heat management polymeric materials of interest in food refrigeration and packaging. J. Appl. Polym. Sci. **131**(16), 406–461 (2014)
3. C. Chen, L. Wang, Y. Huang, Morphology and thermal properties of electrospun fatty acids/polyethylene terephthalate composite fibers as novel form-stable phase change materials. Sol. Energy Mater. Sol. Cells **92**(11), 1382–1387 (2008)
4. C. Chen, L. Wang, Y. Huang, Ultrafine electrospun fibers based on stearyl stearate/polyethylene terephthalate composite as form stable phase change materials. Chem. Eng. J. **150**(1), 269–274 (2009)
5. R. Cheng, X. Wang, Y. Zhang, Energy-efficient building envelopes with phase-change materials: new understanding and related research. Heat Transfer Eng. **35**(11–12), 970–984 (2014)
6. G. Fang, H. Li, F. Yang, X. Liu, S. Wu, Preparation and characterization of nano-encapsulated n-tetradecane as phase change material for thermal energy storage. Chem. Eng. J. **153**, 217–221 (2009)
7. H. Ke, Y. Cai, Q. Wei, Y. Xiao, J. Dong, Y. Hu, L. Song, G. He, Y. Zhao, H. Fong, Electrospun ultrafine composite fibers of binary fatty acid eutectics and polyethylene terephthalate as innovative form-stable phase change materials for storage and retrieval of thermal energy. Int. J. Energy Res. **37**(6), 657–664 (2013)
8. A.M. Khudhair, M.M. Farid, A review on energy conservation in building applications with thermal storage by latent heat using phase change materials. Energy Convers. Manag. **45**(2), 263–275 (2004)
9. M.J. Laudenslager, R.H. Scheffler, W.M. Sigmund, Electrospun materials for energy harvesting, conversion, and storage: a review. Pure Appl. Chem. **82**(11), 2137–2156 (2010)
10. S. Mondal, Phase change materials for smart textiles – an overview. Appl. Therm. Eng. **28**(11–12), 1536–1550 (2008)
11. R. Perez-Masia, A. López-Rubio, J.M. Lagarón, Development of zein-based heat-management structures for smart food packaging. Food Hydrocoll. **30**(1), 182–191 (2013)
12. R. Perez-Masia, M.J. Fabra, A. López-Rubio, J.M. Lagarón, Use of electro-hydrodynamic processing to develop nanostructured materials for the preservation of the cold chain. Innov. Food Sci. Emerg. Technol. **26**, 415–423 (2014)
13. N. Sarier, E. Onder, S. Ozay, Y. Ozkilic, Preparation of phase change material-montmorillonite composites suitable for thermal energy storage. Thermochim. Acta **524**, 39–46 (2011)

Chapter 12
Co-electrospun Brain Mimetic Hollow Microfibres Fibres for Diffusion Magnetic Resonance Imaging

Feng-Lei Zhou, Penny L. Hubbard Cristinacce, Stephen J. Eichhorn, and Geoff J.M. Parker

Abstract Diffusion magnetic resonance imaging (dMRI) provides a non-invasive tool to explore biological tissues, including brain with its highly organised hierarchical fibrous structures. An MR phantom is a test object with known size and material for the calibration of MR scanners and the validation of image processing algorithms. Despite extensive research on the development of brain-mimicking phantoms, there are significant problems with using the existing phantoms for dMRI. This chapter is designed to lead the reader through the development of brain-mimetic phantoms for application in dMRI. Our starting point is a brief introduction to the dMRI technique and phantoms previously developed to mimic brain tissues. The second section focuses on the preparation and characterization of novel physical phantoms composed of co-electrospun hollow microfibres. Finally, the evaluation of the developed co-electrospun phantoms is presented in the third section.

F.-L. Zhou (✉)
Centre for Imaging Sciences, The University of Manchester, Manchester M13 9PT, UK

The School of Materials, The University of Manchester, Manchester M13 9PL, UK

CRUK-EPSRC Cancer Imaging Centre in Cambridge and Manchester, Manchester M20 3LJ, UK
e-mail: fenglei.zhou@manchester.ac.uk

P.L. Hubbard Cristinacce
Centre for Imaging Sciences, The University of Manchester, Manchester M13 9PT, UK

School of Psychological Sciences, University of Manchester, Manchester M13 9PT, UK

S.J. Eichhorn
College of Engineering, Mathematics and Physical Sciences, University of Exeter, Exeter EX4 4QF, UK

G.J.M. Parker
Centre for Imaging Sciences, The University of Manchester, Manchester M13 9PT, UK

CRUK-EPSRC Cancer Imaging Centre in Cambridge and Manchester, Manchester M20 3LJ, UK

12.1 Introduction

12.1.1 Diffusion MRI

Diffusion magnetic resonance imaging (dMRI) is a mature MRI technique, which was introduced in the 1980s but with the first applications realised in the early 1990s [1]. This technique combines a diffusion measurement with MRI and can characterize water diffusion properties at each picture element (pixel) of an image. It therefore provides a non-invasive tool to explore biological tissues, including brain and muscle with their highly organised hierarchical structures characterised by an orientationally anisotropic arrangement in vivo, both in animals and in humans. In these tissues, water does not diffuse equally in all directions, which is often defined as a property called anisotropic diffusion. For example, brain white matter consists of highly ordered bundles at the molecular (filaments), microscopic (axons), and macroscopic (tracts) length scales with orientationally coherent structures often persisting for more than the MRI voxel length scale. Brain water diffuses preferentially along axonal fibre directions but randomly in grey matter (Fig. 12.1).

MRI is the only imaging modality that allows visualization and calculation of molecular diffusion in vivo directly from molecular translational movement of water. Two key parameters as listed below are usually measured in dMRI:

1. Apparent Diffusion Coefficient (ADC): it measures the magnitude of diffusion of water molecules within tissue. The value of ADC is usually expressed in units of $mm^2 s^{-1}$ and is lower than free diffusion (and therefore the true diffusion coefficient), and closely reflects tissue microstructure, which impedes water diffusion;
2. Fractional Anisotropy (FA): FA is an index of the degree of alignment across structures and its value ranges from zero (isotropic diffusion, no coherent
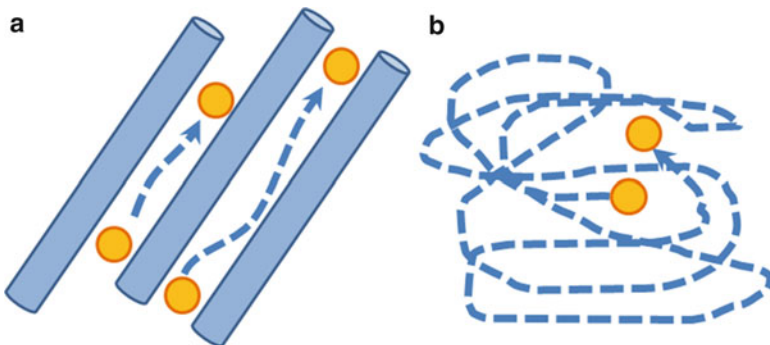
Fig. 12.1 Water diffusion in brain tissue: (**a**) white matter and (**b**) grey matter [2] (©2013 Gracian Garcia-Marti, Angel Alberich-Bayarri, Luis Marti-Bonmati. Originally published in the book edited by Kostas N. Fountas, ISBN 978-953-51-0923-5, under CC BY 3.0 license. Available from: http://dx.doi.org/10.5772/53079)
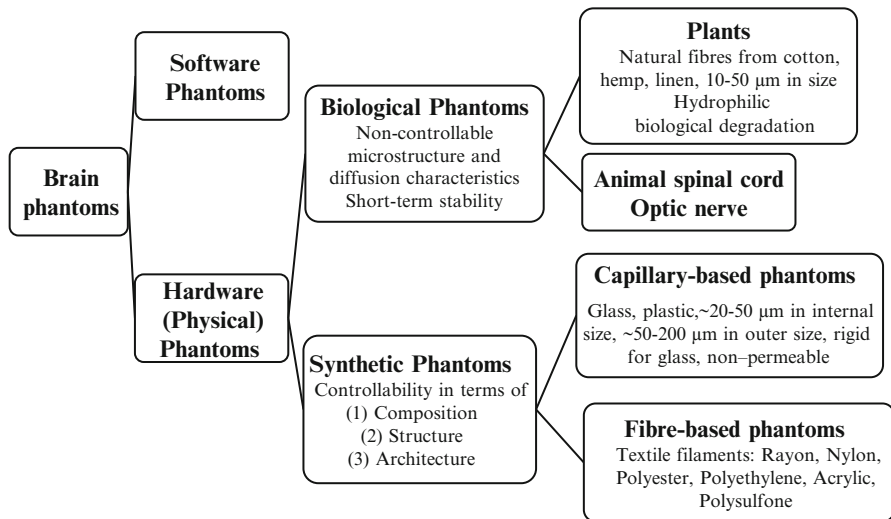
Fig. 12.2 Summary of MR phantom classifications and their characteristics

alignment within the voxel) to one (highly coherent alignment within the voxel). For isotropic water diffusion, the water displacements are equal in every direction and the FA value is zero, whereas diffusion in ordered structures has a higher FA.

12.1.2 MRI Phantoms

12.1.2.1 Imaging Phantoms

Imaging phantoms are artificial objects of known size and composition that are scanned in the area of medical imaging to evaluate the performance of various imaging devices including MRI, CT, Ultrasound, PET, and other modalities. MR phantoms can be a fluid-filled container or tube containing structures of various materials, sizes and shapes, for the calibration of MR scanners and the validation of image processing algorithms. Existing dMRI phantoms have been made from animal tissues, plant stems and textile filaments. Figure 12.2 above summarises imaging phantom classifications and their characteristics.

12.1.2.2 Brain Mimicking Phantoms

Tissue-mimicking phantoms for neurological use have to date proved to be a promising, but limited, tool for calibration and validation of MR scanners and

methods. These phantoms aim to mimic the cellular structure of tissues on the micrometre scale and the long-range connections within the brain on the centimetre scale. It is desirable to have a phantom that exhibits the same or similar properties ("cell" size, "tract" structure, "membrane" permeability, etc.) to human and/or animal tissue, but there are significant problems with using the existing brain phantoms, i.e., the uncontrollable structure of natural phantoms and the large diameters of synthetic phantoms [3, 4].

12.1.2.3 Natural and Synthetic Phantoms

Plant materials and animal tissues have been used as biological phantoms [5–9]. However, they are poor choices for calibration purposes as the exact microstructure and diffusion characteristics of these materials do not closely match with in vivo human tissue, and they are inherently uncontrollable in experimental use and chemically unstable during storage.

Synthetic phantoms of brain white matter are usually made from glass or plastic capillary and textile filament fibres [8, 10–12]. However, glass capillaries are usually rigid and plastic capillaries have larger diameters than typical axons, which limits the macroscopic and microscopic geometry of phantom design. All these available textile filament fibres (see Fig. 12.3) are solid, and none of existing synthetic options have non-negligible and tuneable membrane permeability. It also remains a challenge to regulate the angular distribution of fibres and construct complex fibre geometries such as crossing, kissing or branching present in brain tissue. As a result, the dissimilarity between the microscopic geometry of the existing phantoms and that of brain tissue sets a limit on the degree of validation that they can provide and, to date, has necessitated the use of live animal studies in which the measured diffusion characteristics can be validated against tract tracer methods and post-mortem histology.
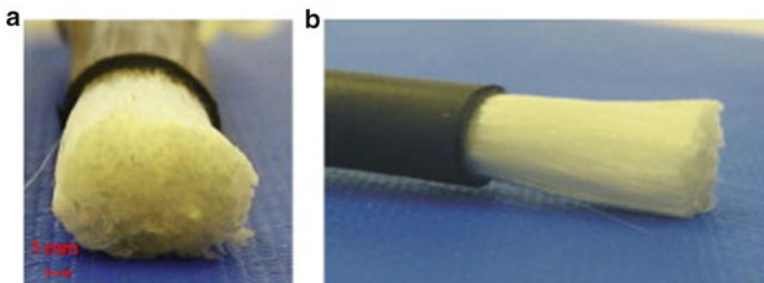
Fig. 12.3 Photographs of a fiber phantom with the shrinking tube partly removed: (**a**) transversal; (**b**) longitudinal view (Reprinted with permission from [8]. Copyright (2008) Elsevier)

12.2 Hollow Microfibres by Co-electrospinning

12.2.1 Co-electrospinning

Electrospinning is a technique employing electrostatic forces to preparing polymeric fibres having diameters in the range of around 100 nm to a few microns from polymer solutions or melts. As a modified process, co-electrospinning (co-ES) can be used to fabricate polymeric fibres with unique core–sheath or hollow structures. Figure 12.4a depicts a schematic of the co-electrospinning process. In coaxial electrospinning, one of the key components lies in its spinneret, consisting of two concentric needles with one located inside another (Fig. 12.4b). A DC high voltage is applied to the spinneret, and it deforms the compound droplet. A compound jet is generated on the tip of the deformed droplet, and in an ideal case, a core–shell or hollow nano/microfibre is created (Fig. 12.4c). In order to obtain a stable compound jet, there are a few general features for designing a coaxial spinneret: (1) better concentricity of the inner and outer needles; (2) controllable flow rates for both the inner and outer solutions, respectively; (3) adjustable protruding length of the inner needle along the axis; and (4) changeable tubular gap between the needle tip openings (see right bottom of Fig. 12.4b).

12.2.2 Co-ES Hollow Microfibres

12.2.2.1 Random Hollow Microfibres

Random hollow microfibres are straightforward produced on a static grounded fibre collector in the co-ES process due to its inherent jet trajectory comprised of straight and spiral sections. Optical and electron microscopes are widely used tools to characterize
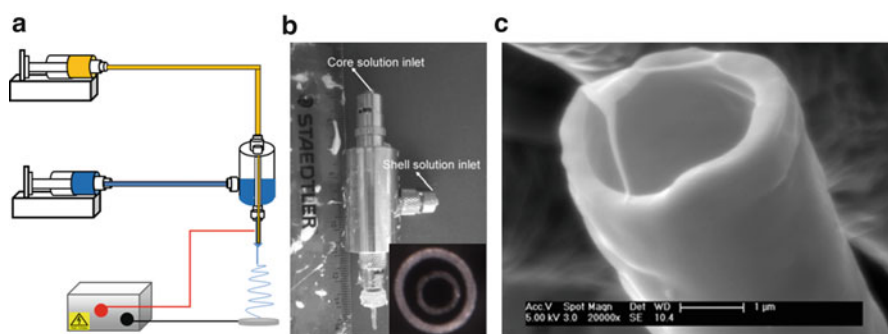
Fig. 12.4 (**a**) Schematic of a co-electrospinning process; (**b**) A spinneret for coaxial electrospinning used in our laboratory (*inlet*: spinneret tip); (**c**) SEM micrograph of cross-section of one hollow fibre by coaxial electrospinning
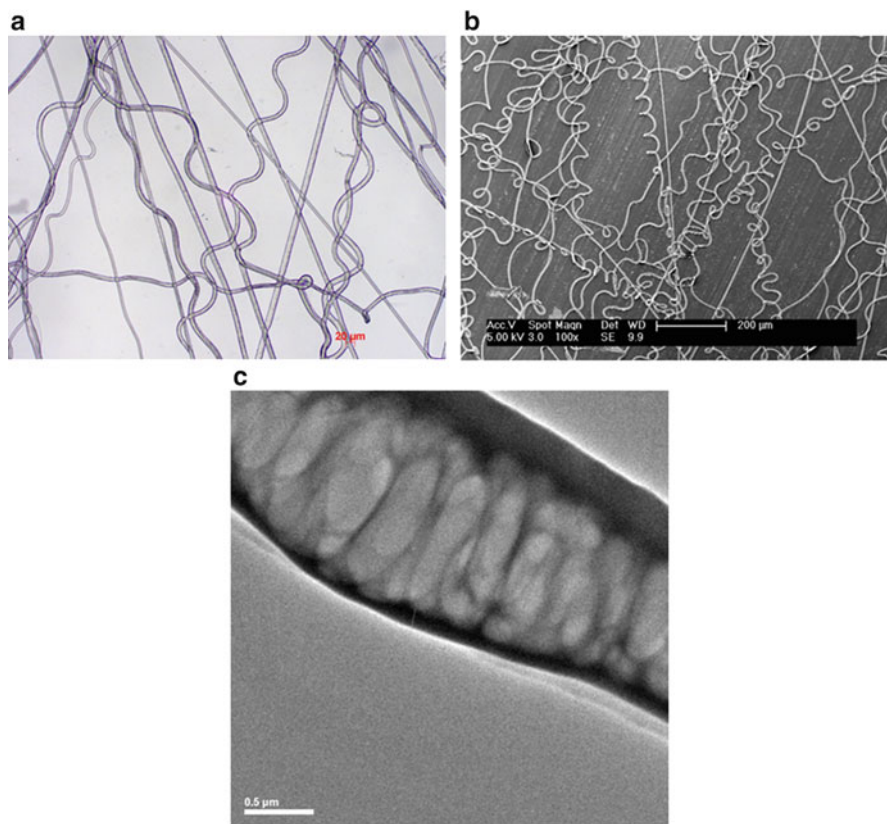
Fig. 12.5 (**a**) Optical image of co-ES polycaprolactone(shell)/polyethylene oxide (core) microfibres (9.0 and 3.0 mL h^{-1} shell and core flow rates, 11.4 kV applied voltage, 12.0 cm working distance); (**b**) SEM image of co-ES polycaprolactone(shell)/polyethylene oxide (core) microfibres (5.0 and 0.2 mL h^{-1} shell and core flow rates, 18.0 kV applied voltage, 20.0 cm working distance); (**c**) TEM image of co-ES polycaprolactone(shell)/sugar (core) microfibres (1.0 and 0.1 mL h^{-1} shell and core flow rates, 9 kv applied voltage, 10.0 cm working distance)

the surface morphology of the resultant co-ES hollow microfibres. Typical optical and scanning electron microscope (SEM) images of the surface morphology of a random co-ES hollow microfibre mesh are shown in Fig. 12.5a–b. In order to confirm the core-shell structures, a transmission electron microscope (TEM) is often used, as shown in Fig. 12.5c, revealing the sugar-polycaprolactone core-shell structured fibre.

To date, four different combinations of core-shell materials (two categories: polymer-polymer and non polymer-polymer) have been successfully used to produce hollow microfibres in our recent studies. SEM, together with freeze fracture, is very useful to examine the cross-sectional morphology of co-ES fibres. The cross-sections of these co-ES fibre meshes are presented in Fig. 12.6, from which cross-sectional pore sizes and distributions can be measured. In general, in order to obtain a stable co-ES and thus well-defined core-shell fibre structure, it is necessary for
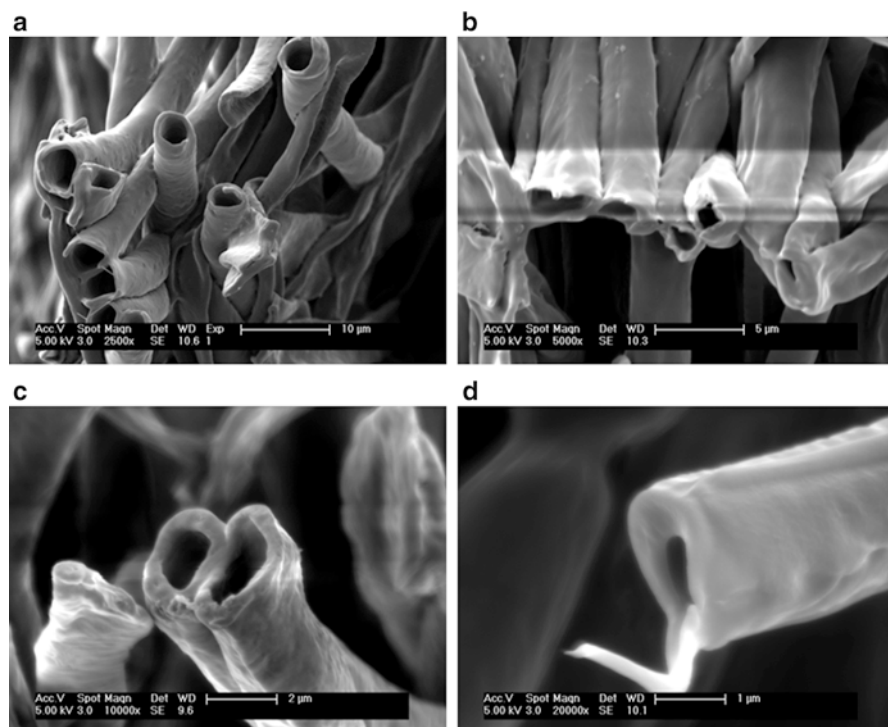
Fig. 12.6 SEM images of cross-sections of co-ES hollow microfibre meshes from (**a**) PCL shell – PEO (polyethylene oxide) core; (**b**) PCL shell – olive oil core; (**c**) PCL shell – mineral oil core; (**d**) PCL shell – sugar aqueous solution core

shell materials to have good fibre spinnablity (e.g., polycaprolactone (PCL) used in our study) and for core materials (e.g., polymer solutions preferably, olive oil, mineral oil or sugar solution) to be sufficiently viscous to withstand high stretching forces exerted on the core fluid. More interestingly, inner diameters (I.D.s) of hollow microfibres can be tuned by both co-ES process parameters (i.e. core solution flow rate) and core-shell solution materials. Figure 12.7 shows a few typical co-ES hollow microfibres with different sizes ranging from ~1 to ~12 μm. Most recently, random hollow microfibres have been successfully used to mimic brain grey matter [13].

12.2.2.2 Aligned Hollow Microfibre Bundles and Strips

Aligned hollow microfibre bundles have been produced by co-electrospinning of PCL shell and PEO core by using a rotating collector as shown in Fig. 12.8. In our recent studies, extensive efforts have been devoted to the exploration of the values of the electric field and core-shell flow rates in order to obtain their operating
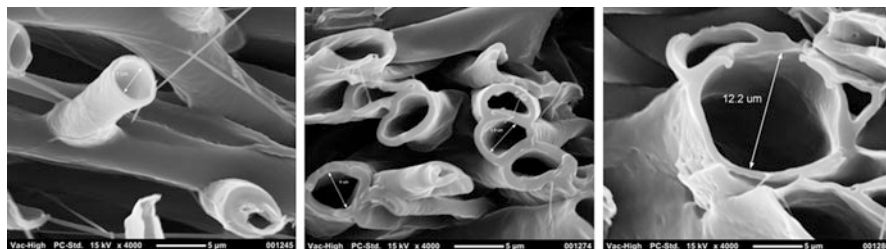
Fig. 12.7 SEM images of co-ES hollow PCL shell – PEO core microfibre meshes with various inner diameters
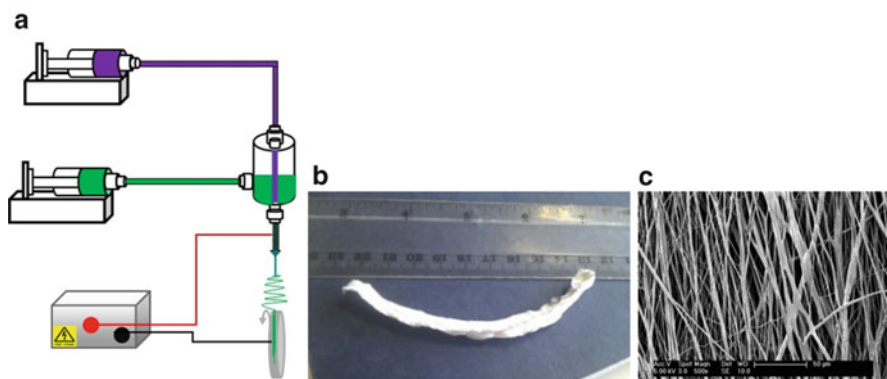
Fig. 12.8 (**a**) Schematic of co-ES process for production of aligned hollow fibre bundle; (**b**) Photo of fibre bundle; and (**c**) SEM image showing surface morphology of fibre bundle

diagrams, where a stable co-ES process could be achieved to produce an effective phantom material [4]. Within the operating diagrams, the core flow rate of PEO solution was adjusted to produce hollow PCL fibres with various inner diameters, while the PCL shell flow rate was maintained constant, since the inner diameter of hollow PCL fibres is expected to be one of key factors affecting the diffusion of the solvent in dMRI.

SEM images in Fig. 12.9a–h reveal that the inner diameters of PCL fibres increased from ~3.3 to ~10.2 μm (Fig. 12.9i) as the core flow rate increased from 0.1 to 2 mL h^{-1}, when the shell flow rate was maintained at 3 mL h^{-1}. There was a similar tendency for the effect of core flow rate when the shell flow rate was increased to 6 mL h^{-1} (Fig. 12.9j). As shown in Fig. 12.9i, the reproducibility of the inner diameters of eight hollow PCL samples produced using different core flow rates was good. Based on these results, the inner diameters of the PCL fibres were easily adjusted to suit the application of axon-mimicking phantoms, by fine-tuning the core-shell flow rates. Compared with the effect of the core flow rate, it can clearly be seen from Fig. 12.9k that the shell flow rate had a less significant impact on the inner diameter of co-ES hollow PCL fibres. This finding was in line with previous reports by Zussman et al. [14, 15]. However, it must be pointed out that the
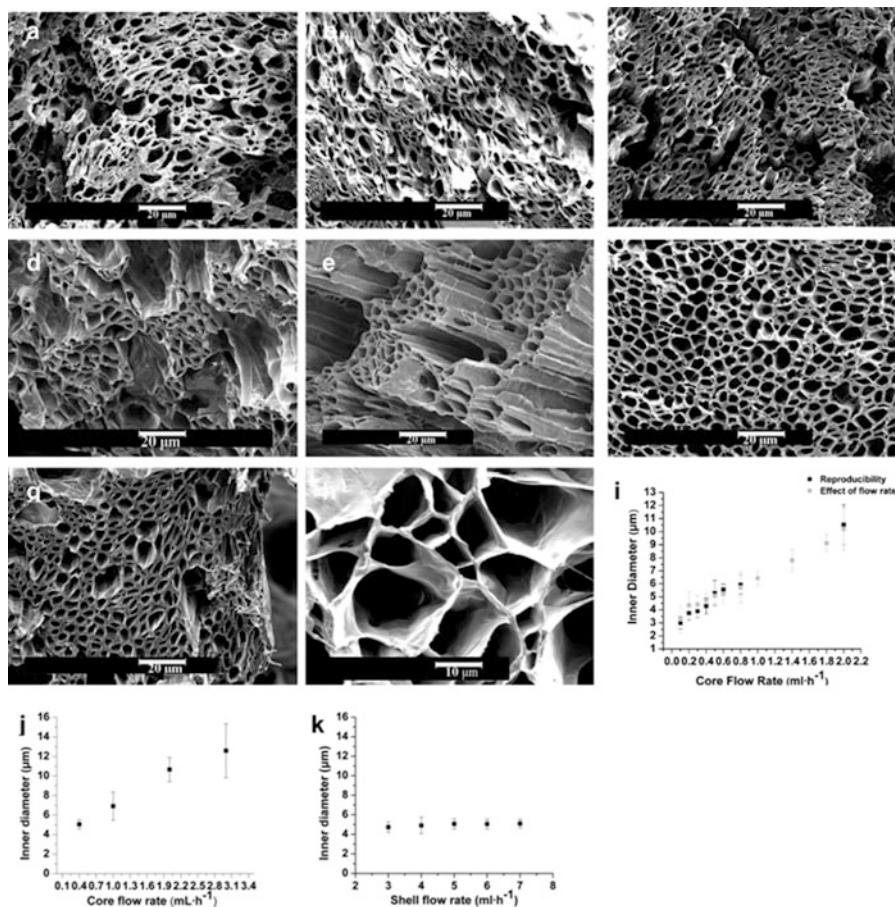
Fig. 12.9 SEM images of hollow PCL fibres produced at different core flow rates: (**a**) 0.1; (**b**) 0.2; (**c**) 0.3; (**d**) 0.4; (**e**) 0.5; (**f**) 0.6; (**g**) 0.8; (**h**) 2 mL h^{-1}; (**i**) the relationship between the inner diameter of hollow PCL fibres and core flow rate at a 3 mL h^{-1} shell flow rate, showing good reproducibility; (**j**) the relationship between the inner diameter of hollow PCL fibres and PEO core flow rate at 6 mL h^{-1} shell flow rates; (**k**) the relationship between the inner diameter of hollow PCL fibres and shell flow rate. Experimental parameters: 9 kV applied voltage, 5 cm working distance, 3 mL h^{-1} PCL shell flow rate (Reprinted with permission from [4], Copyright (2012) American Chemical Society)

range of shell flow rates used in our studies had to be narrow in order to maintain the stability of the co-ES process, whereas the core flow rate and electric field were fixed.

Another form of aligned hollow microfibre assembly – fibre strip has been also prepared from PCL shell and PEO core with core flow rates of 0.8, 1.4, and 2.0 mL h^{-1} by using a rotating drum mounted on an *x-y* translation stage, as shown in Fig. 12.10. Using the SEM images in Fig. 12.11a–c the area-weighted mean inner diameters of the fibres in the three strips are found to be 9.5, 11.9, and
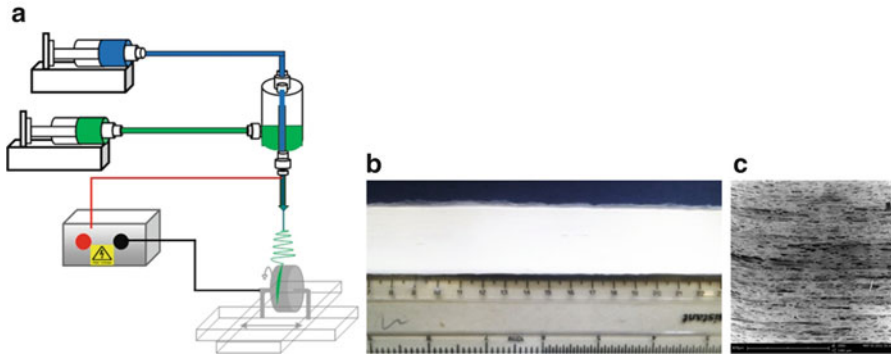
Fig. 12.10 (**a**) schematic of co-ES process for production of aligned hollow fibre strip; (**b**) photo of fibre strip; and (**c**) SEM image showing surface morphology of fibre strip
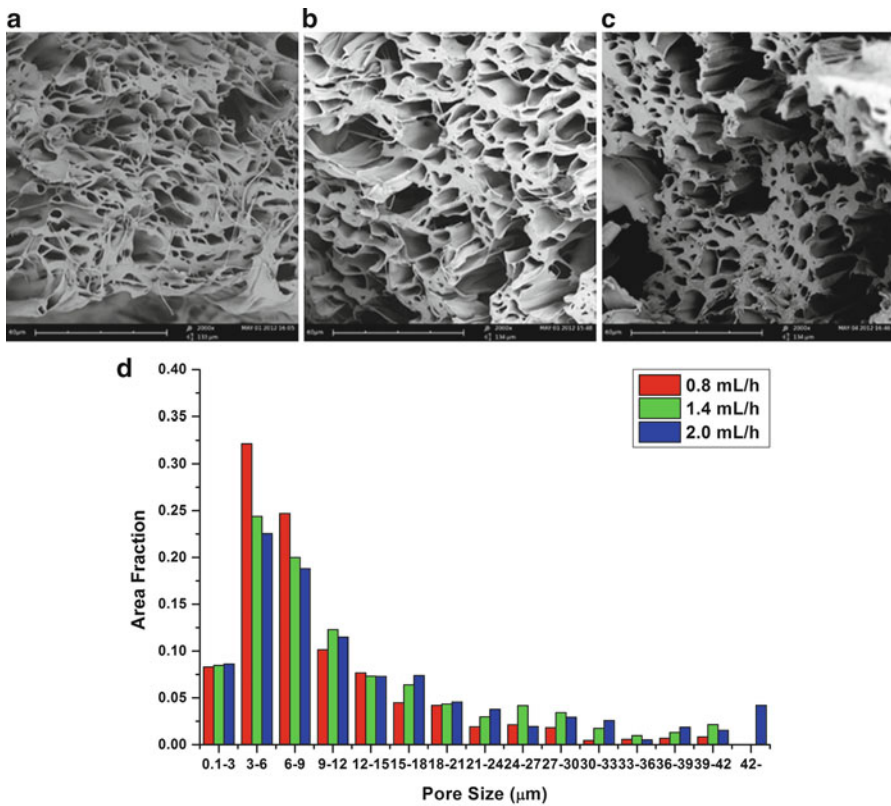
Fig. 12.11 Electron micrographs of co-ES hollow fibre strips produced using the core flow rate of (**a**) 0.8 mL h^{-1}, (**b**) 1.4 mL h^{-1}, (**c**) 2.0 mL h^{-1}, (**d**) A histogram of the area-weighted mean pore size measurements for each strip. (Reprinted with permission from [17]. Copyright (2015) John Wiley and Sons)

13.4 μm, respectively. Figure 12.11d shows the range of inner diameters for each of these strips as a normalized histogram. There is a broad range of fibre inner diameters within the strip, reminiscent of real tissue [16], but it is clear that the mean diameter tends towards higher values for the strips prepared with higher core flow rates. In order to investigate the reproducibility of co-ES hollow microfibres, five strips were prepared with an inner flow rate of 0.8 mL h^{-1}. Figure 12.12 shows
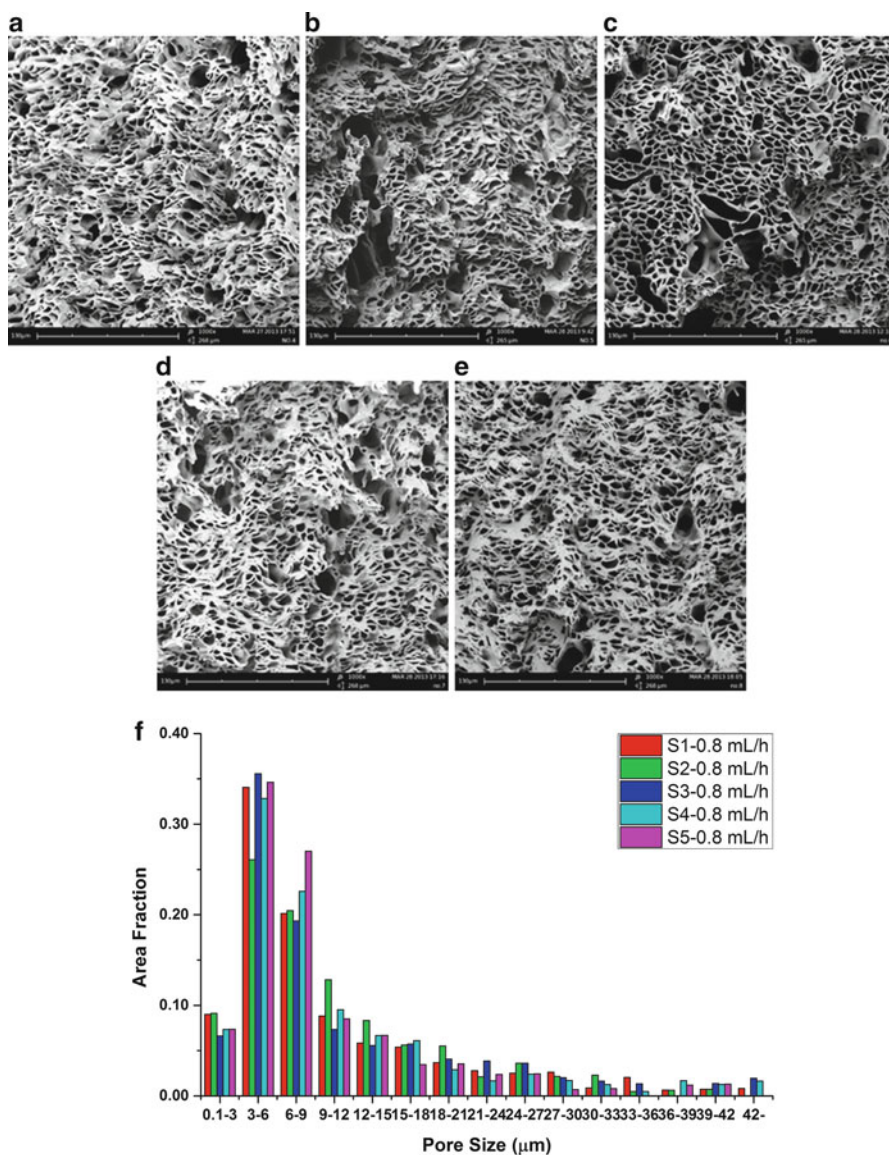
Fig. 12.12 (**a–e**) Representative electron micrographs of five co-ES hollow fibre strips reproducibility using 0.8 mL h^{-1} core flow rate, and (**f**) the histogram of their inner diameters

cross-sectional SEM images with ×1,000 magnification through a strip, cut perpendicular to the axis of the fibres, revealing a microporous structure. Using the SEM images the range of inner diameters for each of these strips is shown as a normalised histogram (Fig. 12.12f).

12.3   Co-ES Microfibre Phantoms and MR Evaluation

Two types of MR phantoms have been developed using co-ES hollow microfibres, which are fibre-bundle based and fibre-strip based, as shown in Fig. 12.13.

12.3.1   Fibre Bundle Based MR Phantoms

MR phantoms were constructed by inserting fibre bundles into MR test tubes, with the fibres aligned along the axis of the tubes. The tubes were filled with the diffusion model liquid, cyclohexane, which is a proton rich solvent capable of infusing into the hydrophobic polymer, with a suitable MRI properties to mimic the free liquid in axonal bodies. Figure 12.14a shows the fibres packed in a glass tube filled with cyclohexane. In dMRI, MR signal is sensitive to the molecular diffusion of

Fig. 12.13 (**a**) Fibre bundle-based MR phantom; (**b**) Fibre strip-based MR phantom
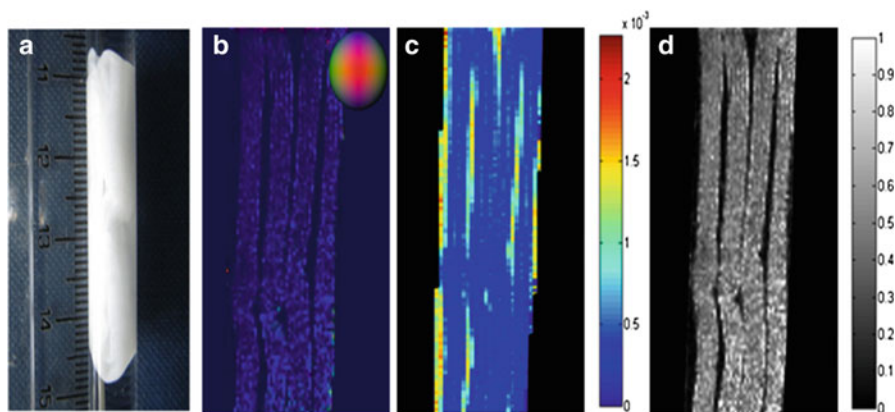
Fig. 12.14 (**a**) Fibre phantoms in a glass tube filled with solvent, cyclohexane; (**b**) Single slice through the phantom, revealing the consistent preferential alignment of the micrometre-scale fibre along the axis of the tube; (**c**) A mean diffusivity map revealing lower values in the phantom compared with the free solvent; (**d**) A fractional anisotropy map showing that diffusion within the phantom is anisotropic (approaching 1) and in the solvent is isotropic (approaching 0). (Reprinted with permission from [4]. Copyright (2012) American Chemical Society)

cyclohexane and can change when the free diffusive passage of these solvent molecules is restricted or hindered by surrounding barriers. The measurement of ADC in multiple directions allows us to determine the orientation of these barriers. Due to the anisotropic structure, the least hindered diffusion (or highest diffusion coefficient) in the hollow aligned co-ES fibre bundles is expected to be parallel to the fibre alignment direction. Figure 12.14b shows a colour map of the orientation of the least restricted diffusion and, therefore, the principal direction of the fibres in the bundles as anticipated from the construction of the phantom. The colour key ball in the figure reveals that fibres in red run into and out of the page, in green run from left to right, and in blue run up and down. The figure clearly shows the principal direction of the aligned fibres to be along the axis of the tube.

Figure 12.14c shows the mean diffusivity (MD) of cyclohexane in the hollow microfibres, revealing that the average parallel and perpendicular apparent diffusion coefficients are significantly lower than that for free cyclohexane. Figure 12.14d shows the fractional anisotropy (FA). The MD value in the our study is higher and FA value lower than the average MD and FA values of the ex vivo optic nerve of a rat, respectively, measured by Richardson et al. [18]. These values are, however, in the approximate in vivo biological range for white matter [19]. Considering the fact that the average diameter of hollow microfibres in the phantom is $10.2 \pm 1.6\,\mu m$, which is consistent with large axons in white matter [20], the MD value is expected to be a little higher and FA value a little lower than in the optic nerve. These ex vivo MD and FA values of the optic nerve are however respectively lower and higher than what is generally observed in tissue in vivo. It is worth noting that the phantom sample testing temperature in our study is relatively low (22 °C vs body temperature in the Richardson study), suggesting that the

factors including the use of cyclohexane as a solvent and the relative lack of microstructural complexity in the phantom when compared with biological tissue may also influence the parameter values.

12.3.2 Fibre Strip-Based MR Phantoms

A similar procedure as described in Sect. 12.3.1 has been followed to prepare MR phantoms using strips with difference fibre diameters (Fig. 12.15a). Diffusion tensor imaging (DTI) has been carried out on a Bruker 7 T horizontal bore magnet (Bruker Biospin, Germany).

The FA and the radial diffusivity calculated from diffusion-tensor images are plotted against the area-weighted mean inner diameters measured from SEM images. As shown in Fig. 12.15b–c, the radial diffusivity increases with the increasing mean inner diameter of the fibres, whereas FA decreases linearly. This trend is expected as, dependent on the diffusion time of the acquisition, an increase in inner diameter reduces the restriction to the diffusion of cyclohexane molecules perpendicular to the axis of the fibres. This leads to a subsequent decrease in FA: from 0.45 ± 0.05 to 0.33 ± 0.04, and increase in the measured apparent diffusion coefficient perpendicular to the fibres from $0.38 \pm 0.05 \times 10^3$ cm s^{-1} to $0.61 \pm 0.06 \times 10^3$ cm s^{-1}.

We have carried out a study investigating whether the phantoms prepared under the same co-ES conditions could lead to a reproducible dMRI signal. Five fibre strips prepared in the Sect. 12.2.2.2 using an inner flow rate of 0.8 mL h^{-1} (see Fig. 12.12) and were then prototyped into five phantoms. These phantoms were scanned concurrently on a 3 T clinical scanner using the manufacturer's high
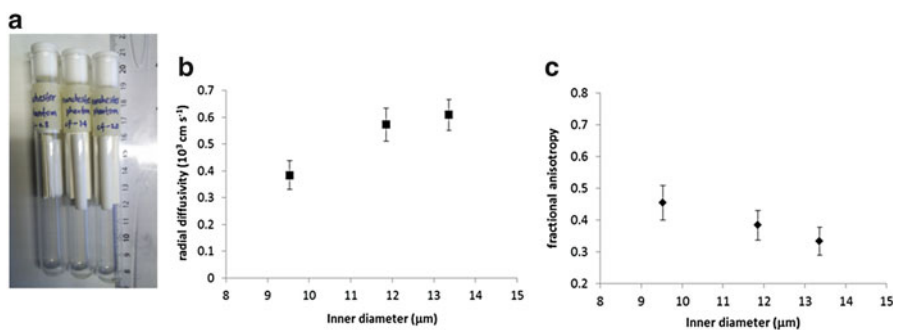
Fig. 12.15 (**a**) Three tubes containing phantoms with fibers of increasing inner diameter; (**b**) area-weighted mean pore inner diameter (measured from SEM) against fractional anisotropy (measured from DTI); (**c**) area-weighted mean pore inner diameter against radial diffusivity (Error bars are standard deviations from the mean; Reprinted with permission from [17]. Copyright (2014) John Wiley and Sons)

resolution DTI protocol. The results of both the SEM and DTI have shown that there is only a small amount of variation between the samples (see details in [17]).

A final point of consideration for a useful phantom material is the long-term stability of the fiber material in the diffusion solvent. It is important that the material does not degrade or change structure within a reasonable time window. Short-term stability of PCL fibres in cyclohexane has been shown to be good over both a 1-week [4] and 12-month period, but further study of the long term stability is desirable.

12.4   Conclusions

In summary, we have developed a novel brain white matter mimicking phantom comprising co-ES hollow polymeric fibres, which can be constructed and used as reference materials for diffusion magnetic resonance imaging. The inner diameter of co-ES hollow fibres can be tuned by controlling the core flow rate and core-shell solution pairs in order to provide structures with similar inner diameters to axon fibres in brain white matter. Our study has demonstrated that the developed phantoms can mimic the cellular barriers imposed by axonal cell membranes and myelin, and can result in expected responses (ADC and FA values) of MR scanner by changing their size. The developed phantoms are reproducible and have been tested in other imaging centres in the UK, EU and US. Research in this area can potentially enable the development of biomimetic phantoms that can mimic a range of biological structures within the body, potentially providing substitutes for animal tissues, and allowing the stable and reproducible validation and calibration of diffusion MRI in other organs and cellular structures.

References

1. S. Mori, P.B. Barker, Diffusion magnetic resonance imaging: its principle and applications. Anat. Rec. **257**(3), 102–109 (1999). doi:10.1002/(sici)1097-0185(19990615)257:3<102::aid-ar7>3.0.co;2-6

2. G. García-Martí, A. Alberich-Bayarri, L. Martí-Bonmatí, Brain structure MR imaging methods: morphometry and tractography. Nov. Front. Adv. Neuroimaging (2013). doi:10.5772/53079

3. H. Johansen-Berg, T.E.J. Behrens (eds.), *Diffusion MRI: From Quantitative Measurement to In-Vivo Neuroanatomy The Validation of Tractography* (Academic, Amsterdam, 2009)

4. F.-L. Zhou, P.L. Hubbard, S.J. Eichhorn, G.J.M. Parker, Coaxially electrospun axon-mimicking fibers for diffusion magnetic resonance imaging. ACS Appl. Mater. Interfaces **4** (11), 6311–6316 (2012). doi:10.1021/am301919s

5. S. Boujraf, R. Luypaert, H. Eisendrath, M. Osteaux, Echo planar magnetic resonance imaging of anisotropic diffusion in asparagus stems. MAGMA **13**(2), 82–90 (2001). doi:10.1007/bf02668156

6. Y. Assaf, R.Z. Freidlin, G.K. Rohde, P.J. Basser, New modeling and experimental framework to characterize hindered and restricted water diffusion in brain white matter. Magn. Reson. Med. **52**(5), 965–978 (2004). doi:10.1002/mrm.20274

7. M. Descoteaux, E. Angelino, S. Fitzgibbons, R. Deriche, Apparent diffusion coefficients from high angular resolution diffusion imaging: estimation and applications. Magn. Reson. Med. **56**(2), 395–410 (2006). doi:10.1002/mrm.20948

8. E. Fieremans, Y. De Deene, S. Delputte, M.S. Özdemir, Y. D'Asseler, J. Vlassenbroeck, K. Deblaere, E. Achten, I. Lemahieu, Simulation and experimental verification of the diffusion in an anisotropic fiber phantom. J. Magn. Reson. **190**(2), 189–199 (2008). doi:10.1016/j.jmr.2007.10.014

9. P. Pullens, A. Roebroeck, R. Goebel, Ground truth hardware phantoms for validation of diffusion-weighted MRI applications. J. Magn. Reson. Imaging **32**(2), 482–488 (2010). doi:10.1002/jmri.22243

10. C. Poupon, B. Rieul, I. Kezele, M. Perrin, F. Poupon, J.-F. Mangin, New diffusion phantoms dedicated to the study and validation of high-angular-resolution diffusion imaging (HARDI) models. Magn. Reson. Med. **60**(6), 1276–1283 (2008). doi:10.1002/mrm.21789

11. P. Fillard, M. Descoteaux, A. Goh, S. Gouttard, B. Jeurissen, J. Malcolm, A. Ramirez-Manzanares, M. Reisert, K. Sakaie, F. Tensaouti, T. Yo, J.-F. Mangin, C. Poupon, Quantitative evaluation of 10 tractography algorithms on a realistic diffusion MR phantom. NeuroImage **56**(1), 220–234 (2011). doi:10.1016/j.neuroimage.2011.01.032

12. E. Fieremans, Y.D. Deene, S. Delputte, M.S. Özdemir, E. Achten, I. Lemahieu, The design of anisotropic diffusion phantoms for the validation of diffusion weighted magnetic resonance imaging. Phys. Med. Biol. **53**(19), 5405 (2008)

13. A. Ye, P.L. Hubbard Cristinacce, F.-L. Zhou, Z. Yin, G.J.M. Parker, R. Magin, Diffusion tensor MRI phantom exhibits anomalous diffusion. *The Proceeding of The 36th Annual International IEEE EMBS Conference*, Chicago, IL, USA, 26–30 August 2014, pp. 746–749

14. A. Arinstein, R. Avrahami, E. Zussman, Buckling behaviour of electrospun microtubes: a simple theoretical model and experimental observations. J. Phys. D. Appl. Phys. **42**(1), 015507 (2009)

15. S.N. Reznik, A.L. Yarin, E. Zussman, L. Bercovici, Evolution of a compound droplet attached to a core-shell nozzle under the action of a strong electric field. Phys. Fluids **18**(6), 062101 (2006). doi:10.1063/1.2206747

16. Y. Assaf, T. Blumenfeld-Katzir, Y. Yovel, P.J. Basser, Axcaliber: a method for measuring axon diameter distribution from diffusion MRI. Magn. Reson. Med. **59**(6), 1347–1354 (2008). doi:10.1002/mrm.21577

17. P.L. Hubbard, F-L. Zhou, S.J. Eichhorn, G.J.M. Parker, Biomimetic phantom for the validation of diffusion magnetic resonance imaging. Magn. Reson. Med. **73**(1), 299–305 (2015). doi:10.1002/mrm.25107

18. S. Richardson, B. Siow, A.M. Batchelor, M.F. Lythgoe, D.C. Alexander, A viable isolated tissue system: a tool for detailed MR measurements and controlled perturbation in physiologically stable tissue. Magn. Reson. Med. **69**(6), 1603–1610 (2013). doi:10.1002/mrm.24410

19. D.K. Jones, Studying connections in the living human brain with diffusion MRI. Cortex **44**(8), 936–952 (2008). doi:10.1016/j.cortex.2008.05.002

20. J.A. Perge, J.E. Niven, E. Mugnaini, V. Balasubramanian, P. Sterling, Why do axons differ in caliber? J. Neurosci. **32**(2), 626–638 (2012). doi:10.1523/jneurosci. 4254-11.2012

Chapter 13
Turning Nanofibres into Products: Electrospinning from a Manufacturer's Perspective

Thomas R. Hayes and Iain C. Hosie

Abstract In recent years, the interest in electrospinning research and development has grown dramatically, with new nanofibrous materials and applications being reported in peer-review journals every month. Application areas are as broad ranging as medical devices, filtration, electronics, composites, energy generation and storage, sensing, acoustics and more. Despite the clear potential for nanofibres to be used in each of these industries, the uptake in terms of the number of commercialised products that use electrospun nanofibre remains very limited, with air filtration being the only sector in which they are used extensively. In this chapter, the current state of the electrospinning industry is discussed, including recent advances in commercial-scale electrospinning and other competing technologies. The challenges that are faced by commercial electrospinning companies are highlighted, helping to explain the limited commercialisation and uptake of electrospinning by industry. To finish, some examples of nanofibre products that are currently available or being commercialised are given, with an outlook on what the future may hold for electrospun nanofibre technologies in the years to come.

13.1 Introduction

Since the early 1990s, the subject of electrospinning has attracted an increasing amount of interest within academia, and with it an ever-deepening understanding of the exploitable properties of nanofibres and nano-scale textiles, and the important processing principles from lab to pilot-scale production. As such a growing range of innovative applications are being discovered and developed. It is clear that the nanofibre industry is growing, but remains hard to define and is growing in a disparate manner.

T.R. Hayes (✉) • I.C. Hosie
Revolution Fibres Ltd, 9A Corban Ave, Henderson, Auckland 0612, New Zealand
e-mail: thomas@revolutionfibres.com; iain@revolutionfibres.com

Despite the great potential of electrospun nanofibre that has been demonstrated in many peer-review journals for use in applications as broad ranging as filtration, medical devices, electronics, composites, energy generation and storage, and sensing, to name just a few, the number of commercialised products using electrospun nanofibre remains extremely limited.

The only exception to this being air filtration products, which have included electrospinning technologies in their manufacture for several years. Electrospun nanofibres were first discovered in the 1930s (Formahls, etc.) and quickly found a use in filters in the USSR (Petranov filters) from the 1940s–1980s. Surprisingly, the technology never expanded out of air filtration, or Russia for that matter, until the 1980s.

One reason for this lack of commercialisation of electrospun fibres was the small scale at which nanofibres could be produced using the conventional electrospinning method, which predominantly limited its use to the production of small samples within laboratories. As electrospinning was borne from the textiles and filtration industry, the high expectations that were placed on the production rate, and low expectations of the cost, meant it was not a favoured technology. Nevertheless, academia persevered with electrospinning, intrigued by the potential of nano-scale textiles; and no doubt buoyed by the relative ease of lab-scale production.

Another reason for the slow uptake of electrospun nanofibres was that, aside from filtration, there was no obvious use for nanofibres. Now, as we understand the new and exciting properties of materials at the nano-scale and aided by the development of accessible and affordable analysis tools such as the bench-top SEM, we inevitably seek to apply these innovative materials to everyday products to increase performance, reduce size and weight and achieve more commercial return.

In recent years, a number of companies have attempted to address the problem of nanofibre production rates and have developed new methods, adapted from conventional electrospinning, which are capable of significantly faster production than methods previously reported within academia. With these new technological advancements, the potential for the use of electrospun nanofibre in industrial applications has become more achievable and there are a growing number of companies being formed to develop an industry for nanofibre use.

Also in recent years our technologies, devices and consumer goods are getting smaller. Coupled with humanities relentless quest for improvement, we are in an age where we continually explore new properties of materials, especially at the nano-scale. The potential to take the vast array of non-woven textiles to the nano-scale is an intriguing prospect and a strong commercial opportunity in diverse sectors.

In this chapter, the commercialisation of electrospinning will be discussed along with the challenges that are faced by commercial nanofibre developers and manufacturers in developing nanofibre-based technologies for industrial application. Furthermore, we will feature examples of new and emerging nanofibre-based products being commercialised.

13.2 The Electrospinning Industry

The creation and use of nanofibres in the air filtration industry dates back to the 1930s and continues to the present day, and is a fascinating story of a "forgotten" technology riding the wave of "nanotechnology" and becoming rediscovered in research circles. Rather than map this story of development and use in air filters, we shall focus on the emerging uses of nanofibre and the infrastructure required to create and support them.

In order for electrospinning to be adopted by industry, the process must be robust; capable of continuous production of nanofibre with uniform fibre diameter distribution at controlled deposition rates and thickness. The production process must be controllable without the need for highly-trained experts to supervise the production. It must be safe for workers, end users and the environment. It must offer significant performance advantages over existing technologies, and, in most applications the nanofibre must either be supplied as a rolled good or customised to suit industrial production systems. And in many cases it must also comply with a myriad of international regulations.

To be commercially viable, the electrospinning process must be able to produce nanofibre at large enough volume and for a cheap enough cost to be commercially viable when competing with existing alternative technologies or products. Nanofibre is borne out of the centuries-old, very competitive and cost-centric textiles market. In order to compete with existing textiles (and specialty films), nanofibres must offer distinct performance or production advantages such as:

- Improvements in surface area, porosity and reduced thickness and/or weight
- Use of materials and functional additives that would not withstand traditional fibre making techniques (e.g. high heat, high pressure)
- Textiles or membranes small enough to be used in miniaturised devices (e.g. electronics, implantable medical devices etc.)

The requirements for production scale and price is highly dependent on the specific application being considered. Typically, the more technically advanced or complex end products, such as medical devices or consumer electronics, can demand higher market prices and require smaller production volumes. In these cases, the allowable cost of manufacture can be higher and the rate of production less challenging, compared with more commodity products such as conventional textiles or filters.

However, there are clear exceptions to this generalisation, such as in applications where the electrospun nanofibre is competing with existing, established technologies. One example of this is the case of Li-ion battery electrodes, in which there is technical potential for the use of inorganic electrospun nanofibre, but where the cost president has been set by the existing carbon electrode materials, which have become very cheap and easily manufactured in tonne-quantities.

It is also worth noting, that whilst there may be good potential for profitability in manufacturing nanofibre for more demanding applications, such as medical

devices, there are often more demands on the manufacturing process in terms of conformation to regulatory standards, which can come with significant cost during development and prior to any manufacturing agreements.

Nevertheless, nanofibres are increasingly being scaled and delivered cost-competitively to the market. The air filter industry adopted the technology early and was responsible for high-scale production. The first examples of this were the Petryanov filter in Russia in the 1930s and Donaldson Co.'s filters in the 1980s, and since then, many more companies now boast what are considered mass-scale production capabilities for electrospun nanofibres. Air filtration was a well-suited industry because nanofibre offered an obvious performance advantage over larger fibres. In addition, the filter industry is a dominant player in the advanced textiles sector, with much of the expertise and supporting infrastructure already in-place to take electrospinning further than ever seen before.

Many industries, however, have not developed from the textiles or non-wovens markets, and so producing nanofibre is a huge technical leap, not to mention expense. For the new wave of commercial-scale electrospinning companies, the identification of the appropriate applications is therefore critical to their sustainability as a business, and many companies will rely on public funding or externally sourced private investment before they are able to establish commercially viable manufacturing processes and contracts.

Currently, the nanofibre industry is a fledgling "technology push" market where hundreds of academic papers per annum are published, many exploring or referencing commercial applications. The main contributing factor to this technology push is the fact that electrospinning at the lab scale is very easy compared with most fibre manufacturing techniques, and most nanotechnologies. Conventional needle based electrospinning is a cheap, achievable "entry" into nanotechnology. Unfortunately, needle-based electrospinning rarely translates into commercial scale electrospinning, so most research has to be re-configured to be commercially viable.

BCC Research has estimated that global revenues for nanofibre-enabled products were an estimated US$382.1 million in 2011, growing to around $852.3 million by 2017. TechNavio's analysts, in 2013, found the compound annual growth rate (CAGR) for nanofibres is 38 %, compared with 21 % for nanotechnology, and electrospinning remains the preferred method for nanofibre production (Nafigate estimates over 90 % of patents and products). Currently, polymeric nanofibres account for the main bulk of the current revenues for nanofibres, finding applications across a number of sectors, with their main markets being air and water filtration, composites and textiles.

However the nanofibre market is very hard to define. Rather than being defined by end-users needs or the emergence of nanofibre products, it is becoming heavily influenced by lab-to-pilot scale electrospinning machine manufacturers following behind Czech Republic's pioneers Elmarco in providing the research community with the tools to upscale production. The "technology push" is likely to continue for some time, and nanofibre is far from becoming a commodity such as microfiber.

In most cases the ability to produce nanofibre is not enough. Nanofibre alone is not a product. It is a platform technology that requires adaptation and customisation to fit a wide variety of uses such as filtration, skin health, composites, acoustics in building materials and electronics, biotech and energy. The requirements of these sectors are vastly different, and this presents a challenge for nanofibre manufacturers. In response, some manufacturers including New Zealand's Revolution Fibres Ltd have developed Nanofibre Customisation Services designed to help nanofibre get out of the laboratory and into the marketplace. In this example, Revolution Fibres can accommodate nanofibre product development from idea generation through to large-scale manufacture.

13.2.1 Commercial-Scale Electrospinning

One of the biggest criticisms of electrospinning has been the pace of nanofibre production – widely seen as the most significant barrier to the adoption of nanofibres in commercial applications. Researchers and companies are taking innovative new approaches to adapt the traditional approach to electrospinning in order to address the issue of production scale, whilst still maintaining good quality non-woven textiles.

The general concept of electrospinning, in its simplest form, is the introduction of a polymer solution (usually in the form of a droplet) into a high voltage field – drawing a fibre from the droplet and collecting onto a surface.

Conventional, laboratory-based electrospinning using a charged capillary, such as a needle or pipette tip, is well established and well understood, yet remarkably difficult to perfect. However, with typical solution flow rates in the region of 3 milliliters per hour, this method is only capable of producing a small area of electrospun nanofibre and sample preparation can often require several hours of spinning to achieve the required deposition weight. In order to produce commercially relevant quantities of nanofibre, it is therefore necessary to scale-up the electrospinning process. There are two main categories by which this has been achieved: needle-based electrospinning and needleless electrospinning and the basic principles of each are discussed below.

13.2.1.1 Needle-Based Electrospinning

The scale-up of conventional capillary electrospinning was most simply achieved by increasing the number of spinning capillaries. Rather than spinning a single nanofibre from a single charged needle, solution is fed to several charged needles simultaneously so that each needle produces an individual spinning jet and nanofibre. Provided that the needles are spaced far enough away from each other to avoid detrimental interaction of their respective electrostatic fields, the

production rate can therefore be linearly scaled according to the number of spinning needles and there is theoretically no limit to the number of needles that can be combined. Many research groups have conducted research to determine the optimum packing density and pattern for the spinning needles, to achieve the maximum productivity for a given area. In the author's experience, the optimum distance between adjacent spinning needles is not a fixed parameter; instead it can change with different polymer solutions, most likely as a result of the differences in solution parameters such as conductivity or dielectric constant.

As with conventional laboratory-scale electrospinning, there are some potential problems that could seriously affect the ability to achieve a robust process capable of continuous nanofibre manufacture. The needle-based process relies on the continuous flow of polymer solution through the capillary needles. When the solution reaches the tip of the needle and a Taylor cone is formed, the solvent begins to evaporate. In the case of water-based solutions this evaporation is slow enough to allow for the stable and prolonged formation of nanofibre. However in order to electrospin a greater range of polymers, more volatile solvents are often required. In these cases, the solvent can evaporate quickly from the tip of the needle, causing the precipitation of polymer, which eventually blocks the capillary and prevents the continued jet formation and nanofibre production. In a laboratory setting, this is not a significant issue as the needle can easily be unblocked and spinning resumed. In commercial production, where there could be hundreds or thousands of capillaries, needles would not be able to be unblocked without stopping the entire production for cleaning, causing significant downtime and probably also impacting on deposition weight over time. Increasing the internal diameter of each capillary can reduce blockages, but this may then affect other electrospinning parameters, such as the required solution viscosity, which then impacts on the necessary electrospinning voltage and the resulting fibre diameter.

Nevertheless, some commercial electrospinners have kept the needle-based approach and are indeed perfecting it, such as BioInicia, whose FluidNatek® branded electrospinning machines offer users the ability to produce various types of nanofibre at laboratory, pilot or mass-production scales.

An advantage of the scaled-up needle-based electrospinning process is that the process is directly scalable from the laboratory method, which means that the wealth of published literature available, generated by researchers using needle-based laboratory apparatus, can be used to provide appropriate solution recipes, reducing the solution development time during the development of new commercial nanofibre products. It also allows for the simple scale-up of spinning technology enhancements that have been developed on laboratory apparatus, such as the use of co-axial capillaries to produce core-shell nanofibres, which have been successfully scaled-up by BioInicia and which open up new application areas compared with standard single component nanofibres, such as food, pharmaceutical or agrochemical encapsulation or materials for hydrogen storage.

13.2.1.2   Needleless Electrospinning

To address some of the difficulties with needle-based electrospinning, a new electrospinning technology was developed by the Technical University of Liberec and commercialised in 2004, by Elmarco under the brand name Nanospider.™ Elmaro's method of "free-surface" electrospinning does not require capillaries. Instead a rotating drum or wire electrode is partially submerged in a bath of polymer solution. As the electrode rotates, its surface is coated with a thin film of solution. When an electric field is applied, Taylor cones spontaneously form from the film and nanofibres are formed. The electrode continues to rotate so that spinning jets are continuously formed and stopped and the solution film is replenished.

Without the need for capillaries, there is no risk from blockages forming during production. However, due to the larger surface area of solution exposed in the free-surface electrospinning apparatus, both on the electrode surface and in the solution bath, evaporation of volatile solvents from solutions can still cause problems in prolonged production runs. As the solvent evaporates from the polymer solution, the concentration of polymer in the remaining solution increases over time, leading to progressively larger diameter and less uniform fibres. The drying solution on the electrode can also affect the spinning jets and, because the Taylor cones form naturally, rather than from defined spinneret tips, the number of spinning jets that form can also change over time leading to a reduced deposition weight.

Alternative methods of needle-less electrospinning, such as that developed by Revolution Fibres, address the disadvantages of both needle-based electrospinning and free-surface electrospinning, by eliminating the need for capillaries, whilst maintaining control over the number and location of Taylor cones that form on the spinnerets. Revolution Fibre have scaled-up their process from lab-scale to industrial-scale and are now able to achieve continuous production runs over several hours, and several hundred square meters of non-woven nanofibre mat without a reduction in deposition weight or a significant change in fibre diameter.

Other interesting examples of needle-less electrospinning include the regenerating bubble method, developed at Stellenbosch University, and polymer coated wires recently seen in Elmarco machines.

These techniques allow for water-based and solvent-based solutions to be processed controllably and reliably. One disadvantage of this method, compared with needle-based systems, are that due to the difference in solution handling and Taylor cone formation, the solutions developed in research laboratories and reported in published literature often require significant modification before the optimum solution and processing variables can be achieved. Thus, the majority of academic findings must be adapted to suit various needleless techniques, adding time and cost to the initial development of new nanofibre products.

Until recent advances by Arsenal Medical in 2012, the use of needle-less electrospinning techniques had been limited to single component nanofibres. Their high-throughput slit-surface electrospinning method is now capable of large

volume production of core-shell nanofibre without the use of capillaries, predominantly for wound care and medical devices.

In addition to purely electrostatic spinning methods, as discussed above, some nanofibre spinners have combined electrostatics with alternative means of spinning fibre, such as centrifugal force, in the case of rotary jet electrospinning, or air pressure, both of which encourage the polymer solution to form a jet and thereby reduce the requirement for such high electrospinning voltage. These methods are capable of great production rates, but can be more difficult to control fibre diameter and diameter distribution, typically resulting in non-woven mats consisting of fibres with a broad range of diameters from tens of nanometers to several micrometers.

13.3 Companies Involved in the Electrospinning Industry

At the latest count there are in excess of 100 companies selling electrospinning machines or electrospun nanofibre-based products, a majority of which service the laboratory research market with small-scale needle-based machines. Fewer companies have commercialised industrial-scale electrospinning, whether that is selling large machines, for example Elmarco (Czech Republic), Fuence (Japan), BioInicia (Spain), Inovenso (Turkey), amongst others, or manufacturing nanofibre-based products for commercial application, for example, DuPont, 3M, Donaldson, Hollingsworth & Vose, Arsenal Medical, and several more.

An increasing number of companies are starting to also offer bespoke nanofibre development or contract manufacturing services, with the hope of bridging the gap between a promising R&D outcome and a commercial product. Some of these emerging companies include E-Spin Technologies, SNS Nanofibre Technology, FineTex Technology, Revolution Fibres, Kertak Nanotechnology, BioInicia, Soft Materials, YFlow, Electrospunra and IME Technologies.

13.4 Alternative Industrial Nanofibre Manufacturing Technologies

Electrospinning has without a doubt become the most popular nanofibre production technique, most likely because of its relative simplicity and accessibility at laboratory scale. However, there are alternative methods for nanofibre manufacture, some of which show great potential for the mass production of nanofibre products for some applications in the future.

13.4.1   Islands-in-the-Sea or Segmented Pie Extrusion

Hills Inc. (USA) is a well-established industry leader in the field of polymer extrusion processes. They have developed a number of melt processing techniques for the production of submicron fibres. The "islands-in-the-sea" method involves the bi-component melt extrusion of polymer fibres within fibres, where one polymer is soluble in a selected solvent and a second polymer is insoluble. Using this method they are able to produce up to 1,200 fibres within a single filament. Once the bi-component filaments are formed, a subsequent solvent soaking step dissolves the soluble component leaving only the submicron diameter insoluble polymer fibres.

In a similar approach, Hills Inc. are also able to produce submicron fibres by extruding bi-component filaments (either with an islands-in-the-sea or segmented pie configuration) and then splitting them into their component fibres using pressurised gas or water jets to force the segments apart.

Both methods use conventional melt extrusion technology with special adaptations to the die in order to create the bi-component filaments. While these techniques are able to achieve good control over fibre diameter and large production scale, for thermoplastic polymers that cannot easily be electrospun, the high capital cost of the machinery is prohibitive for most companies involved in the development and commercialisation of new nanofibre-based technologies. As such, its uptake in the market has been somewhat limited.

13.4.2   Melt Blowing

The method for producing melt blown microfibre was developed in the 1950s and first used at commercial scale by Exxon in the 1970s. Since then it has become one of the "conventional" textile manufacturing technologies, used widely by many manufacturers including Vose, 3M, Kimberley-Clark, Cummings and Johns Manville. The process involves extruding a polymer melt through a die orifice and drawing the extrudate with high-pressure hot air. This method can achieve staggeringly fast production rates in the order 30,000 m per min for 3 μm diameter fibres.

By modifying the process to reduce the internal diameter and increase the number of orifices per die area (in the region of 100 holes per in.), submicron fibres can be produced. However, due to the smaller holes, the pressure required to extrude the polymer melt is much higher than for microfibers and the melt flow index must be much greater (i.e. lower melt viscosity). In addition, the relative flow rate of the hot air compared with the melt flow rate has to be increased significantly, making the process extremely energy intensive. The resulting fibres tend to have a relatively broad size distribution with fibres ranging from 500 nm to several microns. This limits the use of melt blown fibre to applications where controlled

fibre diameter and narrow size distribution are not required, such as textiles and absorbent materials.

As with the other melt extrusion methods discussed, the range of polymers that can be processed is limited and the high heat required to extrude the polymer means that it is not suitable for temperature sensitive polymers or functional additives.

13.4.2.1   Forcespinning and Rotary Jet Spinning

Two very closely related recent developments for nanofibre production that are gaining significant attention are Forcespinning, developed at the University of Texas Pan American and since commercialised by FibeRio Technology Corporation, and Rotary Jet Spinning, developed at the Harvard School of Engineering and Applied Sciences. Both methods employ the same principles; using centrifugal forces to drive a polymer melt or solution through orifices in a rotating spinneret, in a similar way to the machines used for spinning sugar syrup to make candy floss.

One of the marketed advantages of Forcespinning over electrospinning is the ability to spin polymer melts or polymer solutions with much lower concentrations of solvent, reducing the cost and environmental issues associated with solvent waste in conventional electrospinning. It also enables the production of nanofibres from many thermoplastic polymers e.g. PP, PE, PET, PTFE, that cannot be electrospun due to being insoluble or having low dielectric constant.

While melt electrospinning is possible, and is becoming more widely available to researchers thanks to the recent commercialisation of a laboratory scale melt electrospinning machine by Spraybase (Ireland), the resulting fibre diameters tend not to be in the submicron range.

As such, the centrifugal spinning techniques seem to be an attractive approach that is sure to find application in the production of many nanofibre materials. Having said that, it remains a relatively new technique only currently commercialised by FibeRio, so is yet to be thoroughly examined by the market.

13.5   Challenges Faced by Commercial Electrospinning Companies

With a large number of nanofibre applications successfully demonstrated in published literature and a growing number of companies now with the capability to manufacture commercial volumes of electrospun nanofibre, the availability of commercial electrospun nanofibre and nanofibre-based products is improving. However there are several challenges that commercial electrospinning companies face in developing and manufacturing nanofibre-based products for industrial applications, and which are therefore preventing greater uptake of electrospun material. Some of these challenges have been identified by the authors and are discussed below.

13.5.1 *Building a New Market for Nanofibre*

While nanofibres are not a new concept and are well established in some areas, such as the filtration industry, there is not really an existing market for nanofibre. In fact, most of the innovative nanofibre-based developments in academia have been made without the involvement of an industrial partner providing the "market-pull", or need. Despite the promise, in many cases the commercial viability of these developments is yet to be seen. . . or hard to imagine!

Although the innovation and market growth signs are very encouraging, it is still not clear what products or services the nanofibre market entails. The current state of the market sees early adopters of the technology, bar the filtration industry, primarily selling electrospinning machines, rather than nanofibre products. This then puts the onus on end users to become producers, or researchers to become manufacturers.

A novel nanofibre-based technology can be scaled-up by a commercial electrospinning company, but without an engaged industrial client requesting the technology the developers are relying on finding a suitable customer, and bearing the cost of commercialisation and sales, in markets not suited to their skill-set. Furthermore, end users are not readily willing to invest in the as-yet commercially unproven technology without having had any previous involvement in its design or development.

While few end-users of nanofibre are technically capable or willing to make the commercial leap to becoming nanofibre producers, some examples (outside of air filters) are emerging. These are in areas where the uses have reached scale rapidly, and end-users are adopting electrospinning in their production lines or in their vertically integrated supply chains. The best example of this is in batteries where Samsung and DuPont are manufacturing nanofibre separator membranes.

The more preferred method for the commercialisation of a new electrospun product is therefore one of collaborative development from an early stage. Early engagement between a nanofibre manufacturer and an industrial client who has a real need for nanofibres (whether for performance enhancement in their product or market differentiation) is critical. By involving the end customer from an early stage, the nanofibre can be tailored to the clients' specific requirements, which increases the chances of it providing significant benefits to their product or business. Furthermore developing the product with a manufacturer rather than a research institute can identify the commercial problems earlier, and lead to earlier prototyping and pilot scale production.

Due to the need for significant customisation of nanofibre for many industrial customers, the optimisation of the process required to develop and manufacture a new nanofibre-based product can be time-consuming and expensive. Unless the industrial client is engaged from the start and willing to fund the development, this can be impossible for a small electrospinning company to proceed with, even if

there is great potential for the resulting product. In many cases, an industrial partner may require proof-of-concept along with thorough testing of prototypes before they are willing to engage in a development project with an electrospinning company, again because it is unlikely that there would be existing nanofibre-based products in the market for comparison.

To raise the profile of nanofibres outside of academic circles, and thus more investment into the technology, requires a unified voice from researchers and commercial manufacturers alike. Promising developments include the Nafigate portal, a platform that connects nanofibre experts from around the world and enables the formation of new projects and clusters to focus on the development of modern applications of nanofibre and build a global nanofibre community.

Research activities and direction is also fragmented, with far too much duplication across the world. Researchers too can contribute to a coordinated effort to bring nanofibres closer to commercial reality, by engaging manufacturers and contributing to a pool of research where each party has specific, complementary R&D objectives towards a larger commercial goal. An encouraging development is the European funded COST Action MP1206 network, which forms an interdisciplinary knowledge platform of representatives from around the world, from academia and industry, to generate progress in the state of the art by working in a unified and collaborative manner.

The opportunities for funding available through the Horizon2020 framework are also likely to play an important role in the building of a nanofibre market throughout the next decade, both by reducing the funding gap that exists in the development and commercialisation of new nanofibre products, and also by again encouraging collaborative development between academics, nanofibre manufacturers and end-users or "route-to-market" companies, who are often missing from new development projects.

13.5.2 Production Rates and Solvents

Despite the recent advancements in mass-production of nanofibre by electrospinning it has still come under criticism for its relatively low production rate in comparison with traditional textile manufacturing techniques.

Nanofibres, in particular those made through electrospinning, will always struggle to compete on price and production rate, but should it need to? This perhaps is a misconception that only considers production rate, and not the additional benefits that nanofibres offer. Nanofibres will be able to command higher margins when the technology development is focused on areas where they offer distinct advantages – such as high surface area, ultra-thin membranes, specific porosity, and added functionality.

We are seeing fascinating properties that can be achieved by incorporating only very little nanofibre, and it acts as a great enhancement to existing fibres (micro-fiber, textiles) in many cases.

Some applications require a very definite fibre diameter and density (e.g. filters and composite reinforcement) and so suit electrospinning, while some require mass production to keep cost down (e.g. absorbent pads) but don't have a major need for precision. In this case there are faster methods (gas assisted, force spinning, etc.). The key is in finding those applications where the advantages of using electrospun nanofibre are able to command a premium.

13.5.3   Managing a Platform Technology

Nanofibre is not a product in itself, but rather a platform technology that can enhance another product. The vast range of potential applications for electrospun nanofibre is fantastic, but also makes it difficult to thoroughly explore the opportunities.

Each application requires a different investigation with different types of nanofibre, different degrees of integration with other materials and different types of expertise in testing and characterisation. Despite referencing the promise of academic discoveries in papers and journals, the commercial viability is rarely discussed. Factors such as cost versus benefit, competition of alternative technologies, supply chain, IP and regulatory considerations also need thorough investigation to assess the commercial viability of using electrospun nanofibre versus other techniques. In some cases, the cost and expertise required for nanofibre producers to do the necessary business case and R&D to show the benefits of nanofibre versus competing technologies is too high, and can stifle innovation.

The vast number of uses for nanofibre can make for a fragmented industry, and this is a challenge for nanofibre manufacturers. Quite often nanofibre manufacturers must stick to specific industries and channel their expertise into particular sectors, such as The Electrospinning Company (UK) who is devoting its attention to the biomedical sector (scaffolds, etc.).

13.5.4   Engaging with Manufacturers Too Late in Development

Another issue faced by commercial nanofibre manufacturers is that other companies or academic groups will often conduct research and development on a new nanofibre-based technology, using laboratory apparatus, to a point where they have proven the concept and are ready to scale up, only then engaging with a manufacturer. Due to the differences in spinning technology between laboratory-scale and

commercial scale electrospinning apparatus, there is often a significant amount of additional development required to scale up the technology, sometimes requiring changing materials completely. This introduces additional costs and delays, which could be avoided by including a commercial manufacturer in discussions and development activities much earlier in the project, before the process is optimised.

Another similar trend is for researchers to "spin out" their nanofibre research into new commercial ventures. While this is exactly what the technology requires, quite often the spinout company decides to become a manufacturer and has to then devote huge resources, new infrastructure and different skill-sets to produce their invention. In some cases it could be faster and cheaper to sub-contract the manufacture of their nanofibre invention in order to devote their time and resources on the (not-insignificant) cost of commercialisation. This will reduce start up costs, allow for prototyping and pilot-scale production for samples, and bring new expertise into the venture.

13.5.5 Papers, Patents and PhD's

The growth in the number of publications relating to electrospinning and nanofibre each year since 2000 has been remarkable, as highlighted by Fig. 13.1, showing the trend for electrospinning related journal articles, and Fig. 13.2, showing the trend for nanofibre related patents. In 2013 alone more than 2,300 journal articles were published on electrospinning and more than 760 patents were published relating to nanofibre, suggesting that a lot of innovative research and development is being
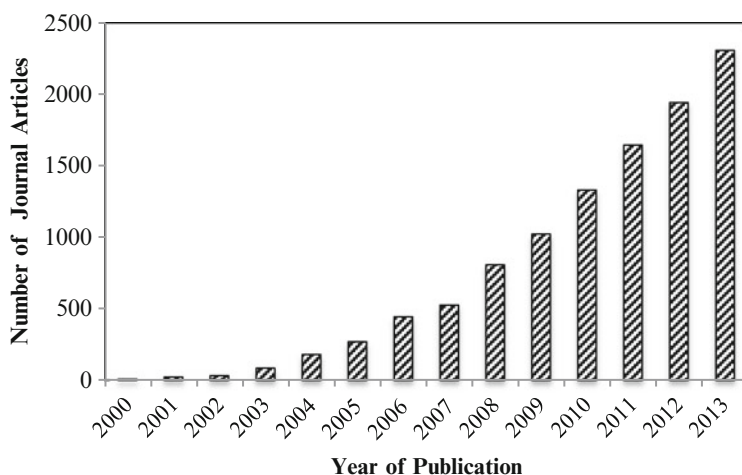
Fig. 13.1 Chart showing the number of electrospinning related journal articles published between 2000 and 2013 (Data generated from Thomson Reuters' Web of Science on 30th August 2014. Keywords: electrospinning OR electrospun OR "electrostatic spinning")
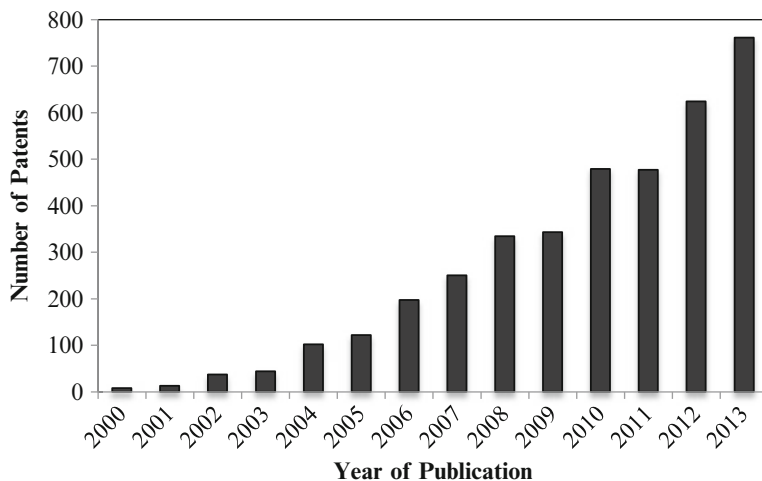
Fig. 13.2 Chart showing the number of nanofiber related patents published between 2000 and 2013 (Data generated from the European Patent Office Espacenet Patent Search database on 30th August 2014. Keywords: nanofiber OR nanofibre OR nanofibrous OR "submicron fiber" OR "submicron fibre")

carried out to develop nanofibres that address industrial challenges and to broaden their potential application. Clearly this is a technology push market, with the rate of innovation (or invention) far surpassing the rate of commercialisation.

While the large number of publications provides endless inspiration for the emerging nanofibre developers and manufacturers, they also represent a significant problem for the nanofibre market, and consequently investment in the sector. Disclosure of commercially valuable intellectual property (IP) creates hurdles for end users because they will commonly have to navigate tricky licensing and royalty arrangements with inventors (typically universities) who often have no use for the IP themselves once the research is over. Similarly, many patents are filed by academic institutions or large multinational corporations who have no obvious plans or routes for commercialisation. For many smaller companies unwilling to accept the enormous legal risks or hurdles, this restricts the commercialisation potential in many application areas and therefore slows industry growth.

13.5.6 Lack of Control Over Raw Materials Supply and Consistency

Even when manufacturing nanofibre at commercial-scale, the use of raw materials can be relatively small, in the region of kilograms of polymer, rather than tonnes. As such, there are some materials that prove difficult to secure reliable sources. Where an existing industry dominates the use of a particular material, such as

carbon fibre manufacture with polyacrylonitrile (PAN) or cigarette filter manufacture with cellulose acetate (CA), the suppliers of these raw materials are unwilling to supply in the relatively small batches required for electrospinning. When materials are available, it is often difficult to secure a consistent supply, especially when it comes to naturally derived polymers such as cellulose acetate, where batch variation can have a significant impact on the spinnability of the polymer. As such, some very common materials that are easy to source in a few gram quantities for academic work, and which might have been shown to provide the ideal properties for a particular application, can prove to be extremely difficult to manufacture in a commercially viable manner.

In some cases, useful polymers have been treated or synthesized to be resistant to most solvents – a key determinant of a polymer being able to be electrospun. As it is rare for polymers to be synthesized specifically for electrospinning, commercial nanofibre manufacturers are quite often at the mercy of the demands of the other users of the polymer. The emergence of melt-electrospinning and other techniques such as "Force-spinning", and the pioneering work of Seema Agarwal and Andreas Greiner in the electrospinning of suspensions and emulsions, are therefore an exciting prospect.

13.5.7 Nano-fear and the Absence of Regulation

In 2012, researchers at the University of Edinburgh reported that nanofibres shorter than 5 nm did not cause harm to living cells, whereas longer fibres could result in pulmonary inflammation and disease, similar to that caused by inhalation of asbestos. This journal article resulted in widespread news stories, including in main-stream media such as the BBC, reporting the danger of nanofibre, when in fact the researchers were investigating nickel and silver nanofibres and carbon nanotubes, all of which should be considered short fibre.

Electrospun polymeric nanofibre, having a continuous length and being deposited in the form of a non-woven mat has never been found to cause any adverse affect on living cells, beyond that of the standard inflammatory foreign-body reaction. Further more, electrospun nanofibre is used as a biomimetic scaffold material for the growth of cells for use in tissue engineering and tissue repair. While the industry spoke out against the findings (through nanofibre web-portal Nafigate) the damage was done.

One of the causes of this confusion is the lack of any internationally agreed terminology for nanotechnology, which leaves terms such as nanofibre, nanorod and nanoparticle open to interpretation. Despite definitions having been proposed by the International Organisation for Standardisation (ISO) and taken up by the European Agency for Safety and Health at Work, they are insufficient to be able to separate potentially hazardous short nanofibre from more inert long fibre. A nanofibre is simply defined as a "flexible nanorod" and a nanorod as a nano-

object with two similar external dimensions in the nano scale (<100 nm) and a third dimension significantly longer than the other two.

To make matters worse, the current risk assessment methodologies are not suited to the hazards associated with nanomaterials. In particular, existing toxicological and eco-toxicological methods are not relevant; exposure evaluation (dose) needs to be expressed as quantity of nanomaterial and/or surface area rather than simply mass. In addition, the equipment used for routine detection and measurement of nanomaterials in air, water, and soil is often inadequate. Regulatory bodies in the US the EU have concluded that nanoparticles form the potential for an entirely new risk and that it is necessary to carry out an extensive analysis of the risk. The challenge for regulators is whether a matrix can be developed which would identify the different types of nanomaterial that are likely to have special toxicological properties or whether it is more reasonable for each new material to be tested separately.

A truly precautionary approach to regulation could severely impede development in the field of nanotechnology if safety studies are required for each and every nano-science application. While the outcome of these studies can form the basis for government and international regulations, a more reasonable approach might be development of a risk matrix that identifies the highest risk materials.

As a result of this uncertainty around the safety of nanomaterials, some potential users of electrospun fibre may be scared off, and the international transportation and sale of nanofibre could be jeopardized by over-cautious regulation. In reality, electrospun nanofibre poses a significantly smaller risk than other nanomaterials and once formed into a non-woven mat should perhaps be treated the same way as the bulk chemicals from which they are made, or as nonwovens.

13.6 Commercially Available Electrospun Products

The main markets for polymer nanofibres are air and water filtration, medical devices, composites, batteries and textiles. Polymeric nanofibres account for the main bulk of the current revenues for nanofibres, finding applications across a number of sectors. Although there are also many applications in which inorganic nanofibres have been shown to be of value for example in high temperature filtration applications. Carbon nanofibres are also beginning to find application across a raft of industries including electronics (heat management, EMI shielding, conductors), composites (polymers, resins, glass, ceramics, plastics), energy (batteries, catalysts and fuel cells) and medicine and life sciences (drug delivery, tissue engineering, implants). Carbon nanofibres represent the fastest growing market for nanofibres, especially in Li-Ion battery applications. Cellulose nanofibres are also beginning to make an impact in composites and electronics applications.

Leading players in the market include Ahlstrom, DuPont, Donaldson, Hollingsworth & Vose, Johns Manville, Kuraray, Mitsubishi Rayon, Teijin and Toray, but innovative up and coming companies involved in both the production

and application of nanofibres are emerging. Notable examples include Elmarco, FibeRio Technology Corporation, Finetex EnE, BioInicia and Revolution Fibres Ltd.

Revolution Fibres, in particular, has developed and commercialised a number of electrospun nanofibre products and platform technologies, both with and without industrial clients involved, some of which are discussed below together with other notable nanofibre-based products and technologies currently being commercialised.

13.6.1   Nanofibres in Filtration Applications

Nanofiber air filters have been on the market for a number of years. Main producers include Donaldson's Ultraweb®, Exceed, eSpin Technologies and Hollingsworth & Voses' Nanoweb® filter media. Nanofiber based air filtration technology are most effective at stopping particles smaller than 3 μm with minimal impact on pressure drop. They can adsorb volatile organic compounds (VOCs), microorganisms, allergens, and other pollutants (e.g., tobacco smoke) With the continual rise in air pollution and the IARC's recent classification of air particulates below 2.5 micron as "probable carcinogens", the demand for high efficiency filtration for buildings and personal use shows no signs of abating.

The next phase of growth is in functional, "intelligent" filters that selectively capture pollutants of concern (VOC's, microbes and viruses, heavy metals, etc.) using active ingredients. Examples of functional additives include nanoparticles (silver, platinum), metal-organic frameworks and bioactives. An example of this is Seta™ air filtration, developed for a New Zealand-based home ventilation company, which is a range of air filtration products that incorporate a fine web of electrospun nanofibre loaded with antimicrobial manuka extract.

An emerging area for nanofibre is in liquid filtration, where nanofibre membranes can be used to replace existing porous microfiltration membranes with great benefits in terms of reduced pressure drop and therefore reduced energy consumption. Perhaps one of the most important applications is in the production of drinking water from non-potable sources, such as standing water or seawater. This industry seems to be dominated by large established companies with a background in filtration materials and systems. As such, there are several commercialised nanofibre products in the market already e.g. Nitto Denko, who produce nano-membranes for water desalination, Hollingsworth & Vose, who manufacture NanoWeb for liquid filtration using a proprietary nanofibre coating process, DuPont with their Hybrid Membrane Technology, and Veolia Water, a world-leading in waste-water management. Other specialist electrospinning companies, such as eSpin and FineTex EnE also have liquid filtration offerings.

13.6.2 *Nanofibres in Composite Applications*

The composites industry, particularly carbon fibre, continues to experience rapid growth internationally as industries strive for stronger, lighter, and more energy efficient materials. The use of composites is seeing exponential growth in recent years in aerospace, automotive, and wind turbine sectors, in addition to continued growth in applications that were early adopters of composite materials, such as marine and watersports hardware and other sporting goods.

The benefits of fibre reinforced polymer composites are well known and their use has become commonplace in high-tech applications requiring low weight as well as high strength, high stiffness and corrosion resistance. Despite these attributes, fibre reinforced composites generally suffer from poor impact resistance, poor fracture toughness and poor delamination strength. This is particularly the case when brittle thermosetting matrix resins are used.

Currently, these problems are addressed by altering the chemical formulation of the resin to improve toughness, by adding toughening particles to the resin or by inserting microfiber interleaves into the interlayers between the plies of the laminate.

Much work has been done over the last decade to improve the formulations of resin systems to improve toughness, but in many cases, this does not fully address the problems of poor composite impact resistance, fracture toughness and delamination. Toughening particles are difficult to disperse evenly in the resin, resulting in regions with high and low concentrations of toughening particles, which can reduce the performance of the composite. Furthermore, toughening particles are also free to flow with the resin during the curing process resulting in further uneven particle distribution.

Microfibre interleaves used in a laminate can improve impact resistance but often have detrimental effects on other composite mechanical properties. Furthermore, the addition of bulky microfiber veils can cause undesirable increases in weight and thickness of the laminate.

Lightweight veils made from nano-sized thermoplastic fibres can be used as an alternative to currently used composite toughening methods. Electrospun thermoplastic nanofibre interleaving veils have been shown to improve the compression after impact (CAI), delamination resistance and the Mode I and Mode II interlaminar fracture toughness of composites. Nanofibre veils have also been shown to improve the fatigue resistance and vibration-damping properties of fibre reinforced composite materials. It is also possible to make electrically conductive nanofibre veils for composite applications such as aircraft structures and wind turbines where improvements in the through thickness electrical conductivity and lightening damage reduction are required.

The first commercial electrospun nanofibre product aimed at composites reinforcement Xantu.Layr™ interlamina composite reinforcement is an electrospun nanofibrous veil that can be easily incorporated between the carbon fibre layers of a composite structure. During curing, the resin infiltrates through the nanofibre veil

and the result is a composite with increased impact damage resistance and fracture toughness without additional weight. The first products to make use of Xantu. Layr™ are a range of high performance fishing rods made by Kilwell and Synit, exported from New Zealand. In their testing of the rods, the presence of Xantu. Layr™ increased the breaking load of the rods by 100 %.

13.6.3 Nanofibres in Acoustic Applications

Sound is the basis of all human communication. The voices we hear, the music we listen to, the ambient vibrations that tell us about our environment. Creating sound is something that comes naturally to us. Controlling sound is another story.

Sound control is a growing concern in many industries around the globe. Ambient sound can be both distracting and discomforting at excessive levels. Conventional methods of sound control including foams and fabrics have been used to date to absorb, reflect and diffuse sound to a certain degree. However, as our electronic devices, buildings and transportation get slimmer and lighter our needs for hearing protection from environmental/industrial noise, or improved acoustic performance, increase The challenge for traditional acoustic layers such as foams and batts of various fibres, is to increase performance whilst becoming smaller, lighter and less dense.

Phonix™ acoustic products, developed by Revolution Fibres Ltd, have been found to increase the sound absorbency of existing acoustic materials such as foams and non-wovens. Using the nanofibrous Phonix™ material, the furniture manufacturer Finewood has developed the Return Focus Pod, a sound absorbing office cubicle for reducing noise in open-plan offices. In addition, Phonix™ nanofibre technology has been shown to reduce the unwanted high frequency noise in sound recording and playback.

13.6.4 Nanofibre for Medical and Skincare Applications

Nanofibres are uniquely suited to many medical applications due to their structure, which closely mimics that of the extracellular matrix of many of the tissues in our body. When used within the body, for regenerative medicine for example, the high porosity and pore interconnectivity allow nutrient and waste transport and cell communication, although cell penetration into a nanofibrous scaffold for three dimensional tissue growth is not usually possible without additional spacing materials to increase pore size. Using electrospinning allows for a wide variety of natural or synthetic polymers, including many FDA-approved materials, to be spun as well as for functional additives, such as antimicrobials or growth factors, to be incorporated.

Tissue engineering remains in its infancy, but there can be no doubt that this is a fast growing market and it will require suitable scaffold materials as it develops. Some companies have already commercialised nanofibre based scaffold materials, such as Xylos Corporation, who produce biomaterial solutions for the treatment, repair and replacement of human tissue based on biocellulose, not electrospun but instead synthesized naturally by a micro-organism (*Acetobacter xylinium*). These nanofibres are approximately 200 times finer than cellulose derived from cotton and are highly absorbent. Teijin is also using nanofibres, for bone and cartilage regeneration, and are planning preclinical trials in 2014.

Another medical field well suited to the use of nanofibre is wound care. There are a number of companies producing nanofibre based wound dressings to exploit the advantages of nanofibres, which include inducing haemostasis, due to the high surface area exposed to the blood, high liquid absorption, good barrier properties to reduce the risk of microbial colonisation, excellent moisture vapour permeability and the option of bioresobability. Companies include Xylos Corporation, HemCon Med. Tech, Inc., Covidien and Smith and Nephew.

Revolution Fibres, too, has developed nanofibre dressings, not currently targeted towards medical applications, but for cosmetics and natural health. actiVLayr™ skin delivery platform is a water soluble marine collagen fibre patch that can be loaded with a wide range of plant and fruit extracts that are clinically proven to improve skin elasticity, moisture retention and reduce the appearance of wrinkles and sun spots. actiVLayr® Anti-aging patches and Skin Repair dressings are examples of the myriad of potential products using nanofibres as the delivery platform. By adjusting the extract types (grapes, kiwi, blackcurrant, seaweed, etc.), actiVLayr® can target various skin appearances/benefits. A broad range of products is conceivable and achievable, including:

- Skin moisture and elasticity face masks
- Skin brightening patches (under-eye or full face)
- Anti-inflammatory patches
- Natural health – delivery onto skin of plant extracts, essential oils, and enzymes
- Acne treatment
- Nappy liners that reduce irritation
- Burn treatment with antimicrobial extracts or additives
- Multi-layered wound dressings with different functional additives to aid the various stages of healing
- Drug delivery

Drug delivery is another emerging area of medical application. The controlled release of a drug into the body over time requires careful design of the implanted material and the dispersion of the drug within the material. Encapsulating drugs within nanofibres, in particular within core-shell nanofibres, allows for uniform distribution of drug throughout the implant and also enables a targetted release profile by controlling the degradation of the core and shell components of the fibres. BioInicia has developed the capability to mass produce core-shell nanofibre, under GMP conditions, by coaxial electrospinning so are in a strong position to be able to service this application area.

13.6.5 Nanofibres for Sensing Applications

Sensing is another area where electrospun nanofibre technologies show great promise, as is highlighted throughout the other chapters of this book. Their high surface area and porosity allow for exceptional interaction with their environment (liquid or gas), which means that, with the appropriate functionalisation, they are able to react with their target substance with great sensitivity. This natural fit between the inherent high surface area of electrospun nanofibre and the requirements for a sensing material, along with ability to produce nanofibres from a wide range of materials and incorporate a variety of functional additives means that they can be applied in a multitude of sensing devices. Therefore the commercialisation potential is significant, provided the nanofibres can be integrated into the devices in a cost effective manner.

Collaboration between the ERDF-funded project, iSMART, based at Nottingham Trent University and Nano Products Ltd (UK) has lead to some interesting developments in the commercialisation of nanofibre sensing devices. Using an existing offset lithographic printing facility, modified to print conductive inks onto plastic sheet, Nano Products are able to mass-produce flexible electronic circuits. By overlaying a web of functional electrospun nanofibres, they are able to very cost-effectively create electrochemical devices at commercial scale. It is easy to see how this type of combination of technologies could be an effective commercialisation route for low cost sensing devices, e.g. for disposable medical diagnostics.

Cutting edge work by Professor Il-Do Kim at the Korea Advanced institute of Science and Technology has demonstrated the mass-market potential for nanofibre-based sensing. Using platinum-loaded SnO_2 nanofibres, which are sensitive to acetone and toluene, he created an exhaled-breath sensor that can detect raised levels of acetone or other biomarkers in the breath, to detect diabetes, lung cancer and potentially a range of other diseases. The especially exciting development is that they have not stopped at testing the nanofibre material on its own, but have integrated it into a USB-enabled electronic device to allow it to be connected to a smart phone. It is this extra step that helps end users imagine the mass-market potential and makes future commercialisation more likely.

For many sensing applications, including biomedical diagnostics in particular, functionalisation of the sensing material's surface is required to impart the desired reactivity between it and the target substance. Ideally, this functionalisation step should be quick, inexpensive and be usable on a variety of substrate chemistries. In a promising R&D collaboration, KODE Biotech Ltd (New Zealand) has partnered with Revolution Fibres to explore the benefits of combining their unique biofunctionalisation technique with mass-produced electrospun nanofibre.

KODE Biotech has developed and commercialised a patented technology platform that enables the rapid incorporation of biofunctional molecules onto biological and synthetic surfaces, by simple contact. KODE™ Function-Spacer-Lipid (FSL) constructs are readily dispersible in water or solvents to facilitate easy application

onto a variety of different surfaces by standard coating methods, including inkjet printing, and by adding to nanofibre textiles, either pre or post manufacture, Koded Nano-Textiles are created. With the attachment of a wide array of functional groups made possible, this presents a potential revolution in medically functional fibres, with almost limitless potential, including:

- anti-microbial medical textiles
- protein or growth-factor functionalised tissue engineering scaffolds or wound care products
- delivery of therapeutic agents e.g. anti-cancer
- blood group and other diagnostic assays
- controlled delivery of pharmaceuticals and therapeutic agents e.g. anti-cancer
- immobilisation of cells-on-a-chip

Importantly, initial trials of Koded Nano-Textiles in various immunological biosensing assays showed that nanofibres have outstanding specificity and sensitivity compared with previously modified materials such as papers. This demonstrates the potential to revolutionise diagnostic (and environmental testing) kits worldwide – making them simple to use, simple to manufacture and easy to interpret with clear words and graphics (through inkjet or other printing methods), as shown in Fig. 13.3, on a high definition substrate – reducing the risk of misdiagnosis and misinterpretation. Additionally it shows that a post manufacture technique of simple spraying of the KODE™ constructs onto nanofibres will

Fig. 13.3 Photograph showing three samples of Koded Nano-Textile, inkjet printed with KODE™ Function-Spacer-Lipid biotin (FSL-biotin) and subsequently reacted in an immunological assay to stain for the presence of FSL

immediately cause them to become stably biofunctionalised. This technique is simple, commercially ready and accessible to virtually any medical device including diagnostics.

13.7   Summary and Future Outlook

Over the last 15 years electrospinning has received a great deal of attention from researchers and as a result, our understanding of the process and the potential applications of the resulting nanofibre has developed dramatically. Now the technology is mature, it is increasingly progressing beyond the laboratory and into the industrial setting, as start-ups and large multinationals are recognising the commercial potential of electrospun products. Despite this, the number of nanofibre products that have made it to market is rather disappointing. This has been partly due to the lack of commercially viable manufacturing capabilities. As a result, there has been a recent surge in companies developing and commercialising electrospinning machines for both laboratory scale and mass-production of nanofibre.

Some of the challenges that are faced by electrospinning companies in commercialising nanofibre products include the difficulty in exploring the vast array of potential applications without significant funding, the perceived danger of working with nanofibres, which is exacerbated by the lack of clearly defined terms, the lack of control over material supply as a result of the relatively small volume requirements for electrospinning compared with other industries, the creation of legal hurdles by large companies and universities eager to patent innovations without clear intentions for commercialisation, and the lack of involvement of manufacturers in nanofibre development projects until the final stages of laboratory-scale optimisation. Any or all of these challenges will have slowed the commercialisation of products in this predominantly "technology push" emerging industry.

Despite these challenges, the nanofibre industry is growing rapidly and products are now reaching the market in areas that include filtration, composites, electronics and energy generation, acoustics and medical. As the industry grows, and more end users are made aware of the potential of electrospun nanofibre, more of the applications that have been proven at laboratory scale will be adopted and the market will recognise the need for nanofibre.

Some particular areas where the application of nanofibre is likely to see growth in the next few years are: smart filters that are able to remove specific hazardous substances from the air– addressing the problems of pollution in densely populated cities; biomedical devices – as the years of clinical research are coming to fruition; functional composites – as the use light weight materials grow in the aerospace and automotive sectors; energy storage – to address the ever increasing global energy demands and growth of renewable energy generation; acoustics – as modern living requirements demand higher performance noise management with thinner and

lighter materials; and sensing – to satisfy our ever growing demands to monitor our health and environment.

It is our hope that more industries will work with nanofibre manufacturers to progress ideas further beyond where the research ends and to realise the potential that nanofibre has, so that we see an emergence of new and innovative nanofibre products in the future.